Technical University of Munich
TUM School of Natural Sciences

Scintillator-Based Particle Detectors for Radiation Measurements on the International Space Station and for the Exploration of the Moon

Martin J. Losekamm

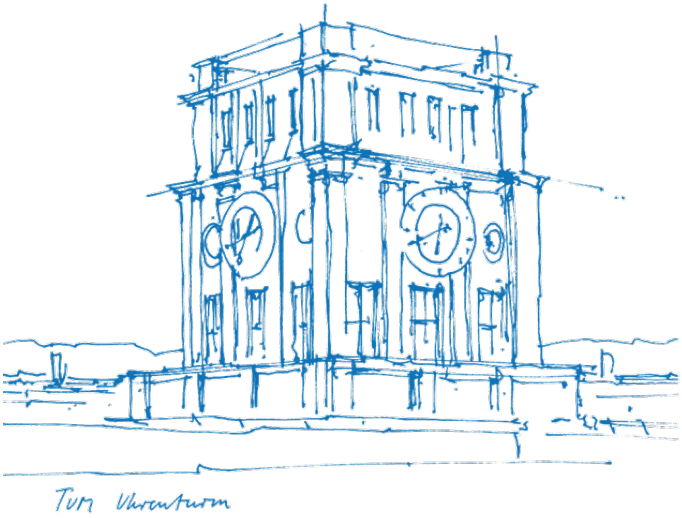

Technical University of Munich
TUM School of Natural Sciences

Scintillator-Based Particle Detectors for Radiation Measurements on the International Space Station and for the Exploration of the Moon

Martin Jan Losekamm

Complete reprint of the dissertation approved by the TUM School of Natural Sciences of the Technical University of Munich for the award of the

Doktor der Naturwissenschaften (Dr. rer. nat.).

Chair: apl. Prof. Dr. Norbert Kaiser

Examiners:

1. Prof. Dr. Stephan Paul
2. Prof. Dr. Ulrich Walter

The dissertation was submitted to the Technical University of Munich on 22.08.2024 and accepted by the TUM School of Natural Sciences on 17.09.2024.

Bob, this is Gene, and I'm on the surface; and, as I take man's last step from the surface, back home for some time to come—but we believe not too long into the future—I'd like to just (say) what I believe history will record. That America's challenge of today has forged man's destiny of tomorrow. And, as we leave the Moon at Taurus-Littrow, we leave as we came and, God willing, as we shall return, with peace and hope for all mankind.

Eugene A. Cernan, Commander of Apollo 17, 1972.

Abstract

Cosmic and solar radiation allow us to investigate myriad phenomena in astrophysics and heliophysics, serving as a remote probe for processes that we cannot study *in situ*. Secondary radiation created in their interaction with matter allows us to investigate the surface composition of the Moon and other airless bodies. Mitigating the exposure of spacecraft and crew to high-energy radiation is, however, one of the greatest challenges to crewed and robotic exploration of the solar system.

In this thesis, I present my work developing two instruments for studying cosmic and solar particles and the secondary radiation created by them. The RadMap Telescope is a compact radiation monitor for characterizing the environment inside the International Space Station. At its heart is a tracking calorimeter that can resolve the charge and energy of cosmic-ray nuclei with omnidirectional acceptance, allowing detailed studies of the radiation field's temporal and spatial variations. I also analyze data gathered during a nine-month operational period on the space station. The Lunar Cosmic-Ray and Neutron Spectrometer is a versatile instrument designed for deployment on mobile and stationary surface assets. It can detect areas of increased hydrogen abundance via neutron spectroscopy, which we use to search for water-ice deposits in the Moon's polar regions. I also present a reference mission to the Shoemaker-Faustini ridge at the lunar south pole.

Both instruments have active elements made from organic and inorganic scintillators that generate light in response to charged particles and neutrons, which is detected by silicon photomultipliers. I present measurements of relevant scintillator properties, including the characterization of ionization quenching and the influence of coating on the light yield of scintillating fibers. I also describe the advantages and challenges of adapting Bragg curve spectroscopy for event-wise particle identification.

Contents

Abbreviations and Acronyms

ABS acrylonitrile butadiene styrene
AC alternating current
ADC analog-to-digital converter
ADSH Airbus DS Space Systems, Inc.
ADU Active Detection Unit
AFIS Antiproton Flux in Space
ALTEA Anomalous Long Term Effects in Astronauts
AMS-02 Alpha Magnetic Spectrometer
APD avalanche photodiode
ARS acute radiation syndrom
ASIC application-specific integrated circuit

BGA ball grid array
BNL Brookhaven National Laboratory
BVC bias voltage converter

CAD Crew Active Dosimeter
CALET CALorimetric Electron Telescope
CAN Controller Area Network
CC current comparator
CCD charged-coupled device
CCP Central Command Processor
CCSDS Consultative Committee for Space Data Systems
CDAS common data acquisition system
CDP Communications Data Processor
CERN European Organization for Nuclear Research
CI current integrator
CKT convergent kinetic theory
CLPS Commercial Lunar Payload Services
CME coronal mass ejectionn
CMIS current-mode input stage
CNC computer numerical control
CNES Centre National d'Études Spatiales

CNS compact neutron spectrometer
CNSA China National Space Administration
CPD Crew Passive Dosimeter
CPD Charged Particle Detector
CPDS Charged Particle Directional Spectrometer
CPT charged-particle telescope
CRAND cosmic-ray albedo neutron decay
CRaTER Cosmic Ray Telescope for the Effects of Radiation
CSDA continuous slowing-down approximation

DAC digital-to-analog converter
DAMPE Dark Matter Particle Explorer
DAN Dynamic Albedo of Neutrons
DC direct current
DCR dark count rate
DDR4 SDRAM Double Data Rate 4 Synchronous Dynamic Random-Access Memory
DEM digital elevation model
DLR German Aerospace Center
DNS Domain Name System
DOSTEL DOSimetry TELescope
DraGNS Dragonfly Gamma-ray and Neutron Spectrometer

EAD ESA Active Dosimeter
EAD Ethernet Ancillary Data
EC European Commission
eFDP enhanced Functionally Distributed Processor
EFT-1 Exploration Test Flight-1
EMI electromagnetic interference
eMMC embedded MultiMediaCard
ENF excess noise factor
ePVT external Private (LAN)
ESA European Space Agency

FIFO first in, first out
FND Fast Neutron Detector
FPGA field-programmable gate array
FRET Förster resonance energy transfer
FRM II Forschungsreaktor München II
FWHM full width at half maximum

GCR galactic cosmic rays
GCU gain calibration unit
GPD general-purpose dosimeter
GPS Global Positioning System
GPU graphics processing unit
GRaND Gamma Ray and Neutron Detector

GRS Gamma-Ray Spectrometer

HDPE high-density polyethylene
HEAO-3 High Energy Astronomy Observatory 3
HEND High Energy Neutron Detector
HERA Hybrid Electronic Radiation Assessor
HERD High Energy cosmic Radiation Detector
HiRes High Resolution Fly's Eye
HOSC Huntsville Operations Support Center
HPEG HOSC Payload Ethernet Gateway
HRDL High Rate Data Link
HTTPS Hypertext Transfer Protocol Secure

I2C Inter-Integrated Circuit
IC integrated circuit
ICRP International Commission on Radiological Protection
ICRU International Commission on Radiation Units & Measurements
IDEAS Integrated Detector Electronics AS
ILRS International Lunar Research Station
IO input–output
IP Internet Protocol
ISRU in-situ resource utilization
ISS International Space Station
ISS-RAD International Space Station Radiation Assessment Detector
ISS-CREAM Cosmic Ray Energetics and Mass for the International Space Station
ITMS ion-trap mass spectrometer
IVoDS Internet Voice Distribution System

JEM Japanese Experiment Module
JSL Joint Station LAN
JTAG Joint Test Action Group

KCU Ku-band Communications Unit

LAN local area network
LCNS Lunar Cosmic-Ray and Neutron Spectrometer
LCROSS Lunar Crater Observation and Sensing Satellite
LDO low-dropout regulator
LE-CPT low-energy section of the CPT
LED light-emitting diode
LED low-energy dosimeter
LEND Lunar Exploration Neutron Detector
LEO low Earth orbit
LET linear energy transfer
LGAD low-gain avalanche diode
LHC Large Hadron Collider

LIBS laser-induced breakdown spectroscopy
LIDAL Light Ion Detector for ALTEA
LND Lunar Lander Neutron and Dosimetry
LOLA Lunar Orbiter Laser Altimeter
LRO Lunar Reconnaissance Orbiter
LROC Lunar Reconnaissance Orbiter Camera
LS Lindhard-Sørensen
LSB least significant bit
LSS Lindhard-Scharff-Schiøtt
LUVMI-X Lunar Volatiles Mobile Instrumentation – Extended
LVS Lunar Volatiles Scout

MAPS monolithic active-pixel sensor
MAPT Multi-Purpose Active-Target Particle Telescope
MCC-H Mission Control Center – Houston
MCNP Monte Carlo N-Particle
MESSENGER MErcury Surface, Space ENvironment, GEochemistry, and Ranging
MIP minimum-ionizing particle
MO molecular orbital
MOSFET metal-oxide-semiconductor field-effect transistor
MPV most probable value
MRAM magnetoresistive random-access memory
MRDL Medium Rate Data Link
MSL Mars Science Laboratory
MSolo Mass Spectrometer Observing Lunar Operations
MUX multiplexer

NAND NOT-AND
NAS network-attached storage
NASA National Aeronautics and Space Administration
NFS Network File System
NGD neutron and gamma dosimeter
NIEL non-ionizing energy loss
NIST National Institute of Standards and Technology
NMLS Neutron Measurements at the Lunar Surface
NRVISS Near-Infrared Volatiles Spectrometer System
NS neutron spectrometer
NSRL NASA Space Radiation Laboratory
NSS Neutron Spectrometer System
NTP Network Time Protocol

OLTARIS On-Line Tool for the Assessment of Radiation In Space
OS operating system

PAMELA Payload for Antimatter Matter Exploration and Light-nuclei Astrophysics
PAN Penetrating particle ANalyzer

PAO Pierre Auger Observatory
PCB printed circuit board
PCIe Peripheral Component Interconnect Express
PDE photon detection efficiency
PDS power distribution system
PDS Planetary Data System
PDSS Payload Data Services System
PDU power distribution unit
PEEK polyether ether ketone
PEHG Payload Ethernet Hub Gateway
PEI polyetherimide
PEN polyethylene naphthalate
PET polyethylene terephthalate
PET positron emission tomography
PGA programmable gain amplifier
PHITS Particle and Heavy Ion Transport code System
PIN positive-intrinsic-negative
PL NAS Payload Network-Attached Storage
PL MDM Payload Multiplexer/Demultiplexer
PMMA poly(methyl methacrylate)
PMT photomultiplier tube
POIC Payload Operations and Integration Center
POM polyoxymethylene
POPOP 1,4-bis(5-phenyloxazol-2-yl) benzene
PROSPECT Package for Resource Observation and in-Situ Prospecting for Exploration, Commercial exploitation and Transportation
PS polystyrene
PSD pulse shape discrimiation
PSI Paul Scherrer Institute
PSR permanently shadowed region
PTFE polytetrafluoroethylene
PVT polyvinyltoluene

QC charge comparator
QCD quantum chromodynamics
QED quantum electrodynamics

RADFET radiation sensing field-effect transistor
RBE relative biological effectiveness
REM Radiation Environment Monitor
RF radiofrequency
RICH ring-imaging Cherenkov
RMS root-mean-square
ROI region of interest

SAA South Atlantic Anomaly
SAR successive-approximation register
SC system controller
SDRAM synchronous dynamic random-access memory
SEE single-event effect
SEFI single-event functional interrupt
SEL single-event latch-up
SEP solar energetic particles
SEU single-event upset
SiPL Planar Silicon Sensors
SiPM silicon photomultiplier
SiPX Silicon-Pixel Sensor
SLPA shell-wise local plasma approximation
SNR supernova remnant
SNSA Swedish National Space Agency
SOFIA Stratospheric Observatory For Infrared Astronomy
SPAD single-photon avalanche diode
SPDT single-pole double-throw
SPI Serial Peripheral Interface
SRAG Space Radiation Analysis Group
SRAM static random-access memory
SRIM Stopping and Range of Ions in Matter
SSC Swedish Space Corporation
SSH Secure Shell
SWIP solar-wind implanted particle
SYSCLK system clock

TA Telescope Array
TADF thermally activated delayed fluorescence
TC telecommand
TCP Transmission Control Protocol
TCS thermal control system
TDC time-to-digital converter
TDRSS Tracking and Data Relay Satellite System
TEPC tissue-equivalent proportional counter
TH track-and-hold
TID total ionizing dose
TM telemetry
TOF time-of-flight
ToT time-over-threshold
TRD transition radiation detector
TReK Telescience Resource Kit
TRIDENT The Regolith and Ice Drill for Exploring New Terrains
TRL technology readiness level

TUM Technical University of Munich
TVS transient-voltage suppression

UART universal asynchronous receiver-transmitter
UCA unitary-convolution approximation
UDP User Datagram Protocol
USB Universal Serial Bus
USL U.S. Laboratory
USOS U.S. Orbital Segment
USSR Union of Soviet Socialist Republics
UV ultraviolet

VCAS Volatiles and Context Analysis Suite
VIPER Volatiles Investigating Polar Exploration Rover
VLAN virtual LAN
VOILA Volatiles Identification by Laser Analysis
VPN Virtual Private Network

WAP Wireless Access Point
WSGT White Sands Ground Terminal

ZARM Center of Applied Space Technology and Microgravity

Preface

Humanity left the lunar surface for the final time when Eugene A. Cernan, commander of the Apollo 17 mission, climbed up the ladder of the Lunar Module *Challenger* in the early hours of December 14, 1972. He worked with fellow astronaut Harrison H. "Jack" Schmitt to close the module's hatch one last time, making sure that none of the aggressive lunar dust had compromised the tightness of the silicone compound seal. The two of them had spent 22 hours, three minutes, and 57 seconds walking the Moon's surface and performing a broad range of experiments and investigations during three seven-hour extravehicular activities. Schmitt, a geologist, had been the first scientist to land on the Moon and the mission was the scientifically most productive of the entire Apollo program. Some 14 hours after Cernan had entered the module, the motor of the ascent stage ignited to lift him and Schmitt back up the Moon's gravity well. About two hours later, after docking *Challenger* to the Command Module *America* waiting in orbit, they re-joined Ronald E. Evans, who had been circling the Moon for the past three days in the arguably quite uninspiring company of five mice, and started preparations for the trip to Earth. They began their journey home in the late hours of December 16, 1972 and safely splashed down in the Pacific Ocean nearly three days later. The subsequent recovery of the three astronauts by the USS *Ticonderoga* marked the end of the last Apollo mission.

No human has ventured beyond Earth orbit since, let alone set foot on the surface of another planet. Apollo 17 was the last of a series of (mostly) successful crewed missions to the Moon that saw the United States take first place in the now-iconic Space Race against the former USSR. The incredible dedication and ingenuity of the thousands of engineers and scientists working on the Apollo program, as well as the Mercury and Gemini programs preceding it, had primarily been fueled by the geopolitical rivalry of the two Cold-War superpowers, as had the U.S. government's willingness to provide the vast

amounts of money required to finance the creation of a human space program from the ground up. With the race won and American supremacy over the USSR established, President Richard Nixon felt it was hard to further justify the quite significant expenditures needed to keep Apollo running purely to satisfy scientific curiosity, especially in light of waning public interest. The budget of the National Aeronautics and Space Administration (NASA) also came under increasing pressure by the financial demands of the nascent Skylab and Space Shuttle programs, ultimately leading to the cancellation of missions 18 through 20. NASA administrator James E. Webb had barely managed to secure funding for a first batch of 15 Saturn V boosters, enough for nine more Moon landings after Apollo 11, to begin with. Plans to continue the program beyond these flights with loftier ambitions, such as establishing a lunar base or sending a crewed mission to Mars, had been axed by the government early on. In the following decades, human space flight was to a large extent shaped by the capabilities of the Shuttle—whose design was heavily influenced by requirements of the U.S. Air Force and which was not meant to leave Earth orbit—and those of the Soviet Soyuz spacecraft, which to this day ferries Russian cosmonauts to the International Space Station (ISS). Even though Soviet engineers had originally designed Soyuz for lunar missions, the USSR never managed to successfully launch their N1 heavy-lift rocket, confining the spacecraft to missions in Earth orbit. As a consequence of the shifting of priorities away from high-stakes exploration to militarily and commercially more relevant applications in Earth orbit, the Apollo missions remain the only excursions of humanity to another planet to this day.

In the decades since the retirement of Project Apollo, NASA repeatedly tried to revive lunar exploration, most notably through the Constellation program, which was formulated in response to the Vision for Space Exploration of President George W. Bush and his administration [Bus04]. Though Constellation's immediate focus lay on the completion of the space station and on preparatory lunar missions, the overall objectives were the establishment of a permanent human presence in space and the first landings of humans on Mars [04]. The program was strongly criticized by those who felt that going back to the Moon would be repeating past achievements with little added value. Among them was none other than Apollo 11 astronaut Edwin E. "Buzz" Aldrin Jr., the second man to walk on the Moon. Aldrin and others pushed for a more direct approach to the manned exploration of Mars, in which the Moon played only a peripheral role [Ald13]. The Constellation program was ultimately scrapped by President Barack Obama in favor of a more flexible policy with Mars at its center. The

administration's decision was to a large extent based on the recommendations of the Augustine Commission, which found that the Constellation program was so over budget and lagging behind schedule that none of its objectives could reasonably be met without a massive increase in funding [Aug+09]. The administration of President Donald J. Trump, though not completely scrapping the work begun under President Obama, yet again changed the focus of NASA's human exploration program by demanding that a crewed lunar landing take place by 2024. Based on this decision, the agency initiated the Artemis program, whose goal is the establishment of a permanent and *sustainable* human presence on the Moon through a combination of publicly and privately funded missions. Though acknowledging that the initial schedule of Artemis may have been overlay ambitious, President Joseph R. Biden so far did not announce a major revision of U.S. space policy and seems to support the continuation of the program.

Outside of the U.S., the space exploration programs of the Western European countries—most importantly those of France, Germany, Italy, and the UK—have historically been closely linked to that of NASA. The European Space Agency (ESA) initiated early stages of a crewed spaceflight program in 1987 when it approved an initial phase of concept development for the Hermes spaceplane proposed by the French Centre National d'Études Spatiales (CNES). Hermes, however, never got past the drawing board and its only lasting legacy is the impact it had on the design of the Ariane 5 launch vehicle, which was meant to carry the spacecraft into orbit. European astronauts participated in a number of Space Shuttle missions before and during the construction of the ISS and today are part of the station's regular crew rotation. Yet, even though the crewed and un-crewed exploration of the Moon is promoted with renewed vigor by ESA and European industry, the continent still lacks a clear vision for a human spaceflight program. Despite their industrial, academic, and financial might, European governments for now seem to be content with sending a handful of astronauts to the Moon on Artemis missions.

After setting the Space Race in motion through their early spaceflight successes, the USSR secretly pursued separate programs to achieve the first crewed lunar flyby and the first crewed lunar landing using different versions of the Soyuz spacecraft. Beaten to these achievements by the Apollo 8 and Apollo 11 missions, respectively—and after four catastrophic failures of the N1 launch vehicle—the Soviet leadership brought the programs to an end before the first crewed flight to the Moon was attempted. Despite these setbacks, the Soviets successfully launched Salyut 1, the world's first space station, on

19 April 1971, kicking off a largely successful series of single-module stations serving both civilian and military purposes. The final *Salyut* modules formed the core of the highly successful *Mir* station and of the Russian section of the ISS. The future of Russia's manned spaceflight program, beyond the current participation in the space station, is not as well known as that of the U.S. or Europe. Officials of Roscosmos, the state corporation responsible for all matters concerning spaceflight, publicly deliberated a departure from the ISS program in 2024 in favor of a new Russian space station in Earth orbit to be constructed between 2025 and 2035. In 2021, Roscosmos and the China National Space Administration (CNSA) signed an agreement concerning the development of the International Lunar Research Station (ILRS), a program to establish a research facility on the lunar surface with as yet very broadly defined objectives and timelines.

Bringing Humanity to the Moon and Beyond

Surely, the technological advances of the past decades and the experience of operating the ISS for more than 20 years ought to make crewed spaceflight beyond Earth orbit a lot easier than during the Apollo era. Establishing a permanent and sustainable human presence in cis-lunar space and on the lunar surface, however, presents challenges that far exceed those encountered at any time during humanity's past efforts to conquer the stars. Even the infrastructure required to support a semi-permanently crewed station in lunar orbit like the Gateway, whose construction is set to begin in the next few years, is orders of magnitude more complex than running the ISS in low Earth orbit. There are many factors contributing to the complexity of lunar missions; chief among them, though, is the cost of bringing material and supplies across the vast distance between Earth and the Moon. Parts of my work is in support of current efforts to make use of locally available resources, in particular water, to reduce the number of supply flights needed to sustain crewed outposts. Another challenge is that we have little idea of the effects that long-term stays on the Moon or in lunar orbit will have on astronauts. Though we can extrapolate, to some degree, from the studies performed on the ISS, there is nonetheless a plethora of open questions. One of the biggest risks is the exposure to cosmic and solar radiation and their influence on the human organism. A large part of my work is focused on improving our understanding of this complex field.

As with nearly every major program or mission in the space sector, the schedule of the Artemis program keeps shifting as development delays add

up. I will therefore refrain from making any predictions concerning the timing of planned missions. One thing should be clear, though: The earlier we find solutions to overcome the challenges we face, the more likely it is that Artemis will not only return humanity to the Moon but also lay the foundation for a long-term human presence in cislunar space. From my perspective, establishing such presence is a prerequisite for the crewed missions to Mars and other deep-space destinations.

Funding

My work was financially supported by:

German Research Foundation (Deutsche Forschungsgemeinschaft, DFG):

- Research grant 414049180;
- Cluster of Excellence 'ORIGINS: From the Origin of the Universe to the First Building Blocks of Life' – EXC 2094 – 390783311;
- Cluster of Excellence 'Origin and Structure of the Universe' – EXC 153 – 24799710; and
- Collaborative Research Center 'Neutrinos and Dark Matter in Astro- and Particle Physics' – SFB 1258 – 283604770.

European Commission:

- Horizon 2020 program, grant 822018.

German Federal Ministry of Education and Research (Bundesministerium für Bildung und Forschung, BMBF):

- High-D consortium – 05H21WORD1.

The deployment of the RadMap Telescope to the International Space Station was sponsored by the ISS National Laboratory, administered by the Center for the Advancement of Science in Space (CASIS) on behalf of the National Aeronautics and Space Administration (NASA).

Own Contributions

I fulfilled a variety of roles working on the projects presented in this thesis. As project manager, I applied for external and internal grants, administered finances, wrote the required technical and legal documentation, and coordinated with our partners. Towards NASA, I act as the principal investigator of the RadMap Telescope. I also (co-)supervised many of the students listed below. The scientific objectives of our projects I developed in cooperation with my colleague Thomas Pöschl.

Nearly all detector and instrument hardware (electronics, mechanics, and otherwise) presented in this thesis was designed, constructed, and commissioned by me. The rest of it was designed by students under my supervision. I devised the architecture of our instruments, their operational principles, and their integration into the respective spacecraft or probes. I coordinated the production of components with internal and external partners, assembled and tested most of the electronics myself, and led the integration of the detectors and instruments. I also led our team through five test-beam campaigns at Paul Scherrer Institute, several smaller tests at CERN, and during acceptance testing at Johnson Space Center. The analysis of the RadMap Telescope's data presented in this thesis was performed solely by me.

Throughout the document, I expressly point out whenever I present work that was largely performed by my colleagues, either in the text or in the form of footnotes. In the cases where I quote results obtained by students I supervised, I cite their respective theses.

Acknowledgements

The manuscript in front of you is the result of many years of hard work. To be honest, many more than I would have agreed committing to back when I was ready to leave university for a job at the European Space Agency after the completion of my Master's degree. I would like to thank my thesis advisor, Prof. Stephan Paul, for convincing me to stay for 'just a few more years' and pursue a career in science. I also thank him for giving me the freedom of conducting research that had surely not been at the core of his interest until then, and for entrusting me with the responsibility to lead the respective projects.

While my research would have been difficult without the help of a great many people, it would have been impossible without my longtime colleague Thomas Pöschl. For many years, we worked together on the projects presented in this thesis—and on many others. We would surely not have achieved all that we did without his steadfast commitment to our work. I am also immensely grateful to Hans-Jürgen Zachrau, who not only helped to bring the idea for the RadMap Telescope to life but also introduced me to the world of the ISS program. I learned to appreciate that he can always be relied on for personal advice, too. Another person who made indispensable contributions to the RadMap Telescope is Sebastian Rückerl; he pretty much all by himself implemented the project's software framework and is one of the most reliable persons I know. Thanks also to Peter Hinderberger for his work on the instrument's FPGA firmware.

I would like to acknowledge the great cooperation with our colleagues from the Radiation Biology department at the German Aerospace Center, and in particular Thomas Berger, Karel Marsalek, Michael Wirtz, and Moritz Kasemann. Launching the RadMap Telescope to the ISS would not have been possible without the support of our colleagues at Airbus in Houston: Thomas Kendelbacher, Brian Mutz, Joakim Andreassen, Carl Kuehnel, and Kris Kuehnel. The instrument's integration into the ISS infrastructure was supported by many people at NASA, among them Matthew Villaverde, John Selmarten, Tyler Dorval, John Lauber, Adolphus Murphy, Katherine Larson, Tishawn Webb, Jade Conway, Melissa Hopper, Karl Roth, Lewis Croog, Katrina Whitlock, Andrea Kelly, and Janice Makinen.

Thanks also to the LUVMI-X consortium and external partners, and especially to Janos Biswas, Christian Gscheidle, Jeremi Gancet, Thibaud Chupin, David Vogt, Simon Sheridan, Anthony Evagora, Marine Joulaud, and Jessica Flahaut. I regret Covid-19 prevented us from seeing each other more often during our time working on the project.

I am greateful to Prof. Laura Fabbietti, Stephan Königstorfer, Joana Wirth, Thomas Klemenz, Berkin Ulukutlu, and Roman Gernhäuser for their help with assembling and testing the detector modules for the RadMap Telescope; and to Prof. Markus Czupalla for supporting the design of the instrument's thermal control system. Our late colleague Dieter Renker was an indispensable source of knowledge about silicon photomultipliers.

I want to acknowledge the work of all students who contributed to our research through internships and theses: Moritz Adams, Manoram Agarwal, Marius Anger, Lukas Bierwirth, Liesa Eckert, Verena Eiblmeier, Felix Firmbach,

Michael Gareis, Christopher Gottschaldt, Alexander Hahn, Matthias Hanke, Benjamin Hanrieder, Philipp Hauptmann, Maximilian Hoch, Lucas Hollender, Maximilian Höschler, Jakov Kholdkov, Sabrina Kressierer, Maximilian Kronmüller, Andrea Meraner, Lingxin Meng, Luise Meyer-Hetling, Michael Milde, Jan Henrik Müller, Alicia Pechan, Lea Prüfer, Philipp Schmette, Franz von Silva-Tarouca, Patrick Wastian, and Aileen Wolf.

No hardware project can be successful without good technicians, which is why I would like to highlight the excellent work of the team at our mechanical workshop: Manfred Pfaller, Manfred Reither, Michael Novotny, Andreas Kienle, Sebastian Saller, Thomas Fechter, Gabriel Reingen, and Nicolas Siart. Thanks also to Igor Konorov, Stefan Huber, and Dmytro Levit for their support and troubleshooting in many aspects related to data acquisition. At Paul Scherrer Institute, we were always excellently supported by Thomas Rauber, Manuel Schwarz, and Davide Reggiani.

Thanks to Karl Eichhorn, Dominic Ecker, Karina Bernert, Christian Dreisbach, and Philipp Haas for the many hours of discussions—work-related or otherwise—for countless lunch breaks, and for supporting us whenever we were short on manpower and time.

Last but certainly not least, I would like to thank my wife, Ann-Christin, for always supporting me, for tolerating my sometimes crazy work schedule, and for showing up unannounced with coffee and moral support when I need it.

Chapter 1

Introduction

The exploration of our solar system via crewed and robotic missions comes with myriad challenges. Some are related to the unique environments encountered in interplanetary space and on the surface of foreign planets. Others are due to the large distances and mission durations of interplanetary travel. Yet others are caused by the (still) severely limited mass and volume that we can launch into space, even though significant advances have been made in the past decade. Often, the challenges we face are rooted in a combination of two or more of these aspects.

My research presented in this thesis focuses on two challenges that are particularly important to human spaceflight but also have connections to astrophysics and planetary science. The first is the risk that the radiation environment in space poses to the health of astronauts spending months or years in spacecraft bound for the Moon, Mars, or other destinations. Although we have learned much about the effects of radiation on the human body from the crews who have lived and worked on the International Space Station (ISS) for more than 20 years, the risk predictions for missions beyond low Earth orbit (LEO) are still shrouded in uncertainty. Many unknowns lie in the field of radiation biology, but some are also connected to limited capabilities of the instrumentation we use to monitor the crews' exposure.

The second challenge is the provision of one of the most important commodities required for the survival of a human crew: water. Beyond hydration and hygiene, water can be used as a highly effective radiation shield and as rocket fuel. Yet, launching large quantities of it from a planet with a gravity well as deep as Earth's is prohibitively expensive. Water is thus at the focus of

the nascent research into in-situ resource utilization (ISRU), with many in the field hoping that it can be extracted either from the Moon or from asteroids in cislunar space. A first step is to deepen our limited understanding of the lunar water cycle and of the nature, size, and accessibility of water deposits in the Moon's polar regions. Current model predictions are severely constrained by the almost total lack of *in-situ* data; even high-resolution orbital measurements are only available to a limited extent. One of the tools that can help alleviate this lack of data is neutron spectroscopy.

At first sight, these two research areas seem to have little in common. Yet, they are intimately connected by the need for characterizing radiation fields created by cosmic rays and solar energetic particles. This requires an understanding of the primary radiation sources and their interaction with natural and artificial structures—such as the surface of the Moon and the shielding of spacecraft. It also requires the operation of detectors for charged particles and neutrons on crewed spacecraft, robotic probes, landers, and rovers. The focus of my work is the development of such instrumentation.

The study of extraterrestrial radiation is, of course, an interesting topic in itself. Even though we typically pay little to no attention to them in our daily life, cosmic rays and solar particles have a profound impact on life on Earth. They likely played a large role in the formation and evolution of life as we know it [Dar11; GB20], and they interact with our home planet's atmosphere and magnetosphere in myriad ways [Mir+15]. On Jupiter's moon Europa, the bombardment of the planetesimal's icy surface with cosmic-ray particles provides the energy required for the dissociation of water-ice molecules into hydrogen and oxygen [Sza+24], potentially generating the conditions for habitability. And ultra-high energy cosmic rays more than a million times more energetic than particles accelerated in the largest human-made research facilities [Abb+23] are a particularly hot topic in the field of astroparticle physics these days. Their study can help us understand the processes leading to the creation and acceleration of cosmic rays throughout the galaxy, thereby providing crucial data on the life cycles of stars and on the properties of the interstellar medium.

Our work at the Technical University of Munich (TUM) focuses on the parts of the cosmic-ray and solar radiation spectra that are relevant to the protection of astronauts and to the study of lunar surface, which is why we can unfortunately only contribute little to many of these fascinating research topics. I want to stress that the instrumentation we develop is meant for operational purposes and as such must be as compact and power-efficient as

possible. Though one of the central aspects of my work is to improve the resolution with which we can resolve the cosmic radiation field in compact detectors, the capabilities of large astrophysics experiments like the Alpha Magnetic Spectrometer (AMS-02) on the ISS are by design far superior, at least in the range of particle energies that is at core of their sensitivity. Vice versa, many of the instruments developed for astrophysics investigations can contribute little to our research.

The first part of my thesis deals with the development of the RadMap Telescope, a compact yet highly capable radiation monitor for crewed spacecraft. To highlight why the focus of our work is on improving the resolution for the charge of cosmic-ray nuclei, I begin this part with a brief review of radiation biology, shielding strategies, and start-of-the-art instrumentation (Chapter 5). I then introduce the working principle of the instrument's main detector—a tracking calorimeter made from scintillating plastic fibers and silicon photomultipliers—and present the results and lessons learned from early demonstrations and prototypes (Chapter 6). The performance of scintillator-based detectors depends strongly on two main properties: the material's light yield and ionization quenching. I present our detailed studies of these aspects in Chapter 7, before describing the design, production, and calibration of the flight detectors in Chapter 8. Though it is still work in progress, I discuss our approach for analyzing the instrument's data in Chapter 9 before presenting the design of the flight instrument, including a detailed description of its main detector's read-out electronics (Chapter 10). An initial analysis of the data gathered during a nine-month operational period on the ISS, with a focus on checking the consistency of our measurements against those of a flight-proven detector, is given in Chapter 11. Lastly, I discuss the potential for future improvement, studies we still need to perform to fully understand the RadMap Telescope's measurements, a comparison to other state-of-the-art instruments, and next steps in Chapter 12.

The second part of this thesis encompasses my work developing the Lunar Cosmic-Ray and Neutron Spectrometer. To motivate the use of neutron spectroscopy to search of the signatures of hydrogen (and thus water), I begin by briefly reviewing the current status of the search for water on the Moon and explain how neutrons generated in the interaction of cosmic rays with the lunar surface can help us identify (sub-surface) areas of increased hydrogen abundance (Chapter 13). I then present the design of a scintillator-based neutron spectrometer and charged-particle, discuss their anticipated performance based on simulation studies, and briefly describe first tests (Chapter 14). To

show how our instrument can contribute to the search for water on the Moon, we helped design a rover-based reference mission to the Shoemaker-Faustini ridge at the lunar south pole, an overview of which I give in Chapter 15. Lastly, I compare both the rover and the instrument to other research in the field and discuss future prospects for flight missions (Chapter 16).

Before starting with the detailed description of these two projects, I briefly summarize the current state of research into cosmic rays and solar energetic particles (Chapter 2), comprehensively summarize the interaction of radiation with matter with a particular focus on heavy nuclei (Chapter 3), and introduce the detector components that we use to construct our instruments (Chapter 4).

Chapter 2

A Brief Review of Cosmic and Solar Radiation

Cosmic rays are charged particles and atomic nuclei that are created and accelerated primarily by exploding stars throughout our galaxy. They were first discovered in 1912 by Austrian-American physicist Victor Franz Hess during several balloon flights to altitudes of about 5 km, where he found that radiation levels are twice as high as on the ground [Hes12]. The now universally accepted term *cosmic rays* was introduced by Robert A. Millikan and G. Harvey Cameron, who showed that the observed increase of the radiation intensity is caused by an influx of particles from space [MC28]. Contrary to the assumptions of some of his contemporaries, Arthur H. Compton in the early thirties of the past century first determined that cosmic-ray particles must be charged [AC33]—a fact that has since been confirmed by numerous experiments, though we also know that significant sources of uncharged particles (neutrinos and high-energy photons) exist throughout our galaxy and that they are closely connected to the origin of cosmic rays[1]. Before the emergence of accelerators capable of producing particle beams of sufficiently high energies in controlled environments, cosmic-ray research has been one of the primary means for studying particle physics. During its early heyday, a

Some sections of this chapter are based on a reference entry on cosmic rays that I contributed to the Encyclopedia of Lunar Science [LB23].

[1] Some authors include neutrinos and gamma rays in the definition of cosmic rays. I, however, follow the more widely accepted convention that cosmic-ray research, gamma-ray astronomy, and neutrino astronomy are part of the broader field of *astroparticle physics* [GER16].

number of important discoveries were made via the observation of charged radiation of extraterrestrial origin. Perhaps the most famous example is the discovery of the positron in cloud chamber images by Carl David Anderson in 1932 [And33]. Other particles, too, were discovered, such as muons in 1936 [AN36], kaons in 1947 [RB47], and pions in 1947 [Lat+47] and 1950 [Bjo+50]. The first observation of antiprotons at the Bevatron accelerator in 1955 [Cha+55] marked the end of this era, with subsequent discoveries almost exclusively happening in laboratory experiments powered by accelerators that have been continuously increasing in size and performance.

Renewed interest in cosmic rays was sparked by the launch of the Payload for Antimatter Matter Exploration and Light-nuclei Astrophysics (PAMELA) in 2006 and by the installation of the AMS-02 on the ISS in 2011. These experiments—and others following them, such as the CALorimetric Electron Telescope (CALET) and the Dark Matter Particle Explorer (DAMPE)—have made it possible for the first time to accurately and directly study the high-energy phenomena at the focus of gamma-ray and neutrino astronomy that, supposedly, are closely linked to the origin of cosmic rays. Previously, space-based experiments had hardly been sensitive to the particle energies of interest to these disciplines. If they were, their resolution at such energies was completely insufficient for drawing scientifically valid conclusions. For decades, scientists interested in particles with energies beyond a few GeV thus needed to rely on measurements made by balloon-borne experiments and air-shower telescopes. And although especially the latter remain an increasingly important tool in the arsenal of astroparticle physics, the highly accurate measurements provided by AMS-02 herald the beginning of a new era. Future experiments, such as the envisioned AMS-100 [Sch+19], will extend the energy range of direct measurements (in space) even further and significantly improve resolutions at the highest energies accessible by AMS-02 today. Between the advent of cosmic-ray research at the beginning of the past century and now, the interest in studying particles (and nuclei) of cosmic origin has thus shifted from taking the first steps in developing the Standard Model of particle physics to understanding the high-energy astrophysical processes that govern how matter is synthesized and distributed across the universe.

Despite studying cosmic rays for more than a century, there are many aspects about them that we have not yet fully understood. Especially their origin and acceleration to very high energies remain a field of intense study, with the aforementioned close connections to the disciplines of gamma-ray astronomy and neutrino astronomy [GER16]. An in-depth discussion of these

aspects goes beyond the scope of this thesis and I will focus my review of cosmic and solar radiation on the aspects relevant to the work presented here.

2.1 Observations of Cosmic Rays

I start my discussion of cosmic rays with a summary of the latest observational evidence upon which most of the theories described in later sections are based. Cosmic-ray research is a discipline in which most of the experimental setup—the processes governing the creation, acceleration, and propagation of particles and nuclei—cannot be controlled by the experimenter. Even worse, there is no direct experimental access to these processes that would allow us to test hypotheses of their workings, and only little to no in-situ data to work with. Any theory on the origin of cosmic rays and their propagation through galactic and extragalactic space can thus only rely on the observational data produced in the wider field of astroparticle physics. This data consists of a mix of measurements that allow us to remotely probe the creation, acceleration, and propagation processes of cosmic-ray particles (neutrino and gamma-ray astronomy) and measurements of the cumulative effect of all these processes on particles arriving at Earth or at the location of various spacecraft throughout the Solar System (direct and indirect measurements of cosmic rays). Additional information is provided by astronomical observations across the whole electromagnetic spectrum. A clear understanding of what data are available (and what are not) must thus be the starting point for every discussion of the current state of cosmic-ray research and of the future direction of the discipline.

The data on cosmic rays we have collected so far stems from three types of experiments: charged-particle detectors operating in space, balloon-borne particle detectors, and large air shower telescopes. Space-based and balloon-borne systems are usually either magnetic spectrometers or calorimeters (with a limited ability to track particles). The advantage of launching such detectors aboard spacecraft is that they operate beyond Earth's atmosphere—and sometimes even beyond the influence of its magnetic field—giving us direct access to primary particles across (almost) the whole cosmic-ray spectrum. To some extent, this is also true for balloon-borne experiments, though the effect of the residual atmosphere and of Earth's magnetic field at typical flight altitudes of a few tens of kilometers makes it impossible to measure particles at the lower end of the spectrum. Though magnetic spectrometers like AMS-02 can deliver the most precise measurements, their sensitivity and resolution

are limited by the strength of their magnetic field. The larger the field, the higher the momentum, and hence energy, that can be resolved. Stronger fields, however, require more massive and power-hungry magnets, which becomes a challenge if experiments are launched on balloons or satellites (see the proposed AMS-100 instrument referenced above). Missions aiming to measure at energies higher than a few TeV are thus forced to employ instruments centered around calorimeters, usually with added layers of tracking detectors (see, for example, CALET and DAMPE). Such systems are less precise than spectrometers but require no magnetic field and can hence be designed for sensitivities in the TeV region without violating the (current) mass constraints of space missions. Cosmic rays with the highest energies, however, cannot be detected by either type of detector (yet). One reason is that the sensitivity to such high energies is extremely challenging to achieve—even calorimeters must be extremely massive to be able to fully absorb the energy of particles beyond the TeV region. More important, though, is the fact that the flux at the far end of the spectrum is so low that the sensitive area of detectors would need to be prohibitively large if data sets of statistical significance were to be collected. The latter problem is circumvented by air shower telescopes, which effectively use Earth's atmosphere as a calorimeter to estimate the energy of cosmic-ray nuclei [Spu18]. This is achieved by measuring the total energy of the cascade-like shower of secondary particles created when a high-energy primary particle interacts with the atmosphere. Though the maximum detectable energy is practically limitless, a major challenge with this technique is its limited ability to provide information about the relative abundance of different nuclei. A precise analysis of the composition of cosmic rays at the highest energies is therefore not possible based on the measurements we have access to today.

2.1.1 Spectrum and Composition

Cosmic rays, often referred to as *galactic cosmic rays* (GCR)[2], comprise all stable charged particles and fully ionized atomic nuclei (atoms stripped of all their orbital electrons) with sufficiently long lifetimes—that is, longer than the average time it takes them to propagate from their point of creation anywhere in the galaxy to the Solar System. Based on current assumptions about the average density of matter in the galaxy, this time is estimated to be roughly five to ten million years [Lon12]. The cosmic-ray spectrum has a leptonic and

[2]As opposed to *solar cosmic rays*, a term that in the past was often used to describe charged particles emanating from the Sun but has largely fallen out of use.

a hadronic component, with the latter contributing about 98% of all particles[3]. The leptonic component consists of electrons and positrons, which are of minor importance for the work presented here but have in recent years elicited significant interest—not least because the latter might hold clues about the nature of dark matter [Cho+09; Bou+15], though this is a strongly debated possibility [DBG21; GHY20; Hoo+17; KC23; CK22]. The hadronic component is dominated by protons, or hydrogen nuclei, which account for 87% of all cosmic-ray hadrons. Helium nuclei make up a further 12%, and only about 1% are heavier nuclei [Lon12]. A very minor contribution is made by antiprotons [Cow16] and, possibly, by heavier antinuclei [Šer+22; Doe+20].

The spectrum of cosmic-ray particles and nuclei observed at Earth (see Figure 2.1) is very steep; it spans more than eleven orders of magnitude in kinetic energy and well above thirty orders of magnitude in flux. Above about $30\,\mathrm{GeV}$ per nucleon[4], it can be approximately described by a sequence of power laws, with each segment spanning multiple decades in energy [Spu18]. In differential form, the spectrum per element i is defined as the number of nuclei, $\mathrm{d}N_i(E)$, per unit area, $\mathrm{d}A$, per unit solid angle, $\mathrm{d}\Omega$, per unit time, $\mathrm{d}t$, and per energy interval, $\mathrm{d}E$ [Gri01]:

$$\Phi_i(E) = \frac{\mathrm{d}N_i(E)}{\mathrm{d}A\,\mathrm{d}t\,\mathrm{d}\Omega\,\mathrm{d}E}\ \frac{\text{nuclei}}{\mathrm{cm}^2\,\mathrm{s}\,\mathrm{sr}\,\mathrm{GeV}} \propto K_i \left(\frac{E}{1\,\mathrm{GeV}}\right)^{-\alpha_i} \tag{2.1}$$

Here, E is the *kinetic* energy of the particle or nucleus, K_i a normalization factor, and α_i the spectral index [GER16]:

$$\alpha_i \simeq \begin{cases} 2.7 & 10\,\mathrm{GeV} < E < 3\cdot 10^6\,\mathrm{GeV} \\ 3.1 & 3\cdot 10^6\,\mathrm{GeV} < E < 3\cdot 10^9\,\mathrm{GeV} \\ 2.6 & 3\cdot 10^9\,\mathrm{GeV} < E < 10^{11}\,\mathrm{GeV} \end{cases}$$

The power-law nature of the spectrum can be physically motivated from widely accepted assumptions about the basic nature of the acceleration and propagation processes (see [Gru20] and brief discussion in Section 2.2). The value of the spectral index is determined by these processes and can thus (slightly) differ for different elements. The all-particle spectrum (i.e., the sum of the individual elemental spectra) shown in Figs. 2.1 and 2.2 illustrates the

[3] For brevity, I often use the terms *particles* and *nuclei* synonymously in the context of cosmic rays.
[4] In cosmic-ray research, the kinetic energy of nuclei is often normalized to their number of nucleons (protons and neutrons) to facilitate the comparison of different elements, see Section 3.1.

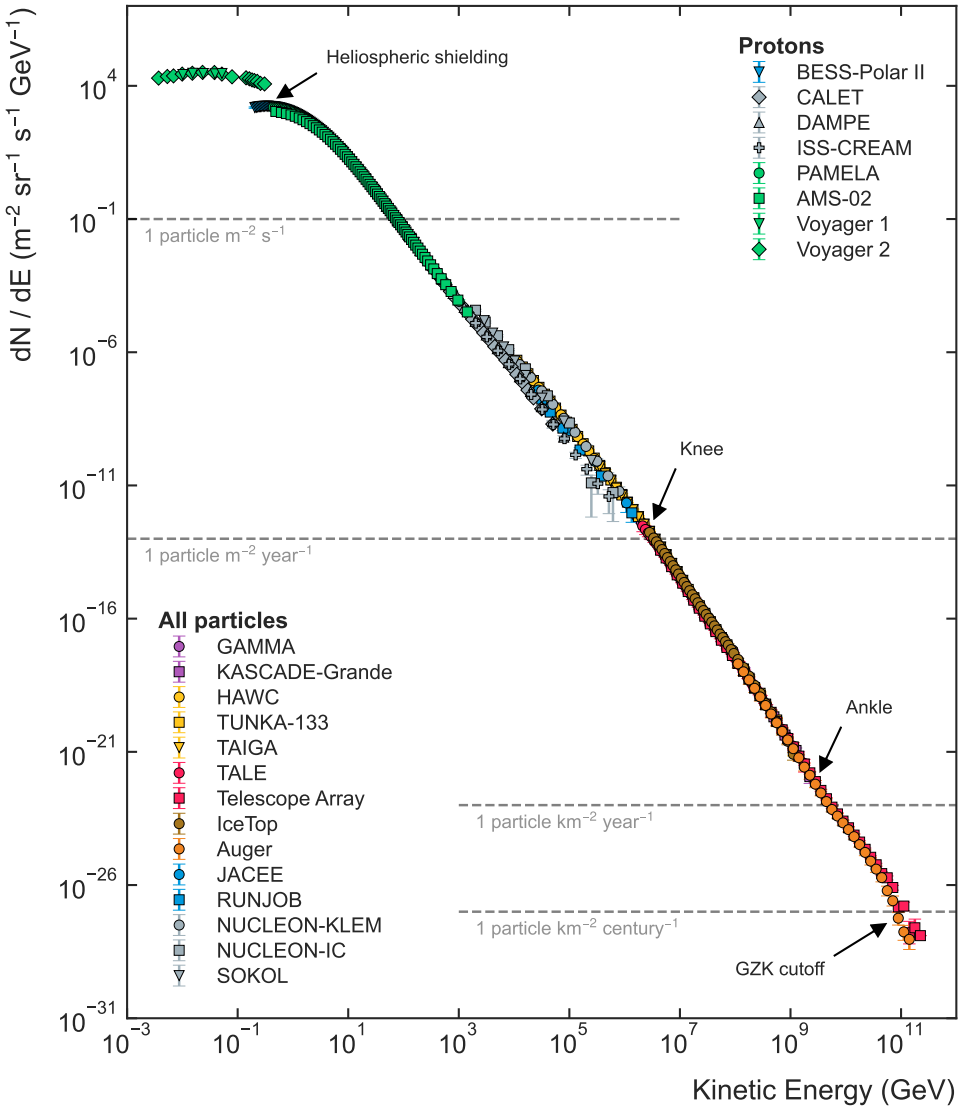

Figure 2.1: Proton and all-particle spectrum measured by experiments on ground, in the atmosphere, and in space.[5] Colors indicate different types of experiments: purple—particle detector array, yellow—air Cherenkov array, red—hybrid (detector & fluorescence), orange—hybrid (water Cherenkov & fluorescence), brown—ice Cherenkov array, blue—balloon, grey—space (calorimeter), green—space (spectrometer).

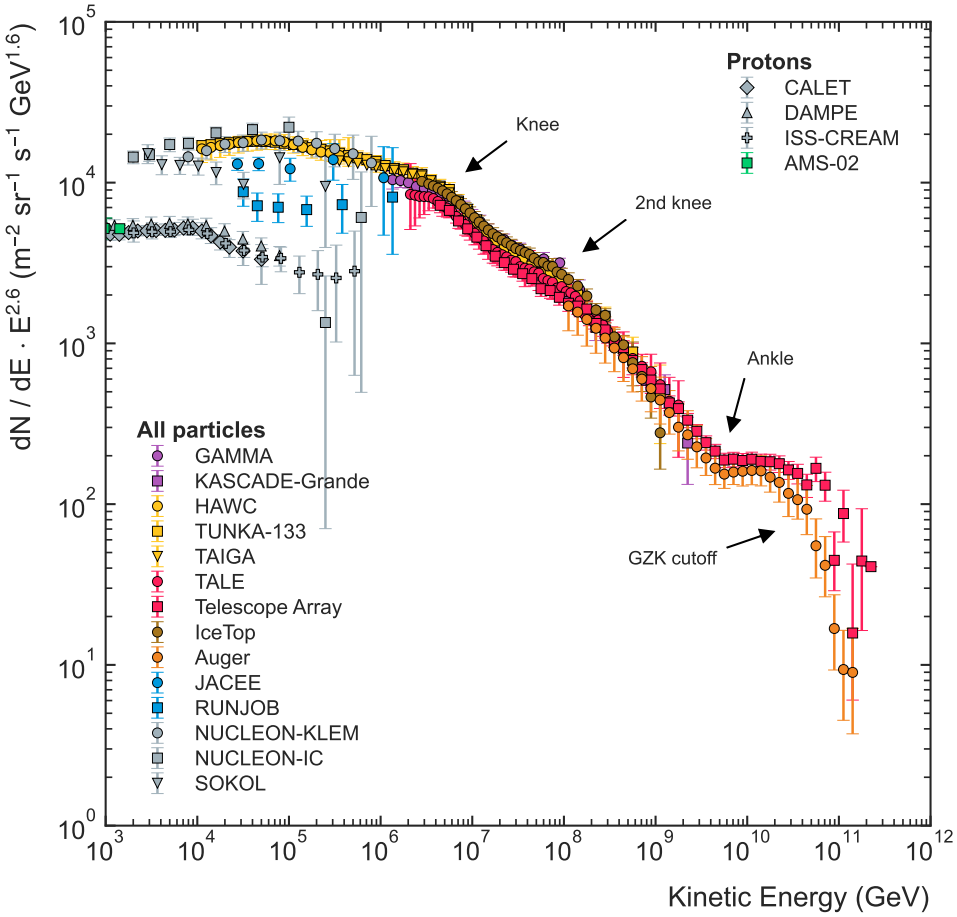

Figure 2.2: Same data[5] as shown in Figure 2.1, but zoomed in and multiplied by $E^{2.6}$ to better reveal features at the high-energy end of the spectrum. See Figure 2.1 for explanation of colors.

two primary transitions of α: the *knee* at around $3 \cdot 10^6\,\mathrm{GeV}$ and the *ankle* at around $3 \cdot 10^9\,\mathrm{GeV}$. The origin of these transitions is still being investigated; in the following, I briefly summarize what we currently know about the spectral features above about 10 GeV and the various theories of their origin. The lower end of the spectrum, which is strongly influenced by the magnetic fields of the Sun and Earth, is discussed in Section 2.3.

(Ultra-)High Energies: 10^6 to 10^{11} GeV

Though the existence of the spectral change at the knee is well established, different experiments register it at slightly different energies and with different shapes—i.e., some results show a sharp break and others a broad transition region [GER16; Sta21]. Partially due to these inconsistencies in the available data, there is no ultimate consensus yet on its origin. One of the most widely discussed theories goes back to Peters [Pet61] and postulates that the knee arises due to a rigidity-dependent maximum energy to which cosmic rays can be accelerated in galactic sources that provide the bulk of cosmic rays [BV07]. If $E_{\mathrm{k}}^{\mathrm{p}}$ is the maximum attainable energy for protons, the spectrum would steepen at energies $E_{\mathrm{k}}(Z) = Z \cdot E_{\mathrm{k}}^{\mathrm{p}}$ for nuclei with charge Z (an effect known as the Peters cycle) and the mass composition would thus shift to heavier elements at energies beyond the knee. The KASCADE air-shower detector was the first experiment to see hints of the Peters cycle in their data [Ant+05], and other experiments appear to have seen similar trends since (e.g., [Aar+19]). An alternative theory suggests that particles with energies beyond the knee cannot be contained in the interstellar magnetic field and thus start to leak from the galaxy [Gru20]. This would similarly lead to a rigidity-dependent sequence of knees in the individual elemental spectra but would require, somewhat problematically, that a second class of galactic sources capable of accelerating particles to energies beyond the knee exists [Alv+19]. Based on these two general possibilities, there is a plethora of models that try to explain in detail how the existence of the knee might be connected to the acceleration process of cosmic rays, to their propagation through the galaxy, or to altogether different processes [Hör04; CD13; GY18]. Reliable estimates of the mass composition at these energies are crucial for judging the validity of the different theories. The experimental data from air shower experiments, however, are far from conclusive so far [Ape+09; Bar+15], mostly because the technique intrinsically has a lower mass separation power than direct measurements. The question of the knee's origin thus still remains an unanswered one [Alo+18; Alv+19], though most measurements at least appear to be consistent with a broad transition region formed by the successive spectral changes of hydrogen and helium—which are almost equally abundant in this energy region—at $3 \cdot 10^6\,\mathrm{GeV}$ and $6 \cdot 10^6\,\mathrm{GeV}$, respectively [MR19].

[5] Data sources: [Ter14; Ape+13; Mor+21a; Alf+17; Pro+14; Ast+22; Abb+18; Iva16; Aar+19; Abr+21; Asa+98; Der+05; Gre+19; Iva+93; Abe+16; Adr+22c; An+19; Cho+22; Adr+11; Agu+21a; Sto+19; Cum+16; Mau+20].

The existence of the ankle has long been believed to be due to a maximum energy to which galactic sources can accelerate cosmic-ray nuclei, with particles at higher energies postulated to originate outside our galaxy [Hil84a]. The extragalactic origin of cosmic rays with the highest energies is widely accepted [ABG12], with potential acceleration mechanisms connected to neutrons stars, black holes, gamma-ray bursts, active galactic nuclei, or diffusive shock acceleration at intergalactic shock fronts [GB23; Alo17]. A minor contribution may come from the decay of super-heavy dark matter [SM19]. Where exactly the transition from galactic to extragalactic sources takes place is, however, a topic of strong debate. It seems possible that an ankle-like feature naturally occurs in the spectrum of extragalactic cosmic rays [BGG06; Alo+07], in which case the maximum energy of galactic particles would need to be considerably lower than the ankle [Kac19]. This would be consistent with the observation of an additional spectral feature between the knee and the ankle, the so-called second knee (see Figure 2.2). Its position roughly coincides with the iron knee of the Peters cycle, $E_{\mathrm{k}}(Z = 26) = 26 \cdot E_{\mathrm{k}}^{\mathrm{p}} \simeq 8 \cdot 10^7\,\mathrm{GeV}$ [BB07], seemingly lending credibility to the model of a single class of galactic sources accelerating protons up to the knee. Such a scenario would elegantly dispense with the requirement for a second class of galactic accelerators, and extragalactic sources would dominate at energies above the second knee [Kac19]. Again, however, the experimental data available, especially with respect to the elemental composition, are far from conclusive [CD13; Alo17; Alo23] and credible alternate theories persist [Eic+16; Tho+16]. Recent measurements have revealed an additional feature at energies beyond the ankle that I will not discuss here [Aab+20; LC23].

Until a few years ago, only little data was available at what we believe to be the far end of the cosmic-ray spectrum. Recent measurements by the High Resolution Fly's Eye (HiRes) experiment [Abb+08], the Pierre Auger Observatory (PAO) and the Telescope Array (TA), however, suggest that there is a cutoff in the spectrum at around $10^{11}\,\mathrm{GeV}$ ($10^{20}\,\mathrm{eV}$) [VIT17], often referred to as the Greisen-Zatsepin-Kuz'min (GZK) cutoff. Independently predicted by Greisen [Gre66] and by Zatsepin and Kuz'min [ZK66] in 1966, this cutoff was postulated to be caused by the interaction of cosmic-ray protons, $\mathrm{p_{gcr}}$, with photons of the cosmic microwave background, γ_{cmb}, and with protons of the interstellar and intergalactic media, $\mathrm{p_{im}}$. Such interactions lead to the intermediate production of Δ^+ hadronic resonances, which subsequently decay to pions, kaons, and protons [Spu18]:

$$\begin{aligned} \mathrm{p_{gcr}} + \gamma_{\mathrm{cmb}}/\mathrm{p_{im}} \longrightarrow \Delta^+ \longrightarrow \mathrm{n/p} + \pi^\pm + \pi^0 + K^\pm + ... \\ \mathrm{n} \longrightarrow \mathrm{p} + \mathrm{e}^- + \overline{\nu}_\mathrm{e} \end{aligned} \tag{2.2}$$

Pions and kaons are unstable hadrons and further decay into gamma rays, electrons, positrons, and neutrinos, allowing to probe the interactions of ultra-high energy cosmic rays via multiple messengers [Més+19]:

$$\begin{aligned} \pi^+ &\longrightarrow \mu^+ + \nu_\mu \\ &\quad\ \mu^+ \longrightarrow \mathrm{e}^+ + \nu_\mathrm{e} + \overline{\nu}_\mu \\ \pi^- &\longrightarrow \mu^- + \overline{\nu}_\mu \\ &\quad\ \mu^- \longrightarrow \mathrm{e}^- + \overline{\nu}_\mathrm{e} + \nu_\mu \\ \pi^0 &\longrightarrow \gamma + \gamma \\ \mathrm{K}^\pm &\longrightarrow \mu^\pm + \nu_\mu/\overline{\nu}_\mu \\ &\quad\ \mu^+ \longrightarrow \mathrm{e}^+ + \nu_\mathrm{e} + \overline{\nu}_\mu \\ &\quad\ \mu^- \longrightarrow \mathrm{e}^- + \overline{\nu}_\mathrm{e} + \nu_\mu \end{aligned} \tag{2.3}$$

Since protons are present in both the initial and the final states of the above interactions, these two processes effectively lead to an energy loss of cosmic-ray protons (of extragalactic origin) that have energies above the threshold for the so-called photoproduction of pions, which is approximately $E_{\mathrm{GZK}} \simeq 5 \cdot 10^{10}\,\mathrm{GeV}$ ($5 \cdot 10^{19}\,\mathrm{eV}$) [Spu18]. For nuclei, E_{GZK} linearly scales with the number of nucleons. Additional, less significant energy losses are caused by the direct production of electron-positron pairs and by adiabatic losses due to the expansion of the universe. For nuclei, photon-induced disintegration may also play a role [Anc19]. Yet again, the experimental data, especially concerning the mass composition at these ultra-high energies, are ambiguous and also allow interpretations that would point to an intrinsic rigidity-dependent maximum energy of extragalactic accelerators [Alo+18; Alv+19]. To complicate matters, the Auger and TA data disagree on the shape of the cutoff (see Figure 2.2), which could either be due to systematic effects in one or both experiments, or possibly be caused by a local source of ultra-high energy cosmic rays in the Northern Hemisphere [Plo+23].

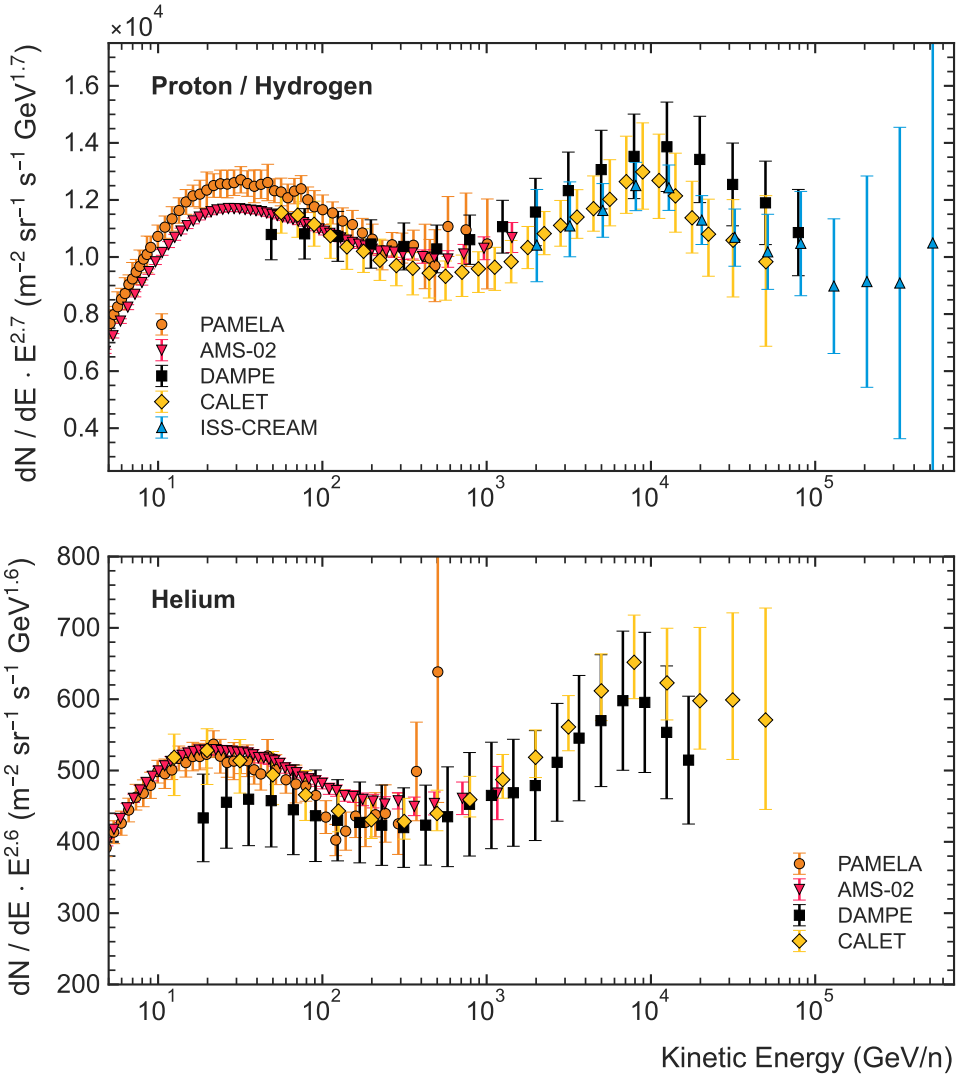

Figure 2.3: Spectral features of the cosmic-ray proton and helium spectra between $10\,\mathrm{GeV/n}$ and $10^6\,\mathrm{GeV/n}$, showing deviations from simple power laws with spectral indexes of 2.7 and 2.6, respectively. The plots only show measurements by space-based experiments.[6]

Medium Energies: 10 to 10^6 GeV

The regions between these spectral breaks were long thought to be well-described by power laws with different spectral indices, partially motivated by assumptions about the nature of galactic accelerators. Especially the range up to the knee, making up the bulk of cosmic rays, was assumed to be characterized by $\alpha_\mathrm{H} \simeq 2.7$ for protons and $\alpha_\mathrm{He} \simeq 2.6$ for helium and heavier nuclei [Sta21]. The advent of high-precision, space-based spectrometry and calorimetry in the GeV-to-TeV range, however, has changed that paradigm. Additional features in the spectra of the two lightest elements, hydrogen (protons) and helium, were independently measured by the space-based experiments PAMELA [Adr+11], AMS-02 [Agu+21b], DAMPE [An+19; Ale+21], CALET [Adr+22c; Adr+23], and ISS-CREAM [Cho+22]. Additional evidence with somewhat larger uncertainties was provided by NUCLEON [Atk+18; Atk+19] and earlier by at least two balloon-borne experiments [Ahn+10; Pan+09; Yoo+17]. Figure 2.3 shows the respective proton and helium measurements from space-based experiments, except for that of NUCLEON. Lipari and Vernetto [LV20] used the combined experimental data to fit the proton spectrum with a 'two-break' expression:

$$\Phi_\mathrm{H}(E) = K_\mathrm{H} \left(\frac{E}{E_0}\right)^{-\alpha_1} \left[1 + \left(\frac{E}{E_\mathrm{b}}\right)^{\frac{1}{w}}\right]^{-(\alpha_2-\alpha_1)w} \left[1 + \left(\frac{E}{E'_\mathrm{b}}\right)^{\frac{1}{w'}}\right]^{-(\alpha_3-\alpha_2)w'} \tag{2.4}$$

where E_0 is an arbitrary reference energy, K_H gives the absolute normalization, α_i are the spectral indeces of the three power-law segments, E_b and E'_b are the break energies at which the spectral shape changes, and w and w' parametrize the width of the two transitions [Lip18]. Their fit yields a spectral hardening from $\alpha_1 = 2.80 \pm 0.03$ to $\alpha_2 = 2.57^{+0.04}_{-0.06}$ at an energy $E_\mathrm{b} = 670^{+260}_{-150}\,\mathrm{GeV}$ and a softening to $\alpha_3 = 2.87^{+0.15}_{-0.10}$ at $E'_\mathrm{b} = 16^{+13}_{-8}\,\mathrm{TeV}$. The origin of these two features is not at all clear yet. The fact that a similar hardening and softening was observed in the spectra of nuclei heavier than helium [Agu+17; Atk+19] does, however, point to a rigidity-dependent universal behavior. Naively, it could be explained by the existence of three classes of galactic sources or by different propagation parameters at low, mid, and high rigidity. Another possibility is the existence of an ensemble of sources with different spectral shapes that in combination yield the spectrum we observe [LV20]. Additional precision measurements, especially beyond the knee, are required to further investigate these hypotheses.

[6] Data sources: [Agu+21a; Adr+22c; An+19; Cho+22; Adr+11; Mau+20; Ale+21; Adr+23].

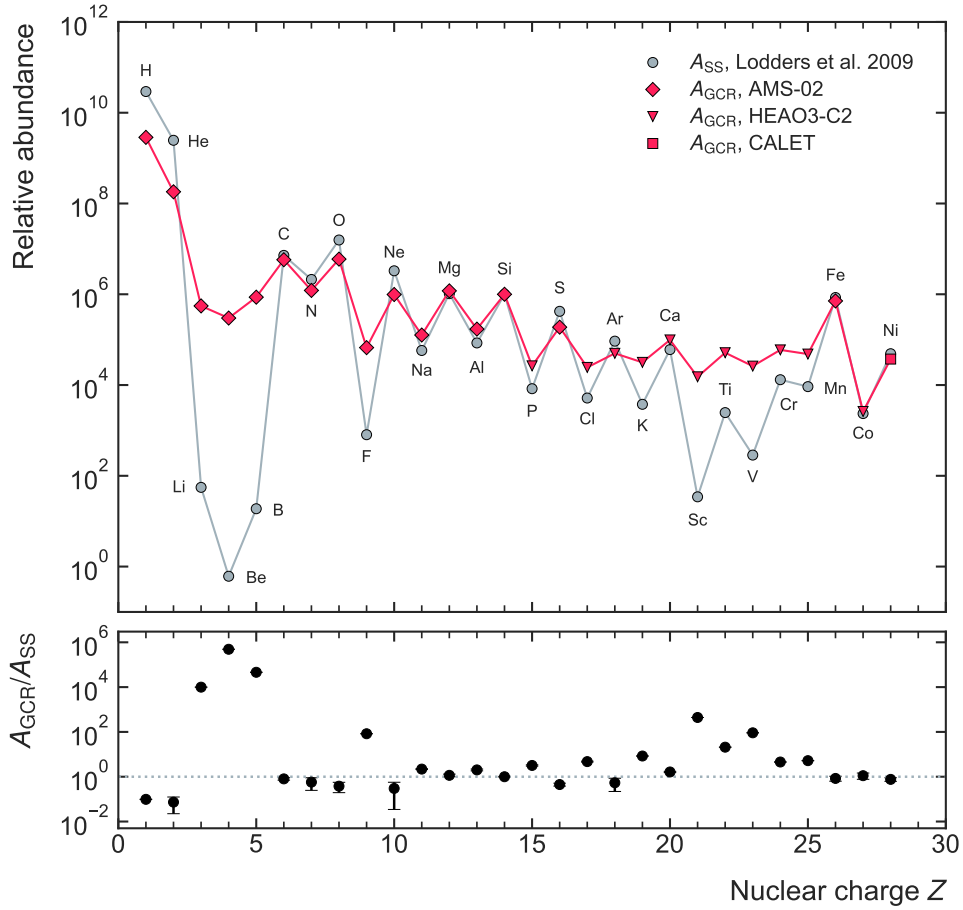

Figure 2.4: Elemental cosmic-ray abundances, A_{GCR}, compared to the abundances of elements in the Solar System, A_{SS} [LPG09]. GCR abundances are calculated at an energy of 20 GeV/n from fits to measurements of AMS-02 [Agu+21a; Agu+21b; Agu+21c; Agu+23], HEAO-3 [Eng+90], and CALET [Adr+22b]. For tabulated values, see Table 2.1.

2.1.2 Elemental Abundances and Individual Spectra

Cosmic rays effectively constitute a sample of extraterrestrial—and at the highest energies even extragalactic—matter, albeit somewhat modified by the processes governing the acceleration and propagation of particles throughout the universe. Their composition is in many aspects very similar to the

abundance of elements in our Solar System, though there are significant differences for some of them. This is highlighted by Figure 2.4, which compares the relative elemental abundances of cosmic-ray nuclei from hydrogen (H) through nickel (Ni) to those of the average matter in the Solar System. Both data sets are normalized to $A_{\mathrm{Si}} = 10^6$ to allow a direct comparison. Though all trans-iron elements up to uranium (U) and beyond have been detected in cosmic rays [Fow+87; Bin+89; Kea+97], I will not discuss them here. Their abundances are two to three orders of magnitude lower than that of cobalt (Co) [Hör03], rendering them largely irrelevant for the work presented in this thesis. Their study is, however, important for understanding the synthesis of ultra-heavy elements, many of which are overabundant in cosmic rays [KM18].

In the range from H through Ni, the elemental abundances in cosmic rays closely resemble those in the Solar System for many elements. The characteristic alternation between relative abundance and scarcity of elements with adjacent charge number Z is due to the nuclear binding energy: Nuclei with even number of protons and neutrons are most stable and hence more abundant, those with odd numbers of both are the least stable and almost not present at all [Pov+15]. The stability and abundance of even-odd combinations lies somewhere in between. In addition, nuclei with filled nuclear shells are particularly stable and are called magic nuclei [Hey90]; double-magic nuclei like He and O are extremely stable and correspondingly abundant [Gru20]. The general trend towards increasing stability for elements with larger binding energy (e.g., Fe) is somewhat obscured by the two abovementioned effects. The resulting abundance pattern can be observed in the elemental composition of both the Solar System and of cosmic rays. Three significant differences in the cosmic-ray composition do, however, stand out: the relative overabundance by orders of magnitude of the light elements lithium (Li), beryllium (Be), and boron (B); the overabundance of the sub-iron elements scandium (Sc), titanium (Ti), vanadium (Va), chromium (Cr), and manganese (Mn); and the underabundance of hydrogen and helium.

The origin of the overabundace of the Li-Be-B and sub-iron (Sc-Ti-V-Cr-Mn) groups is well understood: These elements are essentially absent as end products of stellar nucleosynthesis [Joh19; JFT20] and hence are significantly less abundant throughout the galaxy (and, likely, the universe). They are, however, present in cosmic rays due to the spallation of heavier elements—mostly carbon (C) and oxygen (O) in the case of Li-Be-B [MAR71; Rol+08] and iron (Fe) in the case of the sub-iron group [Ben+16]—in interactions of cosmic rays with interstellar matter. To distinguish them from *primary* cosmic-ray

Table 2.1: Elemental abundances: The values shown in 2.4 are compared to those obtained by Grieder [Gri01], Hillier [Hil84b], and Simpson [Sim83].

Element (Z)		**This Work**	**Grieder**	**Hillier**	**Simpson**
H	(1)	$2.87 \cdot 10^9$	-	$1.86 \cdot 10^9$	-
He	(2)	$1.81 \cdot 10^8$	-	$2.57 \cdot 10^8$	$2.70 \cdot 10^8$
Li	(3)	$5.53 \cdot 10^5$	-	$1.29 \cdot 10^6$	$1.36 \cdot 10^6$
Be	(4)	$2.99 \cdot 10^5$	$4.18 \cdot 10^5$	$7.50 \cdot 10^5$	$6.70 \cdot 10^5$
B	(5)	$8.63 \cdot 10^5$	$9.24 \cdot 10^5$	$2.00 \cdot 10^6$	$2.33 \cdot 10^6$
C	(6)	$5.77 \cdot 10^6$	$5.46 \cdot 10^6$	$7.14 \cdot 10^6$	$7.60 \cdot 10^6$
N	(7)	$1.21 \cdot 10^6$	$1.15 \cdot 10^6$	$1.79 \cdot 10^6$	$2.08 \cdot 10^6$
O	(8)	$5.96 \cdot 10^6$	$5.70 \cdot 10^6$	$6.50 \cdot 10^6$	$7.07 \cdot 10^6$
F	(9)	$6.67 \cdot 10^4$	$7.70 \cdot 10^4$	$1.21 \cdot 10^5$	$1.70 \cdot 10^5$
Ne	(10)	$9.88 \cdot 10^5$	$8.78 \cdot 10^5$	$1.14 \cdot 10^6$	$1.13 \cdot 10^6$
Na	(11)	$1.26 \cdot 10^5$	$1.32 \cdot 10^5$	$1.93 \cdot 10^5$	$2.58 \cdot 10^5$
Mg	(12)	$1.19 \cdot 10^6$	$1.14 \cdot 10^6$	$1.36 \cdot 10^6$	$1.42 \cdot 10^6$
Al	(13)	$1.71 \cdot 10^5$	$1.76 \cdot 10^5$	$2.00 \cdot 10^5$	$2.82 \cdot 10^5$
Si	(14)	$1.00 \cdot 10^6$	$1.00 \cdot 10^6$	$1.00 \cdot 10^6$	$1.00 \cdot 10^6$
P	(15)	$2.64 \cdot 10^4$	$3.02 \cdot 10^4$	$4.29 \cdot 10^4$	$5.30 \cdot 10^4$
S	(16)	$1.86 \cdot 10^5$	$1.78 \cdot 10^5$	$2.14 \cdot 10^5$	$2.31 \cdot 10^5$
Cl	(17)	$2.44 \cdot 10^4$	$2.85 \cdot 10^4$	$3.57 \cdot 10^4$	$6.40 \cdot 10^4$
Ar	(18)	$4.99 \cdot 10^4$	$5.53 \cdot 10^4$	$1.07 \cdot 10^5$	$1.02 \cdot 10^5$
K	(19)	$3.16 \cdot 10^4$	$3.76 \cdot 10^4$	$5.71 \cdot 10^4$	$7.20 \cdot 10^4$
Ca	(20)	$9.85 \cdot 10^4$	$1.04 \cdot 10^5$	$1.57 \cdot 10^5$	$1.61 \cdot 10^5$
Sc	(21)	$1.52 \cdot 10^4$	$1.60 \cdot 10^4$	$2.86 \cdot 10^4$	$4.50 \cdot 10^4$
Ti	(22)	$5.15 \cdot 10^4$	$5.70 \cdot 10^4$	$1.21 \cdot 10^5$	$1.02 \cdot 10^5$
V	(23)	$2.61 \cdot 10^4$	$3.02 \cdot 10^4$	$5.00 \cdot 10^4$	$6.70 \cdot 10^4$
Cr	(24)	$5.95 \cdot 10^4$	$6.73 \cdot 10^4$	$1.07 \cdot 10^5$	$1.18 \cdot 10^5$
Mn	(25)	$4.81 \cdot 10^4$	$5.13 \cdot 10^4$	$6.43 \cdot 10^4$	$8.20 \cdot 10^4$
Fe	(26)	$7.12 \cdot 10^5$	$7.16 \cdot 10^5$	$7.71 \cdot 10^5$	$6.08 \cdot 10^5$
Co	(27)	$2.62 \cdot 10^3$	$3.48 \cdot 10^3$	$< 1.43 \cdot 10^4$	-
Ni	(28)	$3.73 \cdot 10^4$	$3.94 \cdot 10^4$	$2.86 \cdot 10^4$	$3.70 \cdot 10^4$

particles and nuclei that are accelerated in the sources[7], these overabundant elements are known as *secondary* cosmic rays. Knowing the nuclear spallation cross-sections, and hence the probability for secondary nuclei to be produced through spallation per unit of matter traversed, we can estimate the average amount of matter encountered by cosmic rays on their way to Earth that would lead to the observed overabundances. One of the most widely used quantities for such calculations is the ratio of boron to carbon [Sta21].

Hydrogen and almost all helium were synthesized early in the evolution of the universe in a process called Big Bang nucleosynthesis [Joh19]. They are by far the most abundant elements in the universe and their underabundance (relative to elements with $Z > 3$) in cosmic rays is not yet fully understood. A less pronounced suppression is, however, also evident for other elements, for example nitrogen (N), oxygen, and neon (Ne). Possible explanations mostly concern the efficiency with which particles are injected into the cosmic-ray acceleration process, which is why I will discuss them in Section 2.2.

Figure 2.5 shows the spectra of a selection of cosmic-ray nuclei at Earth as measured by space- and balloon-borne experiments. So far, high-precision data from direct measurements with magnetic spectrometers over a broad energy range is only available for a selection of light elements—up to sulfur (S), in the case of AMS-02—and for iron. Despite the large ranges in energy and flux depicted, the figure indicates the challenges of combining data from instruments with different and, in some cases, unknown systematic uncertainties that operated at different times, sometimes decades apart. It nonetheless illustrates that the spectra of the individual elements up to Ni all have roughly the same shape, shifted to the right for larger Z (and mass). Above energies of about 10 GeV/n, the spectra are mostly undisturbed by solar modulation [Spu18] and therefore remain constant over time.

The spectral index $\alpha_i \simeq 2.7$ is almost the same for the majority of elements. Notable exceptions are the (significantly) softer spectra of protons and (light) secondary elements (e.g., Be and B). This is further highlighted by Figure 2.6, which shows a selection of individual elemental spectra measured by AMS-02. The fluxes are multiplied by $E^{2.7}$ to enhance the visibility of deviations from a power law with index 2.7. Each spectrum was fitted with Equation 2.4 in the range of 30 GeV to 300 GeV to determine the spectral index of the respective element. The resulting power laws, evaluated for energies between 10 GeV and 3 TeV, and their values of α_i are shown in the figure as well. The indices

[7] Sometimes also referred to as *primordial* cosmic rays.

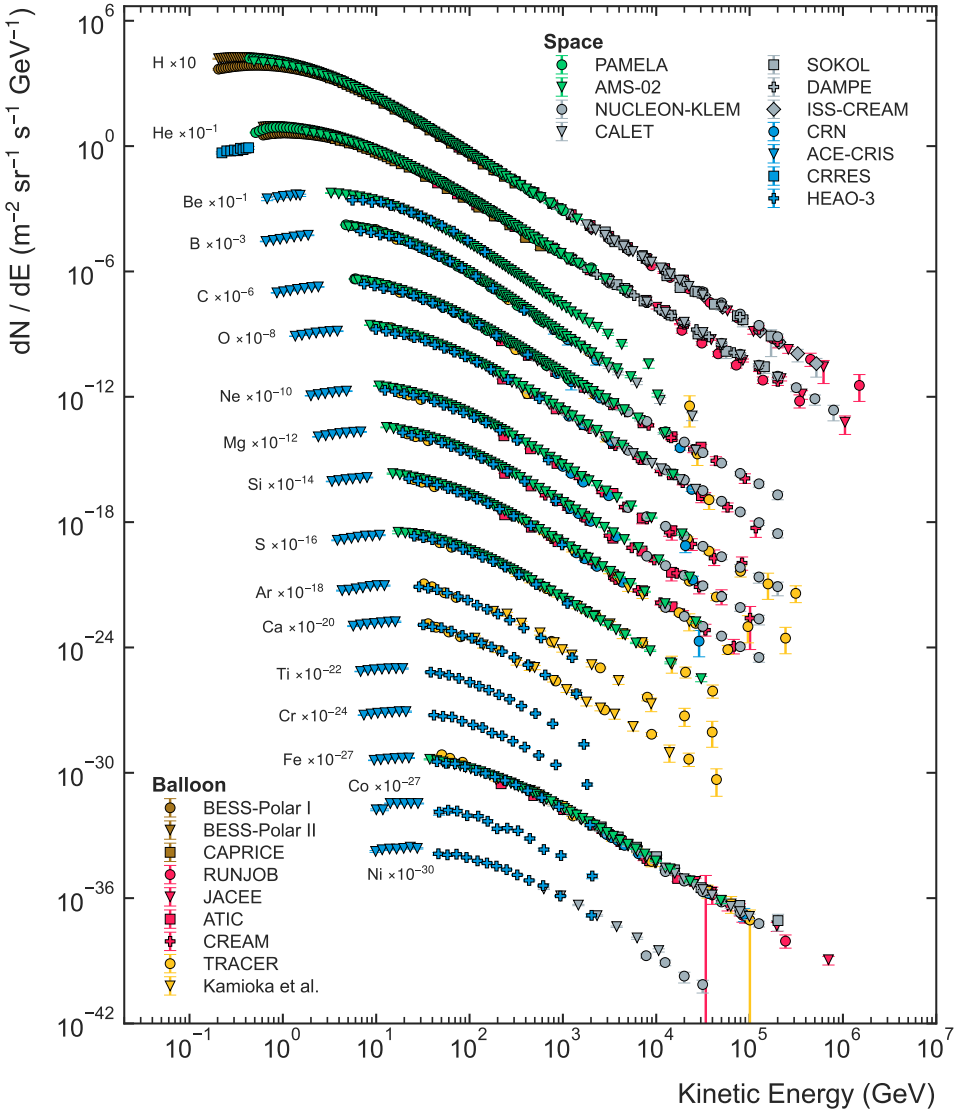

Figure 2.5: Scaled fluxes of individual cosmic-ray nuclei at Earth as measured by space- and balloon-borne experiments.[8] Colors indicate different types of experiments: green & brown—spectrometers, gray & red—calorimeters, blue & yellow—others.

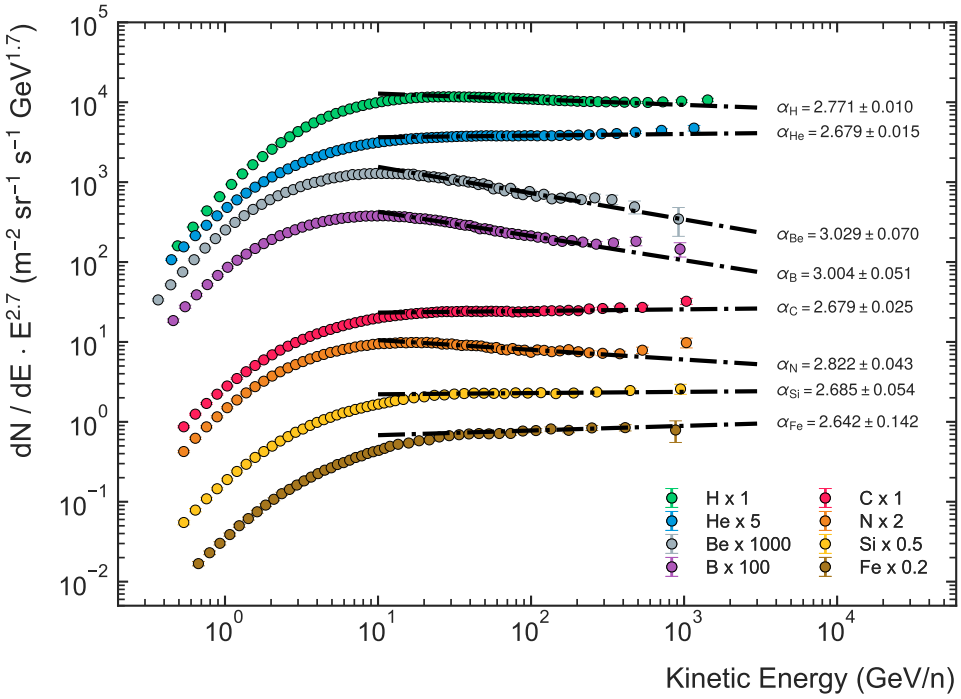

Figure 2.6: Scaled individual spectra of selected elements as measured by AMS-02 [Agu+23; Agu+21b]. Each spectrum was fitted with Equation 2.4 in the range of 30 GeV to 300 GeV to determine the spectral index of the respective element.

of He, C, Si, and Fe are all compatible with an average value of $\alpha_{\mathrm{avg}} = 2.67$. Hydrogen, however, has a slightly steeper spectrum with $\alpha_{\mathrm{H}} = 2.771 \pm 0.010$, most likely because protons have a different acceleration history than heavier nuclei [Sta21]. With $\alpha_{\mathrm{Be}} = 3.029 \pm 0.070$ and $\alpha_{\mathrm{B}} = 3.004 \pm 0.051$, the spectra of Be and B are even steeper (softer), which is likely due to their secondary nature. N has an index ($\alpha_{\mathrm{N}} = 2.822 \pm 0.043$) somewhere between those of primary and secondary elements, suggesting that its origin is of mixed nature.

The fits shown in Figure 2.6 are for illustration purposes only and do not represent an in-depth analysis of AMS-02 data, nor do they take into account

[8]Data sources: [Agu+21a; Agu+23; Agu+21b; Abe+16; Adr+11; Adr+14; Asa+98; TC98; Der+05; Pan+09; Cho+22; Yoo+17; Ahn+09; An+19; Ale+21; Adr+22c; Adr+23; Adr+22a; Adr+20; Adr+21b; Adr+22b; Eng+90; Obe+11; Ave+08; Swo+90; Mue+91; Iva+93; Kam+97; CGW00; Boe+03; Gre+19; Tur+21; Lav+13; Nol+06; Mau+20].

the observed differences between the data of AMS-02 and other instruments. The quite noticeable differences in spectral shape of H and He in measurements by space-borne experiments can, for example, be seen in Figure 2.3. The AMS collaboration itself has analyzed their H [Agu+15b] and He [Agu+15a] data using a simplified version of Equation 2.4 with only a single spectral break, yielding $\alpha_{\mathrm{H}}^{\mathrm{ams}} = 2.849^{+0.010}_{-0.008}$ and $\alpha_{\mathrm{He}}^{\mathrm{ams}} = 2.780 \pm 0.010$, as well as a hardening in both spectra that is roughly consistent with that found by Lipari and Vernetto [LV20], though not exactly. Indications of such a hardening are visible in nearly all spectra shown in Figure 2.6.

2.2 Origin of Cosmic Rays

The origin of cosmic rays is one of the major unanswered questions of modern astrophysics. Any proposed theory attempting to answer it must address two aspects of this question: Where are cosmic rays created? And where are they accelerated to the (ultra-high) energies we observe? It is not at all clear that the mechanisms that create cosmic-ray particles must be the same as those accelerating them. On the contrary: It is reasonable to assume that they are, at least to some degree, separate; while the former process must take place at a specific site (the source), the latter can, and likely does, happen anywhere along a particle's path from the source to Earth. Over the years, many theories of creation and acceleration were proposed, though I will focus my discussion here on the most widely accepted ones and only briefly mention alternative theories whenever warranted. For in-depth treatments of different aspects of cosmic-ray physics, I refer the interested reader to a number of comprehensive textbooks on the matter: [Lon12; GER16; Spu18; Sta21].

2.2.1 The Birth of Cosmic Rays

The light elements of the cosmic-ray spectrum are, like all nuclear matter in the universe, synthesized in the core of stars [NKT13]. The heaviest elements, however, can only be created in supernovae—i.e., the explosion of massive stars at end of their life when all hydrogen and helium have been fused to heavier elements and the star's outer layers collapse onto the core [BV21]. It is in this process that the temperatures (i.e., energies) required to efficiently overcome the fusion barrier for heavy elements are reached [Mey94; Joh19]. The elements created in the supernova are blown out into the space surrounding the dead star, where they can be swept up by younger ones. The life cycle

of stars, including their explosive death, is still a field of active research, which is why many questions concerning the creation of elements are not yet fully answered and the underlying physical processes are often only known qualitatively [JFT20].

2.2.2 Acceleration Mechanisms

The processes accelerating the elements created in stars and supernovae to cosmic-ray energies are less well understood, though significant advances have been made through multi-messenger astrophysics (i.e., the observation of objects via charged particles, gamma rays, X-rays, and neutrinos) [Més+19; Bec21]. It is widely believed that the bulk of cosmic rays is accelerated by shock fronts in supernova remnants (SNRs) [Aha13; TG18; Liu+22]. The question whether this acceleration mechanism can produce the observed spectrum over all energies is far from answered, though, with many alternative mechanisms proposed [BZB17; Car18; FM18; Kan18; AYO19; Acc+22]. What most models have in common is their common physical mechanism, diffusive shock acceleration [KD01; Hil05; TK15; Per+22]; it is mainly the nature of the shock-creating processes that is not yet fully understood.

On their way from the primary acceleration site to Earth, the spectrum of cosmic rays is altered significantly by interactions with the interstellar medium [AB18]. The transport (propagation) through regions of hot and cold gas, plasmas, and magnetic irregularities is diffusive [AB18; Che+18; SMP07; GAP07], and spallation reactions alter the composition as well [Com+05].

2.3 Cosmic Rays in the Heliosphere

The *heliosphere* is the vast bubble-like region of space surrounding the Sun that is altered by it, most notably by the ever present wind of charged particles blown out from our star (the *solar wind*) and the magnetic field created by it [KB14; Ric+22]. It extends well beyond the Kuiper belt and the only two human-made objects to ever leave it are the Voyager 1 and 2 probes [RB11]. The plasma-generated magnetic field deflects the lowest-energy cosmic rays and prevents them from entering our solar system. In a process called *solar modulation*, the energy spectrum of particles that reach the inner planets varies depending on the solar activity, i.e., the strength of the solar wind [Par58; Pot13]. The modulation follows a roughly 11-year cycle, half of the 22-year Hale cycle [Owe+15; GM17]; this short-term cycle is overlaid by several

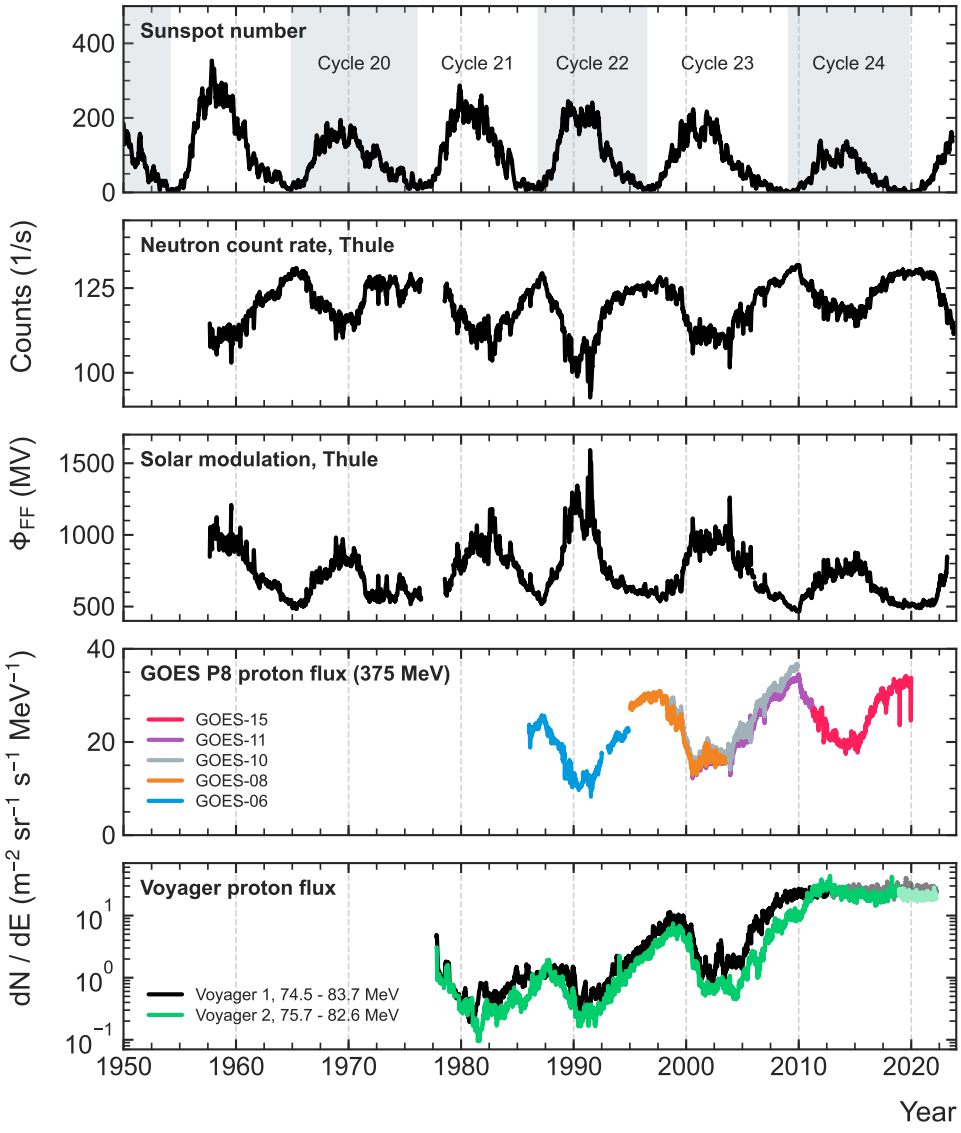

Figure 2.7: Overview of solar modulation in the heliosphere. The upper panel shows the time evolution of the sunspot number [SIL24], used as an indicator for the solar activity. The next two panels show the counts of atmospheric neutrons at Thule station[9] and the solar modulation parameter derived from it. The lower two panels show GCR proton fluxes recorded by GOES satellites[10] and the Voyager probes[11] [Seo+94; Cum+16].

long-term cycles spanning hundreds to thousands of years [Bis+23]. The flux intensity of cosmic rays with energies of less than about 30 GeV/n [Pot13] is anti-correlated with the solar activity because a larger solar-wind plasma density leads to stronger shielding of low-energy particles.

Figure 2.7 gives a qualitative overview of the effect of solar modulation. The upper panel shows the average daily number of observed sunspots, typically used as indicator of the solar activity (the more sunspots, the stronger the solar wind) [Hat15; CH18]. The second panel from the top shows the count rate of neutrons created in Earth's atmosphere by high-energy cosmic rays—which is anti-correlated with the solar activity [Man+16; VUM21]—recorded at Thule station in Greenland. From the neutron counts one can derive the parameter Φ_{FF} (see middle panel), which encodes the strength of the solar modulation calculated in a force-field approximation [Mau+15; Ghe+17]. The lower two panels show the flux of 375-MeV and 83-MeV protons recorded by the GOES satellites and the two Voyager probes, respectively. Both show that the particle flux is correlated with the neutron-monitor count rates and hence anti-correlated with the solar activity. The lower panel also shows that the flux measured by the Voyagers remained roughly constant after 2012, which is one of the indicators for them leaving the heliosphere (and therefore the region influenced by the solar wind).

Figure 2.8 illustrates how particles of lower energy are affected stronger by solar modulation. It covers the period around the last solar maximum in 2014. The lower two panels show the sunspot number and the solar modulation parameter (this time derived from the neutron count rates registered at Oulu [Mau+20]). The upper panel shows the proton flux (daily averages) in five different energy bins recorded by the AMS-02 experiment [Agu+21d]. The much stronger change in flux at lower energies can be seen clearly.

2.4 Solar Energetic Particles

Besides the Sun's constant emission of electromagnetic radiation and very-low-energy charged particles—the solar wind—our star also produces sudden

[9] Data provided by the University of Delaware Department of Physics and Astronomy and the Bartol Research Institute.

[10] `https://www.ngdc.noaa.gov/stp/satellite/goes/index.html` and `https://www.ngdc.noaa.gov/stp/satellite/goes-r.html`

[11] `https://voyager.gsfc.nasa.gov/download.html`

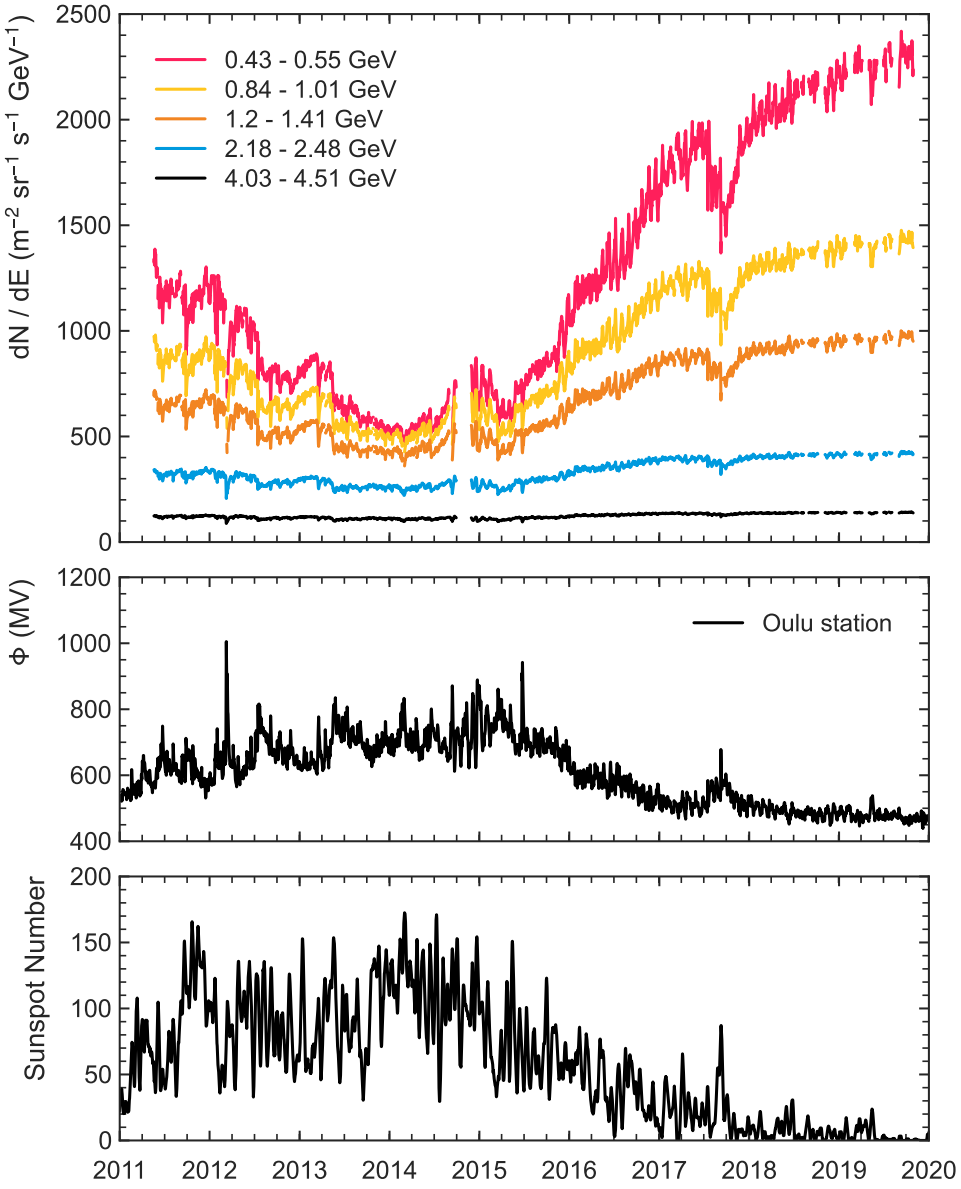

Figure 2.8: Effect of solar modulation of protons with different energies. Lower two panels: Neutron flux recorded at Oulu and modulation parameter derived from it [Mau+20]. Upper panel: Daily-average proton fluxes recorded by the AMS-02 experiment [Agu+21d].

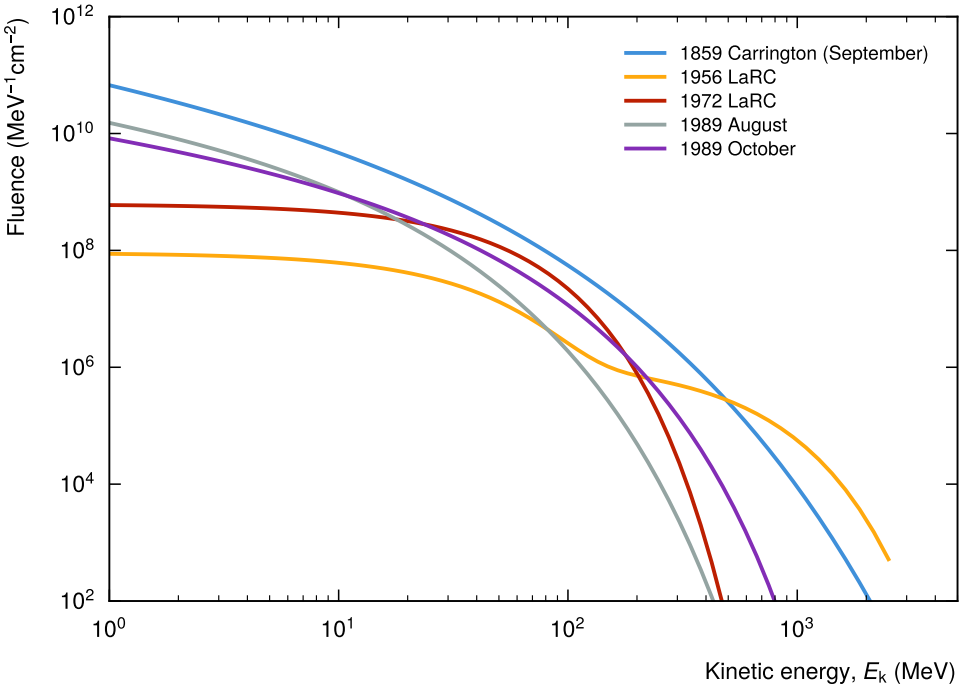

Figure 2.9: Total-fluence spectra (i.e., integrated over the entire event) of selected historic solar energetic particles (SEP) events. Data retrieved from OLTARIS [Sin+10].

intense bursts of charged particles (mostly protons, electrons, and some light nuclei [Rea18; Rea19]) with energies of typically several hundreds of MeV/n [Rea21]; proton energies can reach several GeV in extreme cases. The so-called SEP are accelerated by multiple processes in the solar corona, most importantly by the sources of flares [Chu90; Jon15] and coronal mass ejectionns (CMEs) [GNZ19], though their exact nature is not yet well understood [Che+15; Rea15; Vla+19; Whi+22; Yar22]. The onset of the events is usually sudden (minutes to hours), and they occur randomly [Jig+18; Ver20], albeit much more often during phases of high solar activity.

The intensity of a burst of SEP depends not only strongly on the intensity of the event but also on how well Earth's magnetosphere is magnetically connected to the acceleration site [Dro94; BSE20]. So does the spectral shape, which can often be described by a single or double power law. Figure 2.9 shows the total-fluence spectra of selected historic SEP events for illustration. The

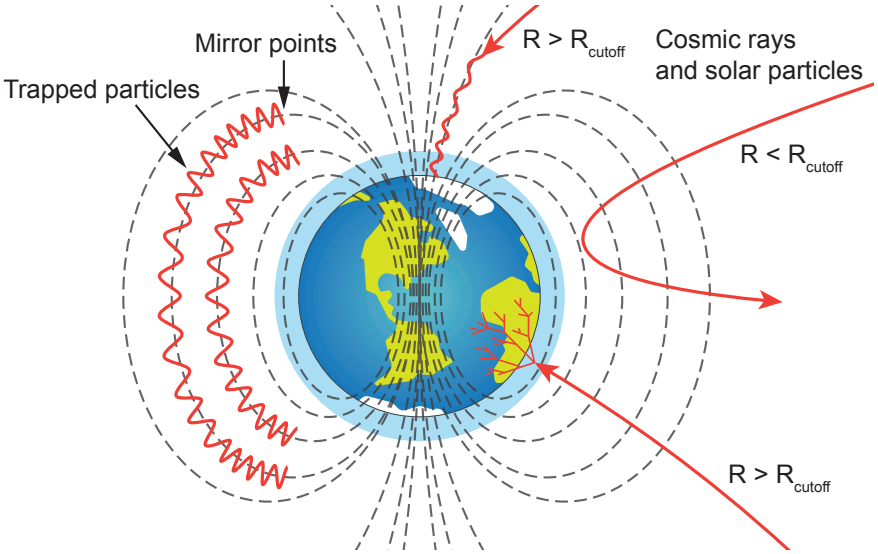

Figure 2.10: Interaction of charged particles with Earth's magnetic field. Left: Low-energy particles moving about the field lines can become trapped because the increasing field densities at the poles act as magnetic mirrors. Right: Only cosmic-ray and solar particles with rigidity higher the effective cutoff rigidity can reach the Earth; particles with lower rigidity are deflected.

probability for events of a given severity to happen scales inversely with the hardness of the spectrum, with extreme events happening only in frequently [Whi+17; Cli+22]. The temporal evolution of the flux intensity also varies widely [DD16].

2.5 Cosmic and Solar Particles Close to Earth

Close to Earth, cosmic rays and solar particles are strongly influenced by its *magnetosphere*, i.e., its magnetic field. The right side of Figure 2.10 summarizes the different outcomes of this interaction, which are best discussed as a function of *rigidity* [Büt18],

$$R = \frac{pc}{Ze}\,, \tag{2.5}$$

where p and Ze are the particle's momentum and charge, respectively, and c is the speed of light. Particles of the same rigidity and charge sign behave exactly the same in a magnetic field, irrespective of their other properties.

In the equatorial regions of Earth's magnetic field, particles traverse the magnetosphere roughly perpendicular to the field lines. If they have low rigidity, they are deflected such that they cannot closely approach the planet; particles with high rigidity can penetrate the field and interact with the atmosphere, leading to the creation of *air showers*, i.e., cascades of secondary particles created in hadronic interactions with atmospheric molecules. The transition between the two extremes is at the *effective (vertical) cutoff rigidity*, which is approximately given by [HKH13; Büt18]:

$$R_{\mathrm{c}} = \kappa \frac{1}{L^{\alpha}} \,. \tag{2.6}$$

Here, $\kappa \approx 14.823\,\mathrm{GV}$, $\alpha = 2.0311$, and L is the McIllwain parameter, which specifies the distance at which a magnetic field line crosses the equatorial plane [SSG87]. The cutoff rigidity therefore depends on the latitude, longitude, and height of a point above Earth. Precisely calculating the cutoff rigidity requires precise knowledge of the field configuration, which varies with time. Both models for doing so [Fin+20; LMU23] and tabulated values [Ger+21] are available.

Towards the poles, trajectories are increasingly parallel to the field lines, which minimizes the action of the magnetic field on them. Low-rigidity particles can therefore spiral (gyrate) along the field lines deep down into the atmosphere. At the poles, the cutoff rigidity is practically zero.

2.5.1 Radiation Belts

Particles with sufficiently low energies can (temporarily) become trapped in Earth's magnetic field [KB14], leading to the creation of the radiation belts [LH19] (often named after their discoverer James van Allen [VF59]). This is illustrated on the left side of Figure 2.10. The particles gyrate around and move along the field lines; the increasing density of lines (i.e., the field gradient) in the polar regions (of the magnetic field) acts as magnetic mirror and reverses the motion along the lines, resulting in a bouncing motion of the particle between the polar regions [RZ14].

Typically, Earth is surrounded by two toroidal radiation belts, and inner and an outer one. The inner belt contains mostly protons with energies up to several GeV and a small fraction of electrons; the outer one is populated primarily by electrons [Hel+20]. The prevalent source of protons (and electrons) in the inner belt is a process known as cosmic-ray albedo neutron decay (CRAND)—the decay of secondary neutrons created by high-energy cosmic rays in Earth's

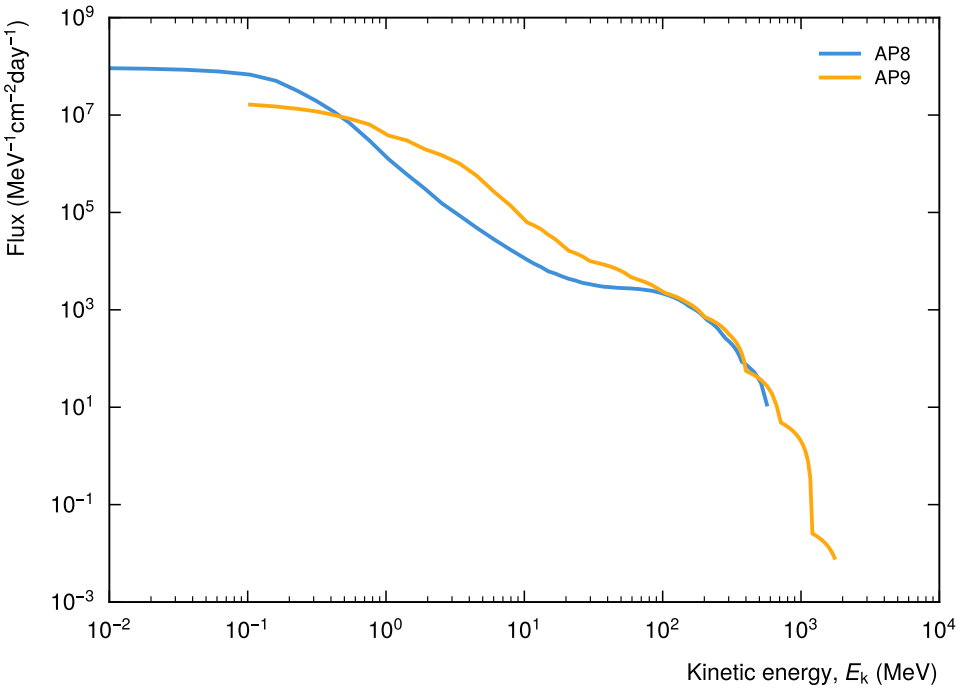

Figure 2.11: Cumulative spectra of protons trapped in Earth's inner radiation belt over one day for a spacecraft at 400 km and with an inclination of 51.6°. The AP8 model was evaluated on 1 July 2022. The AP9 model does not capture variations with solar activity. Data obtained from OLTARIS [Sin+10].

atmosphere [SHK13; Zha+19a]—though other sources also contribute. The belts are dynamic structures [Rip+20] that are affected by the solar activity, changes in Earth's magnetic field, and the cosmic-ray intensity [Bak+17; Zha+19b].

The tilt and shift of the magnetic field's dipole axis relative to the planet's rotational axis results in a somewhat asymmetric field configuration. As a consequence, the inner radiation belt is significantly closer to Earth's surface in a region over the south-eastern part of South America and over the South Atlantic. In this region, called the South Atlantic Anomaly (SAA) [PD16], spacecraft in LEO pass through the belt and are exposed directly to the radiation-belt particles. Figure 2.11 shows the spectra of trapped protons seen by the ISS (in an orbit with 400 km altitude and 51.6° inclination) according to the AP/AE8

and AP/AE9 models [SJE17]. The energy of electrons is generally less than about 10 MeV, which is why they can be easily shielded [Hel+20].

Chapter 3

Interaction of Radiation with Matter

The main focus of our work is the development of particle detectors for the characterization of cosmic rays and secondary radiation created in interactions of cosmic rays with some medium, for example Earth's atmosphere or the lunar surface. This chapter provides a brief primer on the fundamentals of radiation interactions, with particular emphasis on aspects relevant to the work described in this thesis. The focus lies on a somewhat detailed summary of the interaction of charged particles, and in particular heavy ions, with matter. In-depth knowledge of this complex topic is required for understanding the working principle of our detectors and the challenges associated with it. Building on this discussion, I also summarize the interactions of neutrons with matter. A brief review of relativistic kinematics and interaction cross-sections is given in Appendix A.

3.1 Units

In particle physics, the energy, momentum, and mass of particles are commonly expressed in *natural units*, in which the constants c (speed of light) and $\hbar$ (reduced Planck constant) are dimensionless and $c = \hbar = 1$ [KW20]. In this system, Equation A.8 reduces to

$$E = \sqrt{m_0^2 + p^2}, \tag{3.1}$$

with the energy given in GeV, the momentum in GeV/c, and the mass in $\mathrm{GeV/c^2}$ (or, analogously, with other unit prefixes).

In cosmic-ray research, and in space physics in general, the kinetic energies of nuclei, E_k, are often expressed in terms of MeV per nucleon (MeV/n) or GeV per nucleon (GeV/n), also referred to as the *specific energy*:

$$\frac{E_\mathrm{k}}{A} \simeq \mathrm{u}c^2(\gamma - 1), \tag{3.2}$$

where A is the atomic mass number and $\mathrm{u} = 1.6605 \cdot 10^{-27}\,\mathrm{kg}$ is the unified atomic mass unit [LR16]. In Equation 3.2, no (practical) distinction is made between the energy per atomic mass unit and the energy per nucleon because the difference between them is (much) smaller than 0.25% for stable isotopes of all elements heavier than helium [ICRU73].

3.2 Interaction of Charged Particles with Matter

Comprehensive knowledge of the processes governing the passage of charged particles through matter is not only a prerequisite for designing sensors that can detect and analyze cosmic rays. It is also important for understanding how radiation interacts with biological organisms and with matter surrounding it (e.g., in the form of shielding).

A charged particle (in the following called *projectile*) traversing a medium (the *target*) loses some or all of its kinetic energy in interactions with the medium's atoms. According to [ICRU73], these energy-loss processes can be roughly classified into five groups:

1. Electronic excitation and ionization of the target's atoms,
2. Excitation and ionization of the projectile,
3. Electron capture by the projectile,
4. Nuclear-scattering interactions,
5. Emission of electromagnetic radiation.

Protons and light ions lose energy dominantly via electromagnetic interactions with shell electrons and thereby excite or ionize atoms along their path through the medium (process 1). Radiative interactions (process 5), for example the emission of bremsstrahlung, are relevant at very high velocities, but only for relatively light particles. Nuclear losses—i.e., the transfer of energy to recoiling nuclei (process 4)—are negligible for light ions but become significant for

heavy ions at low and moderate velocities. Likewise, the contributions of projectile excitation (process 2) and electron capture (process 3) rise with increasing projectile mass and charge.

In addition, particles may lose energy in nuclear and chemical reactions. While the latter are irrelevant at the energies of interest here, the probability for the fragmentation of projectile (and target) nuclei is significant at typical cosmic-ray energies. Fragmentation is rarely discussed in the context of energy loss because it changes the identity of the projectile, and there is often little sense in relating the stopping of the fragments to that of the mother nucleus [ICRU73]. It does, however, significantly influence the energy-deposition profile in the stopping medium and is therefore important for particle detectors. I will discuss fragmentation in some detail, as it also affects the ability to identify particles in the detectors we are developing.

The following review is restricted to the discussion of the passage of *heavy* charged particles (all particles and nuclei except electrons and positrons) through matter. For the latter, bremsstrahlung (process 5) and annihilation (in case of positrons) must be taken into account [ICRU37]. Since the detection of electrons is not a goal of the projects presented in this thesis, these processes are only treated superficially. The only radiative process discussed in some detail is the emission of Cherenkov radiation for charged particles moving faster than the speed of light in a medium. Though unimportant for energy loss [Wor+22], it is often used in particle detectors.

The strength of the interaction between a particle of a given type and energy with a medium of density ρ is given by the *mass*[1] *stopping power* [ICRU90]

$$\frac{S}{\rho} = \frac{1}{\rho}\left\langle \frac{\mathrm{d}E}{\mathrm{d}x} \right\rangle , \tag{3.3}$$

where $\langle \mathrm{d}E \,/\, \mathrm{d}x \rangle$ is the mean energy lost by the particle per distance $\mathrm{d}x$ in the material. The quantity $S = \langle \mathrm{d}E \,/\, \mathrm{d}x \rangle$ denotes the *linear stopping power*. As discussed above, the stopping power for heavy charged particles comprises three major components [ICRU90]

$$\frac{1}{\rho}S = \frac{1}{\rho}S_{\mathrm{el}} + \frac{1}{\rho}S_{\mathrm{rad}} + \frac{1}{\rho}S_{\mathrm{nuc}} \tag{3.4}$$

$$= \frac{1}{\rho}\left\langle \frac{\mathrm{d}E}{\mathrm{d}x} \right\rangle_{\mathrm{el}} + \frac{1}{\rho}\left\langle \frac{\mathrm{d}E}{\mathrm{d}x} \right\rangle_{\mathrm{rad}} + \frac{1}{\rho}\left\langle \frac{\mathrm{d}E}{\mathrm{d}x} \right\rangle_{\mathrm{nuc}} , \tag{3.5}$$

[1] The adjective “mass” if often omitted.

where $(1/\rho)\langle \mathrm{d}E \,/\, \mathrm{d}x\rangle_{\mathrm{el}}$ is the *mass electronic*[2] *stopping power* due to Coulomb interactions with atomic electrons, $(1/\rho)\langle \mathrm{d}E \,/\, \mathrm{d}x\rangle_{\mathrm{rad}}$ the *mass radiative stopping power* due to the emission of bremsstrahlung in the electric field of atomic nuclei and electrons, and $(1/\rho)\langle \mathrm{d}E \,/\, \mathrm{d}x\rangle_{\mathrm{nuc}}$ the *mass nuclear stopping power* due to elastic Coulomb interactions with atomic nuclei.

In the following, I will discuss the electronic stopping power at some length, and briefly summarize the current knowledge of the radiative and nuclear stopping powers. I will then discuss important aspects of heavy-ion stopping, before closing with a brief treatment of Cherenkov radiation.

3.2.1 Electronic Energy Loss and Stopping Power

In the 1930s, Hans Bethe [Bet30] and Felix Bloch [Blo33a; Blo33b] provided the first quantum-mechanical treatment of the electronic energy loss of charged particles passing through matter. Though their work is largely still valid today, there have been numerous refinements—notably by Niels Bohr [Boh48] and Ugo Fano [Fan63]—that resulted in corrective terms for various kinematic regimes. Roughly following the summary in [KW20], I only review the aspects most relevant to the design of the particle detectors presented in this thesis. Comprehensive treatments can, for example, be found in [LR16; And+17; Wor+22; ICRU37; ICRU49; ICRU73].

A particle traversing a medium loses energy in a stochastic series of Coulomb interactions with the electrons of the medium's constituent atoms that, for practical purposes, often cannot (and need not) be treated individually. We thus define the *mean electronic energy loss* per path length, which depends on the properties of the medium and of the particle, in terms of the cross-section $\mathrm{d}\sigma_{\mathrm{el}}/\,\mathrm{d}T$ for collisions with atomic electrons [KW20; ICRU49]:

$$-\left\langle \frac{\mathrm{d}E}{\mathrm{d}x} \right\rangle_{\mathrm{el}} = n \int_{T_{\min}}^{T_{\max}} T \frac{\mathrm{d}\sigma_{\mathrm{el}}}{\mathrm{d}T}(m, \beta, T)\, \mathrm{d}T \tag{3.6}$$

Here, n is the number density of the medium, and m and β are the particle's mass and velocity, respectively. The integral from $T_{\min}$ to $T_{\max}$ covers all allowed energy transfers. Note the minus sign, which shows that energy is lost by the particle.

The integral of Equation 3.6 can be divided into two regions of energy loss. For energy transfers much larger than the binding energy of shell electrons

[2] In the old nomenclature of the International Commission on Radiation Units & Measurements (ICRU) also referred to as the *collision stopping power* [ICRU49; ICRU90].

($T \geq T_1$), the latter can be neglected, and the integral can be computed straightforwardly. For $T < T_1$, the binding energies must be taken into account in a quantum mechanical treatment and the integral cannot be solved classically. T_1 is typically in the range of 0.01 MeV to 0.1 MeV [KW20]. Equation 3.6 can hence be rewritten as [KW20]

$$-\left\langle \frac{\mathrm{d}E}{\mathrm{d}x} \right\rangle_{\mathrm{el}} = n_e \int_{T_1}^{T_{\max}} T \frac{\mathrm{d}\sigma_{\mathrm{el}}}{\mathrm{d}T} \,\mathrm{d}T - \left\langle \frac{\mathrm{d}E}{\mathrm{d}x} \right\rangle_{T<T_1} \tag{3.7}$$

where n_e is the electron density of the medium,

$$n_e = Z_2 \frac{\rho N_{\mathrm{A}}}{A_2}, \tag{3.8}$$

with ρ being the medium's mass density, A_2 its atomic mass number, and Z_2 its atomic number (the number of protons in the nucleus).

Rutherford Scattering Off Shell Electrons ($T \geq T_1$)

For $T \geq T_1$, the transferred energy is always large enough to free a shell electron from its atom and impart some kinetic energy on it. Since T_1 is much larger than the binding energy of the electron, the latter can be neglected and the electron can be regarded as free. The scattering of the incoming projectile particle off the electron can therefore be treated as *Rutherford scattering* [KW20]. Using the Mott cross-section (to take into account possible spin flips of the target electron), we can solve Equation 3.6 for $T \geq T_1$ [KW20]:

$$-\left\langle \frac{\mathrm{d}E}{\mathrm{d}x} \right\rangle_{T \geq T_1} = n_e \int_{T_1}^{T_{\max}} T \frac{2\pi Z_1^2 \alpha^2 \hbar^2}{\beta^2 m_e T^2} \left(1 - \beta^2 \frac{T}{T_{\max}}\right) \mathrm{d}T \tag{3.9}$$

$$\simeq \frac{2\pi Z_1^2 \alpha^2 \hbar^2}{\beta^2 m_e} n_e \left(\ln \frac{T_{\max}}{T_1} - \beta^2\right) \tag{3.10}$$

Here, Z_1 is the charge of the projectile particle or nucleus, m_e the mass of the electron, and α the fine structure constant.

Maximum Energy Transfer

In the above approximation, the maximum energy transfer can be derived from the kinematics of elastic scattering. Again neglecting the binding energy, we

obtain [KW20]:

$$T_{\max} = \frac{2m_e c^2 \beta^2 \gamma^2}{1 + 2\gamma m_e/m + (m_e/m)^2} \tag{3.11}$$

$$\simeq \begin{cases} 2m_e c^2 (\beta\gamma)^2 & \text{for} \quad \gamma m_e < m \\ \gamma m c^2 = E & \text{for} \quad \gamma \to \infty \\ m_e c^2 (\gamma - 1) = E - m_e c^2 & \text{for} \quad m = m_e \end{cases} \tag{3.12}$$

Equation 3.12 shows that the full energy of the incoming particle can be transferred to a single shell electron only in the relativistic limit ($\gamma \to \infty$).

Minimum Energy Transfer ($T < T_1$)

Below the ionization threshold, energy can be transferred to the target atom only in discrete, non-zero quantities that correspond to the energies required to lift electrons to allowed excites states. For particle velocities comparable to or smaller than the electron orbit velocities, interference effects also become relevant [KW20]. Describing the energy loss via atomic excitations is thus a highly complex task that was first attempted comprehensively by Bethe [Bet30]. For the low-energy-transfer region of Equation 3.7, his calculations yielded

$$-\left\langle \frac{\mathrm{d}E}{\mathrm{d}x} \right\rangle_{T<T_1} = \frac{2\pi Z_1^2 \alpha^2 \hbar^2}{\beta^2 m_e} \left[\ln \frac{2m_e c^2 \beta^2 T_1}{I^2} - \ln \frac{1}{\gamma^2} - \beta^2 \right], \tag{3.13}$$

where I is the mean excitation energy of the atom. Its logarithm is defined by the logarithmic sum of the excitation energies, E_n, for transitions to the energy levels n, weighted by the corresponding oscillators strengths, f_n:

$$\ln I = \sum_\mathrm{n} f_\mathrm{n} \ln E_\mathrm{n} \tag{3.14}$$

Since Equation 3.14 is difficult to compute analytically, the mean excitation energy is usually determined from experimental data. Values for a wide range of elemental and compound media are published by the National Institute of Standards and Technology (NIST) [HS04].

The Bethe Equation for the Electronic Energy Loss

With Eqs. 3.8, 3.10, and 3.13, we can re-write Equation 3.7 to arrive at an equation that describes the mean rate of electronic energy loss of moderately

relativistic charged (heavy) particles in matter [KW20; Wor+22; ES12]:

$$-\left\langle \frac{\mathrm{d}E}{\mathrm{d}x} \right\rangle_{\mathrm{el}} = K \frac{Z_2}{A_2} \frac{Z_1^2}{\beta^2} \left[\frac{1}{2} \ln \frac{2 m_e c^2 \beta^2 \gamma^2 T_{\max}}{I^2} - \beta^2 - \frac{\delta(\beta\gamma)}{2} \right] \tag{3.15}$$

This equation is usually called the *Bethe equation* and its full derivation is based on a fist-order Born approximation[3]. The corrective term $\delta/2$ is the *density correction* and is relevant at high particle energies. For easier reference, I repeat here the definition of all quantities used in Equation 3.15:

- $K = 4\pi N_{\mathrm{A}} r_e^2 m_e c^2 = 0.307\,\mathrm{cm}^2/\mathrm{mol}$, with the classical electron radius $r_e = \alpha\hbar/(m_e c) \simeq 2.8\,\mathrm{fm}$.
- Z_1 and β are the charge and velocity of the projectile particle.
- Z_2 and A_2 are the atomic number (proton number) and mass number of the traversed medium.
- I is the mean excitation energy of the medium's atoms.
- $T_{\max}$ is the maximum possible energy transfer to a shell electron (see Equation 3.12).
- δ is the density correction, relevant at high particle energies.

The Bethe equation is accurate to a few percent in the region of $0.1 < \beta\gamma < 1000$ (corresponding to proton kinetic energies of about 5 MeV to 1 TeV). At $\beta\gamma \simeq 0.1$, the projectile speed is comparable to the electron orbit velocities; at $\beta\gamma \simeq 1000$, radiative effects start to become relevant [Wor+22]. Both limits depend on the atomic number of the traversed medium.

Equation 3.15 can be re-written as

$$-\left\langle \frac{\mathrm{d}E}{\mathrm{d}x} \right\rangle_{\mathrm{el}} = K \frac{Z_2}{A_2} \frac{Z_1^2}{\beta^2} L(\beta), \tag{3.16}$$

where L is a dimensionless parameter called the *stopping number* that describes the essential physics of the electronic interactions [LR16]. In the form given here, Eqs. 3.15 and 3.16 define the mass electronic stopping power of a particle in a medium, a quantity of dimension [energy · mass^{-1} · area] for which typical units are $\mathrm{MeV g^{-1} cm^2}$. It is roughly the same for most materials, decreasing

[3]The first-order Born approximation assumes free electrons, a condition that is not met for $T < T_1$ in Equation 3.13. It was, however, shown by Mott that the Born approximation can be applied at energies much smaller than the electron binding energies [Mot31], as long as the projectile speed is not large compared to the speed of electrons in the K shell [LB37].

only slowly with Z [Wor+22]. The linear electronic stopping power is hence defined as

$$S_{\mathrm{el}} = \left\langle \frac{\mathrm{d}E}{\mathrm{d}x} \right\rangle_{\mathrm{el}} \rho, \tag{3.17}$$

has dimension [energy $\cdot$ cm^{-1}], and is typically given in MeV/cm.

Corrections at High and Low Energies

The Bethe formula can be modified by higher-order corrections to extend its validity to lower and higher energies. One of these, the density correction [Ste52; CF70; SSB82], is already included in the definition of Equation 3.15 and accounts for the screening of the expanding electric field of highly relativistic projectile particles by the polarization of the medium [KW20]. For very high energies ($\gamma \to \infty$, $\beta \to 1$), it takes the form [Wor+22]

$$\frac{\delta(\beta\gamma)}{2} \xrightarrow{\gamma\to\infty} \ln\frac{\hbar\omega_{\mathrm{p}}}{I} + \ln\beta\gamma - \frac{1}{2}, \tag{3.18}$$

where $\hbar\omega_{\mathrm{p}} = \sqrt{4\pi N_e r_e^3} m_e c^2/\alpha$ is the medium's plasma energy and N_e is its electron density. The density correction truncates the relativistic rise of the energy loss by replacing the $\ln\beta^2\gamma^2 T_{\max}$ term in Equation 3.15 with $\ln T_{\max}$. It is significant only when the kinetic energy of the particle is of the same order or larger than its rest energy. For protons, it reaches the one-percent level above 500 MeV and the ten-percent level above 10 GeV [ICRU49].

More important, however, are corrections at low energies, as the detectors presented in this thesis need particles to (almost) stop in their active volumes to identify them. They can be added to the Bethe equation by extending the definition of the stopping number in Equation 3.16 [Wor+22; ICRU49]:

$$L(\beta) = L_{\mathrm{a}}(\beta) - \frac{C(\beta)}{Z_2} + Z_1 L_1(\beta) + Z_1^2 L_2(\beta) \tag{3.19}$$

Here, L_{a} is the terms in square brackets in Equation 3.15, C/Z_2 is the sum of shell corrections, and $Z_1 L_1$ and $Z_1^2 L_2$ are the Barkas and Bloch corrections, respectively. With these additional terms, the Bethe equation is accurate to the percent level down to $\beta \simeq 0.05$, or about 1 MeV for protons [Wor+22]. Table 3.1 summarizes the magnitude of the corrections, which I briefly discuss below, for protons in aluminum. The energy-dependent magnitudes are nicely illustrated in [And+17].

Shell Corrections Shell corrections amend the requirement of Bethe's theory that the projectile velocity be much greater than the bound electron velocity. With decreasing velocity of the projectile, approaching that of the K-shell electrons, the contribution to the energy loss of collisions with these electrons begins to fall off. If the velocity falls below that of the K-shell electrons, the latter cease participating in the stopping process altogether and the contributions of the L and higher shells start to become reduced as well [And+17]. There exist several methods to compute the term $C(\beta)/Z_2 = (C_\mathrm{K} + C_\mathrm{L} + ...)/Z_2$, where C_i are the individual corrections for each atomic shell [Bic02; Por87; Bon67; McG83; AZ77], though ultimately most of them rely to some degree on experimental data [ICRU49]. The magnitude of the shell corrections is substantial: For a 30-MeV proton traversing aluminum it is 0.6%, increasing to almost 10% as the proton's energy decreases to 0.3 MeV [Wor+22; Zie99].

Barkas-Andersen Correction The Barkas-Andersen correction[4] accounts for the difference in Coulomb interaction of shell electrons with positively and negatively charged projectile particles [JM72; ARB72; ARB73; Lin76]. The repulsive nature of the latter interaction leads to a lower energy loss for negative particles. As a consequence, a particle and its antiparticle do not have the same range in matter [And+89; Møl+97]. No complete theory exists that would allow the analytic calculation of the correction [Bic90]. Basbas even argued that the shell and Barkas corrections probably cannot be treated as unrelated effects [Bas84], further complicating their mathematical description. Several semi-empirical approaches based on experimental data have been developed and yield different results [ARB72; Lin76; MS89; Bic90; ICRU49]. For protons in aluminum, the magnitude of the Barkas correction is less than 0.1% at 30 MeV but increases to about 17% at 0.3 MeV in the widely used model of Ashley et al. [ARB72; Wor+22]. A more recent and straightforward expression by Ziegler [Zie99] yields similar results.

Bloch Correction The Bloch correction takes account of perturbations of the atomic wave functions in close collisions of the projectile with shell electrons. It stems from Bloch's energy-loss theory—derived without the first-order Born approximation [Blo33a; Blo33b]—and is valid when the projectile velocity is large compared to the velocities of the electrons [LS96; ICRU49]. The theoretically derived mathematical form must be evaluated numerically [Ahl80], but a

[4]The Barkas-Andersen effect is often simply called the Barkas effect. I follow the naming recommendation of the ICRU to highlight Andersen's instrumental role in finding the effect.

	30 MeV	**0.3 MeV**
Shell corrections	0.6%	9.9%
Barkas correction	<0.1%	17%
Bloch correction	<0.3%	7%

Table 3.1: Magnitude of corrections to the Bethe equation (Equation 3.15) for protons with kinetic energies of 30 MeV and 0.3 MeV in aluminum. Values taken from [Wor+22].

simplified analytical expression was developed by Bichsel and Porter [BP82]. The correction's magnitude is less than 0.3% for protons of 30 MeV kinetic energy in aluminum and rises to 7% at 0.3 MeV [Wor+22].

No adequate theory exists for $0.01 < \beta\gamma < 0.05$ (about 100 keV to 1 MeV for protons) [Wor+22]. Andersen and Ziegler developed a phenomenological function based on fits to experimental data that is widely used instead [AZ77]. Lindhard et al. provided a successful framework for projectile velocities lower than the electron velocities ($\beta < 0.01$) [LSS63].

In addition to the nuclear stopping power (see Section 3.2.4), several corrections primarily relevant for fast, heavy ions [Bic02] can be added to the Bethe equation by further extending the stopping number in Equation 3.19 [Ahl80]. One example is the close-collision Mott cross-section [Ahl78], the inclusion of which may result in corrections of up to 2% for Fe ions with kinetic energies of 300 MeV per nucleon [Bic02].

Electronic Energy Loss of Electrons and Positrons

The electronic energy loss of electrons and positrons can be derived analogously to that of heavy charged particles. Interactions with shell electrons are likewise dominating but the different kinematics of collisions between particles of the same mass need to be taken account of. Therefore, the Mott [Mot30] and Møller [Møl32] differential cross-sections for electron-electron scattering and the Bhabha [Bha36] differential cross-section for electron-positron scattering must be used for the derivation of the energy loss. For small energy transfers, the cross-sections are similar to the one for heavy charged particles [KW20].

3.2.2 δ Electrons and Restricted Electronic Energy Loss

In near-central collisions of the projectile with shell electrons, large energies can be imparted on knocked-out electrons. The kinetic energy of these so-called *δ electrons* follows a distribution proportional to $1/T^2$, with a tail up to $T_{\max}$ (in the relativistic limit) [KW20]. Such high-energy electrons have a large range in matter; they can thus carry significant portions of the energy lost by the projectile away from the interaction site and cause secondary ionization [And+17; LR16]. In thick targets (detectors) and for highly relativistic particles, this potentially leads to a deterioration of the spatial resolution. In thin targets, δ electrons may have sufficient energy to leave the medium altogether, leading to a discrepancy between energy lost by them and the energy measurable in the detector, and hence to a deterioration of the energy resolution [LR16].

We can determine the maximum energy T_{cut} that may be imparted on an electron such that its range is restricted to a local region around the track of the incident particle. The value of T_{cut} depends strongly on the application at hand [And+17]. The corresponding *restricted mass electronic stopping power* (without low-energy corrections) is then defined as [KW20]:

$$\frac{1}{\rho} S_{\mathrm{el}}(T_{\mathrm{cut}}) = \frac{1}{\rho} \left\langle \frac{\mathrm{d}E}{\mathrm{d}x} \right\rangle_{T<T_{\mathrm{cut}}} \tag{3.20}$$

$$= -K \frac{Z_2}{A_2} \frac{Z_1^2}{\beta^2} \left[\frac{1}{2} \ln \frac{2 m_e c^2 \beta^2 \gamma^2 T_{\mathrm{cut}}}{I^2} - \frac{\beta}{2} \left(1 + \frac{T_{\mathrm{cut}}}{T_{\max}} \right) - \frac{\delta(\beta\gamma)}{2} \right] \tag{3.21}$$

The restricted stopping power saturates at high energies in the so-called *Fermi plateau* because $T_{\max}$, which increases with γ, is replaced by a fixed T_{cut} [KW20]. In general, Equation 3.20 describes the energy loss of highly relativistic particles in *thin* targets more accurately than Equation 3.15. Its validity is, however, severely limited for values of T_{cut} close to or smaller than the K-shell binding energies [And+17; ICRU37].

3.2.3 Linear Energy Transfer

A concept that is widely used in radiation dosimetry is that of the *linear energy transfer (LET)*. Traditionally, the LET has been defined as being identical to the restricted electronic stopping power (see Equation 3.20) [And+17; ICRU37]. However, the ICRU has more recently updated its definition—based on the work by Kellerer et al. [KR90; KHR92; CKR95]—to exclude only the *kinetic*

energy of δ electrons when it is larger than T_{cut}. Contrary to Equation 3.20, the *binding energy* that must be expended to free the electrons is not excluded [ICRU85a]. With $T_{\mathrm{cut}} \equiv \Delta$, the definition of LET thus becomes [And+17]

$$L_\Delta = \rho N_{\mathrm{A}} \frac{Z_2}{A_2} \int_{T_{\mathrm{min}}}^{T_{\mathrm{max}}} T \frac{\mathrm{d}\sigma_{\mathrm{el}}}{\mathrm{d}T}\, \mathrm{d}T - \epsilon_{\mathrm{ke}>\Delta} = S_{\mathrm{el}} - \epsilon_{\mathrm{ke}>\Delta}, \tag{3.22}$$

where $\epsilon_{\mathrm{ke}>\Delta}$ is the sum of the kinetic energies of δ electrons with energies exceeding Δ.

The LET is generally larger than the restricted stopping power because it includes the binding energy for *all* interactions, also those for which the δ electron kinetic energy is larger than Δ. Consequently, the LET more accurately reflects the energy that is deposited locally (i.e., close to the primary interaction site) in the target and is thus a more meaningful quantity in radiation dosimetry than the restricted stopping power [And+17]. For $E_{\mathrm{k}} < \Delta$, no energy transfer larger than Δ can occur and hence $L_\Delta = S_{\mathrm{el}}$. Similarly, for $\Delta \to T_{\mathrm{max}}$, the LET approaches the stopping power, often written as $L_\infty \equiv S_{\mathrm{el}}$ [And+17].

3.2.4 Radiative Energy Loss and Stopping Power

Radiative energy loss is mostly caused by bremsstrahlung, which is emitted when a charged particle is accelerated (or decelerated) in the electric fields of a medium's constituent atoms. Since the Coulomb acceleration strongly depends on the mass of the projectile particle, bremsstrahlung is practically only relevant for electrons (and positrons) [And+17], for which it is the dominant energy-loss channel over a large range of kinetic energy [Wor+22].

For both electrons and positrons, the mass radiative stopping power can be calculated from [ICRU37; And+17]

$$\frac{1}{\rho} S_{\mathrm{rad}} = \frac{1}{\rho} \left\langle \frac{\mathrm{d}E}{\mathrm{d}x} \right\rangle_{\mathrm{rad}} \tag{3.23}$$

$$= N_{\mathrm{a}} \left[\int_0^{E_{\mathrm{k}}} k \frac{\mathrm{d}\sigma_{\mathrm{e}}}{\mathrm{d}k}\, \mathrm{d}k + Z \int_0^{E'_{\mathrm{k}}} k \frac{\mathrm{d}\sigma_{\mathrm{n}}}{\mathrm{d}k}\, \mathrm{d}k \right], \tag{3.24}$$

where $\mathrm{d}\sigma_{\mathrm{n}}/\,\mathrm{d}k$ is the differential cross-section for the emission of a photon with energy k due to the interaction of the projectile with the screened electric field of the atomic nucleus and $\mathrm{d}\sigma_{\mathrm{e}}/\,\mathrm{d}k$ is the corresponding differential cross-section for the interaction with shell electrons [ICRU37]. E_{k} is the kinetic

energy of the incident electron (positron) and $E'_\mathrm{k} < E_\mathrm{k}$ is the maximum energy of a photon that can be emitted in electron-electron interactions [ICRU37].

The first quantum-electrodynamical calculation of Equation 3.23 was carried out by Bethe and Heitler [BH34]. Many additions and corrections to the original Bethe-Heitler theory have since been made, for example by Elwert [Elw39], Schiff [Sch51], Koch and Motz [KM59], and Pratt et al. [Pra+77]. The most complete treatment—which continues to be widely used today—was published by Seltzer and Berger [SB85] and builds on many of the previously published works. Besides their original publication, the interested reader may consult the comprehensive summaries in [And+17; KW20; LR16; ICRU37].

In the following, I will briefly motivate why the radiative stopping power is irrelevant for my work. Irrespective of the type of incident particle, the radiative and electronic energy losses have different dependencies on the mass, m, and the kinetic energy, E_k, of the projectile particle and on the atomic number, Z, of the medium [KW20]:

$$\left\langle \frac{\mathrm{d}E}{\mathrm{d}x} \right\rangle_\mathrm{el} \propto Z_2 \ln \frac{E}{m} \tag{3.25}$$

$$\left\langle \frac{\mathrm{d}E}{\mathrm{d}x} \right\rangle_\mathrm{rad} \propto Z_2^2 \frac{E}{m^2} \tag{3.26}$$

Consequently, the electronic energy loss dominates at low energies and the radiative one at high energies. The *critical energy*, E_c, is often defined as the energy for which the two energy losses are equal in magnitude [BS64; KW20]. In an alternative definition (for electrons) by Rossi, the critical energy is the energy at which the electronic energy loss after one radiation length[5] is equal to the energy of the radiating electron [Ros52]. See [Wor+22] for a comparison of the two definitions. Using Rossi's definition, the critical energy for electrons in solids and liquids can be approximated by

$$E_\mathrm{c}^{e^-} \simeq \frac{610\,\mathrm{MeV}}{Z_2 + 1.24}, \tag{3.27}$$

with average deviations of the values for individual elements from this function of about 2.2% [Wor+22]. In materials up to iron ($Z_2 \leq 26$), it thus lies in the range of tens to hundreds of MeV, rendering it a dominant effect in many experiments involving electrons.

[5]The radiation length is the distance after which an electron on average possesses $1/\mathrm{e}$ of its initial kinetic energy [KW20].

Due to their higher mass ($m_e = 511\,\mathrm{keV}$ vs. $m_\mu = 105.7\,\mathrm{MeV}$), the critical energy for muons, E_c^μ, in most materials is already in the range of several hundred GeV to a few TeV[6]. The critical energy for protons ($m_\mathrm{p} = 938.3\,\mathrm{MeV}$) is much higher, approximately though not exactly reflected by the $\ln(1/m)$ and $1/m^2$ dependencies of the electronic and radiative energy losses, respectively [Wor+22]. The latter can therefore be neglected at the energies relevant to the work presented in this thesis.

3.2.5 Nuclear Energy Loss and Stopping Power

Charged particles also lose energy in elastic collisions with the atomic nuclei of a medium. As a result, they can be deflected considerably. Though these interactions are strictly speaking no proper nuclear reactions, the term *nuclear energy loss* has historically been used to describe them [And+17].

The energy transferred in a Coulomb interaction between a projectile and a recoiling nucleus is proportional to the ratio of their masses and is thus negligible for light particles like electrons [And+17]. For heavy particles, however, it constitutes a significant mode of energy loss if the projectile's speed is smaller than the orbital velocities of the atomic electrons [And+17; LR16]. At higher velocities, where the electric potential of the nucleus is almost fully screened by the Coulomb fields of the electrons, it accounts for less than 0.05% of all energy loss [ICRU73].

The *mass nuclear stopping power* is defined in terms of the differential elastic-scattering cross-section for collisions with atomic nuclei [And+17]

$$\frac{1}{\rho} S_\mathrm{nuc} = \frac{1}{\rho} \left\langle \frac{\mathrm{d}E}{\mathrm{d}x} \right\rangle_\mathrm{nuc} \tag{3.28}$$

$$= 2\pi n \int_0^\pi Q(\theta, E_\mathrm{k}) \frac{\mathrm{d}\sigma_\mathrm{elast}}{\mathrm{d}\Omega} \sin\theta \,\mathrm{d}\theta \,, \tag{3.29}$$

where θ is the deflection angle in the center-of-mass system. $Q(\theta, E_\mathrm{k})$ is the energy transferred to the recoiling nucleus and is given by [Sig14; And+17]

$$Q(\theta, E_\mathrm{k}) = \left[4E_\mathrm{k} \frac{m M_\mathrm{t}}{(m + M_\mathrm{t})^2} \right] \sin^2 \frac{\theta}{2}. \tag{3.30}$$

[6] Examples are $E_\mathrm{c}^\mu = 612\,\mathrm{GeV}$ in aluminum and $E_\mathrm{c}^\mu = 1.183\,\mathrm{TeV}$ in polystyrene. Values are taken from https://pdg.lbl.gov/2023/AtomicNuclearProperties/index.html.

The term in brackets is the maximum possible energy transfer in an elastic collision, where m and M_t are the masses of the projectile and the nucleus, respectively. The scattering cross-section, $\mathrm{d}\sigma_\mathrm{elast} \,/\, \mathrm{d}\Omega$, encodes the Coulomb interaction between the projectile and the screened electric field of the nucleus. The screening depends on the impact parameter, which is defined as the perpendicular (radial) distance between the path of the projectile and the center of the electric potential field of the nucleus. Since the energy transfer to the recoiling nucleus is larger than ionization losses only in close collisions, the impact parameter can be used to approximately separate the regimes of nuclear and electronic losses in impact-parameter space [LSS63; Lin+63].

The scattering off the nucleus' screened Coulomb potential can be treated classically for low projectile energies. At higher energies (in the MeV range), the quantum-mechanical elastic-scattering cross-section[7] can be used [Mol47], though the resulting differences are marginal [ICRU49]. The electric potential—often called the *inter-atomic potential* [Sig14] in the implicit assumption that the projectile is a nucleus heavier than a proton because nuclear losses for protons are small—can be described by [ICRU49; ICRU73]

$$V(r) = \frac{Z_1 Z_2 e^2}{4\pi\epsilon_0 r} \Psi_\mathrm{s}\left(\frac{r}{r_\mathrm{s}}\right), \tag{3.31}$$

where r is the radial distance to the nucleus, ϵ_0 is the vacuum permittivity, e is the elementary charge, and z and Z are the charge numbers of the projectile and the nucleus, respectively. The screening function, $\Psi_\mathrm{s}(r/r_\mathrm{s})$, depends on the *screening length*, r_s. The screening length, in turn, depends on z and Z, a dependency that is often exploited to scale [LNS68; Sig14] universal screening functions to different projectile-target combinations [Boh48; Fir57; ZBL85]. More complicated expressions than Equation 3.31 have been derived to take into account that the projectile and the target nucleus are embedded in a medium [DB84; SW85; JNP87], though the resulting differences are generally negligible except at particle energies well below 1 keV [ICRU73], as well as for some metals and semiconductors [SW85; Sig14].

Figure 3.1 compares the electronic, nuclear, and total stopping powers of protons (H nuclei) and alpha particles (He nuclei) in hydrogen and aluminum. The data presented was taken from the PSTAR and ASTAR databases of NIST [Ber+17]. The figure not only demonstrates that the nuclear stopping power is

[7] See Section 2.11 of [And+17] for well-written summary treatments of both classical and quantum-mechanical theories of elastic and inelastic scattering of heavy charged particles.

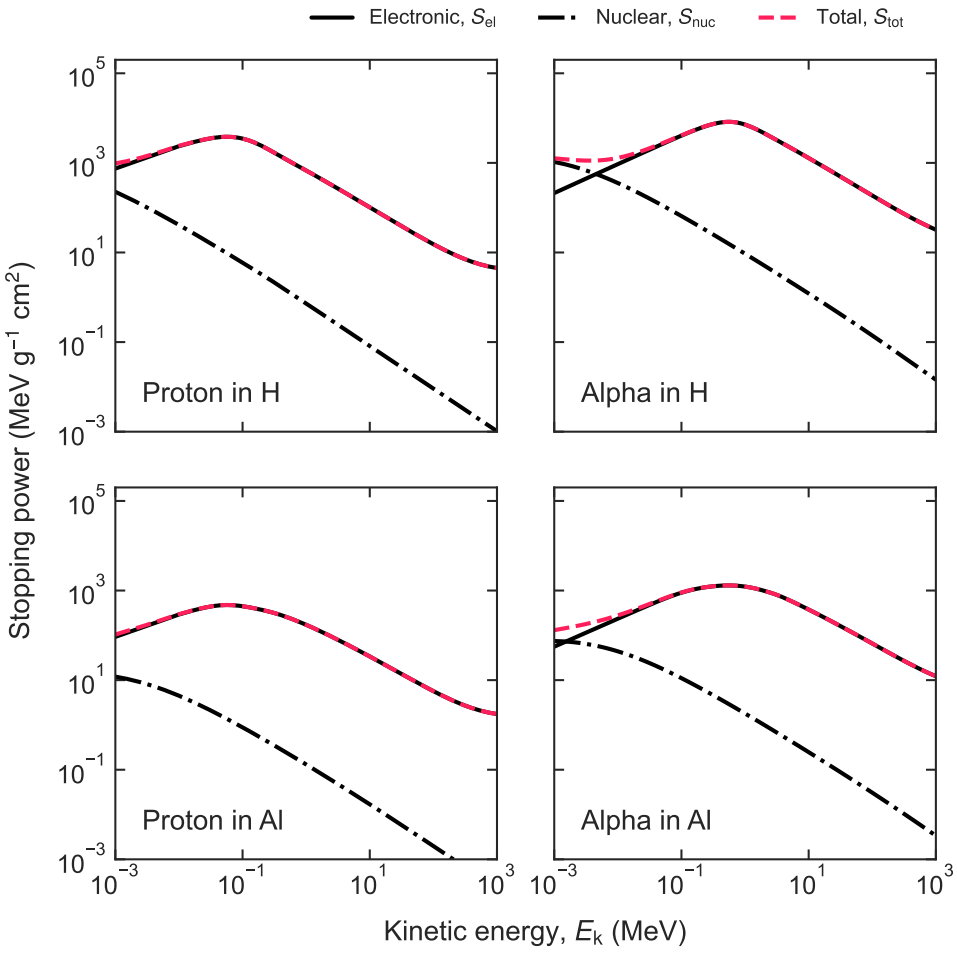

Figure 3.1: Electronic, nuclear, and total mass stopping power of protons (left) and alpha particles (helium nuclei; right) in hydrogen (top) and aluminum (bottom). Data taken from the PSTAR and ASTAR databases [Ber+17].

generally only relevant at small projectile energies but also illustrates its mass dependence: the heavier the projectile and the lighter the target nuclei, the larger the contribution of nuclear losses to the total stopping power.

One or several nuclear scattering events can lead to a large energy loss (relative to the projectile's incident energy) and hence to a large deflection of

the projectile [ICRU49]. This is especially important for thin absorbers placed in front of detectors with limited solid-angle coverage.

3.2.6 Important Features of the Stopping Power

Since the radiative and nuclear energy losses for heavy charged particles are significant only at high and very low particle energies, respectively, the total stopping power defined by Equation 3.5 is dominated by the electronic energy loss over many orders of magnitude. The discussion in the following sections will thus focus on the electronic stopping power, unless noted otherwise.

In Figure 3.2, which shows the stopping power of aluminum for muons with kinetic energies from keV to PeV, the region for which Equation 3.15 adequately describes the energy loss is highlighted as the 'Bethe' region. Above the muon critical energy, radiative losses dominate. Below about 1 MeV, Bethe theory without the low-energy corrections breaks down; at the lowest energies, the Andersen-Ziegler and Lindhard-Scharff-Schiøtt (LSS) formalisms, which rely on experimental data to derive phenomenological functions, must be used to describe the total stopping power. Depending on the projectile-target combination, nuclear losses may play a role, though they do not for muons.

In the Bethe region, the stopping power exhibits a broad minimum at energies corresponding to $\beta\gamma \sim 3 - 3.5$ ($\beta \sim 0.95$), a value that inversely scales with the atomic number of the traversed medium, Z [Wor+22; KW20]. Particles with mean energy loss rates close to that minimum are often called minimum-ionizing particles (MIPs). At higher energies, the electronic stopping power rises as a result of the logarithmic term in Equation 3.15, both because of the explicit $\beta^2\gamma^2$ dependence and because T_{mx} effectively is a function of $\beta^2\gamma$ (see Equation 3.12) [Wor+22]. Thanks to the density correction (Equation 3.18), this relativistic rise of the electronic energy loss is truncated (see dashed line in Figure 3.2) but is in any case dwarfed by radiative losses above the critical energy. Since the stopping power increases only little for energies corresponding to $\beta\gamma > 3.5$—keep in mind that the critical energy for protons and heavier nuclei is much higher than for muons and radiative losses can thus effectively be neglected—in many fields all particles with energies above the minimum are treated as MIPs. A large portion of the cosmic-ray spectrum falls into the region between minimum ionization and the onset of radiative losses. The electronic energy loss thus gives a good approximation of the total stopping power for many applications in cosmic-ray research.

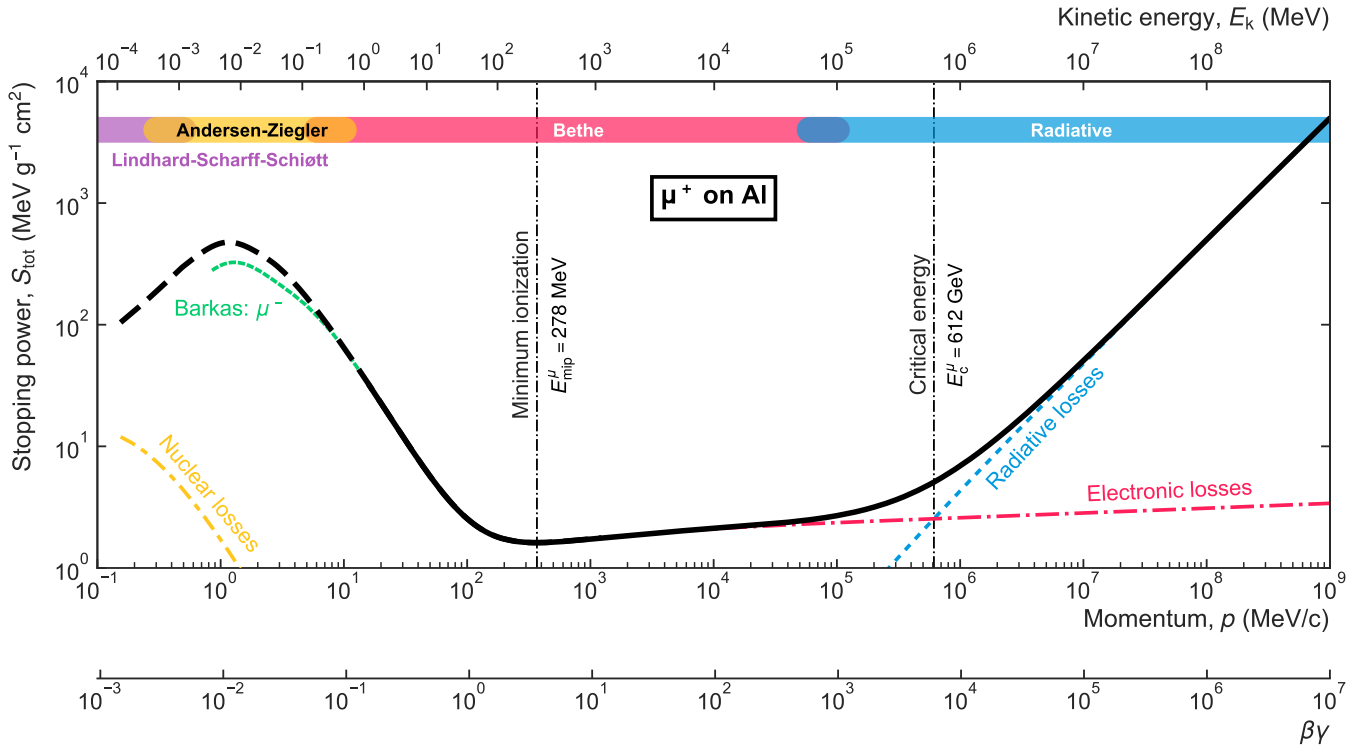

Figure 3.2: Stopping power of (positive) muons in aluminum as a function of momentum, kinetic energy, and $\beta\gamma$ (see Equation A.7). The solid and dashed black curves show the total stopping power, the colored curves the individual contributions by different energy-loss mechanisms. The dashed green line shows the deviation at low energies for negative muons due to the Barkas correction. Data in the Bethe and radiative regimes taken from [GMS01; Wor+22], data in the Andersen-Ziegler and Lindhard-Scharff-Schiøtt (LSS) regimes taken from [ICRU49; Ber+17; SS01a; Cse02]. Figure adapted from [Wor+22; GMS01].

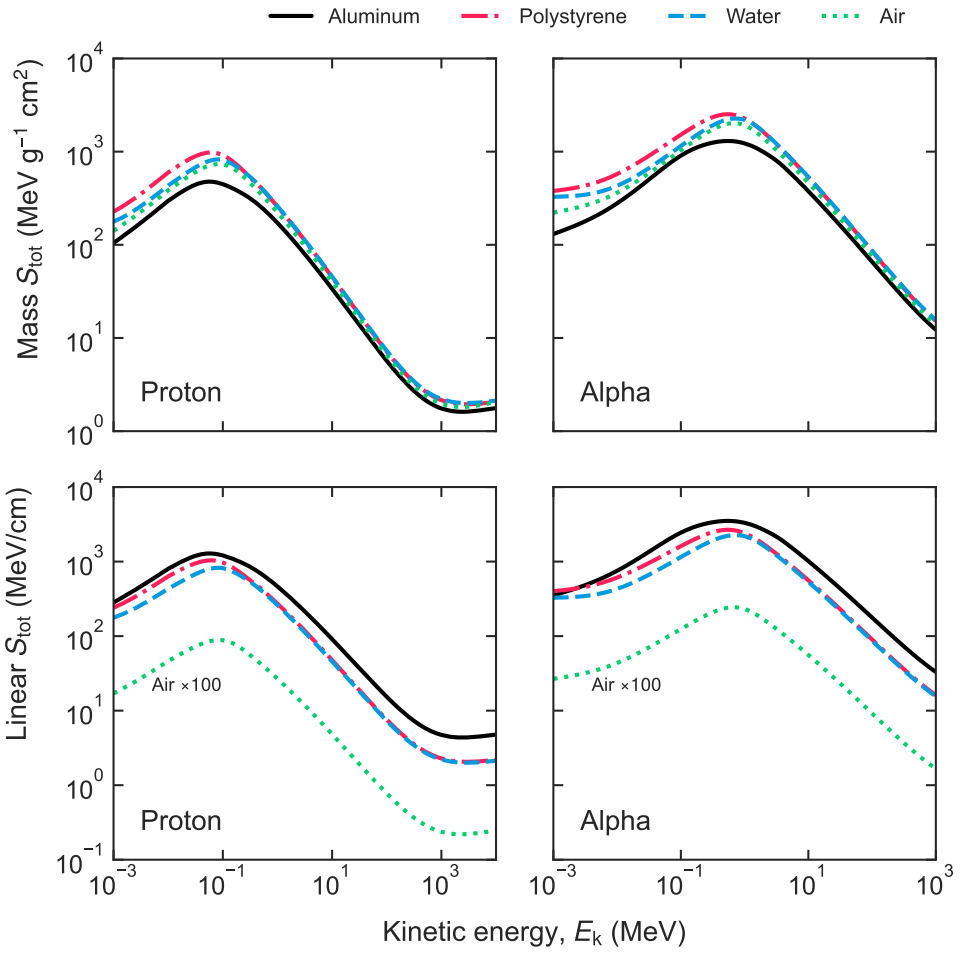

Figure 3.3: Total mass and linear stopping power of protons in aluminum, polystyrene, water, and air. The linear stopping power in air is multiplied by 100. Data taken from the PSTAR and ASTAR databases [Ber+17].

At energies below $\beta\gamma \sim 3$, the electronic stopping power increases steeply with decreasing energy, roughly as a function of $1/\beta^\alpha$, where $\alpha \sim 1.5 - 1.7$ decreases with increasing Z [Wor+22]. This velocity dependence can be explained by the increased interaction time for slower particles [KW20]. Since the momentum transfer in collisions is directly proportional to the interaction time, the energy loss increases until it reaches a maximum at $\beta\gamma \sim 0.01$—often

called *Bragg maximum*—and falls off steeply thereafter until the projectile thermalizes and stops [LSS63]. This deviation from the $1/\beta^\alpha$ dependence is due to the low-energy corrections discussed above.

It is helpful to understand how the (electronic) stopping power depends on the properties of the projectile particle and the target medium:

Dependence on the Traversed Medium The total mass stopping power decreases noticeably with increasing Z_2 (see upper panels of Figure 3.3) for two reasons. The first is the Z_2/A_2 dependence of the electronic stopping power (Equation 3.15), which results in a proportionality to the number of electrons per unit mass of the medium. The latter decreases substantially for heavier elements.[8] The second and stronger cause is the dependence on the mean excitation energy, I, which also decreases with increasing Z_2. The lower panels of Figure 3.3 show, however, that the Z-dependent decrease of the mass stopping power is outweighed by the larger density of heavier elements when using the linear stopping power.

Dependence on Particle Charge Due to the Z_1^2 term in Equation 3.15, the stopping power increases quadratically with the charge of projectile. This simple dependence can be used to obtain the stopping power for heavy nuclei from that of protons. This approach is generally valid for medium and high energies but overestimates the energy loss in the region where the various low-energy corrections dominate [And+17]. Semi-empirical scaling approaches try to correct for this discrepancy [And+17; Zie77].

Dependence on Particle Mass The stopping power does not directly depend on the mass of the projectile. At a given kinetic energy, however, the velocity, β, of a particle depends on its rest mass. What follows is that particles with the same velocity and (effective) charge—and not necessarily the same kinetic energy—have the same stopping power, except at very low energies [And+17]. Isotopes of the same element therefore have slightly different stopping powers.

3.2.7 Energy Loss Fluctuations and their Distribution

When developing particle detectors, we want to know what the energy loss of a particle with energy E_k in a material is. Even though Equation 3.15 determines the mean energy loss per path length, it does not take into account that the energy loss is a statistical process with inherent fluctuations. The total energy

[8] For example, $Z_2/A_2 = 0.499542$ for carbon and $Z_2/A_2 = 0.395753$ for lead [And+17].

loss, ΔE, experienced by a particle over a distance Δx is the sum of many small losses, δE_n, due to individual ionization and excitation events [KW20]:

$$\Delta E = \sum_{n=1}^{N} \delta E_n \tag{3.32}$$

When particles traverse matter, fluctuations occur in the number of ionization and excitations events, N, and in the energy transfer per interaction.

The fluctuations in N often follow a Poisson distribution, especially in thin or low-density detectors (targets). It hence follows for the resolution with which a detector can measure the mean energy loss of particles [KW20]:

$$\frac{\sigma(\Delta E)}{\Delta E} \approx \frac{1}{\sqrt{N}} \tag{3.33}$$

The fluctuations in energy transfer follow a $1/(\delta E)^2$ distribution between a lower bound, $\delta E_{\min}$, and an upper bound, $\delta E_{\max}$ [KW20]. The former is given by the minimum ionization or excitation energy of the medium, the latter by $T_{\max}$ (see Equation 3.12). The most probable energy transfer is in fact near $\delta_{\min}$, but occasionally a particle may lose much or all of its energy in a single central collision with an orbital electron.

For a fixed Δx, the energy loss ΔE follows a probability density $f(\Delta E; \Delta x)$ that is normalized in the interval between the minimum, $\Delta E_{\min}$, and maximum, $\Delta E_{\max}$, allowed total energy transfer. The fluctuations of the δE_n per collision lead to an asymmetric distribution: The predominantly occuring interactions with small δE_n give a Gaussian part, and the infrequently occuring collisions in which much of the particle energy is transferred to single electrons (δ electrons, see above) cause a long tail to large ΔE. Though rare, these high-energy-transfer collisions—with ΔE extending to $T_{\max}$—drive the mean energy loss in thin targets far into the tail of the distribution [Wor+22]. The *most probable value* of the energy loss, ΔE_{mpv}, corresponds to the maximum of the distribution and lies close to $\Delta E_{\min}$. The statistical fluctuations leading to this highly asymmetric distribution are called *energy-loss straggling*; $f(\Delta E; \Delta x)$ is correspondingly called the *straggling function* [Fan63; ICRU49].

The shape of the distribution depends on the ratio of the mean total energy loss given by Equation 3.15, $\langle \Delta E \rangle$, to the maximum possible energy loss in a single collision, $T_{\max}$. It thus varies with the nature of the projectile and the target, and with the projectile's path length in the medium, Δx (and hence the

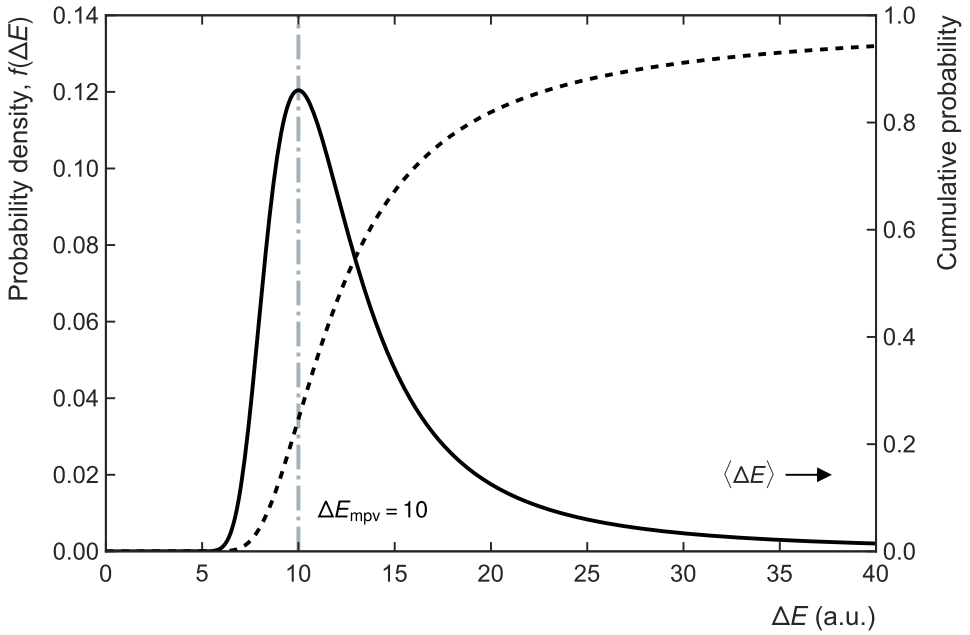

Figure 3.4: Probability density (solid line) and cumulative probability (dashed line) of a Landau distribution with $\Delta E_{\mathrm{mpv}} = 10$ and $\xi = 1.5$, describing the energy loss of particles with small Δx (i.e., in thin targets). Though mathematically not defined for this distribution, the mean energy loss, $\langle \Delta E \rangle$, would lie to right of the shown ΔE range because of the long tail.

target thickness). A measure of the ratio is given by [Vav57; CF70]

$$\kappa = \frac{\xi}{T_{\mathrm{max}}}, \tag{3.34}$$

where ξ is the *straggling parameter* [KW20; Wor+22]:

$$\xi = \frac{1}{2} K \frac{Z_2}{A_2} \rho \frac{z^2}{\beta^2} \Delta x. \tag{3.35}$$

The parameter κ can be used to distinguish between different forms of the straggling function [And+17]:

1. $\kappa \geq 1$. In this case, the number of collisions is so large that small energy transfers completely dominate due to their much larger probability of

occuring. Williams first found that the long tail to large ΔE vanishes and the straggling function is hence practically given by a Gaussian with a full width at half maximum (FWHM) of $\Gamma = 3.9\xi$ [Wil29].

2. $\kappa \leq 0.01$. For very small κ, the number of collisions is small, straggling is maximal, and the energy-loss distribution thus highly asymmetric. Under the simplifying assumption that $T_{\max}$ (and hence ΔE) can become infinitely large, Landau first found an analytic solution to the transport equation and derived a universal function to describe energy-loss straggling in thin targets, widely known as the *Landau distribution* [Lan44]. Figure 3.4 exemplarily shows such a distribution for $\Delta E_{\text{mpv}} = 10$ and $\xi = 1.5$. The FWHM is given by $\Gamma = 4.018\xi$ [KW20]. The tail to $\Delta E = \infty$ makes the Landau distribution cumbersome to work with; a mathematically simpler but not very good approximation is the *Moyal distribution* [Moy54].
3. $0.01 < \kappa < 1$. In this intermediate region, neither the solution of Landau nor the model of Williams adequately describe the energy-loss distribution. Without the assumption of infinite $T_{\max}$, Vavilov found a general theory that bridges the two extremes [Vav57] and reduces to the Landau and Gaussian distributions for small and large κ (and hence small and large Δx), respectively [And+17]. Though it is even more cumbersome to work with than Landau's solution, the Vavilov distribution is valid over the entire kinematics and thickness ranges [KW20] and is thus the preferred approach for most straggling calculations [And+17].

When working with real-life particle detectors, it is often practical and computationally advantageous to approximate the straggling function with a convolution of a Gaussian and a Landau distribution. Blunck and Leisegang showed that doing so improves the accuracy of the Landau function particularly for short path lengths [BL50]; Shulek et al. found the same for the Vavilov distribution [Shu+67]. Another accurate and computationally efficient approach is the numerical convolution method, used and compared to the Blunck-Leisegang and Shulek corrections by Bichsel and Saxon [BS75; Bic88].

Though giving (slightly) different shapes for the energy-loss distribution, the various theories agree that its most probable value can be described by [And+17; KW20; Wor+22]

$$\Delta E_{\text{mpv}} = \xi \left[\ln \frac{2m_e c^2 \beta^2 \gamma^2}{I} + \ln \frac{\xi}{I} + j - \beta^2 - \delta(\beta\gamma) \right]. \tag{3.36}$$

This was shown by Bichsel, who provided a comprehensive treatment and modern derivation of the stopping power and energy straggling in thin silicon detectors [Bic88]. He added the density correction, $\delta(\beta\gamma)$, which was not included in Landau's and Vavilov's original work. Different values for the parameter j are given in the literature [Ros52; Tal79; Bic88], though ΔE_{mpv} is not very sensitive to it [Wor+22]. Bichsel gives $j = 0.200$ [Bic88].

Due to the behavior of $\delta(\beta\gamma)$ in the high-energy limit ($\beta\gamma \gtrsim 100$) (see Equation 3.18) [KW20; Wor+22], the most probable energy loss behaves like

$$\Delta E_{\mathrm{mpv}} \xrightarrow{\beta\gamma \gtrsim 100} \xi \left[\ln \frac{2 m_e c^2 \xi}{\hbar \omega_{\mathrm{p}}} + j \right]. \tag{3.37}$$

As for the density correction, the excitation energy, I, is replaced by the plasma energy, $\hbar\omega_{\mathrm{p}}$, to account for the polarization of the medium for highly relativistic particles. Equation 3.37 shows that the most probable energy loss, like the restricted energy loss (Equation 3.20), does not rise indefinitely but reaches a Fermi plateau. Eqs. 3.36 and 3.37 also show that $\Delta E_{\mathrm{mpv}}/\Delta x$ scales logarithmically with Δx, since $\xi \propto \Delta x$ and $\Delta E_{\mathrm{mpv}} \propto \xi \ln \xi$ [Wor+22].

Mean vs. Most Probable Energy Loss vs. Energy Deposition

The above discussion makes it necessary to issue a note of caution on using the Bethe equation to describe the energy loss of particles in matter. To quote Workman et al., "few concepts in high-energy physics are as misused as $\mathrm{d}E \,/\, \mathrm{d}x$" [Wor+22]. This is to say that the mean electronic energy loss as given by Bethe's theory (Equation 3.15) is often used to describe the energy loss of single particles. The mean is, however, strongly affected by rare events with large single-collision losses, as evident by the long tail of the Landau distribution. For relativistic particles, T_{max} can reach several GeV or more, while the most probable energy loss for a majority of materials is on the order of 20 eV; in light elements, as much as 80% of losses are smaller than 100 eV [ICRU49]. The disproportionate weight assigned to events with large energy transfer leads to large fluctuations and a strong sensitivity to cuts even in experimental distributions with a few hundred events or more, rendering Equation 3.15 experimentally ill-defined [Wor+22]. It should thus not be used to describe the energy loss by single particles. The better and more easily determinable quantity is the most probable energy loss given by Equation 3.36.

A distinction must also be made between the energy lost by a particle and the energy deposited in some region of the target [ICRU49]. A large fraction of

the lost energy is converted into kinetic energy of δ electrons (see Section 3.2.2 on restricted energy loss), which can travel a long way from the interaction site and thus determine the spatial pattern of energy deposition [WMP88; AMB14]. Secondary photons (created by fluorescence or bremsstrahlung) can likewise carry energy over long distances. In addition, not all deposited energy can (easily) be measured; a fraction of it may be converted into excitation modes that are not detectable in a given application.

3.2.8 Stopping Power of Compounds

To first order, the stopping power of compound materials can be approximated using the *Bragg additivity rule* [BK05]. It states that the atoms of different elements in a compound contribute to the stopping power nearly independently. The total stopping power for a compound consisting of n different elements can thus be calculated by [And+17]

$$\frac{S_{\text{tot}}}{\rho} = \sum_{i=1}^{n} w_i \left(\frac{S_{\text{tot}}}{\rho}\right)_i , \tag{3.38}$$

where w_i are the weight fractions of the n elements. Likewise, the effective values for the mean excitation energy and density effect of the compound can be calculated by [And+17; KW20]

$$\ln I_{\text{eff}} = \frac{1}{Z_{\text{eff}}} \sum_{i=1}^{n} w_i Z_i \ln I_i \tag{3.39}$$

$$\delta_{\text{eff}} = \frac{1}{Z_{\text{eff}}} \sum_{i=1}^{n} w_i Z_i \delta_i, \tag{3.40}$$

where Z_{eff} is the weighted sum of the elements' atomic numbers.

This approach, however, neglects the influence of chemical binding and thus underestimates I_{eff}; it also does not take the effective change in the electron density into account, resulting in an incorrect value for δ [And+17; Wor+22]. Tabulated values [SSB82; SBS84; SB84] and calculation recipes [SP71] are available for a broad range of compounds that allow to determine the effective mean excitation energy and density correction with accuracies at the percent level.

3.2.9 Multiple Scattering, Range, and Bragg Peak

The ansatz in Equation 3.6 for the calculation of the electronic stopping power assumes that a particle traversing a medium loses energy at a continuous rate per unit length. This simplification is called the *continuous slowing-down approximation (CSDA)* [And+17] and is the basis for the derivation of the Bethe theory.

During its passage through a medium, a particle undergoes single Coulomb interactions with atomic nuclei. In each interaction, it is scattered by predominantly small angles [Wil39] according to the Rutherford cross-section [Rut11]. For hadronic projectiles, strong (nuclear) interactions also contribute but are generally not considered in the CSDA [Wor+22]. If the target is thick enough for the particle to undergo at least 20 scatters, we speak of multiple or Moliére scattering [KW20]. In the central limit [Beh+13] of an infinite number of scatters, the distributions of the net scattering angle and the displacement are Gaussian. The distribution for the general case of a limited number of scatters was derived by Moliére [Mol48] and can be approximated by a Gaussian with long tails produced by less frequent hard collisions with large deflections [Sco63; MOK64; KW20]. Though precise distributions and values for single particles are best achieved with a Monte Carlo simulation [Str05], approximate analytic solutions can be used to estimate the effect of multiple scattering.

In the small-angle approximation, the spatial scattering angle—the angle between the particle direction before and after traversing the scattering volume—can be decomposed into [KW20]

$$\theta_{\text{space}} \approx \sqrt{\theta^2_{\text{plane},x} + \theta^2_{\text{plane},y}}, \tag{3.41}$$

where $\theta_{\text{plane},x}$ and $\theta_{\text{plane},y}$ are the projected angles on the planes perpendicular to the direction of motion. The deflections in these planes are independent and identically distributed, and hence $\mathrm{d}\Omega = \mathrm{d}\theta_x \, \mathrm{d}\theta_y$ [Wor+22]. The spatial and projected angular distributions are then approximately given by [Bet53]

$$\frac{1}{2\pi\theta_0^2} \exp\left(-\frac{\theta^2_{\text{space}}}{2\theta_0^2}\right) \mathrm{d}\Omega \tag{3.42}$$

$$\frac{1}{\sqrt{2\pi}\theta_0} \exp\left(-\frac{\theta^2_{\text{plane},i}}{2\theta_0^2}\right) \mathrm{d}\theta_{\text{plane},i}\,. \tag{3.43}$$

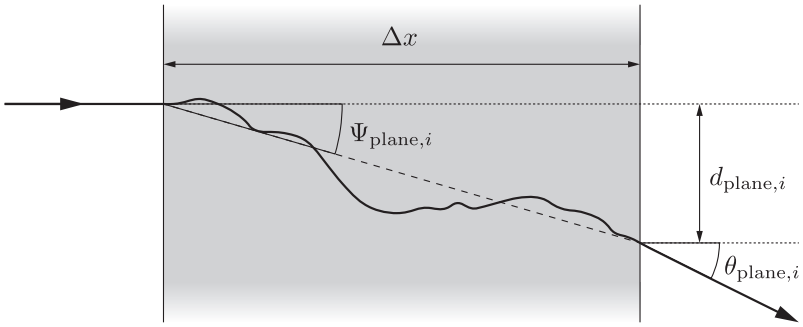

Figure 3.5: Characteristic quantities used to describe multiple scattering at a macroscopic level. Adapted from [Wor+22].

Here, θ_0 is the root-mean-square (RMS) width of the projected angular distribution in the Gaussian approximation and is given by [Hig75; LD91]

$$\theta_0 = \frac{13.6\,\text{MeV}}{\beta cp} z \sqrt{\frac{\Delta x}{X_0}} \left[1 + 0.088 \ln\left(\frac{\Delta x}{X_0} \frac{Z_1^2}{\beta^2}\right)\right], \tag{3.44}$$

where x/X_0 is the thickness of the scattering medium in radiation lengths. X_0 has been determined for many elements [Tsa74; Tsa77] and tabulated values are widely available.[9] For mixtures and compounds consisting of n elements, it is given by the weighted sum of the elemental X_i [Wor+22]:

$$\frac{1}{X_0} = \sum_{i=1}^{n} \frac{w_i}{X_i}. \tag{3.45}$$

To calculate θ_0 for compounds, first use Equation 3.45 to calculate the effective $\Delta x/X_0$, then insert it into Equation 3.44.

Figure 3.5 shows the quantities of interest when calculating the effect of multiple scattering on the passage of particle through a medium with thickness Δx: the deflection angle $\Psi_{\text{plane},i}$, the offset from the original entrance point $d_{\text{plane},i}$, and the width of the effective scattering angle, $\theta_{\text{plane},i}$. They can be

[9] See, for example, https://pdg.lbl.gov/2023/AtomicNuclearProperties/index.html.

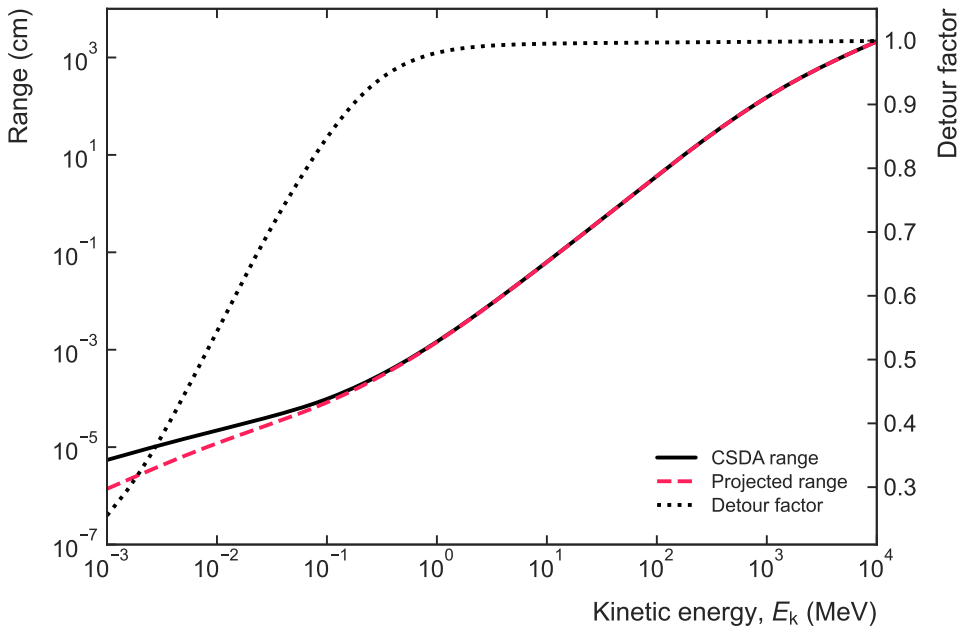

Figure 3.6: CSDA range, projected range, and detour factor of protons in aluminum. Data taken from the PSTAR database [Ber+17].

approximately calculated from [Wor+22]

$$\Psi^{\mathrm{rms}}_{\mathrm{plane},i} = \frac{1}{\sqrt{3}}\theta_0 \tag{3.46}$$

$$d^{\mathrm{rms}}_{\mathrm{plane},i} = \frac{1}{\sqrt{3}}\Delta x\theta_0 \tag{3.47}$$

$$\theta^{\mathrm{rms}}_{\mathrm{plane},i} = \theta_0 \tag{3.48}$$

These estimates are only valid in the limit of small $\theta^{\mathrm{rms}}_{\mathrm{plane},i}$ and in the absence of large-angle scatters. More realistic values can be achieved with a simulation using Monte-Carlo methods.

A concept that is tightly coupled to multiple scattering is the range, R, of particles in a medium. It can be understood as the total length of the path that a particle follows until it stops. A related quantity is the *mean forward* or *projected range*, R_{proj}, which is the expectation value of the maximum penetration depth of a particle in its initial direction [And+17]. In the CSDA, the range represents the average path length traveled by a particle as it slows down from its initial

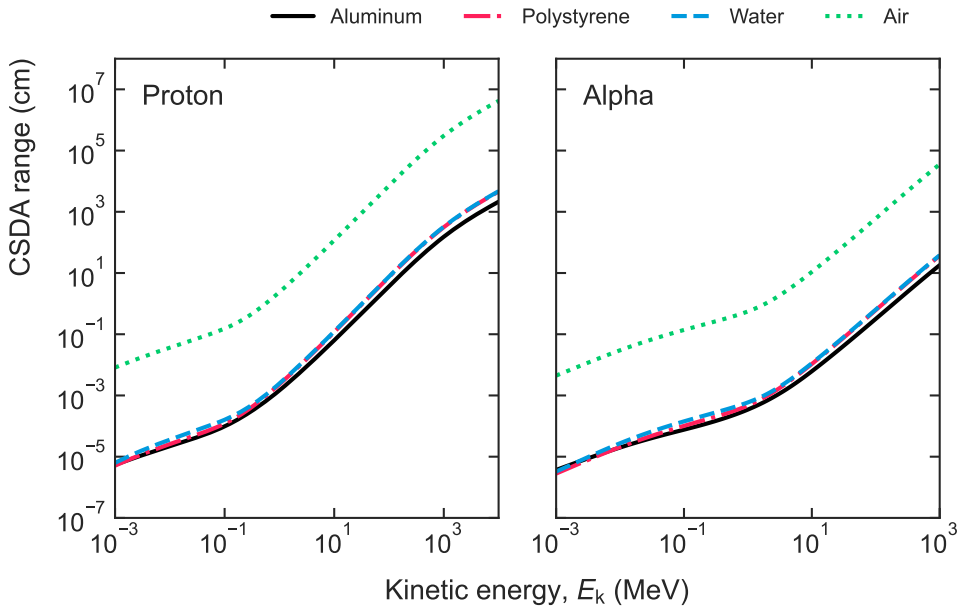

Figure 3.7: CSDA range of protons (left) and alpha particles (right) in aluminum, polystyrene, water, and air. Data taken from the PSTAR and ASTAR databases [Ber+17].

velocity (defined by its initial energy, E_0) to zero. Neglecting nuclear stopping, it is given by [And+17]

$$R_{\mathrm{CSDA}}(E_0) = \rho \int_{E_0}^{0} \frac{\mathrm{d}E}{S_{\mathrm{tot}}(E)} = \rho \int_{E_0}^{0} \frac{\mathrm{d}E}{S_{\mathrm{el}}(E) + S_{\mathrm{rad}}(E)}. \tag{3.49}$$

The natural unit of the range is thus $\mathrm{g/cm^2}$, though it is often more intuitive to use R_{CSDA}/ρ in units of [length]. R_{CSDA} underestimates the true R by less than 0.2% for protons and heavier nuclei [Fan63; And+17]. Similar to the stopping power (see Section 3.2.7), the CSDA range represents the mean of a range-straggling distribution.

For light particles (electrons), multiple scattering leads to a substantial difference between R_{CSDA} and R_{proj}. When neglecting nuclear interactions, however, the effect of multiple scattering is much smaller for heavy particles at medium to high energies, though it increases somewhat for heavier target materials. The ratio $R_{\mathrm{proj}}/R_{\mathrm{CSDA}}$ is called the detour factor and effectively

allows to gauge the effect of multiple scattering [And+17]. Figure 3.6 shows the CSDA range, projected range, and detour factor for protons in aluminum. It can be seen that the difference between R_{csda} and R_{proj} is all but negligible above energies of about 1 MeV.

At high energies, the range of two particles with masses m_1, m_2 and charges z_1, z_2 having the same velocity is related by the scaling law [ICRU49]

$$\frac{R_{\mathrm{CSDA},1}(\beta)}{R_{\mathrm{CSDA},2}(\beta)} = \frac{m_2}{m_1}\left(\frac{z_1}{z_2}\right)^2. \tag{3.50}$$

Figure 3.7 shows the effect of this scaling on the range of protons and alpha particles in aluminum, polystyrene, water, and air. It also shows how R_{CSDA} scales inversely with the stopping power (compare to Figure 3.3).

Bragg Curve

The strong $1/\beta^{\alpha}$ dependence of the stopping power at energies below the minimum-ionization point (see Section 3.2.6) leads to a strong increase of the energy loss experienced by a particle when it stops in a medium. The CSDA approximation allows to estimate the energy loss between two points $A(x_i, y_i, z_i)$ and $B(x_{i+1}, y_{i+1}, z_{i+1})$ according to [And+17]

$$\Delta E = E_i - E_{i+1} \approx E_i - sS_{\mathrm{tot}}(E_i), \tag{3.51}$$

where s is the path length between the points A and B. Using Equation 3.51 to iteratively calculate the energy lost by a particle until it stops results in a characteristic energy-loss profile, called the *Bragg curve*. Figure 3.8 shows such a profile, albeit based on an interpolation of experimental data. The figure illustrates how the stopping power increases sharply when the remaining kinetic energy of the particles decreases to the MeV regime, before abruptly falling to zero. The peak at the end of the energy-deposition profile is known as the *Bragg peak*.

Understanding the characteristics of the Bragg curve is important for deriving the working principle of the RadMap Telescope's central detector. I will discuss their dependence on various parameters in detail in Section 6.2. The Bragg peak also plays a role in determining the damage caused by different particles and nuclei in biological tissue, as discussed in Section 5.2.

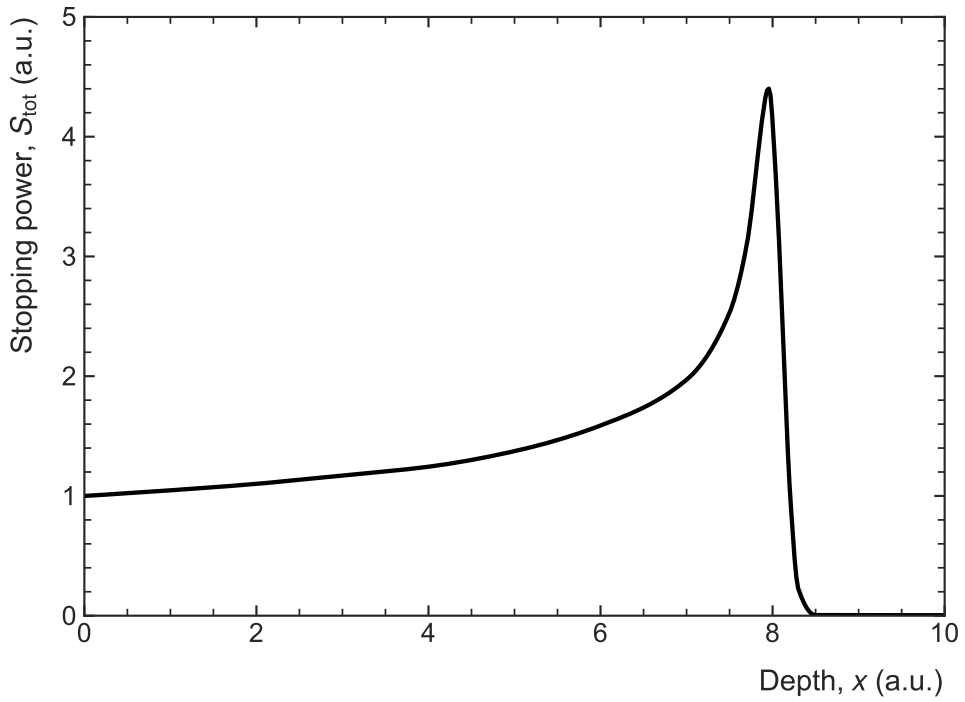

Figure 3.8: Characteristic energy-loss profile of particles stopping in a medium, known as the Bragg curve.

3.2.10 Interaction of Hadrons with Matter

Hadrons—i.e., composite particles such as protons, neutrons, and pions that consist of two or more quarks—not only lose energy due the ionization of the medium they traverse but also via hadronic interactions with its nuclei, leading to the development of so-called *hadronic showers* [Wig17].[10] If treating those particle initiating a shower as being "absorbed" by the medium, hadronic interactions have no effect on the behavior of the electronic energy loss but rather cause a fraction of particles to have a shorter range [KW20].

In analogy to the radiation length for electromagnetic interactions, X_0, the *hadronic absorption length*, λ_a, defines the attenuation of a hadron beam in

[10] In analogy to *electromagnetic showers* that are induced by, for example, electrons and photons but are not relevant for my work and thus not discussed here.

matter after a penetration depth Δx [KW20]

$$N(x) = N_0 \mathrm{e}^{-\Delta x/\lambda_\mathrm{a}}, \tag{3.52}$$

where N_0 is the initial number of particles entering the medium (compare with Beer-Lambert law, Equation A.21). λ_a (see definition of mean free path, Equation A.20) can be derived from the inelastic hadronic cross-section, σ_inel [KW20]:

$$\lambda_\mathrm{a} = \frac{A_2}{N_\mathrm{A}\rho\sigma_\mathrm{inel}}. \tag{3.53}$$

Hadronic interactions only dominate over other forms of energy loss when the ionization range (see Equation 3.50) becomes much larger than the absorption length at high energies. They are thus largely irrelevant for the instruments we develop. They are, however, of great importance for the measurement of ultra-high-energy cosmic rays with air-shower telescopes [Lip14; EHP11].

3.3 Stopping Power and Fragmentation of Heavy Ions

The passage of heavy ions—generally understood to be ions of elements heavier than helium—through matter cannot be adequately described by Bethe's theory of the stopping power as discussed in Section 3.2.1. The primary reasons are:

1. For increasing atomic number of the projectile, Z_1, the Coulomb force cannot be treated as a weak perturbation of the medium, as is common practice for protons and other singly-charged particles in the quantum-mechanical descriptions of Bethe [Bet30; Bet32] and Bloch [Blo33a; Blo33b], and in the classical description of Bohr [Boh13b; Boh15].
2. The validity range of the Born approximation used in Bethe's theory diminishes rapidly with increasing Z_1 [Sig17].
3. Ions are composite particles and the projectile therefore cannot generally be treated as a point charge [SS16].
4. Ions carry electrons except at high speed, leading to complex electronic interactions with bound and free electrons of the target medium that were not foreseen in any of the aforementioned theories [ICRU73].

The ongoing search for an accurate theoretical—or even semi-empirical—description of the heavy-ion stopping process has therefore been challenging. Since giving a detailed assessment of the current state of knowledge is beyond

the scope of my thesis, I only selectively summarize the aspects most relevant to the working principle of our detectors. For comprehensive summaries, I refer the reader to [Ahl80; ICRU73; SS16; Sig17].

Efforts to theoretically describe heavy-ion stopping date back to Bohr [Boh40], Lamb [Lam40], as well as Brunings, Knipp, and Teller [KT41; BKT41]. The role of the projectile charge and of charge exchange between projectile and target were first comprehensively highlighted by Bohr and Lindhard [BL54]. In the absence of a single theory valid over the full range of projectile energy, the treatment of heavy-ion stopping is often divided intro three broadly defined energy regions based on the Thomas-Fermi velocity [Gom56; Bet68]

$$v_{\mathrm{TF}} = v_0 Z^{2/3}, \tag{3.54}$$

where Z is the atomic number of either the projectile, Z_1, or the target, Z_2, and v_0 the Bohr velocity.[11] According to [ICRU73] and using $v_{\mathrm{TF},1}$ for the projectile, these regions are ($v = \beta c$ is the projectile speed):

1. $v \lesssim v_{\mathrm{TF},1}$. At very low projectile energies—below the Bragg maximum—the electronic stopping power is approximately [FT47; LS61] though not exactly [SS15a] proportional to the projectile speed, v. Theoretical descriptions are often based on the original LSS theory [LS61; LSS63; Til95], though with a number of modifications [Sig17]. More recent calculations exist for an alternative approach that models the shells of the target atoms as a free electron gas [Ech+86; Ari02]. Neither approach, however, can fully describe the charge-dependent structure of the stopping cross-section found in experimental data [OD63; Eis68; Ale+78; SS16]. A model based on an extended Friedel sum rule can reproduce the observed Z_1 oscillations to some degree [LA98], though a proof of the rule's applicability is pending [Sig17].
2. $v \sim v_{\mathrm{TF},1}$. At energies around and above its maximum, the stopping power was initially described by a modified version of Bethe's theory, in which screening by the projectile electrons was taken into account via the introduction of an empirically determined effective ion charge [Nor60; MN62; Nor63]. Attempts were made to justify this approach from a theoretical perspective [YRB78; BK82; MP95], though it was later realized that using the effective charge instead of Z_1 likely leads to an underestimation of the Bloch correction [ICRU73], among other

[11] $v_0 = e^2/(4\pi\epsilon_0\hbar) = c/137.036$ [Boh41; ICRU73].

shortcomings [SS01b; SS20a]. A brief review of current theoretical approaches is given in Section 3.3.2 below.

3. $v \gg v_{\mathrm{TF},1}$. At highly relativistic energies, the stopping power can be well described by Bethe theory (see Section 3.2.1) in the corrected form of Lindhard and Sørensen [LS96]. Successful comparisons have been made with experimental data over a wide range in energy [Wei+00].

3.3.1 Regimes of Heavy-Ion Stopping

In heavy-ion stopping, a number of processes that are either less significant or completely absent in the case of light projectiles (electrons, protons, and alpha particles) must be taken into account. Figure 3.9 is adapted from [ICRU73] and qualitatively summarizes these effects in a carbon target as a function of the projectile's charge and specific kinetic energy. The lines indicate the approximate limits between regimes of applicability; arrows point into the regime where the respective effect is dominant or significant. Like the figure, the following discussion is closely adapted from [ICRU73].

The horizontal line labelled 'Slow' is at $E_{\mathrm{k}}/A_1 = 25\,\mathrm{keV}$ and roughly corresponds to $v = v_0$. Below, the ion speed is lower than the orbital velocity of all but the outermost shell electrons of the target. Similarly, the line labelled 'Shell corrections' marks the Thomas-Fermi velocity of the target electrons, below which their motion cannot be ignored. The third horizontal line (labelled 'Relativistic') at $E_{\mathrm{k}}/A_1 = 1\,\mathrm{GeV}$ is close to the projectile's rest energy and marks the transition to the highly relativistic regime where the modified Bethe theory alone is sufficient to describe the energy loss for all Z_1 shown [LS96].

The 'Screening' limit corresponds to the Thomas-Fermi velocity of the projectile. At energies exceeding this limit, the latter is stripped of most or all of its electrons. Below, an ion in charge equilibrium carries a non-negligible number of electrons, the presence of which allows the projectile to become excited or further ionized. These effects are significant whenever the number of electrons accompanying the projectile is comparable to or greater than that of the target atoms. The latter limit is roughly indicated by the line labelled 'Projectile excitations'. The transition to dominating nuclear stopping is marked as 'Nuclear losses' and was estimated based on the LSS theory for velocity-proportional electronic stopping [LS61; LSS63].

The most important limit is that of the applicability of the first-order Born approximation, upon which the quantum-mechanical treatment of scattering in Bethe's theory is based. It is, however, easier to define the upper validity

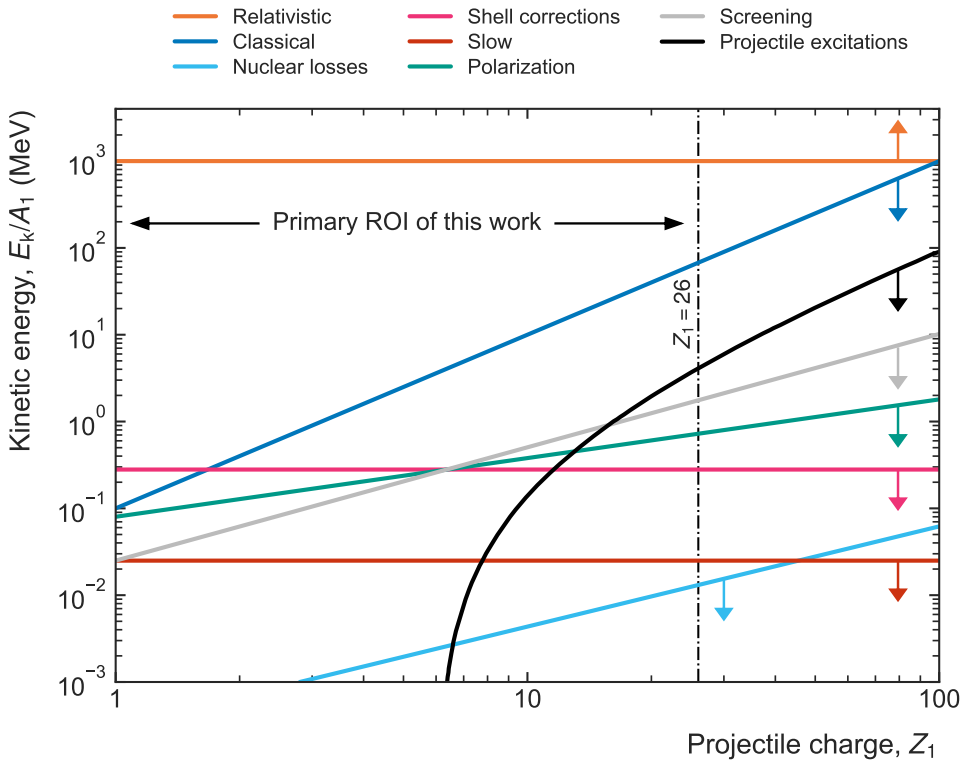

Figure 3.9: Approximate limits between regimes of ion stopping in a carbon target as a function of the projectile's charge and (specific) kinetic energy. Arrows point into the regime where the respective effect is either dominant or at least significant. See text for explanations of the effects. The region of interest (ROI) of this thesis is $1 \leq Z_1 \leq 26$. Adapted from [ICRU73].

limit of Bohr's classical theory, which is given by [ICRU73]

$$\frac{E_\mathrm{k}}{A_1} < Z_1^2 \times 100\,\mathrm{keV}. \tag{3.55}$$

This criterion is known as the *Bohr criterion* and is marked in Figure 3.9 by the line labelled 'Classical'. The transition between the classical and the Born regimes defined by Equation 3.55 extends the applicability of Bethe theory for light-ion projectiles to lower energies by several orders of magnitude (with respect to the 'Relativistic' limit).

Another factor limiting the validity of the Born approximation—and hence of the uncorrected Bethe theory—is the Barkas-Andersen effect, which becomes substantial for [ICRU73]

$$v \lesssim (Z_1 Z_2)^{1/3} v_0. \tag{3.56}$$

The corresponding limit is included under the label 'Polarization' but is always lower than the 'Classical' limit. The regime between these lines is thus a region of more or less smooth transition between the classical and the Born regime.

Though Figure 3.9 is largely a qualitative summary, it can be seen that the uncorrected Bethe formula (Equation 3.15) is valid down to the sub-MeV regime for light ions. It also shows, however, that for heavier ions in the ROI of this thesis (up to $Z_{\mathrm{Fe}} = 26$), the Bohr model is applicable up to energies of almost 100 MeV per nucleon. In addition, the effects of projectile excitations, screening, polarization, and shell corrections cannot be ignored and are substantial for the heaviest elements in the ROI.

3.3.2 Theories for Intermediate Energies ($v \sim v_{\mathrm{TF}}$)

Finding a theoretical description of heavy-ion stopping at intermediate energies ($v \sim v_{\mathrm{TF}}$) has been difficult for a variety of reasons. Among them are problems in understanding the relation between ion charge and energy loss, uncertainty about the role of the Barkas-Andersen effect, and a lack of knowledge about the contribution of charge exchange and projectile excitation [ICRU73].

Bethe's quantum-mechanical theory [Bet30; Bet32], which treats projectile-target interactions via quantal perturbation theory to the lowest order, very successfully describes the energy loss of relativistic point-like charged particles. With corrections applied, it is used to predict the stopping of electrons, protons, alpha particles, and other singly-charged particles over a wide range of energies [ICRU37; ICRU49]. It also works reasonably well for highly relativistic heavy ions but fails to accurately describe the energy loss for ions with $Z_1 > 2$ at low speeds. Bohr's theory [Boh13b; Boh15], on the other hand, performs well in the classical limit, where scattering of the projectile off the target electrons can be treated based on his classic model of the atom [Boh13a; Boh21]. Though it also cannot fully describe the stopping of heavy ions, in the extended form of Sigmund [Sig96] its predictions are much closer to experimental data than those of Bethe's theory [SS16].

As early as 1948, however, Bohr realized that the regimes of validity—at least for singly-charged, point-like particles—of the classical-orbit and the

quantum-mechanical theories are roughly complementary [Boh48]. Even earlier, Bloch had provided an approach that was, in fact, capable of connecting the two theories by replacing Bohr's classical impact parameter with a quantized angular momentum [Blo33a; Blo33b]. This ansatz does not affect distant collisions, where the results of Bethe's and Bohr's theories match, but produces different results for close collisions at low speed. This led to the formulation of the Bloch correction to Bethe's theory that I already briefly discussed in Section 3.2.1 [SS20a]:

$$\Delta L_{\mathrm{Bloch}} = L_2 = \Psi(1) - \mathrm{Re}\,\Psi\left(1 + i\frac{Z_1 v_0}{v}\right). \tag{3.57}$$

Here, Ψ is the digamma function, defined as the logarithmic derivative of the gamma function, $\Psi(\zeta) = \mathrm{d}\ln\Gamma(\zeta)/\,\mathrm{d}\zeta$ [Olv+10], and Re denotes the real part. This correction vanishes at high velocities and behaves like $\ln(Cv/Z_1 v_0)$ at low velocities, where $C = 2e^{-\gamma}$ and γ is Euler's constant [ICRU73]. With Equation 3.57, the stopping number for Bloch's theory can be written as [ICRU73]

$$L_{\mathrm{Bloch}} = L_{\mathrm{Bethe}} + \Delta L_{\mathrm{Bloch}} \tag{3.58}$$

$$= \ln\frac{Cmv}{Z_1 v_0 \hbar\omega} + \ln\frac{2Z_1 v_0}{v} - \mathrm{Re}\,\Psi\left(1 + i\frac{Z_1 v_0}{v}\right) \tag{3.59}$$

$$= L_{\mathrm{Bohr}} + \Delta L_{\mathrm{invBloch}}, \tag{3.60}$$

defining an inverse Bloch correction, $\Delta L_{\mathrm{invBloch}}$, that can be added to Bohr's theory to achieve results identical to Equation 3.58. An accurate approximation to Equation 3.59 was found by de Ferrariis and Arista [FA84]. The Bloch formula as defined in Equation 3.58 has only selectively been expanded to include the shell, Barkas-Andersen, and density corrections [ICRU73], though an extension to relativistic velocities was found by Lindhard and Sørensen [LS96].

However, Bohr's and Bethe's theories, and hence Equations 3.58 and 3.60, ignore physical phenomena that are important in heavy-ion stopping [SS16]:

1. Electrons bound to the projectile partially screen the Coulomb interaction between projectile and target. This is important at low projectile energies because electrons with orbital velocities smaller than the projectile speed tend to be stripped [Boh40]. Since Bohr and Bethe both treat the projectile as a point charge, a screening correction must be applied for $v \lesssim v_{\mathrm{TF},1}$ [SS16].

2. Bohr's theory ignores the orbital motion of target electrons, which is included in Bethe's theory via the shell correction. It becomes relevant for $v \lesssim v_{\mathrm{TF},2}$ [SS16].
3. With increasing Z_1, the projectile's electronic potential can no longer be well approximated by that of a point charge, even if screening corrections are applied [SG98a].

Efforts to make up for these fundamental shortcomings in a comprehensive theory of heavy-ion stopping have not been fully successful thus far but led to a number of promising approaches.

Binary Theory Among them is the binary theory of Sigmund and Schinner [SS00; SS02], which is a reformulation of Bohr's model and hence starts in the classical limit. It reproduces the results of Bohr's theory but avoids the formal division into regimes of close and distant collisions (an inherent feature of both Bohr's and Bethe's approaches) by treating the effect of electron binding as screening of the interaction [ICRU73]. This reduces the complex many-body problem (two nuclei plus one or more electrons) to a binary-scattering interaction between the projectile and a single target electron. The effective potential used to describe the projectile charge was tuned to work well for varying ion charge states [SS20a]. The Barkas-Andersen correction is inherent to the model, and shell corrections have been incorporated [SS01a]. An extension of this non-perturbative classical model to the Born regime is achieved via the inverse Bloch and the relativistic Lindhard-Sørensen corrections [LS96].

Unitary-Convolution Approximation The unitary-convolution approximation (UCA) of Grande and Schiwietz [GS02] attempts the opposite and starts from Bethe's theory, covering the transition from the Born to the classical regime [ICRU73]. It does so via the Bloch correction but uses an impact-parameter-dependent version of Bloch's theory [GS98]. The model was extended to screened ions via the introduction of a screened potential [AGS00] and allows for projectile excitation and ionization [ICRU73]. It does, however, neither include shell and Barkas-Andersen corrections [ICRU73], nor the relativistic Lindhard-Sørensen correction [SS20a].

Nonlinear Fermi-Gas Model A third theory attempts to extend the validity range of transport-cross-section calculations valid for $v \lesssim v_{\mathrm{TF},1}$ (e.g., [FT47; Fir57; LSS63; CGA94]) to intermediate velocities. Arista and Lifschitz model the target as a nonlinear electron gas and use a generalized Friedel sum rule to describe screening and scattering [LA98]. The original model was extended

to heavier ions [Ari02] and natively incorporates shell corrections. It does, however, not include projectile excitation and ionization [ICRU73]. Though powerful in describing low-speed stopping, it struggles to properly account for interactions with bound electrons at intermediate velocities [ICRU73; AL02].

Shell-Wise Local Plasma Approximation Likewise building on the description of target electrons as a Fermi gas, Montanari et al. use a shell-wise local plasma approximation (SLPA) to extend calculations to bound electrons [LS53; CP72; MM06], thus implicitly taking into account the binding forces ignored in other models. The contribution of valence electrons is accounted for via the extended Friedel sum rule for the transport cross-section [Mon+08; Can+11], as in the previously described theory. SLPA also includes the Barkas-Andersen effect and projectile excitations but does not allow for charge exchange [SS16].

Convergent Kinetic Theory The fifth category of models, often collectively referred to as convergent kinetic theory (CKT), provides extensions to the Bethe theory that allow stopping-power calculations for partially ionized projectiles in partially ionized targets [ICRU73]. Many of these models were originally developed for the description of plasma interactions [Cha+98; Gar+98; May+02] and thus describe processes like the projectile charge state and charge exchange particularly well. The Barkas-Andersen effect and shell corrections are included, but the range of validity is restricted to $Z_2 < v/v_0 < Z_1$ [ICRU73].

Even though some of these calculations—and others not mentioned here (e.g., [Hat+08; SKC15; Gra16; SUC19; Zin+20; MCB20])—can claim successes in describing selected projectile-target combinations over more or less wide ranges in velocity (energy), none can yet provide a comprehensive theory. It has, for example, been established that SLPA fails for projectiles heavier than C [Can+11]. Binary theory, on the other hand, has been shown to work for a wider range of Z_1 but still does not always agree well with experimental data [Fet+06; Sig17; SS19]. Though the latter seems to be one of the better-performing models, I do not attempt to provide a qualitative or quantitative assessment of the different theories here. Direct comparisons between (some of) them can be found in [ICRU73; SS16; Sig17; SS20a].

3.3.3 The Role of Corrections

Figure 3.9 succinctly illustrates that corrections become significantly more important the heavier the projectile gets, even when restricting Z_1 to values of interest to our work. The central role of the Bloch correction in connecting

the low-speed, classical regime with the relativistic one is discussed in Section 3.3.2 above. The importance of the *inverse* Bloch correction as addition to Bohr's theory for the calculation of heavy-ion stopping cross-sections has been highlighted in [SS20a]. I likewise do not discuss shell corrections in detail here, as they are equally important for light and heavy ions. They are also inherent to many of the theories discussed in Section 3.3.2.

Much attention has been given to the Barkas-Andersen effect after Andersen et al. found that the stopping powers for alpha particles were *slightly more* than four times higher than those for protons [ASS69]. The difference was found to significantly increase with decreasing projectile speed and could be quantified as a contribution to the stopping power that is proportional to Z_1^3, much like the one observed for particles and their antiparticles [ICRU73]. The latter observation initially posed a severe obstacle to the theoretical treatment of heavy-ion stopping because the respective corrective term threatened to exceed the Bethe term even for moderately large Z_1 [SS03b]. In a seminal attempt to describe the effect, Ashley et al. developed a Z_1^3 extension to the Bohr model and postulated that deviations from Coulomb scattering were to be expected exclusively from distant collisions [ARB72]. Disputing the restriction to large impact parameters, Lindhard provided an alternative estimate of the Z_1^3 correction and claimed that an additional Z_1^4 term, derived from Bloch's theory, was needed [Lin76]. More recent and more complete evaluations are based on the electron-gas model [ES90] or the harmonic-oscillator model [MS89]. The increase of the Barkas-Andersen correction with decreasing speed eventually leads to a negative stopping force in the velocity-proportional regime ($v \lesssim v_{\mathrm{TF},1}$), resulting in the breakdown of theories based on expansions in Z_1 and in the need for nonlinear stopping theory [Ech+86; MF92; LA98; AL99; SS02; ICRU73]. The Barkas-Andersen effect is still being investigated, both theoretically and experimentally. Contrary to initial fears, however, Sigmund and Schinner could show that its importance actually decreases with increasing projectile charge, mostly because of increased screening [SS03b]. They also found, though, that corrections due to the inner target shells may be at the percent level even for energies on the order of 1 GeV per nucleon [SS20a].

The original extension of Bethe's theory to relativistic velocities [Fan63; Jac99] produces accurate results for the slowing down of projectiles with low Z_1, such as protons and alpha particles. It does, however, not describe well the more complicated case of relativistic heavy nuclei [Sch+94] because the scattering cross-section resulting from the Born approximation differs significantly from the exact one for large nuclear charges [SG98a]. This problem can be

addressed by finding an exact solution of the Dirac equation for the scattering of a relativistic electron off the potential of a point-like nucleus, as first found for electron projectiles by Mott [Mot29; Mot32]. Approximate solutions for ion projectiles were later derived by Ahlen [Ahl80]. The most up-to-date and comprehensive treatment is that of Lindhard and Sørensen, who showed that the slowing down of highly relativistic heavy ions is affected by the nuclear charge distribution of the projectiles [LS96], necessitating a modification to the Mott cross-section for point-like particles. Since the aforementioned low-energy corrections can be neglected for large β, the stopping number for relativistic, fully ionized (i.e., bare) nuclei is hence given by [SG98a]

$$L_{\mathrm{rel}} = L_{\mathrm{Bethe}} + \Delta L_{\mathrm{Mott}} + \Delta L_{\mathrm{LS}} - \frac{\delta}{2}, \tag{3.61}$$

where L_{Bethe} is the L term in Equation 3.16 without the density correction, ΔL_{Mott} the Mott correction, and ΔL_{LS} the Lindhard-Sørensen (LS) correction. Equation 3.61 is often referred to as LS theory for the heavy-ion stopping power and was shown to be in good agreement with experiments [Dat+96; Sch+96; Wei+00].

3.3.4 The Role of Ion Charge and Charge Exchange

A distinct feature of heavy-ion stopping is the presence of electrons on the projectile at all but the highest energies, even if it initially entered the target in a fully ionized state. This is because ions pick up and lose electrons during their passage through the medium in a process called *charge exchange* [ICRU73]. The energy loss of ions can thus only be described in a dynamic *charge-state equilibrium* (see discussion below), which is characterized by the probabilities $P(v, q_1)$ for an ion with velocity v to have a charge $q_1 e$. Using these, we can define an average equilibrium charge—not to be confused with the questionable concept of effective charge [SS01b; SS20a]—via [ICRU73]

$$\langle q_1 \rangle = \sum_{q_1} P(v, q_1)\, q_1 \tag{3.62}$$

and an equilibrium stopping cross-section via

$$\langle \sigma \rangle = \sum_{q_1} P(v, q_1)\, \sigma(v, q_1). \tag{3.63}$$

Here, the *frozen-charge stopping cross-section* $\sigma(v, q_1)$ defines the energy loss between two charge-changing events and can be determined experimentally via measurements of the energy loss in thin targets [ICRU73] or via theoretical calculations [SS20a].

Equilibrium charge states have been studied intensively, and it was found that they are on average higher in solids than in gases [Las51a; Las51b]. Bohr and Lindhard attributed this difference to a density effect [BL54]. Though disputed and intensely debated because of inconclusive data [BL70], increasing evidence appears to support this theory [MCG00; Bim+89a; Bim+89b]. In a Thomas-Fermi estimate, the charge state of ions (at least) up to Ar in solid matter can be approximated by [SS20a]

$$\langle q_1 \rangle = Z_1 \left(1 - e^{-v/Z_1^{2/3} v_0}\right). \tag{3.64}$$

The definition of an ion charge state requires the clear distinction between electrons that move with the ion and those that do not. This is to some degree complicated by the existence of so-called *convoy electrons* that are emitted from a target with a velocity close to that of the projectile [Lau+81; Sel85].

Charge Exchange

Charge exchange—i.e., the projectile's capture and loss of electrons—plays an important role in heavy-ion stopping because virtually all interaction cross-sections directly or indirectly depend on the projectile charge state. Unlike for point-like particles (e.g., protons), the stopping power of a partially or fully ionized nucleus therefore does not vary continuously but fluctuates along the projectile's path [SG98b]. For sufficiently thick targets, the ion approaches a dynamic charge-state equilibrium—a state in which the cross-sections and hence rates of electron capture and electron loss are equal [SG98b]—and the stopping power stabilizes, though residual fluctuations persist (see discussion on straggling below). Upon slowing, the equilibrium shifts to states of decreasing charge until the ion fully neutralizes, at which point nuclear scattering becomes the dominant energy-loss mechanism [Ahl80].

The capture and loss of electrons cause energy loss, which contributes to the stopping power. Also, charge exchange is inevitably accompanied by projectile excitation and de-excitation, further adding to the energy loss [SG98b] though not necessarily to the energy deposition in the target [KC80]. These effects were first predicted to result in a shorter range of alpha particles by Flamm and

Schumann [FS16], and later discussed more comprehensively by Rutherford [Rut24], Bohr [Boh48], and others. Sigmund and Glazov found that the energy loss due to excitation and ionization was probably overestimated in the theoretical literature [ICRU73], though they calculate that these processes still contribute as much as 1% to the equilibrium stopping cross-section at energies of 5 MeV per nucleon, and 10% or more at energies below 100 keV per nucleon [SG03]. The contribution of electron capture varies more significantly for different projectile-target combinations and is therefore more difficult to quantify in general terms—but it can be quite substantial, as highlighted, for example, in [Sig14].

Energy Loss

Initially, it was believed that the difference in stopping cross-section for an ion in different charge states must be proportional to q_1^2 (based on Bethe's energy-loss formula). But this is true only in the case of $Z_1 \gg Z_2$; generally, the q_1-dependence is (much) weaker than quadratic [ICRU73; SS20a].

To account for all possible charge states of an ion passing through matter, the energy-loss spectrum as a function of path length, x, must be expressed as a matrix [Sig92; SOS11]

$$\mathbf{F}(\Delta E, x) = \|F_{uw}(\Delta E, x)\|, \tag{3.65}$$

where u and w denote the state of the ion at depth 0 and x, respectively. In this description, the term 'state' includes both charge and excitation states. For $\Delta E \ll E_\mathrm{k}$, the matrix can be expressed as a Bothe-Landau integral [Sig92]

$$\mathbf{F}(\Delta E, x) = \frac{1}{2\pi} \int_{-\infty}^{\infty} e^{ik\Delta E} e^{Nx\mathbf{Q}(k)} \,\mathrm{d}k\,, \tag{3.66}$$

where N is the target's atom density and $\mathbf{Q}(k)$ a matrix with elements [SOS11]

$$Q_{uw}(k) = Q_{uw} - \int \left(1 - e^{-ikT}\right) \,\mathrm{d}\sigma_{uw}(T) \tag{3.67}$$

$$Q_{uw} = \sigma_{uw} - \delta_{uw} \sum \sigma_{uw}. \tag{3.68}$$

Here, $\sigma_{uw}(T)$ is the differential cross-section for an energy loss $(T, \mathrm{d}T)$ in a transition from state u to w and $\sigma_{uw} = \int \mathrm{d}\sigma_{uw(T)}$ the total cross-section. The mean energy loss summed over all exit states is then defined as [SG98b]

$$\left(-\frac{\mathrm{d}E}{\mathrm{d}x}\right)_u = \sum_w F_{uw}(x) S_w, \tag{3.69}$$

where $S_w = \sum_v S_{wv}$ is the total stopping cross-section of an ion in state w and

$$S_{wv} = \int T \, \mathrm{d}\sigma_{wv}(T) \tag{3.70}$$

a partial stopping cross-section. An explicit connection between ion charge and stopping force can be established via the screened Coulomb potential of the projectile [BK82]

$$V(r) = -\frac{q_1 e^2}{r} - \frac{(Z_1 - q_1)e^2}{r} e^{-r/r_\mathrm{s}}, \tag{3.71}$$

where the screening radius r_s is determined on the basis of a modified Thomas-Fermi model. This potential, together with the (outdated) effective-charge concept, is the basis for many tabulations of heavy-ion stopping powers [ZBL85]. More general screening functions have been explored by others [Kan99; GS02; Ari02]. Sigmund incorporated Equation 3.71 into Bohr's classical theory with a charge-dependent screening radius [Sig97],

$$r_\mathrm{s} = 0.8853 \, a_0 Z_1^{-1/3} \left(1 - \frac{q_1}{Z_1}\right), \tag{3.72}$$

though this approach eventually proved problematic and was superseded by binary theory [ICRU73].

Mean Excitation Energy vs. Oscillator-Strength Spectra

In the context of heavy-ion stopping, characterizing the excitation spectrum of the target medium by a single value for the mean excitation energy, as given by Equation 3.14 in the context of Bethe's theory, is inadequate [ICRU73]. In general, the sum over f_n can be replaced by an integral over the continuous spectrum of oscillator strengths, $f(\hbar\omega)$, that is related to the complex refractive index $\mathrm{n}(\omega) + i\mathrm{k}(\omega)$ via [ICRU73]

$$f(\hbar\omega) = 1.5331 \times 10^{-3} \, \frac{A_2}{\rho} \frac{\hbar\omega \mathrm{nk}}{(\mathrm{n}^2 + \mathrm{k}^2)^2}. \tag{3.73}$$

Here, $f(\hbar\omega)$ is normalized such that

$$\int_0^\infty f(\hbar\omega) \, \mathrm{d}(\hbar\omega) = Z_2. \tag{3.74}$$

Tabulated values of the oscillator strengths can be found in [ICRU73]. In an alternative approach, the dielectric theory by Lindhard and Scharff replaces the summation over excitation frequencies by an integration in space over the plasma frequency and the electron density [LS53].

3.3.5 Energy-Loss Straggling

The energy-loss distribution for light particles is predominantly determined by the collision statistics of Coulomb scattering (see Section 3.2.7). Depending on the impact parameter and projectile speed, other effects can contribute but are of minor importance. For heavier ions, on the other hand, charge exchange constitutes a complicating effect, primarily for two reasons [ICRU73]:

1. The cross-sections for energy loss and angular deflection depend on the charge state and thus are not constant along the projectile path. Even in charge equilibrium, the true ion charge fluctuates around the mean given by Equation 3.64. These fluctuations of the charge state directly translate into fluctuations of the energy loss [SOS11], commonly known as *charge-exchange straggling*.
2. Charge-exchange events themselves can give rise to significant energy loss and scattering. These are usually not treated as part of the above point but must be added separately.

Experimental evidence for charge-exchange straggling abounds [Cue+64; BAB80; SCF81; Oga+91; Fre+96]. Some theoretical studies even suggest that it might exceed collisional straggling under certain conditions [Win77], a conclusion which is at least partially supported by measurements [BBO00].

Other, non-Poissonian effects, such as *bunching* of target electrons and *packing* of target atoms are more pronounced for heavy ions than for lighter projectiles [SS10]. As of today, neither experimental nor theoretical studies of these processes are comprehensive enough to allow accurate predictions. Available results, however, suggest that both effects depend stronger than quadratically on the ion charge and can therefore become quite significant, though they partially compensate each other [SS10]. Especially at low energies (projectile speeds), deviations from free-Coulomb scattering also become more pronounced for higher Z_1 than for light projectiles [SS03a].

As a consequence of all these effects, the mathematical description of energy-loss straggling must be expanded considerably. For fully stripped

projectiles with $v \gg v_{\mathrm{TF}}$, this is achieved by finding solutions to the general Bothe-Landau formula for the energy loss [Lan44]

$$F(\Delta E, x)\ \mathrm{d}(\Delta E) = \frac{\mathrm{d}(\Delta E)}{2\pi} \int_{-\infty}^{\infty} e^{is\Delta E - nx\sigma(s)}\ \mathrm{d}s\,, \tag{3.75}$$

where s is a variable in Fourier space, x the path length, and n the number of target atoms per volume. $\sigma(s) = \int (1 - e^{-isw})\ \mathrm{d}\sigma(w)$ is the transport cross-section, w the energy loss in an individual interaction, and $\mathrm{d}\sigma(w)$ the differential cross-section per atom for an energy loss in the interval $(w, \mathrm{d}w)$. Solutions for the transport cross-sections of protons and light ions are given in Section 3.2.7. More general solutions have been found by Lindhard [Lin85], Glazov [Gla00], and others.

In the general case of partially stripped ions, this approach is, however, only valid for frozen charges—i.e., between charge-changing events. The effective collisional stopping power hence becomes a weighted mean of frozen-charge stopping powers, resulting in an energy-loss spectrum as described by Equations 3.65 and 3.66 above. Different approaches for solving these equations have been found by Sigmund and Glazov [Sig92; Sig94; GS97; Gla02]. Though differing in the exact mathematical form, the energy-loss distribution for heavy ions in charge equilibrium is qualitatively similar to the one shown in Figure 3.4, though the Gaussian part tends to be (much) wider.

3.3.6 Nuclear Reactions and Fragmentation

One of the largest qualitative differences between the interaction of light and heavy ions with matter is the substantial role of nuclear reactions in the latter case. Such non-elastic interactions can occur whenever the incoming ion's kinetic energy is large enough to overcome the mutually-repulsive Coulomb force acting between projectile and target nuclei [BEH84]. This so-called *Couloumb barrier* typically lies at center-of-mass energies of tens of MeV per nucleon or less [VAS81; Qu+14], though nuclear interactions at energies insufficient to overcome the barrier are possible due to tunneling [Lil82; Rol07]. The Coulomb barrier effectively marks the transition between the regime of electromagnetic interactions—ultimately described by quantum electrodynamics (QED)—and the regime of the strong interaction, described by quantum chromodynamics (QCD).

Depending on the centrality of the ion–ion collision, different processes lead to a modification of the interacting nuclei. At large impact parameters,

and hence in peripheral collisions, the ions merely graze each other and, in doing so, may exchange one or more nucleons [Win94]. Such *transfer reactions* lead to a change in mass and charge, and hence modify the nuclei's elemental or isotopic identity [Zuc60]. Simple single-transfer reactions, where only one proton or neutron is transferred from projectile to target or vice versa, were studied as early as the 1950s [RSZ53; CF54]. The more complicated cases of double and multiple transfer, where two or more nucleons move in an unidirectional transfer from one to the other ion, were studied later and are still a field with many open questions [Cor+13; Mij22]. Even more challenging to investigate are exchange transfer and complex transfer, in which pairs or clusters of nucleons are exchanged bidirectionally between the ions, respectively [Zuc60].

At smaller impact parameters, the ions partially overlap and the interaction becomes deeply inelastic. A meta-stable di-nuclear system is formed that may break up—forming, after the exchange of a considerable number of nucleons, projectile-like and target-like fragments [BEH84; Sab24]—or fuse to create a compound system [Wil+95; Hei+10a; Hei+10b]. The more central the collision is, the higher is the probability for partial or complete fusion of the di-nuclear system. At higher center-of-mass energies, the energy density in the compressed nuclear matter rises and the colliding nuclei decompose into single nucleons [BEH84]. At some point, the density becomes so high that the nucleons' constituent quarks are deconfined [Bay82]. This ultimately leads to the formation of a quark-gluon plasma [BS07; PŠ17], though the ultra-high center-of-mass energies required for its creation are of little relevance here.

The modified (via nucleon transfer) or fused nuclei emerging from the interaction are practically always in highly excited states and are often heavily deformed. They de-excite primarily via the evaporation of nucleons and light nuclei like deuterons or alpha particles [KQA60; Fer+96; Wen+19]. If the excitation energy is too large, the system becomes unstable against fission and breaks apart into two (or more) larger fragments [BEH84]. In fusion reactions, the amalgamated system has no memory of its formation history; the end state of the interaction—and hence the identity of the fission fragments—is solely determined by the properties of the compound system and not by the specific reaction leading to its creation [BEH84].

Nuclear reactions have been and still are a widely used tool for studying the structure of nuclei [AT70; LHO23] and the processes governing nucleosynthesis [ZG08; Bac+14; HD22]. In the context of this thesis, we are, however, not so much interested in the exact interaction processes but in their end states,

as well as in the energy-dependent interaction cross-sections. Theoretical calculations and predictions are, however, hardly possible: Despite the fact that QCD is the fundamental theory governing nuclear interactions, it is only really usable in the limit of large momentum transfers and has not yet been applied to nucleus–nucleus collisions at the energies relevant to our work [ZL16]. In general, the complex nature of exactly solving the equations underlying many-body nuclear interactions defies present-day computational methods. At energies relevant to experiments at the Large Hadron Collider (LHC) and other high-energy accelerators, progress has been made in the discretized space of *lattice QCD* [GL10], though such calculations typically do not extend down to energies of interest here. We thus need to rely on a variety of semi-empirical nuclear-reaction models that are based to a large extent on experimental data (for examples, see [Wil+94; Her+07; Wer+21; KHG23]), which in some areas is far from complete [ZL16]. The lack of a fully theoretical description leads to uncertainties in the prediction of interactions for which no or only few measurements have been made.

In the context of developing detectors capable of measuring and identifying cosmic-ray nuclei, it is important to understand the overall, macroscopic effect nuclear reactions in the detector material have on the incident particles that shall be analyzed. Any of the processes described above at minimum leads to a change in mass and charge of the projectile, which consequently has a different stopping power and hence energy-loss profile. Even for grazing collisions, the projectile in most cases fragments into two or more particles (nucleons and nuclei lighter than the original ion) due to excitation-induced fission. These fragments retain, to a large degree, the velocity and direction of the projectile, though small angular deflections are possible [ZL16]. The corresponding changes in transverse and longitudinal momentum with respect to the incident projectile are essentially normally distributed and well described by the statistical theory of Goldhaber [Gol74], as confirmed by experimental data [Zei+01; Zei+07; Zei+08]. In the extreme case of high-energy head-on collisions (i.e., with small impact parameter), a large multiplicity of projectile-like fragments is created, each having a stopping power that is significantly lower than that of the pre-collision projectile (due to the Z_2^2/β^2 scaling of the energy loss in Equation 3.15).

Target (or target-like) fragments are created when the struck nucleus substantially participates in the interaction, either due to excitation resulting from nucleon transfer or in close collisions where most of the nuclear matter of the interacting ions is re-arranged. They have much lower energies than projectile

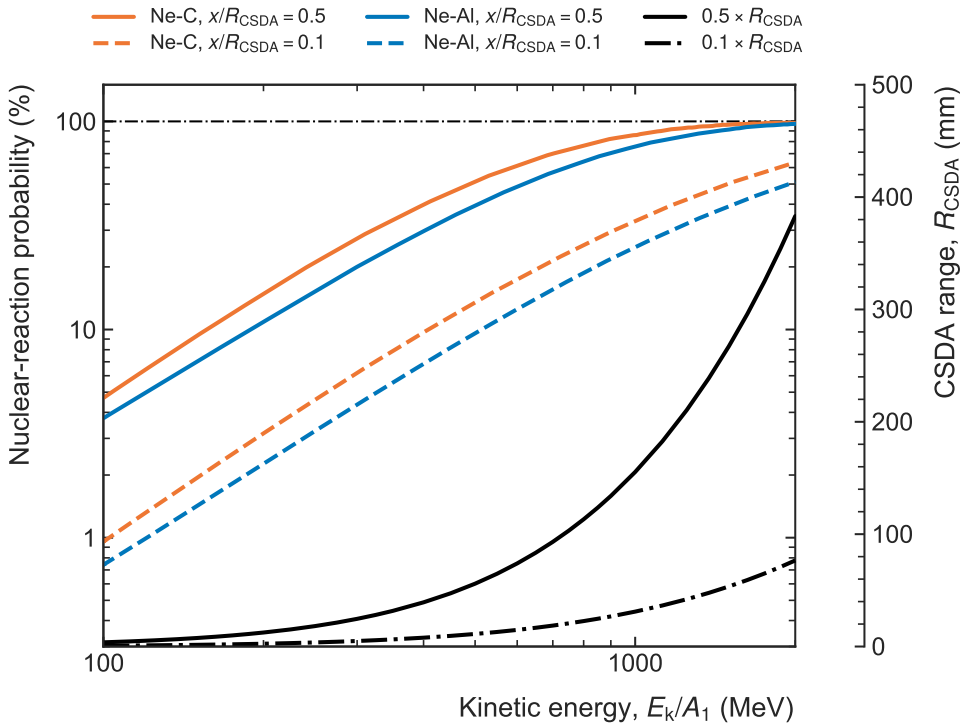

Figure 3.10: Nuclear-reaction probability for neon nuclei in carbon (orange) and aluminum (blue) targets as a function of energy. Curves are shown for two target thicknesses, x, as fixed fractions of the CSDA range, $x/R_{\mathrm{csda}} = 0.1$ and $x/R_{\mathrm{csda}} = 0.5$. The physical thickness thus varies with energy. The black line shows the scaled ranges in aluminum for comparison. Data taken from [Gei+02; ZZB10].

fragments (on the order of tens of MeV or less [ZL16]) and consequently have a high stopping power and short range. Since they are evaporated from a de-exciting nucleus that is essentially at rest, they are also emitted more or less isotropically, creating a star-like pattern of energy deposition around the interaction site. Only neutral fragments (neutrons) can have a longer range and cause energy deposition far away from the projectile track when they hit another target nucleus and initiate a secondary nuclear interaction.

Overall, fragmentation leads to an energy-loss behavior that is significantly different from the one for electromagnetic interaction alone, as discussed in the previous sections of this chapter. For projectile fragmentation, the sum of

the stopping power of the fragments is always lower than that of the incident nucleus [ZL16]. Paired with the longer range of the fragments, this leads to a flatter and deeper energy-deposition profile. Target fragmentation, on the other hand, leads to large, localized energy depositions at random locations along the projectile's path. Both processes are usually not covered in the discussion and parametrization of the energy loss of ions in matter and, specifically, are not included in the mathematical description of energy-loss straggling referred to in Section 3.3.5 above. In the literature, this omission is usually justified with the identity-changing nature of nuclear reactions. The above treatment of the heavy-ion stopping power thus applies to the pre-collision projectile and to the projectile and target fragments separately but not to the projectile–fragment system as a whole.

The probabilities for possible end states of a nuclear reaction can be quantified by a plethora of interaction cross-sections, such as the elemental and isotopic fragment-production cross-sections and various differential cross-sections in angle, energy, and momentum [Nor+12]. In our work, we are primarily interested in the probability for a nuclear reaction to take place in the interaction of a given projectile–target combination as a function of the projectile's kinetic energy. Likewise, we would like to know the probability for such a reaction to change the elemental nature of the projectile, which requires an alteration of its nuclear charge, Z_1. These probabilities are given by the *total nuclear-reaction cross-section* and by the *charge-changing cross-section*, respectively. Different semi-empirical parametrization for both exist and a brief but good overview is given in [Luo+21].

Figure 3.10 exemplarily shows the total nuclear-reaction probability for neon nuclei in carbon and aluminum for two target thicknesses (given as fixed fraction of the CSDA range). The data was taken from Geissel et al. [Gei+02], who performed calculations based on the widely used parametrization by Shen et al. [She+89]. The data illustratively highlights that (1) nuclear reactions are percent-level processes even at energies below 100 MeV per nucleon and that (2) they are dominating processes in targets of more than 10 cm thickness and for energies close to or exceeding 1 GeV per nucleon. Incidentally, the latter value coincides rather well with the region of maximum cosmic-ray flux (see Figure 2.5) and with the upper end of the sensitivity range of our detectors. This quite clearly demonstrates the importance of nuclear reactions, and in particular target fragmentation, to our work.

3.4 Interaction of Neutrons with Matter

The interaction of neutrons with matter differs substantially from that of charged particles. It is dominated by elastic and inelastic scattering off nuclei of a material's constituent atoms, and by the triggering of nuclear reactions such as capture, spallation, and fission [And+17]. Neutrons can only indirectly deposit energy through a two-step process: They impart energy on protons or nuclear fragments and these heavy charged particles—which have a high stopping power and short range—then deposit this energy via electronic losses.

The dominant interaction and intermediate and high energies is elastic scattering with atomic nuclei. In this case, the average energy transferred to the recoiling nucleus is [And+17]

$$\overline{Q} = E_\mathrm{i} \frac{2 m_\mathrm{n} M}{(m_\mathrm{n} + M)^2} = \frac{Q_\mathrm{max}}{2} \,, \tag{3.76}$$

where E_i is the incident neutron energy, m_n the neutron mass, M the mass of the nucleus, and Q_max the maximum possible energy transfer. The energy transfer is thus largest for low-Z materials (with correspondingly low M). For hydrogen, for example, approximately half the kinetic energy is transferred in a single collision because $M = m_\mathrm{p} \approx m_\mathrm{n}$. This effect is exploited for the *moderation* of neutrons, i.e., for the degradation of their energy to thermal levels (around 0.025 eV): The average number of collisions to thermalize a neutron with 1 MeV initial energy is about 25 for hydrogen, 114 for carbon, and 2092 for uranium [And+17]. Shielding against neutrons must therefore contain a high proportion of low-Z materials. The differential cross-section for a single-neutron elastic scattering is given by [And+17]

$$\frac{\mathrm{d}\sigma_\mathrm{el}}{\mathrm{d}\Omega} = |l|^2 \,, \tag{3.77}$$

where l is the *scattering length* that contains all physics of the interaction a varies greatly between different nuclei.

At energies larger than a few MeV, neutrons can impart sufficient energy on a nucleus to lift it into an excited state. In such inelastic collisions, a neutron with lower energy is emitted in a random direction [And+17]:

$$\mathrm{n} + {}^{A}_{Z}\mathrm{X} \rightarrow {}^{A+1}_{Z}\mathrm{X}^* \rightarrow {}^{A}_{Z}\mathrm{X}^* + \mathrm{n}' \rightarrow {}^{A}_{Z}\mathrm{X} + \mathrm{n}' + \gamma \,. \tag{3.78}$$

Here, n is the incident neutron, n' the emitted neutron, ${}^{A}_{Z}\mathrm{X}^*$ the target nucleus in the excited state, and ${}^{A+1}_{Z}\mathrm{X}^*$ the unstable intermediate product after the

neutron has entered the nucleus. Typically, a large fraction of the incident neutron's energy are lost and emitted as secondary radiation upon de-excitation of the target nucleus.

At lower energies than required for inelastic scattering, thermal neutrons can be *captured* by a nucleus, leading to an excited intermediate product that decays via the emission of a proton or a gamma ray. In neutron-induced *nuclear fission*, a heavy nucleus splits into two or more smaller nuclei, releasing large quantities of energy because of the larger binding energy of the fission products [Joy18]. This process is largely irrelevant for the work described in this thesis. Much more relevant is *spallation*, which is the term used to describe neutron-induced fragmentation of a target nucleus (see Section 3.3.6 above).

Concluding Remarks

My review of the interaction of radiation with matter may seem somewhat detailed for a dissertation focusing on detector development and not on the theoretical description of such processes. I would like to point out, however, that I barely scratched the surface of many effects that ultimately determine the (theoretical) performance of our sensors. Especially the stopping of heavy ions, though increasingly well understood, is still an area of active research. Uncertainties remain even in seemingly fundamental aspects of stopping theory. It will become evident in the remainder of my thesis that few of these uncertainties can cast serious doubt on the general working principle of the detectors we develop. Some, however, may significantly affect the precision and accuracy of our measurements.

It is important to keep in mind that interest in stopping theory has waned in recent decades. Many modern simulation tools were optimized for the description of highly relativistic particles—as relevant to experiments at the LHC and other high-energy accelerators—for which corrected forms of Bethe's theory provide adequately accurate predictions. In addition, little high-precision data at low energies has become available apart from what is needed to improve cancer therapy (mostly concentrating on protons and carbon). Care must thus be taken when relying on simulation frameworks developed for these applications.

Chapter 4

Relevant Detector Technologies

Almost all devices for detecting charged particles exploit the fact that a charged particle ionizes the material along its track—hence the often-used distinction between ionizing radiation (charged particles and photons above a certain threshold energy) and non-ionizing radiation (photons below the ionization threshold). With few exceptions[1], modern detectors collect, and in some cases multiply, the created electron-ion pairs or electron-hole pairs (in the case of semiconductor detectors). The collected charge is then used as a measure of the energy the particle lost in the detector through ionization.

The most common detector materials are gases and solids; liquids are seldom used, but if they are, then often at larger scales (for example in the liquid-Argon calorimeter of the ATLAS experiment [WC09]). Gases are often employed to construct detectors with large volumes and an acceptable price tag but have the disadvantage of requiring pressure vessels and systems for mixing, handling, and purifying gases. Solid-state detectors, on the other hand, are used to construct detectors of the highest resolutions but are often expensive and difficult to scale. Though gaseous detectors are used in space (for example in the transition radiation detector of the AMS-02 experiment [Agu+21a]), the rigorous safety requirements typically encountered in space missions and the small sizes of most instruments favor the use of solid-state materials.

Our work focuses on the development of detector systems based on solid-state materials, with a particular focus on the use of various organic and inorganic scintillators. I therefore introduce the physical principles of the

[1] Nuclear track-etch detectors, for example, do not collect charges but make use of the damage to their base material caused by the ionization [HW80].

scintillation mechanism, with a particular emphasis on organic scintillators. As many of our detectors are based on scintillating fibers, I also discuss the principles of light transport in fibers and summarize the current state of knowledge about using them in space applications. We exclusively use silicon photomultipliers (SiPMs) to detect scintillation light in our detectors, and I introduce them at the end of the chapter.

4.1 Detection Efficiency and Geometric Factor

In the fields of cosmic-ray research, astrophysics, and in radiation protection, we want to determine absolute fluxes of particles in a certain region of space. To do so, we use detectors that are imperfect. Particles traversing a detector's active volume may not sufficiently interact with it for us to be able to determine their type, energy, and direction of incidence. In some cases, they may not interact at all. The so-called *detection efficiency*—the probability for a particle to leave a reconstructable trace in the detector—may in general depend on the particle type, energy, and direction, and on the location of the first interaction in the detector [Leo94; Kno10].

We thus need to understand what *count rate*—i.e., the number of particles detected per unit time—we expect in a detector for a given energy- and direction-dependent flux. Conversely, if we want to calculate an absolute flux from a measured count rate, we need to know the detector's energy- and direction-dependent sensitivity. We hence consider a detector subjected to a particle flux with spectral intensity $J(E, \theta, \varphi) = J_0(E)F(\theta, \varphi)$, with $F(\theta, \varphi)$ normalized such that

$$\int_{\theta=0}^{\pi} \int_{\varphi=0}^{2\pi} F(\theta, \varphi)\, \mathrm{d}\Omega = 4\pi, \tag{4.1}$$

where $\mathrm{d}\Omega = \sin\theta\, \mathrm{d}\theta\, \mathrm{d}\varphi$, and θ and φ are the polar and azimuth angles encoding the direction. $J(E)$ thus describes the energy spectrum of the flux, assumed to be constant in time. We also assume that both $J(E)$ and $F(\theta, \varphi)$ have no spatial dependence—or that the detector is fixed in space—such that we do not need to take into account spatial coordinates.

In this scenario, the count rate of the detector is given by [Sul71; CO71]

$$C = \int_{E_1}^{E_2} \left[\int_{\Omega} \mathrm{d}\Omega \int_{\mathrm{S}} F(\theta, \varphi)\, \hat{\mathbf{r}} \cdot \mathrm{d}\boldsymbol{\sigma} \right]_E J_0(E)\, \epsilon(E)\, \mathrm{d}E\,, \tag{4.2}$$

where Ω is the full solid angle considered, S is the total area of detector's entrance aperture, $\hat{\mathbf{r}}$ the unit vector in direction (θ, φ), and $\hat{\boldsymbol{r}} \cdot \mathrm{d}\boldsymbol{\sigma}$ the effective element of area oriented into that direction. In the general case, $\hat{\boldsymbol{r}} \cdot \mathrm{d}\boldsymbol{\sigma}$ may depend on the particle energy. $\epsilon(E)$ is the energy-dependent detection efficiency, which we here assume to be independent of θ and φ, though this is often not true in real detectors. E_1 and E_2 are the lower and upper bounds of the range of particle energies being considered, respectively. If calculating the total count rate, E_1 is the minimum detectable kinetic energy and $E_2 = \infty$.

The term in square brackets is the *gathering power* of the detector for a flux whose intensity has an angular dependence given by $F(\theta, \varphi)$ [Sul71]:

$$\Gamma_{\mathrm{F}}(E) = \int_{\Omega} F(\theta, \varphi)\, \mathrm{d}\Omega \int_{\mathrm{S}} \hat{\mathbf{r}} \cdot \mathrm{d}\boldsymbol{\sigma} = \int_{\Omega} F(\theta, \varphi)\, A(E, \theta, \varphi)\, \mathrm{d}\Omega \tag{4.3}$$

Here, we define the *directional response function* of the detector as

$$A(E, \theta, \varphi) = \int_{\mathrm{S}} \hat{\mathbf{r}} \cdot \mathrm{d}\boldsymbol{\sigma}\,. \tag{4.4}$$

Once determined, the response function allows to calculate the gathering power of a detector for any given flux $J_0(E)$. This is especially useful in numerical simulations.

In the simplifying case of an isotropic flux, $F(\theta, \varphi)$ is unity and the gathering power is independent of θ and φ. If we further assume that the detection efficiency is unity and independent of energy, we can define the detector's *geometric factor*, often also called the *geometric acceptance*, as

$$G_{\mathrm{F}}(E) = \int_{\Omega} \mathrm{d}\Omega \int_{S} \hat{\boldsymbol{r}} \cdot \mathrm{d}\boldsymbol{\sigma} = \int_{\Omega} A(E, \theta, \varphi)\, \mathrm{d}\Omega\,, \tag{4.5}$$

such that the count rate is simply given by

$$C = \int_{E_1}^{E_2} G_{\mathrm{F}}(E)\, I_0(E)\, \mathrm{d}E\,. \tag{4.6}$$

$I_0(E)$ is intensity of the particle flux at a given energy E that is constant in space and in time. An often used simplification assumes that the response function (Equation 4.4), and thus the geometric factor, are energy-independent, as is for example the case for a particle telescope consisting of two or more planar detectors without a magnetic field. In this case, Equation 4.6 reduces to

$$C = G_{\mathrm{F}} \int_{E_1}^{E_2} I_0(E)\, \mathrm{d}E\,. \tag{4.7}$$

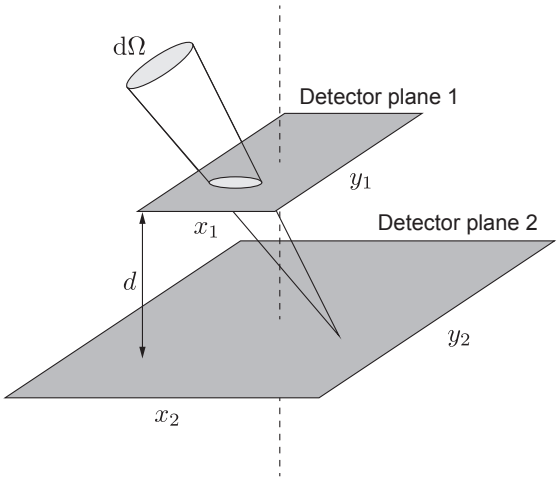

Figure 4.1: Definition of variables used for the analytic calculation of the geometric factor of two co-planar detectors.

Though not always reflecting the true response function, the geometric factor is—due to its simplicity—often the parameter of choice for comparing the gathering power of different detectors used in cosmic-ray research.

4.1.1 Analytic Solutions

Since Equations 4.4 and 4.5 are difficult to compute analytically, especially if they depend on the particle energy, the response function and geometric factor are often determined numerically. There exist, however, analytic solutions for simple cases that can help to approximate more complex geometries.

One of them is a single planar detector, whose geometric factor for an isotropic particle flux is simply given by [Sul71]

$$G_{\mathrm{F}}^{\mathrm{plan}} = 2\pi A, \tag{4.8}$$

where A is the total area of the detector. Another simple geometry is that of a particle telescope consisting of two co-planar detectors with side lengths x_i and y_i that are separated by a distance d (see Figure 4.1). An analytic expression for an isotropic flux and for the general case where the two detectors do not have the same size ($x_1 \neq x_2$) was found by Thomas and Willis [TW72], and independently by Sullivan [Sul71]. In the case of equally sized detectors

($x_1 = x_2 = x$ and $y_1 = y_2 = y$), their expressions are identical to those found earlier by Witmer and Pomerantz [WP48]:

$$\begin{aligned} G_{\mathrm{F}}^{\mathrm{tel}} = {} & \frac{2x\sqrt{d^2+y^2}}{d^2} \arctan \frac{x}{\sqrt{d^2+y^2}} \\ & + \frac{2y\sqrt{d^2+x^2}}{d^2} \arctan \frac{y}{\sqrt{d^2+x^2}} \\ & - \frac{2x}{d} \arctan \frac{x}{d} - \frac{2y}{d} \arctan \frac{y}{d} - \ln \frac{d^2(d^2+x^2+y^2)}{(d^2+x^2)(d^2+y^2)} \end{aligned} \tag{4.9}$$

Such analytic expressions can be used to check numeric determinations for consistency, as I will do for the calculation of the geometric factors of our detectors in Section 9.2.

4.2 Scintillators for Charged-Particle Detection

Despite being one of the oldest techniques for particle detection [Pri50; Bel50], scintillation detectors still play a significant role in all areas of scientific research that involve the detection of charged (and uncharged) particles. The use of scintillators dates back to the early days of experimental nuclear physics [RCE30], and they remain one of the most versatile radiation-sensitive materials to this day [Kha15]. At the same time, they are simple to use, often relatively inexpensive, and can be the basis for rugged detectors operating in a wide range of environmental conditions without the maintenance requirements associated with, for example, gas detectors.

In a scintillator, the energy deposited by a charged particle through the ionization and excitation of the material's constituent atoms or molecules is partially dissipated via *luminescence*—i.e., the emission of photons with a characteristic wavelength spectrum. There are essential differences in the scintillation process in organic and inorganic materials [Bir64], though I will here focus on the former, as relevant to the charged-particle detectors described in this thesis. The ideal (organic or inorganic) scintillator should possess the following properties [Kno10]:

1. The material should convert the energy deposited by a (charged) particle into detectable light with high efficiency.
2. The conversion should be linear—i.e., the light yield should be directly proportional to the deposited energy over a wide range of energies.

3. The scintillator should be transparent to its own light emission.
4. The decay time of the induced luminescence should be short, resulting in fast pulses that allow the detection of particles at high rates and with good time resolution.

Scintillating materials differ widely in their properties, and no single material is the perfect fit for every conceivable application. Because of the high Z-value of their constituents and their high density, inorganic scintillators are widely used in medical physics, X-ray and gamma-ray spectroscopy, and for calorimetry [Sch21; Sve+17; Shw17]. They tend to have the highest light yield (up to 100,000 photons per MeV of energy deposition in extreme cases [Yan+22]) and linearity, though they often have a long decay time (several hundred nanoseconds to microseconds) that prevents their use in high-rate applications [Duj+18]. In the past decade or so, however, several inorganic materials were found that show decay times of only a few nanoseconds, albeit often at the cost of a lower light yield [Yan+22].

Organic scintillators, on the other hand, are favored for the detection of charged particles and neutrons due to their lighter constituents, lower density, and high hydrogen content [Kno10; Ham21]. They are generally faster than inorganic materials, with decay times of a few to tens of nanoseconds, but tend to have a lower light yield (typically on the order of 10,000 photons per MeV or less for plastics and slightly higher for organic crystals [Ham21; YWF15]). Improving the latter is one of the primary drivers of current materials research in the field of organic scintillators [Kos22].

4.2.1 Scintillation Mechanism in Organic Scintillators

The scintillation mechanism in organic materials is closely associated with conjugated and aromatic organic molecules, in particular those containing one or several benzene (C_6H_6) rings. In contrast to most inorganic materials—which require a regular crystalline lattice—scintillation from a given molecular species can thus be observed independent of its physical state [Kno10]. This is because organic materials form compounds or molecular crystals in which the molecules are only loosely bound by Van der Waals forces and retain their individual identity, electronic structure, and luminescent properties [Tsa+18]. The latter can thus be observed in the vapor state, in liquid and solid solutions, in the liquid, plastic and glassy states, and in the crystalline state [Bir64].

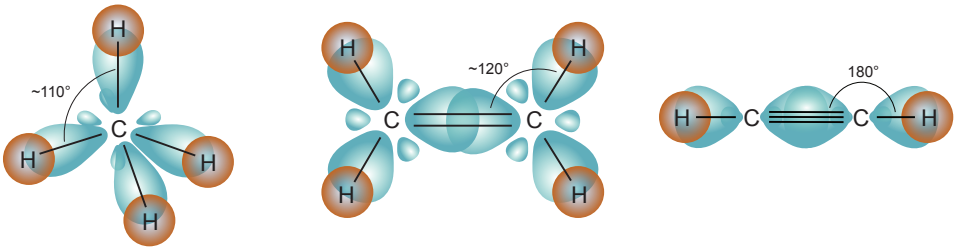

(a) Methane – sp^3 (b) Ethylene – sp^2 (c) Acetylene – sp

Figure 4.2: Examples of the three different hybridizations of valence-electron orbitals in simple hydrocarbons. The four σ bonds in the non-luminescent sp^3 hybridization are arranged in a (three-dimensional) tetrahedral geometry. The luminescent sp^2 and sp hybridizations lead to planar geometries. Only the C–H and C–C σ bonds are shown; the π molecular orbitals (MOs) forming the double and triple bonds are omitted for clarity.

The structure and luminescent properties of organic molecules is largely determined by the electronic structure of the carbon atom and its ability to form hybridized electron orbitals [Bir64]. In carbon, one of the electrons in the 2s state can be considered promoted to a 2p orbital because the atom can then form energetically favorable saturated, double-bonded, or triple-bonded hydrocarbons [CGW12]. Figure 4.2 shows the three ways in which the resulting four valence-electron orbitals (one 2s and three 2p) can overlap and form covalent bonds, using simple hydrocarbons as illustrative examples.

In methane, the four orbitals overlap in equal parts—each taking three quarters of its character from a 2p orbital and one quarter from the 2s orbital—to form four equivalent sp^3 hybrid orbitals [CGW12]. These overlap with the 1s orbitals of hydrogen atoms to form four σ bonds of equal length and strength. Molecules containing only σ bonds are not luminescent. In ethylene, one of the 2p orbitals remains unchanged, and three equivalent sp^2 hybrid orbitals are formed by mixing the other two 2p orbitals and the 2s orbital [CGW12]. The sp^2 orbitals participate in the C–C and C–H σ bonds, while the remaining 2p orbitals of the two atoms overlap to form a π molecular orbital (MO), providing the second part of the C–C double bond. In acetylene, only one 2p orbital mixes with the 2s orbital to form two sp hybrid orbitals that participate in the C–H and C–C σ bonds. The remaining four 2p orbitals from both carbon atoms combine to form two π MOs, resulting in a C–C triple bond.

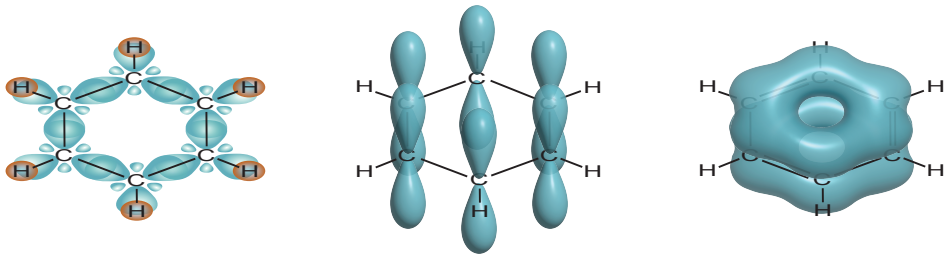

(a) σ bonds (b) 2p orbitals (c) Delocalized π MOs

Figure 4.3: π MOs in benzene: The six carbon atoms are sp^2 hybridized and form a planar ring via σ bonds. The six free 2p orbitals combine to form six delocalized π MOs, giving the molecule its luminescent properties.

It is the excited states of these π MOs that give organic molecules their luminescent properties [Bir64]. The most important luminescent molecule is the aromatic benzene ring, whose six carbon atoms are sp^2 hybridized and form a planar ring via σ bonds (see Figure 4.3). The six free 2p orbitals combine to form six π MOs, and the electrons in these orbitals are *delocalized*—i.e., they are spread equally over all the carbon atoms [CGW12]. Similar systems of delocalized π electrons occur in other aromatic and conjugated systems.

The electronic energy levels of a molecule with such a π-electron structure and the transition between these levels can be schematically represented by a Jabłoński diagram (sometimes called Perrin-Jabłoński diagram), as shown in Fig 4.4. Energy deposited by a particle can be absorbed by lifting the system from its ground state, S_0, to any of the excited singlet (S_2, S_3, ...) states. In typical organic scintillators, the energy spacing between the S_0 and S_1 states is about 3 or 4 MeV [Kno10]; the spacing between higher-lying states is somewhat smaller. Superimposed on each of the electronic levels are vibrational sublevels with a typical spacing of about 0.16 MeV, denoted by a second subscript (S_{00}, S_{01}, ...) [Bir64]. The transition between singlet and triplet (T_1, T_2, ...) states is spin-parity-forbidden, though it may occur under certain conditions [GL68]. Because the spacing between vibrational levels is large compared to average thermal energies (0.025 eV), the predominantly populated level at room temperature is the S_{00} ground state [Kno10]; the molecule is thus primarily excited via $S_{00} \to S_{1x}$, $S_{00} \to S_{2x}$, ... transitions.

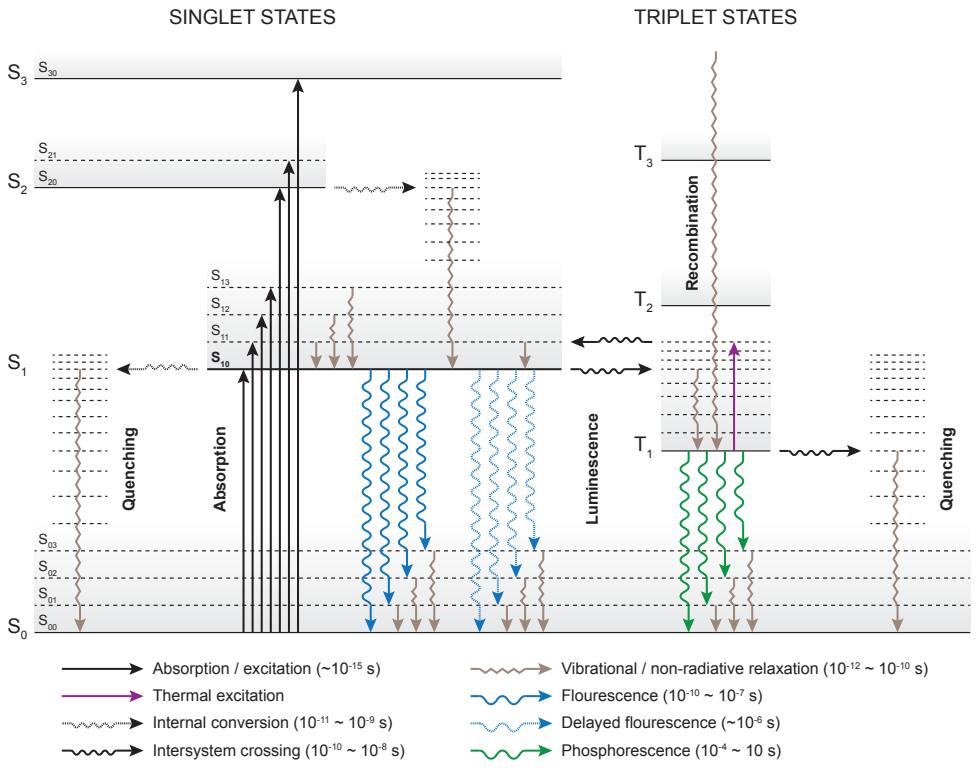

Figure 4.4: Jabłoński diagram of the energy levels and transitions between them in an organic scintillator. Higher-lying vibrational sublevels are only shown when needed to indicate internal conversion. See text for explanation.

Types of Luminescence

In a scintillator, kinetic energy of a charged particle passing near luminescent molecules is absorbed via the excitation of their π-electron system into any of the singlet states S_1, S_2, ... (see the upward-pointing arrows in Figure 4.4). Despite their short radiative lifetime, the higher singlet states ($S_2, S_3, ...$) can efficiently and quickly (on the order of picoseconds) de-excite via non-radiative internal conversion to the S_1 state due to the overlap of adjacent excited states [Bir64]. Sublevels with excess vibrational energy (e.g., S_{11} or S_{12}) are not in thermal equilibrium with their neighbors and quickly relax non-radiatively to the state's lowest vibrational level [Kno10]. The excitation process thus

produces—in a very short time—a population of molecules in the S_{10} state.

The S_{10} state has a lifetime on the order of a nanosecond (or less) and can de-excite radiatively to any of the vibrational sublevels of the ground state (S_{01}, S_{02}, ...), which then quickly relax non-radiatively to S_{00}. The photons emitted in this prompt luminescent process, called *fluorescence*, make up the largest part of a scintillator's light emission. Their wavelength spectrum reflects the vibrational structure of the S_0 state. Though the resulting spectral structure is roughly the inverse of the $S_0 \rightarrow S_1$,... absorption band, the whole spectrum is shifted to somewhat lower energies (longer wavelengths) because (1) excitation starts exclusively from the S_{00} state and (2) energy is lost in internal conversion and vibrational relaxation to the fluorescent S_{10} state.[2] This so-called *Stokes shift* can intuitively be understood when comparing the length of the absorption and fluorescence arrows in Figure 4.4 and is the reason why scintillators are partially transparent to their own light emission. The intensity of the fluorescence emission decays exponentially with time according to [Bir64]

$$I(t) = I_0 e^{-t/\tau} \,, \tag{4.10}$$

where I and I_0 are the intensities at time t and $t = 0$, respectively, and τ is the decay time, which typically is on the order of a few nanoseconds.

A fraction of the molecules excited to the S_{10} state undergo a non-radiative transition into the triplet state T_1 in a process called *intersystem crossing* [LK44]. Though spin-parity-forbidden, such transitions are made possible by the reversal of electron spins through spin–orbit coupling in overlapping excited states [Kas50]. Another path to T_1 is the recombination after ionization of the π-electron system, which preferentially populates the triplet state [Ham21]. T_1 is long-lived, with lifetimes ranging from microseconds to seconds [Bir64], and can radiatively decay to the S_0 state (and its vibrational sublevels), a process known as *phosphorescence* [Jab35; Kas47]. Because T_1 lies below S_1, the spectrum of phosphorescence light, though also exhibiting a structure reflecting the S_0 vibrational sublevels, is shifted to longer wavelengths. Its intensity decays exponentially (see Equation 4.10) but with a much longer decay time of up to several seconds.

While in T_1 or some other metastable state, molecules may during their excitation lifetime acquire sufficient thermal energy to return (via a reverse intersystem crossing) to S_1 and subsequently decay radiatively to S_0. The resulting luminescence spectrum is the same as that of fluorescence but decays

[2] There are materials that are known to show luminescence from higher excited states [Ito12].

non-exponentially with a period on the order of microseconds or longer [Bir64]. The process is hence known as *delayed fluorescence*, and its intensity and timing depend on a number of parameters, including the T_1–S_1 energy gap, the lifetime of T_1, and the temperature [Bir64].

The *scintillation efficiency* of a scintillator is defined as the fraction of energy deposited by a charged particle that is converted into visible light—i.e., via any of the three mechanisms discussed above [Kno10]. This definition disregards that for many applications, only prompt fluorescence is desirable, while delayed fluorescence and phosphorescence are often unwanted byproducts[3] that may lead to a degradation of measurement resolution because of their long decay times. The scintillation efficiency of typical materials is low—mostly in the single-digit percent regime after excitation by charged particles [Cla74], though it can reach up to 90% upon excitation via ultraviolet (UV) radiation [Bir64]—because excited molecules can relax via a number of non-radiative processes. Figure 4.4 exemplarily shows vibrational relaxation after internal conversion and intersystem crossing from the S_1 and T_1 states to higher-lying vibrational levels of S_0, respectively. All such non-radiative de-excitation processes are collectively called *(ionization) quenching* [Bir51]. They decrease mainly the intensity of the fast scintillation component (prompt fluorescence); the slow components and all decay times remain largely unaffected [Bir64]. To achieve high scintillation efficiency, care must be taken during the production of scintillators to avoid impurities that generate additional avenues for quenching.

Classification of Organic Scintillators

There are unitary, binary, and ternary organic scintillators. *Unitary* systems, the most important being pure crystals such as anthracene, consist of a single fluorescent material. A range of widely available materials—for example plastics like polystyrene or poly(methyl methacrylate)—scintillate, but their efficiency is often too low to be of practical use. In *binary* systems, this deficiency is compensated by mixing scintillating materials in liquid, plastic, or crystalline solutions. Often, the scintillation efficiency can be further improved by adding a third material. Such *ternary* systems can come in the form of liquid

[3] There has, however, recently been an increased interest in materials exhibiting thermally activated delayed fluorescence (TADF) for applications ranging from X-ray imaging to highly efficient organic light-emitting diodes (LEDs) [Abr+22; Ma+22; Men+23].

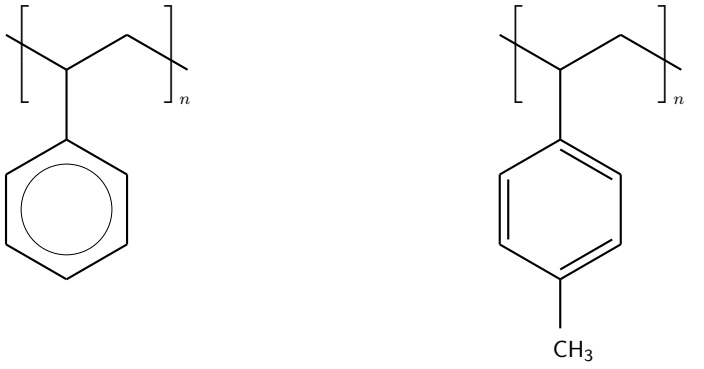

(a) Polystyrene (PS) (b) Polyvinyltoluene (PVT)

Figure 4.5: Molecular structure of the two most widely used polymer matrices for plastic scintillators. On the left, the π-electron MOs of the aromatic benzene ring are drawn as circle in the ring, visualizing the de-localization of the MOs. In the field of chemistry, however, it is often preferable to draw them as alternating single and double bonds (see right) [CGW12].

and plastic solutions, and I will discuss their scintillation mechanism using the example of plastic scintillators below.

4.2.2 Plastic Scintillators

Plastic scintillators are broad class of mostly ternary plastic solutions that offer several advantages over many other organic materials. Most importantly, they are relatively inexpensive and can be fabricated or machined into arbitrary shapes. The majority of plastic scintillators are ternary systems, consisting of a solvent (or *matrix*) and two solutes. The matrix, which makes up the bulk of the material, typically has a rather low scintillation efficiency or is largely opaque to its own luminescence emission. The two most commonly used plastics are the aromatic polymers polystyrene (PS) and polyvinyltoluene (PVT) [Bir64], whose molecular structures are shown in Figure 4.5. Other options include the non-aromatic poly(methyl methacrylate) (PMMA)[4] [SK05] and, more recently, cheap materials like polyethylene naphthalate (PEN) and polyethylene terephthalate (PET) [Nak+11; Nak+13], as well as polysiloxanes

[4]Often, aromatic co-solvents are added to compensate for PMMA's comparatively low intrinsic scintillation efficiency [Mos+93].

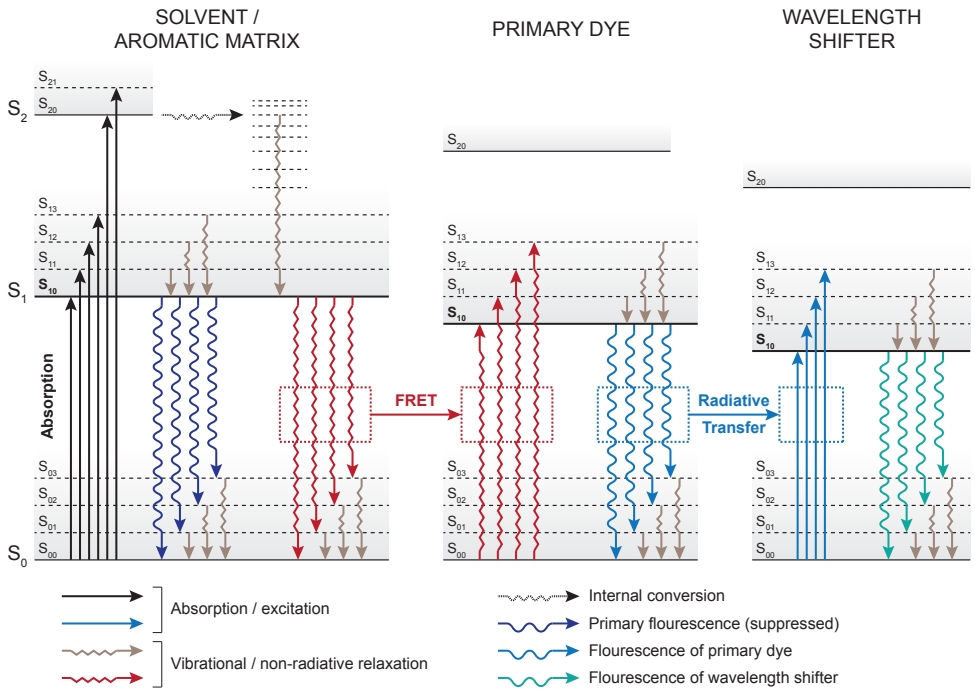

Figure 4.6: Jabłoński diagram of the energy transfer in ternary plastic scintillators. Excitation energy is transferred from the plastic matrix to the primary dye via a non-radiative process called Förster resonance energy transfer (FRET). The fluorescence light of the dye is absorbed by the wavelength shifter and re-emitted at longer wavelengths. The length of the arrows is not to scale.

with higher radiation hardness [Kos22]. Plastics can also be mixed or otherwise modified to achieve a higher overall performance [Nak+13; BHS14; Zai+20].

The primary solute, often called the *primary dye*, is added to increase the scintillation efficiency. It is typically a *fluorophore*, a chemical compound that comprises multiple aromatic groups or other molecular structures containing several π-electron systems [Kau93; Mos+93]. Recently, significant progress has been made in using nanomaterials or heavy element-enriched dyes to increase the scintillation efficiency in certain applications [Par+14; Dem+16; Haj+18; Min+21]. Excitation energy moves from the matrix to the dye in a process called Förster resonance energy transfer (FRET) [För06], in which it is transferred non-radiatively via intermolecular dipole-dipole coupling [SSN22].

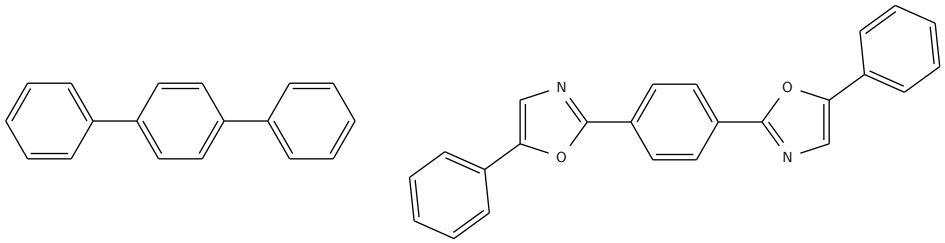

(a) p-terphenyl (b) POPOP

Figure 4.7: Molecular structure of two fluorophores that are commonly used as primary dye (p-terphenyl) and wavelength shifter (POPOP) in plastic scintillators.

Since this transfer is the more efficient process, the intrinsic fluorescence of the matrix is largely suppressed (see Figure 4.6). FRET can only happen when the emission spectrum of the matrix and the absorption band of the dye (partially) overlap [SSN22]. Its efficiency depends strongly on the distance between the donor and the acceptor molecules and thus varies significantly with the concentration of the dye [SSN22]. In most cases, optimal concentrations range from 0.3 to 4% by weight [Mos+93].

The fluorescence of the primary dye typically lies in the UV (with a maximum between 300 and 400 nm) and is much brighter than that of the matrix. The material is, however, often still largely opaque to its own emission. To compensate for the strong self-absorption, a *wavelength-shifting* fluorophore is added as a secondary solute at concentrations of 0.1% or less. This wavelength shifter efficiently absorbs the photons emitted by the dye and re-emits them at a longer wavelength, usually in the blue to blue-green part of the visible spectrum (400 to 500 nm) [Mos+93]. Thanks to this shift, the self-absorption in the material can be greatly reduced, and the emission spectrum also matches better to the sensitivity range of most photosensors.

Figure 4.7 shows the molecular structures of two commonly used fluorophores, p-terphenyl [Wak82] and 1,4-bis(5-phenyloxazol-2-yl) benzene (POPOP). p-Terphenyl is one of the most efficient primary dyes and can be added to a wide range of plastics [Gal13]. POPOP is used as a wavelength shifter [HYP22] and has a fluorescence spectrum that matches well to the peak sensitivity of modern silicon-based photosensors (see Section 4.5 below). Figure 4.8 compares the absorption bands and emission spectra of these two

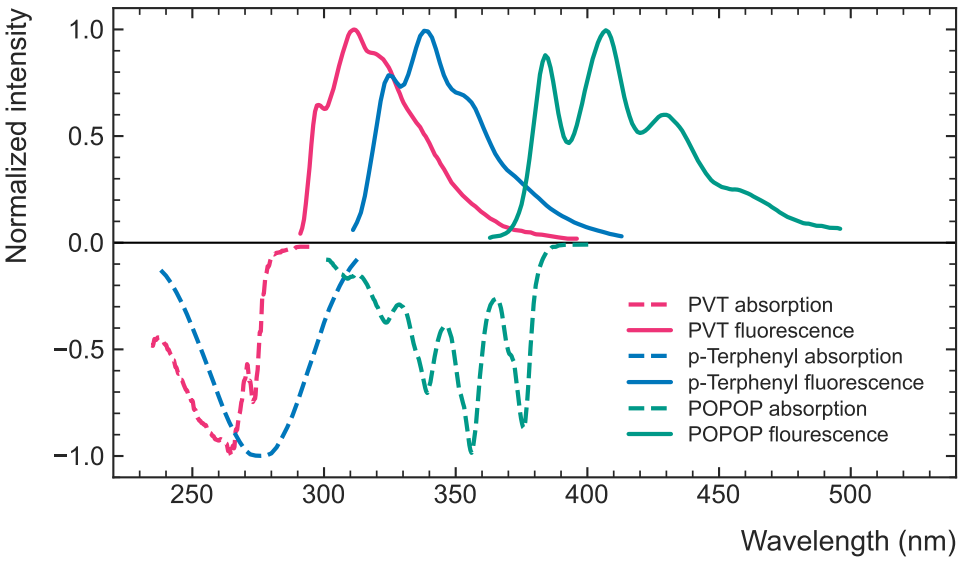

Figure 4.8: Fluorescence and absorption spectra of PVT, p-terphenyl, and POPOP. Data taken from [AAT24].

fluorophores to the intrinsic fluorescence spectrum of PVT, illustrating how the scintillation light gets shifted form the UV to the blue region. Ideally, the emission of a scintillator is primarily that of the wavelength shifter. The shape of the spectrum, though, is determined by the folding of the emission and absorption bands of the matrix and the fluorophores and thus is not exactly that of the shifter [Bir64].

The true nature of the scintillation process is often more complicated than the simplified picture I present here, which has a clear-cut transfer path for the excitation energy. In reality, different processes, for example fluorescence and FRET in the matrix, compete with each other, resulting in a scintillation spectrum that is a mix of those of the solvent and the solutes [HB78; Mon+19]. Alternate, radiative transitions that compete with FRET can exist, and the relative strength of the different processes is often concentration-dependent [Bir64]. Plastic scintillators are also not restricted to ternary systems [HYP22; Kos22]. The above picture does, however, reflect the scintillation process in plastics accurately enough for the purposes of this thesis.

Degradation due to Radiation Exposure

Transient and permanent molecular damage in a scintillator creates quenching centers, causing a deterioration of the scintillation efficiency that is induced gradually under the prolonged exposure to ionizing and non-ionizing radiation [BB51]. Sometimes referred to as *aging* [BB92], the magnitude of this deterioration depends on many parameters, including the chemical nature of the matrix and the solvents [Bri+93; Kha19], the environmental conditions (e.g., temperature, presence of oxygen or other reactive gases) [Tom+93], the type of radiation [Sai+22], and the rate of exposure [GWC93; TH93]. The transparency of the scintillator to its own emission is likewise affected by the formation of so-called color centers that absorb fluorescence light and lead to a visible discoloration of the material [Zor93; Jiv+17]. The scintillation and transmission efficiencies can partially recover after exposure in processes collectively known as *annealing* [Bri+93; TSJ93; HJS93]. Like the deterioration under exposure, the annealing process can strongly depend on environmental parameters like the temperature and the presence of oxygen [Wic+91; Wal+93].

Significant efforts have been made to find and develop radiation-hard scintillators for current and future high-luminosity accelerator experiments [Mar+93; Che93; Dec15; Det+17], from which the astroparticle and cosmic-ray communities can profit immensely. Even for plastic scintillators, which are among the most susceptible to radiation damage, acceptable doses of up to several Mrad ($\sim 10^5$ Gy) can be achieved [Zor+89; Mar+93; Bil+18; Zhm+19], vastly exceeding the requirements in typical space applications.

4.2.3 Response of Organic Scintillators

In a scintillator, only a small fraction of the kinetic energy lost by a charged particle is converted into scintillation light. The remainder is dissipated non-radiatively, mainly in the form of (lattice) vibrations or heat [Kno10]. The scintillation efficiency generally depends on the particle type and its energy, and in the ideal case it is independent of energy—leading to a linear relationship between light yield and particle energy.

Mathematically, the response of a scintillator to excitation by a charged particle can be characterized by its light yield (i.e., the number of photons created) per unit distance traveled by the particle, $\mathrm{d}L\,/\,\mathrm{d}x$. It is, however, sometimes more useful to express the light yield as a function of deposited

energy, $\mathrm{d}L \,/\, \mathrm{d}E$. The two quantities are related via

$$\frac{\mathrm{d}L}{\mathrm{d}x} = \frac{\mathrm{d}L}{\mathrm{d}E} \cdot \frac{\mathrm{d}E}{\mathrm{d}x}, \tag{4.11}$$

where $\mathrm{d}E \,/\, \mathrm{d}x$ is the total energy lost by the particle per unit distance. In the absence of quenching and potential other non-linear effects, the light yield is directly proportional to the energy loss [Bir64]:

$$\frac{\mathrm{d}L}{\mathrm{d}x} = S\frac{\mathrm{d}E}{\mathrm{d}x}. \tag{4.12}$$

Here, $S \equiv \mathrm{d}L \,/\, \mathrm{d}E$ is the overall scintillation efficiency of the material in the regime of proportionality, that is, at high particle energies and thus low energy loss. It has the dimension of [photons $\cdot$ energy^{-1}]. Since $\mathrm{d}E \,/\, \mathrm{d}x$ depends on the kinetic energy and the charge of the particle, the light yield is a function of these parameters as well.

In this regime, the total light yield (number of photons) of a particle losing an amount of energy E_1 is given by [Kno10]:

$$L = \int_0^{E_1} \frac{\mathrm{d}L}{\mathrm{d}E}\, \mathrm{d}E = SE_1. \tag{4.13}$$

Quenching

To account for ionization quenching, we need to modify the definition of the light yield per unit of deposited energy to reflect its non-linear dependence on the kinetic energy of the particle:

$$\left.\frac{\mathrm{d}L}{\mathrm{d}E}\right|_{E_\mathrm{k}} = S \cdot Q\left(\frac{\mathrm{d}E}{\mathrm{d}x}\right). \tag{4.14}$$

Q is the unit-less *quenching function* that goes to unity at small energy loss (and hence large E_k). With this modification, we can rewrite Equation 4.11 as [Pös+21]

$$\left.\frac{\mathrm{d}L}{\mathrm{d}x}\right|_{E_\mathrm{k}} = S \cdot Q\left(\frac{\mathrm{d}E}{\mathrm{d}x}\right) \cdot \frac{\mathrm{d}E}{\mathrm{d}x}. \tag{4.15}$$

Birks was the first to propose a semi-empirical relation of the light yield and the specific energy loss [Bir51] and his model is still widely used. He assumed that quenching is an unimolecular process in which excited molecules

relax non-radiatively without interacting with their neighbors (see Figure 4.4) [Bir64]. He parametrized this process in terms of the density of ionized or excited molecules along the particle track, $B \cdot \mathrm{d}E \,/\, \mathrm{d}x$, and the probability for non-radiative relaxation, k:

$$Q_{\mathrm{Birks}} = \frac{1}{1 + kB \cdot \frac{\mathrm{d}E}{\mathrm{d}x}} \tag{4.16}$$

With this simple quenching function, Equation 4.15 approximates Equation 4.12 at small $\mathrm{d}E \,/\, \mathrm{d}x$. At large specific energy loss, it becomes [Bir64]

$$\frac{\mathrm{d}L}{\mathrm{d}x} = \frac{S}{kB} = \text{const.} \tag{4.17}$$

In Birks' model, there thus exists a maximum light yield in every scintillator that is solely determined by its own properties and not by the type or energy of the incident particle. k and B can neither be derived from first principles nor be measured independently. Their product, kB, thus acts as one parameter known as *Birks' coefficient*, which has the dimension of [distance $\cdot$ energy^{-1}] and is determined via fits to experimental data [Hir+92].

In many cases, this single adjustable parameter can adequately describe the shape of experimentally observed energy-loss profiles [Kno10]. There exist, however, a number of more complicated models that try to compensate for the shortcomings of Birks' model. I describe them in the context of the measurements we performed to precisely determine the quenching behavior of the scintillators we use (see Section 7.1).

Time Response

To first order and for most applications, it can be assumed that the luminescent states in an organic molecule are populated instantaneously. If only fluorescence is observed, the time response of a scintillator is thus a quasi-instantaneous leading edge followed by a simple exponential decay (see Equation 4.10) [Kno10]. In a more refined picture, the time it takes to populate the S_{10} level from which prompt fluorescence arises (half a nanosecond or less) can be taken into account via [Kno10; KR64]

$$I = I_0 \left(e^{-t/\tau} - e^{-t/\tau_1} \right), \tag{4.18}$$

where τ_1 is time constant for the population of the optical levels and τ is the *decay time* of the fluorescence emission that is typically stated by manufacturers.

An alternative approach describes the population step by folding Equation 4.10 with a narrow Gaussian distribution [MB79]. Most plastic scintillators are quite fast and have decay times well below 5 ns.

The longer decay time of delayed fluorescence, typically measured in hundreds of nanoseconds, does not play a large role in most applications because scintillators are usually engineered to predominantly de-excite via prompt fluorescence. One can, however, make use of the fact that the probability for populating long-lived triplet states, and hence the intensity of the delayed component, depends on the energy-loss density [Kno10]. Since prompt and delayed fluorescence both decay exponentially, the time evolution of the total scintillation intensity can be modeled by the sum of two exponential decays. The relative strength of the longer decay component can then be used to distinguish between different types of particles (gamma rays, neutrons, heavy nuclei) in a method called *pulse shape discrimiation (PSD)*. A range of materials is specifically designed for PSD, mostly for separating neutrons from gamma rays [RWH64] and alpha particles from electrons[5] [Bag+10].

4.3 Scintillating Fibers

In the late 1950s, it was realized that the spatial resolution of scintillator detectors could be improved if they were constructed from bundles of scintillators drawn into long fibers instead of larger pieces of bulk material [RC57; Rey60]. After initially losing out to spark and bubble chambers due to inferior performance, in the late 1980s material and production improvements [BPS81; BS82; All+84] led to a resurgence of proposals to use such fibers—made from plastic, glass, or liquid materials (the latter inside thin glass capillaries)—for constructing large tracking detectors [Ali+88; Mus+95], active targets [Ang+89; Ang+90], and calorimeters [Kir87; Her+90; App+97]. Nowadays, the majority of applications use fibers made from plastic scintillators, taking advantage of the relatively inexpensive raw materials and the much easier production and handling (compared to glass fibers). Though glasses and other inorganic materials continue to be used [Die+14; Lv+24], I will not discuss them here because they are not relevant to our work.

Modern scintillating-plastic fibers consist of a core of polymer scintillator,

[5] These two applications are effectively the same, as neutrons and gamma rays are identified via the separation of secondary alphas and electrons.

mostly ternary fluorescent systems based on a PS matrix[6], surrounded by one or multiple thin layers of cladding material, usually PMMA or fluorinated poly(meth)acrylate [Kno10]. Since the cladding material has a lower refractive index than the core, a fraction of the scintillation photons can be reflected at the core–cladding interface and the system thus acts as a light pipe. In fibers with multiple layers of cladding (with sequentially lower refractive index), additional reflections take place at the cladding–cladding interfaces, leading to a higher trapping efficiency [Ruc93]. Each layer must be several wavelengths thick to allow the electromagnetic wave to extend into the material [Kir87], leading to typical thicknesses of a few micrometers [Reb+99].

Fibers are produced from preforms of bulk scintillator—rods of PS (with additives) of several centimeters thickness—around which a layer of cladding material is placed. The latter can either be an extruded cylinder whose inner diameter closely matches the core preform, or a coating that is directly applied to the polished surface of the core [Kir87]. The preform is slowly heated to the softening point of the core and cladding materials and then pulled at an appropriate, constant speed to form the fibers [Reb+99]. In this process, the ratio of the physical dimensions of the preform core and cladding are preserved. The minimum thickness of the final product (for a given preform geometry) is thus limited by the minimum thickness to which the cladding can be reduced without affecting the reflection condition at the core–cladding interface [Reb+99]. The smallest commercially available diameter is 200 μm, though so-called microfibers with diameters as small as 50 μm have been produced [Blu+89]. By varying the pulling speed, virtually any final diameter can be achieved, though a two-step pulling process may be necessary to produce very thin ones [Kir87]. Variations in the fiber diameter stem from inconsistent pulling speed and typically are on the order of ∼1%, though values down to 0.1% are possible [Kir87]. As the geometry of the preform is preserved, a multitude of fiber cross-sections can be produced, though round and square ones are most common.

4.3.1 Photon Transport and Trapping Efficiency

Photons incident on an interface between two transparent materials with different refractive index are reflected if their angle of incidence (with respect

[6] In the early days of fiber development, PVT was used as matrix [BPS81] but was soon replaced by PS due to its superior mechanical properties.

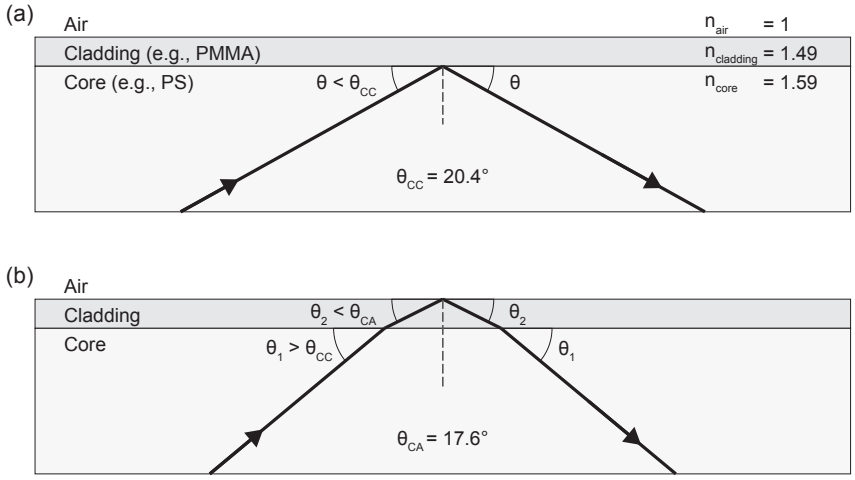

Figure 4.9: Reflection of photons at the core–cladding (a) and cladding–air (b) interfaces of a scintillating fiber with single cladding. θ_{CC} and θ_{CA} are the critical angles for reflection at the core–cladding and cladding–air interfaces, respectively.

to the interface surface[7]) is smaller than the *critical angle* of refraction [BW20]:

$$\theta < \theta_{\mathrm{crit}} = \frac{\pi}{2} - \arcsin\left(\frac{n_2}{n_1}\right), \tag{4.19}$$

where n_1 and n_2 are the refractive indices of the materials, and $n_1 > n_2$. The larger θ_{crit}, the larger the fraction of photons that can be trapped and thus transported down the fiber.

This would suggest that a scintillating fiber (e.g., made from PS with $n_{\mathrm{PS}} = 1.59$) without cladding should be preferable over one with a cladding made, for example, from PMMA because of the larger change in refractive index ($n_{\mathrm{PMMA}} = 1.49$ vs. $n_{\mathrm{air}} = 1$). The challenge, however, lies in the perfectly polished surface that is required for reflection to occur. An unprotected core–air interface is damaged easily, leading to large scattering losses that outweigh the gain in (theoretical) trapping efficiency. The cladding thus primarily protects

[7] In the field of optics, angles are usually measured from the surface normal, not from the surface. In the context of fiber optics it is, however, more intuitive to measure angles from the surface (i.e., from the center axis of the fiber) because emission angles are typically referenced to the center axis as well. The definition of the critical angle in Equation 4.19 therefore differs from the that found in textbooks by a factor of $\pi/2$.

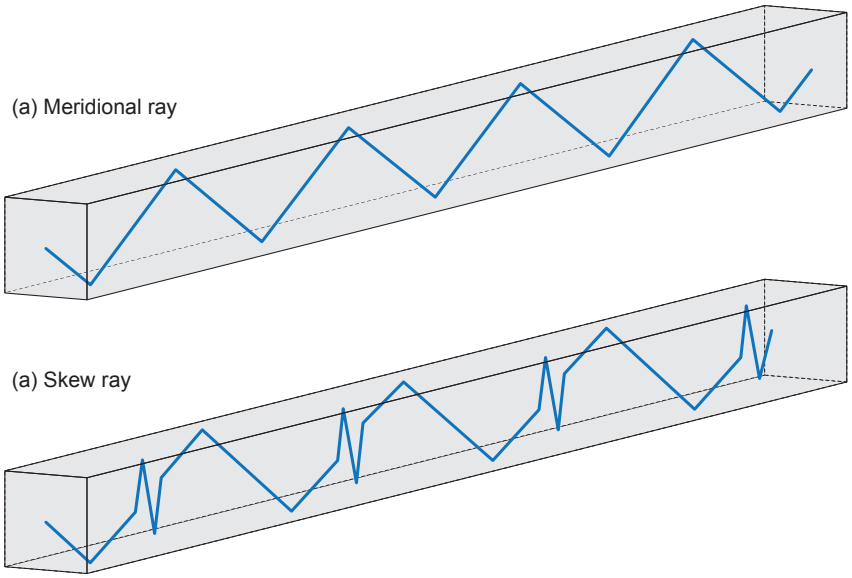

Figure 4.10: Geometric conditions under which light can travel down a fiber. Meridional rays travel in a plane that is parallel to one of the fiber's side faces. Skew rays follow a spiral path that is propagated along the length of the fiber.

the core–cladding interface against abrasion and other damage to keep the reflection conditions intact [Leu95]. Some of the light escaping into the cladding can be trapped by the cladding–air interface, though it is generally assumed that the inferior optical quality of the cladding's outer surface leads to most, if not all, being lost [Reb+99; Kno10]. I discuss the trapping of photons in scintillating fibers in more detail in Section 7.2.

Figure 4.10 shows the two geometric conditions under which light can travel down a fiber, using the example of a square cross-section. *Meridional rays* are photons that, in the case of round fibers, always pass through the center axis of the fiber, even after many reflections [Kno10]. In square fibers, the equivalent condition is that the photon travels in a plane that is parallel to one of the fiber's side faces. Meridional rays are typically used to illustrate the transmission properties of optical fibers and require a minimum number of reflections per distance traveled. *Skew rays*, on the other hand, do not travel in a single plane but instead follow a spiral path that is propagated along the length of the fiber. They theoretically have a higher capture fraction

and would thus outnumber meridional rays. In practice, however, they have a longer propagation path and need to undergo many more reflections at the core–cladding interface and are thus more strongly attenuated [Whi88; Kno10]. Many authors argue that they can be completely neglected [Reb+99]. This assumption at least holds for long fibers, though I discuss in Section 7.2 why it is oversimplified in the case of short ones.

For round fibers, the fraction of photons trapped as meridional rays can be determined by calculating the fraction of solid angle, Ω, subtended by the critical angle [Whi88; Kno10]:

$$f_{\mathrm{core}} = \frac{\Omega}{4\pi} = \frac{1}{4\pi} \int_{\varphi=0}^{\varphi=\theta_{\mathrm{crit}}} \mathrm{d}\Omega = \frac{1}{2} \left(1 - \sin\theta_{\mathrm{crit}}\right) = \frac{1}{2} \left(1 - \frac{n_{\mathrm{cladding}}}{n_{\mathrm{core}}}\right) \quad (4.20)$$

Assuming isotropic emission of the scintillation light, equal amounts are captured in both directions, so that the total light yield is double that given by the above expression. For fibers with a PS core and a cladding made from PMMA, Equation 4.20 yields a capture fraction of 3.1%. As skew rays somewhat contribute to the light transmission, some authors claim that the true capture fraction is about 10 to 30% higher [Kir87; Whi88; Kno10].

Rebourgeard et al. developed a more refined mathematical model of light propagation in the core of a fiber that includes skew rays [Reb+99]. For the total capture fraction, their calculations yield

$$f_{\mathrm{core,tot}} = \frac{1}{2} \left[1 - \left(\frac{n_{\mathrm{cladding}}}{n_{\mathrm{core}}}\right)^2\right]. \quad (4.21)$$

This expression yields a capture fraction of 6.1% for a PS–PMMA fiber, which is not only more than 30% higher than the value given by Equation 4.20 but also significantly larger than achieved in commercial products [Kur14; Lux23e].

Eqs. 4.20 and 4.21 only apply to round fibers and cannot straightforwardly modified for other geometries. A treatment of the theoretical capture fraction of fibers with a square cross-section is provided in Section 7.2.4.

4.3.2 Attenuation

The intensity of the scintillation light guided along a fiber is attenuated due to several extrinsic and intrinsic effects, which are discussed in detail in Section 7.2. Generally, these include self-absorption by the dye and the wavelength-shifter, scattering losses at impurities, and Rayleigh scattering from (small)

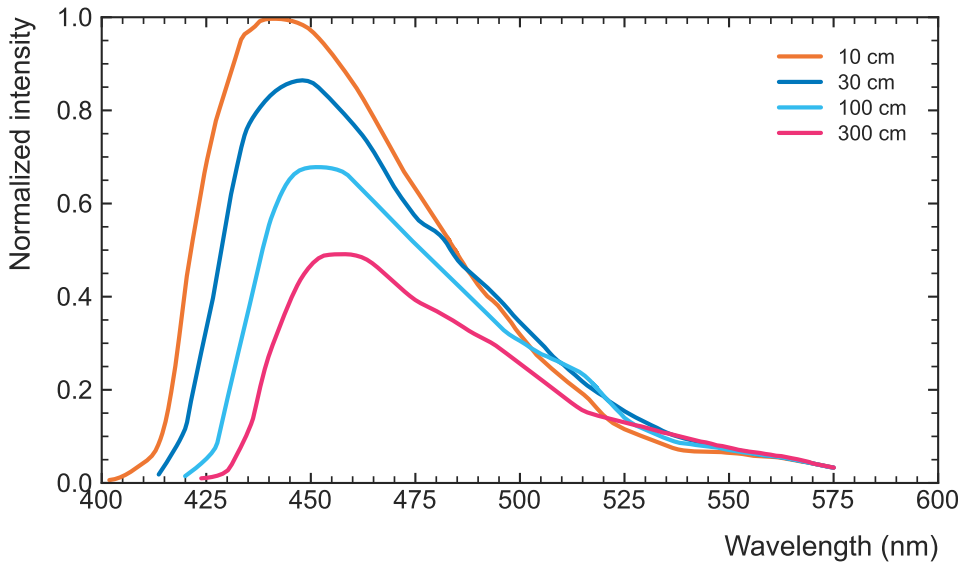

Figure 4.11: The spectrum of SCSF-78 scintillating fibers after 10 cm, 30 cm, 100 cm, and 300 cm of transmission, showing the stronger absorption of light with shorter wavelengths. Data taken from [Kur14].

density fluctuations in the core [Kno10]. Self-absorption is typically higher than in bulk scintillators because dyes and wavelength shifters are added at higher concentrations to maximize the light yield in fibers of small diameters [Kno10]. Figure 4.11 exemplarily shows the emission spectrum of SCSF-78 fibers after 10 cm, 30 cm, 100 cm, and 300 cm of transmission, highlighting how self-absorption leads to the stronger attenuation of light with shorter wavelengths.

The cumulative effect of the different attenuation processes is usually parametrized in a material-specific *attenuation length*, Λ_{att}. In the simplest mathematical picture, a constant absorption probability per path length, x, results in an exponentially decaying emission intensity [Kno10]:

$$I(x) = I_0 \cdot e^{-x/\Lambda_{\mathrm{att}}} \tag{4.22}$$

Here, I_0 is the initial intensity of (trapped) scintillation light close to the emission site (i.e., the particle interaction point). Typical values for Λ_{att} range from tens of centimeters to several meters. This approximate picture often does not adequately describe attenuation.

Rebourgeard et al. have attempted to derive the attenuation length in a fiber from first principles, given knowledge of the attenuation in the core material for the mean emission wavelength, $\Lambda_{\mathrm{core}}(\bar{\lambda})$ [Reb+99]. Taking into account interface losses and other effects, they found reasonable agreement of their predictions and measurements. In practice, however, the attenuation length depends on so many hard-to-quantify parameters that it is nearly always determined experimentally.

4.3.3 Radiation Damage

In addition to the general decrease of scintillation efficiency in plastic scintillators due to radiation exposure (see discussion in Section 4.2.2 above), radiation-induced absorption centers play a relatively larger role in fibers than in bulk material. It has been observed that exposures at doses of 10^3 to 10^4 Gy (10 to 100 krad) can lead to significant decreases of the attenuation length [Wic+91; MYG93], some of which can be reversed by annealing [Kno10].

4.4 Scintillators for Neutron Detection

Since neutrons do not electromagnetically interact with materials, virtually all neutron detectors rely on the detection of a recoil nucleus or charged secondary particles—such as protons, alpha particles, and light fission fragments—emitted as the result of a neutron-induced nuclear reaction.

4.4.1 Slow Neutrons

For slow neutrons (with energies smaller than 0.5 eV), one of the most widely used conversion reactions is [Kno10]

$$ {}^{3}_{2}\mathrm{He} + {}^{1}_{0}\mathrm{n} \rightarrow {}^{3}_{1}\mathrm{H} + {}^{1}_{1}\mathrm{p} \quad 0.764\,\mathrm{MeV}\,, \tag{4.23} $$

which releases an energy of 0.764 MeV. Conservation of energy and momentum leads to oppositely directed reaction products with energies of

$$ E_{\mathrm{p}} = 0.573\,\mathrm{MeV} \quad \text{and} \quad E_{{}^{3}\mathrm{H}} = 0.191\,\mathrm{MeV}\,. \tag{4.24} $$

Though this ^{3}He(n, p) reaction has a higher cross-section than many other conversion reactions, the high cost of ^{3}He is sometimes prohibitive, as is the fact that it is best employed in gas detectors.

For scintillator-based neutron detectors, two conversion reactions based on elements that can be incorporated into solid-state materials are widely used: ^{10}B(n, α) and ^{6}Li(n, α). For the former, the reaction can be written as [Kno10]

$$ {}^{10}_{5}\mathrm{B} + {}^{1}_{0}\mathrm{n} \rightarrow \begin{cases} {}^{7}_{3}\mathrm{Li} + {}^{4}_{2}\alpha & 2.792\,\mathrm{MeV} \\ {}^{7}_{3}\mathrm{Li}^{*} + {}^{4}_{2}\alpha & 2.310\,\mathrm{MeV}\,. \end{cases} \tag{4.25} $$

For thermal neutrons, about 94% of reaction lead to the excited state and 6% to the ground state of ^{7}Li. In either case, the energy of the incident neutron is orders of magnitude smaller than the energy released in the reaction and thus cannot be determined. For the excited branch, the energies of the reaction products are [Kno10]

$$ E_{\mathrm{Li}} = 0.84\,\mathrm{MeV} \quad \text{and} \quad E_{\alpha} = 1.47\,\mathrm{MeV}\,. \tag{4.26} $$

The ^{6}Li(n, α) reaction, on the other hand, only proceeds to the ground state [Kno10],

$$ {}^{6}_{3}\mathrm{Li} + {}^{1}_{0}\mathrm{n} \rightarrow {}^{3}_{1}\mathrm{H} + {}^{4}_{2}\alpha \quad 4.78\,\mathrm{MeV}\,, \tag{4.27} $$

with reaction-product energies of

$$ E_{^{3}\mathrm{H}} = 2.73\,\mathrm{MeV} \quad \text{and} \quad E_{\alpha} = 2.05\,\mathrm{MeV}\,. \tag{4.28} $$

Though the cross-section of the ^{6}Li(n, α) reaction is the lowest of the three presented here, the significantly higher energy release has advantages in many applications and results in a larger number of scintillation photons. ^{10}B and ^{6}Li can be incorporated into a wide variety of organic [Mab+16; Nem+21; Ngu+21] and inorganic [Son+24; FLS22; Kan+23] scintillators, though the latter are often preferred due to the former's sensitivity to fast neutrons.

4.4.2 Fast Neutrons

The conversion reactions discussed in the previous section have cross-sections that decrease considerably with the incident-neutron energy and are thus not particularly useful for detecting fast neutrons. In many applications that do not require a measurement of the neutron energy, thermal-neutron detectors are simply embedded into moderators of appropriate thickness, yielding a counting device that can determine the flux of neutrons within a certain energy range (that depends on the moderator thickness) [Kno10]. A noteworthy example is

the Bonner sphere, which exploits the fact that a polyethylene-clad thermal-neutron detector has a response curve that is similar to the energy-dependent dose equivalent delivered by neutrons [BEB60; Kno10]. Detectors based on moderation usually cannot determine the energy of incident neutrons, which is mostly lost in passive material.

Despite its much smaller cross-section at fast energies, the ^{6}Li(n, α) reaction can be used to detect and measure the energy of fast neutrons, albeit with comparatively low efficiency. The excess energy brought by the neutron into the reaction is imparted on the reaction products, such that observable energy is larger than the 4.78 MeV released for thermal neutrons. This is exploited in a range of fast-neutron scintillators, many of which are based on a glass or crystal matrix, both in bulk and in fiber for, though plastic are also used [BTG62; Kno10; Gia+16; FLS22; For+23].

The most widely used technique to detect fast neutrons without prior moderation is based on elastic scattering and the subsequent detection of the recoil nucleus [Kno10]. Because of the large energy transfer in neutron-proton scattering (see Section 3.4), organic (plastic) scintillators are the most widely used material for fast-neutron detection [Law+14; Sim+16; Zhm17; Mon+19]. In general, the incident-neutron energy can be reconstructed from the response function, though deconvolution and unfolding may be required [Kno10]. Pulse shape discrimination can be used to distinguish neutron from gamma-ray interactions [Bla+14; Mon+19; Kim+23].

4.5 Silicon Photomultipliers

Photodetectors are perhaps the most prevalent class of sensor for detecting non-ionizing radiation. Usually, we refer to any device that can detect photons with wavelengths in the UV and optical regimes as photodetectors; those sensitive to higher photon energies are referred to as X-ray or gamma-ray detectors, though their functional principle is often similar. In nuclear, particle, and astroparticle physics, photodetectors are mostly used for the detection of scintillation and Cherenkov light. The majority of them employs the photoelectric effect—i.e., the complete absorption of a photon's energy by an atom, leading to the excitation and subsequent emission of an electron. In semiconductors, these electrons are not released from the material but are lifted from the valence band to the conduction band, hence generating moveable charge carriers that cause a detectable signal [KW20].

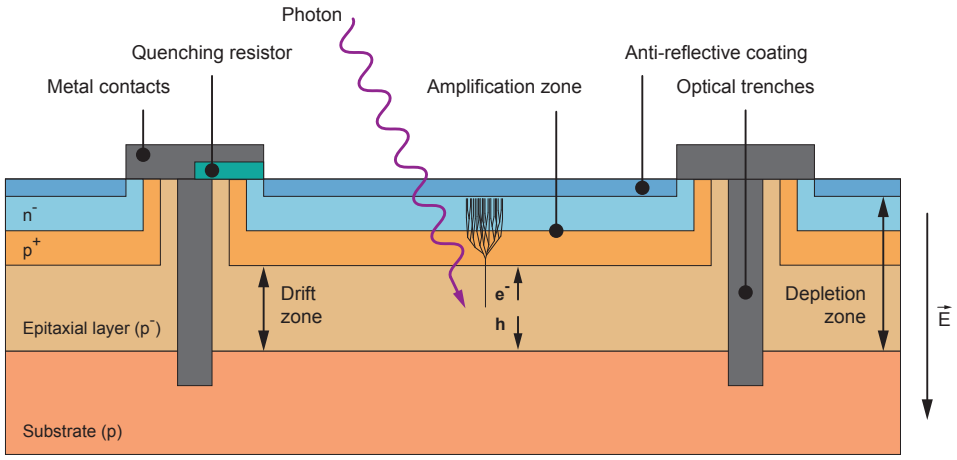

Figure 4.12: Simplified schematic layout of an n-on-p SPAD structure in a SiPM (an equivalent layout can be drawn for a p-on-n structure). The electron avalanche is drawn only for visualization only and is not a realistic representation.

Historically, the most widely used photodetector has been the photomultiplier tube (PMT), in which an electron released from a photocathode is accelerated by an electric field and multiplied in a cascading amplification system consisting of several so-called *dynodes* [Leo94]. PMTs continue to be some of the best low-background detectors for signals consisting of only few photons, especially in applications that require good time resolution. Their use in space applications, however, is complicated by their comparatively large size, their inherent and often undesirable sensitivity to magnetic fields, and the fact that they are mechanically not very stable. In the past two decades, silicon photomultipliers (SiPMs) have matured into devices that rival the performance of PMTs in many respects but are much smaller and easier to use. SiPMs are arrays of independent single-photon avalanche diodes (SPADs), called *microcells* or pixels, that are connected to a common readout [RL09]. These SPADs are essentially Geiger-mode avalanche photodiodes (APDs) operated at very high gain [Ren06; Mus09].

Figure 4.12 shows a simplified schematic layout of the SPAD structure in a SiPM. Each SPAD microcell is photodiode with an additional buried pn-junction (called a *metallurgical junction*) with high p and n doping [KW20]. The high doping causes a correspondingly high electric field at the junction when a reverse bias voltage is applied across the cell. In this high-field region,

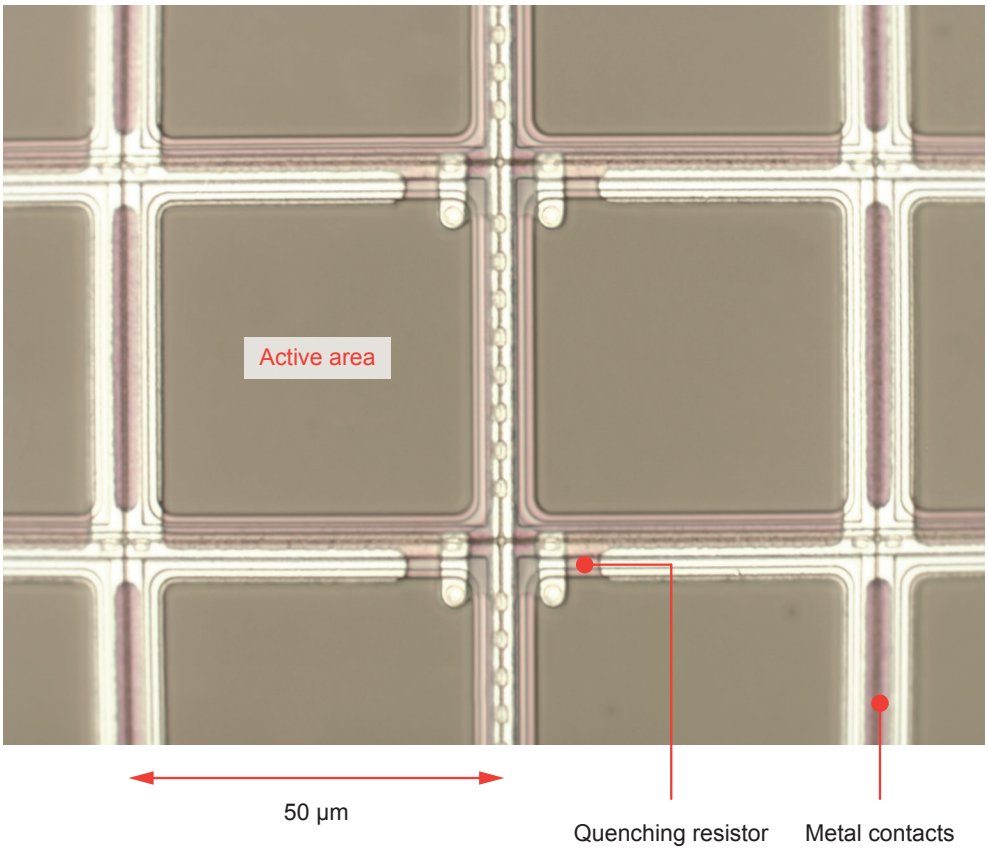

Figure 4.13: Microscopic image of the microcell structure of a KETEK PM3350 SiPM by KETEK, showing the active areas of each cell and structure for bias-voltage distribution and charge collection between them. Adapted from [Hah14].

electrons gain sufficient energy for inducing avalanche amplification [McI61; Hai+63]. In APDs, the applied voltage is often chosen such that the output signal is proportional to the number of photons hitting the diode. The SPADs of SiPMs, however, operate in Geiger mode [McI85]: The bias voltage is chosen about 10% to 20% above the breakdown voltage of the junction. A single photon hitting a microcell can thus initiate a self-sustaining avalanche. To stop the avalanche, the generated charge is collected through a *quenching resistor*[8];

[8]Another option is to use active quenching circuits [Sti09], though they are practically not used in SiPMs because of their large size.

the high current through the resistor causes the operating voltage to drop below the breakdown voltage, allowing the cell to recharge [Cov+96].

Operating the SPADs in Geiger mode has three primary advantages: (1) The efficiency for detecting photons is drastically increased over devices operating in proportional mode [Dau+93]; the intrinsic amplification is typically on the order of 10^5 to 10^7 [GH20], essentially rendering each microcell a binary (yes/no) photodetector; and (3) the amplification becomes insensitive to magnetic fields [KW20], which is highly desirable in many applications.

In a SiPM, the SPAD microcells are packed tightly together on a common substrate (see Figure 4.13). In the most commonly used *analog*[9] SiPMs, both their anodes and cathodes are connected in parallel. Since each cell releases a charge that is essentially defined by the cell size, doping concentration of the pn-junction, and the applied bias voltage (and is thus constant for a fixed value of the latter), the detector generates pulses with discrete amplitude spacing (see Figure 4.14). SiPMs are thus ideal for detecting (and quantifying) signals of only few photons. They are available commercially with microcell sizes of 10 µm to 75 µm and total sensitive areas of up to $6\times6\,\mathrm{mm}^2$, allowing the detection of single to more than 10 000 photons with a single device.

4.5.1 Relevant Performance Parameters

A full description of the signal-generation and noise characteristics of SiPMs is well beyond the scope of my thesis. I thus introduce only the few parameters relevant to the operation of our detector. For more comprehensive treatments, I refer the reader to several comprehensive review articles available in the literature [RL09; AG19; Ace+19; PG19; GH20].

One of the most important parameters of a SiPM is its breakdown voltage. That is because its gain, detection efficiency, and others parameter depend on the *overvoltage*, which is defined as

$$V_{\mathrm{ov}} = V_{\mathrm{bias}} - V_{\mathrm{br}}\,, \tag{4.29}$$

where V_{bias} and V_{br} are the bias and breakdown voltage, respectively. The breakdown voltage depends on the junction thickness, and hence on the doping concentration, and may therefore vary slightly for devices produced from different silicon wafers. It also changes with temperature, with typical coefficients of $20\,\mathrm{mV\,K^{-1}}$ for shallow and $60\,\mathrm{mV\,K^{-1}}$ for thick junctions, respectively [GH20].

[9] In *digital* SiPMs, the individual read-out electronics for every microcell are integrated into the device, effectively treating the cells as binary switches [KW20].

Gain

The gain of a SPAD microcells of SiPMs with integrated quenching resistors is generally defined as [GH20]

$$G = \frac{V_{\mathrm{ov}} \cdot (C_{\mathrm{q}} + C_{\mathrm{d}})}{q}, \tag{4.30}$$

where $V_{\mathrm{ov}} = V_{\mathrm{bias}} - V_{\mathrm{br}}$ is the overvoltage at which the SiPM is operated, C_{q} the parasitic capacitance of the metal contacts, C_{d} the depletion layer capacitance, and q the elementary charge. C_{q} and C_{d} are usually in combined form as the cell capacitance. From Equation 4.30, it is evident that the gain stability is directly proportional to variations of the applied bias voltage. A stable voltage supply with low ripple[10] and drift is therefore imperative for achieving good energy resolution in a SiPM-based detector.

Photon Detection Efficiency

In applications where only few photons must be detected, for example when MIPs traverse thin scintillators, it is important to optimize the photon detection efficiency (PDE) of a SiPM, which quantifies the efficiency with which photons incident on the sensor are detected. The PDE is simply the ratio of detected photons to incident photons [Yan+14], and is defined as [PG19; GH20]:

$$\mathrm{PDE}(V_{\mathrm{ov}}, \lambda) = \mathrm{QE}(\lambda) \cdot P_{\mathrm{T}}(V_{\mathrm{ov}}, \lambda) \cdot \mathrm{FF}_{\mathrm{eff}} \tag{4.31}$$

Here, QE is the quantum efficiency, P_{T} the avalanche trigger probability, $\mathrm{FF}_{\mathrm{eff}}$ the effective geometric fill factor, λ the wavelength of the incident photon. The quantum efficiency is the probability for a photon to generate a charge carrier capable of triggering an avalanche; it can be maximized by optimizing the doping structure of the silicon [PG19]. The avalanche trigger probability encodes the probability that a charge carrier (electron or hole) traversing the high-field region triggers an avalanche; it is a function of the size of the avalanche region (and hence of V_{ov}) and of the energy of the charge carrier (and hence of λ) [PG19]. The fill factor is defined as the ratio of the active area of all SPADs to the total area of the SiPM. Because the inactive area between microcells does not scale with their size, $\mathrm{FF}_{\mathrm{eff}}$ is higher the larger the cells are. Typical values range from 40% for 10-µm cells to 80% for 50-µm ones [GH20].

[10] Ripple is the residual periodic variation of a voltage generated by the rectifier in a DC–DC (or AC–DC) switching converter. Its periodicity follows that of the switching frequency of the converter, which usually operates at tens to hundreds of kHz [EM20; Dai22].

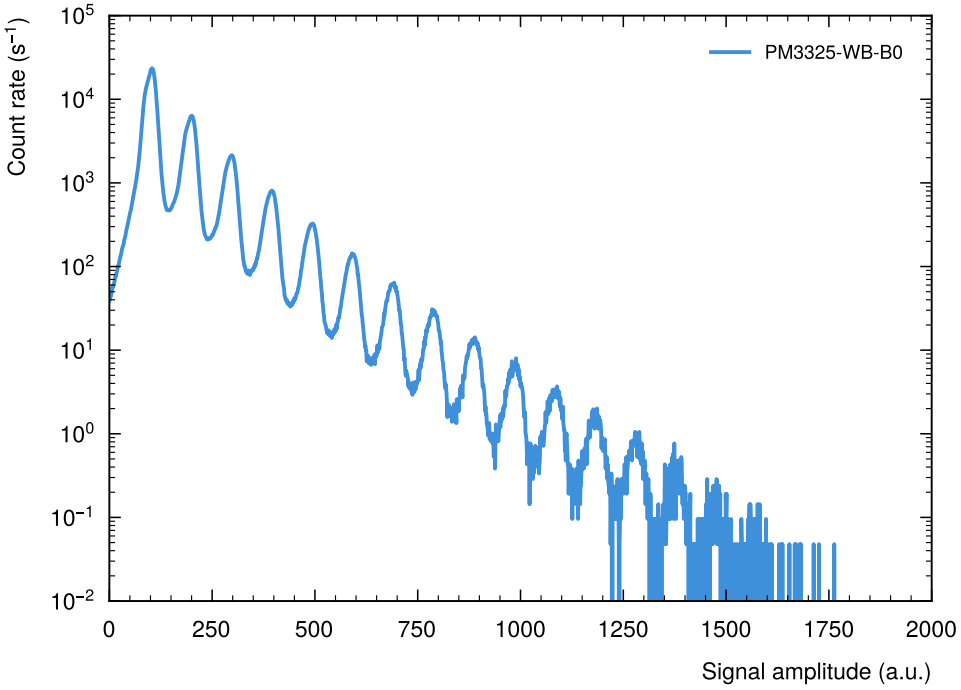

Figure 4.14: Dark count spectrum of the PM3325-WB-B0 SiPM by KETEK. The data was recorded at a bias voltage of 31 V and at room temperature with a A1423B preamplifier and a DT5730S digitizer, both manufactured by CAEN.

The spectrum shows the discrete peaks typical for a SiPM: The first one corresponds to the signal amplitude for one SPAD firing, the second one to that of two SPAD being triggered coincidentally, and so on.

Dark Counts

One parameter that is particularly important in low-light applications is the dark count rate (DCR), i.e., the rate at which a SiPM produces a signal without being struck by a photon. Dark counts are caused by the generation of charge carriers in the depletion region of an SPAD that diffuse into the junctions and trigger an avalanche [PG19]. There are two processes responsible for the generation of free charge carriers; one is inversely proportional to the temperature, the other is primarily proportional to the field strength (and hence bias voltage) and only weakly depends on the temperature [RL09]. Thus, if the DCR is a critical parameter for a given application, a SiPM should

be operated at low temperature and bias voltage. The DCR for typical SiPMs is on the order of several hundred kilohertz per mm^2 or higher, and can be lowered by a factor of two for a temperature reduction of eight to ten degrees [RL09; GH20].

Figure 4.14 shows a dark count spectrum of a KETEK PM3325-WB-B0 SiPM recorded at a bias voltage of 31 V and at room temperature. The spectrum highlights one important aspect: To keep the trigger rate due to dark counts in a detector below 100 Hz or 1 Hz, thresholds of at least six or eleven cells must be applied, respectively. The number of photons that shall be detected must be correspondingly higher.

Crosstalk and Afterpulsing

In a SiPM, *crosstalk* is a form of correlated noise, that is, noise which is induced by the avalanche process in one or multiple SPADs and which cannot easily be distinguished from the primary event, except for a shift in time. *Prompt* crosstalk is caused by photons produced in an SPAD avalanche [Lac+93; PG19] traveling to a neighboring microcell and triggering an avalanche there (with a maximum delay of a few hundred picoseconds [Ing+11]). *Delayed* crosstalk is caused by secondary photons being absorbed in the undepleted region of a neighboring SPAD, leading to a much more delayed (up to tens of nanoseconds) triggering of an avalanche because the charge carriers must first diffuse to the multiplication zone [GH20]. *External* crosstalk is induced by secondary photons exiting the active area of one SPAD and being reflected of the SiPM's protective epoxy or glass window (or some attached scintillator), thus being able to trigger avalanches in far-away microcells [Mas+21; TOF23]. Lastly, *afterpulsing* is conceptually very similar in nature to delayed crosstalk but is caused by charge carriers being trapped in the high-field region and released (in the same microcell) tens to hundreds of nanoseconds later [Ace+15; PG19]. In many devices, prompt crosstalk is the most prevalent noise source but can be suppressed quite effectively by introducing *optical trenches* between the SPAD microcells (see Figure 4.12) [GH20]. The other effects can be reduced by optimizing the layer structure, carefully selecting materials, and lowering the SPAD gain.

Crosstalk and afterpulsing cause the measured number of microcells to be larger than the number of SPADs triggered by primary charge carriers, often referred to as *photoelectrons*, that are generated by incident photons. This excess charge appears as an artificial gain in the system degrading the

resolution of the counting statistics, which is called the excess noise factor (ENF) [GH20]. It is unity for a bias voltages close to the breakdown voltage and increases with the overvoltage. The introduction of optical trenches has led to the development of SiPMs whose ENF is close to unity for overvoltages up to 5 V [GH20].

Saturation and Non-Linearity

If the number of photons incident on a SiPM, N_{ph}, approaches its number of microcells, N_{tot}, we observe a saturation of the photosensor. For a uniform illumination, the number of triggered SPADs is given by [RL09; GH20]

$$N_{\mathrm{fired\,cells}} = N_{\mathrm{tot}} \cdot \left(1 - \exp\left[-\frac{N_{\mathrm{ph}} \cdot \mathrm{PDE} \cdot \mathrm{ENF}}{N_{\mathrm{tot}}}\right]\right) . \tag{4.32}$$

This relation is approximately linear for small N_{ph} and becomes highly nonliner for large N_{ph} [Gru+14; Bre+16]. Appropriate corrections can significantly extend the range of linearity [Bri+24]. For non-uniform illumination, describing the saturation is more complex and generally requires simulations or measurements to get the model parameters right [GH20]. Light sources with pulse widths longer than the SPAD recovery time further complicate the situation, as microcells may be triggered multiple times.

4.5.2 Radiation Damage

SiPMs are silicon-based semiconductor detectors and as such are susceptible to damage by both ionizing and non-ionizing radiation [Lin03]. Since we have not paid much attention to this topic so far in the context of the detectors presented in this thesis, I here only give a very brief overview. A concise but comprehensive summary is given in [GM19].

There are two major effects of radiation damage in SiPMs. The first is a significant increase in the DCR, which is caused by the creation of transient and permanent defects in the bulk silicon lattice of the depletion region and by an increase in the surface current [Mus+07; Mat+08; RL09; Qia+13; Pag+14]. It also manifests itself as an increase in the dark current both above and below breakdown [GM19] and an increased probability for dark counts with large amplitudes [Mat+08]. The major second effect is the loss of single-photon resolution due to increased noise, which leads to larger fluctuations of the

effective charge released by a triggered SPAD [Pag+14; Tsa+16]. It also appears to be connected to bulk damage in the silicon [GM19].

Minor effects include the increase of the breakdown voltage (and hence decrease of the effective gain) due to changes in the doping concentration [Hee+16], a reduction of the PDE due to changes in the entrance layer [Mus09], a larger leakage current due to an increasing junction temperature, and a higher cell occupancy due to the increased DCR [GM19]. These effects are generally not significant for medium particle fluences (up to $10^12\,\mathrm{cm}^{-2}$) and their determination is complicated by the increased dark current [GM19]. Significant annealing—i.e., the (partial) reversal of radiation-induced effects—happens at room temperature [Nak09; Sán+09; Boh+09; Hir+21], with an exponential decrease of the annealing time observed for increasing temperature [Qia+13; Tsa+16; Cal+19].

The exact relation of radiation effects to particle type, energy, and dose (rate) is not yet well understood [GM19; Mit+22] and partially lacks a comprehensive empirical basis. To my knowledge, experimental studies have so far been limited to exposure by neutrons, electrons, protons, and gamma rays, assuming that these results can be scaled to heavier particles and nuclei [GM19]. For space applications [Bar+20; Alt+23], comprehensive tests with heavy ions are required to confirm this hypothesis.

Part I

Addressing the Space Radiation Challenge

Introduction to Part I

Exposure to cosmic and solar radiation and its effect on the human body is one of the biggest challenges that must be overcome before our quest to establish a permanent human presence in space can begin in earnest. Despite significant advances in the past decades, the urgency of addressing this challenge has only increased now that NASA and others plan to send astronauts beyond the protective embrace of Earth's magnetosphere on long-term missions to the Moon, Mars, and other deep-space destinations. Our inability to accurately predict both a crew member's radiation exposure during a deep-space mission and the health effects resulting from this exposure can be traced to two separate but interconnected knowledge gaps. One is the lack of detailed data on the space radiation environment—including its spectral, temporal, and spatial variations—almost everywhere except in LEO. The other is our incomplete understanding of the biological processes governing the interaction of space radiation with the human organism.

The first part of my thesis summarizes our efforts to help address this 'space radiation challenge' by developing new instruments for characterizing the environment in LEO and beyond. It is worth pointing out that our pursuit of this goal is somewhat accidental. We originally started developing the detector technology that now forms the heart of the RadMap Telescope—the instrument at the focus of this part of my thesis—for a mission to detect antiprotons trapped in Earth's inner radiation belt. Due to chronic funding uncertainties in the early phases of the project, we were looking for ways to demonstrate that the new detector concept we had devised would indeed provide the capabilities required for this astrophysical investigation. Our efforts to combine an on-orbit verification with scientifically relevant measurements ultimately led to the formulation of the science case for the RadMap Telescope.

It is due to this historic entanglement that the development of the RadMap detector and instrument cannot be fully separated from our earlier (and future)

work on this astrophysics mission. Especially the requirements and constraints imposed on the detector design are largely derived from the original mission concept, though I will show in Chapter 6 that in hindsight most of them would have read very similar had we started from a blank sheet. I nonetheless need to draw on the mission's requirements for some of the design decisions we took, even though Antiproton Flux in Space (AFIS) is not a central part of my thesis.

To motivate the need for new radiation monitors that can provide detailed measurements of the radiation environment in LEO and beyond, I begin this part by reviewing the topic of space radiation and its risk to astronauts in Chapter 5, before giving an overview of state-of-the-art instrumentation. Chapter 6 contains descriptions of the working principle of RadMap's central detector, in-depth characterization studies of the materials used, and the final detector design. I present the actual RadMap Telescope instrument in Chapter 10, including its objectives and capabilities, the design of its electronics, the production of flight hardware, and its integration into the ISS infrastructure. Finally, Chapter 12 provides some initial performance data and a comparison to the capabilities of instruments currently in operational use by NASA and ESA. I conclude with a summary of plans and prospects for future instruments based on the RadMap Telescope design.

Chapter 5

The Risk of Radiation in Space

The risk that cosmic and solar radiation pose to astronauts has been known since the early days of the Space Age [Eng+73; BHB75]. Its severity, however, has often been misjudged due to the lack of detailed data and, more importantly, an incomplete understanding of radiation biology [Cha+18]. Today, we know that current exposure limits, rooted in an assessment of the risk for radiation-induced late effects like cancer and cardiovascular diseases, threaten to severely limit the total duration of crewed missions beyond Earth orbit [Cuc15b; Cuc+15]. In this chapter, I give an overview of astronauts' exposure to radiation and its consequences, briefly describe the effects on microelectronic devices, and discuss the state-of-the-art instruments for dosimetry and radiation monitoring.

5.1 Sources of Radiation Exposure

In interplanetary space—that is, far away from planetary bodies that alter the radiation field due to their atmosphere, magnetosphere, and bulk shielding—the only relevant components of the space radiation environment are cosmic rays (in the context of radiation protection nearly always referred to as GCR) and SEP. In the vicinity of Earth and other planets, an additional component may be contributed by particles trapped in the planetary magnetic field, if present. On airless bodies like the Moon, secondary radiation is also produced in interaction of GCR and SEP with the surface. This additional radiation field consists of a variety of particles, including fragments of cosmic-ray nuclei, electrons, gamma rays, and neutrons.

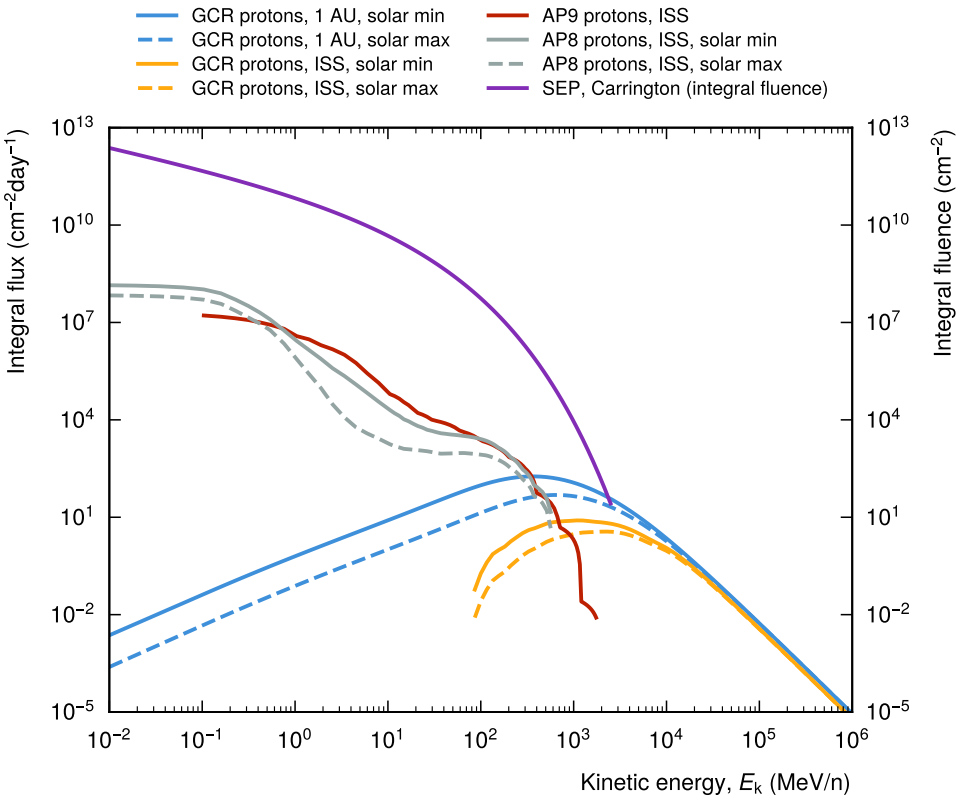

Figure 5.1: Qualitative overview of the different radiation-field components. The flux (per day) of GCR protons is shown in free space at 1 AU and for the ISS orbit (400 km at 51.6°) for solar minimum and maximum. For trapped particles, the AP8 and AP9 models are evaluated for the ISS orbit. As an example for SEP, the total fluence of protons during the Carrington event is shown. Data obtained from OLTARIS [Sin+10].

Figure 5.1 shows a qualitative summary of the different components of the radiation environment in LEO. GCR have by far the smallest flux, though their high biological effectiveness (see below) makes them the largest contributor to the radiation dose. Since particle with energies of less than about 10 MeV can be easily shielded, trapped protons (encountered inside the SAA) make up the largest part of the incident particle flux. In addition to the components shown in the figure, secondary radiation created in a spacecraft's shielding can also significantly contribute (see below).

5.2 Radiation Biology: The Risk to Astronauts

Understanding the health risks resulting from exposure to the space radiation environment is a multi-faceted and cross-disciplinary area of research that is still subject to a great deal of uncertainty. Most limitations in our understanding of radiation biology and the consequences of radiation exposure are due to the complex nature of the interaction of radiation particles with the human organism. Even without these limitations, predicting acute and latent effects of radiation interactions in a biological system is notoriously difficult. I can give but a brief overview of this wide field of research, highlighting the aspects most relevant to our work. More comprehensive introductions are given in [DC11; Cha19; Hel+20; Nat21; Hel+23].

5.2.1 Dosimetric Quantities

The primary dosimetric quantity used in radiation protection is the *absorbed dose*. It is defined as the mean energy, $\mathrm{d}\epsilon$, absorbed per unit mass, $\mathrm{d}m$, from any kind of ionizing radiation in any kind of material [ICRP123; Bog+22]:

$$D = \frac{\mathrm{d}\epsilon}{\mathrm{d}m}\,. \tag{5.1}$$

The unit of the absorbed dose, which is often simply referred to as the dose, is the *Gray*: $1\,\mathrm{Gy} \equiv 1\,\mathrm{J\,kg^{-1}} = 100\,\mathrm{rad}$. The older unit, the *rad*, is still widely used, especially in non-biological contexts. To determine the biologically effective dose, the absorbed doses in organs and tissue must be weighted by the *relative biological effectiveness (RBE)* of different types of radiation, as well as by tissue weighting factors [ICRP123]. The differences in male and female organ tissue may also be taken into account.

The resulting effective doses values are, however, not measurable in practice and can therefore not be used in radiation monitoring. Instead, the operational quantity is the *dose equivalent* [ICRP123]

$$H = QD\,, \tag{5.2}$$

where D is the absorbed dose at the point of interest in tissue and Q is the mean quality factor encoding the biological effectiveness of radiation particles at that point. Q is a dimensionless quantity; to distinguish it from the absorbed dose, however, the dose equivalent is measured in *Sievert*: $1\,\mathrm{Sv} \equiv 1\,\mathrm{J\,kg^{-1}}$.

Since the absorbed dose can be measured directly, the dose equivalent can be straightforwardly calculated given knowledge of Q.

The biological effectiveness of ionizing radiation depends on the type and energy of radiation particles, on the total dose and the rate at which it is absorbed, and on the tissue type. The main area of interest for radiological protection is the effectiveness at the low doses and dose rates that are typically encountered in space. At high dose rates, for example as a result of direct exposure to an SEP event, the large energy deposited in tissue leads to prompt biological reactions and the stochastic description of radiation exposure is no longer valid [ICRP123]. The RBE is referenced to low-LET radiation, for example high-energy gamma rays, and allows to define the radiation quality and risk factor for a radiation type of interest.

The radiation quality is strongly correlated with the ionization density along a particle track, and therefore with the unrestricted LET, L. This correlation is reflected in the definition of the quality factor by the International Commission on Radiological Protection (ICRP) as a function of LET in water [ICRP123]:

$$Q(L) = \begin{cases} 1 & L < 10\,\mu\mathrm{m}^{-1} \\ 0.32L - 2.2 & 10\,\mu\mathrm{m}^{-1} \leq L \leq 100\,\mu\mathrm{m}^{-1} \\ 300/\sqrt{L} & L > 100\,\mu\mathrm{m}^{-1} \end{cases} \tag{5.3}$$

With this definition, the quality factor of a given radiation field at a certain point in tissue is given by

$$Q = \frac{1}{D} \int_{L=0}^{L=\infty} Q(L)\, D_L \, \mathrm{d}L \;, \tag{5.4}$$

where D is the absorbed dose in tissue and $D_L = \mathrm{d}D \,/\, \mathrm{d}L$ is the distribution of D in L (in water) at the point of interest [ICRP123].

Based on the dose equivalent, the whole-body effective dose equivalent, H_E, is defined as the weighted sum over the organ dose equivalents using the tissue weighting factors w_T [Hel+20]:

$$H_\mathrm{E} = \sum_\mathrm{T} w_\mathrm{T} H_\mathrm{T} = \sum_\mathrm{T} w_\mathrm{T} Q_\mathrm{T} D_\mathrm{T} \,. \tag{5.5}$$

The sum is over four different reference tissues given in [ICRP110], for each of which a sex- and age-averaged weighting factor based on experimental data is defined. This approach recommended by the ICRP was adopted by most space agencies worldwide.

NASA, however, uses a different definition of the quality factor that takes into account the physical properties of the radiation particles, namely their (nuclear) charge and energy [Cuc11; Cuc15c]. Instead of relating Q only to the ionization density, and hence LET, it also considers the track structure, i.e., the spatial pattern of the energy deposition, which was found to play a significant role in the biological effectiveness [Nat12; Geo+13; Cuc13; Cuc15a; Goo21]. In this model, the quality factor function is defined as [ICRP123; Cuc15c]

$$Q_{\mathrm{NASA}}(Z,E) = (1 - P(Z,E)) + 6.24 \cdot \frac{(\Sigma_0/\alpha_\gamma)}{L} P(Z,E)\,, \tag{5.6}$$

with [Cuc15c; Cuc15b]

$$P(Z,E) = (1 - \mathrm{e}^{-Z^{*2}/\kappa\beta^2})^m (1 - \mathrm{e}^{-E/E_{\mathrm{TD}}})\,. \tag{5.7}$$

Here, Z, E and β are the charge, energy, and velocity of a particle, respectively, and Z^* is the effective charge number that includes a velocity-dependent correction to account for the pickup of electrons by nuclei at low energies (see Section 3.3.4). The parameters Σ_0/α_γ, E_{TD}, m, and κ define the shape of the function and must be derived empirically from fits to data from radiobiology experiments [Cuc15c].

What is important in the context of my thesis is that the reason for introducing Q_{NASA} was to be able to more accurately calculate the effective dose equivalent, and to better describe the biological effectiveness of a radiation field. Determining Q_{NASA} does, however, require the measurement of a particle's Z and E; many devices currently used for radiation monitoring cannot perform such measurements (see below). To illustrate the importance of correctly treating heavy ions, Figure 5.2 shows the contribution of nuclei (up to iron) to the total particle fluence, absorbed dose, and dose equivalent.

5.2.2 Biological Effects of Radiation Exposure

The constant flux of GCR causes a chronic whole-body exposure of astronauts during space missions. Though the dose and dose rate are on average (relatively) low, heavily ionizing cosmic-ray nuclei cause locally very high doses on a microscopic level that lead to permanently damaged tissue. In LEO, radiation-belt particles inside the SAA are another source of chronic exposure. Much of the uncertainty in estimating the risk posed by the space radiation environment stems from our still limited understanding of the associated late biological effects of such low-dose exposure. In interplanetary space, high

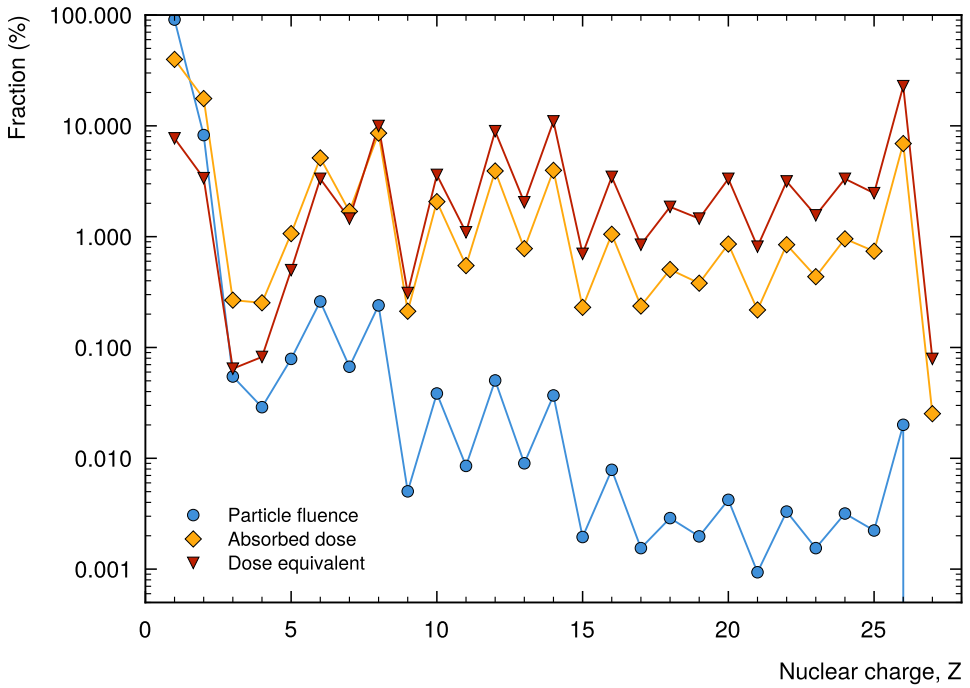

Figure 5.2: Contribution of nuclei (up to iron) to the total particle fluence, absorbed dose, and dose equivalent. Adapted from [Cuc11].

doses may be accumulated within hours or days due to SEP events, potentially leading to acute effects.

Acute Effects

Exposure to a large single dose of radiation causes acute radiation syndrom (ARS), colloquially known as *radiation sickness*. The first stage of ARS is nearly always hallmarked by a rapid onset of nausea and vomiting, which can be life-threatening to astronauts in space suits [Hel+20]. Other effects include the disturbance of the neurochemical metabolism of the central nervous system. The development of later stages depends on the received dose and can last days to weeks [HBS20]. Doses of 3 to 4 Gy lead to the death of 50% of exposed humans within 30 days, mostly due to functional depression of the bone marrow [Ker+22] and the associated suppression of the immune system [Hel+20]. After exposure to doses of 5 to 12 Gy, disturbances of the

gastrointestinal tract arise quickly [MPG21], resulting in systemic inflammation and blood poisoning, which ultimately leads to multiple organ failure and death within three to ten days. At very high doses, the central nervous system is severely affected, including loss of coordination, confusion, and eventually coma. Above 10 to 12 Gy, survival is impossible [Hel+20]. Acute effects were observed in a large population of atomic-bomb survivors and are hence among the best-studied effects of radiation exposure.

Chronic and Late Effects

Chronic and late effects of prolonged exposure to the space radiation environment are much less well understood than acute effects because of the lack of clinical data. That is because the damage induced by highly ionizing cosmic-ray particles is so much higher than that of terrestrial radiation sources that essentially none of the data collected on Earth can be relied upon. A nucleus with high charge, Z, and energy, E_{k}, traversing organic matter produces a broad trail of high ionization density along its track, which is surrounded by an even broader penumbra of lower ionization density created by δ electrons [KKS92; Nik+98]. The energy imparted on the system leads to biomolecular changes in the traversed tissue. Most importantly and in contrast to terrestrial radiation, high-LET cosmic radiation can break DNA molecules in multiple locations at the same time, creating a complex damage pattern that is difficult to repair [HG08; Gar+10; Zad+18; Sum+20]. The broader track structure of nuclei with higher Z is the reason for relating the RBE and quality factors not only to the LET but also to the particle type.

Unrepaired DNA damage can lead to a number of biological outcomes, including arrests in the cell cycle, cell death, senescence, and mutations [Hel+20]. The accumulation of these outcomes during long-term exposure then leads to observable late effects. Cancer is most widely known and publicized one, though the role of highly ionizing radiation in tumor promotion and progression is not well established [Hel+20; GZH22]. Human cancer risk data for heavy ions are not available and radiobiological data are limited. Risk estimates are therefore mostly derived from atomic-bomb survivors that were exposed to high doses in a short time [Pie+96] and projected to the conditions in space; they therefore suffer from large uncertainties [Nat21; SS21; GZH22]. Other effects include degenerative tissue effects like the formation of cataracts [BC21], cognitive deficits and neurological damage [Par+15; Par+18; Ala+23], and cardiovascular diseases [Del+16; Rik+20].

5.3 Effects on Microelectronic Devices

The response of microelectronic devices to radiation is a complex field of research, albeit a little more predictable and better understood than the response of biological systems. Though it not of primary interest to my research, the effects of radiation on non-biological systems must nevertheless be kept in mind when designing instruments that must operate reliably in the space radiation environment. Being (mostly) silicon-based devices, electronic integrated circuits are susceptible to a variety of transient effects and permanent damage in response to radiation exposure. The major underlying processes are cumulative ionization, the displacement of atoms in the semiconductor lattice, and single event effects. I here discuss very briefly only the most important parameters to consider when selecting electrical components; many aspects I do not mention at all. A comprehensive high-level overview of radiation effects on electronics is given in [BK20].

5.3.1 Total Ionizing Dose

The interaction of ionizing radiation, both via electronic and nuclear energy loss, with the semiconductor lattice results in the creation of charge carriers (electron-hole pairs). A fraction of the generated holes can accumulate in insulating parts of circuits, for example oxide gate structures, or at the interfaces of different materials, leading to the slow buildup of net charges in regions of the device where electrons and holes cannot recombine (because they are not mobile) [EBS00; BK20]. This charge buildup can then affect the circuit's performance, for example result in a voltage shift of gate thresholds in field-effect transistors or in a reduction of the current gain of bipolar transistors [HA02]. The cumulative action of ionization is determined via the total ionizing dose (TID), which is defined as the energy absorbed by a unit mass of material. It is typically measured in rads or in Gray. TID effects lead to the slow degradation of device performance. They often depend on the dose rate, the ionization energy density—i.e., on the type and energy of the incident particle—the applied bias voltage (electric field) in a device, and the temperature [BK20].

5.3.2 Displacement Damage

Another cumulative effect of radiation exposure is displacement damage, which results in the gradual degradation of a semiconductor's properties due to accumulated physical damage in its crystal structure [EBS00]. In contrast to TID, displacement damage is a volumetric effect, changing the electrical properties of the bulk material [BK20]. Atomic displacement is the result of non-ionizing energy loss (NIEL); it creates low-mobility vacancies in the crystal lattice and mobile interstitial defects (displaces silicon nuclei), both of which can be electrically active and create traps in the silicon band gap. They also have the tendency to combine with other vacancies, intrinsic impurities, and other defects [HA02]. Much like dopants, these accumulations lead to changes in critical semiconductor properties. In interactions with extremely high NIEL, the bulk silicon can partially melt and turn amorphous, thereby completely changing the band structure in that region [BK20].

5.3.3 Single Event Effects

A single-event effect (SEE) occurs whenever a single particle deposits enough energy in a device to produce an observable (transient) effect [EBS00]. SEEs can be nondestructive or destructive. Nondestructive SEEs cause an observable event or corruption in the output state of a circuit that is transient and self-recovering [BK20]; the only exception are memory cells, which need to be written to clear the erroneous state. Nondestructive events thus do not damage the device in any way, which is why they are often called *soft errors* [AM15]. Destructive SEEs, on the other hand, permanently degrade or destroy circuit components and are thus sometimes referred to as *hard errors*.

One of the most important effects are reversible but persistent single-event upsets (SEUs). They happen when radiation events occur in a storage component, for example in one or multiple bits of random access memory or a latch, causing them to change their state until they are overwritten with new data [BK20]. If undetected, such *bit flips* can lead to serious malfunctions of computer systems. The probability for single-bit and multi-bit SEUs depends on the particle and energy, on the angle of its track to the semiconductor [Pet11]. SEUs in critical system registers, which more or less instantly lead to a wider disruption of a digital system, are called single-event functional interrupts (SEFIs).

A potentially catastrophic class of SEEs are single-event latch-ups (SELs). They occur when the charge carriers generated by a charged particle cause the development of a self-sustaining low-impedance path between power and ground that is only stopped when power is removed or the device suffers catastrophic failure due to overheating [BK20; Pet11]. The probability for SELs to occur rises with increasing energy deposited by a particle, and thus depends on its type and energy. Often, external circuits are used to monitor the supply current of SEL-sensitive devices and shut them down once an out-of-bounds increase is detected [BK20].

5.4 Shielding

Shielding against the space radiation environment is a complicated business that often involves scenario-specific trade studies. The guiding motto seems to be intuitively clear at first: the more shielding, the better. While this maxim would perhaps be true if arbitrarily thick layers of shielding could be employed, it is certainly not if we consider the mass limitations of today's launchers. The greatest challenge is the large range of particle types and energy encountered in cosmic and solar radiation [Zei21]. The low-energy protons and light ions found in SEP and in Earth's (and other planets') radiation belts can be shielded relatively easily by a few centimeters of aluminum equivalent [Tro+06].[1] One challenge, however, is the generation of secondary radiation, most importantly neutrons [Hei+98; Get+04; Hor+22]. In the SAA, for example, neutrons created by radiation-belt particles absorbed in the shielding of the ISS make up a significant fraction of the crew's radiation exposure [Tro+06; PB10; Zei21].

The situation is much more complicated for medium to high-energy cosmic rays. Since particles at these energies can induce a range of nuclear interactions and fragmentation (see Section 3.3), a detailed comparison of the radiation dose received before and after the shielding is required. Such studies are usually performed using simulations tools [Cuc+06] and show that shielding configurations adhering to the volume and mass constraints of average space missions often increase the GCR-induced radiation dose received inside a spacecraft [DS20; Zei21; DB24]. This is primarily because the multiplicity of particles is higher due to fragmentation and other production of secondary

[1] For better comparability, the effective stopping power of a material is usually expressed in the equivalent thickness of aluminum (being the most common structural material used in space) that has the same stopping power.

radiation, and because the latter usually consists of particles with shorter range and higher stopping power [Hei+06]. The design of an optimal shielding configuration for a given mission therefore must involve a careful comparison of the (anticipated) radiation fields inside and outside the shielded volume [ELT19; SS20b]. Besides nuclear fragments [Hei+06], electrons, gamma rays, and neutrons [Bos+20; Hor+22], the significant contribution of pions has recently been investigated [Voz+24]. Modern concepts often try to minimize the generation of secondary radiation through a carefully chosen layered structure of multiple different high-Z and low-Z materials [Sla+17; Bon+19a; MS20; Luo+22; AlZ+23]. Though active shielding, i.e., the generation of a strong magnetic field mimicking Earth's magnetosphere, continues to be studied theoretically [Spi10; Was+15; Pal+23], it seems unlikely that the current densities required to create such a field can be generated at the required scales in the foreseeable future.

While shielding strategies are not at the focus of the work presented in my thesis, the large role of secondary radiation highlights that detectors deployed for assessing the crew's radiation exposure should at best be sensitive to this secondary radiation field.

5.5 State-of-the-Art Instrumentation

Many charged-particle detectors for space applications have traditionally been built based on two general architectures: particle telescopes and spectrometers. Particle telescope comprise several layers of energy-sensitive detectors, with planar silicon sensors being the most widely used option. These detectors can either consist of one large active area or they can be position-sensitive (via a segmentation into strips or pixels) to allow the determination of the angle under which a particle traverses the stack. With the energy-loss information in the different layers, a particle telescope can be used to accurately determine the LET of a particle. If the total energy must be measured, a calorimeter can be added at one end of the telescope. A telescope's ability to accurately identify the type of particle (or nucleus) that traversed it is, however, somewhat limited as the LET is not an unambiguous quantity. Often, an identification is not possible based on the information from a single interaction alone but only using a statistically meaningful ensemble of many events.

A spectrometer is used when a more comprehensive determination of the radiation particles' properties is required. The core of a spectrometer is a stack of

position-sensitive detectors inside a strong magnetic field that deflects charged particles. The particles' momentum can be determined based on the measured deflection. Combined with at least the information from a calorimeter, not only a particle's energy can measured, but a precise determination of the particle type can be made. Adding additional detectors—such as Cherenkov detectors, transition radiation detectors, or time-of-flight detectors—can enhance the particle-identification capabilities.

5.5.1 Spectrometers

Today's flagship cosmic-ray detector is, of course, AMS-02 on the ISS [Bat08; Tin13; Bat20]. Its high-precision tracking detector and strong magnet give it capabilities similar to those of ground-based spectrometers used in high-energy physics experiments. The additional detectors required for particle identification and energy measurement—a transition radiation detector (TRD), a ring-imaging Cherenkov (RICH) detector, a time-of-flight (TOF) system, and an electromagnetic calorimeter—make it a highly complex system. The precision with which AMS-02 can measure particle-dependent energy spectra is unprecedented and allows to probe many of the unsolved questions in cosmic-ray physics. Its data is, however, not ideally suited for crew radiation monitoring (and never was meant to be used for such purposes, though recently efforts are being made to use AMS-02 data in a radiation-protection context [Che+23; Bar+23; Bar+24]). This is because the instrument's lower sensitivity limit for protons is at a rigidity of about 1 GV (corresponding to an energy of 427 MeV) [Bat20]. The limit for helium is at about 2 GV (433 MeV/n) [Agu+19]. A substantial part of the energy range relevant to radiation protection is thus not accessible to AMS-02. Similar constraints exist for other astrophysics spectrometers—for example CALET [TM19], DAMPE [Cha+17], and the upcoming High Energy cosmic Radiation Detector (HERD) on China's Tiangong space station [Kyr22]. That is not to say that the data provided by these instrument cannot be useful to understand, for example, the creation of secondary radiation in a spacecraft's structures and shielding. Other uses include the real-rime monitoring of SEP [Fal+23].

Generally, spectrometers are at the upper end of the capability scale. They are, however, seldom used for operational radiation monitoring because of the required magnetic field, whose strength dictates the size of the system. Even if a spectrometer is optimized for the energy range of interest and uses state-of-the-art electromagnets and low-power sensors, the size, mass, and

power consumption of the system usually exceed many if not all constraints for a high-availability system that is critical to crew health. A possible exception could be the Penetrating particle ANalyzer (PAN) concept [Amb+19; Suk+23].

5.5.2 Dosimeters

At the other end of the capability scale are a variety of crew-worn and area-monitoring dosimeters. These systems can be both active and passive, with the latter often requiring detailed analysis to determine the absorbed dose. The use of passive sensors goes back to the early days of the space program [Eng+73]. Today, they are used in the form of thermoluminescent materials [Nag+13; Pug+14; Pin+24], optically stimulated luminescent materials [Yuk+06; Ber+16a; Yuk+22], and track-etch detectors [Nag+13; Ber+16a], among others [Ako+05; CH11]. The main drawback of nearly all these systems is that the complexity of the necessary processing (sometimes involving chemicals) requires them to be brought back to Earth for analysis (exceptions include, for example, the Pille-ISS thermoluminescent dosimeter system [Pin+24]).

Due to this limitation, there is a persistent trend toward using active dosimeters [VV22]—i.e., sensors that can be read out fully automatically and in real time—though passive ones continue to be in widespread use in current and upcoming missions [Gaz+17], and are the detectors of choice for high-resolution measurements with anthropomorphic phantoms [Rei+09; Sem+10]. In contrast to passive instruments that exploit radiation-induced damage or reversible changes in the material's molecular structure, active dosimeters rely on the ionization of the sensor material and the subsequent collection of the created charge, either on a cumulative or event-by-event basis. Nowadays, they often consist of some form of silicon sensor, though gas and scintillation detectors are occasionally used as well. Perhaps the most important advantage of active devices, besides the fact they do not need processing on ground, is that they not only provide measurements of the (integrated) absorbed dose but also of the dose rate, thus enabling studies of time-dependent effects.

A historically widely used class of detectors used for dosimetry are tissue-equivalent proportional counters (TEPCs). They usually consist of a hollow sphere made from tissue-equivalent plastic that is filled with tissue-equivalent gas at very low pressure [Mal+19; Hay+22]. The gas volume acts as ionization detector [KWB95; Str+15] that is in principle capable of microdosimetric measurements (depending on the size of the system) [RZ96]. Today, silicon diodes—capable of collecting (and sometimes amplifying) the charged created

via ionization by a passing particle—are the most prevalent class of sensors under development for dosimetry [Lus+10; Rit+14; Jam+19; Ben+22; Gaz+23; SBD24]. Their sensitivity range and resolution can vary widely depending on the diode type and on the stability and resolution of the read-out electronics. Generally, though, they have the advantage of being much easier to construct than gas detectors.

Two examples of modern active dosimeters are the devices used by the European and American space agencies. NASA's Crew Active Dosimeters (CADs) [Gaz+23], a direct replacement for the Crew Passive Dosimeters (CPDs) that have been used since the launch of the first ISS expedition, contain modified versions of commercially available direct-ion storage dosimeters based on floating-gate MOSFETs (which are functionally very similar to the European RADFETs [HA86]). The ESA Active Dosimeters (EADs) are more complex devices, containing two silicon diodes of different thickness, one RADFET, and one direct-ion storage dosimeter [SBD24]. Both systems are worn by the American and European astronauts on the ISS, respectively, and will also be used for future missions to the Moon.

5.5.3 Telescope-Like Detectors

The most widely used class of instruments used to characterize the radiation environment on spacecraft for operational purposes are variants of particle telescopes. The complexity of these devices varies significantly, ranging from simple instruments containing a single telescope that comprises two or three silicon diodes [Dok+01; Bea+02; Rit+14] to complex ones with multiple telescopes, each made up of multiple layers of (position-sensitive) detectors [Lee+07; Dac+15; Nar+17]. Instruments currently active on the ISS include the Light Ion Detector for ALTEA (LIDAL), a version of the earlier ALTEA telescope [Nar+17] with added TOF detectors [DiF+23], and the Charged Particle Detector (CPD) of the International Space Station Radiation Assessment Detector (ISS-RAD) (see Figure 5.3), which combines silicon and scintillation detectors (and is paired with the Fast Neutron Detector (FND)) [Has+12; Zei+23a]. All these devices measure the energy loss of particles in multiple detector layers and from this information try to reconstruct a particle's identity and energy. Few of them, however, contain enough material to stop cosmic-ray nuclei with energies in the region of interest to radiation protection and fully absorb their energy.

A fairly recent development is the use of silicon-pixel sensors as standalone

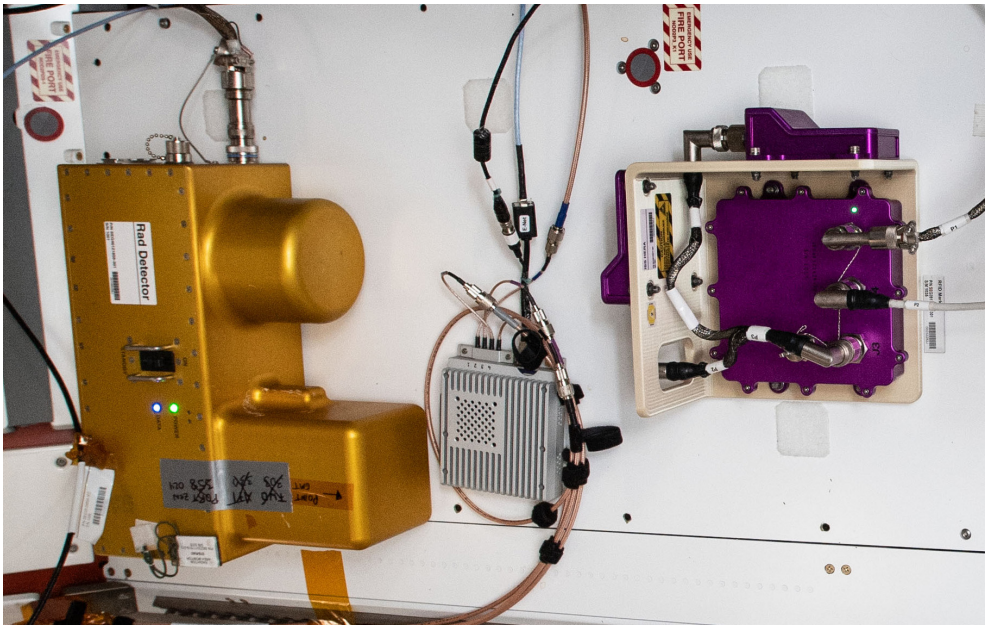

Figure 5.3: The ISS-RAD (left, gold) and HERA reference (right, purple) instruments operating in the Node 2 module of the ISS. Image credit: NASA.

radiation detectors. NASA deployed the first generation of Radiation Environment Monitors (REMs) on the ISS in 2012 [Kro+15; Sto+15]. These instruments are based on the Timepix series of silicon detectors developed at CERN [Llo+07; Poi+14; BCL20; Won+20]. In 2015, an updated instrument design was deployed on the first Orion spacecraft to reach space as part of Exploration Test Flight-1 (EFT-1) [Kro+15; Bah+15]. Several other missions also carried Timepix-based radiation detectors [Gra+16; Fur+19; Ber+24]. A single Timepix can primarily measure the energy deposited by a charged particle traversing it—and hence the absorbed dose in silicon. In contrast to unsegmented sensors, its pixel structure does, however, allow to estimate the direction the particle was coming from and thus to normalize the energy deposition to the track length, yielding a more precise measurement of the LET [Kro+18; Gra+18]. A partial identification of the particle type is possible based on the pattern of energy deposition (for particles with nearly perpendicular incidence) or from the track structure (for particles traveling in the detector plane) [Geo+18; SP18; Ber+24]. A stack of two or more sensors with absorbers in

between can improve the separation of hydrogen and helium ions [PP20]. In the Hybrid Electronic Radiation Assessor (HERA) system, NASA plans to use Timepix-based instruments as standard area monitors on the Artemis missions to the Moon [Sto+23]. A first version was part of Artemis 1, and a reference instrument is currently being operated on the ISS (see Figure 5.3).

Concluding Remarks

Even the rather brief review of our current understanding of the risk that cosmic and solar radiation pose to astronauts on missions beyond LEO show that further research is urgently needed. Many uncertainties are primarily rooted in radiation biology, though advances in dosimetry are also required.

The two key takeaways motivating our research are: (1) The biological effectiveness of cosmic and solar radiation not only depends on the LET but varies strongly with a particle's charge and energy; and (2) there is a lack of instruments that allow monitoring the radiation environment inside a spacecraft with sufficient resolution in Z (up to iron) to allow a determination of Q_{NASA} with acceptable uncertainty. Even the newest generation of devices developed by NASA and other space agencies lacks that capability. In the absence of real-time, Z-resolved measurements, either the ICRP quality factor must be used or a particle's charge and energy must be derived from a measurement of its LET. This cannot be done unambiguously and not for single particles. Especially in shielded environments, relying solely on models and simulations to propagate the (assumed) cosmic-ray environment through spacecraft walls and structures is questionable. There is thus a need for compact, low-power detectors that provide better resolutions in charge and energy.

Chapter 6

A Compact Tracking Calorimeter

The brief overview of state-of-the-art instruments in the previous chapter shows that there already is a broad range of technologies that can provide detailed information about the space radiation environment. So why bother developing another one? The caveat with the devices currently in operation is that virtually none of them can by itself provide all the information mission planners and the medical personnel supporting them would like to have access to. That is particularly true in future missions beyond LEO, for which only limited data on the respective radiation exposure is currently available. Assembling an adequate picture of the radiation environment therefore requires them to rely on data from a variety of sensors. That, in turn, necessitates knowledge of the locations throughout the spacecraft these sensors were positioned at during the time the data was taken, of the way each sensor's data was filtered and corrected for instrument-specific response characteristics, and of the sensitivity ranges and spatial, temporal, and energy resolutions of each instrument. In many cases, instruments are operated by different groups that do not necessarily share the same, or even similar, approaches for cleaning up, analyzing, and normalizing their data. They may even base their analyses on different assumptions regarding, for example, local shielding conditions, which can have a significant impact on the reported measurements. Data from sensors based on different technologies must also be treated differently in all but a few cases, as detector technologies exhibit significantly dissimilar responses to radiation. Though efforts are being made to calibrate different sensors at the same facilities to improve their interoperability [Ben+19], this cross-calibration can only partially alleviate the aforementioned challenges.

The current patchwork of instruments thus leads to a somewhat incoherent knowledge of the radiation environment inside a spacecraft and to largely unknown uncertainties resulting from the combination of data that may have undergone completely different treatment by the different groups building and operating them. Recently, discrepancies between the cosmic-ray fluxes at higher energies measured simultaneously by astrophysical investigations—in particular AMS-02, CALET, and DAMPE—also seem to indicate that systematic effects of different detector systems are not being treated correctly.

The development of new instruments with broader capability sets and larger sensitivity ranges could help to substantially improve this situation. While it is unlikely that someone will design a one-size-fits-all solution for space radiation monitoring anytime soon—there will very likely always be a need for small and lightweight personal dosimeters, for example—reducing the number of different sensors will certainly improve the accuracy of the gathered data. It will also result in operational advantages by reducing the number of instruments mission planners must accommodate at locations of interest throughout a spacecraft. A less diverse range of detector technologies employed in instruments would also make it easier to compare the sensor data and hence increase the possibilities of interoperability.

In this chapter, I describe the general working principle of a detector concept we devised that promises to address this challenge. I also discuss, in general terms, our implementation of it and briefly summarize the development and test of early prototypes. This includes a detailed summary of measurements we performed to demonstrate the fundamental detection principle.

6.1 General Requirements and Constraints

The central theme of our work on the detectors for the RadMap Telescope (and the AFIS mission) has been to develop functionally simple and robust instruments that can be constructed from commercially available and inexpensive[1] components. While later chapters will show that finding low-cost solutions to demanding functional and operational requirements has at times been challenging, we nevertheless were able to devise a working principle that is simple and mostly straightforward to implement.

Many of the requirements and constraints placed on the detector design have evolved historically from the specific requirements of the CubeSat-

[1] If measured against typical prices in the spaceflight industry.

based astrophysics mission we worked on. In hindsight, the overlap in required capabilities between both applications—despite their somewhat different objectives—does, however, allow them to be well motivated in more general terms:

Particle Identification. Both our objectives in radiation monitoring (for the RadMap Telescope) and those in astrophysics require the identification of (anti-) protons and nuclei, albeit with different separation power. Common to both applications is the near-perfect separation of (anti-)protons and helium from heavier ions, as they are the most abundant cosmic-ray particles. In radiation monitoring, even small uncertainties in determining their flux can lead large errors in calculating the absorbed dose; for AFIS, the derivation of the antiproton flux from the antiproton-to-proton ratio suffers from a similar sensitivity to misidentification. For radiation-monitoring purposes, the identification of ions up to iron is required, although the separation power can be worse for neighboring species (i.e., those with adjacent nuclear charge) of similarly low flux. Sensitivity to different isotopes is not needed. In addition, secondary particles like pions must be detected but not identified. The detection of electrons is not generally required but is an optional objective relevant to radiation monitoring, especially for missions that venture beyond Earth's protective magnetosphere or spend a long time in planetary radiation belts with a large electron population.

Energy Resolution. The desired sensitivity range and energy resolution somewhat vary between the two applications. The AFIS mission profile provided the initial reference, namely a sensitivity in the range of tens to hundreds MeV per nucleon at a resolution of better than 10%. These values not only match well to those of operational radiation monitoring but also to those of many heliophysics applications. In both cases, a better resolution, on the order of a few percent, is desirable but not strictly necessary.

Tracking. The tracking of primary (protons, antiprotons, and nuclei) and secondary (pions) particles is central to the measurements we want to perform, both in the fields of radiation monitoring and astrophysics. The required position and angular resolutions are, however, not well-defined. A value of 2° for the latter is a somewhat arbitrary goal that would allow performing directionally resolved measurements of the shielding efficiency in radiation-monitoring applications. The position resolution is not of interest in itself but is largely driven by the angular-resolution requirement. A second driver is the

need for separating closely spaced tracks of secondary pions created in the annihilation of antiprotons.

Geometric Acceptance. A limitation of many detectors used for radiation monitoring, as well as for (space-based) cosmic-ray and heliophysics research is their gathering power, parametrized in the geometric acceptance (or geometric factor, see Section 4.1). The smaller the acceptance, the longer the measurement time required for achieving a desired resolution. Investigations using detectors with small geometrical factor thus either suffer from large statistical uncertainties or cannot resolve transient phenomena well. There is no well-defined lower limit on the acceptance; for every design option, the detector size must be traded off against the time needed to achieve a given precision of flux measurements. Our objective is to develop detector concepts that have the largest possible acceptance while meeting the volume and mass constraints summarized below.

Volume and Mass. The starting point of our work on cosmic-ray detectors was the idea for the AFIS mission, which we envisioned to be based on a 3U CubeSat form factor [CDS14]. We hence initially assumed a maximum volume of $9 \times 9 \times 9\,\mathrm{cm}^3$ and a mass limit of 1 kg for the detector of such a mission. With the extension of the CubeSat standard towards larger form factors and in light of our evolving research focus, these constraints have somewhat relaxed but still provide a good guideline. Generally, volume and mass are severely constrained commodities in the spaceflight business, especially on crewed spacecraft. There are thus strong incentives for designing instruments to be as compact as reasonably possible. Similar limitations exist for electrical power but are not discussed here because they are only relevant to electrical systems and not to the detector itself.

Launch and Space Environments. Bringing an instrument into orbit and operating it in space is associated with several unique challenges. The first is the high degree of mechanical stability required to survive the vibration, shocks, and acoustic pressure experienced during launch. Their intensities differ somewhat from vehicle to vehicle but tend to be lower for crewed launches. The second is the on-orbit thermal environment. In the vacuum of space, convective heat transfer is impossible and heat can thus only be removed from a system via radiative transfer to free space, which is much less efficient. Even in pressurized spacecraft, the absence of Earth's gravitational pull means that convection does not take place, necessitating a careful thermal

design. Another challenge is the exposure to the space radiation environment and the extreme UV emissions of the Sun, which can lead to increased material degradation. Damage due to debris or micrometeoroid impacts can also occur but is largely irrelevant to our instruments because they are deployed inside the protective hull of spacecraft.

Materials. The choice of materials that can be used in space applications, especially aboard crewed spacecraft, is limited. Most restrictions are on the grounds of flammability and outgassing, which render many plastics inadmissible. The increased corrosion risk for some aluminum and steel alloys can also be a limiting factor. Aboard crewed spacecraft, the use of materials that could potentially present health hazards is severely restricted, also rendering the use of many gases difficult.

The detector design we devised can satisfy all the above requirements and constraints. For the RadMap Telescope, some constraints (e.g., concerning the launch environment) were relaxed to a certain degree (Section 10.1.3).

6.2 Working Principle

The underlying idea of the detector concept—which we initially called the Multi-Purpose Active-Target Particle Telescope (MAPT) and later renamed to Active Detection Unit (ADU) for the RadMap Telescope—is to use a single, homogenous volume for tracking, energy measurement, and particle identification. To achieve this, the volume must be segmented[2] in three dimensions and large enough (or finely segmented enough) to achieve an acceptable tracking performance. It must also be sufficiently dense for nuclei with energies in the range of interest to lose a significant fraction of their energy to enable energy measurements and particle identification.

We also needed to identify or develop a particle-identification method that does not require the use of a magnetic field to determine charge and momentum. This was because the initially assumed limitations in size and weight would not have allowed the use of a sufficiently strong permanent magnet. Though potentially resulting in a smaller setup, the use of an electromagnet was not possible because of power limitations and would still have exceeded the mass budget of the AFIS mission.

[2] If using solid-state detector materials. Gas detectors do not necessarily need to be segmented.

6.2.1 Bragg Curve Spectroscopy

The technique that promises to address all our requirements and constraints is called *Bragg curve spectroscopy* and was developed by Gruhn et al. with the help of an ionization chamber at the Lawrence Berkeley Laboratory in the early 1980s. In their 1982 paper, Gruhn and his collaborators summarized the technique's strengths as follows [Gru+82]:

> "Several advantages are realized in this type of heavy ion detector. [...] Large solid angles are easily achieved. The resolution for identifying particles is intrinsically high because all the measurements are made in one medium, eliminating window or dead layer effects. Particle identification can in principle be achieved over a large dynamic range of energies and particles."

The original technique requires particles to fully stop within the detector, losing all their kinetic energy in a characteristic Bragg curve (see Section 3.2.9). If that curve is fully recorded by the detector, one can determine the following parameters of the particle (see Figure 6.1): its range from the length of its track in the detector; its total kinetic energy from the integral over the Bragg curve; its specific energy loss, $\mathrm{d}E/\mathrm{d}x$, at the beginning of the track; and its maximum energy loss from the height of the Bragg peak. The range, R, is a characteristic function of the particle's nuclear charge Z_1, its mass number A_1, and its initial velocity β; the kinetic energy, E_{kin}, is a function of A_1 and β; the $\mathrm{d}E/\mathrm{d}x$ depends on Z_1 and β; and the height of the peak depends solely on Z_1. A single record of the Bragg curve therefore allows to determine the three parameters (Z_1, A_1, and β) that unambiguously describe a particle or nucleus stopping in the detector.[3] It cannot, though, determine the *sign* of Z_1 because the interaction between particle and material only depends on Z_1^2 (see Equation 3.15). The separation of particles from their antiparticles is therefore not possible using only the information contained in the Bragg curve.

If a particle does not fully stop within the detector volume because its initial energy was too high, an extrapolation of the curve can still yield acceptable results [Hag+08]. The energy of the particle cannot be arbitrarily high, though, as the $\mathrm{d}E/\mathrm{d}x$ must change significantly over the track length for the extrapolation to be sufficiently accurate. This requirement sets an upper limit

[3] I use subscripts on Z_1 and A_1 to be consistent with the nomenclature in Chapter 3, where the subscript '1' denotes the properties of a projectile ion and '2' those of a target ion.

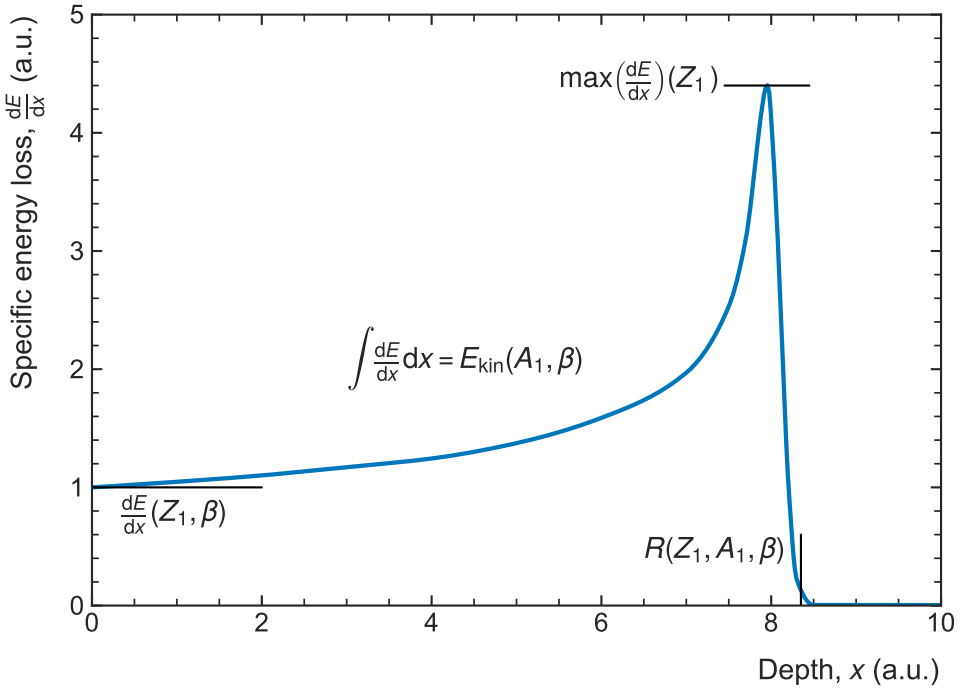

Figure 6.1: Parameters that can be extracted from a Bragg curve. The figure is adapted from [Gru+82]. The Bragg curve is based on an interpolation of data taken from the NSRL user guide [Bro24].

on the reconstructable energy that mostly depends on the detector's energy and spatial resolutions. At high energies, particles with similar momentum but different mass can also be separated by their (nearly constant) energy-loss density alone [AC80]. This technique, however, requires independent knowledge of a particle's momentum and is thus of little use to us.

To illustrate the influence of kinetic energy and nuclear charge on the shape of the Bragg curve, Figure 6.2 shows the energy-loss profiles of protons, silicon nuclei, and iron nuclei with different energies in high-density polyethylene (HDPE). The data shown was recorded at the NASA Space Radiation Laboratory (NSRL) [LaT+16] at the Brookhaven National Laboratory (BNL) with the help of ionization chambers and polyethylene absorbers of different thicknesses; it is freely available from the NSRL user guide [Bro24]. The data points represent the average ionization energy loss of many particles, not the value of a single

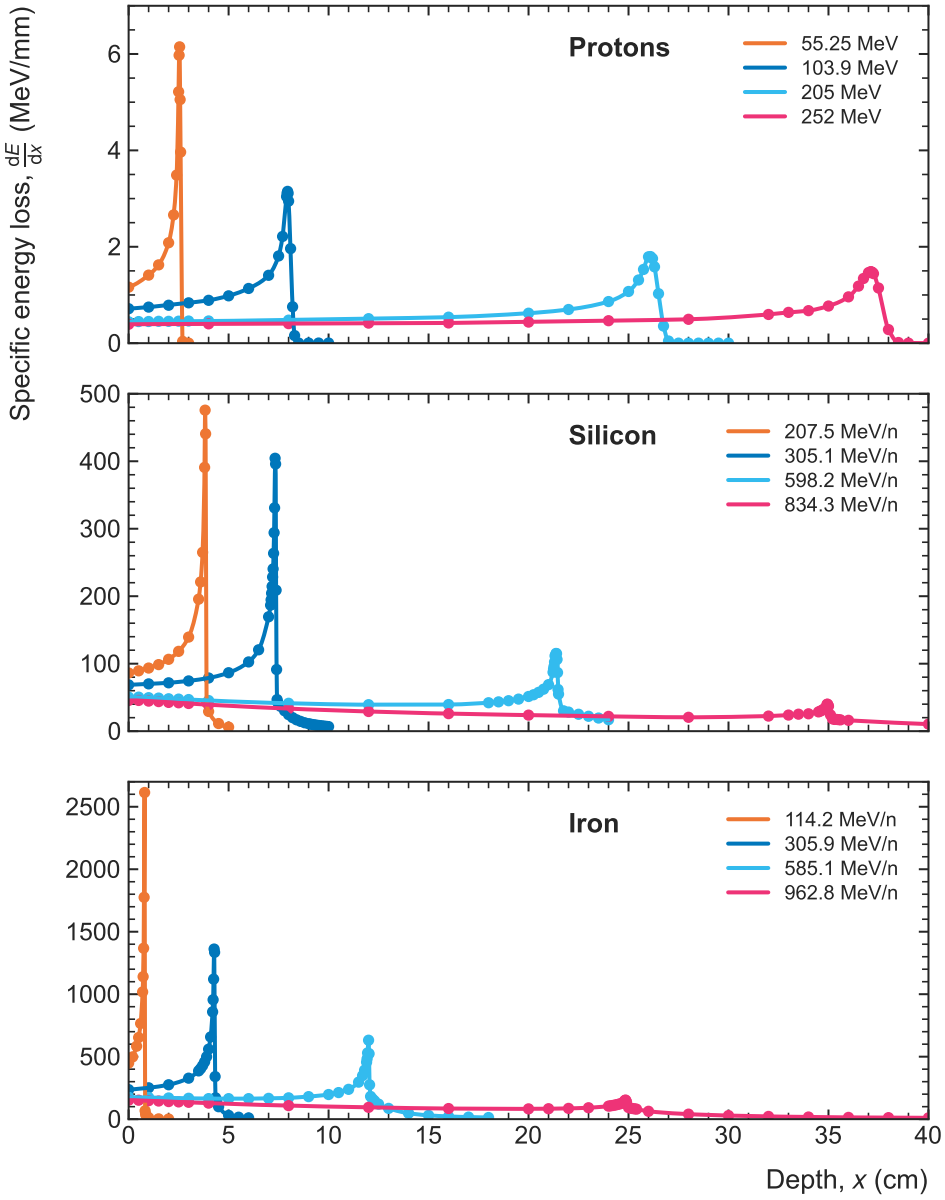

Figure 6.2: Bragg curves for protons, silicon nuclei, and iron nuclei of different energies in high-density polyethylene (HDPE). The data shown is from a large ensemble of particles. It was taken from the NSRL user guide [Bro24] and interpolated with a cubic spline for visualization purposes.

measurement. Uncertainties are not given in the user guide.

The upper panel of Figure 6.2 illustrates that most of the protons' energy is deposited in the last few millimeters of their tracks, leading to a very sharp Bragg peak at low energies. At higher energies, the peak is increasingly broadened by statistical fluctuations of the energy loss (energy-loss straggling, see Section 3.2.7), and the average maximum $\mathrm{d}E/\mathrm{d}x$ decreases accordingly. Despite the broadening, the energy-loss densities drop rather sharply to zero at depths beyond the peak. The middle panel of Figure 6.2 shows analogous measurements for silicon. Though the stopping curves look very similar for low energies, two differences can be observed: Beyond the Bragg peak, the energy loss does not drop to zero as sharply as it does for protons, and the shape of the energy-loss profile changes significantly for nuclei with higher energies. Both differences are even more pronounced for iron nuclei, as shown in the bottom panel of Figure 6.2.

Challenge #1: Fragmentation

These two differences are caused by the fragmentation of beam nuclei into nuclei with lower Z_1 (see Section 3.3.6). Projectile fragments, which have a lower stopping power in the target material, retain—to a large degree, though not exactly—the velocity and direction of the projectile. It is hence intuitively comprehensible how the longer range of projectile fragments produces the tail beyond the Bragg peak. As long as the fraction of projectiles that fragment remains small, the shape of the energy-loss profile otherwise roughly resembles that of protons. For higher beam energies, however, most of the incident nuclei fragment before the target material can stop them. The resulting mix of projectile fragments has a significantly lower energy-loss density than unfragmented nuclei, leading to a decrease of the mean $\mathrm{d}E/\mathrm{d}x$ compared to the initial value at the entrance point, where the higher energy-loss density of the beam nuclei dominates. Target fragments, on the other hand, are emitted isotropically in the rest frame of the target nucleus; they have a high stopping power and, correspondingly, a short range. Even though they therefore significantly increase the energy density close to the interaction site, their probability is almost constant along the projectile's path, which is why they add only little to the deformation of the energy-loss profile.

Figure 6.3 allows a closer look at the deformed Bragg curve of 962.8-MeV iron nuclei and clearly illustrates the drop of the energy-loss density for increasing depth caused by projectile fragmentation. A small fraction of nuclei

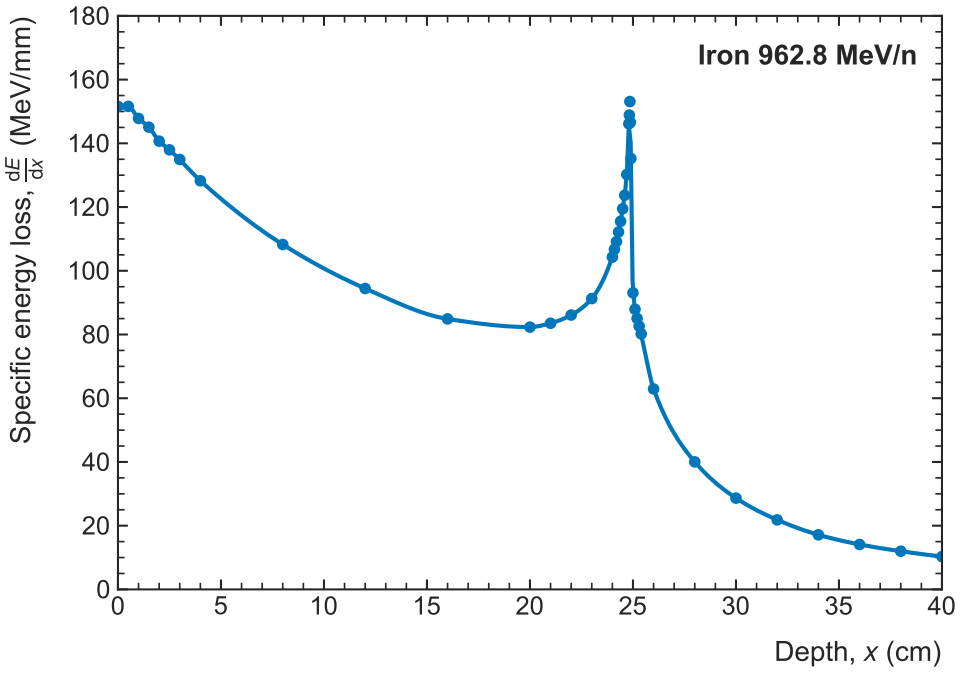

Figure 6.3: Bragg curve of iron nuclei with an energy of 982.8 MeV/n in HDPE, illustrating the effect of fragmentation on the shape of the energy-loss profile. The data shown is from a large ensemble of particles; the energy-loss profiles of single ions vary significantly. The data points were taken from the NSRL user guide [Bro24] and interpolated with a cubic spline for visualization purposes.

survives and stops, leading to the formation of a Bragg peak that barely exceeds the initial energy loss. The fragmentation hence limits the accuracy of particle identification and energy measurement at higher projectile energies, as the energy-loss profiles for nuclei of the same species and energy can look very different. At one end of the range of possible profile shapes is a nucleus that does not fragment at all and thus produces a picture-perfect Bragg peak. At the other end is one that fragments immediately upon entering the material, producing several lighter particles whose energy-loss density barely changes along their path through the detector. The profile shown in Figure 6.3 is the weighted average over all possible shapes in between these extremes. There is thus no single template that can be used to identify the energy-loss profile of nuclei that are prone to fragmentation.

This is a fundamental weakness of Bragg spectroscopy if the technique is applied to single particles, as in our case, and not to ensembles of particles, as originally proposed by Gruhn at al. Particle-identification algorithms must be able to cope with the broad range of potential energy-loss profiles for ions of the same energy and species, significantly complicating the analysis of the data gathered by our detectors. Figure 3.10 illustrates that for light ions like neon, which lies in the middle of our nuclear-charge sensitivity range, the nuclear-reaction (and hence fragmentation) probability approaches 100% for 10-cm thick carbon targets at energies of 1 GeV/n or more. Even for neon ions that just about stop in a target of such thickness, the probability exceeds 10%. The situation gets worse for higher nuclear charge, for which increasingly larger fractions of ions fragment at lower energies.

Figure 6.2 does, however, show that for nuclei stopping in a detector less than 10 cm in size, the Bragg peak is only minimally distorted even for elements as heavy as iron. An analysis restricted to such stopping nuclei thus promises to deliver precise measurements. Using the example of iron, this stopping condition translates into an upper energy limit of about 450 MeV/n (less for lighter ions). It would, however, be highly desirable to extend the measurement range to larger energies, in which case fragmentation must be taken into account during data analysis to achieve any meaningful result.

Challenge #2: Energy-Loss Straggling

A similar challenge likewise arises from the fact that the characteristic Bragg curve describes the mean energy-loss profile of particles with a given energy. The profile for individual particles, even in the absence of fragmentation, can be significantly different from this average behavior due to energy-loss straggling. Especially in the region around the Bragg peak, the distribution of the energy-loss density is rather broad. Consequently, the exact shape of the Bragg peak differs from event to event, though the variation is far smaller than that caused by fragmentation. Straggling is, however, more severe for stopping ions than it is for high-energy ones that pass through the detector and only lose an insignificant amount of their kinetic energy.

Challenge #3: Dynamic Range

A third challenge of the technique is illustrated by Figure 6.4. The figure shows energy-loss profiles for hydrogen, carbon, oxygen, silicon, and iron nuclei at

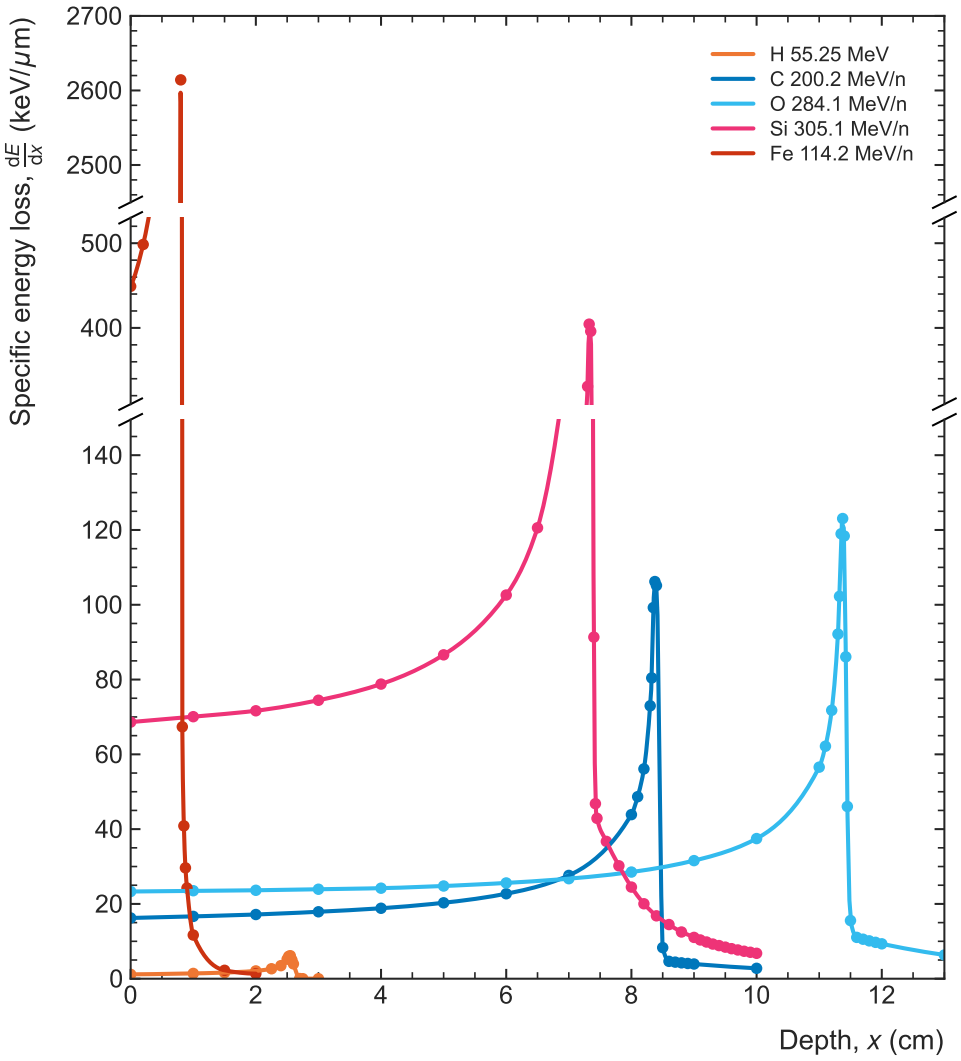

Figure 6.4: Comparison of Bragg curves for hydrogen (protons), carbon, oxygen, silicon, and iron nuclei in HDPE, highlighting the large dynamic range required for separating ion species via Bragg curve spectroscopy. The data points were taken from the NSRL user guide [Bro24] and interpolated with a cubic spline.

various energies and highlights that their maximum specific energy loss differs by up to three orders of magnitude. While this large separation is in principle helpful for the accurate identification of nuclei, it does require high-resolution detectors with a large dynamic range if both light and heavy nuclei shall be detected with the same system. Especially in space applications—where mass, power, and the range of usable detector technologies are limited—constructing such a system may present a challenge given the particular requirements and constraints of a given mission.

Despite these challenges, Bragg curve spectroscopy promises to be a particle-identification technique that can deliver the separation accuracy required for the RadMap Telescope. Besides the advantage of not requiring a magnetic field, the energy-loss profile can potentially be recorded with sufficient detail by a detector with only moderate spatial resolution (in contrast to the high resolutions required in compact magnetic spectrometers). This simplifies the construction of a homogenous detector consisting of a single, robust, and inexpensive material.

6.3 Implementation

Instead of using an ionization chamber like Gruhn and his collaborators, we realized that a detector volume made of a solid material has several critical advantages for space-borne systems. Most importantly, it neither requires a pressure vessel nor a system for handling gases. Both are challenging to implement on spacecraft, where they may present catastrophic hazards to both vehicle and crew and therefore must be designed with a number of redundancies and safety features. An additional hazard is posed by the high voltages (typically several hundred to a few thousand Volts [HR20]) required to accelerate the ionized gas. Depending on the type of chamber and on the desired field configuration, the required wires or foils are oftentimes quite delicate, with typical diameters of a few tens of micrometers [HR20]. Designing them to withstand the vibrations and shocks encountered during a launch and the thermal environment in orbit is certainly a challenge, though not an insurmountable one—as, for example, the AMS-02 experiment demonstrated with the successful deployment of a large array of straw tubes [Kir+04].

The disadvantage of using solid detector materials is that it is harder to construct a continuously sensitive volume that allows to precisely measure

the energy-loss profile of a particle along its track. A solution is to segment the detector in two or three dimensions. By choosing an adequate size of the individual segments, an almost arbitrarily good spatial resolution can be achieved, though at the cost of many insensitive layers between the segments. These 'dead' layers can significantly decrease the detector's energy resolution because the energy a particle loses in them is not recorded. In addition, a smaller segment size often leads to a worse signal-to-noise ratio in each segment, again resulting in a decrease of the energy resolution. At some point, the deposited energy that can be detected also becomes so small that there is an effective lower limit on the (theoretical) segment size. Often, though, mechanical and electrical limitations arise well above this limit.

The choice of materials that allow to construct the three-dimensional detector volume required for omnidirectional sensitivity at an acceptable cost is limited. Semiconductors are increasingly the material of choice for constructing large tracking detectors [All19] and calorimeters [BRS18] with excellent spatial and energy resolutions, respectively. So far, however, they cannot be used to construct large monolithic volumes with (fine) three-dimensional segmentation. Silicon-strip or silicon-pixel detectors can provide superior tracking in two dimensions and also achieve good energy resolutions but are made from wafers with a typical maximum thickness of a few hundred micrometers [Mos09]. Densely packing a macroscopic volume with such detectors to construct a homogenous calorimeter is prohibitively expensive, especially for projects with limited budget like ours. In high-energy physics experiments, they are thus typically used in sampling calorimeters, where layers of silicon detectors are separated by (thick) layers of passive, heavy materials like lead [BRS18]. Another disadvantage of using silicon-based sensors with fine segmentation is the amount of power required to digitize their signals; in space applications, this has so far confined their use to tracking detectors.

Recent developments like the upgrade of the ALICE inner tracker with monolithic active-pixel sensors (MAPS) show that large tracking detectors with integrated read-out systems and low power densities can be realized [Fan20; Agl23]. A rival technology are low-gain avalanche diodes (LGADs), which promise to deliver superior timing performance [Car+20; Gia23]. To achieve such low power consumption, however, these new detectors are designed to provide only spatial information—with each pixel simply indicating whether it was hit by a particle or not. The much more power-intensive digitization of the collected charge is not performed at all. To construct a calorimeter from such sensors, a sampling-calorimeter-like layout with energy-sensitive

layers separating the tracking layers could be chosen but would require a more complex setup with two different detector technologies. It is also questionable whether the high spatial resolution of such silicon detectors is required for the identification of ions via Bragg curve spectroscopy.

Scintillators (both organic and inorganic), on the other hand, can easily be produced to fill large volumes and can be segmented more or less arbitrarily, though generally with much coarser segmentation than possible for silicon detector. Chapter 9 shows that the latter aspect is completely acceptable for the RadMap Telescope and the better spatial resolution of silicon detectors is indeed not necessarily required. The rather broad range of available scintillator materials allows to fine-tune a detector's sensitivity range (in terms of particle energy) by choosing one with an adequate density.

Generally, plastic scintillators are easier to work with than crystals (or ceramics). Plastics can be cast or extruded and then machined into almost arbitrary shapes while crystals must be grown and then ground into their final shape. Due to their brittleness, this process is very time-consuming and the range of shapes that can be produced with comparable effort is limited. The hygroscopicity of some materials also makes their handling more complicated. In addition, the higher price of inorganic scintillators is another aspect that restricts their use in large-scale systems, though some proposed space-based instruments would make use of them nonetheless [Adr+21a]. Plastic scintillators, on the other hand, have two main disadvantages that complicate their use in space applications: They have a much narrower operational temperature range (with temperatures exceeding 100°C being critical[4]) and are more susceptible to radiation damage, especially in the mixed-radiation field encountered in space. In applications requiring a large temperature working range or high radiation hardness, inorganic scintillators may thus be a better choice. Table 6.1 summarizes the advantages and disadvantages of using organic (plastic) and inorganic (crystal) scintillators for space applications.

For the MAPT detector principle employed in RadMap's ADU, we chose to use organic scintillators in the form of scintillating-plastic fibers. Such fibers have been, and still are, used for particle tracking in high-energy physics experiments [DAm+96; Ruc96]. They can easily be procured from manufacturers in standard diameters with round and square cross-sections. Due to its superior

[4]The softening temperatures of PS and high-temperature PVT, the two most widely used plastic matrices, are 90°C and 99°C, respectively [KMN17; Elj23]. Glass transition occurs above these temperatures, significantly changing their mechanical and optical properties [Pla65; Rie96]. Manufacturers often quote maximum operational temperatures of 50°C to 70°C.

Table 6.1: Advantages and disadvantages of using organic (plastic) and inorganic (crystal) scintillators for space applications.

	Organic Scintillators	**Inorganic Scintillators**
Advantages	Easy to form/machine Easy to handle Emission can be fine-tuned Inexpensive	Large temperature range High radiation hardness
Disadvantages	Small temperature range Low radiation hardness	Hard to form/machine Often hygroscopic Expensive

mechanical stability (compared to PVT), they are usually based on a PS matrix. Most are ternary systems, with dyes and wavelength shifters added such that the emission maximum is in the blue range of the optical spectrum, though the exact chemical composition is in most cases a closely guarded secret. The advantage of using fibers instead of machined and polished pieces of bulk scintillator is twofold: (1) They require less mechanical work (a simple cutting to the required length and polishing of the end faces) and (2) have a higher light-collection efficiency thanks to their cladding. This comes at the cost of a smaller range of readily available matrix–dye–shifter combinations, which means their properties (in terms of light yield and mechanical properties) cannot be matched as well to the application at hand as the wider range of commercially available bulk scintillators allows. This limitation has not been an issue for us, as several commercially available fiber types are well suited to the detection of heavy charged particles (protons and nuclei).

6.3.1 Fiber Selection

The particular fiber type we chose, SCSF-78 manufactured by Kuraray [Kur14], has a square cross-section and a thickness of 2 mm. It has a single cladding made of PMMA, an attenuation length of longer than 4 m, and a decay time of 2.8 ns. Its emission maximum at 450 nm matches well to the sensitivity range of most modern photosensors. The only other commercially available product with a square cross-section at the time we started developing the MAPT concept was the BCF-12 fiber by Saint-Gobain Crystals (now Luxium Solutions) [Sai11]. Table 6.2 compares the properties of the two fiber types and shows that the differences are marginal in most cases, at least for our applications.

Table 6.2: Properties of square SCSF-78 and BCF-12 fibers per manufacturer data sheet [Kur14; Sai11]. Kuraray does not quote an intrinsic light yield for the SCSF-78 fiber, though it should not differ strongly from that of BCF-12.

	SCSF-78 Single cladding	**BCF-12** Single cladding	**BCF-12** Multi-cladding
Core material	PS	PS	PS
Cladding	PMMA	PMMA	PMMA, fluor-acrylic
Cladding thickness	2%	4%	6%
Trapping efficiency	4.2%	4.4%	7.3%
Intrinsic light yield	?	∼8000 ph./MeV	∼8000 ph./MeV
Emission peak	450 nm	435 nm	435 nm
Decay time	2.8 ns	3.2 ns	3.2 ns
Attenuation length	>4 m	2.7 m	2.7 m

The only significant difference is the higher trapping efficiency[5] of the multi-cladded BCF-12, which comes at the cost of a thicker cladding (i.e., insensitive volume) and thus a lower detection efficiency if used in fiber arrays. A simple estimate shows that the associated higher light output is not necessarily advantageous. Assuming an approximate energy loss of 200 keV/mm in PS [Ber+17] and neglecting the insensitive volume of the cladding, a MIP traversing the fiber produces at least

$$N_{\mathrm{ph}} = 0.2\,\mathrm{MeV/mm} \cdot 2\,\mathrm{mm} \cdot 8000\,\mathrm{photons/MeV} = 3200\,\mathrm{photons}. \tag{6.1}$$

For the multi-cladded BCF-12 with a trapping efficiency of 7.3%, this translates into 234 photons reaching a photosensor at one end of the fiber, if attenuation is not taken into account. At 4.4% efficiency for the single-cladded version, the light output is about 141 photons. Even if accounting for attenuation (which is minimal if only light transport in the core is considered) and assuming a conservative photon detection efficiency of 40%, a MIP produces a signal of about 50 photoelectrons in single-cladded BCF-12. Considering the noise levels in modern photodetectors, this yields an excellent signal-to-noise ratio.

At the lower end of the energy-loss sensitivity range, there is thus no reason to choose multi-cladded fibers. The discussion in Section 6.2.1 shows that, at the other end of the range, the maximum energy-loss density of heavy ions is

[5]This is the trapping efficiency of the core–cladding interface. Both Kuraray and Saint-Gobain assume that the cladding–air interface does not contribute to the light transport.

more than three orders of magnitude larger than that of MIPs. Even though much of this energy is lost to quenching (see Section 6.3.4 below), such a huge range entails that the lower trapping efficiency of single-cladded fibers is actually helpful in keeping the required dynamic range of the photosensors as small as possible, leading to a better resolution for small $\mathrm{d}E \,/\, \mathrm{d}x$.

Kuraray does not specify the intrinsic light yield of the SCSF-78 core material in their data sheet, and we could not find one published in the literature. It is, however, reasonable to assume that it does not strongly differ from that of the BCF-12 fiber, as manufacturers typically optimize dye and wavelength-shifter concentrations for maximum light yield to compensate for the limited thickness of the active material in a fiber [Kno10; Sai11]. Assuming that the two fiber types not only share the same matrix material but are also doped with solutes of comparable efficiency, their intrinsic light yield likely only differs by a few percent at most. With the difference in trapping efficiency being minimal, the above light-output estimate for the BCF-12 fibers should thus roughly hold for the SCSF-78 type as well, at least to a degree where we can confidently assume a good signal-to-noise ratio for MIPs.

The two fiber types should thus perform equally well in most cases. For some applications, the SCSF-78's longer attenuation length and the thinner cladding could be advantageous. Even though we did not expect these parameters to have a significant impact on the performance of our detectors, we ultimately chose the SCSF-78 fiber. This choice was, however, primarily based on the fact that our group had some experience in using it.

6.3.2 Detector Layout

Our goal was to construct a detector volume that allows the three-dimensional tracking of particles with a sensitivity and resolution (both in tracking performance and energy determination) that is as constant over the full solid angle as possible. Using commercially available fibers, this can be achieved by simply arranging them in a three-dimensional array (see Figure 6.5), with every second layer turned by 90°. To increase the detection efficiency and tracking resolution, every second layer of the same orientation is shifted by half the fiber pitch.[6] This ensures that particles traversing the insensitive material between fiber cores (i.e., the cladding and the space between adjacent fibers) in one layer are detected in the next. Such a layout can be used to construct

[6] The center-to-center distance of two adjacent fibers.

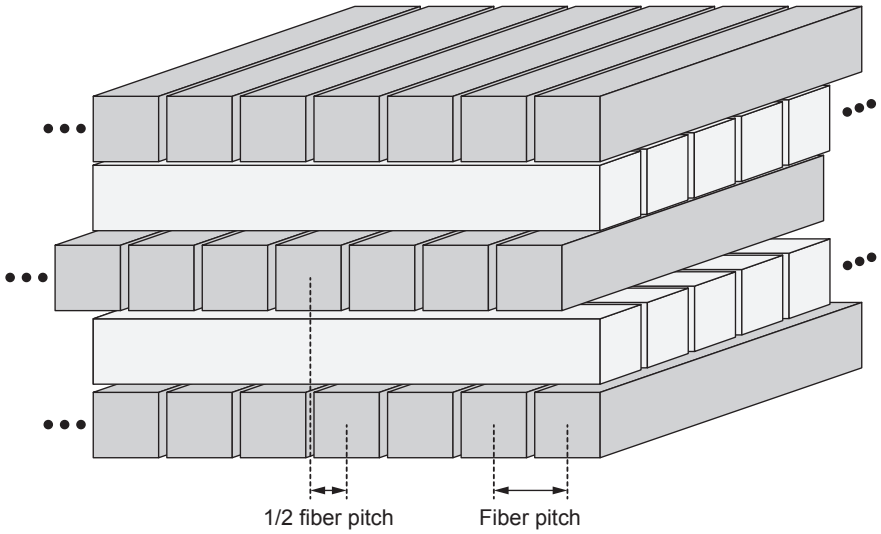

Figure 6.5: General principle of constructing a tracking calorimeter from scintillating fibers: Fiber arrays are stacked in alternating orientation, with every second layer in each orientation shifted by half the fiber pitch to increase the detection efficiency and tracking resolution.

cuboid detector volumes of almost arbitrary dimensions. For applications like the RadMap Telescope, we mostly attempt to achieve a roughly cubic shape because it is best suited to the detection of isotropic particle fluxes.

Multi-layer arrays of scintillating fibers are obviously not a new invention. They have been used for the two-dimensional tracking of charged particles in accelerator-based experiments for decades [Ruc96]. There are, however, key differences in how we make use of the general concept of stacking fibers. First, virtually all scintillating-fiber trackers built so far are only meant to determine two-dimensional coordinates on a (flat or curved) plane, for example the coordinates of a particle-interaction point relative to the beam axis [Hon+15; Coh+16]. Second, the information provided by multiple fiber layers with the same orientation is often only used to improve the spatial resolution and detection efficiency, not to determine the angle of a particle track [Bei+10; DB17]. Single fibers with, for example, lower detection efficiency thus have little impact on the overall performance of the system. Third, typical fiber trackers provide hit information only [Bis+02; Ort+20]; the differences in energy loss of traversing particles are seldom made use of. In contrast, in our

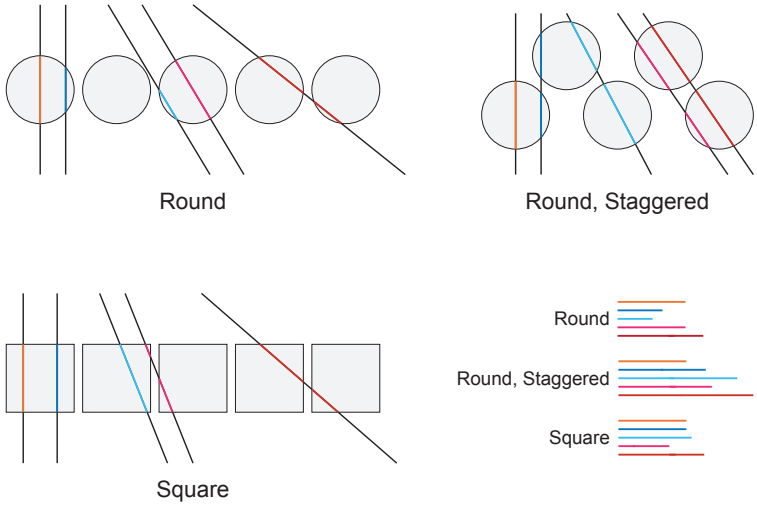

Figure 6.6: Schematic illustration of the path-length differences in layers of round and square fibers. The total length is shown for tracks traversing two or more fibers, even though in some cases the number of photons produced in short path segments may not be large enough to be reliably detected in photosensors.

approach every fiber (layer) acts as an independent sub-detector that provides both hit information and an energy-loss measurement, which is why we use the term *tracking calorimeter* to describe the detector concept. The requirements on the light-yield uniformity, signal-to-noise ratio, and energy resolution in each detector channel are thus a lot stricter than in the typical applications of scintillating fibers referred to above. Individual underperforming or 'dead' channels consequently have a much larger impact.

The stacking concept shown in Figure 6.5 motivates our choice of fibers with a square cross-section. Since each layer acts as an independent position-sensitive detector, the detection efficiency along its segmented coordinate should be as uniform and high as possible. A round cross-section, however, would result in a strongly position-dependent path length in the core material for a particle traversing the layer in perpendicular direction. This, in turn, leads to a non-uniform light yield and hence to a position-dependent detection efficiency. Even worse, the very short path length for some particles would lead to locally very low detection efficiencies. A solution to overcome this limitation would be the use two staggered layers of round fibers per array

(see illustration in Figure 6.6), which would shift the average path length to larger values. This approach would mostly alleviate the problem of very short path lengths but still result in strong angle-dependent differences. It would also require roughly twice the number of detector channels as a single layer of square fibers. The second reason for using the latter is the higher fill factor (i.e., volumetric fraction of active material) that can be achieved, which results in a larger material budget and hence higher measurable particle energies.

The detector layout does not result in angular and energy resolutions that are fully uniform over the complete solid angle. Particles entering the detector at small angles to array planes (i.e., nearly horizontally in Figure 6.5) may only traverse fibers of one layer, thus not producing the hits in both orientations (which we often refer to as *projections*) needed to accurately determine track parameters. In the worst case, they may travel along a single fiber, depositing all their energy in it. Particles traversing the detector at small angles to the stacking direction (i.e., vertically in Figure 6.5), on the other hand, will in most cases hit many fibers in both orientations, allowing a precise determination of their track parameters. I discuss the detector acceptance and resolution in more detail in Chapter 9, after introducing the exact mechanical layout of the RadMap Telescope's flight detectors.

6.3.3 Photodetectors and Optical Crosstalk

One aspect that prevented the construction of very compact fiber detectors in the past was the size of PMTs, which for decades were the only photodetectors capable of detecting single or few photons. The individual read-out of every fiber in an array thus required a mechanical fan-out of the fibers to an array of PMTs that occupied a volume orders of magnitude larger than the detector's active one. Another aspect was the prohibitively high price tag of photomultipliers, which sometimes led to clever but complicated schemes being employed to read out spatially distant channels with the same sensor to save costs [LoP+14; Coh+16]. An alternative were even more expensive position-sensitive photomultipliers [Sal+89; Hor+04] or charged-coupled device (CCD) image sensors [Ang+89; Res+95], though the latter's low sensitivity rendered the detection of single particles challenging. A final challenge are the bias voltages of several hundreds to thousands of volts required to operate PMTs, which can be a safety issue in spaceflight applications.

The limitations that often arose from these challenges were overcome by the advent of single-photon-sensitive silicon sensors, first in the form of APDs

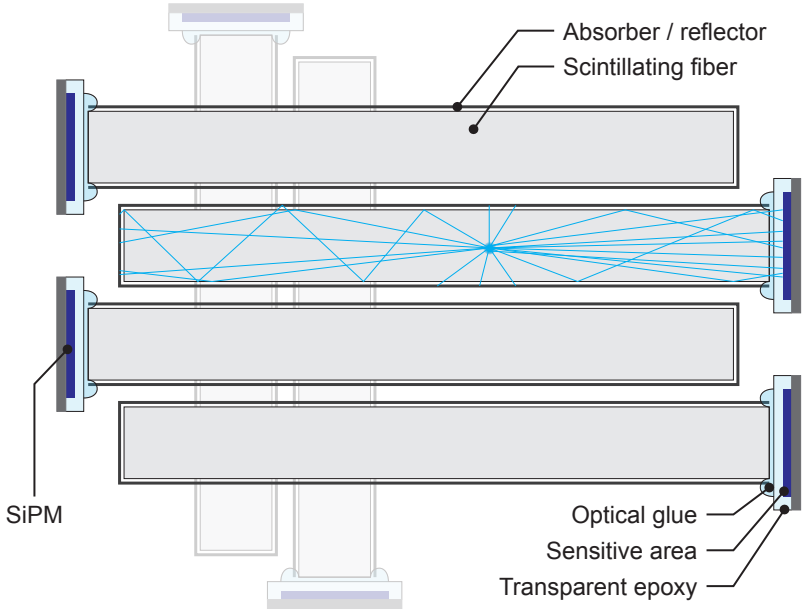

Figure 6.7: Since the SiPMs have a sensitive area and mechanical package that are slightly larger than the fiber cross-section, they are attached on alternating sides of each fiber array with optical glue. The fibers, including their end face at the far end of the SiPM, are wrapped in or coated with an absorbing or reflecting material to prevent optical crosstalk.

and then SiPMs. Such devices are not only smaller and less expensive than PMTs, and require lower operating voltages; they are also mechanically more stable, are insensitive to magnetic fields, and have a comparably high gain. The only disadvantages are their lower detection efficiency and larger dark-count rate, which for large-area SiPMs can reach the MHz regime at room temperature. For applications like ours, where even for MIPs more than 100 photons arrive at the end of a fiber, the latter two aspects are not an issue.

The maturation of SiPMs into commercially available products in the years prior to the kick-off of our work was the enabling technology development that made the construction of detectors based on the MAPT concept possible. Building a detector with the same layout of the active volume but read out by PMTs would just not have been possible. Though the performance of SiPMs

has continued to improve drastically in the past decade—and we consequently switched products (and manufacturers) frequently—their use in the ADU has remained the same.

Every scintillating fiber in our tracking calorimeters is read out by a single SiPM that has an active area that is slightly larger than the fiber's cross-section. The small size of the sensors allows us to keep the length of the fibers as short as needed for constructing the three-dimensional tracking volume because they can be attached with optically transparent glue to the fiber ends directly at the edge of the tracking volume. The sensors' slightly larger size does, however, require that neighboring fibers are read out at opposite ends (see Figure 6.7), leading to a partial overlap of an 'open' fiber end with the SiPMs of the two neighboring ones. To prevent optical crosstalk arising from this overlap or, more generally, from untrapped photons, each fiber must be wrapped in or coated with an absorbing or reflecting material. I present our studies of different crosstalk-preventing materials and their effect on a fiber's light yield in Section 7.2.

6.3.4 The Role of Ionization Quenching

One of the main challenges of working with plastic scintillators is the strong effect of ionization quenching (see Section 4.2.3) for large energy-loss densities because it reduces the separation power for (stopping) ions with large $\mathrm{d}E \,/\, \mathrm{d}x$. Quenching is, on the other hand, also the effect that makes the identification of MIPs and heavy ions with a single scintillator–photodetector combination possible in the first place. Without the quenching-induced reduction of the scintillation efficiency, the huge dynamic range (in terms of energy-loss density) of more than three orders of magnitude (see Figure 6.4) would otherwise be impossible to resolve with a single type of photosensor. We therefore studied the quenching behavior of SCSF-78 fibers in some detail. I present these studies and discuss the implications of their results in Section 7.1. Here, I only use the simple model of Birks (introduced in Section 4.2.3) and our measured value of Birks' coefficient, kB, to illustrate the effect of quenching on the data gathered by our detectors.

Quenching reduces the fraction of energy deposited by a charged particle that is converted into scintillation light. The light yield per unit distance, $\mathrm{d}L \,/\, \mathrm{d}x$, is described by Equation 4.15, where I assume Q to be the quenching function proposed by Birks (Equation 4.16) for the purposes of this discussion.

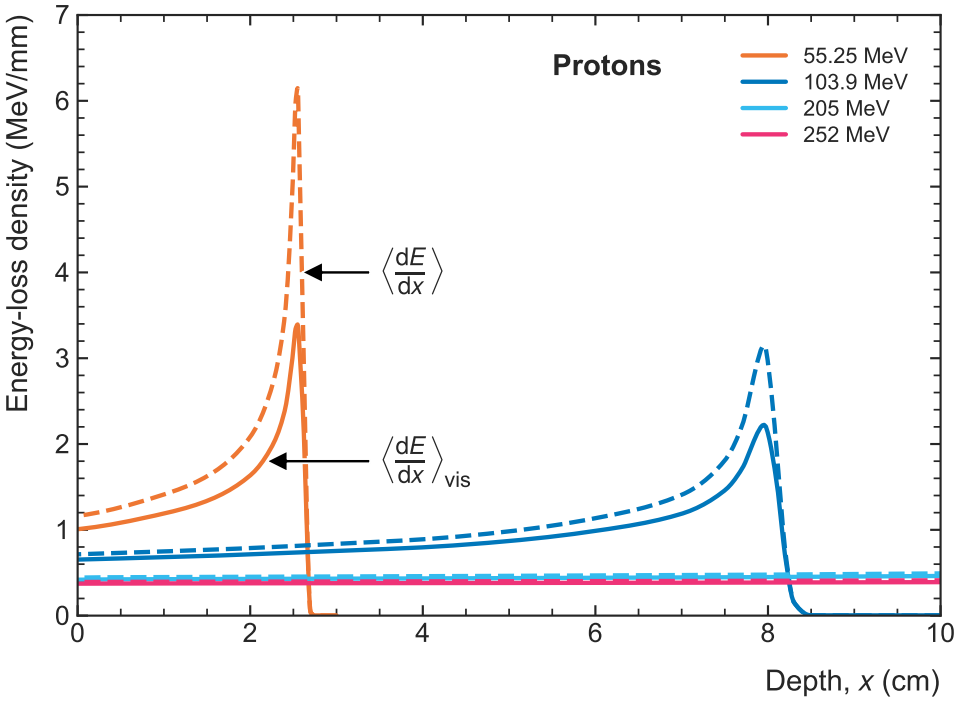

Figure 6.8: Effect of ionization quenching in SCSF-78 core material on the energy-loss profile of protons. The dashed curves show the experimentally measured deposited energy density from NSRL [Bro24], as presented in the upper panel of Figure 6.2. The solid curves show the visible energy density, determined by applying the quenching correction for SCSF-78 according to Birks' model (using the kB-value determined by us, see Section 7.1).

Since we do not know the scintillation efficiency[7] of the SCSF-78 core material, S, I use a modified version of this equation:

$$\left.\frac{\mathrm{d}L}{\mathrm{d}x}\right|_{E_\mathrm{k}} = S \cdot \left\langle \frac{\mathrm{d}E}{\mathrm{d}x} \right\rangle_\mathrm{vis}, \tag{6.2}$$

where $\langle \mathrm{d}E \,/\, \mathrm{d}x \rangle_\mathrm{vis}$ is the *visible (specific) energy density* that I define as

$$\left\langle \frac{\mathrm{d}E}{\mathrm{d}x} \right\rangle_\mathrm{vis} = Q\left(\frac{\mathrm{d}E}{\mathrm{d}x}\right) \cdot \left\langle \frac{\mathrm{d}E}{\mathrm{d}x} \right\rangle. \tag{6.3}$$

[7] Somewhat confusingly, the intrinsic scintillation efficiency is often referred to as the (intrinsic) light yield, under the assumption that quenching is insignificant.

It represents the quenching-corrected energy-loss density that can be converted into scintillation light (hence the term *visible* energy density). Since S is assumed to be constant, we can without loss of generality compare the visible energy density to the deposited energy density in lieu of comparing the quenching-corrected light yield to the uncorrected one.

Figure 6.8 visualizes the effect of ionization quenching on the energy-loss profiles of protons stopping in HDPE. Since HDPE and PS are very similar in their chemical composition, their difference in stopping power is negligible for the purposes of this illustration. The dashed curves show the experimentally measured, unquenched[8] deposited energy density from NSRL [Bro24], as presented in the upper panel of Figure 6.2. The solid curves show the visible energy density, determined by applying Equation 6.3 to the experimental data. The figure illustrates the significance of quenching even at the small energy densities generated by protons, though a clear Bragg curve-like profile is retained nonetheless.

The much more pronounced effect of quenching on the energy-loss profiles of (heavy) ions like silicon and iron is illustrated by Figure 6.9. Since the difference between the deposited and the visible energy density can be orders of magnitude, I here only show the latter; the original unquenched energy-loss profiles are shown in Figure 6.2. To illustrate how strongly quenching reduces the energy available to the scintillation mechanism, the small panels show the ratio of visible to deposited energy density:

$$\epsilon_{\text{vis}} = \frac{\langle \mathrm{d}E \,/\, \mathrm{d}x \rangle_{\text{vis}}}{\langle \mathrm{d}E \,/\, \mathrm{d}x \rangle} \tag{6.4}$$

Figure 6.9 illustrates that the energy convertible into scintillation light can be a sub-percent fraction of the deposited energy, completely distorting the shape of the Bragg curves. It also shows that there seems to be an intrinsic limit to the visible energy-loss density of about 8 MeV/mm.

There are several implications for ADU-style tracking calorimeters:

1. The dynamic range that must be covered by the photosensors is limited to a mean energy deposition of about 8 MeV/mm (multiplied by the scintillation efficiency).
2. High-resolution measurements at the upper end of that range are required to resolve what remains of the Bragg peak.

[8] I assume that quenching in the ionization chambers used at NSRL can be neglected.

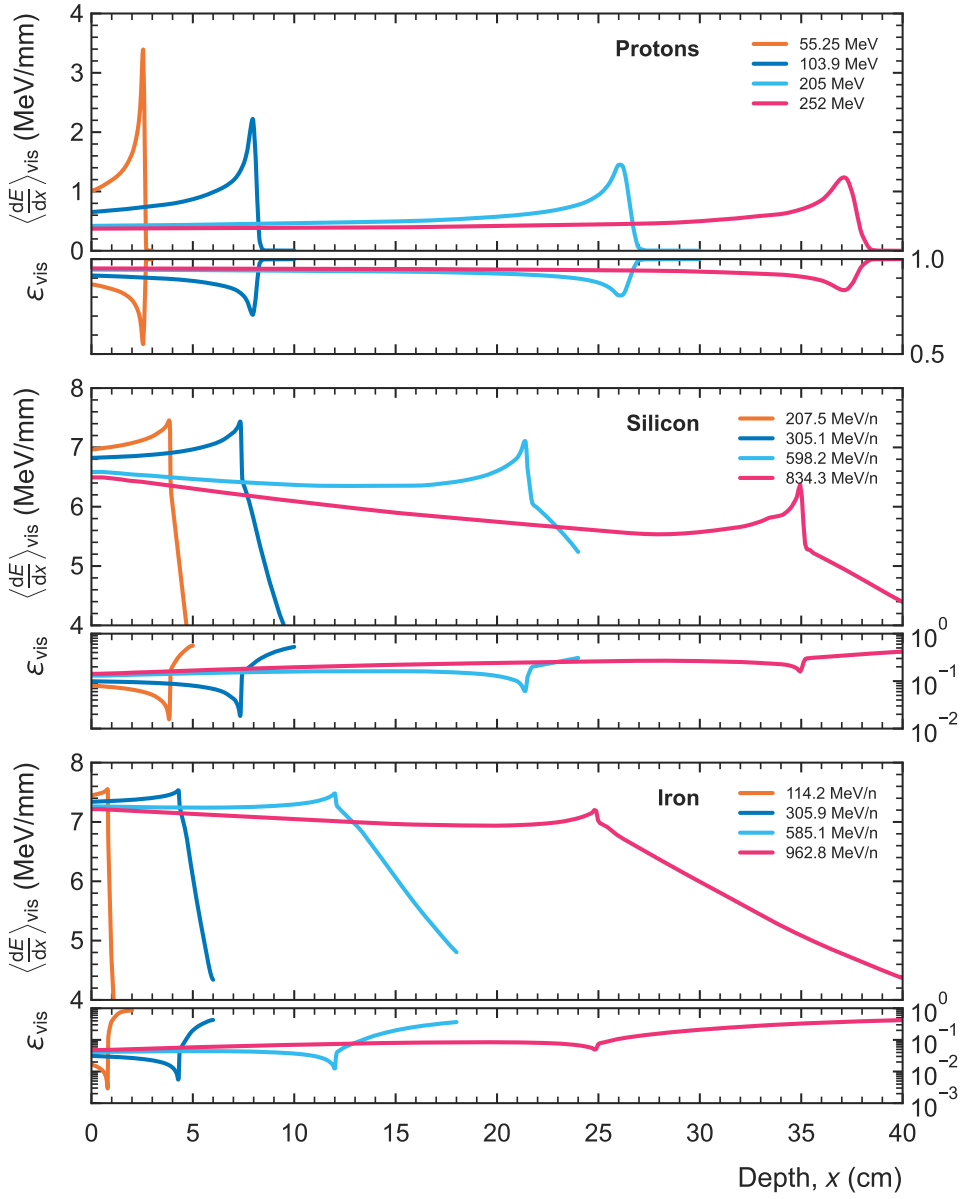

Figure 6.9: Visible energy loss of protons, silicon ions, and iron ions in SCSF-78 core material. The large panels show the data from NSRL presented in Figure 6.2 [Bro24] with the quenching correction for SCSF-78 according to Birks' model applied (using the kB-value determined by us, see Section 7.1). The small panels show ϵ_{vis} (Equation 6.4).

3. The tail beyond the peak created by light projectile fragments has a relatively larger size because it is mostly unquenched.

As stated at the beginning of this section, these aspects render the application of Bragg curve spectroscopy harder but also make our detector concept viable in the first place by reducing the dynamic range.

Figs. 6.10 and 6.10 illustrate how quenched, discretized energy-deposition profiles of different particles look like in a tracking calorimeter constructed from scintillating fibers with a 2-mm thickness. The data was generated using a Geant4 [Ago+03; All+16] simulation, with quenching implemented according to Birks' model and using the kB-value determined by us (see Section 7.1). The upper panels show the mean total energy deposited in each fiber:

$$\Delta E = \left\langle \int_{\Delta x} \frac{\mathrm{d}E}{\mathrm{d}x}\, \mathrm{d}x \right\rangle, \tag{6.5}$$

where the integral over the path length, δx, is calculated for each particle individually, and ΔE is the mean value of the resulting distribution. The visible energy is consequently calculated via

$$\Delta E_{\mathrm{vis}} = \left\langle \int_{\Delta x} Q\left(\frac{\mathrm{d}E}{\mathrm{d}x}\right) \cdot \frac{\mathrm{d}E}{\mathrm{d}x}\, \mathrm{d}x \right\rangle. \tag{6.6}$$

Figure 6.10 confirms what is shown in Figure 6.8, namely that Bragg peaks for stopping protons are still clearly visible after the quenching correction was applied. Figure 6.11, however, shows that the situation is much more complicated for ions. What remained of the Bragg peak in the non-discretized data shown in Figure 6.9 is effectively gone when the energy deposition of heavy ions is integrated over 2-mm fibers. Even though peak-like and clearly separable profiles are still visible for light ions, the curves for carbon ($Z_{\mathrm{C}} = 6$) and oxygen ($Z_{\mathrm{O}} = 8$) look pretty similar already. The curves for silicon ($Z_{\mathrm{Si}} = 14$) and iron ($Z_{\mathrm{Fe}} = 26$) are nearly indistinguishable if we take into account that the figures only show the mean deposited energy and not the variance caused by straggling.

In summary, there are two key conclusions concerning the overall viability of the ADU detector concept that can be drawn from this discussion:

1. The identification of light ions up to, and perhaps including, carbon based on their energy-loss profiles in 2-mm thick scintillating fibers is for sure feasible, even when accounting for ionization quenching.

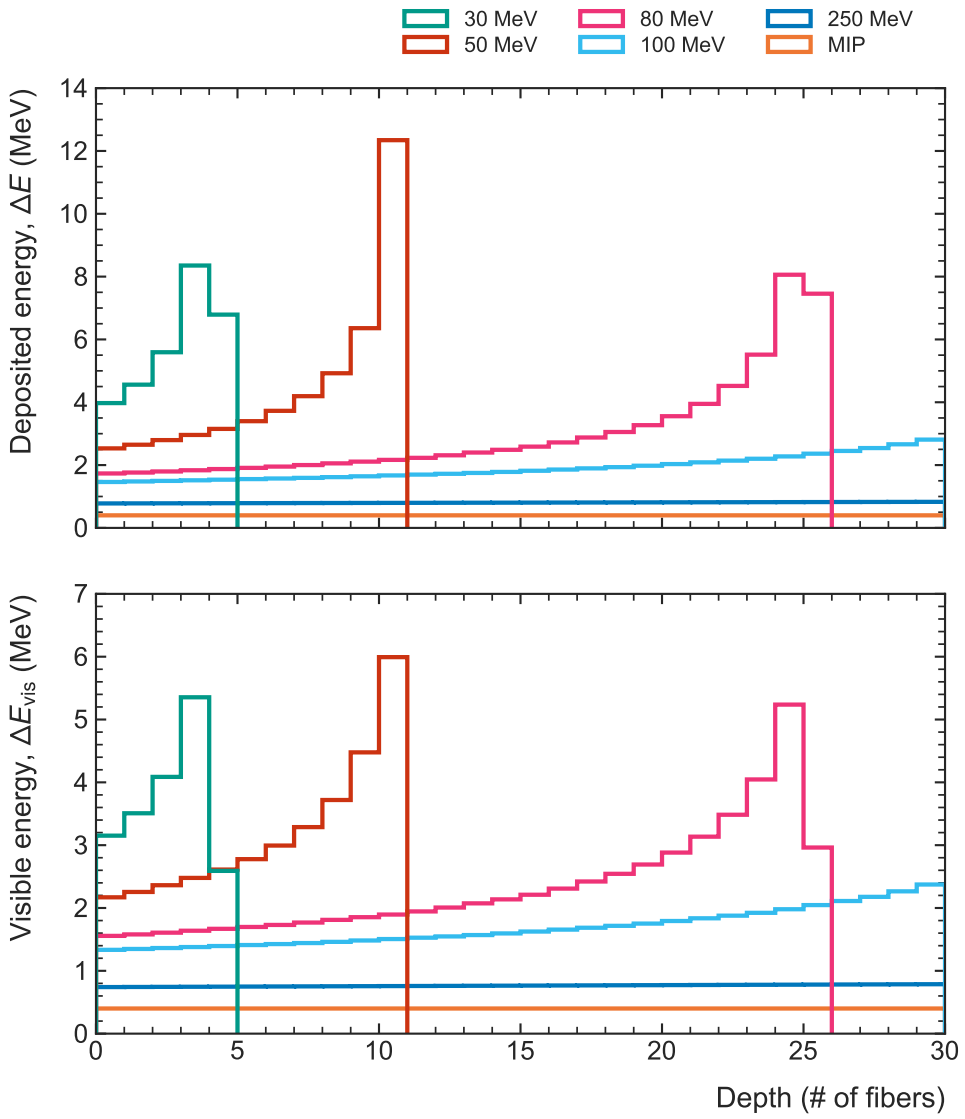

Figure 6.10: Energy-deposition profiles for protons in ADU-style tracking calorimeters simulated with Geant4. The upper panel shows the energy deposited in successively traversed fibers. The lower panel shows the visible energy in each fiber after correction with Birks' quenching function.

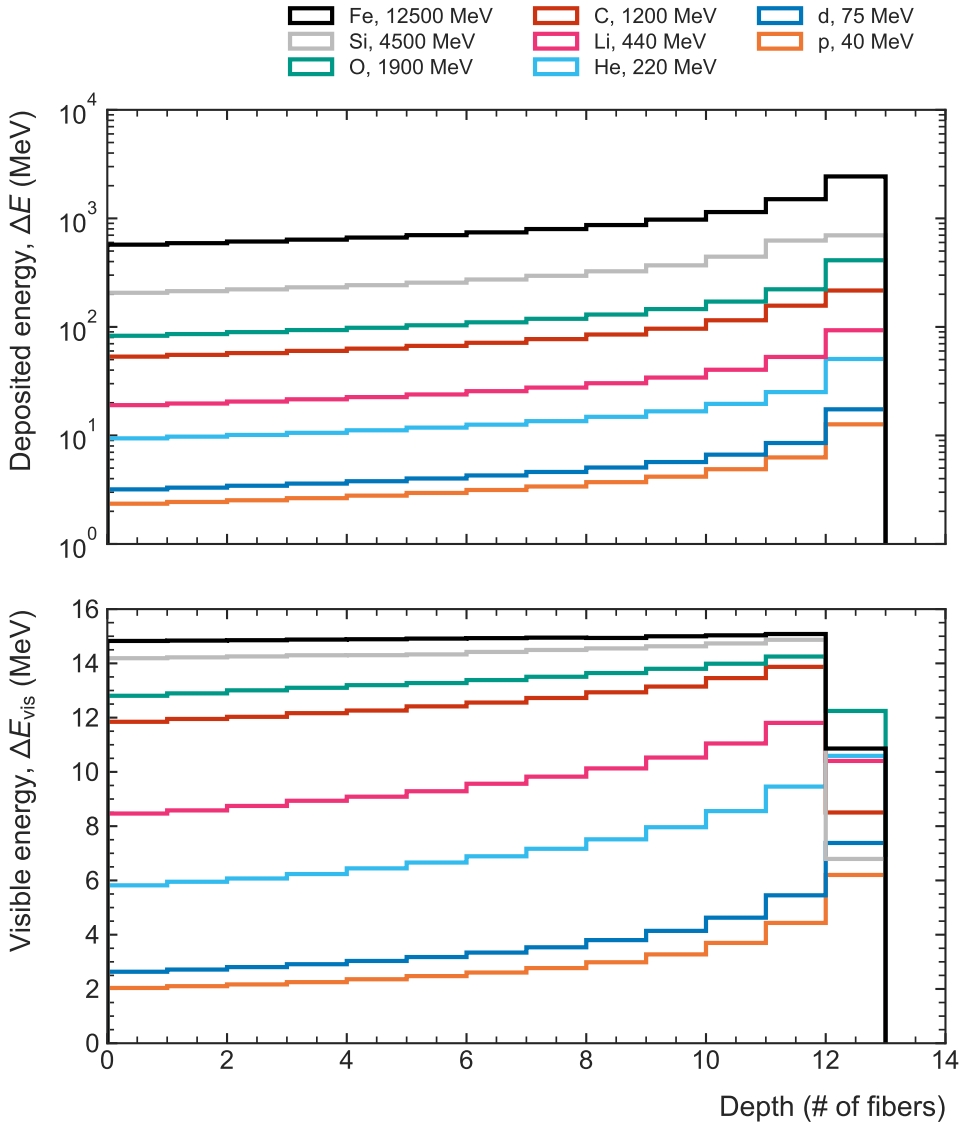

Figure 6.11: Energy-deposition profiles for different ion species with the same range in ADU-style tracking calorimeters simulated with Geant4. The upper panel shows the energy deposited in successively traversed fibers. The lower panel shows the visible energy in each fiber after correction with Birks' quenching function.

2. The identification of heavier ions is complicated by the severe distortion of their energy-loss profiles by quenching. It is thus questionable whether individual elements can be separated with high accuracy, though reliably detecting differences of $\Delta Z = 1$ or $\Delta Z = 2$ may be realistic. For radiation-monitoring purposes, the latter would already be a major step forward.

What is apparent from these conclusions is that accurate knowledge of the quenching behavior of the scintillating fibers is crucial for interpreting the data gathered by the ADU. This is the primary reason for which we performed a respective experimental study.

6.4 Proof-of-Principle Demonstration

To demonstrate that we can indeed record clean energy-loss profiles of stopping particles using scintillating fibers, we conducted a proof-of-principle test. For this experiment, we used the same measurement setup as for our quenching studies (see Section 7.1.3 for details). The detector consisted of a planar array of 16 SCSF-78 scintillating fibers, each read out individually at one end with a Hamamatsu Photonics S13360-4935 SiPM. Their microcell pitch of 25 μm ensured that saturation effects are negligible even at the highest energy-loss densities. The fibers were neither coated nor treated in any other way. We suppressed optical crosstalk solely by placing them apart by several millimeters and blocking stray light from hitting the SiPMs of neighboring fibers with an opaque plastic structure. The whole setup was placed inside a vacuum chamber to suppress beam–air interactions that would result in scattering and energy loss between fibers.

We exposed the detector to a beam of protons at the πM1 beam line of the high-intensity proton accelerator at the Paul Scherrer Institute (PSI). To constrain the spot size and position of the beam on the fibers, we used a copper collimator with a 2-mm bore placed at a distance of 20 cm upstream of the first fiber (see Figure 7.2). We selected the beam intensity such that the probability for pile-up events[9] was negligible.

Figure 6.12 shows the energy-deposition profile of a beam of 56.25-MeV protons in the fiber array. For each fiber, the plot shows along the vertical axis the distribution of the visible energy, ΔE_{vis}, created by single protons. The

[9] Multiple protons traversing the detector (nearly) simultaneously.

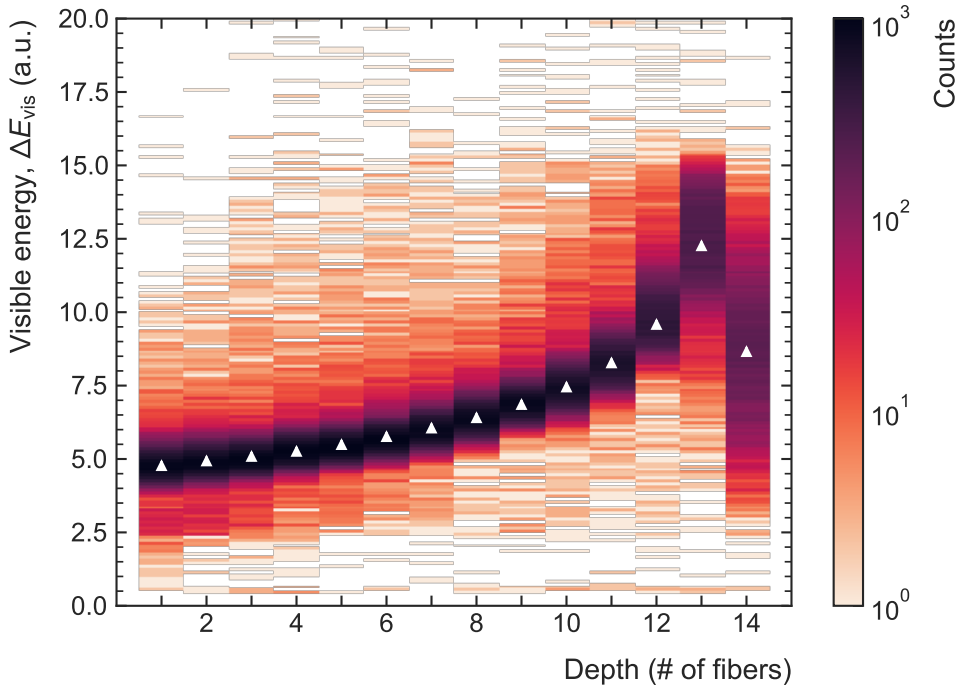

Figure 6.12: Energy-loss profile of a beam of 56.25-MeV protons in a planar array of SCSF-78 scintillating fibers. For each fiber, the plot shows along the vertical axis the distribution of the visible energy, ΔE_{vis}, created by single protons. The white triangles indicate the most probable energy loss in each fiber. The data is from the analysis of 10 000 events. Adapted from [Los+21].

profile has the expected peak-like structure, which is, however, substantially 'washed out' by energy straggling and quenching. The combination of these two effects most strongly affects the fibers around the Bragg peak, where quenching is the strongest and straggling leads to slight differences in the range of the particles. Figure 6.13 (note the logarithmic vertical scale) more clearly illustrates the broadening of the energy-deposition distribution in successive fibers along the path of the protons: The initially Landau-like distribution develops an increasingly stronger tail at higher ΔE_{vis}, which eventually fully dominates in the 13th fiber, where the particles deposit most of their energy yet do not fully stop. The almost symmetric distribution around a lower mean ΔE_{vis} in the 14th fiber can be explained by the fact that the protons traverse only a (small) fraction of the fiber width. Though their energy-loss density is

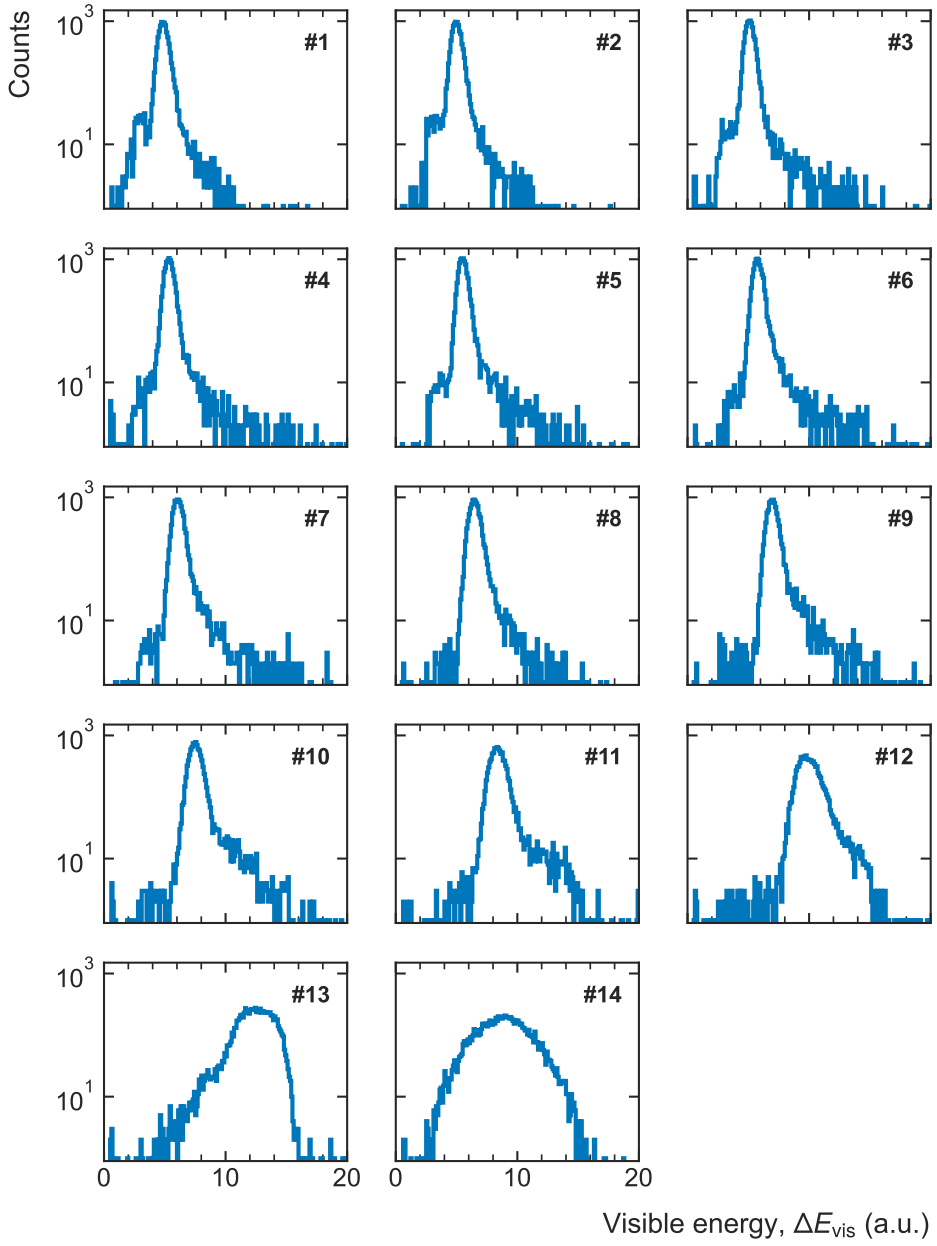

Figure 6.13: Energy-loss distributions of 56.25-MeV protons in each fiber of the test array. Same data as presented in the vertically oriented distributions in Figure 6.12.

at its maximum—as is the effect of quenching—the much shorter path length results in an integrated visible energy that is smaller than in the previous fiber. The results of this experiment demonstrate several important aspects:

1. The rather narrow energy-loss distributions in the fibers (note the logarithmic scales in Figs. 6.12 and 6.13) show that particle identification and energy measurement for protons is possible. Based on the simulations presented in Figure 6.11, this conclusion can likely be extended to light ions, though an experimental confirmation is needed.
2. For protons, and when the broadening due to straggling and quenching effects is correctly accounted for, the mean-ΔE_{vis} profile can describe the majority of events well. A percent-level fraction, however, deviates more strongly from the average behavior, in a few cases seemingly randomly and by several standard deviations. This variation must be taken into account if high-precision particle identification shall be performed with high efficiency. If, on the other hand, the occurrence of such outliers could be statistically accounted for (based on real or simulated data), the failure to correctly identify them might not matter as much.
3. Though likely acceptable for protons and light ions, the substantial broadening of the energy-deposition profile complicates the separation of heavier ions with similar nuclear charge. Further (experimental) studies are required to determine from which element on the ΔE_{vis} distributions created by ions with $\Delta Z = 1$ overlap so substantially that a separation with high confidence becomes impossible.

The test thus showed that Bragg curve spectroscopy should in principle work well for protons and light ions (though the definition of 'light' in this context is still an open question). It also further highlighted the challenges that complicate the identification of heavier ions and, consequently, the urgent need for test measurements with such particles.

Ultimately, however, it is unrealistic to assume that we can gather test data like that shown in Figure 6.12 for every element from hydrogen to iron. Even the NSRL at BNL, which at the moment works with the broadest range of ions, only offers nine species across this range. We thus need to rely on simulations to develop our particle-identification algorithms. To be able to do so, we nonetheless need to gather experimental data with at least a few ion species to benchmark our simulation models, especially the one for quenching (see discussion in Section 7.1).

6.5 Early Prototypes

Over the years, we developed several prototype detectors of different scale. The reason for building them was not only to test and demonstrate various aspects of the tracking calorimeter concept but also to mature the mechanical construction of the ADU and to incrementally develop suitable read-out electronics. I here present the two detectors that most substantially contributed to the evolution from the idea of building a scintillating-fiber tracking calorimeter to the construction of the flight detectors for the RadMap Telescope.

6.5.1 CubeZero

The very first prototype we ever built, called CubeZero, was meant to demonstrate the overall viability of the tracking-calorimeter concept, including its ability to track charged particles with reasonable accuracy. The following is only a very brief summary of its design and of the tests we performed. A detailed description can be found in the Diploma thesis of Lingxin Meng [Men14]. Additional data analysis was conducted by Thomas Pöschl and is described in his Master's thesis [Pös15].

Mechanically, CubeZero had little in common with the detectors that would eventually fly to the ISS. It consisted of 128 SCSF-78 square scintillating fibers of about 68 mm length, arranged in 16 arrays of 8 fibers each. Every second layer was rotated by 90 degrees to allow tracking, but the arrays in each orientation were not shifted against each other as illustrated in Figure 6.5 above. As such, CubeZero would have had a lower detection efficiency than our original concept, though we never performed a comparative measurement with setups that were sufficiently similar for isolating this effect. The fibers were read out on alternating sides of each array (layer) with early versions of the PM3350 SiPMs manufactured by KETEK GmbH [KET14; Sch+14]. To prevent optical crosstalk, we aluminized the fiber ends opposite of the SiPMs and wrapped each fiber individually with conventional aluminum foil. The resulting fiber stack is shown in the center of Figure 6.14; the SiPMs are soldered onto the red printed circuit boards (PCBs) surrounding the fibers.

Since this was the first prototype we built, we did not attempt to develop read-out electronics compatible with the space and power constraints nor with the reliability requirements of a space mission. Instead, each SiPM was individually connected to a shaping preamplifier that matched its signal characteristics to the input capabilities of a multichannel sampling analog-to-

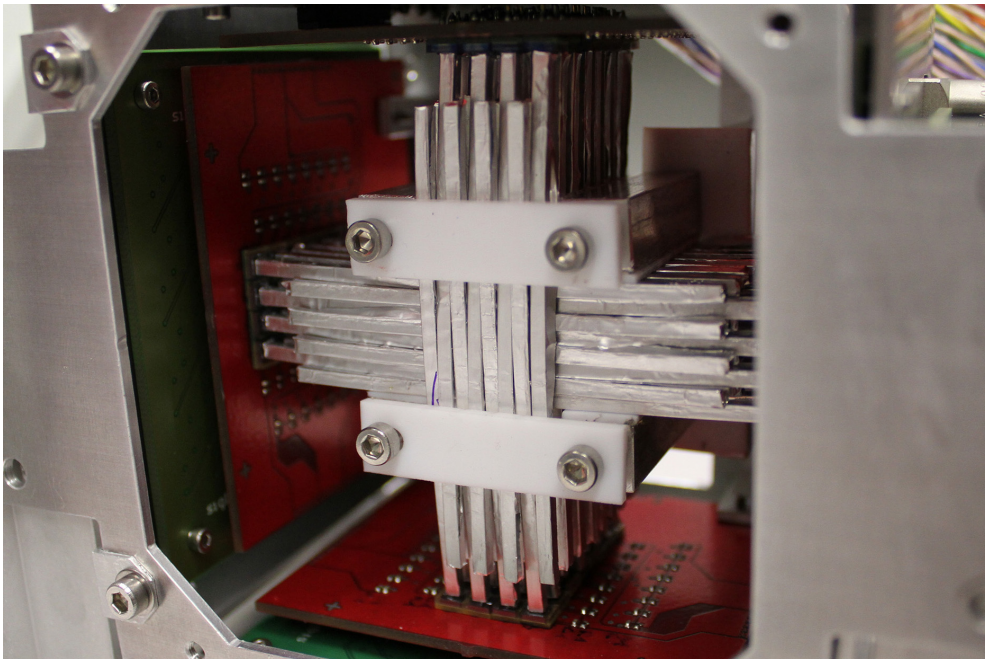

Figure 6.14: Fiber stack of the CubeZero prototype. 128 SCSF-78 square scintillating fibers with a 2-mm thickness were arranged in 16 layers of 8 fiber each, with every second layer rotated by 90 degrees. The fibers were wrapped in conventional aluminum foil to prevent optical crosstalk.

digital converter (ADC) [Man+09]. This discrete solution allowed us to digitize the signal waveforms of all SiPMs with high resolution. It is, however, by far too space- and power-intensive to allow the construction of larger detectors within the constraints of our applications.

We tested the detector at the πM1 beam line at PSI with beam of protons and negative pions. For the latter, we chose a beam momentum of 375 MeV, which corresponds to $\beta\gamma \sim 3$. The pions were thus MIPs and had a constant energy-loss density throughout the detector, which was ideal for investigating its tracking capabilities. For protons, we chose beam momenta between 300 and 375 MeV/c, which was low enough for them to stop in the detector's active material. We used scintillator plates that had the same size as the fiber arrays' overlapping area (about $16 \times 16\,\mathrm{mm}^2$) and were read out by PMTs to trigger the sampling ADCs (either individually or in coincidence).

Results and Lessons Learned

Despite bandwidth issues with the data-acquisition system (see [Men14]), we were able to demonstrate the detector's ability to record tracks of MIPs that are clearly distinguishable from noise and background events. Using the first and the last fiber layers as reference, we determined an average per-channel detection efficiency of about 99.2% [Men14]. One must, however, refrain from interpreting this result as indicative of the general performance of the detector concept: The probability for a particle to (1) hit a fiber in the first and in the last layer but to (2) not hit the ones in between is fairly low, and is mainly determined by the uncertainty of mechanically placing the fibers in their holding structure.[10] Particles that traverse the first layer of the detector in the insensitive space between two fiber cores, however, are not accounted for at all. The efficiency value cited above thus certainly overestimates the absolute detection efficiency. Unfortunately, the trigger detectors placed upstream and downstream of the prototype, though roughly having the same size as its tracking area, were not aligned well enough for using their hit information to correct this effect.

The analysis of the proton measurements was complicated by the fact that we had expected a significantly lower light yield than we ultimately observed and thus chose SiPMs with a microcell pitch of 50 μm to achieve a higher detection efficiency. The higher-than-expected light output led to saturation effects at large energy-loss densities, in addition to the unavoidable quenching of the Bragg peak. We nevertheless were able to record energy-loss profiles for stopping protons, though with lower statistical significance than during the proof-of-principle demonstration discussed in Section 6.4 above (which we performed later). The SiPM saturation, uncertainties due to wrapping the fibers (see below), and substantial beam–air interactions over a distance of 1.2 m between the beam line exit window and the detector also resulted in larger uncertainties.

A combined analysis of the four proton data sets recorded at different beam momenta and of one calibration measurement with pions allowed us to determine estimates of several crucial performance parameters [Pös15]:

1. We calculated a mean of 218 ± 42 photons arriving at the end of a fiber per MeV of ΔE_{vis}—i.e., after taking into account the reduction of the

[10] The discussion in Section 6.3.1 shows that the light yield of the fibers for MIPs is so high that any inefficiencies related to it can be neglected.

energy deposition due to quenching. The rather large uncertainty is only partially due to statistical fluctuations; much of it is caused by the light-yield differences of the fibers (see discussion below). The value we obtained is significantly higher than the one calculated in Section 6.3.1 above, where I followed the manufacturer's assumption that light is only trapped by the cladding–air interface. What causes the increased light yield—contributions of the cladding–air interface, reflections at the aluminized fiber end, or light trapped by the aluminum foil—cannot be determined based on the data.

2. We performed a first determination of the Birks' coefficient of SCSF-78 fibers and obtained a value of 0.127 ± 0.03 mm/MeV. Considering that the strong saturation of the SiPMs may have led to an underestimation of systematic effects, this value is compatible with the one we determined based on our much more precise measurements presented in Section 7.1.
3. Despite the limited amount of data we collected, we were able to reconstruct the four different beam energies with sub-MeV precision. We could not check the accuracy of this reconstruction because we did not measure the beam parameters with an independent, calibrated detector. Instead, we relied on the momentum filter of the beam line to determine the momentum of the incident particles and accounted for energy loss and straggling due to beam–air interactions based on a simulation with the SRIM software [ZZB10].

Besides determining these important parameters, we also learned a lot about the construction of a scintillating-fiber tracking calorimeter. A detailed look at Figure 6.14 reveals that we underestimated the intrinsic variation of the fiber geometry, as well as the added thickness of the aluminum foil. It also shows the substantial curvature of the fibers, which occurred because we had them delivered on a coil. In addition to these purely mechanical aspects, we observed unacceptably large fiber-to-fiber variations of the light yield [Pös15], which we tried correcting for in our data analysis though they still led to large and (to some degree) unknown systematic uncertainties.

Despite these shortcomings, the first prototype demonstrated the general feasibility of using a single stack of scintillating fibers for the track reconstruction and energy measurement of protons. The sub-MeV precision of the energy reconstruction, if extendable to the full range of energies we aim to cover with the RadMap Telescope's ADU, would be more than sufficient to fulfill the requirements of radiation-monitoring applications.

6.5.2 A Stratospheric Balloon Flight

We developed the second prototype I present here as part of our participation in the REXUS/BEXUS program, which gives (graduate) students the opportunity to perform experiments on sounding rockets and stratospheric balloons. The program is run by the German Aerospace Center (DLR), the Swedish National Space Agency (SNSA), and ESA, with support from the Swedish Space Corporation (SSC) and the Center of Applied Space Technology and Microgravity (ZARM) of the University of Bremen. Our objective was to measure the intensity profile and angular distribution of cosmic-ray-created secondary radiation (mostly muons and electrons) [Rei93; EHP11; KW12] at altitudes of up to 27 km using a full-scale tracking calorimeter aboard a stratospheric balloon [Los+15]. The second goal was to demonstrate that we could operate a detector with flight-like read-out electronics in the demanding near-space environment of the stratosphere. This particularly included the extreme ambient temperatures, the almost complete absence of convective heat transport, and the low-pressure environment at altitudes above 20 km [But22].

Detector Design and Fiber Treatment

The detector we constructed for this mission consisted of 30 layers, each comprising 30 SCSF-78 square scintillating fibers with a thickness of 2 mm, for a total of 900 detector channels. Fiber arrays (layers) with the same orientation were not shifted against each other. To keep the inter-fiber spacing as small as possible, we used a single 3D-printed structure made from acrylonitrile butadiene styrene (ABS) as mechanical support (see Figure 6.17). The resulting tracking volume had a size of $65 \times 65 \times 65\,\mathrm{mm}^3$. Though ABS is a flammable plastic that requires safety-related exceptions in human spaceflight missions, it was the only material that we could print with sufficient precision at the time.

As for the CubeZero prototype, we wrapped each fiber into aluminum foil and aluminized the ends opposite of the SiPMs. This time, however, we took more care in controlling the quality of our fiber production. In the first step, we needed to straighten the fibers to remove the curvature (due to delivery on a coil) that had complicated the integration of the CubeZero detector. We achieved this by heating them to about 80 °C while pressing them between two aluminum plates for about 1.5 hours. This removed much of the bending for most of the fibers, and we assumed it had little effect on their optical characteristics. For some fibers, however, small irregularities of the aluminum

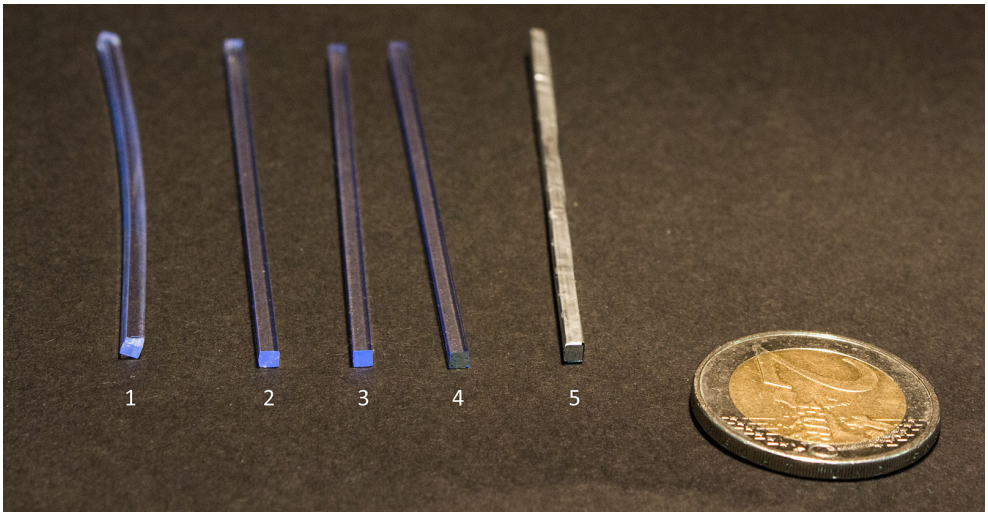

Figure 6.15: Five steps of preparing scintillating fibers for the 900-channel prototype: (1) bent fiber after cutting from the coil, (2) straight fiber after heating, (3) polished fiber, (4) fiber with sputter-coated end, (5) fiber wrapped with aluminum foil.

surfaces were imprinted on the cladding, which in hindsight (see Section 7.2) may have had an adverse effect on the light yield. Afterwards, we polished the fibers on both ends and sputter-coated one end with a 40-nm thick aluminum layer. Finally, we wrapped each fiber with 50-μm thick aluminum foil; it overlapped on one longitudinal surface, where it was held together by small dots of glue. These five steps of treating the fibers are illustrated in Figure 6.15.

We knew from the tests of the CubeZero prototype that SiPM saturation was not an issue for MIPs. Since the radiation environment in the stratosphere consists mostly of high-energy muons and electrons (positrons) with energy-loss densities comparable to those of MIPs [Rei93], we determined that it was reasonable to again rely on PM3350 SiPMs from KETEK, which we already had experience with and had characterized thoroughly [Hah14]. The SiPMs were soldered to PCBs with 30 (two rows) and 45 (three rows, see Figure 6.16) photodetectors, each of which was in addition equipped with four temperature sensors. There was no other circuitry on these sensor arrays except for individual R–C–filters to stabilize the bias voltage of each SiPM. The unamplified signals were routed to the read-out electronics via individually shielded micro-coaxial cables (see Figure 6.18). Bias-voltage and temperature-

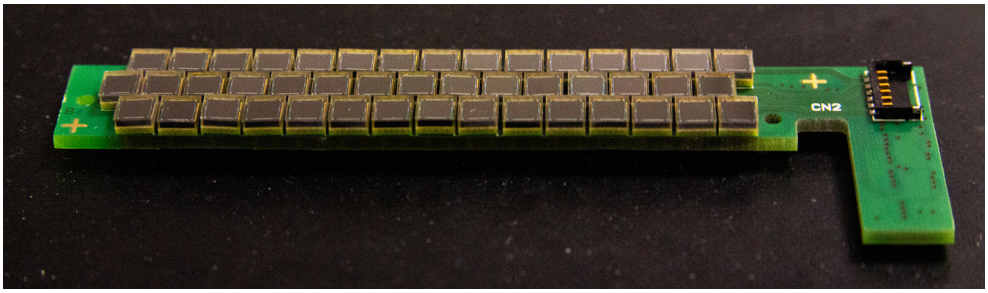

Figure 6.16: Three-row array of 45 KETEK PM3350 SiPMs. The receptacle for the bias-voltage and temperature-sensor connections is visible on the right. The connector for attaching micro-coaxial signal cables is located on the back.

sensor connections were made via separate cables. The support structure had alignment pins for every PCB to ensure that the fibers were well centered on the SiPMs during assembly (see Figure 6.17). To glue the SiPM arrays to the fiber ends, we used NASA-certified EPO-TEK® 301 optical epoxy [Epo23].

In the flight instrument, the detector was mounted to an aluminum structure via eight attachment points on the top and at the bottom of the plastic support (see Figure 6.17). This structure was in turn attached to the instrument's main structure made from aluminum profiles, which also housed all electrical systems. Light tightness was ensured by an outer hull made from carbon fiber plates. Since the balloon flight was anticipated to only last a few hours, thermal control was completely passive. The detector was largely decoupled from the rest of the instrument by the thermally isolating plastic support. No precautions were taken against electromagnetic interference, for example from the balloon's wireless data transmission system.

Read-Out and Data-Acquisition Electronics

For the development of the read-out electronics for digitizing the SiPM signals, we cooperated with Prof. Kenji Shimazoe at the University of Tokyo. His group was in the process of developing an application-specific integrated circuit (ASIC) for the large-scale application of SiPMs in positron emission tomography (PET) [Shi+14]. Since PET scanners require many individual detector channels to achieve high spatial resolution, and the energy resolution is only of secondary interest, their ASIC design used a time-over-threshold (ToT) approach for measuring the SiPM signal amplitudes. For ToT digitization, each

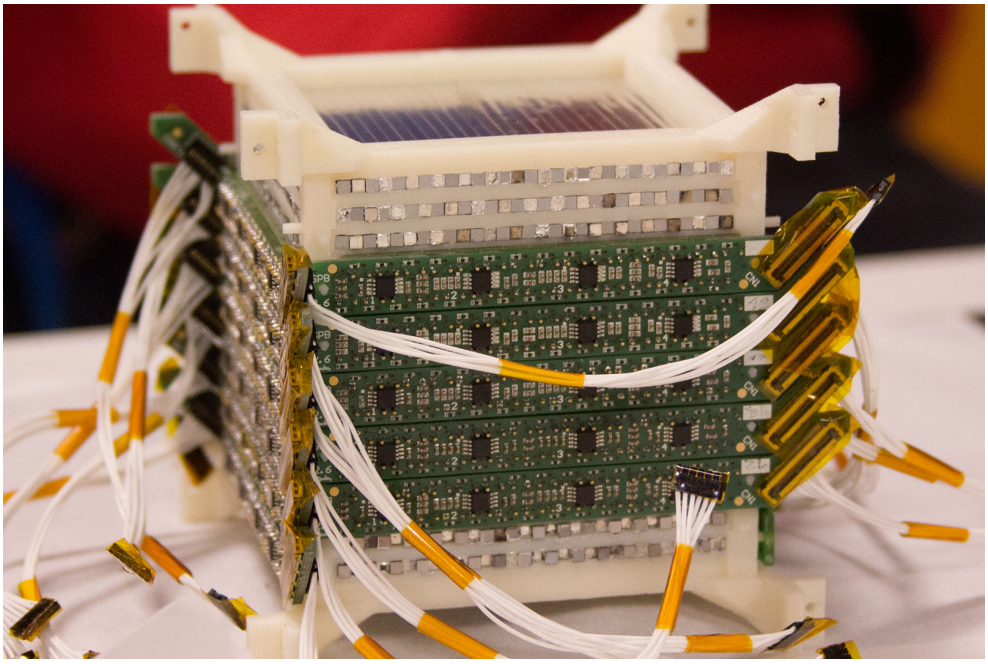

Figure 6.17: Partially assembled 900-channel detector prototype. The scintillating fibers are stacked in a 3D-printed support structure made from ABS plastic. Most SiPM arrays are already attached; alignment pins for them are visible on the side of the detector facing to the left. The exposed layers at the top show the alternating read-out of the fibers (alternating open and aluminized fiber ends). The aluminum on some fiber ends exhibits strong discoloration, which was caused by the sputter-deposition process. The four black components on each SiPM array are the temperature sensors. Attachment points are visible on the top and at the bottom of the support structure.

read-out channel consists of a shaping preamplifier followed by a discriminator. The ASIC simply outputs the discriminated signal fully in parallel, that is, with a dedicated output pin for each input channel. Assuming a (shaped) signal shape that scales nearly linearly with amplitude, the determination of the time a signal is above the discriminator threshold gives an indirect measurement of its amplitude.

The advantage of the ToT method is that it only requires conversion of time difference between the rising and falling edges of the discriminator output to the digital domain. Such time conversion is significantly less power-intensive than a high-resolution measurement of the signal amplitude, not to

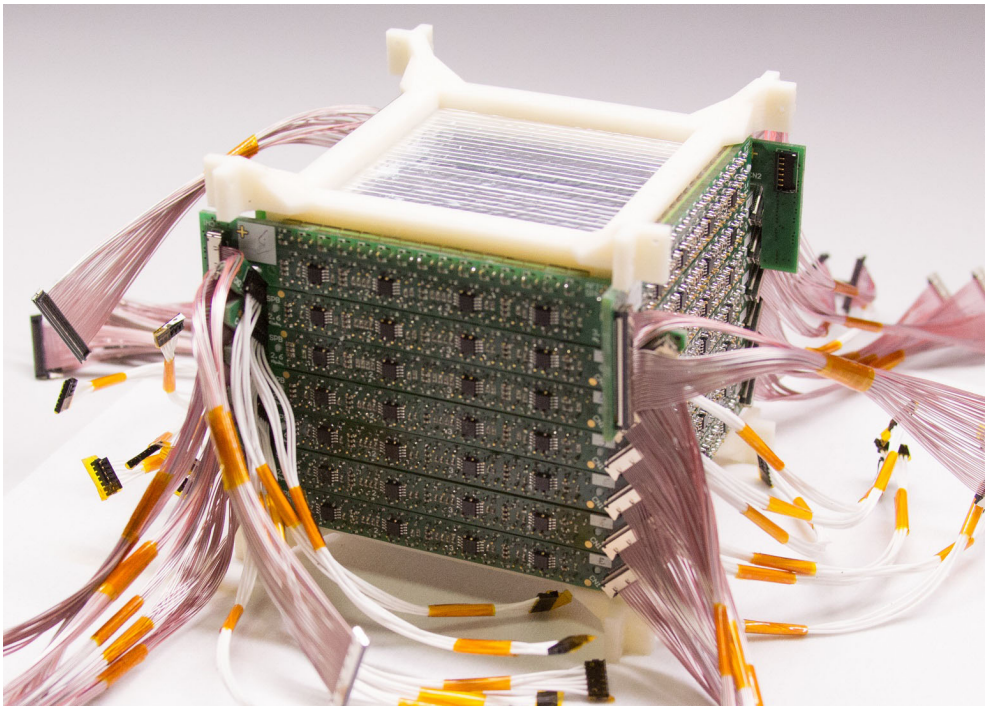

Figure 6.18: Fully assembled 900-channel detector prototype used for our stratospheric balloon flight. The SiPM signals were routed to the read-out electronics via individually shielded micro-coaxial cables (pink). Bias-voltage and temperature-sensor connections were made via separate cables (white).

speak of the time-resolved sampling of signal waveforms. Appropriate time-to-digital converters (TDCs) are commercially available in the form of integrated circuits (ICs) with few channels; a larger number of channels can easily be implemented on field-programmable gate arrays (FPGAs). A fully parallel read-out of many SiPMs at high rate can thus be achieved at a comparatively low power consumption. The major disadvantage of the method is its sensitivity to the exact dependence of the ToT signal length on the amplitude. This relationship is essentially always non-linear, and must be accurately known for a precise digitization of the SiPM signals. Any unknown non-linearity leads to non-linear error of the amplitude measurement, and hence to an energy-dependent resolution uncertainty of unknown magnitude.

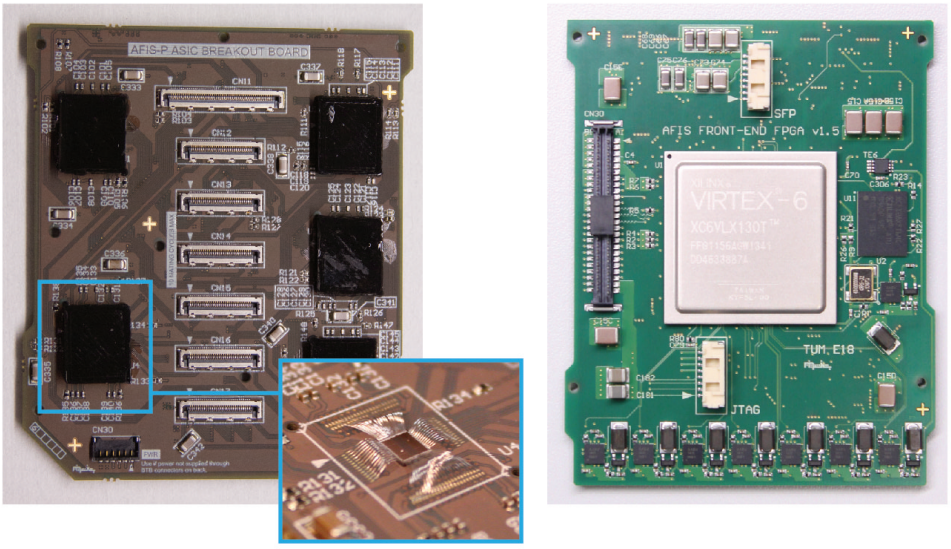

Figure 6.19: Components of the read-out electronics based on the ToT method. Left: 240-channel discriminator PCB, equipped with five 48-channel ToT ASICs developed at the University of Tokyo. The micro-coaxial signal cables shown in Figure 6.18 are plugged into the connectors at the center of the board. The inset shows the wire bonds of a single ASIC. Right: FPGA-based TDC capable of digitizing up to 240 ToT signals. The row of components at the bottom of the PCB are seven bias-voltage converters for supplying the SiPMs.

Despite this challenge, we thought that the perceived advantages of a low-power read-out system capable of sustaining high event rates were an ideal match to the resource constraints of our application. The ASIC developed at the University of Tokyo had 48 channels and allowed a direct connection of the SiPM signals to its input (without blocking capacitors or external termination resistors). The five ASICs required to read out one side of the detector (i.e., a quarter of its channels), were wire-bonded to a custom-designed discriminator PCB (see Figure 6.19), which was hence capable of reading out up to 240 channels. The micro-coaxial cables carrying the SiPM signals were attached directly to this PCB. For the digitization of the ToT signals, we designed a 240-channel TDC based on a Virtex-6 FPGA by Xilinx (see Figure 6.19). Each TDC was also equipped with seven bias-voltage converters to independently supply the seven SiPM arrays on each detector side. We operated the system

Figure 6.20: The BEXUS 18 stratospheric balloon shortly before launch from Esrange Space Center in Kiruna, Sweden. It reached an altitude of about 27 km and stayed aloft for a little over three hours. Image credit: ESA.

at a resolution of 500 ps, with a possible minimum bin width of 350 ps. The data of the four TDCs required to read out the full detector was transmitted to a commercially available data-acquisition system (National Instruments sbRIO 9606) via low-speed serial links. The acquired data was stored on the instrument; a subset was forwarded to the balloon's data-handling system for real-time transmission to the ground.

Results and Lessons Learned

The instrument flew aboard the BEXUS 18 balloon (see Figure 6.20), which was launched from Esrange Space Center in Kiruna, Sweden, and reached an altitude of about 27 km. The flight lasted a little over three hours, half of which was spent at float altitude. Unfortunately, a faulty control line between the data-acquisition system and the front-end electronics rendered the latter inoperable. Though we detected the problem shortly before launch, we did not have enough time to correct it. The only meaningful data collected during

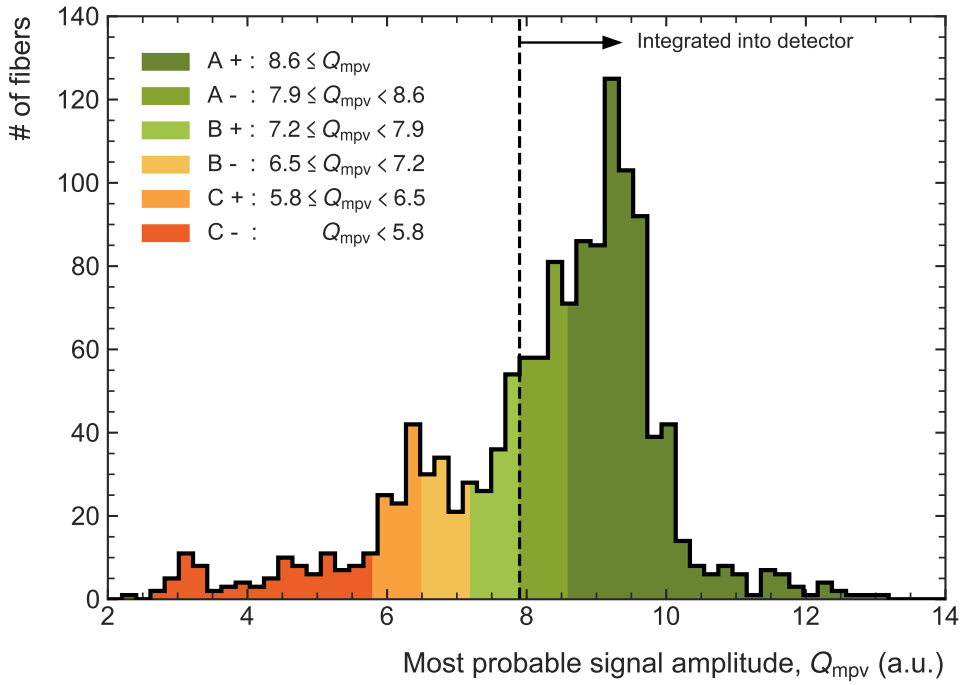

Figure 6.21: Distribution of the most probable signal amplitude of the 1333 fibers produced for the 900-channel prototype upon excitation with a ^{90}Sr source. Colors indicate the quality classification, which we used to select the best 900 fibers for integration into the detector. Adapted from [Pös15].

the flight were thus detailed temperature profiles recorded by more than 120 sensors distributed on the detector and throughout the instrument. This data showed that the overall mean temperature variation was relatively benign, with an observed 8-degree span around approximately 0 °C.

Despite the total loss of detector data, we nevertheless learned a number of important lessons concerning the construction of our tracking calorimeters and the design of the front-end electronics:

Scintillating Fibers. Based on our experience of constructing the CubeZero prototype, we already knew that the treatment of the scintillating fibers—coating one end and wrapping them in aluminum foil—was critical. One problem was that the sputtered aluminum layer tends to peel off if the fiber surface is not perfectly clean or whenever the coating is subjected to mechanical

stress. The other problem is the reduction in light yield we observed for fibers for which glue had crept between the aluminum foil and the cladding (see Section 7.2 for a detailed assessment). Since we were aware of these problems, we tried optimizing our production process to ensure we addressed them as good as possible. Initial tests nevertheless showed that we could not completely avoid them. To compensate, we produced more than 1300 fibers and tested each one of them with beta electrons from a ^{90}Sr source. The respective distribution of the most probable signal amplitudes is shown Figure 6.21. We then used a quality-classification scheme (see colors in the figure) to select the best 900 fibers for integration into the detector. Despite this attempted quality assurance, the light yield of the worst and the best fiber we used deviated by -13% and +42% from the most probable one, respectively. Such a large range is far from ideal; finding better alternatives for suppressing optical crosstalk was thus a focus of our subsequent work (see Section 7.2) in preparation for producing the RadMap Telescope detector.

Fiber Support Structure. For this prototype, we decided to integrate all 900 scintillating fibers in a single support structure. This had the advantage that we could ensure that the fiber-to-fiber and layer-to-layer distances remained the same throughout the whole detector. During the integration process, particularly when gluing the SiPM arrays to the fiber ends, we realized that this approach was more prone to manufacturing uncertainties and handling errors than we had anticipated. One issue was the insufficient mechanical precision of the 3D-printed support structure. The more important one, however, was the fact that a single error in attaching one of the SiPM arrays could render the whole detector unusable. After we had barely been able to correct one such mistake, we concluded that partitioning future detectors into several modules was crucial for achieving an integrating system of good quality.

ASIC Output Buffers. Even though the ToT read-out method seemed appealing because of its high rate capability and low power consumption, we concluded after completion of the balloon mission that it had no future in our application. One reason was a design flaw in the ASICs (the output buffers were too weak), which resulted in a slow rise time of the ToT signals. This made the detection of small-amplitude signals impossible because the output would already be de-asserted before it crossed the voltage threshold for a logic 'high' signal in the FPGAs' input buffers. We had not realized this before the mission because we had only tested the ASICs with an oscilloscope-based setup due to time constraints. So, in hindsight, the read-out electronics would never

have worked correctly even if we had not encountered the issue with the faulty control signal. The problem could possibly have been alleviated by the addition of external driver circuits, but this would have resulted in a prohibitively large and power-intensive system.

Time-Over-Threshold Method. The other reason for discarding the ToT option is its strong non-linearity, or rather its decreasing resolution at large signal amplitudes. Figure 6.22 illustrates this challenge: The upper panel shows SiPM signals with different amplitudes to which a fixed threshold is applied. The lower panel shows the ToT signal length as a function of amplitude of such a signal shape. The key point to observe is the decreasing time difference for constant intervals at increasing amplitudes. The result is a strongly decreasing measurement resolution for large SiPM signals, and hence for large energy-loss densities. The discussion in Section 6.3.4 above shows, on the other hand, that precise measurements at large ΔE_{vis} are crucial for counteracting the effect of quenching. The ToT method thus has its main weakness where we can tolerate it the least. There are approaches that attempt to alleviate this problem by using a threshold that linearly increases with time [Shi+12; PCL23]. Another option could be a stronger shaping of the signal, which would require longer charge-integration times and hence decrease the rate capability. There exists, however, currently no readily available ASIC that could enable the large-scale application of either approach. Implementing a discrete solution, though possible, was no option because of the limited space and power available for the read-out electronics.

Gain Variations. The measurements recorded during the flight showed that even in the relatively short time at float altitude, temperature differences between the hottest and coldest SiPM arrays reached as much as ten degrees. For the AFIS mission, it is reasonable to assume that, depending on the thermal design of the satellite, the variations may be even larger. For the PM3350 SiPMs we used for this prototype (and for the PM3325 we used for RadMap's ADU), a ten-degree temperature difference results in a 3% gain difference (due to drifts in the breakdown voltage, see Section 4.5). If uncompensated, gain fluctuations of such magnitude lead to unacceptably large uncertainties of the energy-deposition measurement in a fiber. Other than many of the ASICs evaluated in Section 10.4, the ToT chip had no input stage that would allow compensating for channel-by-channel changes in the breakdown voltage.

These findings made clear that we needed to introduce several major design

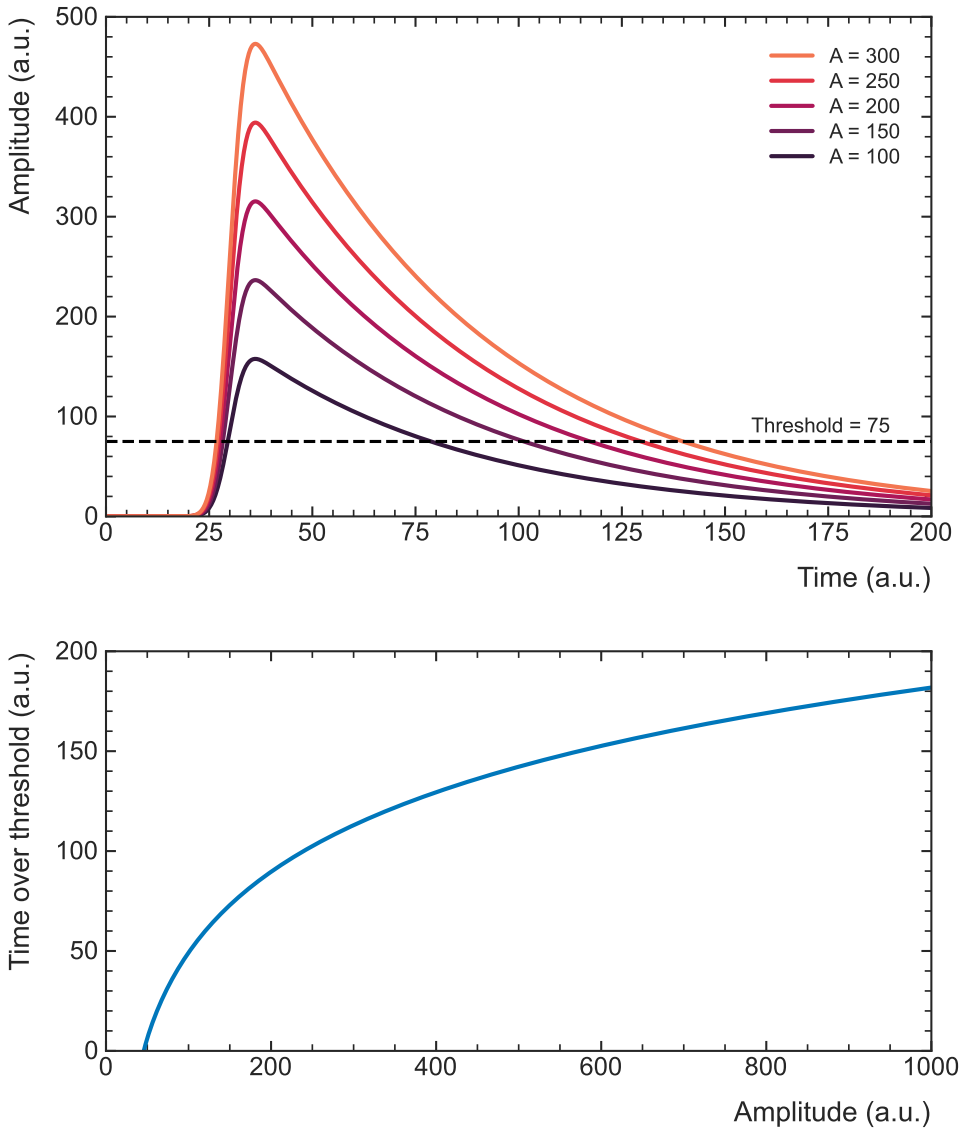

Figure 6.22: Principle of the time-over-threshold (ToT) method. The upper panel shows simulated SiPM signals with different amplitudes to which a fixed threshold is applied. The lower panel shows the ToT signal length as a function of amplitude of such a signal shape. It visualizes the decreasing time difference, and hence the decreasing resolution, for constant intervals at increasing amplitudes.

changes, starting with the way we treated our scintillating fibers for avoiding optical crosstalk. I describe our efforts to find a suitable alternative coating in Section 7.2. A second area for improvement was the mechanical design of the detector, most notably of the support structure. The changes we made in this area are described in Chapter 8. Finally, the most important challenge was finding a better means of reading out the many SiPMs of our tracking calorimeter while adhering to the resource constraints of the intended application as a radiation monitor. I describe the development of a read-out system suitable for spaceflight missions in Section 10.4.

Concluding Remarks

A tracking calorimeter made from scintillating-plastic fibers promises to deliver more precise particle identification than any of the currently used radiation-monitoring systems. At the same, it is significantly more compact than traditional magnetic spectrometers used for astrophysics investigations, and has a much larger geometric factor (and hence gathering power). These aspects could render it an ideal technology for radiation monitoring aboard future (crewed) spacecraft. Bragg curve spectroscopy, which must be used for particle identification in such a detector, is in principle a good method for separating different nuclei but suffers from the unavoidable effects of ionization quenching in (plastic) scintillators. It is thus imperative to understand the quenching mechanism of the fibers used for constructing the detector well if high particle-separation efficiencies are to be achieved.

The experiments we conducted and prototype detectors we built confirm that both the principle of constructing the detector and the method of measuring the energy of protons work well. Mechanical and electrical issues with the prototypes revealed plenty of opportunities for improvement, but the general concept seems feasible. Though we did not perform tests with nuclei, the fact that we can reconstruct the energy-loss profiles of protons of different energies well enough for achieving a sub-MeV energy resolution demonstrates that we are in principle able to identify Bragg curves well. The identification of light ions up to carbon, for which energy-loss profiles are well separated, should thus be possible with high accuracy. For heavier ions, quenching may force us to adopt $\Delta Z = 1$ or $\Delta Z = 2$ classification. This would, however, already be a major improvement over currently used sensors.

Without heavy-ion testing, the influence of projectile fragmentation on the particle identification remains uncertain. What is clear, though, is that we should expect a broad range of possible energy-loss profiles for heavy nuclei, especially if we attempt to extend the energy range of our measurements such that incident particles do not fully stop in the detector. How to exactly deal with this challenge during the analysis of measurements is still unclear and requires further investigation.

Chapter 7

Investigation of Scintillating-Fiber Properties

The performance of the tracking calorimeter described in the previous chapter very much depends on the intrinsic properties of its scintillating fibers. In contrast to applications where they are primarily used to construct position-sensitive detectors for tracking [Ruc96; DAm+96], we rely on the energy a particle loses in each fiber to (1) measure its total energy (loss) and to (2) determine its identity. The resolution with which we can measure the deposited energy thus determines the overall precision and accuracy of our data.

In this chapter, I present experiments we performed to precisely determine the quenching behavior of the type of fiber we use and the position dependence of the light yield in such fibers. Both properties were not previously treated in sufficient detail in the literature, necessitating our own studies.[1]

7.1 Ionization Quenching in SCSF-78 Fibers

In Section 6.3.4 above, I discussed the significant influence of quenching on our ability to separate heavy ions with similar nuclear charge based on their energy-loss profile. The non-linear relation between the light yield and the deposited energy also affects the measurement of the particle energy, with any error in our knowledge of the former directly translating into an uncertainty of

[1] We published the results of our studies in *Nuclear Instruments and Methods A* [Pös+21] and in *Radiation Measurements* [LPP24].

the latter. There were two primary reasons for experimentally investigating the quenching behavior of the fibers we use:

1. There were no previously published studies of quenching in SCSF-78 fibers available in the literature.
2. Birks' model of quenching, introduced in Section 4.2.3, has been shown to inaccurately predict the scintillation response for particles of different charge, among other shortcomings [Bir64; Nyi+14]. Von Krosigk et al., for example, found different kB values for protons and alpha particles in the same material [Kro+16]. Since this and other discrepancies can lead to uncertainties of unknown magnitude in our measurements, an investigation of alternative models and their ability to describe quenching in SCSF-78 fibers was necessary.

For the second aspect, it is helpful to briefly review the different quenching models that have been proposed as extension to (or replacement of) Birks' formalism.

7.1.1 Quenching Models

Birks assumed that quenching is an unimolecular process that can be described simply by the density of the excited or ionized molecules and the probability for their non-radiative relaxation (see Section 4.2.3). For easier reference, I repeat here the quenching function he proposed [Bir51],

$$Q_{\text{Birks}} = \frac{1}{1 + kB \cdot \frac{\mathrm{d}E}{\mathrm{d}x}}, \tag{7.1}$$

which parametrizes quenching with a single parameter, kB.

Chou was the first to propose an extension to Birks' model that takes into account bimolecular quenching—i.e., the interaction between neighboring excited or ionized molecules [Cho52]. Based on a semi-empirical analysis, he proposed to add a term that is second order in $\mathrm{d}E \,/\, \mathrm{d}x$:

$$Q_{\text{Chou}} = \frac{1}{1 + kB \cdot \frac{\mathrm{d}E}{\mathrm{d}x} + C \cdot \left(\frac{\mathrm{d}E}{\mathrm{d}x}\right)^2}, \tag{7.2}$$

where $\sqrt{C}$ has the same dimension as kB. For small specific energy loss, Chou's model approximates Equation 7.1, and Birks himself acknowledged it as a generalization of his model [Bir64].

Wright similarly attempted to take into account bimolecular effects but tried to do so on a slightly less empirical basis. He introduced the parameters a and k for the rates of bimolecular and unimolecular quenching, respectively, and the parameter p to describe the rate of energy dissipation via fluorescence [Wri53]. With these, he writes the light yield per unit distance as

$$\frac{\mathrm{d}L}{\mathrm{d}x} = \frac{p}{a} \ln\left(1 + \frac{a}{p+k} \cdot \frac{\mathrm{d}E}{\mathrm{d}x}\right). \tag{7.3}$$

Shortly after its publication, Kallmann and Brucker questioned the validity of the theoretical derivation of this model on the basis that bimolecular quenching is considered to be in direct competition with fluorescence emission [KB57]. Birks agreed with this objection but claimed that it nonetheless remains a useful semi-empirical relation over a limited range of specific energy loss [Bir64]. For our analysis, we used the fact that Wright assumed $S = p/(p+k)$ at small energy loss to re-arrange Equation 7.3 such that we could separate the quenching function per Equation 4.15:

$$Q_{\mathrm{Wright}} = \frac{1}{W \cdot \frac{\mathrm{d}E}{\mathrm{d}x}} \ln\left(1 + W \cdot \frac{\mathrm{d}E}{\mathrm{d}x}\right), \tag{7.4}$$

where $W = a/(p+k)$ has the same dimension as kB. This one-parametric notation reflects that in Wright's model only the probability for bimolecular quenching depends on the energy-loss density [Wri53].

The fourth model we considered is that of Voltz et al. [Vol+66]. It was the first to distinguish between ionization by the (primary) projectile and by the δ electrons created during the latter's passage through the scintillator. It also includes terms for both the prompt and delayed components of scintillation light, though we did not take into account the latter in our studies and thus omitted these terms. Absorbing the W_{s} parameter of their original notation into S, the quenching function for prompt fluorescence of Voltz et al. reads

$$Q_{\mathrm{Voltz}} = (1 - F_{\mathrm{s}})\, e^{-B_{\mathrm{s}}(1-F_{\mathrm{s}}) \cdot \frac{\mathrm{d}E}{\mathrm{d}x}} + F_{\mathrm{s}}. \tag{7.5}$$

Here, F_{s} is the fraction of singlet excitations (leading to prompt fluorescence, see Section 4.2.3) due to δ electrons that travel beyond the central ionization channel around the track. Voltz et al. assumed the specific energy loss of these electrons to be too small to cause significant quenching, which may not be entirely true. At the same time, the electrons carry energy away from the

central region of the ionization channel, thus reducing quenching there. This is reflected by the $1 - F_{\mathrm{s}}$ term before the exponential function describing the quenching in the channel, parametrized by the quenching parameter B_{s}. F_{s} can be related to the mean excitation energy of the medium, I, to the minimum energy required for an electron to leave the central region of the channel, and to the charge and stopping power of the projectile [Vol+66].

There are several other and mostly more complicated models that we did not consider in our studies. Notable among them is that of Hong et al., which extends Birks' model by a separate treatment of electronic and nuclear stopping, though it does not change the parametrization of the quenching behavior [Hon02]. Yoshida et al. further expanded this approach by accounting for bimolecular quenching of the electronic (but not the nuclear) energy loss in the form proposed by Chou [Yos+10]. A more recent approach by Valdes Santurio et al. is specifically geared towards computing the light yield in thin scintillators via a modified version of Birks' model that accounts for secondary electrons [VPA20]. All these models are of semi-empirical nature.

Attempts have also been made to place models on a more theoretical footing, often via the kinetics of the energy transfer in the scintillator, thus accounting for the temporal aspects and radial diffusion of energy deposition [BCL62; HBK68]. Christensen and Andersen, for example, combined such approaches with models of the track structure and were able to compute quenching correction factors for ions in different scintillators that agree well with experimental data [CA18; Chr+19]. Other approaches are more closely anchored in stopping theory (see Chapter 3) and attempt to describe quenching via the distribution of energy by secondary electrons [MM94; MMB95]. Effects such as surface quenching—the loss of excitation energy in thin scintillators due to δ electrons leaving the material and due to other effects—have also been treated in some detail [Tay+51; Bir52; Wri55].

We decided against using any of these more complicated models for our analysis because we were not interested finding a physically sound theory of quenching but in determining a reasonably accurate yet simple mathematical description for the behavior of our materials. Prior successes (documented in the literature [CS70; Wan+12; Nyi+14; Wes+17; Awe+21]) in using the four quenching functions introduced above compelled us to restrict ourselves to simple semi-empirical approaches.

7.1.2 Measurement Strategy

A detailed description of the experiment we performed can be found in the corresponding journal publication [Pös+21] and in the dissertation of my colleague Thomas Pöschl [Pös22], who was responsible for analyzing the results. I here mostly summarize the measurement strategy and experimental setup, to which I significantly contributed.

To determine the quenching behavior of SCSF-78 scintillating fibers, we measured the light yield as a function of deposited energy, $\mathrm{d}L \,/\, \mathrm{d}E$, of protons at several kinetic energies and fitted the different quenching models to this data using Equation 4.14. Since we could not directly measure $\mathrm{d}L \,/\, \mathrm{d}E$, we instead measured the total light yield, L, in a fiber as a function of the energy a particle loses while traversing it:

$$L(E_\mathrm{k}^\mathrm{in}, E_\mathrm{k}^\mathrm{out}) = S \int_{E_\mathrm{k}^\mathrm{out}}^{E_\mathrm{k}^\mathrm{in}} Q \left(\frac{\mathrm{d}E}{\mathrm{d}x} \right)_{E_\mathrm{k}} \mathrm{d}E_\mathrm{k} \,. \tag{7.6}$$

Here, E_k^in and $E_\mathrm{k}^\mathrm{out}$ are the kinetic energy of the particle before and after traversing the fiber, respectively. To account for the statistical fluctuations of the energy loss and its energy dependence (see the discussion of straggling in Section 3.2.7), we studied the behavior of a large ensemble of particles and analyzed the mean light yield, $\langle L \rangle$, produced by that ensemble given a mean energy loss $\langle \mathrm{d}E \,/\, \mathrm{d}x \rangle$. The underlying assumption is that quenching of the mean energy loss can be described identically to quenching of the stochastic energy loss (of single particles)—i.e., $\langle Q \rangle = Q$.

To cancel out light propagation losses in the fibers and detection inefficiencies in the photosensors, we normalized the measured light yield in each fiber to that of minimum-ionizing reference particles, in our case pions. Using MIPs as a reference has the advantage that their specific energy loss is constant in all samples—independent of their thickness—thus providing a very stable reference energy loss.

To gather granular data over a wide range of specific energy loss, we used a detector consisting of a planar array of scintillating fibers. The minimum-ionizing pions traversed all fibers successively; for protons, we chose energies such that they stopped within the array. This allowed us to observe quenching at the Bragg peak, where $\mathrm{d}E \,/\, \mathrm{d}x$ is the highest. To further improve the granularity, we rotated the detector in the beam to vary the latter's path length, $\langle x \rangle$, in the fibers. Though these changes of $\langle x \rangle$ were small, they strongly affected the particles' energy-loss profile because of the high stopping power

of protons at the Bragg peak. The rotation therefore significantly increased the sensitivity of our measurement.

Since we did not have the means to measure the kinetic energy of the protons in between fibers, we calculated $E_{\mathrm{k}}^{\mathrm{in}}$ and $E_{\mathrm{k}}^{\mathrm{out}}$ for each fiber using tabulated stopping-power values from NIST [Ber+17], thereby accounting for the inactive cladding. This calculation depends on $\langle x \rangle$, and hence on the incidence angle of the beam on the fibers, which is why we treated the path length as a free parameter in our analysis.

7.1.3 Experimental Setup

Our detector consisted of 16 scintillating fibers, arranged in a planar array oriented perpendicular to the beam such that particles passed through them sequentially. Each fiber was 71 mm long and had a square cross-section of 2 mm × 2 mm (the same we use for the ADU). Since we wanted to compare our measurement approach to that of others (and there was no published data on the SCSF-78 fibers), we also cut 2 mm × 3 mm pieces of the same length from a plate of BC-408 scintillator and polished them to achieve a fiber-like state. BC-408 is a widely used PVT-based scintillator manufactured by Saint-Gobain (now Luxium Solutions), for which quenching measurements had been published previously. We oriented these asymmetric scintillator pieces such that the beam passed through them along their shorter edge. Since we could only irradiate 16 fiber samples at a time, we used sample holders that we could easily swap out. Each holder held eight fibers and had a base made from aluminum; the fibers were clamped down on these frames by two structures made from white polyoxymethylene (POM) (see Figure 7.1a).

The light produced in each fiber was detected by a Hamamatsu Photonics S13360-4935 SiPM with an active area of 3 mm × 3 mm glued to one end. The SiPMs had a microcell pitch of 25 µm and a total of 14 400 pixels, of which 6 400 overlapped with the fiber end (in the case of the square SCSF-78 fibers). The slightly larger sensitive area allowed for uncertainties in the positioning of the fibers. The large number of microcells ensured that saturation effects are negligible. We performed all measurements at constant overvoltage and temperature to operate with consistent gains. The SiPMs were mounted to custom PCBs that transmitted their signals without prior amplification to the read-out electronics.

To digitize the signals, we used a multichannel mezzanine-sampling ADC system with a sampling rate of 80 Msps [Man+09]. Since this sampling rate

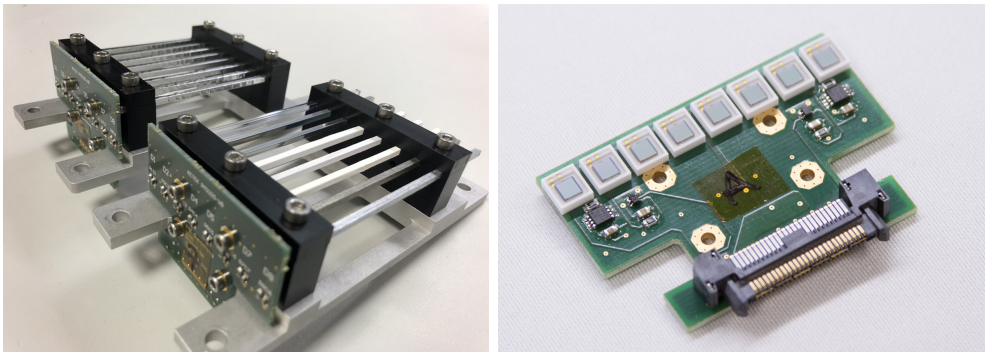

(a) Integrated holder. (b) SiPM array.

Figure 7.1: Sample holder used for the measurement of quenching in SCSF-78 fibers and BC-408 scintillator. The holders, including the SiPM arrays, were installed in the experimental setup using knurled screws and could thus easily be swapped out.

(and the input bandwidth of the ADCs' driver amplifier) were not sufficient for resolving the fast SiPM signals, we used active shapers to match the signal length and amplitude to the system's input range. These shapers consisted of a simple low-pass RC filter to limit the bandwidth of the signals, followed by an operational amplifier with gain $\sim$3.4 to match the signal amplitude to the ADC input range.

We performed the experiment at the πM1 beam line of the high-intensity proton accelerator at PSI. πM1 can deliver beams of protons and (negatively or positively charged) pions with momenta between 100 and 500 MeV/c[2] at a resolution of 1% [Reg+17]. The beam was centered on the sample fibers and had a spot size of 10 mm $\times$ 10 mm at FWHM. To reduce the spot size and beam divergence for protons, we placed a copper collimator with a 2-mm bore at a distance of 20 cm upstream of the detector. We mounted the detector on a motorized rotary table (with the rotation axis in the center of the fiber array), allowing us to vary the incidence angle of the beam on the fibers. Prior to the actual measurements, we calibrated the angular position of the rotary table by observing the changes in light yield upon turning it, with the position where the lowest yield was observed corresponding to an incidence angle of 0°.

[2]These are the theoretically possible values irrespective of the beam composition. The practically achievable lower and upper limits for protons lie closer to 220 and 450 MeV/c, respectively.

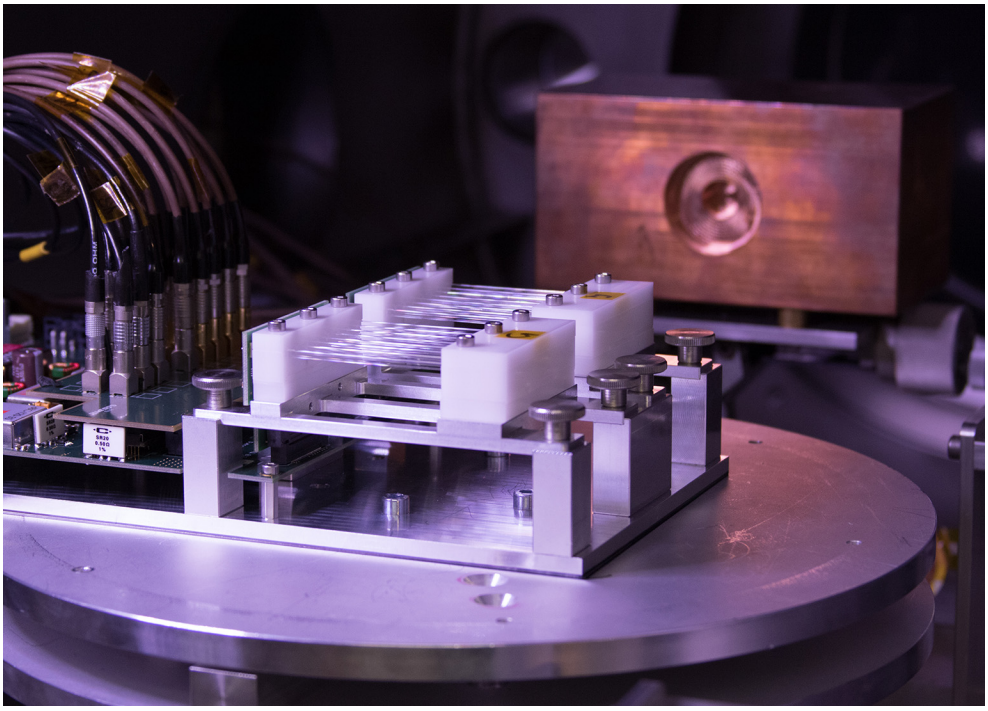

Figure 7.2: Experimental setup of the quenching measurement. The detector is mounted on a rotary table in the center of the vacuum chamber. A copper collimator with 2-mm bore is placed at distance of 20 cm upstream of the detector.

To minimize beam–air interactions—which would lead to a broader momentum distribution of the beam particles and thus to larger uncertainty in determining $E_{\mathrm{k}}^{\mathrm{in}}$ and $E_{\mathrm{k}}^{\mathrm{out}}$ for the first fiber—the entire setup was placed inside a vacuum chamber. Figure 7.2 shows the full experimental setup. We recorded data with beam momenta ranging from 240 to 350 MeV/c, mostly at an incidence angle of 1.6° (chosen for optimal positioning of the Bragg peak for the highest momentum). As additional angles, we chose 3.4° and 8.4° for the SCSF-78 fibers, and 5.4° and 7.9° for the BC-408 samples.

For each momentum, the beam contained both protons and pions, whose digitized signal-amplitude spectra were always well separated. Since the energy-loss density of the pions was to first order constant in all sample fibers, we could use the mean of their distribution as calibration reference for the mean proton light yield.

Table 7.1: Parameter values for the quenching models of Birks, Chou, Wright, and Voltz et al. for SCSF-78 scintillating fibers and BC-408 scintillator, including 1σ-credibility-interval uncertainties and correlation factors (where applicable) [Pös+21]. *These values are at their boundaries, so the credibility interval gives their upper limits.

Model	Param.	Units	SCSF-78	Corr.	BC-408	Corr.
Birks	kB	mm/MeV	0.132 ± 0.004		0.155 ± 0.005	
Chou	kB	mm/MeV	$0.000 \leq 0.001^*$	0.93	0.151 ± 0.040	0.75
	$\sqrt{C}$	mm/MeV	0.129 ± 0.005		$0.000 \leq 0.002^*$	
Wright	W	mm/MeV	0.333 ± 0.009		0.406 ± 0.002	
Voltz et al.	B_s	mm/MeV	0.091 ± 0.006	0.25	0.628 ± 0.108	0.89
	F_s		$0.000 \leq 0.057^*$		0.427 ± 0.019	

7.1.4 Results

The analysis of the experimental data was performed by Thomas Pöschl. I thus only provide a brief summary of the results, as needed for the discussion of the implications that arise for the RadMap Telescope.

Table 7.1 summarizes the results of a rather complex analysis using a Markov-Chain Monte-Carlo algorithm that uses all data sets (at different beam energies and angles) we recorded for each fiber type (see [Pös+21] for details). In addition to the best-fit parameters values, the table lists the 1σ-credibility-interval uncertainties resulting from the analysis and the correlation factors for models with two parameters. Both include statistical and systematic errors. The Birks' coefficient for BC-408 is our benchmark value, as Almurayshid et al. also analyzed quenching in this type of scintillator based on Birks' model [Alm+17]. They obtained $kB = 0.154^{+0.016}_{-0.017}\,\mathrm{mm\,MeV^{-1}}$, which agrees well with our value of $kB = 0.155 \pm 0.005\,\mathrm{mm\,MeV^{-1}}$. When using Chou's model, the behavior of the two scintillators is opposite: For the SCSF-78 fibers, quenching is best described by the quadratic term alone (which is compatible with the kB in Birks' model); for BC-408, the opposite is the case and the linear kB is again compatible with that of Birks' model. When using the model of Voltz et al., the fraction of unquenched energy deposition is zero (as in Birks' model) for SCSF-78, while it is about 50% for BC-408.

To investigate how well each model can approximate the true quenching function, we also performed a model-independent fit that was not subject to the theoretically imposed constraints of the models of Birks, Chou, Wright, and

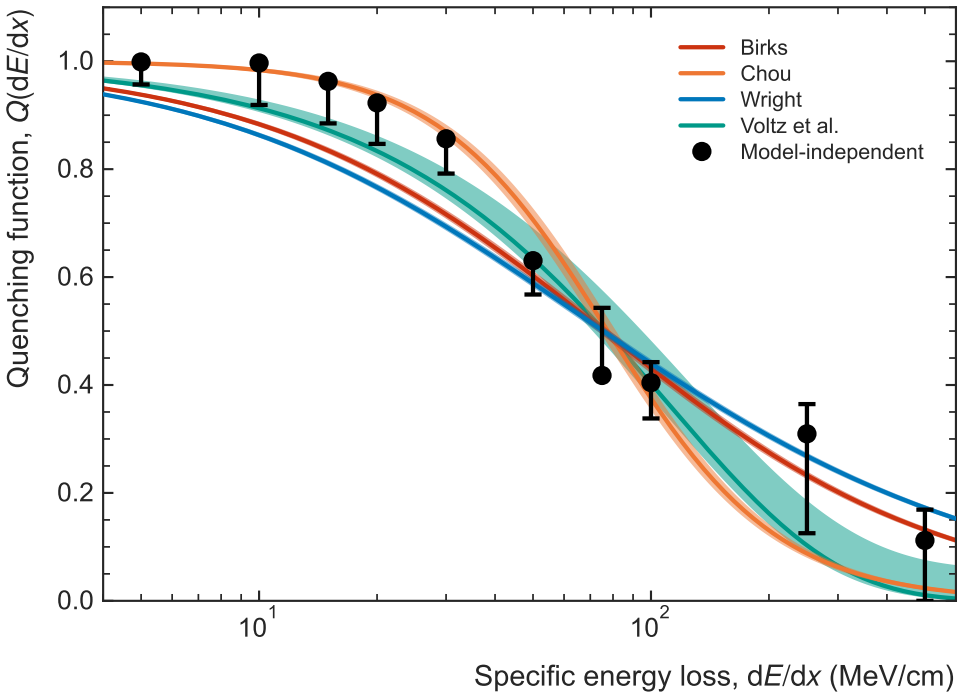

Figure 7.3: 1σ-credibility-interval bands for the model-dependent quenching functions based on the results of our studies. The data points show the best-fit values of the model-independent fit that was not subject to theoretically imposed constraints and thus best approximates the true quenching function. In contrast to the respective figure in [Pös+21], this plot was generated by simply inserting the parameter values listed in Table 7.1 into the model equations.

Voltz et al. We parametrized $Q(\mathrm{d}E\,/\,\mathrm{d}x)$ as a linear spline with eleven knots. We optimized the knot positions such that they cover the complete range of specific energy loss covered by our experiment and have the highest density in the region it is most sensitive to. Figure 7.3 compares the best-fit values for the model-independent function to the 1σ-credibility-interval bands of the model-dependent quenching functions. The bars on the former's results shows the boundary of the smallest credibility interval at each knot position. None of the four models agrees well with the model-independent results over the full energy-deposition range we studied.

Based on these results, we performed a comparison of how well the four models can describe quenching in the two scintillators. This comparison is based on Bayes factors and its mathematical details are described in [Pös+21]. We used Birks' model as a baseline because it is the most commonly used one. Our analysis revealed there is strong evidence that the models of Chou and Voltz et al. better describe quenching in SCSF-78 than Birks' model, with no clear favorite between the two. Chou's model with kB fixed to zero is strongly preferred over all others. Wright's model, on the other hand, is strongly disfavored by our data. For BC-408, Birks' model is clearly better than Chou's; the models of Wright and Voltz et al. are somewhat preferred over Birks', though not strongly.

Our studies revealed that quenching in the SCSF-78 and BC-408 scintillators has different dependencies on the density of the energy deposition. This may be caused by the different base materials or by differences in the chemistry and concentration of the dyes and wavelength shifters—or by a combination thereof. None of the models is decisively favored in fits with both scintillators, and the only model to perform marginally better than Birks' for both materials is that of Voltz et al. We can conclude from these results that none of the semi-empirical models has a mathematical form that is universal to all scintillators, though they may work well for certain materials in a restricted range of specific energy loss.

7.1.5 General Discussion

The discussion of our results in the context of finding a universal model for ionization quenching is rather straightforward. None of the four models we tested seems to be a good candidate for such a function, since none of them works well for both materials we tested. Based on our model-independent fit, we derived mathematical features (slopes, inflections points, etc.) that a phenomenological model must be able to reproduce; these are given in our journal publication. Based on these, it appears that a generic model would need at least four parameters. The merit of our analysis is that it is free of theoretically imposed bias. The apparently necessary development of more refined models can now be partially based on our results, though measurements with a broader range of materials are required. A first step would be the comparison of our data to the more complicated models anchored in quenching kinetics.

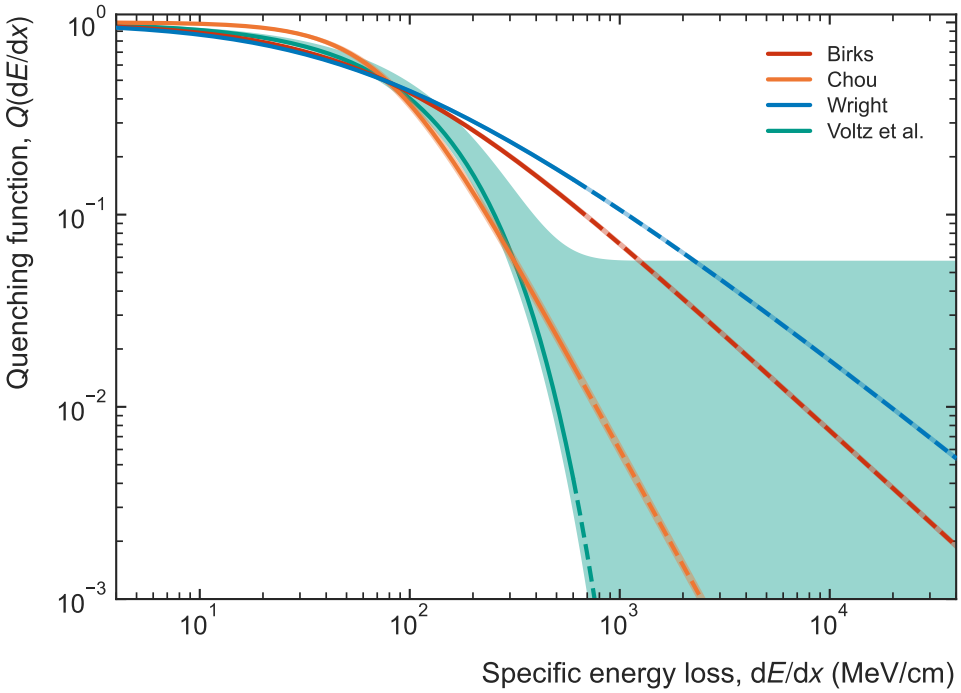

Figure 7.4: Extrapolation of the quenching functions shown in Figure 7.3 to the range of specific energy deposition that is of interest to the RadMap Telescope. The ordinate is shown in logarithmic scale to better visualize the differences between the models.

In the context of the RadMap Telescope, that fact that none of the models works well for both scintillators is not particularly important. Our analysis for SCSF-78 fibers shows that Chou's model with kB fixed at zero is favored over all others, despite the visually obvious deviation from the model-independent behavior at medium and large energy-loss density. It thus seems to be the obvious candidate to use. In Figure 7.4, I nonetheless show an extrapolation of all four models to the range of specific energy loss that is of interest to the RadMap Telescope. The figure also shows exemplary $\mathrm{d}E\,/\,\mathrm{d}x$ ranges for some ions stopping in the ADU. There are, however, two critical weaknesses in extrapolating from our experimental data:

1. The range of specific energy loss in our experiment was limited to that achievable by protons. Chou's model already significantly deviates from the model-independent behavior at the upper end of the energy-loss-

density range we studied. How well it fits experimental data at even higher specific energy loss is unclear. It is therefore an open question whether the true quenching function approaches zero at large $\mathrm{d}E \,/\, \mathrm{d}x$ or whether it settles on a stable non-zero value, as suggested by Birks (see Equation 4.17 [Bir64]). Unfortunately, our model-independent analysis is inconclusive on this question.

2. Our measurements were performed with protons only. An extrapolation to (heavy) ions, even in the range of energy-loss-density we covered, is thus questionable at best. Laplace et al., for example, studied quenching for protons and carbon ions in several plastic scintillators using the models of Birks, Chou, and Voltz et al. (among others) and found that none of the models could adequately describe the behavior for both particle types [Lap+22]. Other studies found that different parameter values are required for different ions types [Nyi+14]. Tammen et al., among others [Dlo+92], observed a similar effect in inorganic scintillators and were able to derive a semi-empirical model based on that of Birks, which can partially predict the quenching behavior of heavy ions in the two materials they tested [Tam+15].

To address these open questions, systematic studies with multiple (organic) materials using ions over a broad range of energy are required. So far, only few, selective studies with ions were performed at all (e.g., [Tam+15; Hit21]), and none has approached quenching systematically. Recently published studies often still rely on Birks' model [Alm+17; Pac+22], even though our analysis and that of others show that better models are needed [Lap+22]. In some of those studies, the same Birks' coefficient is used for different ions even though their experimental data does not support this approach [Biz+12].

In the absence of a systematic experimental treatment of heavy-ion quenching in organic scintillators, we need to rely on our analysis based on the energy-loss density of protons. However, to fully understand to what extent quenching affects measurements of the RadMap Telescope, more comprehensive measurements are needed.

7.1.6 Discussion in the Context of the RadMap Telescope

In light of the model insufficiencies already apparent at the energy-loss densities of stopping protons, it is worth investigating what impact our current lack of knowledge has on the identification of heavy ions via Bragg curve spectroscopy.

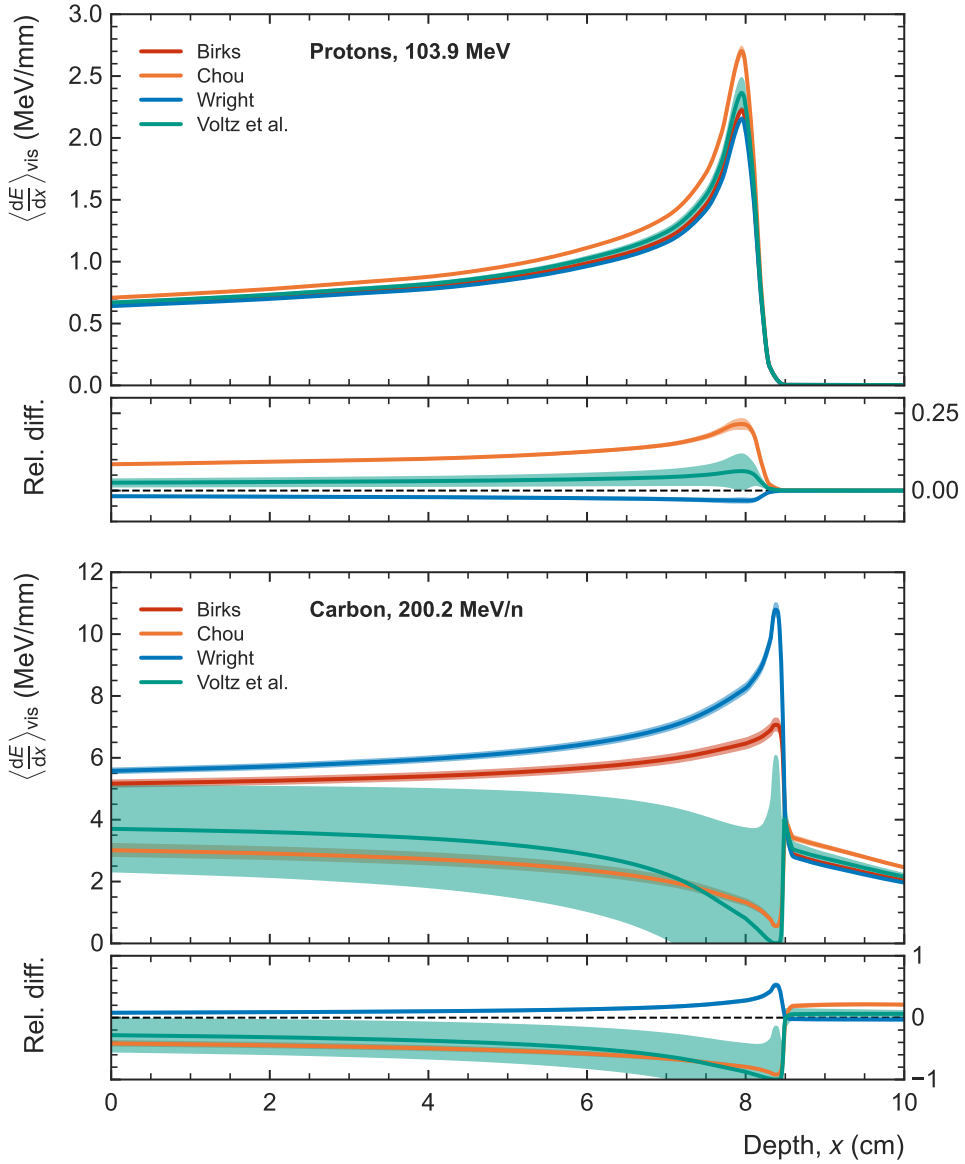

Figure 7.5: Application of the four evaluated quenching models to energy-deposition profiles of protons and carbon ions measured at NSRL [Bro24], using our model parameters determined from proton data (see Table 7.1). The smaller panels show the relative difference of Chou's, Wright's, and Voltz's model to that of Birks.

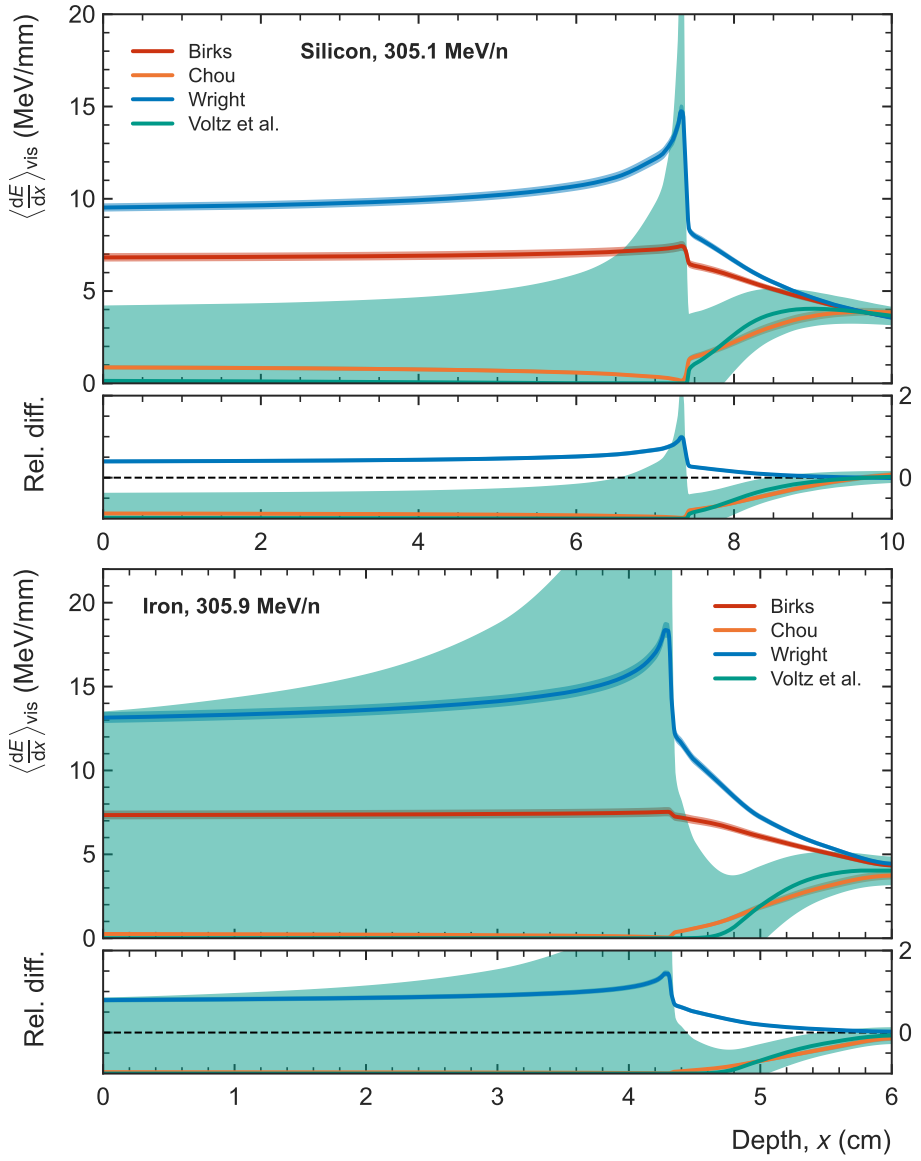

Figure 7.6: Application of the four evaluated quenching models to energy-deposition profiles of silicon and iron ions measured at NSRL [Bro24], using our model parameters determined from proton data (see Table 7.1). The smaller panels show the relative difference of Chou's, Wright's, and Voltz's model to that of Birks.

For this purpose, I again make use of the energy-deposition profiles of stopping ions recorded at NSRL with the help of HDPE absorbers and an ionization chamber [Bro24]. Similar to Figure 6.9, Figs. 7.5 and 7.6 show the four quenching models applied to the (unquenched) energy-deposition profiles of protons, carbon ions, silicon ions, and iron ions. For the model parameters, I use the values listed in Table 7.1. The larger panels show the respective profiles of the visible energy deposition, $\langle \mathrm{d}E \,/\, \mathrm{d}x \rangle_{\mathrm{vis}}$. The smaller panels show the relative difference of Chou's, Wright's, and Voltz's model to that of Birks.

The upper panels of Figure 7.5 demonstrate that the four models result in very similar profiles for protons, with differences between them reaching about 20%. Chou's and Voltz's models predict visible energy densities greater than that of Birks, while Wright's model lies somewhat lower. The relatively good agreement between the Bragg curves predicted by the models is not surprising, given that we used protons to determine their parameters in the first place. The lower panel of the figure, however, shows that this agreement is essentially gone at the energy densities created by carbon ions. Wright's model differs from Birks' one by about 50% in the Bragg peak; the other two models completely invert the energy-deposition profile. In addition, the uncertainties of Voltz's model become so large that it is practically rendered unusable. Figure 7.6 shows that the situation gets worse for heavier ions. In the extreme case of iron ions, Chou's and Voltz's model predict essentially zero visible energy deposition except in the fragmentation tail. This not only seems intuitively unphysical but would also render particle identification and energy measurement impossible. Wright's model, on the other hand, predicts overall weaker quenching, which would likely increase the accuracy of particle identification.

This naive application to heavy ions of models whose parameters were tuned to the small energy-deposition densities of protons is, of course, highly questionable, for reasons discussed in the previous section. It does, however, further highlight the urgent need for comprehensive measurements with heavy ions to precisely understand the quenching mechanism of SCSF-78 fibers (and plastic scintillators in general). The seemingly unphysical behavior of Chou's model at very high energy-deposition densities underlines its disagreement with our measurements that were already apparent in Figure 7.3. Despite their worse agreement with our data at low energy densities, the models of Birks and Wright exhibit behaviors at large energy densities that at least intuitively appear to make more sense. Without experimental data in this regime, however, such a statement is at best an educated guess and must not be relied upon to

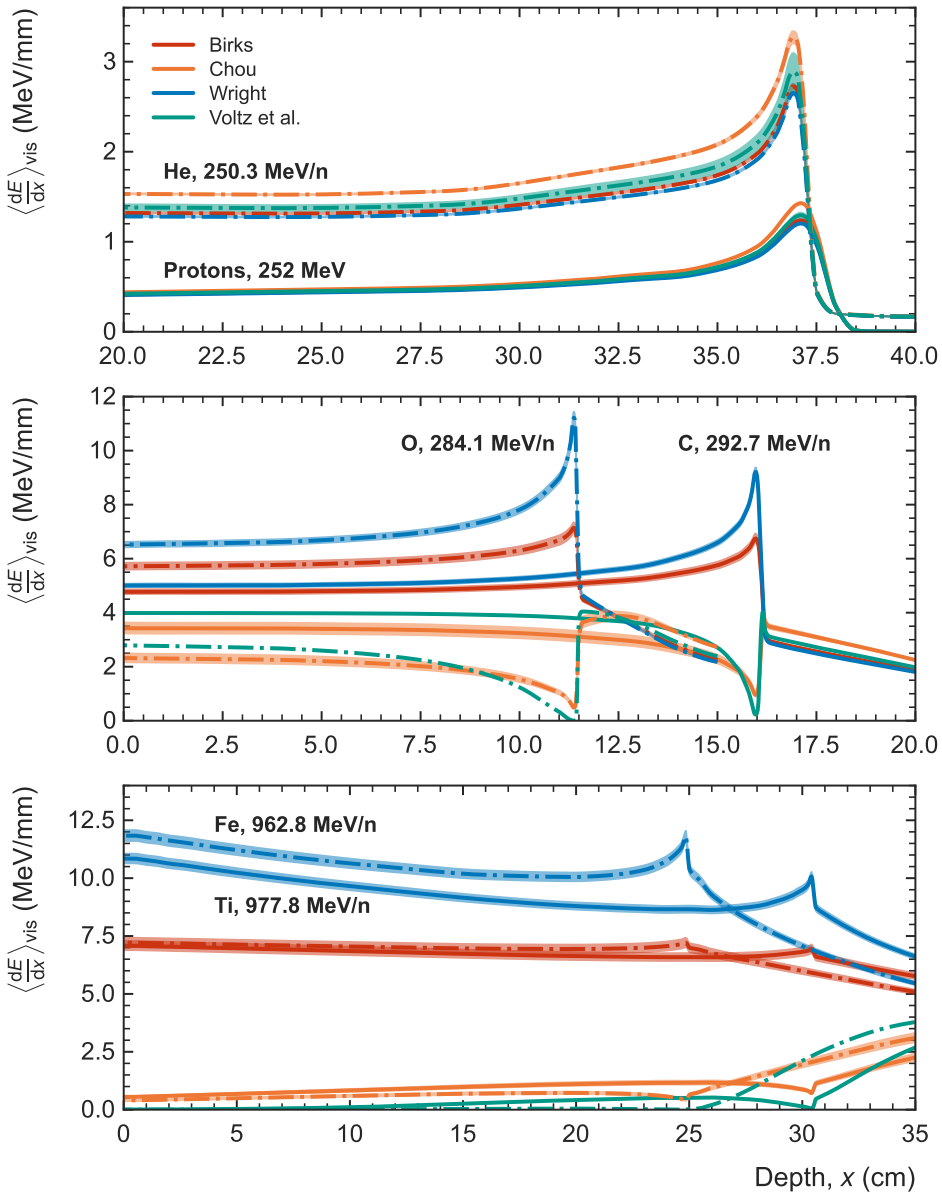

Figure 7.7: Comparison of quenched Bragg curves resulting from the four evaluated models for ions of comparable nuclear charge and range. To maintain readability, the large uncertainties of Voltz's model (see Figs. 7.5 and 7.6) are not shown in the lower two panels. Original data from NSRL [Bro24]; quenching parameters from Table 7.1.

draw definite conclusions about the validity of the models.
Despite the obvious need for better and more generally valid models, we can conclude that the accurate identification of light ions via Bragg curve spectroscopy is certainly possible, no matter which model is closer to the true quenching function. This is illustrated in the upper panel of Figure 7.7, where I compare the quenched energy-deposition profiles of protons and helium ions using all four models. The collections of predicted curves for the two ion species are very well separated, even when considering that the additional uncertainty introduced by straggling is not taken into account here. For carbon and oxygen nuclei (see the middle panel of Figure 7.7), the separation is smaller, though it should still be large enough for a sufficiently accurate identification. For titanium and iron (see the bottom panel of Figure 7.7), however, the curves for Birks' model largely overlap and can surely not be accurately separated. Wright's model, on the other hand, appears to generally forecast a larger separation. Based on its predicted curves, and depending on the strength of straggling for such heavy nuclei, a separation may be possible.

As in Section 7.1.5 above, the extrapolation of quenching models to higher energy-deposition densities severely suffers from the lack of experimental data. I use it here only to illustrate to which extent quenching impedes the identification of heavy nuclei.

7.2 Position Dependence of the Light Yield

In most contemporary applications of scintillating fibers, for example in tracking detectors that only record whether a fiber was hit or not [Ruc96; DAm+96], the impact of attenuation—i.e., the loss of photons due to self-absorption and other effects (see Section 7)—is minimal. Is such systems, the resulting worsening of the signal-to-noise ratio in the photosensors to first order only constrains the permissible length of the system. In our detectors, however, we also need to measure the energy deposition of particles, and attenuation hence necessitates a position-dependent correction of the measured light yield. We must therefore know the attenuation behavior of the fibers we use to a precision matching the energy resolution we want to achieve. Similar challenges arise in other applications of energy-sensitive fiber detectors, for example in the fields of radiation therapy [Arc+05], radiation protection [PMS11; Gil+18], and calorimetry [Kir87; Her+90; App+97].

Another factor relevant to the performance of our detectors is optical crosstalk. For many tracking detectors, photons moving between fibers are not necessarily a detrimental effect, especially in multi-layer ribbons where the distribution of scintillation light in adjacent fibers can provide information that improves the position reconstruction [JHL15; Bei+10; Kir17]. In applications that require good spatial resolution and a high detection efficiency in single layers of fibers, however, optical crosstalk can be a challenge [SHG95]. This is especially true for detectors that must be sensitive to particles creating only few scintillation photons (i.e., MIPs), in which case a single photon moving to an adjacent fiber might not make it through the noise threshold in that channel and is therefore effectively lost.

In our applications, we do not only need to identify the primary particle entering the detector and measure its energy. We also need to reconstruct the tracks of secondary particles, for example created in the annihilation of antiprotons. This requires good energy and tracking resolutions, as well as the separation of closely spaced tracks that may originate from a single vertex. Attenuation and optical crosstalk are therefore key parameters determining the performance of our detectors. In our early prototypes (see Section 6.5), we tried to suppress crosstalk by wrapping fibers with aluminum foil. This was not only a time-consuming process but lead to highly variable, position-dependent light yields. We also observed large reductions in light output whenever glue crept between the foil and the fiber.

This made us realize that—contrary to widely held belief—light trapped by the cladding significantly contributes to the light transport in fibers as short as those in our detectors. The position-dependent light yield of short fibers is thus closely linked to the material used to suppress optical crosstalk. Since we could not find a systematic study of the effect of coating or wrapping fibers with different materials, we needed to perform our own investigation.[3]

7.2.1 Theoretical Considerations

The attenuation of light in scintillating fibers is caused by a combination of intrinsic and extrinsic effects. Intrinsic losses arise from the physical and chemical structure of the fiber material and as such cannot be fully eliminated [Whi+18]; they include self-absorption in the scintillator's matrix or dopants (dyes and wavelength shifters), Rayleigh scattering, and the excitation of

[3] Much of the rest of this section is largely a verbatim copy of our journal publication in *Radiation Measurements* [LPP24], of which I am the lead author.

molecular vibrations and electronic transitions [Reb+99]. Extrinsic losses are caused by impurities and imperfections introduced during the fabrication or handling of the finished product, and can thus be minimized by material purification and through an optimization of the fabrication process [Whi+18]. They include absorption by contaminants and absorbed water, scattering at impurities such as microscopic voids and dust particles, and reflection losses due to imperfections at the core–cladding and cladding–air interfaces [Dec15]. The magnitude of intrinsic effects for a given combination of scintillator matrix and dopants is strongly wavelength-dependent [Whi+18]; for the SCSF-78 fiber, re-absorption in the secondary wavelength shifter is the dominant effect [Eke16]. This leads to the disproportionate loss of photons at the blue end of the emission spectrum for longer propagation paths [Dre+95; PLL08]. All intrinsic and extrinsic losses in the bulk material scale with the integrated path length of the photon through the fiber. Only scattering losses due to imperfections at the core-cladding and cladding-air interfaces scale with the number of reflections and are independent of the bulk material properties.

In a simplified picture, in which we average over the scintillator's emission spectrum and over all possible path lengths of photons trapped under different angles (with respect to the fiber axis), we can define an effective bulk attenuation length, Λ_B, such that the light yield, I, at a distance d from the ionization source is given by

$$I(d) = I_0 \cdot e^{-d/\Lambda_\mathrm{B}}, \tag{7.7}$$

where I_0 is the initial photon intensity at the emission point. Λ_B is the distance over which the intensity of the integrated scintillation spectrum is reduced to $1/e$ and is typically specified by manufacturers. This simple model does, however, ignore the plethora of wavelength- and path-length-dependent effects listed above. In a more refined yet still approximate picture, the observable light yield as a function of distance from the source can be parametrized as

$$I(d) = I_0 \cdot ((1-\alpha) \cdot e^{-d/\Lambda_\mathrm{L}} + \alpha \cdot e^{-d/\Lambda_\mathrm{S}}), \tag{7.8}$$

where Λ_L and Λ_S are two attenuation lengths, and α specifies their relative magnitude [Bau+13]. The introduction of these additional parameters is often motivated by the fact that light with short wavelengths (Λ_S) is attenuated more strongly in the fiber (core) than light with long wavelengths (Λ_L) [ABL90]. This may be justifiable for longer length scales but cannot be generalized. The intrinsic and extrinsic losses cited above all have a different position-dependent attenuation behavior; the losses dominating Λ_L and Λ_S in a three-parametric

Table 7.2: Attenuation lengths for Kuraray SCSF-78MJ round, double-cladded fibers of different diameter D as specified by Kuraray and measured by Beischer et al. (2010), Baulin et al. [Bau+13], Yearwood [Yea13], and Bravar & Demets [BD22]. The parameters listed refer to those used in Eqs. 7.7 and 7.8.

Source	D	α (%)	Λ_B (cm)	Λ_L (cm)	Λ_S (cm)
Kuraray	1 mm	-	467	-	-
Beischer et al. (2010)	$250\,\mu$m	55 ± 8	-	745 ± 194	126 ± 22
Baulin et al. (2013)	1 mm	-	387 ± 26	-	-
Baulin et al. (2013)	1 mm	30	-	486 ± 54	75 ± 22
Yearwood (2013)	$250\,\mu$m	46 ± 4	-	533 ± 57	74 ± 14
Bravar & Demets (2022)	$250\,\mu$m	?	-	337 ± 62	16.4 ± 4.1

model (Equation 7.8) will thus differ depending on the range of path lengths covered in a given study. We therefore prefer to state that a double-exponential model is the simplest model that parametrizes the position-dependent light yield with reasonable accuracy over a broad length range. A more accurate description has been developed, for example, by Rebourgeard et al. but is too complex to be of practical use for our work [Reb+99].

For their round fibers, Kuraray quotes an attenuation length of double-cladded fibers equal to that of fibers with single cladding [Kur14]. In light of our analysis, this may not be true for short fibers (see Section 7.2.4). However, in the absence of a published characterization of single-cladded SCSF-78 fibers, we must use the attenuation lengths for multi-cladded fibers available in the literature as initial references. Table 7.2 lists attenuation parameters obtained from studies performed with untreated fibers that used one-parametric (Equation 7.7) and three-parametric (Equation 7.8) attenuation models. The different results lead to variations in the predicted relative light yield of up to 30 percentage points for propagation lengths in the range of 150 cm to 200 cm. We also expect sizable differences of several percentage points for short fibers with lengths up to 10 cm (see Figure 7.8), as studied in our investigation. These uncertainties in the attenuation translate into uncertainties in the position dependence of the effective light yield, which decrease the energy resolution of fiber-based detectors. They also cast doubt on the validity of extrapolating models based on measurements at long fiber lengths to short distances.

In the following, I briefly review the principle of light transmission in a fiber. At the macroscopic level, the emission of photons in the scintillator core

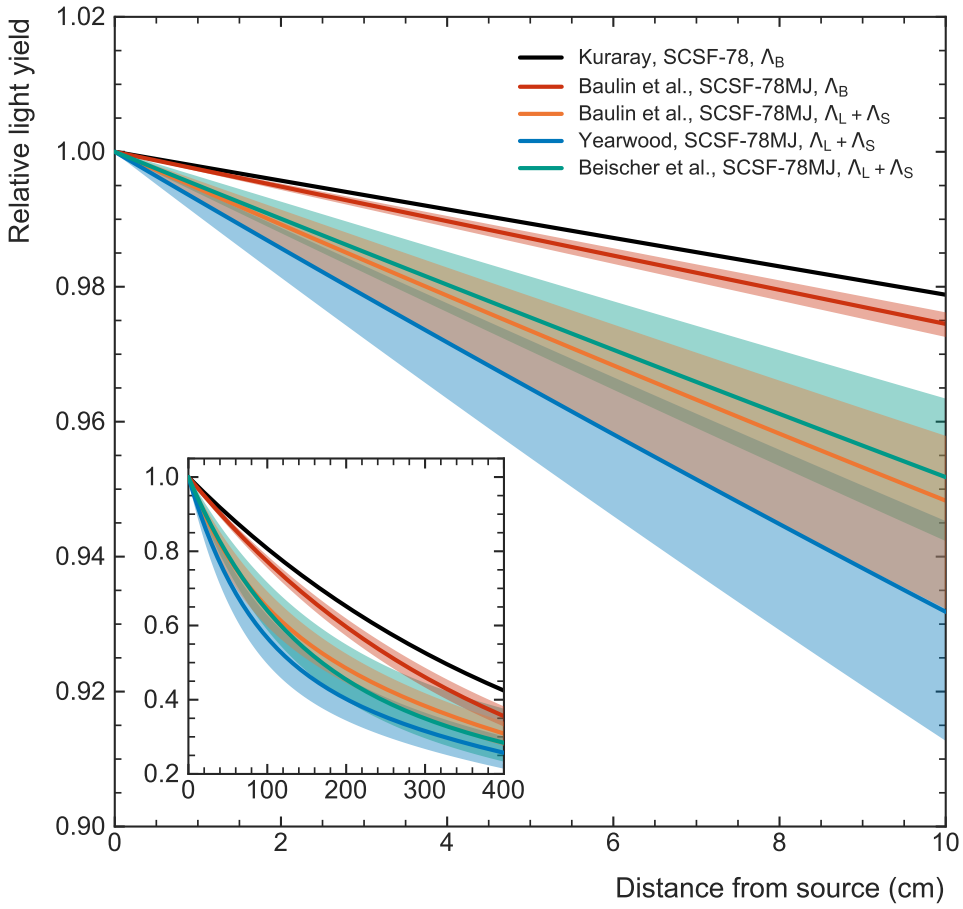

Figure 7.8: Relative light yield of SCSF-78 scintillating fibers as a function of the distance from the ionization source for the different parameter sets listed in Table 7.2. The inset shows the same information for longer distances. Adapted from [LPP24].

is isotropic [Reb+99]. Since the refractive index of the cladding is smaller than that of the core, photons can be totally reflected at the interface between the two and thus travel along the fiber if their emission angle is smaller than the critical angle, θ_{CC} (see Figure 7.9a; note that angles are measured from the surface, not from the surface normal). I refer to Rebourgeard et al. [Reb+99] for a complete mathematical treatment of the trapping process that takes into account the full fiber geometry. In the literature, most authors assume that

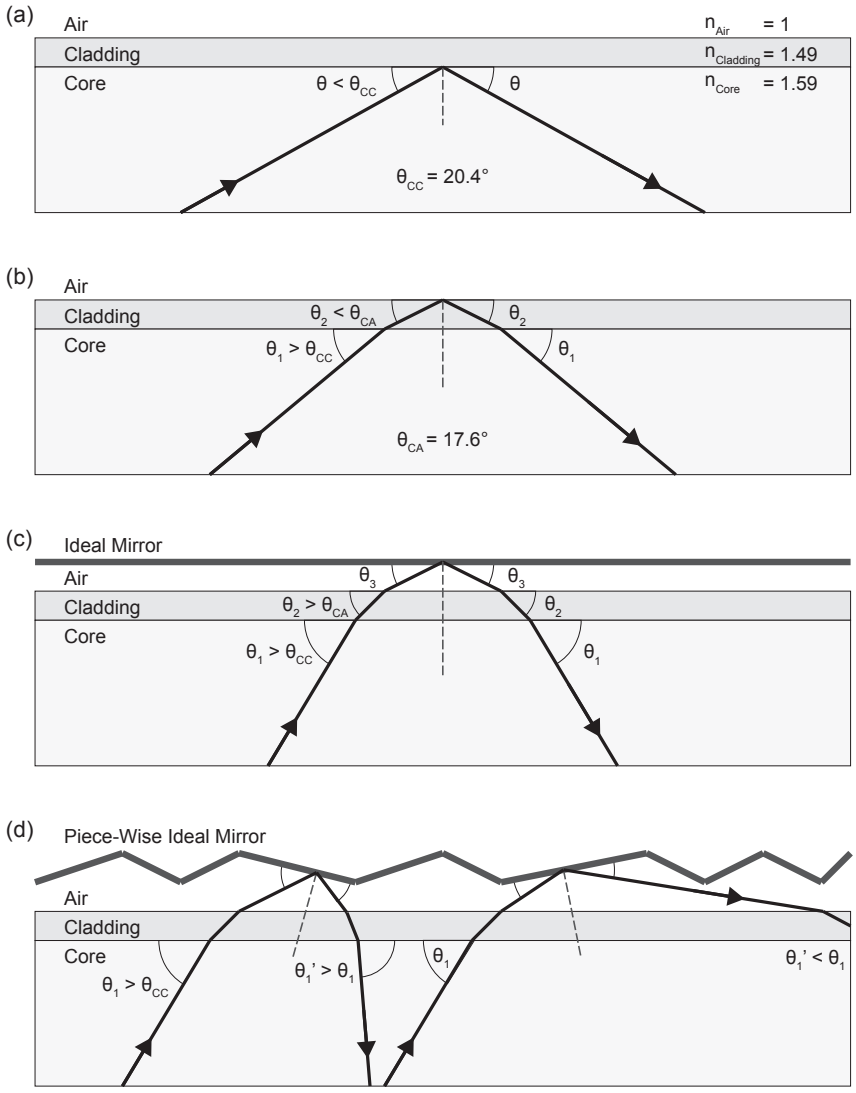

Figure 7.9: Transmission of photons in a scintillating fiber. (a) Reflection at the core-cladding interface; (b) reflection at the cladding-air interface; (c, d) reflection of untrapped photons at mirror surfaces. Scattering at interfaces or in the bulk material, as well as absorption at reflecting surfaces are not shown. Note that angles are measured from the surface, not from the surface normal. Adapted from [LPP24].

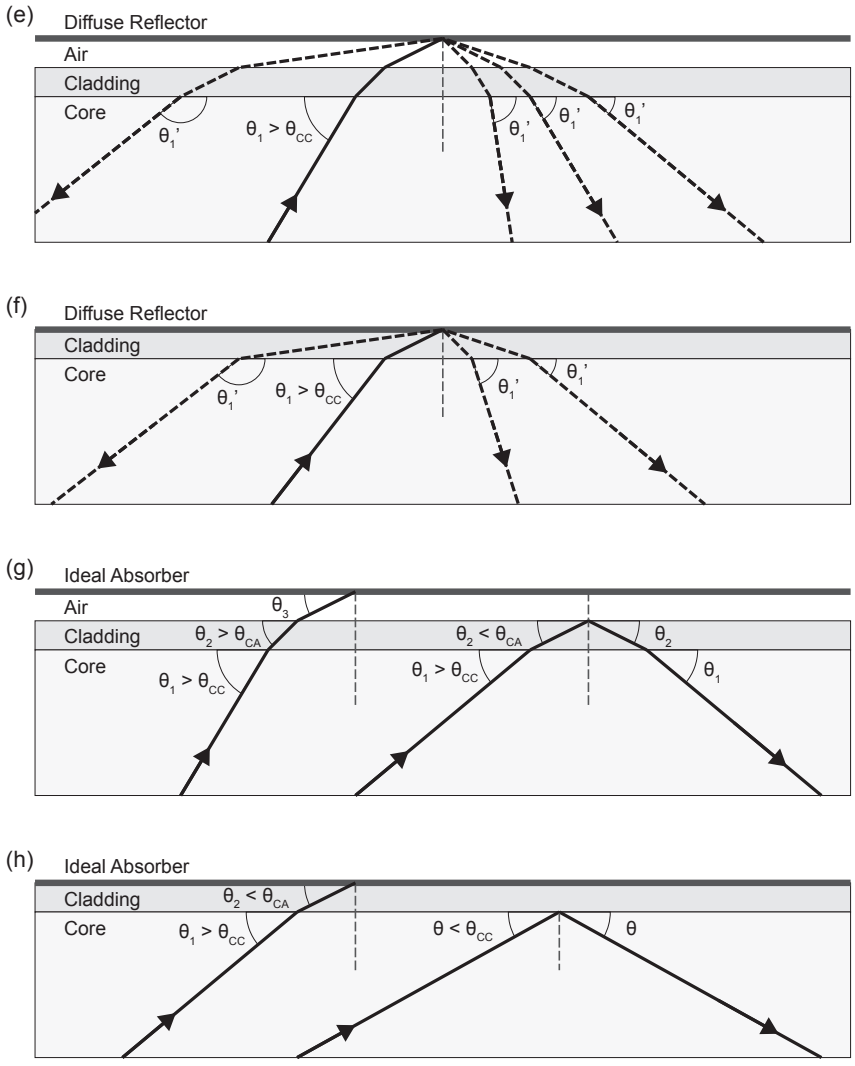

Figure 7.10: Transmission of photons in a scintillating fiber. (e) reflection of untrapped photons at diffuse reflector; (f) reflection of trapped photons at diffuse reflector; (g, h) absorption of untrapped photons. Scattering at interfaces or in the bulk material, as well as absorption at reflecting surfaces are not shown. Note that angles are measured from the surface, not from the surface normal. Adapted from [LPP24].

reflections at the cladding–air interface (for angles smaller than the critical angle θ_{CA}; see Figure 7.9b) do not contribute much to the light propagation in a fiber [Leu95; Eke16; Reb+99]. This assumption is based on two arguments: (1) photons emitted under larger angles must undergo significantly more reflections to reach the end of the fiber and hence are more strongly attenuated by intrinsic losses (because of the longer path length); and (2) the surface quality of the cladding–air interface is inferior to that of the core–cladding interface—due to production defects or damage caused by handling—resulting in a higher loss probability for photons due to scattering. For long fibers, the resulting decrease in trapping efficiency, even if small, eventually leads to the loss of (almost) all photons trapped by the cladding. In short fibers, however, photons must undergo far fewer reflections and have a correspondingly shorter path length, such that a large fraction of those with emission angles smaller than θ_{CA} can reach the end of the fiber and thus contribute to the light yield [ABL90; Reb+99].

The purpose of wrapping or coating fibers is twofold: (1) to improve their light yield by increasing the number of trapped photons and (2) to prevent photons leaving one fiber from entering a neighboring one (optical crosstalk). Supposing that we could wrap a fiber in an ideal mirror, photons would be trapped via specular reflection (see Figure 7.9c) and propagation losses would be due to intrinsic attenuation in the fiber core and the cladding only. For lack of better alternatives, thin reflective foils—e.g., made from aluminum or aluminized Mylar—can be wrapped around fibers. Although not offering a completely flat surface, they can be approximated as piece-wise ideal mirrors, with flat areas of different sizes oriented at small but random angles to each other (see Figure 7.9d). The angle under which photons re-enter the fiber thus depends on the local orientation of the reflecting surface. In addition, there is a small yet significant probability for photons to be absorbed upon hitting the reflector. In combination, these effects result in a randomly fluctuating transmission efficiency along the fiber and thus lead to a non-uniform position dependence of the light yield. The path-length-dependent intrinsic attenuation only exacerbates the effect. If we use a diffusely reflecting material like polytetrafluoroethylene (PTFE) instead, the outgoing direction of a photon is (nearly) independent of its angle of incidence (see Figure 7.10e). The resulting light yield is lower than for an ideal mirror but more uniform than for reflecting foils. If we want to suppress optical crosstalk without enhancing the light yield, we can wrap fibers in an opaque material that efficiently absorbs untrapped photons (see Figure 7.10g). As in untreated fibers, any non-uniformity of the

light yield in this case is only due to intrinsic and extrinsic attenuation losses.

Figs. 7.10e through 7.10h illustrate the effect of directly applying a (diffuse) reflector or absorber (e.g., absorbing paint) to a fiber: Without air gap (Figs. 7.10f and 7.10h), the change in refractive index at the outer cladding surface disappears and photons directly hit the reflector or absorber instead. Total reflection at the cladding–air interface is thus replaced by either diffuse reflection or absorption, leading to an overall light yield that is lower than that of untreated fibers. For this reason, the use of diffuse reflectors for enhancing the light yield of long, fiber-like scintillators without cladding is usually discouraged in the literature: Consistently keeping an air gap in the application of a material like PTFE tape over the length of a fiber is impractical. Yet in any area without air gap, however small, the conditions for total internal reflection at the scintillator–air interface are destroyed, leading to a decrease of the overall light yield. For long fibers, in which reflections at the cladding–air interface do not significantly contribute to the photon transport, this may not be problematic. We, however, expected a measurable impact on the light propagation in short fibers and hence included samples treated with diffuse reflectors in our experiment to study the contribution of the cladding–air interface.

7.2.2 Experimental Setup

We studied the light attenuation in short scintillating fibers and the effect of wrapping and coating them with different materials. We used an experimental setup that allowed us to excite fibers at well-defined locations with a beam of charged pions. All our studies were performed with Kuraray SCSF-78 fibers with a square cross-section and a thickness of 2 mm that we polished at both ends. At about 8 cm, the length of the fibers roughly equalled the size of the RadMap Telescope's main detector (the ADU). At one end of each fiber, we detected the scintillation light with PM3325-WB-B0 SiPMs from KETEK [KET17], which have a pixel size of 25 μm and an active area of $3 \cdot 3\,\mathrm{mm}^2$. We used the same type of sample holders previously described in the context of the measurement of ionization quenching (see Section 7.1.3), holding eight fibers each (see Figure 7.11). On these frames, the fibers were clamped down by two structures made from black POM (white POM in case of the sputter-coated samples). On the side where the SiPMs were attached, the fibers protruded only about 3 mm from the plastic to ensure they were well centered on the photosensors. The SiPMs were soldered to a PCB and glued to the fibers with

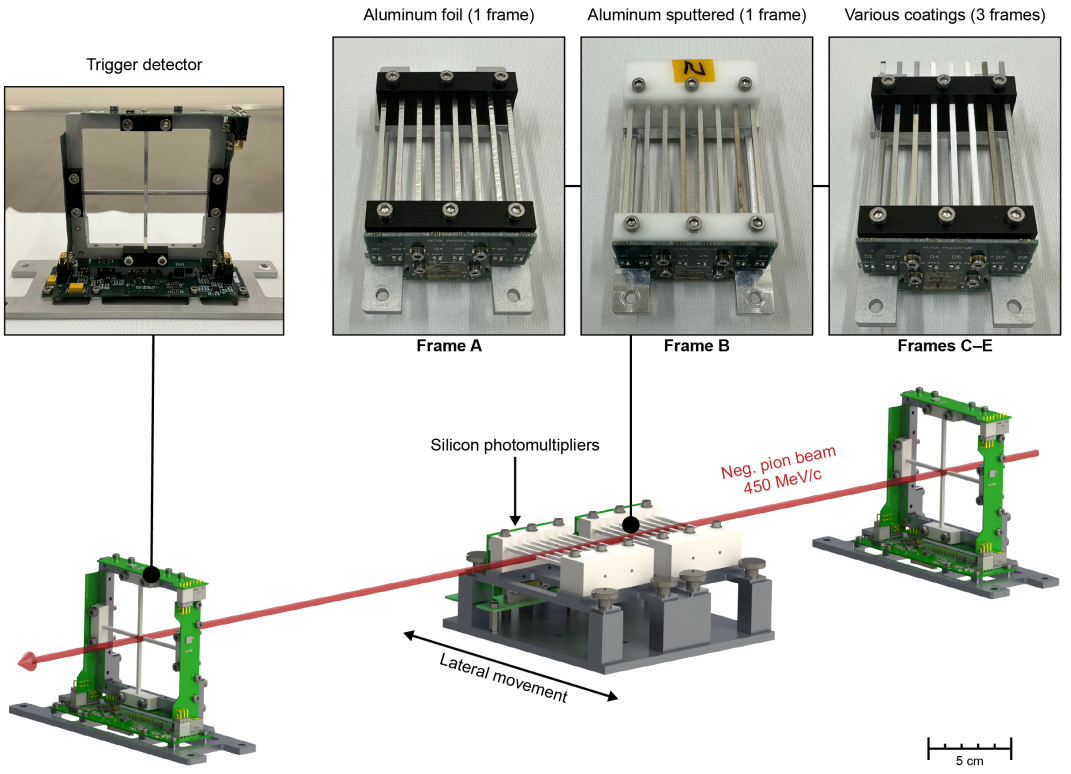

Figure 7.11: Experimental setup for the attenuation measurement, consisting of two trigger detectors and up to two sample frames. The beam traversed the setup from right to left; the samples were moved laterally as indicated. Shown are three examples of sample frames: one with fibers wrapped in aluminum foil, one with sputter-coated fibers, and one with the other coating options we tested (from left to right: untreated, sputter-coated, vapor-coated, PTFE tape, EJ-510, white paint, 996 paint, 995 paint) [LPP24].

EPO-TEK® 301 optical epoxy [Epo23]. Again, the frames were installed in the experimental setup using knurled screws, allowing us to easily swap them out. We tested eight different materials for coating and wrapping fibers. For our early prototypes (see Section 6.5), we wrapped fibers in aluminum foil in a labor-intensive procedure that yielded highly variable quality. We nevertheless wanted to study this solution in detail to better understand the performance of our legacy systems. In preliminary measurements with beta electrons from a ^{90}Sr source, we identified sputter-coating with aluminum as the best-performing alternative (for reasons discussed below). We hence equipped one frame each with fibers treated in these two manners (frames A & B). In both cases, the end faces opposite of the SiPMs were also sputter-coated with aluminum since we already knew this to have a negligible impact on the light yield from the measurements with beta electrons and the samples were already available. As potential alternatives, we identified coating with aluminum by vapor deposition, wrapping with PTFE tape, coating with EJ-510 scintillator paint, and applying various acrylic paints (white, Lascaux Studio Bronze 995 Aluminium, Lascaux Studio Bronze 996 Britannica silver). The latter two incorporate non-oxidizing metallic pigments, which we hoped would provide a higher (diffuse) reflectivity than white paint. We left the end faces of all fibers except for the ones sputter-coated and vapor-coated untreated because we did not know the potential impact of the other surface treatments on the overall light yield in advance. Three samples of each material were distributed among three frames (frames C–E), such that each frame was equipped with one fiber of each sample class in addition to an untreated fiber. We calibrated all SiPMs using an LED flasher before mounting them to the frames and tested all fiber-SiPM assemblies with a ^{90}Sr source after gluing.

To precisely control the position of the primary ionization along the fibers, we used two trigger detectors to select from a wide beam only those particles that traversed the fibers along a well-defined axis. The detectors consisted of two orthogonally mounted SCSF-78 fibers, creating an overlapping area of $2\,\text{mm} \cdot 2\,\text{mm}$. We placed one detector upstream and one downstream of the sample frame (see Figure 7.11) and recorded only those events with coincident signals in the two vertical trigger fibers and all eight sample fibers. We did not use the horizontal trigger fibers to allow for vertical misalignment between the frames and the trigger detectors. The horizontal and vertical positions of accepted beam particles were thus constrained to within 2 mm. We changed the lateral position of the so-defined beam axis by moving the sample frames transversely to the beam using a high-precision motorized linear stage. The

SiPM signals were digitized using the same multichannel mezzanine-sampling ADC system [Man+09] described in Section 7.1.3 above and the same active shapers to match the signal length and amplitude to the ADCs' input range. The whole setup was placed inside a light-tight steel vessel.

We again performed the experiment at the πM1 beam line of the high-intensity proton accelerator at PSI, making use of its ability to deliver beams of (negatively charged) pions with momenta between 100 and 500 MeV/c at a resolution of about 1% [Reg+17]. We selected a momentum of 450 MeV/c, which corresponds to $\beta\gamma \sim 3.2$ and hence to the minimum-ionizing regime (see Section 3.2.6). At this energy, pions have a constant energy-loss density throughout the setup, creating on average an equal number of primary scintillation photons in each fiber. This allows us to directly compare the light yields without applying corrections. The beam intensity was chosen such that the pile-up probability was practically zero. We recorded 13 measurements for each frame, covering distances from the SiPM between 1.2 cm and 6 cm in 4-mm steps.

7.2.3 Results

We determined the signal amplitude of each sample (at every position) by fitting the recorded waveforms with a multi-parametric model of a SiPM signal. Figure 7.12 exemplarily shows the resulting signal-amplitude spectrum at an arbitrary position for a fiber sputter-coated with aluminum. We then determined the most probable signal amplitude of each measurement by fitting a normal distribution to the respective spectrum in the region around the maximum. We interpret these amplitudes as the mean absolute light output in arbitrary units, as given by the model we used to fit the SiPM waveforms. To check the validity of using a Gaussian distribution to approximate the maximum, we fitted a subset of the obtained spectra with a convoluted Landau-Gaussian distribution. The resulting most probable value (MPV) of the signal amplitude in nearly all cases agreed to better than 0.1% with the Gaussian-only approach and never exceeded a 0.5% difference.

Using a single set of calibrated read-out and data-acquisition electronics obviates the need for normalization when comparing absolute light yields of different samples. For the discussion of the position dependence of the light yield, however, we normalized the data of each sample to its light yield closest

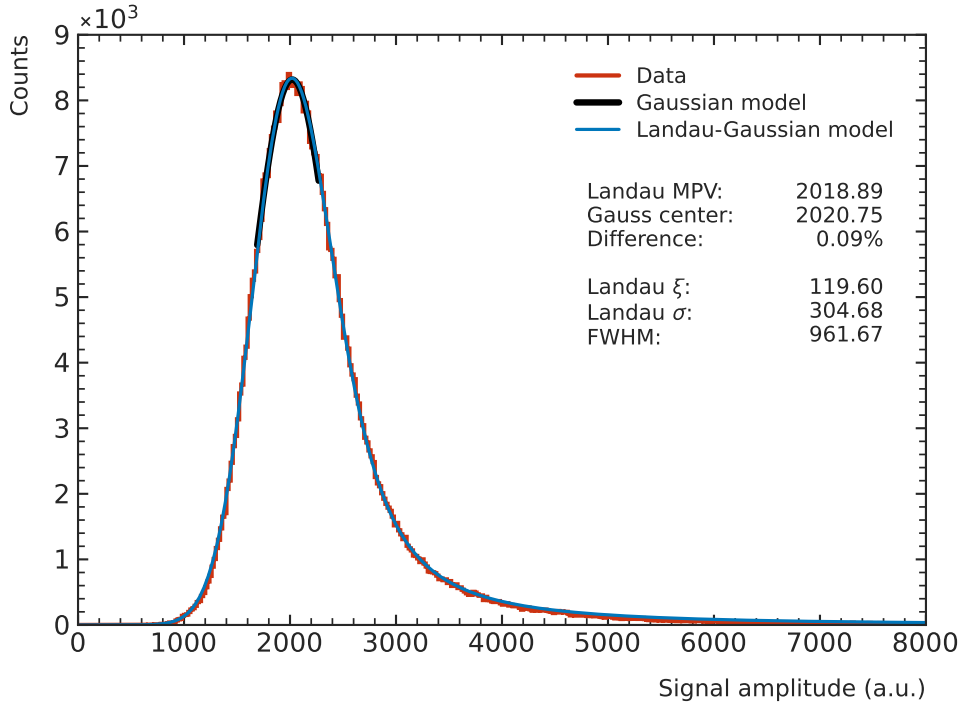

Figure 7.12: Signal-amplitude spectrum for a fiber sputter-coated with aluminum (frame B). The black line shows a fit with a Gaussian distribution in the region around the MPV of the Landau-Gaussian model. Adapted from [LPP24].

to the SiPM. Since it was not relevant to our work, we did not perform a calibration that would allow us to express the light yield in terms of number of photons per unit of energy deposited.

Small Sample Populations (Frames C–E)

Figure 7.13 and 7.14 show the position-dependent absolute and relative (normalized) light yields for the three frames holding differently treated fibers (frames C–E). We observe significant differences in absolute yield and position dependence between sample populations, as well as dissimilar sample-to-sample variations within each population. In the following, I present the results in descending order of absolute light yield:

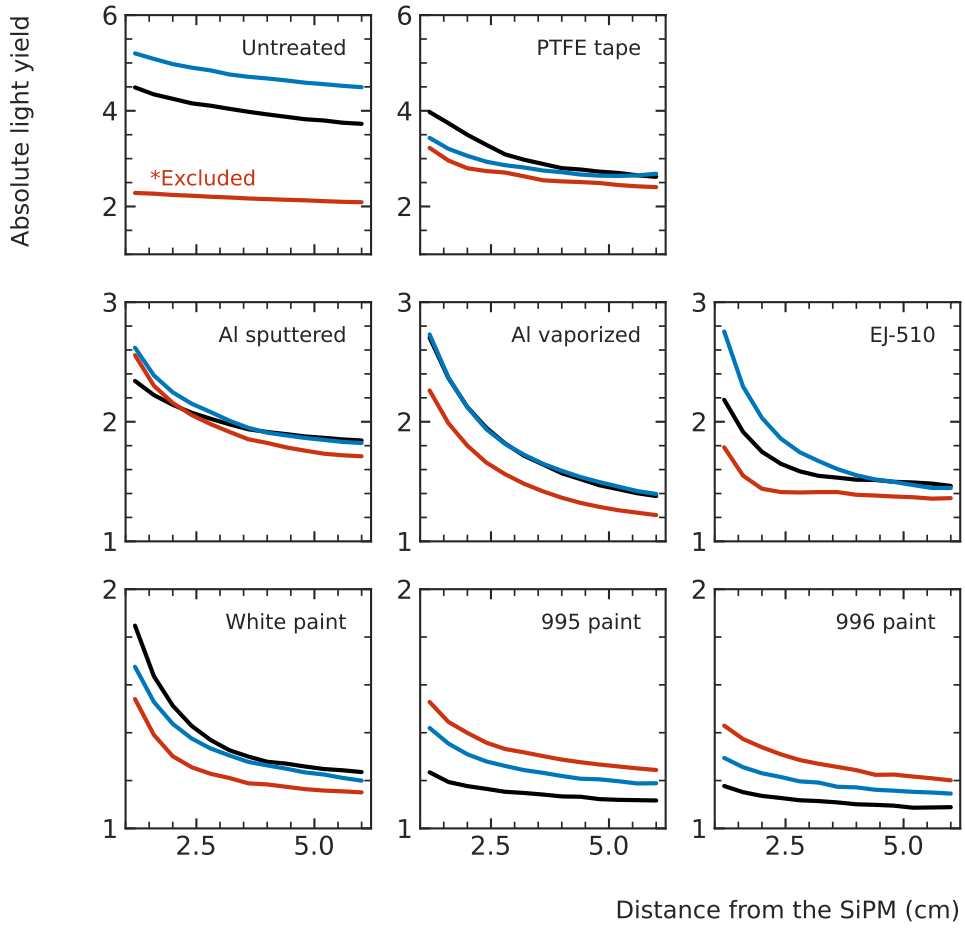

Figure 7.13: Position dependence of the absolute light yield of SCSF-78 fibers wrapped in or coated with different materials. Colors indicate the three different test frames (red – frame C, blue – frame D, black – frame E). The untreated fiber in frame C (marked accordingly) was excluded from further analysis (see Section 7.2.4 for explanation). The sample populations are ordered from high to low yield. Note the different scales for the vertical axes. Adapted from [LPP24].

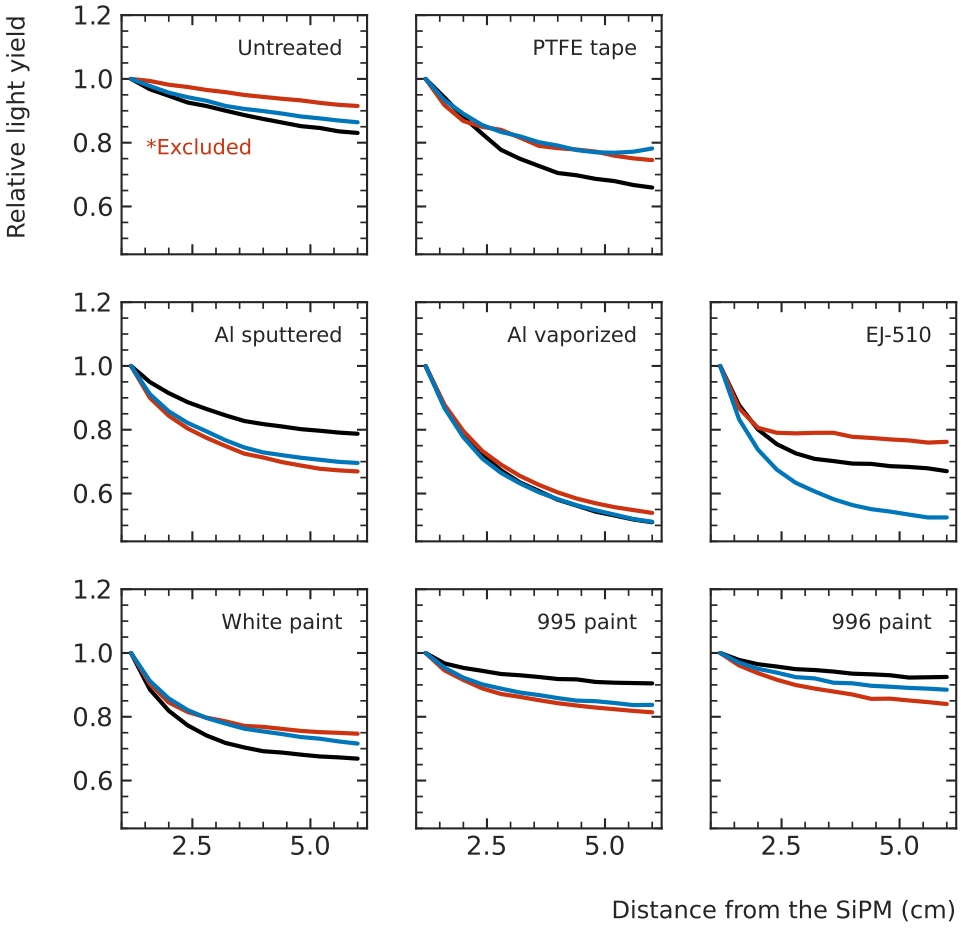

Figure 7.14: Position dependence of the relative light yield of SCSF-78 fibers wrapped in or coated with different materials. Colors indicate the three different test frames (red – frame C, blue – frame D, black – frame E). The untreated fiber in frame C (marked accordingly) was excluded from further analysis (see Section 7.2.4 for explanation). The data for each fiber was normalized to the light yield measured at the beam position closest to the SiPM (1.2 cm). Adapted from [LPP24].

Untreated Fibers The light output of the untreated fibers is the highest of all samples we tested, though there is one outlier with a significantly lower yield. The position dependence is almost linear and, at less than 20% reduction over the full distance range, among the smallest.

PTFE-Wrapped Fibers Fibers wrapped in PTFE have the highest light output of the treated samples but show large sample-to-sample variations in both absolute and relative light yield. For the latter, we observe a reduction of 20% to 35% that is significantly non-uniform.

Fibers Sputter-Coated with Aluminum The absolute light yield of fibers sputter-coated with aluminum is noticeably lower than that of PTFE-wrapped ones but has the lowest spread of all samples. The normalized yield shows a reduction of 20% to 35% over the full distance range.

Fibers Vapor-Coated with Aluminum Fibers that were vapor-coated with aluminum show a light yield comparable to that of sputter-coated ones, but with slightly larger spread. The sample-to-sample variance of the position dependence is the smallest of all sample populations. The 45% to 50% relative reduction in light yield is, however, the largest.

Fibers Coated with EJ-510 The average light yield of samples coated with EJ-510 is slightly lower than that of aluminum-coated ones but exhibits a much larger variance. The position dependence (20% to 50%) is not only the second largest but also has the largest spread of all samples.

Fibers Coated with White Paint The light yield of fibers coated with white acrylic paint is substantially lower than that for samples coated with EJ-510 but has smaller variance. The relative reduction in light yield (20% to 35%) is also smaller and exhibits less variance.

Fibers Coated with Metallic Paint Fibers coated with metallic paints have the lowest overall light output with the largest sample-to-sample variations. Their position dependence of 20%, however, is comparably weak and similar to that of untreated fibers.

Large Sample Populations (Frames A & B)

Figure 7.15 shows the position-dependent absolute light output of the two frames with foil-wrapped (frame A) and sputter-coated (frame B) fibers. Results are shown as standard box plots to illustrate the distribution of the mean light yields of the eight fibers of each sample population. Depending on the distance

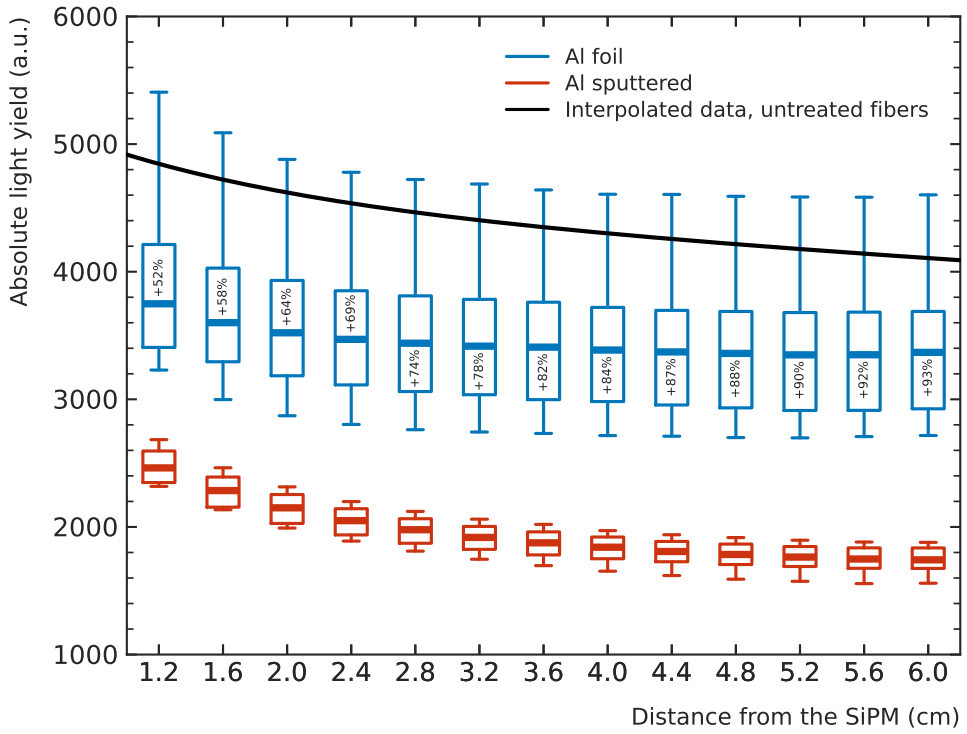

Figure 7.15: Comparison of the absolute light-yield distributions of SCSF-78 fibers wrapped in aluminum foil (frame A) and sputter-coated with aluminum (frame B). The data shown are from all eight fibers in each frame. Whiskers extend to the minimum and maximum value of the respective distribution, boxes extend to the upper and lower quartiles. The black line shows an interpolation of the average data of the untreated fibers shown in Figure 7.13. Adapted from [LPP24].

to the SiPM, the light output of fibers wrapped in aluminum foil is between 52% (at 1.2 cm) and 93% (at 6.0 cm) higher than that of sputter-coated ones. This, however, comes at the cost of larger variations: The average standard deviation of the mean light yield is 17.4 ± 0.4 % and 5.7 ± 0.1 % for foil-wrapped and sputter-coated fibers, respectively—about a factor of three difference. The situation is slightly worse when considering the full range of values at each position: The average difference of the minimum and maximum values relative to the mean of each distribution is 56.7 ± 0.7 % for foil-wrapped samples. At 16.7 ± 1.5 %, the variations for sputter-coated fibers are about a factor of 3.4

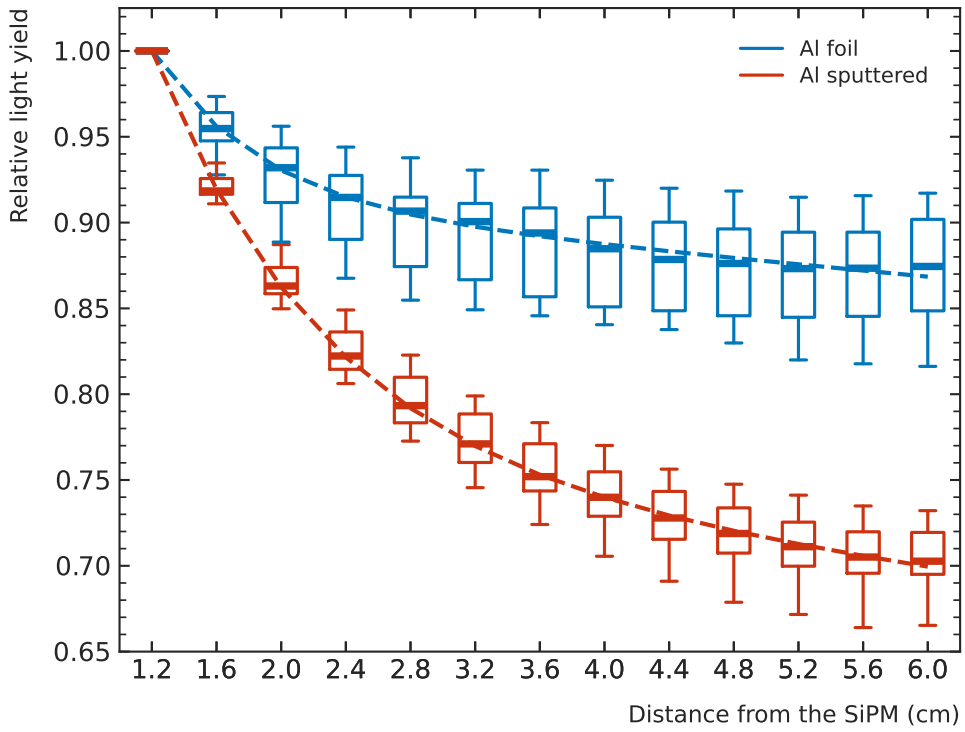

Figure 7.16: Same data shown as in Figure 7.15, but normalized at the position closest to the SiPM (1.2 cm). The dashed lines show fits with a double-exponential attenuation function (Equation 7.8) using the standard deviations of the distributions at each distance as uncertainties. Adapted from [LPP24].

smaller but still significant. The black line in Figure 7.15 is an interpolation of the average data of the untreated fibers in frames D and E, with the outlier of frame C excluded (see Section 7.2.4 for a justification of this exclusion). It reveals that the mean light yield of both sample populations is lower than that of untreated fibers. The light output of some foil-wrapped fibers, however, exceeds that of untreated ones. Figure 7.16 shows the position-dependent relative light yield. For foil-wrapped samples, the yield falls off quickly for short distances but levels off at around 87% for distances larger than 4.5 cm. The sputter-coated samples show a much steeper decrease down to 70% that does not level off in the distance range we studied.

Table 7.3: Results from fitting a double-exponential attenuation function (Equation 7.8) to the relative light-yield distributions of frames A and B (see Figure 7.16). The percentages in parentheses are the relative uncertainties of the parameters.

	Al Foil					**Al Sputtered**				
I_0	1.474	$\pm$	0.076		(5.2%)	1.518	$\pm$	0.133		(0.9%)
Λ_L	98.65	$\pm$	17.52	cm	(17.5%)	54.90	$\pm$	6.10	cm	(11.1%)
Λ_S	0.66	$\pm$	0.07	cm	(10.1%)	1.06	$\pm$	0.03	cm	(2.9%)
α	0.374	$\pm$	0.028		(7.5%)	0.488	$\pm$	0.003		(0.6%)

To quantify the position dependence of the two sample populations, we fitted the data shown in Figure 7.16 with the double-exponential attenuation function of Equation 7.8 using the lmfit package [New+23]. We used the standard deviation of the distribution at each position as uncertainty; since we normalized to the first data point at 1.2 cm, we chose its uncertainty to correspond to the average Gaussian width of the signal-amplitude spectra (see Figure 7.12) and hence set it to 0.1%. The fit results are shown in Figure 7.16 as dashed lines and summarized in Table 7.3, where the percentages in parentheses give the relative uncertainties of the parameter values. The initial photon intensities are larger than unity because we did not normalize at zero distance to the SiPM.

The attenuation lengths for both sample populations are much shorter than reported in the literature (see Table 7.2). The relatively larger attenuation of sputter-coated fibers is mostly reflected in two parameters: a shorter Λ_L (54.90 cm versus 98.65 cm) and a larger α (0.488 versus 0.374), and thus a stronger contribution of Λ_S. The difference in Λ_S further reinforces the impact of the other two parameters but is less pronounced. The fit uncertainties for the sputter-coated samples are generally smaller than those for foil-wrapped fibers. The overall accuracy of our analysis is limited by the fact that we only measured at distances that are about an order of magnitude shorter than Λ_L. We were not able to noticeably improve the fit quality by using attenuation models with fewer or more free parameters (e.g., single- or triple-exponential models).

7.2.4 Discussion of Results

In all tested samples, we expect some light-yield variations to result from the glue coupling between fiber and SiPM, which was not well controlled during

the assembly of our setup. The small variance observed for vapor-coated fibers does, however, show that this effect is likely small. Since such moderate effects can be corrected for if detectors are properly calibrated, we did not study the fiber-SiPM coupling in more detail.

Large reductions of the light yield can occur, however, when glue creeps between the fiber and the material surrounding it, thus destroying the air gap required for internal reflection at the cladding–air interface. This effect explains the untreated fiber with much lower light in frame C (see Figure 7.13): A visual inspection revealed that glue between the fiber and the black POM structure locally replaced the cladding–air interface with a cladding–absorber interface (Figure 7.10h), reducing the efficiency of light transmission and hence the observed light yield. Control measurements with a different set of fibers using beta particles from a ^{90}Sr source confirmed that the light output of untreated fibers (relative to all other treatment options) is in line with the two samples with higher yield. We thus excluded the outlier from further analysis.

The reduced light yield of fibers wrapped in aluminum foil (see Figure 7.15) can be explained analogously. An inspection of many foil-wrapped fibers revealed that in most samples glue had crept between the foil and the cladding. This explains the observed reduction with large sample-to-sample variations instead of the net increase expected in the ideal scenario (depicted in Figure 7.9d). The light output of some samples indeed exceeds that of untreated fibers, confirming the validity of the theoretical scenario and showing that conditions approximating the ideal case can be achieved through careful production. The large variations of the relative light yield (see Figure 7.16) are likely caused by the randomization of reflection angles at the aluminum foil. Likewise, glue creeping between the PTFE tape and the cladding close to the SiPM probably contributes to the observed reduction in light yield of the respective samples in frames C–E. In addition, the application of the tape presumably does not produce a consistent air gap between the cladding and the diffuse-reflecting PTFE, leading to a random mix of the scenarios depicted in Figure 7.10e and f. This might not only explain the relatively high overall light yield but also cause the large sample- and position-dependent variations (see Figure 7.14).

The large reductions in light yield observed for all samples in which we purposely removed the cladding–air interface—i.e., those coated with aluminum or paints—strongly confirm the large contribution of this interface to the light transmission. The paint-coated samples can all be thought of as mixtures between the scenarios depicted in Figure 7.10f and h, with differences primar-

ily stemming from the refractive indices of the paint bases (water-soluble vs. acrylic) and from the optical properties of the pigments (titanium dioxide vs. metallic particles). A visual inspection of the samples indicated that additional variance may be caused by the uneven application of the paints, though its strength relative to the above effects is uncertain.

In sputter- and vapor-coated samples, aluminum atoms are deposited on the cladding surface such that they perfectly follow its microscopic surface roughness, producing a layer that very much acts like an absorber with only little residual (diffuse) reflectivity. Differences lie in the velocity distributions—and hence penetration depths—of the sputtering and evaporation processes [Mat10] and may cause the stronger position dependence of vapor-coated fibers. Despite the larger variance in relative light yield of sputter-coated samples (about 10% at a distance of 6 cm, see Figure 7.16), their smaller overall position dependence (about 30%, compared to almost 50% for vapor-coated ones; see Figure 7.14) makes them the most attractive option for our applications.

Comparison to a Simple Photon Transport Model

To quantitatively assess the role of the cladding–air interface in the light transmission, we determine the theoretical limits to the photon transport in the core and in the cladding and compare them to the fit results summarized in Table 7.3. To do so, we assume that the number of photons arriving at the SiPM is determined purely by the fiber geometry, thus neglecting any losses and inefficiencies. For simplicity, we also assume that for particles traversing the fiber very close to the SiPM, all light emitted towards the sensor (50%) is detected because it covers half the solid angle. To then estimate the fraction of light emitted at some distance d and transmitted in the core to the SiPM (either directly or via internal reflection at the core–cladding interface), we calculate the solid angle covered by a square pyramid (see Appendix C of [BG11]) with opening angles $\varphi_x = \varphi_y = \theta_{\mathrm{CC}}$, where the latter is the critical angle of the core–cladding interface (see Figure 7.17):

$$\Omega_{\mathrm{core}} = 4 \cdot \arcsin\left(\sin\varphi_x \sin\varphi_y\right) = 4 \cdot \arcsin\left(\sin^2\theta_{\mathrm{CC}}\right) \tag{7.9}$$

With $\theta_{\mathrm{CC}} = \pi/2 - \arcsin(n_{\mathrm{clad}}/n_{\mathrm{core}})$ and normalizing to half the solid angle, we obtain the fraction of scintillation light guided to the SiPM in the core:

$$f_{\mathrm{core}} = \frac{\Omega_{\mathrm{core}}}{2\pi} = \frac{2}{\pi} \cdot \arcsin\left(\sin^2\left(\frac{\pi}{2} - \arcsin\left(\frac{n_{\mathrm{clad}}}{n_{\mathrm{core}}}\right)\right)\right) \tag{7.10}$$

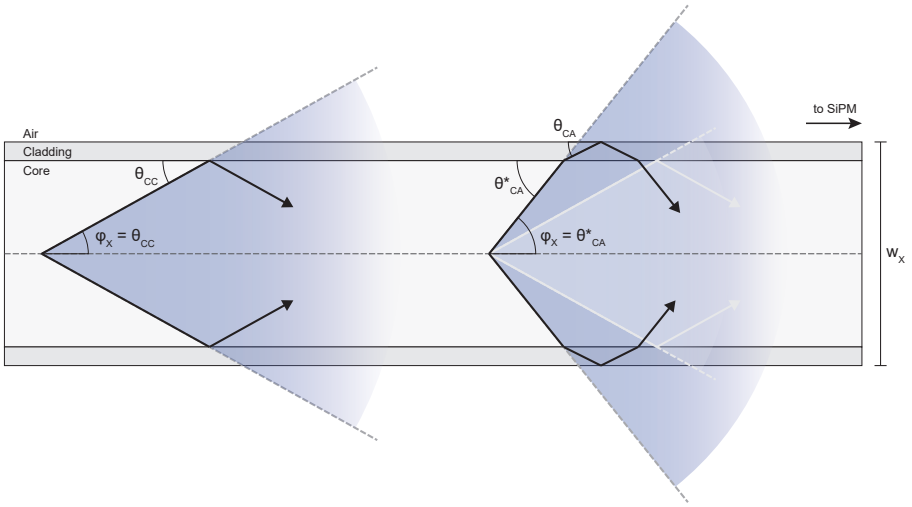

Figure 7.17: Definition of the angle φ_x for reflections at the core–cladding (left) and cladding–air (right) interfaces. φ_y is defined analogously for the other (short) dimension of the fiber. Note that angles are measured from the surface, not from the surface normal [LPP24].

With $n_{\text{clad}} = 1.49$ and $n_{\text{core}} = 1.59$, we obtain $f_{\text{core}} = 7.8\%$. This value is reasonably close to the empirically determined trapping efficiency of 4.2% quoted by Kuraray for long fibers (in which light is mainly transported in the core). For fibers mirrored at the end opposite of the SiPM, Ω_{core} doubles but must be normalized to the full solid angle; the value of f_{core} therefore does not change.

Similarly, we can determine the fraction of light transported in the core *and* in the cladding by calculating the maximum emission angle (in the core) for which photons refracted at the core–cladding interface undergo total reflection at the cladding–air interface. With $\theta_{\text{CA}} = \pi/2 - \arcsin(n_{\text{air}}/n_{\text{clad}})$, we calculate the corresponding angle in the core (see Figure 7.17):

$$\theta^*_{\text{CA}} = \frac{\pi}{2} - \arcsin\left(\frac{n_{\text{clad}}}{n_{\text{core}}} \sin\left(\frac{\pi}{2} - \theta_{\text{CA}}\right)\right) = \frac{\pi}{2} - \arcsin\left(\frac{n_{\text{air}}}{n_{\text{core}}}\right) \tag{7.11}$$

In analogy to Equation 7.10, we then calculate the fraction of scintillation light guided to the SiPM in both core and cladding:

$$f_{\text{core+clad}} = \frac{2}{\pi} \cdot \arcsin\left(\sin^2\left(\frac{\pi}{2} - \arcsin\left(\frac{n_{\text{air}}}{n_{\text{core}}}\right)\right)\right) \tag{7.12}$$

With $n_{\text{air}} = 1$, we obtain $f_{\text{core+clad}} = 41.3\%$. Without attenuation, f_{core} and $f_{\text{core+clad}}$ are constant along the fiber.

At decreasing distance to the SiPM, the maximum emission angle at which photons directly hit the sensor (without reflections) increases sharply and exceeds the critical angles θ_{CC} and θ^*_{CA}, thus dominating the light yield. To assess whether we need to account for this in our model, we calculate the fraction of half the solid angle covered by a square pyramid with base length $w_{\text{x}} = w_{\text{y}} = 2\,\text{mm}$ (ignoring the thickness of the cladding) as a function of the distance to the SiPM, d:

$$f_{\text{direct}} = \frac{2}{\pi} \arctan\left(\frac{w_{\text{x}} w_{\text{y}}}{2d\sqrt{4d^2 + w_{\text{x}}^2 + w_{\text{y}}^2}} \right) \tag{7.13}$$

For f_{direct} to become relevant (larger than f_{core}), d must be less than about 3 mm, and thus much smaller than the distances covered in our measurements. We can therefore assume that the light yield is fully governed by f_{core} and $f_{\text{core+clad}}$.

Finally, we need to scale the initial photon intensities, I_0, of Table 7.3 such that we can compare our fit results for sputter-coated and foil-wrapped fibers to the theoretically derived upper limits of the photon transport. Neglecting attenuation, we assume that the light output of untreated fibers is equal to $f_{\text{core+clad}}$ at the shortest distance covered by our measurements. When normalized to $f_{\text{core+clad}}$, Equation 7.8 evaluated for a treated sample at 1.2 cm distance, $I_{\text{model}}(1.2\,\text{cm})$, must hence be equal to the ratio of the measured light yields of the treated sample population, I_{treat}, to that of untreated fibers, I_{untr}, at 1.2 cm:

$$\frac{I_{\text{treat}}(1.2\,\text{cm})}{I_{\text{untr}}(1.2\,\text{cm})} = \frac{I_{\text{model}}(1.2\,\text{cm})}{f_{\text{core+clad}}} \tag{7.14}$$

Replacing I_{model} with Equation 7.8 in the above expression, we can calculate the scaled values for I_0 that allow us to compare the results presented in Table 7.3 to Eqs. 7.10 and 7.12:

$$I_0 = \frac{I_{\text{treat}}}{I_{\text{untr}}} \cdot \frac{f_{\text{core+clad}}}{((1-\alpha) \cdot e^{-1.2\,\text{cm}/\Lambda_{\text{L}}} + \alpha \cdot e^{-1.2\,\text{cm}/\Lambda_{\text{S}}})} \tag{7.15}$$

The normalization to I_{untr} removes the need for an absolute calibration of our measurements and allows us to ignore the photon detection efficiency of the SiPMs when comparing experimental data to theoretically derived quantities.

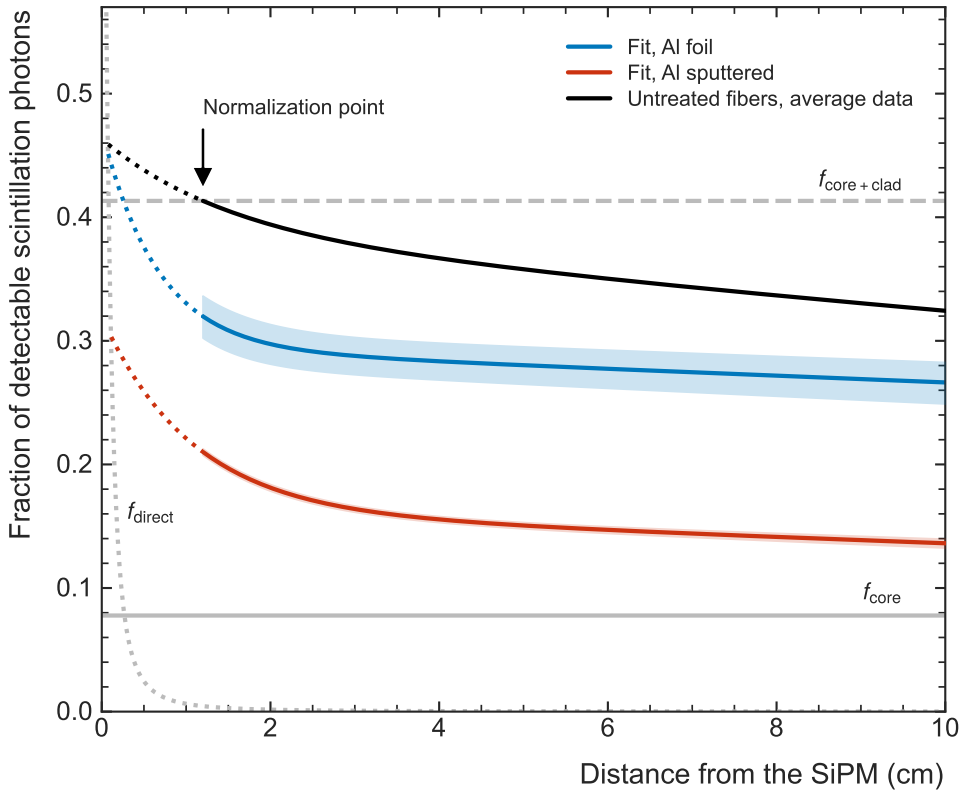

Figure 7.18: Fraction of detectable scintillation photons as a function of the distance of the primary ionization point to the SiPM. The curves for the treated samples are derived from Equation 7.8, with attenuation parameters (Λ_{L}, Λ_{S}, α) obtained by our fits (see Table 7.3) and I_0 scaled via Equation 7.15. The curve for untreated fibers is an interpolation of their average data, matched to $f_{\mathrm{core+clad}}$ at a distance of 1.2 cm. The dotted lines indicate that the extrapolation towards zero distance to the SiPM is for illustration only and is not backed by measurements. Adapted from [LPP24].

Figure 7.18 shows the position-dependent light yield of untreated (frames D and E), foil-wrapped (frame A) and sputter-coated (frame B) fibers in absolute terms—i.e., given as the fraction of detectable scintillation photons as a function of the distance between the point of primary ionization and the SiPM. The curves for the treated samples are derived from Equation 7.8, with attenuation parameters (Λ_{L}, Λ_{S}, α) obtained by our fits to experimental data (see Table 7.3) and I_0 scaled via Equation 7.15. The curve for untreated

fibers is an interpolation of their average data, which we matched to $f_{\mathrm{core+clad}}$ at a distance of 1.2 cm. The extrapolation of all three curves towards zero distance to the SiPM (dotted lines) is for illustration only and is not backed by measurements. Figure 7.18 also shows the theoretically derived fractions f_{core}, $f_{\mathrm{core+clad}}$, and f_{direct}. The results illustrate that the light yield of all three sample populations, though lower than $f_{\mathrm{core+clad}}$, is larger than f_{core} at distances up to 10 cm.

The yield of untreated fibers is more than 25 percentage points higher than f_{core} over the full distance range. This result is roughly in line with measurements performed by Amos et al. [ABL90], who found that in SCSF-81 fibers and for distances shorter than $30\,\mathrm{cm}$ light trapped by the cladding dominates over photons guided in the core alone. It also does not contradict findings for long fibers, in which the cladding–air interface only plays a minor role due to the high density of surface defects of the cladding [Whi+18; Bau+13; Tur+19]. The yield of foil-wrapped fibers is almost 20 percentage points larger than f_{core} at distances between 3 cm and 10 cm, but the large fiber-to-fiber variations—shown as uncertainty band in Figure 7.18—give rise to a 1-σ light-yield uncertainty of 10.6%. In the same distance range, the light output of sputter-coated fibers is only about five percentage points higher than f_{core} but has a lower uncertainty of 2.5%.

Figure 7.18 also illustrates the limitations of our simple model. First, we can only use the data of two untreated fibers for the scaling via Equation 7.15 and therefore cannot calculate reliable uncertainties for I_{untr}. Second, the observed position dependence of their light yield shows that the simplifying omission of attenuation is not generally valid for the distance range we studied. Third, and as a consequence of the previous point, the assumption that the yield of untreated fibers is equal to $f_{\mathrm{core+clad}}$ at a distance of 1.2 cm is flawed and leads to the respective extrapolated curve exceeding $f_{\mathrm{core+clad}}$. The scaling would thus need to be performed as close as possible to the SiPM. Since we lack respective data and did not want to scale using extrapolated models, we chose to accept the uncertainties introduced by the normalization at 1.2 cm. Judging from the extrapolation of the curve for untreated fibers, a normalization at a shorter distance would shift all three curves down by a few percentage points and bring the one for sputter coated-fibers close to f_{core}.

Our simple model demonstrates that internal reflection at the cladding-air interface significantly contributes to light transport in short, cladded scintillating fibers. It also shows that wrapping or coating fibers mostly reduces their light yield, even if only small areas of the cladding surface are altered

(as is the case for foil-wrapped fibers). Measurement uncertainties and model simplifications do, however, limit the accuracy of quantifying these findings.

Conclusion

We demonstrated that reflections at the cladding–air interface significantly contribute to the transport of photons, and hence to the light yield, in short scintillating-plastic fibers. Consequently, we can state that attenuation in short fibers is largely caused by extrinsic effects (i.e., reflection losses) at the outer cladding surface. Though we only tested square samples with a thickness of 2 mm, this finding is applicable to fibers of any shape and diameter. Though not experimentally verifiable based on our measurements, this large contribution of the cladding casts doubt on the assumption that single-cladded and multi-cladded fibers exhibit the same attenuation behavior, at least at short distances. Our results also indicate that models with more free parameters than Equation 7.8 are likely needed to describe the light yield of fibers over long distance ranges.

We found that sputter-coating fibers with aluminum to suppress optical crosstalk gives the most consistent results while being the easiest to achieve. Alternative coatings involving paints of various kinds result in clearly inferior performance. Though wrapping fibers in aluminum foil or PTFE tape leads to a higher overall light yield, it comes at the cost of a significantly larger variance and thus a reduced energy resolution. Only fibers vapor-coated with aluminum deliver a comparable yield and uniformity, though some samples show a larger variance and many were unusable due to production issues. The latter problem may be addressed by using processing parameters better adapted to plastic fibers. Vapor deposition has, for example, successfully been used for bulk scintillators [Kre+05], for which the surface quality may have been more suitable to the deposition process than the relatively inhomogeneous outer surface of cladded fibers.

Our studies are limited by the small number of samples we tested—three for each sample population in frames C–E and eight for those in frames A and B. These limits were imposed by the available measurement time at PSI and the small geometrical acceptance, and hence low count rates, of our experimental setup. The superiority of sputter-coated over foil-wrapped fibers was, however, established using the larger sample populations of frames A and B and is statistically significant. Here, the decisive factor is the smaller light-yield variance of the former, which facilitates the calibration of detectors. For applications that require precise energy resolution, the individual characterization of at least a subset of the fibers used may still be required to study the remaining variation resulting from the coating process. We also did not

study the effect of the coating on the spectrum of the photons arriving at the SiPM, which has a wavelength-dependent detection efficiency. Our results may thus slightly change quantitatively, though likely not qualitatively, if different photodetectors are used.

7.2.5 Discussion in the Context of the RadMap Telescope

Despite the associated lower light yield, our investigation clearly identified sputter coating as the best approach for crosstalk suppression. Especially for the ADU of the RadMap Telescope, we can safely trade a fraction of the light output for a superior uniformity because even for sputter-coated fibers, minimum-ionizing particles will generate signals well above the dark count spectrum of SiPMs. Because an aluminum layer of about 100 nm is sufficiently light-tight to suppress all crosstalk, the process also adds only minimally to the thickness of the fibers (in contrast to wrapping them with foils or tapes, or coating them with paint). This has two advantages: (1) It only adds little insensitive material between fibers and (2) allows us to tightly pack them in their holding structure. These aspects are advantageous for achieving good energy and tracking resolutions, respectively.

Our study also demonstrates that achieving a high energy resolution in our detectors requires careful calibration of the strong position dependence of the light yield in the scintillating fibers. This is nicely illustrated by Figure 7.18, which shows that the fraction of detectable scintillation photons arriving from an interaction site at the far end of a fiber is more than 50% smaller than for a particle crossing close to the photosensor. Using the detected signal amplitudes in their uncorrected form would thus lead to huge uncertainties in determining the particle energy.

Furthermore, our data shows that there are fiber-to-fiber variations of the light yield on the order of a few percent. While these may seem somewhat large at first, it is important to keep in mind that our goal is to perform an event-by-event analysis of the data recorded by the RadMap Telescope. This entails that the fiber-to-fiber variations must be compared to event-level variations, most importantly to the magnitude of energy straggling. An illustration of the latter is given in Figure 7.12, which shows a representative signal-amplitude spectrum of a single fiber with a FWHM of some 48%. The average event-to-event variation of the energy loss of particles with identical energy is therefore an order of magnitude larger than mean variation caused by the sputter-coating process.

Despite these encouraging results, it is nonetheless necessary to perform a careful light-yield calibration of every fiber in a fully assembled detector for several reasons:

1. Even though the standard deviation of the mean light yield is small compared to energy straggling, the average minimum–maximum variations—which is the more relevant quantity—are about 16.7% and thus significant. Figure 7.15 also shows that the outliers are systematically asymmetric, possibly hinting at single fibers with significantly different quality. Lacking an empirical proof for this hypothesis, the best approach is to determine the position-dependent light yield of each fiber.
2. The optical coupling between fiber and SiPM depends on the properties of the glue, which may differ from production batch to production batch. Though we use the same glue used here (EPO-TEK® 301) for the production of the final detectors, we have not systematically studied its influence on the light yield.
3. We also did not perform a systematic study of production variations. All tested samples were sputter-coated in a single batch, which is not possible for the number of fibers needed to produce full detectors (given the limitations of the machinery). It is therefore possible that larger variations occur if fibers from different production runs are used. They may even be larger if fibers are coated on different machines.
4. Last but not least, a reduction of the light-yield uncertainty to negligible levels simplifies the uncertainty propagation in the final data analysis.

Based on the results of this study, we thus determined that a detailed calibration of all detector modules is required (see Section 8.5).

Concluding Remarks

The two studies presented in this chapter show how crucial a detailed understanding of the scintillating-fiber properties is for the interpretation of data gathered with the RadMap Telescope's ADU. Without a careful light-yield calibration, no energy measurement with acceptable resolution is possible, no matter the energy or charge of the particle traversing the detector. Ionization quenching, on the other hand, somewhat influences measurements at the energy-loss densities of protons but becomes disproportionately more important for ions with higher charge. It is exactly in this regime that no systematic studies of the quenching behavior of our fibers (or any others, for that matter) exist yet, though investigations of some inorganic scintillators seem to show that an extrapolation from protons to heavy ions is hardly straightforward. It is thus imperative that such studies be conducted to enable high-precision measurements of heavy-ion fluxes with the tracking calorimeters we develop.

Chapter 8

Flight Detector Design, Test, Production, and Calibration

In the previous two chapters, I summarized the many lessons we learned from constructing and testing prototype detectors, as well as from measurements that furthered our understanding of the various factors affecting the light yield of scintillating fibers. In this chapter, I describe how we incorporated these lessons into the final design of the flight detectors for the RadMap Telescope. Using a simple sensitivity analysis, I also highlight what measurement range and accuracy we expect the instrument to achieve. Lastly, I summarize the tests we conducted to ensure that the detector design meets our requirements in terms of energy resolution and tracking performance.

8.1 Mechanical and Electrical Design

One of the most important lessons we learned while integrating the 900-channel prototype for the stratospheric balloon flight (see Section 6.5) was that using a common support structure for all scintillating fibers is a bad idea, as a single issue during the integration process can render the full detector unusable. Insufficient manufacturing precision—especially when using a 3D-printed structure—can lead to cumulative offsets that not only affect the assembly process but also the final placement of the fibers. The biggest design change we introduced was therefore the division of the detector into four modules of equal size and design. These modules are stacked between two aluminum frames that are held together by four long screws (see Figure 8.1).

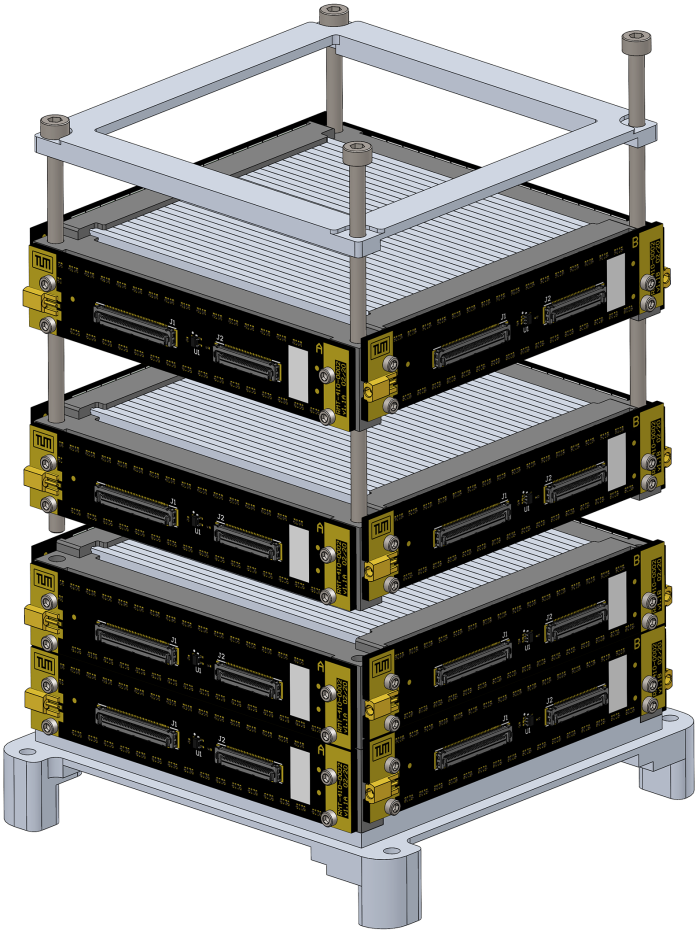

Figure 8.1: Stacking of four 256-channel tracking-calorimeter modules between two aluminum frames for the RadMap Telescope's Active Detection Unit (ADU). The frames are held together by four long screws. The assembled detector is mounted to the instrument's structure via feet on the lower aluminum frame.

The assembled detector is mounted to the instrument's structure via four feet on the lower aluminum frame. One of the biggest challenges of this approach is to ensure not only that the modules can be joined together with high precision but also that, ideally, the spacing between the upper and lower layers of adjacent modules is equal to the layer spacing within each module. The other is to ensure that fibers are well centered on their SiPMs.

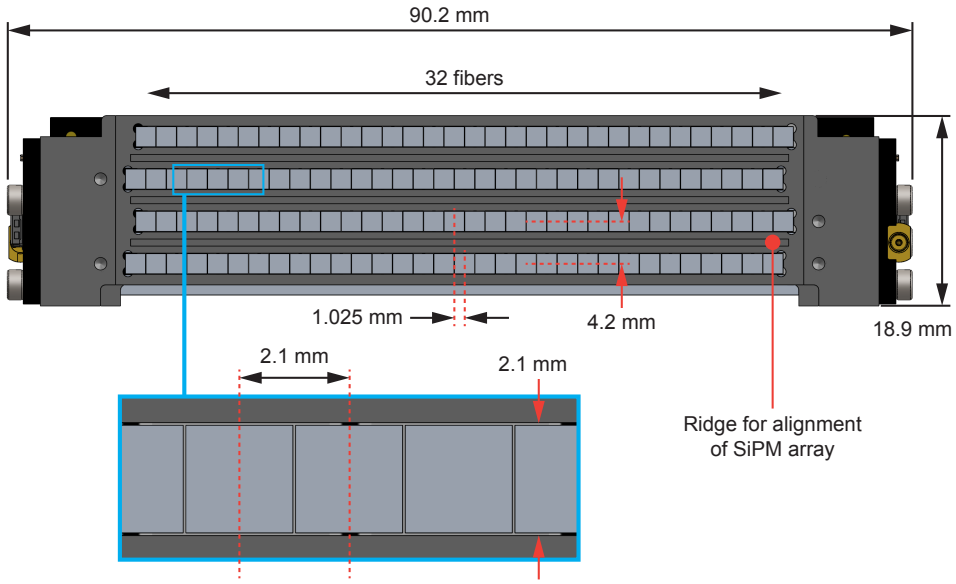

Figure 8.2: Arrangement of fibers in a 256-channel tracking-calorimeter module. Each module has eight layers, with every second one rotated by 90 degrees. The arrangement in the orientation not shown here is identical but shifted down by 2.1 mm.

We introduced other design changes as well, most notably the slight enlargement of each fiber array from 30 to 32 fibers. This we did mainly to better match the number of fibers (and hence sensors per SiPM array) to the number of read-out channels of typical ASICs, which usually is a power of two. Another major change was the shift of each second layer of an orientation, which I introduced in Section 6.3.2, but which we had never implemented in a full-scale detector or prototype before.

8.1.1 Module Design

Each of the four modules shown in Figure 8.1 comprises 256 scintillating fibers of type SCSF-78 with a square cross-section of $2 \times 2\,\mathrm{mm}^2$ and a length of 80 mm. The fibers are sputter-coated with aluminum for crosstalk suppression, with only one end open for the detection of scintillation light via SiPMs. They are arranged in eight layers of 32 fibers each, with every second layer rotated by 90 degrees. As mentioned above, every second layer of each orientation

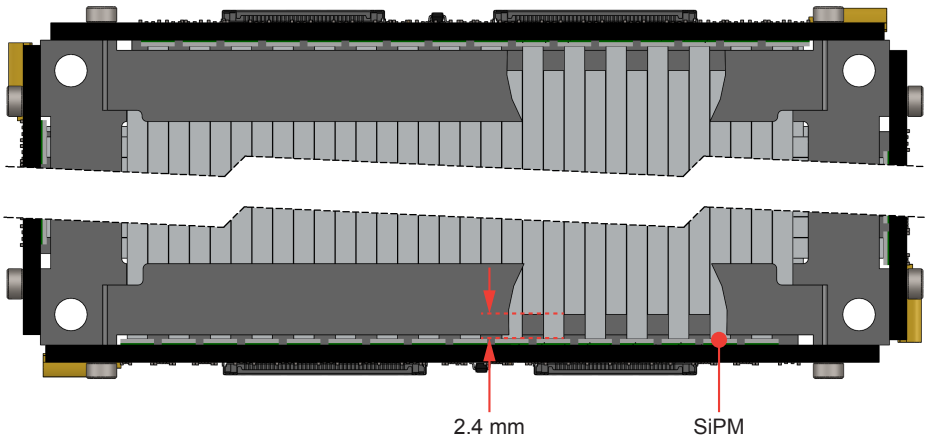

Figure 8.3: Cut-away view of the uppermost fiber layer to reveal the alternating placement of SiPMs at opposite ends of each layer. Such arrangement allows for the use of sensors with a $3 \times 3\,\mathrm{mm}^2$ active area, significantly relaxing the requirements for aligning fibers and SiPMs.

is shifted by half the intra-layer fiber distance (see below) to increase the detection efficiency.

The fibers are held in a single plastic structure, which also provides the mounting points for the SiPM arrays and the features required for precisely joining together multiple modules. The structure has a frame-like layout, with slots for each layer on opposite sides of it (see Figure 8.2). The fibers are therefore held only at their ends, and the region where the layers of different orientation overlap is completely free of additional material. The slots have dimensions of $65.6 \times 2.1\,\mathrm{mm}^2$, which for each fiber translates into 2.05 mm and 2.1 mm room in the horizontal and vertical direction, respectively. These clearances are to account for the 2% variation of the fiber thickness stated by the manufacturer [Kur14], for the additional thickness of the aluminum coating, as well as to absorb any manufacturing tolerances. The intra-layer fiber spacing is hence 2.05 cm, and neighboring layers of the same orientation are shifted by 1.025mm against each other. In vertical direction, the layers are spaced 2.1 mm apart, such that the distance between two layers of the same orientation is 4.2 mm. The fibers are read out on alternating sides of each layer (see Figure 8.3) to allow for the use of SiPMs with a $3 \times 3\,\mathrm{mm}^2$ active area, which significantly relaxes the requirements for aligning fibers

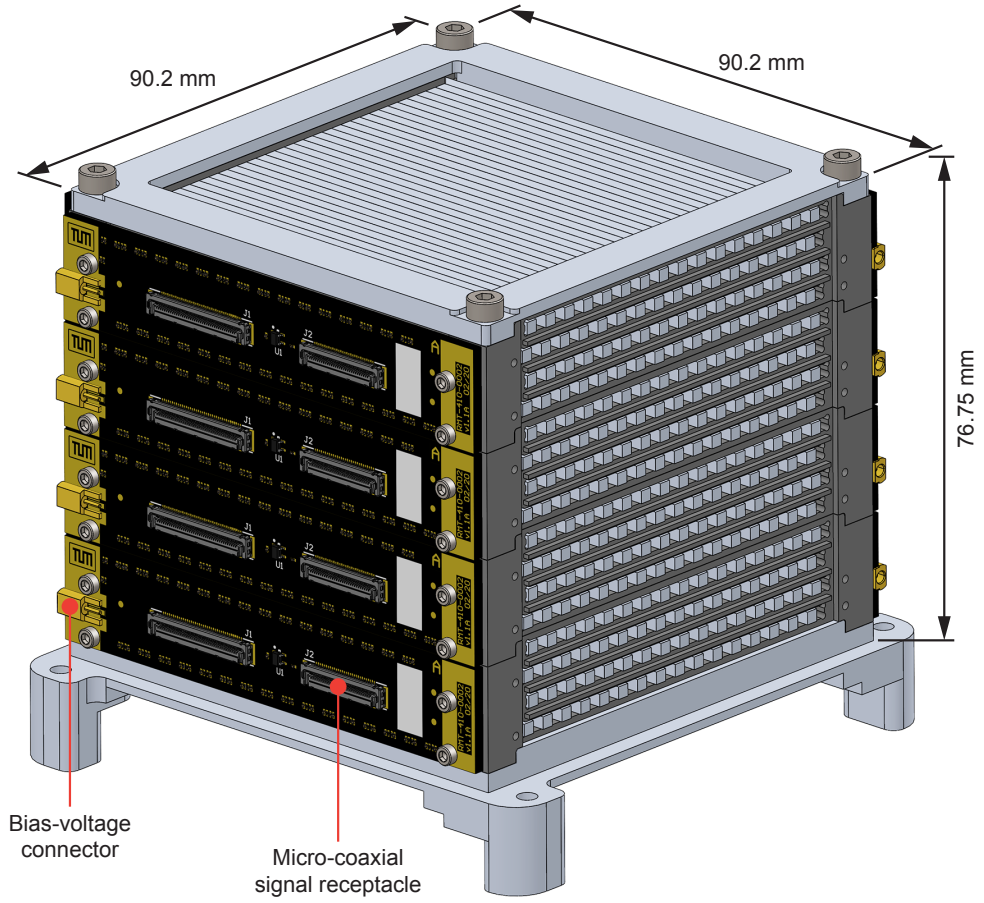

Figure 8.4: Dimensions of the fully stacked RadMap Telescope ADU. The four SiPM arrays on the right are not shown to reveal the scintillating fibers. Only every second fiber is visible because the others are recessed and read out on the opposite side of the detector (see Figure 8.3). The vertical dimension does not include the mounting feet because they are application-specific and are not required for mechanical integrity of the detector itself. The horizontal dimensions include the screws that hold the SiPM arrays. The micro-coaxial signal connectors add about 2.4 mm to the overall horizontal dimensions when plugged into the receptacles.

and photosensors. Fibers read out at the opposite end are recessed by 2.4 mm, preventing glue from forming a light guide between them and the SiPMs. This is to reduce the crosstalk intensity in case their end faces are not fully light tight—e.g., due to scratches or insufficiently thick coating.

The plastic support structure is designed for a gap-less stacking of the modules—i.e., the layer-to-layer distance is the same throughout the detector. The challenge of this design is that the material holding the uppermost and lowermost layers is just 1 mm thick. We initially attempted additive manufacturing using various high-resolution 3D printers, but achieved only mixed results. Most problems we encountered were related to the discrete steps in printing resolution; others were due to deformations upon removing the necessary supports (see Figure 8.5). We then attempted machining with a five-axis CNC mill and found that this 'traditional' manufacturing approach is in principle feasible. The only challenge was the choice of material. To comply with the outgassing and flammability requirements of the ISS program, we initially tried PTFE. Its high elasticity and softness, however, make it difficult to machine and led to significant smearing and deformation of the thinnest parts of the structure (see Figure 8.5). We encountered similar problems with POM, despite its generally better machinability. Ultimately, we found that ABS behaves exceptionally well in our case. After realizing that we needed a safety exception for the use of flammable PS-based scintillating fibers anyway, we thus settled on machining the support structure from black ABS. We also received approval for using it on the space station from the NASA safety engineers, primarily because the total mass of the four structures is only about 83 g and hence well below the limit for 'safety-critical' classification. A similar exception for the use of 358 g of scintillating fibers was made on the same grounds.

8.1.2 SiPM Arrays

The scintillating fibers are read out individually by SiPMs with a sensitive area of $3 \times 3\,\mathrm{mm}^2$. To avoid saturation effects, we chose a microcell pitch of 25 µm, which means that the $2 \times 2\,\mathrm{mm}^2$ end face of a fiber is covered by about 6 400 cells. Assuming that light is only transported in the core (because we destroy the cladding–air interface in the sputter-deposition process, see Section 8.2 below), we expect a light yield of about 134 photons for a MIP with an energy loss of 0.2 MeV/mm traversing a fiber transversally, that is, along one of its short dimensions (see Section 6.3.1). Based on a maximum ΔE_{vis} of 15 MeV for iron nuclei at transversal incidence (see Figure 6.11), this translates into

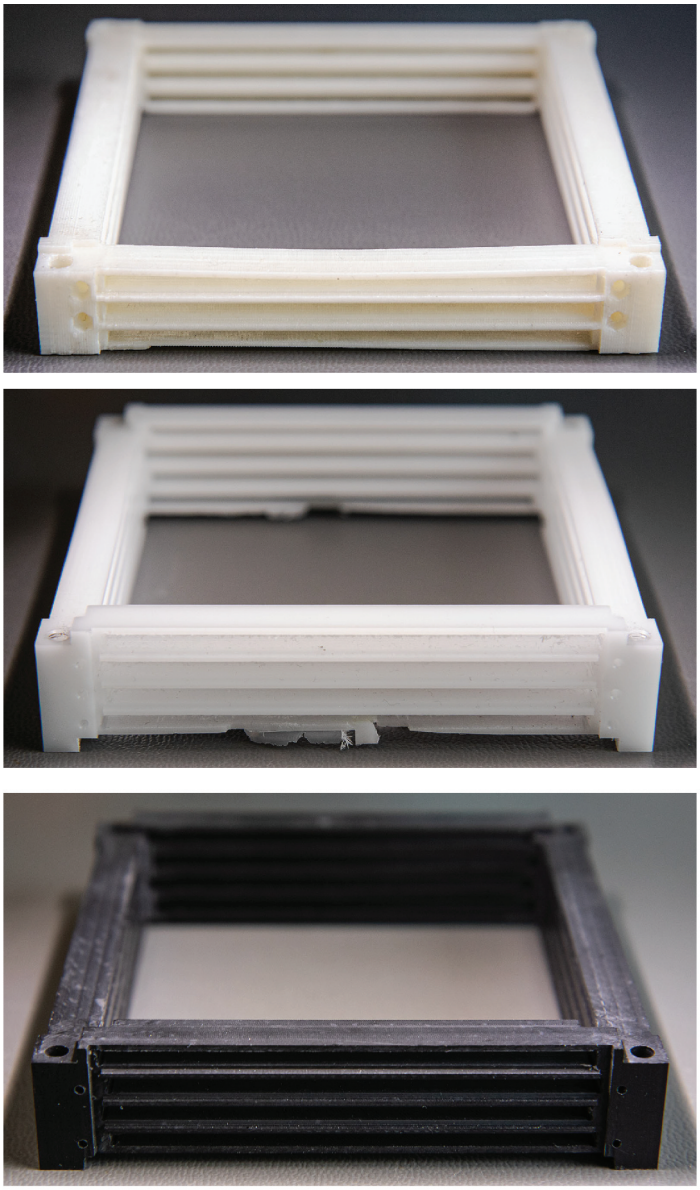

Figure 8.5: Evolution of the plastic support structure holding the SiPMs: initial 3D-printed variant with clearly visible deformations (top), version machined from POM with deformations and material smearing (middle), and final variant machined from ABS (bottom).

Table 8.1: Characteristics of the PM3325-WB-D0 SiPM [KET18].

Parameter		**Value**	**Unit**
Active area		3.0×3.0	mm^2
Microcell pitch		25	μm
Number of microcells		13,920	
Breakdown voltage (V_{br}) at $21\,^{\circ}\mathrm{C}$		min. 24.0, max. 25.0	V
Variation of V_{br}		± 0.125	V
Temperature dependence of V_{br}		22.0	mV/K
Recommended overvoltage (V_{ov})		2.0 to 5.0 (max. 6.0)	V
Gain	at $V_{\mathrm{ov}} = 2.5\,\mathrm{V}$	0.87	$\cdot 10^6$
	at $V_{\mathrm{ov}} = 5.0\,\mathrm{V}$	1.74	$\cdot 10^6$
Temperature dependence of gain		0.3	%/K
Terminal capacitance		1	nF
PDE at 430 nm	at $V_{\mathrm{ov}} = 2.5\,\mathrm{V}$	31	%
	at $V_{\mathrm{ov}} = 5.0\,\mathrm{V}$	45	%
Dark count rate	at $V_{\mathrm{ov}} = 2.5\,\mathrm{V}$	50	$\mathrm{kHz/mm}^2$
	at $V_{\mathrm{ov}} = 5.0\,\mathrm{V}$	125	$\mathrm{kHz/mm}^2$
Dark current	at $V_{\mathrm{ov}} = 2.5\,\mathrm{V}$	0.15 (max. 0.2)	μA
	at $V_{\mathrm{ov}} = 5.0\,\mathrm{V}$	0.7 (max. 1.0)	μA
Crosstalk probability	at $V_{\mathrm{ov}} = 2.5\,\mathrm{V}$	12	%
	at $V_{\mathrm{ov}} = 5.0\,\mathrm{V}$	26	%
Afterpulsing probability	at $V_{\mathrm{ov}} = 2.5\,\mathrm{V}$	1	%
	at $V_{\mathrm{ov}} = 5.0\,\mathrm{V}$	5	%

an upper limit of 5 025 detectable photons. A PDE of 45% then results in a dynamic range of 60 (for MIPs) to 2 262 (for iron nuclei) photoelectrons—i.e., 1% to 35% of the microcells covered by a fiber give a signal for particles with transversal incidence. This, of course, does not take into account that the path length of particles can be much longer than 2 mm, and the amount of light produced correspondingly larger. Using a Geant4 simulation that subjected the detector to an omnidirectional flux of MIPs, we showed that path lengths between zero and 4 mm—twice the fiber thickness—account for more than 95% of all particle tracks. This extends the upper end of the dynamic range to about 70% of the available (i.e., exposed) microcells, for which we do not

expect significant saturation. The tail of the path-length distribution is rather flat beyond this point, and covering it completely would require choosing SiPMs with the smallest microcell pitch available, at the cost of a substantially reduced PDE. This would in turn lead to a reduced sensitivity and resolution for MIP-like particles, which make up the majority of the cosmic-ray spectrum and are thus essential to our measurements.

Our analysis of the light yield of sputter-coated fibers (see Section 7.2) furthermore showed that the number of photons arriving at the SiPM can be significantly higher than for transmission in the core alone if a particle traverses a fiber close to the photosensor. When accounting for the systematic normalization offset, Figure 7.18 in particular shows that the light output of coated fibers is essentially dominated by reflections at the core–cladding interface for distances from the SiPM greater than about 3 cm, thus validating the above calculation of the dynamic range. It can, however, be roughly twice as high very close to the SiPM. For highly non-transversal tracks and for particles hitting a fiber very close to its SiPM, saturation effects can hence become significant. However, the rate of occurrence of such events is so low that we chose not to sacrifice sensitivity at the lower end of the energy-loss spectrum to account for them.

The only other strict requirement was that the SiPMs must have a (nearly) symmetric package that is only slightly larger than their sensitive area. Otherwise, the tight packing of fibers would not have been possible, even when reading them out at alternating ends. At the time when we finalized the ADU design, the only product with a 25-μm microcell pitch fulfilling this requirement was the PM3325-WB-D0 SiPM manufactured by KETEK GmbH [KET18], whose characteristics are summarized in Table 8.1. At $3.315 \times 3.315\,\mathrm{mm}^2$, its packaging is only slightly larger than its sensitive area. This is made possible by the replacement of bond wires used on older generations of sensors with a grid-like structure, which comes at the cost of 480 fewer microcells at the outer edges of the sensitive area (where it is irrelevant to our application).

The 256 scintillating fibers in each tracking-calorimeter module are read out by four 64-channel arrays of PM3325 SiPMs that are attached directly to the plastic support structure. Figure 8.6 shows how the photosensors are arranged in four rows on each array, accounting for the shift of every second fiber layer by half the intra-layer fiber distance. The bias voltage (supplied via one miniature SSMCX coaxial connector) is common to all sensors but is filtered via individual R–C–filters (51 Ω resistance, 10 nF capacitance) placed

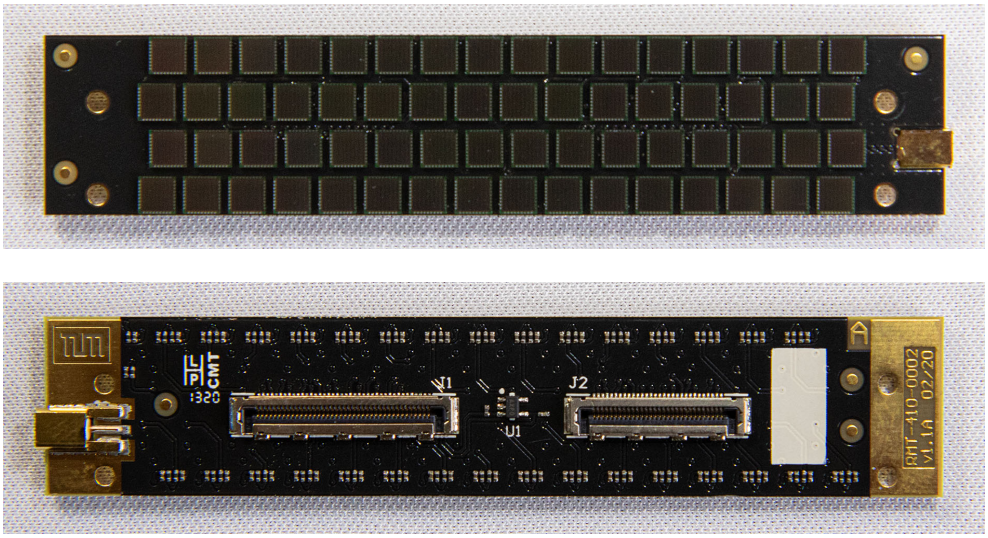

Figure 8.6: 64-channel array made of KETEK PM3325-WB-DO SiPMs. Top: The photosensors are arranged in four rows, accounting for the shift of every second fiber layer by half the intra-layer fiber distance. Bottom: The bias voltage common to all sensors is supplied via one SSMCX connector (left); the unamplified signals are routed to one 50-pin and one 30-pin micro-coaxial connector (center). The IC at the center of the array is a MCP9700A analog-output temperature sensor.

close to the anode[1] of each SiPM. The unamplified signals are routed directly to one 50-pin and one 30-pin receptacle for the micro-coaxial cables used to transmit them to the front-end electronics. In addition, each array has a single Microchip MCP9700A analog-output temperature sensor [Mic21] at its center. The arrays are mounted to the support structure via four M1.6 screws.

8.2 Production of Scintillating Fibers

Our studies of different options for preventing optical crosstalk revealed that sputter-coating them with a thin aluminum layer was not only the best one but also the easiest one to achieve (see Section 7.2). Preparing the fibers for integration into the detector modules was nevertheless a time-consuming effort

[1]The SiPMs are biased with a negative voltage, see Section 10.5 for details.

that required great care. After initial tests with small sample populations, we settled on the following seven-step production process:

Step 1: Cut pieces of about 86 mm length from the coil of SCSF-78 fiber. To keep the mechanical stress on the fibers minimal[2], we used cutters with one flush and one angled edge. Most stress is imparted by the angled edge; during cutting, the flush edge must thus always point to the piece of fiber that is to be used. This requires the cutting of short waste pieces of roughly 10 mm length.

Step 2: Remove the curvature of the fiber pieces by heating them between two aluminum plates to a temperature of 60 °C for four hours. We chose this lower temperature because we discovered that heating to 80 °C (which we previously had done, see Section 6.5) resulted in irregularities on the aluminum surface being imprinted on the cladding.

Step 3: Polish the fibers to the final length of 80 mm. Polishing was done in batches of 255, with the fibers stacked into and held by a support structure of the desired length.

Step 4: Clean the fibers with isopropyl alcohol to remove residue of the polishing paste, as well as any other contamination that may prevent the aluminum layer deposited during the sputter-coating process from sticking. Usually, scintillators must not be cleaned with alcohol because it evaporates at room temperature. The evaporation causes the plastic surface to rapidly cool down, forming microscopic cracks in the process. Acting as scattering centers, these cracks diminish the light yield of the scintillator. This would also apply to the cladding–air interfaces of the fibers. The sputtering process, however, destroys this interface anyway; on the end face where the SiPM is attached, glue fills up any cracks that may form. Using alcohol for cleaning is thus not an issue in our case.

Step 5: Cover one end of each fiber with polyimide (Kapton) adhesive tape to prevent it from being coated with aluminum during the sputter-deposition process. The piece of tape must not be much larger than the $2 \times 2\,\mathrm{mm}^2$ end face to avoid shadowing effects.

Step 6: Sputter-coat the fibers with aluminum of at least 100 nm thickness to ensure the layer is fully opaque.

[2] To ensure, for example, that the adhesion between fiber core and cladding is not weakened.

Step 7: Remove the polyimide tape covers.

Figure 8.7 shows fibers after each production step. Our initial tests showed that we had to expect that at least 10% to 15% of the fibers would have serious production flaws that rendered some unusable. Most of these were either due to peeling of sections of the cladding after polishing or due to large portions of the aluminum coating flaking off. The former was clearly attributable to the mechanical stress and vibrations induced during polishing; the most likely explanation for the latter was remaining contamination of the cladding surface after cleaning.

8.2.1 Module Assembly

The assembly of the ADU modules was performed completely manually, as a semi-automatic production was neither deemed feasible nor necessary. After inserting fibers into the support structure, we used plastic tools (to avoid scratching the coating) to pull each fiber out of its final position by a few millimeters, always on the side where it would be read out. We did this to address the main challenge of mounting the SiPM arrays, namely to ensure that each fiber end is in close contact with its photosensor. Since the friction between them hardly allowed us to move single fibers without changing the position of those surrounding it, we needed to attach the arrays on opposite sides of the detector at the same time. After pulling out the fibers on each layer, we thus loosely attached the two arrays on long screws that acted as guide rails (see lower picture of Figure 8.8). We then pushed them onto the fiber ends and into their intended position, after which we swapped the long screws for shorter ones to hold the arrays in place. This approach ensured that all fibers were pushed back into a final position where they were in contact with the SiPM surface at the same time.

To ensure good optical coupling between fibers and SiPMs, we used EPO-TEK® 301 epoxy, which has a NASA-certified low-outgassing classification [Epo23]. We applied a drop of epoxy onto each SiPM prior to the installation of an array on the guide screws. The surface tension of the glue was high enough to keep it in place during the assembly process (see upper picture of Figure 8.8). The epoxy not only ensures good optical contact but also provides additional mechanical stability because it creeps between adjacent fibers due to capillary action. Though this is advantageous from a structural point of view, it also means that an optical path is provided for photons that inadvertently leave

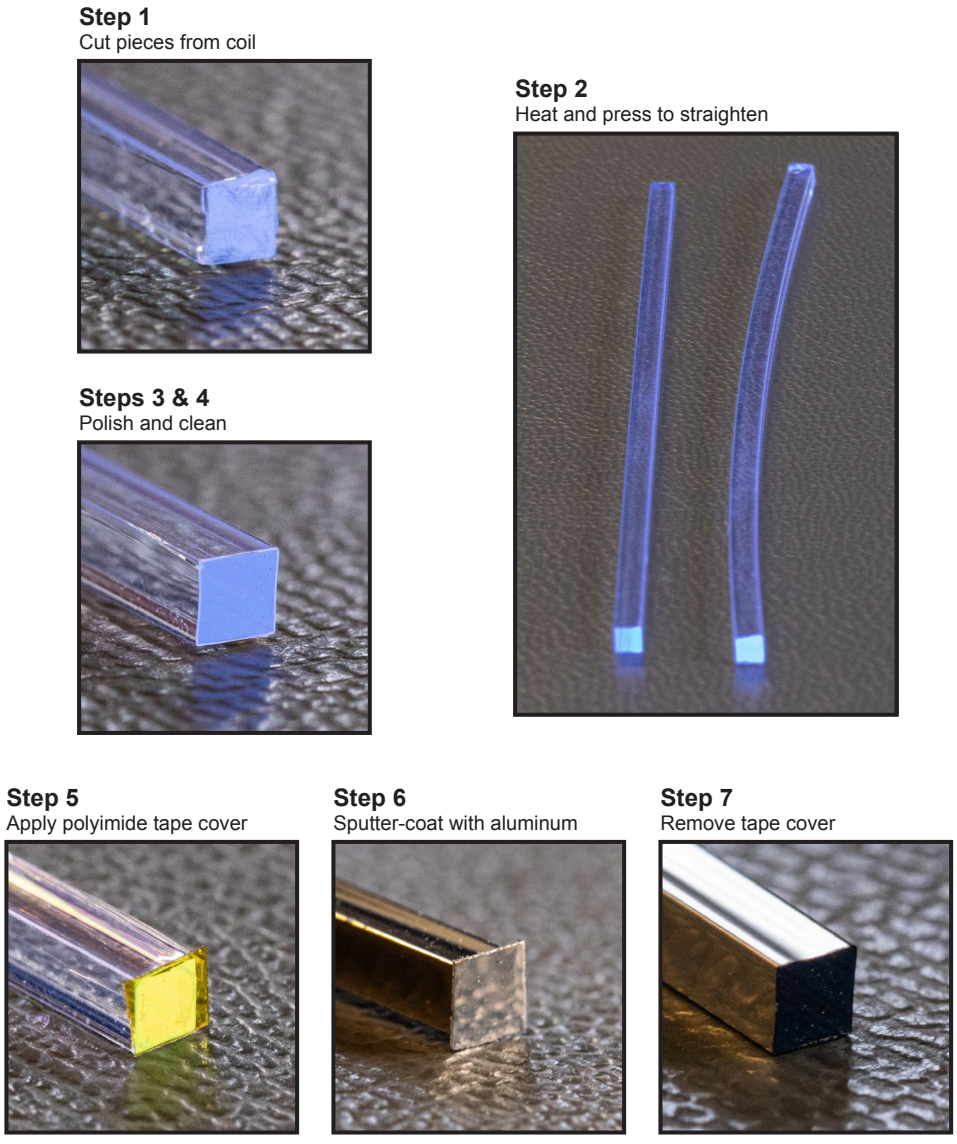

Figure 8.7: Fibers after each of the seven production steps.

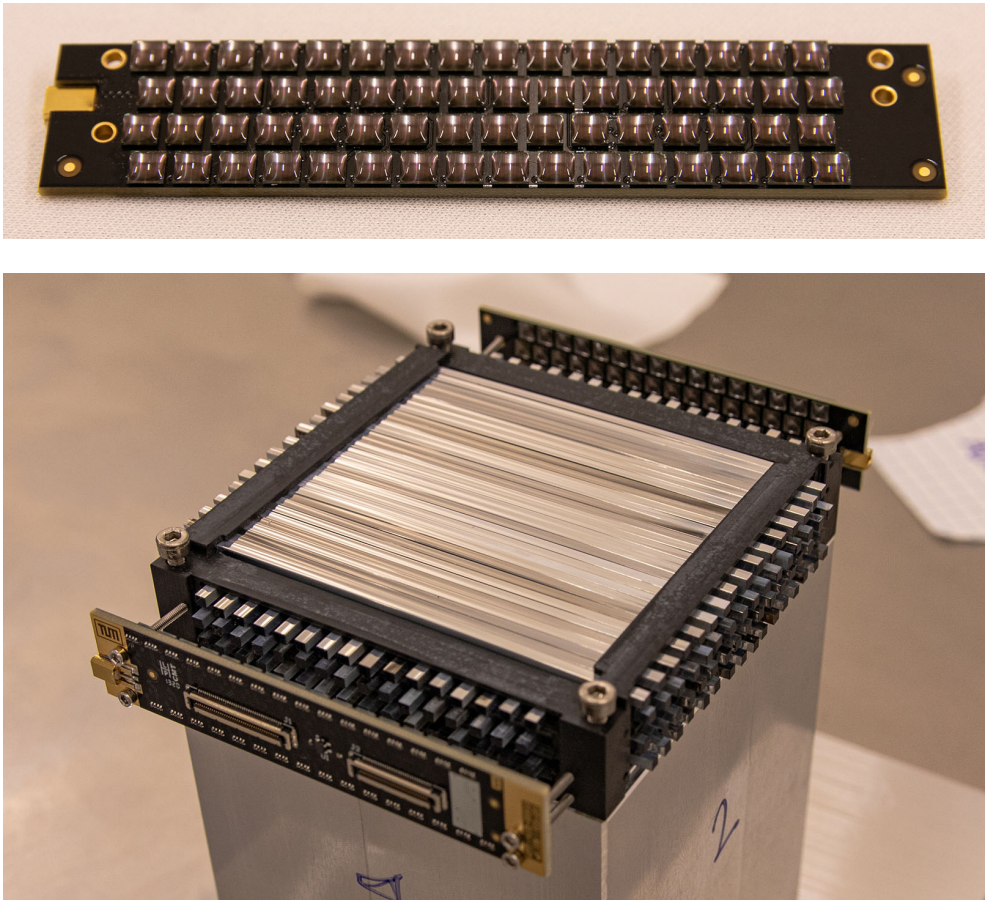

Figure 8.8: Assembly of the tracking-calorimeter modules for the RadMap Telescope's ADU. Top: Drops of EPO-TEK® 301 epoxy on the individual sensors of a SiPM array. Bottom: SiPM arrays on guide screws prior to pushing them into their final position.

a fiber due to defects in the coating, thus enhancing optical crosstalk. Similarly, the glue creeps between adjacent photosensors, creating an optical channel for photons that are reflected and scattered at a SiPM's surface [TRE22]. With the dense packing of fibers we wanted to achieve, these effects are unavoidable. After installation of all four SiPM arrays, we heated the modules to 60 °C for two hours to cure the epoxy.

8.3 Prototype Tests

To validate the major changes we implemented in the design of our tracking calorimeter concept for the RadMap Telescope's ADU, we initially assembled a single 256-channel module. This not only allowed us to try out the various production and assembly processes, but also to qualify the detector's performance. For the latter, we performed another test campaign at the πM1 beam line of PSI, which we had previously used for testing all our prototypes.

This time, our experimental setup was centered around a mechanical support for the ADU module that allowed to move and turn it in the beam (see Figures 8.9 and 8.10). The system had four degrees of freedom (two translations and two rotational ones): Its base was a rotary table that allowed to rotate the rest of the assembly around the vertical axis. Mounted on top of it were two linear axes that allowed to translate the detector laterally to the beam in both horizontal and vertical direction. Finally, the module was mounted to vertical axis via a miniature rotary stage that enabled horizontal rotations. The system thus provided all degrees of freedom required for validating the detector's ability to track charged particles with isotropic incidence. To constrain the trajectory along which particles traverse the module, we used the trigger detectors consisting of two overlapping scintillating fibers (one horizontal, one vertical) that we previously used for our coating studies (see Section 7.2). We thus effectively selected a $2 \times 2\,\mathrm{mm}^2$ portion of the beam, which gave us ample spatial accuracy for testing the detector's capabilities. The setup was again placed in a light-tight vessel, though we did not operate it under vacuum.

To digitize the signals of all 256 SiPMs simultaneously, we used a larger but functionally equivalent version of the multichannel sampling ADC that we had previously used for prototype tests [Man+09].[3] This data-acquisition system was triggered externally by the two trigger detectors. We again used shaping amplifiers (based on the same design we implemented before) to match the SiPM signals' length and amplitude to the input characteristics of the ADCs.

The primary objectives of the test campaign were (1) to assess the channel-to-channel signal variations, (2) to measure the crosstalk probability for each channel, (3) to confirm the module's ability to track charged particles, and (4) to quantitatively assess the achievable angular resolution. For these investigations, we used a beam of negative, minimum-ionizing pions with a momentum of 450 MeV/c. In addition, we recorded a limited amount of data

[3] The system was graciously lent to us by the NA64 collaboration at CERN.

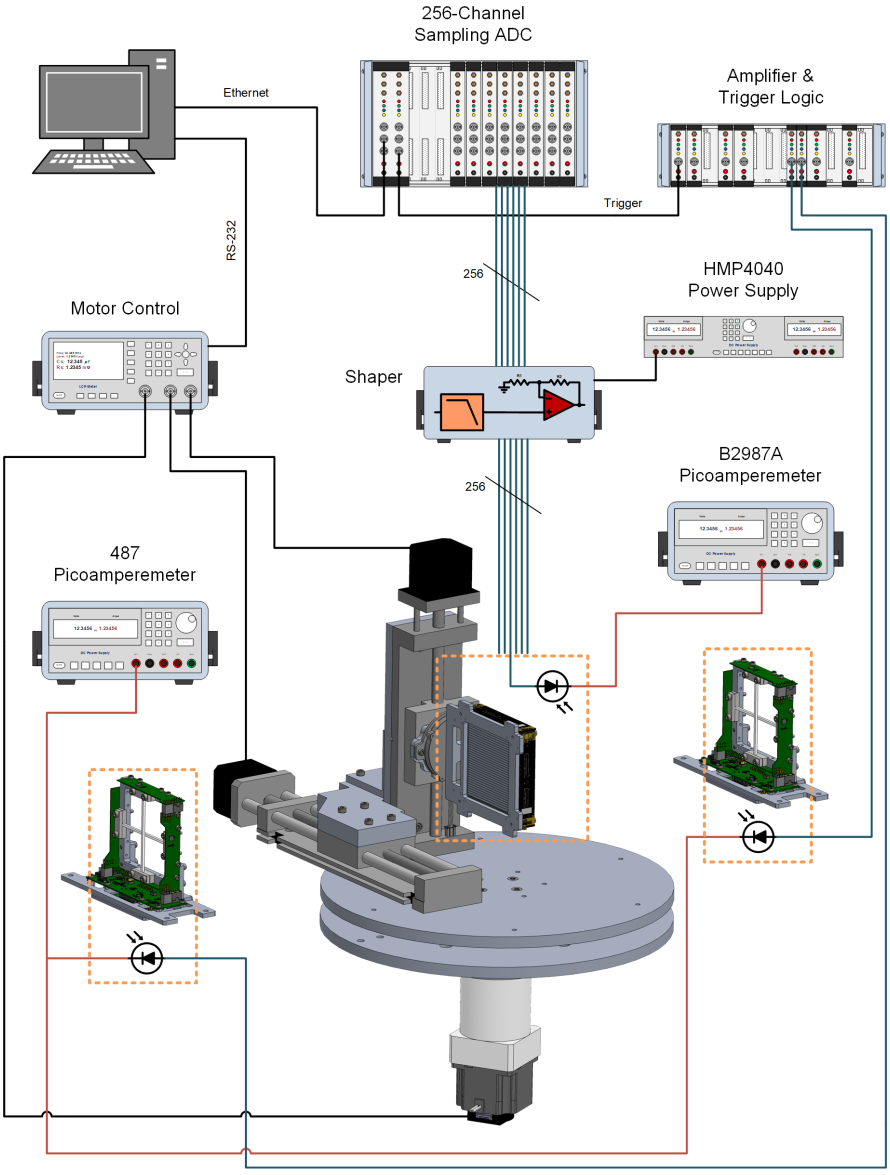

Figure 8.9: Setup used for testing the first ADU prototype module, which is mounted to moving table with four degrees of freedom (two translation, two rotation) that allows to freely orient it in the beam. Trigger detectors placed upstream and downstream from the module define the beam axis.

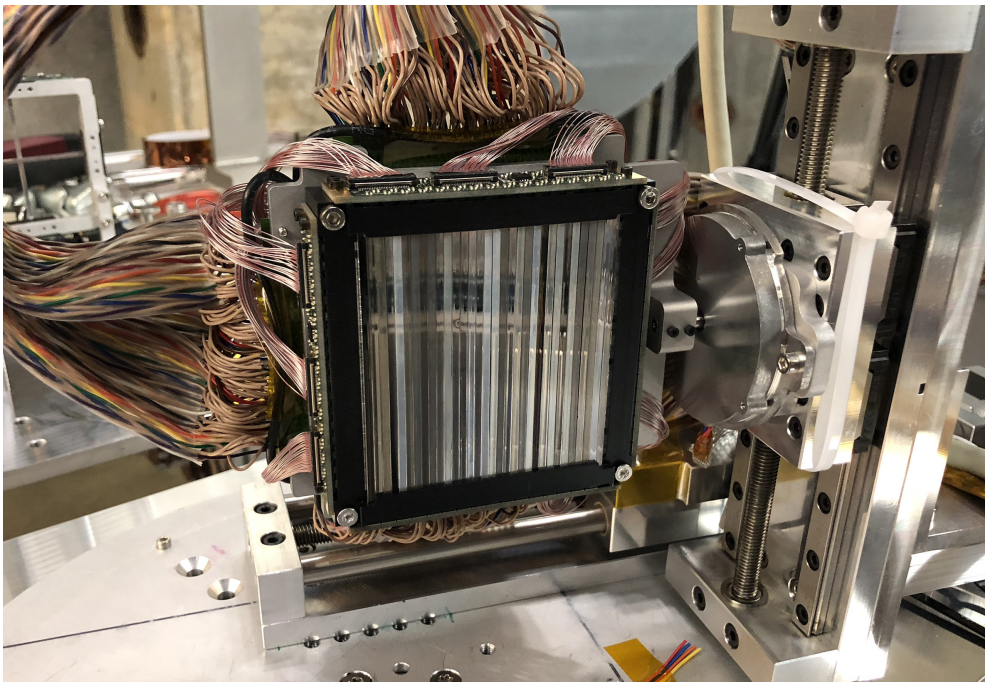

Figure 8.10: ADU prototype during testing at PSI. The module is mounted to a mechanical support with four degrees of freedom. The color-coded signal cables are for the readout via the multichannel sampling ADC.

with 350-MeV/c protons to assess changes of the energy-deposition profile upon rotation of the detector.

8.3.1 Signal-Height Variations

Channel-by-channel variations of the signal height upon excitation with MIPs (which have a constant energy-loss density throughout the detector) have two sources: (1) light-yield variations in the scintillating fibers and (2) variations of the breakdown voltage (and hence gain) of the SiPMs. Testing with a fully integrated detector does not allow to completely disentangle these effects. They can, however, be partially separated by exploiting the position dependence of the fibers' light yield (see Section 7.2). A third source, which we did not investigate in this first test of an ADU module, can be the read-out electronics (see Section 8.4 below).

To investigate the signal-height variation in the test module, we only analyzed data for which the detector was oriented perpendicular to the beam, such that particles traverse the fibers along one of their short axes. This ensures a narrow distribution of the average path length in the fibers, which translates into a small variation of the ΔE_{vis}. Since we know that the light yield of coated scintillating fibers has a strong position dependence (see Figure 7.18), it is also imperative to only compare the data of particles that traversed fibers at (about) the same distance from their SiPM. With this analysis, we were able to gain a first understanding of the light-yield variations in the individual detector channels.

8.3.2 Crosstalk Probability

Crosstalk between neighboring channels can be caused by a variety of effects. The first category, optical crosstalk, encompasses the previously described detection in a SiPM of photons that either inadvertently escaped a directly neighboring fiber (which is read out at the opposite end of the layer) or that were reflected at the surface of neighboring SiPMs. Photons causing optical crosstalk therefore primarily originate in the two channels to left and the two channels to the right of the channel under investigation. The second category encompasses all forms of electrical crosstalk, primarily the induction of signals in PCB traces running closely parallel to each other. As such, electrical crosstalk is not necessarily limited to neighboring channels but depends strongly on the design of the SiPM arrays and read-out electronics, as the signal traces of spatially distant photosensors may run close to each other on a PCB. Based on the test data, we were able to determine that no significant electrical crosstalk was present in the prototype module. We could, however, identify single channels with substantial optical crosstalk.

8.3.3 Tracking Performance

What we describe by the term 'tracking performance' is the detector's ability to record cleanly reconstructable tracks. This measure can be encoded in the probability for a track to be split into multiple tracklets, or fragments, due to fiber layers in which a particle should but does not produce a (measurable) signal. There are many possible causes:

1. Under non-perpendicular incidence, a particle may have a very short path length in a fiber. The number of photons reaching the SiPM is thus small,

and the correspondingly low signal amplitude is indistinguishable from dark counts or noise. It thus does not make it through the background-suppression thresholds of the data-acquisition system.

2. The light yield of a fiber may be small enough for energy-loss straggling to similarly result in a low-amplitude signal that is indistinguishable from noise or dark counts.
3. The particle track may run through the insensitive region between two fibers. The probability for this to happen may be higher if significant irregularities in the placement of fibers are present.
4. A detector channel may be completely 'dead'—i.e., not producing a signal at all. The most likely cause for this scenario is a non-working SiPM or ADC channel.

It can be expected that the tracking performance is not uniform throughout the detector module. In addition, there may be a (strong) dependence on the particles' angle of incidence, primarily due to the effect described in the first item of the above list. Based on the test data, we were able to confirm that some of the above effects may be observable in the prototype module, though the lack of an external high-precision tracking setup providing the exact path of the particles through the detector limited the precision of our analysis.

8.4 Mass Production

For the RadMap Telescope, our objective was to construct two working tracking calorimeters of comparably good quality. This required us to assemble at least eight ADU modules. Because we were aware that the assembly of a single module would not have reliably revealed all possible challenges and issues during the integration process, we aimed for at least twelve fully assembled modules. To account for issues during the integration of fibers into the support structures, we added three additional modules that would not be equipped with SiPM arrays. Since we also knew that we needed to account for at least 15% unusable fibers, the total production volume grew to about 4 500 individual scintillating fibers.

We performed all production and assembly steps exactly as we had done for the prototype module. The only difference in our procedures were the quality-control measures we introduced to ensure that we would end up with eight usable ADU modules.

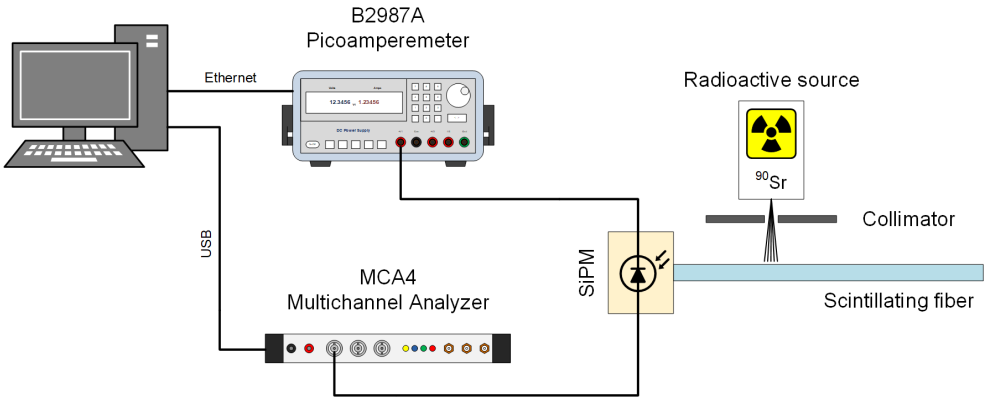

Figure 8.11: Setup used for the quality control of the sputter-coated scintillating fibers. Fiber from each production batch were irradiated by a ^{90}Sr at precisely the same location. We then compared their signal-amplitude spectra recorded by a MCA4 multichannel analyzer.

8.4.1 Quality Control: Scintillating Fibers

We individually inspected every scintillating fiber after each production step (see Section 8.2) to reveal (1) damages of the cladding after heating and polishing, (2) irregularities of the aluminum coating, (3) scratches of the coating due to handling, and (4) any partial coating of the supposedly clean fiber end after removal of the protective polyimide tape. However, we did not individually test all fibers as we had done for the 900-channel prototype (see Section 6.5), simply because of the prohibitively large production volume and the limited manpower available to us. Instead, we tested a randomly selected subset of fibers of each production batch to monitor their quality.

The setup we used to perform these tests consisted of a single PCB with a PM3325-WB-B0 SiPM [KET17] on it, fixed in vertical orientation on an optical bench. A support structure machined from PTFE, which was likewise fixed on the bench, allowed the positioning of the fiber under test such that it was precisely centered on the photosensor. We did not use any means of optical coupling (e.g., grease or silicone) but lightly pressed the fiber against the SiPM's surface. Another holding structure allowed the placement of a ^{90}Sr at precisely the same location above the fiber during every test. We used a Keysight B2987A electrometer to supply bias voltage to the SiPM; the noise on

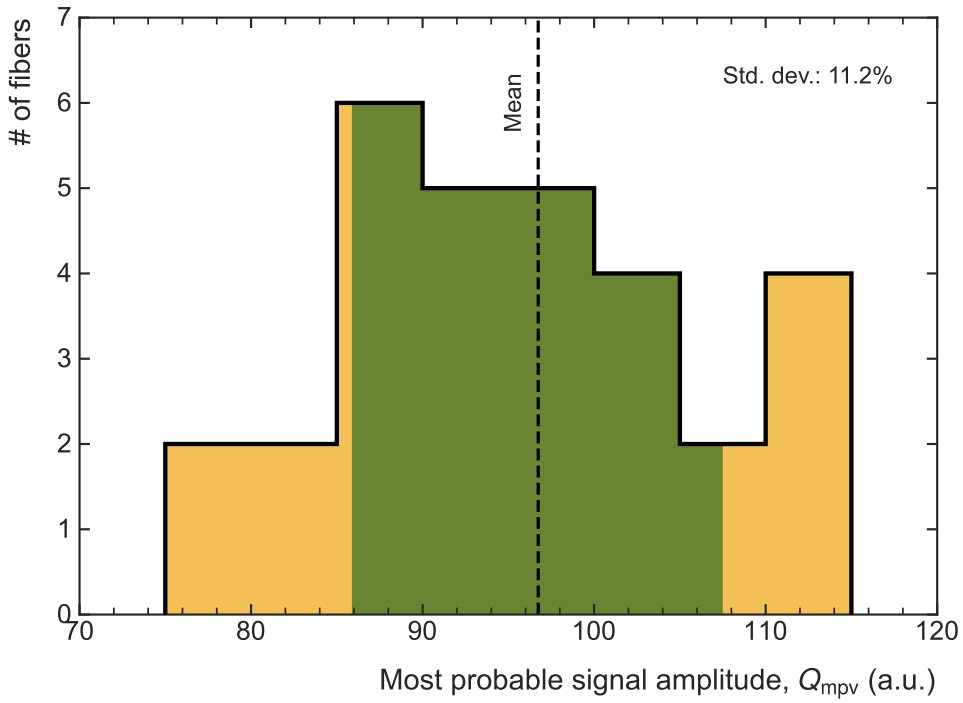

Figure 8.12: Distribution of the peak positions of the ^{90}Sr/^{90}Y spectrum for all 31 randomly selected quality-control fiber samples. The green area marks the range of one standard deviation above and below the mean.

its built-in voltage source is specified at a RMS value of 3.0 mV between 10 Hz and 20 MHz by the manufacturer [Key20]. At our operational point of 4 V overvoltage, this translates into a gain variation of 0.075%, which is negligible for the purposes of quality control. At the same time, the B2987A can monitor the current drawn by the SiPM (in the range up to 2 μA) with a resolution of 1 pA and an accuracy of better than 0.1% of the measurement range. To digitize the SiPM signals, we used a MCA4 multichannel analyzer from FAST ComTec GmbH, which allowed us to perform a pulse-height analysis of the unamplified sensor waveforms at a resolution of 16 bits (over a 10-V input range) and at a rate of more than 10^6 events per second [FAS15]. We operated the setup inside a laboratory that was temperature-controlled to better than 2 °C, where we placed the fibers and the SiPM inside a darkbox.

The beta electrons emitted by ^{90}Sr (with maximum energy of 0.546 MeV) and its decay product ^{90}Y (with a maximum energy of 2.28 MeV) generate a broad ΔE_{vis} spectrum in a scintillating fiber. The central part of such a spectrum can be well approximated by a Gaussian to find the peak of the distribution (corresponding to the most probable energy deposition), which can then be used as a measure of a fiber's (relative) light yield. We used two fibers as references for detecting any changes in the setup or in the noise environment; every time a quality-control measurement was performed, their spectra were measured first and compared to the baselines we established at the start of the production [Eck20]. Figure 8.12 shows the results of the quality-control measurements with a total of 31 fibers. The data reveals a standard deviation of the mean light yield of 11.2%. Though we had initially hoped for a better uniformity, such moderate variation is nevertheless sufficient for our purposes and can be corrected for through calibration of the assembled detector modules.

8.4.2 Quality Control: SiPM Arrays

Variations in the characteristics of the SiPMs can have a significant effect on the measurement accuracy we can achieve. The most important parameters for our application are the breakdown voltage, its temperature dependence, the gain, and the crosstalk probability. To keep the variation in these parameters—and thus, for example, the variation in the overall gain per detector channel—as small as possible, we only used SiPMs produced from a single silicon wafer. This ensured their characteristics stayed within the parameter ranges listed in Table 8.1. Nevertheless, the intrinsic 250-mV range of possible breakdown voltages, for example, leads to an uncertainty of the individual amplification of 5% (at $V_{\text{ov}} = 5\,\text{V}$) to 2.5% (at $V_{\text{ov}} = 10\,\text{V}$), if left uncorrected (see Section 4.5). We did not determine the breakdown voltage individually for each SiPM.

The assembly of the arrays was performed by KETEK, to leverage their in-house expertise in accurately placing and soldering the photosensors. The functional testing we performed ourselves with the help of a pulsed light source [Ulu21; Kre20]. For these tests, each SiPM array was biased to $V_{\text{ov}} = 5\,\text{V}$ with a standard laboratory power supply inside a darkbox. The signal outputs were connected via a test fixture to a 64-channel TRB3 TDC system equipped with PaDiWa leading-edge discriminators [Nei+13] (see Figure 8.13). With this system, we used the ToT method (see Section 6.5.2) to measure the amplitude of the SiPM signals when they were subjected to light pulses generated by a

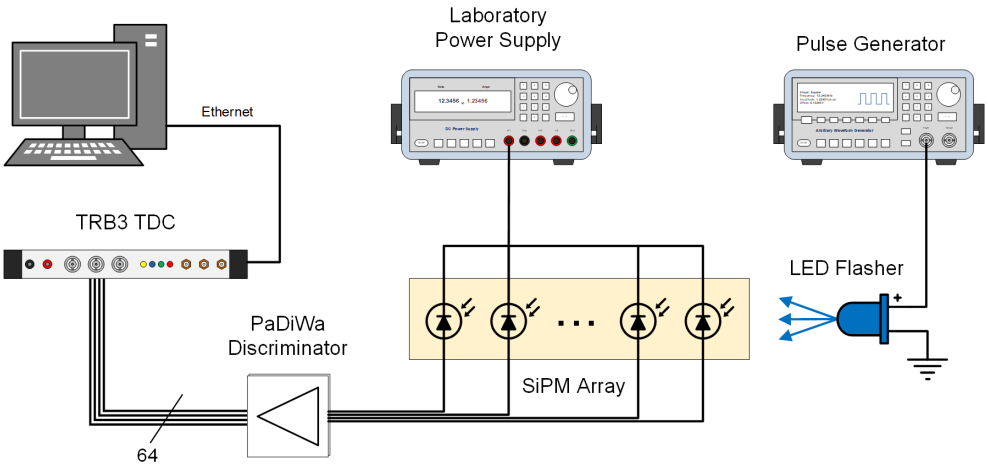

Figure 8.13: Setup used for the quality control of the custom SiPM arrays assembled for us by KETEK. Each array was illuminated with a single LED flasher; the SiPMs were read out via PaDiWa leading-edge discriminators and a TRB3 TDC.

simple flasher circuit [Bec17; Kap+85]. We only used a single LED as light source and did not try to ensure that the light intensity was constant over the array's surface. We simply checked whether each SiPM produced signals that were within ∼20% of the average. As a consequence, the non-linearity of the ToT method was unimportant. Nearly all arrays performed well; only a few had non-functional channels, most of which we could recover through re-soldering the resistor of their bias-voltage filter.

8.4.3 Quality Control: Module Assembly

During assembly of the detector modules, we integrated each fiber into the support structure individually. The two critical challenges were to (1) avoid scratching the aluminum coating and to (2) ensure that each fiber was installed in the correct orientation. The latter was complicated by the fact the sputter-coated and open ends of the fibers are nearly indistinguishable. We inspected each fiber before integration and initially only used those with a perfect coating. We could not, however, discard all fibers that had small defects because it would have increased the required production volume by another 30%. Later modules were thus equipped with an increasing fraction of fibers with a limited number of small defects (abrasions, scratches, flaked-off sections).

Figure 8.14: Assembled modules prior to installation of the SiPM arrays. The fibers in the upper pictures are of good quality; the coating of those in the lower pictures shows substantial signs of abrasion, scratching, and flaking (exemplarily marked in red).

We visually inspected all modules prior to the installation of the SiPM arrays to determine their overall quality. To be able to identify the position of defects in the coating, we illuminated the fibers ends with a high-power UV LED (Thorlabs CS20K2 [Tho20]) to excite the wavelength shifter in them. Figure 8.14 exemplarily shows the result for four different modules. The upper two pictures show modules with fibers of good quality; every second fiber (in a layer) emits light over its entire cross section, the other fiber ends are coated nearly perfectly and therefore do not emit any light. The few visible small defects may cause minor cross talk but not at a significant level. The coating of the fibers in the lower two pictures, on the other hand, shows substantial signs of abrasion, scratching, and flaking. The red arrows and frame exemplarily highlight some of the more severe defects, both on the end and longitudinal faces of the fibers. While the former can cause significant optical cross talk, the latter are of less concern. That is because for photons to be able to move between adjacent fibers, defects on both of them at more or less the same position are required. The probability for a photon to exit a fiber through a defect, reflect back and forth between the aluminum coating of neighboring fibers, and then enter another through a defect is likely very small. We did not, however, experimentally verify this hypothesis.

We preferentially installed SiPM arrays on modules with (near-)perfect fibers. The three ones with the lowest-quality fibers we singled out and did not use at all. During installation, few additional quality-control measured were possible. The only thing we really could do was to check the correct fiber–SiPM alignment in the top and bottom layers of each orientation. Doing this, we realized that in some modules, some fibers still exhibited a slight residual curvature. Since we designed the slots holding the layers wide enough for absorbing any tolerances in fiber thickness—which, as we had painfully learned while assembling previous detectors, could be much larger than the 2% stated by Kuraray—such slightly bent fibers led to irregular spacing in some modules. We tried correcting any substantial misalignment but were obviously only able to do so in the uppermost and lowermost layers. I describe the issue of fiber placement and its implications for the design of future detectors in more detail in Section 12.1.1.

8.5 Calibration

Identifying a particle and determining its energy with an ADU-style tracking calorimeter requires precise knowledge of the energy it lost in each fiber it traversed. It is thus imperative to understand how to determine this energy loss from the signal amplitude generated by each SiPM. A number of factors influence the transfer function from ΔE_{vis} to the signal amplitude:

Fiber coating. The sputter-coated aluminum layer not only affects the overall light yield of each scintillating fiber but also its position dependence (see Section 7.2). Precise knowledge of both is the single most crucial prerequisite for a precise energy reconstruction.

Fiber–SiPM (mis-)alignment. The fact that we use SiPMs with an active area of $3 \times 3\,\mathrm{mm}^2$ allows a misalignment of up to 0.5 mm between each photosensor and its fiber. In some modules, however, the residual curvature of single fibers led to unwanted shifts inside a layer that resulted in larger deviations from the optimal position. In these cases, we observed a few fibers that were only partially covered by their SiPM, leading to a lower overall light yield in these channels but to no changes in the position dependence.

Optical coupling. The optical coupling between fibers and SiPMs is primarily defined by the glue we applied during assembly and can likewise affect the overall light yield. Scattering centers like dust particles and air bubbles cannot be visually detected after assembly, though.

SiPM characteristics. Variations in the characteristics of the SiPMs, most importantly in their breakdown voltage and the dependence of the gain and PDE on it, affect the signal amplitude (i.e., the charge released by the sensor) that is generated for a given number of photons impinging on their active area. Though all SiPMs we used were manufactured from the same wafer, slight variations still occur.

Some of these factors—for example the SiPM characteristics—may to a certain degree be assessed before assembly. Ultimately, however, it is the combination of all of them that determines the channel-to-channel differences in signal amplitude. A careful calibration after assembly is therefore required.

To perform this calibration, we conducted yet another measurement campaign at the πM1 beam line of PSI. The experimental setup was similar to the one we used for testing the first module prototype (see Section 8.3), with only three major differences. First, we did not operate the system inside the steel

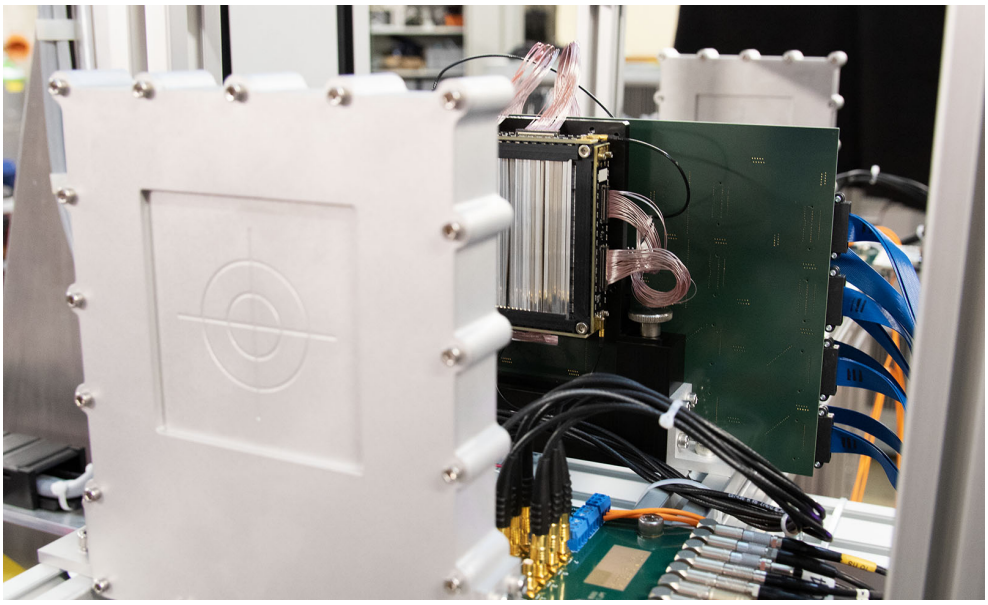

Figure 8.15: Photo of the detector setup used for calibrating the ADU modules. The module under test is visible in the center of the picture. The trigger detectors are housed in the aluminum boxes in the foreground on the left and in the background on the right. All detectors are mounted on aluminum profiles that are somewhat visible at the bottom of the assembly. During operations, the setup was wrapped into a light-tight blanket.

vessel that we used in all previous campaigns, primarily because operations in vacuum were not required, and we needed to be able to quickly swap out the module under test. We instead used an aluminum frame and a blanket to ensure the modules were operated in a completely dark environment. Second, the ADU modules were mounted on a fixed structure, as we did not need to move or rotate them. Third, we used scintillator plates in place of the fiber trigger because we did not need to constrain the beam position on the detector. The plates had dimensions of $8 \times 8 \times 0.5\,\mathrm{cm}^3$ and were thus slightly larger than the active area of the detector modules. Mechanical alignment between the trigger detectors and the modules was ensured via a system of aluminum profiles (see Figure 8.15). We made no changes to the data-acquisition system—i.e., to the shaping amplifiers and the 256-channel sampling ADC—and used a Keysight B2987A electrometer [Key20] for biasing the SiPMs.

We selected a 450-MeV/c beam of negative, minimum-ionizing pions to ensure the test particles had a constant energy-loss density throughout the whole setup. The large trigger scintillators allowed us to record essentially every pion traversing the detector, so we defocused the beam to irradiate as much of it as possible. However, since the maximum beam size was limited by the magnets of the beam line, we needed to record two data sets for each module and move it laterally (both horizontally and vertically) to the beam by a few centimeters in between. For this, we used a precision three-axis translation stage provided by our PSI colleagues, on which we mounted our complete setup.

8.5.1 Calibration of Read-Out Electronics

To be able to separate signal-amplitude variations intrinsic to the detector modules from those caused by the shaping amplifiers and ADCs, we needed to calibrate the latter. We used a test fixture connected to the micro-coaxial cables that the SiPM arrays would be connected to for injecting pulses into the data-acquisition chain. This ensured that our test signals saw exactly the same transmission paths, connectors, shapers, buffer amplifiers, and ADCs as the actual detector signals. For generating the pulses, we used a Keysight 33621A waveform generator [Key23]. We modeled the SiPM signals by a nearly instantaneous rise[4] to a given amplitude, followed by an exponential decay. Since the SiPMs are biased with a negative voltage, we inverted the waveform to test with a signal of negative polarity.

For each of the 256 channels of the read-out electronics, we recorded approximately 2000 test pulses for each of three different amplitudes (-50 mV, -200 mV, and -750 mV) [Eck20]. A combined analysis of the data for all channels revealed that the channel-by-channel variation of the signal amplitude follows a roughly Gaussian distribution. Only at very large amplitudes—much larger than relevant to measurements with MIPs—a non-Gaussian structure emerges. The standard deviation for the three pulse amplitudes we used to calibrate the electronics was between 1.4% and 1.8% [Eck20]. These values must be compared to an intrinsic variation of the amplitudes generated by the waveform generator of, which are of the same order of magnitude. The data-acquisition chain therefore did not have a significant effect on the precision of our final calibration results.

[4] Constrained by the 4-ns minimum rise time of the waveform generator.

Table 8.2: Classification of the produced ADU modules based on our simple analysis of the calibration data. The most probable signal amplitude and its standard deviation are derived from a Gaussian fits to the maximum of the fiber's signal-amplitude spectra; the value given here is the average of all fibers in a module. The ranking is according to the number of channels in a module that belong to the 10% of all fibers with the lowest light yield (across all modules). Adapted from [Eck20]. *ADU013 has a single channel with exceptionally low light yield. **ADU007 has a single non-functional channel.

	Module	**# Fibers in Worst 10%**	**Most Probable Amplitude** (mV)	**Std. Dev.** (%)
●	ADU005	3	33.6	14.6
●	ADU010	4	33.4	16.0
●	ADU004	5	31.7	16.1
●	ADU006	8	32.5	14.9
●	ADU009	16	30.2	18.5
●	ADU003	23	28.4	15.3
●	ADU013*	23	27.9	15.6
●	ADU008	28	29.0	18.2
●	ADU007**	28	27.8	14.8
●	ADU002	42	27.1	15.6
●	ADU015	43	27.3	16.2
●	ADU001	46	26.4	14.8
●	ADU014	64	25.4	15.8

8.5.2 Overall Signal-Amplitude Variations

We initially performed a very simple analysis of the recorded calibration data to assess the overall signal amplitude of each channel upon exposure to minimum-ionizing pions. We fitted the recorded SiPM waveforms with a multi-parametric model of a SiPM signal to determine their amplitudes. We then determined the most probable signal amplitude of a detector channel by fitting a Gaussian to the region around the maximum of the Landau-distributed amplitudes. Finally, we used the calibration of the read-out electronics to convert the value of the most probable signal amplitude from arbitrary units to millivolts.

The results of this initial, simple analysis are summarized in Table 8.2. The 13 modules are ranked based on the number of their channels that belong to the 10% of all fibers with the lowest light yield (across all modules). The table also lists the average most probable signal amplitude of all fibers in a

module, as well as its standard deviation. The four best modules are marked in green, the four next best ones in orange, and the remaining five in red. However, module ADU013, which is generally one of medium quality, has a single channel with exceptionally low signal amplitude; it should thus not be used for flight and is correspondingly marked in red. ADU007 has a single non-functional channel and should similarly not be used. These two channels account for only 0.06% of all detector channels we produced.

Based on this ranking, the four modules marked in green are the primary candidates for constructing the flight detector of the RadMap Telescope. The three modules marked in orange can serve as back up in case one of the 'green' modules cannot be used for some reason. The flight spare can be assembled from the remaining best-ranked modules.

Chapter 9

Sensitivity Analysis

The sensitivity of the ADU, the tracking calorimeter at the heart of the RadMap Telescope, to charged particles of different type and energy, is primarily determined by the size and geometry of its scintillating-fiber stack. The same applies for its ability to identify radiation particles and measure their energy. In this chapter, I summarize the results of a sensitivity analysis of the detector design described in the preceding chapters. This analysis is mostly based on Monte Carlo simulations we performed using multiple software tools, though I also supplement their results with analytic calculations for consistency checks.

9.1 Data Representation & Coordinate System

Each data point generated by RadMap's tracking calorimeter consists of the energy deposition in every fiber per one *event*—i.e., the coincident (within the time resolution of the photosensors and read-out electronics) passing of one or multiple particles through the detector. Before discussing simulated and actual interactions of radiation particles with the ADU here and in the following chapters, it is necessary that I introduce the way we visualize and parametrize the data we gather.

The ADU's scintillating fibers are arranged in two orthogonal directions, as shown schematically in Figure 9.1. The figure also illustrates the orientation of the coordinate system we use. The hit information from the fibers oriented along the x-axis allows us to determine the z-position of a particle in each detector layer. It also allows us to determine which layers along the y-axis were hit, though only for half the layers. The missing information for the other

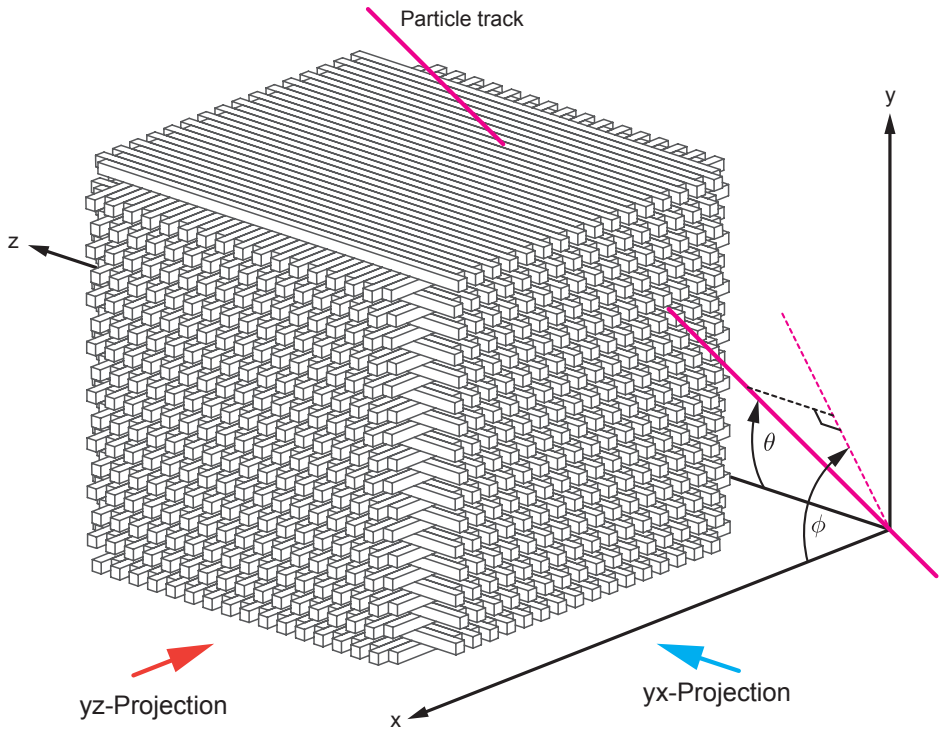

Figure 9.1: Definition of the coordinate system and spherical coordinates θ and ϕ used to parametrize the orientation of particle tracks in the ADU. The red and blue arrows indicate the projections we use to visualize events via two two-dimensional graphs. See text for a description of the coordinate system's origin.

half is provided by the fibers oriented along the z-axis, which also encode the x-position of the track in each layer. Since it is cumbersome to always work with three-dimensional graphs, we usually present the detector data in the form of two projections: In the yz-projection, the information of the fibers oriented along the x-axis is projected onto the yz-plane; correspondingly, the information of the fibers oriented along the z-axis is projected onto the yx-plane in the yx-projection. These projections correspond to what you would see if you looked at the detector along the directions indicated by the red and blue arrows in Figure 9.1.

We use the spherical coordinates θ and ϕ to describe the direction of a particle track in the detector. θ is the angle between the z-axis and the track

and ranges from 0 to π. ϕ is the angle between x-axis and the track's projection into the yx-plane; it can have values between $-\pi$ and π. The absolute position of the track in the detector is not of primary interest to us because our detector is small compared to the spatial variations of the radiation field it observes. The origin of the coordinate system can thus be chosen freely. The only scalar (i.e., spatial) parameters we are interested in is the length of the track, which we typically specify (to first order) via the number of fibers hit. For particles not traversing the detector along one of the coordinate axes, a correction of the length is, however, necessary and requires the choice of a well-defined reference point. Unless stated otherwise, we place the coordinate system's origin at the center of the detector's x- and z-dimensions. For reasons related to how we model the instrument's housing, the origin's position along the y-axis lies about 8 mm below the lowest fiber layer.

9.2 Geometric Factor

One of the most important parameters describing a detector—no matter whether it is used for radiation monitoring or astrophysics investigations—is its geometric factor. It quantifies the system's *gathering power*, and as such allows us to derive the absolute flux of particles (with a specific set of properties) from the count rate registered by it. I introduced the general concept of the geometric factor, G_{F}, in Section 4.1, which in its general form (see Equation 4.5) is often difficult to compute analytically. Due to its large number of individual sensitive elements (the fibers), this is also true for our tracking calorimeter. I therefore introduce a method to compute the ADU's geometric factor using a Monte Carlo simulation. However, before doing so, I approximate G_{F} analytically to have a reference value to compare our simulation results against.

9.2.1 Analytic Calculations

The most naive ansatz for calculating the geometric factor of the four stacked ADU modules is to think of them as three orthogonally arranged planar detectors (see Figure 9.2). This approach is valid if we count any particle that interacts with the detector, no matter how deep it penetrates into the sensitive material. The area of the planar detectors can be considered as the effective sensitive area the stack of fibers presents in a given direction, and each of them is exposed to the full solid angle. The total geometric factor is then simply the

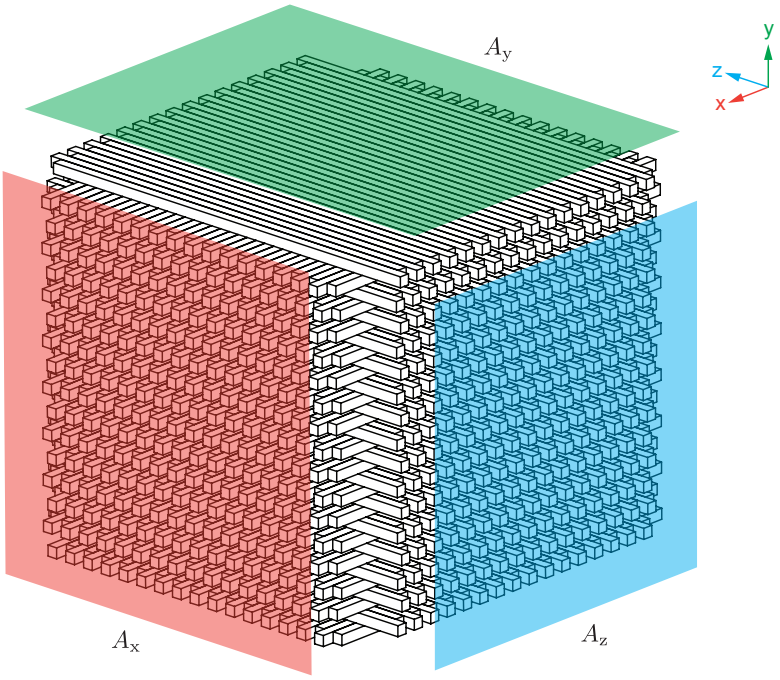

Figure 9.2: Illustration of the decomposition of the geometric factor of RadMap's ADU into that of three orthogonally arranged planar detectors with areas A_x, A_y, and A_z.

sum of the factors of the three planar detectors:

$$G_F = G_x + G_y + G_z \,. \tag{9.1}$$

For the following calculations, I assume a fiber length, l_f, of 80 mm, a core thickness, w_c, of 1.92 mm, and a value of 2.1 mm for both the intra-layer fiber spacing, d_f, and the layer spacing, d_l. With these parameters, the simplest approach is to determine the total fiber-core area facing into the direction of each coordinate axis in Figure 9.2. According to Equation 4.8, the total geometric factor can then be calculated via

$$G_y^1 = 2\pi A_y^1 = 2\pi \cdot 32 w_c l_f \tag{9.2}$$

$$G_x^1 = G_z^1 = 2\pi A_x^1 = 2\pi \cdot \left(16 w_c l_f + 16 \cdot 32 w_c^2\right) \tag{9.3}$$

$$G_F^1 = 2G_y^1 + 4G_x^1 = 854.84\,\mathrm{cm^2 sr}\,. \tag{9.4}$$

Such a simple approach ignores the fiber-to-fiber and layer-to-layer distances of the detector stack, as well as the shift of every second layer of each orientation. Taking these aspects into account, we can calculate the geometric factor in a more refined effective-area ansatz:

$$G_{\mathrm{y}}^2 = 2\pi A_{\mathrm{y}}^2 = 2\pi \cdot (31 d_{\mathrm{f}} + 1.5 w_{\mathrm{c}}) \cdot l_{\mathrm{f}} \tag{9.5}$$

$$G_{\mathrm{x}}^2 = G_{\mathrm{z}}^2 = 2\pi A_{\mathrm{x}}^2 = 2\pi \cdot (31 d_{\mathrm{l}} + w_{\mathrm{c}}) \cdot l_{\mathrm{f}} \tag{9.6}$$

$$G_{\mathrm{F}}^2 = 2G_{\mathrm{y}}^2 + 4G_{\mathrm{x}}^2 = 1\,015.46\,\mathrm{cm}^2\mathrm{sr}\,. \tag{9.7}$$

Even though G_{F}^2 should be closer to the true geometric factor, G_{y}^2 and G_{x}^2 still do not accurately reflect the effective area of the surrogate planar detectors. This is highlighted in Figure 9.3, where the respective areas taken into account are marked by filled rectangles. A supposedly still more accurate approach accounts more truthfully for the shape of the exposed fiber areas:

$$G_{\mathrm{y}}^3 = 2\pi A_{\mathrm{y}}^3 \tag{9.8}$$

$$= 2\pi \cdot ((31 d_{\mathrm{f}} + w_{\mathrm{c}}) \cdot (15 d_{\mathrm{l}} + w_{\mathrm{c}}) + (l_{\mathrm{f}} + s_{\mathrm{f}}) \cdot (15 d_{\mathrm{l}} + w_{\mathrm{c}})) \tag{9.9}$$

$$G_{\mathrm{x}}^3 = G_{\mathrm{z}}^3 = 2\pi A_{\mathrm{x}}^3 = 2\pi \cdot (31 d_{\mathrm{l}} + 1.5 w_{\mathrm{c}}) \cdot (l_{\mathrm{f}} + s_{\mathrm{f}}) - 34 s_{\mathrm{f}} w_{\mathrm{f}} \tag{9.10}$$

$$+ 2 \cdot \left(\frac{l_{\mathrm{f}} - (31 d_{\mathrm{f}} + 1.5 w_{\mathrm{c}})}{2} + \frac{s_{\mathrm{f}}}{2} \right) \cdot (31 d_{\mathrm{l}} + 1.5 w_{\mathrm{c}}) \tag{9.11}$$

$$G_{\mathrm{F}}^3 = 2G_{\mathrm{y}}^3 + 4G_{\mathrm{x}}^3 = 1\,031.22\,\mathrm{cm}^2\mathrm{sr}\,. \tag{9.12}$$

Here, $s_{\mathrm{f}} = 2.4\,\mathrm{mm}$ is the length by which neighboring fibers in a layer are shifted against each other to suppress optical cross talk (see Figure 9.3). It is likely that this ansatz somewhat overestimates the geometric factor, primarily because d_{f} and d_{l} include the insensitive areas between the fiber cores (cladding, coating, etc.). The values of G_{F}^2 and G_{F}^3 should nonetheless provide reasonable reference values for other calculation approaches.

The approach of using three planar detectors as surrogates for the three-dimensional arrangement of scintillating fibers is obviously limited to the scenario where we are interested in the total count rate in the detector. In this case, every particle that hits the surface of one of its side faces produces a count, even if it only has enough energy to penetrate as deep as one fiber (or less). Such events are, however, not *reconstructible*, that is, they do not contain enough information for us to be able to identify the particles or determine their energy (unless we have prior knowledge of their identity).

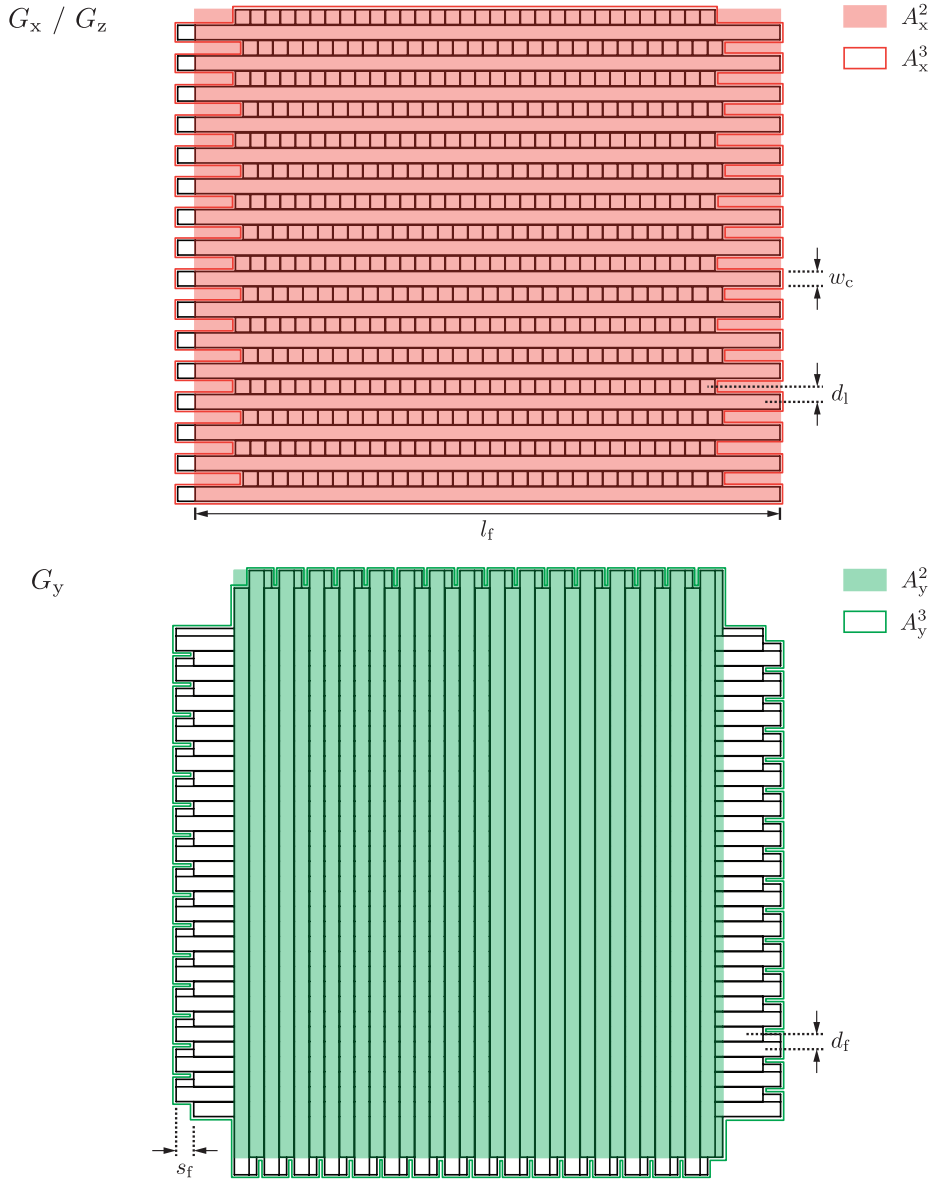

Figure 9.3: Effective areas and variable definitions used for the analytic calculation of the ADU's geometric factor. The color coding is the same as in Figure 9.2.

9.2.2 Simulation-Based Calculation

To assess the more general case, where we require a particle to hit n fibers for reconstruction to be possible, we use a Monte-Carlo method proposed by Sullivan [Sul71] and, independently, by Crannel and Ormes [CO71] in 1971. Their approach has been picked up by multiple authors since [Leh04; Pak+18; ZWX11; Seo+23].

The basis of the method is the definition of the geometric factor as the factor of proportionality between the incident particle flux and the count rate in the detector. As such, it replaces the analytic integration of Equation 4.5. Sullivan summarized the approach in a four-step process [Sul71]:

Step 1: Choose a random point and trajectory on the opening aperture of the detector such that the ensemble of many such choices follows the intensity and angular distributions of the incident particle flux.

Step 2: Follow the trajectory through the detector and determine whether it meets all conditions for being registered. This may include simple parameters like the number of sensitive elements hit, but also more complicated aspects, for example the propagation through the magnetic field of a spectrometer.

Step 3: Record the results of step 2 and, if applicable, calculate any parameter of interest—e.g., the path length of the trajectory in the detector or the number of sensitive elements hit.

Step 4: Repeat steps 1 through 3 enough times to generate a statistically meaningful data set. The required number of simulated events depends on the size and complexity of the detector.

The advantage of this method is that in step 2 conditions for the reconstructibility of events identical to those applied in the analysis of real data can easily be taken into account. Using the results of this simple process, the geometric factor of a detector with arbitrary geometry is given by [CO71]:

$$G_{\mathrm{F}} = \pi A_{\mathrm{F}} \cdot \frac{\text{number of detected trajectories}}{\text{total number of simulated trajectories}} \,. \tag{9.13}$$

Here, A_{F} is the aperture of the detector, and πA_{F} its geometric factor. Since the number of 'detected' trajectories only includes those that fulfill all conditions for full registration in the detector, the aperture can in principle be chosen larger

than the true one (which may be defined, for example, by the first element of a particle telescope). This, however, increases the number of simulated events required to generate a data set of adequate size.

Modern simulation software—such as Geant4, PHITS, or the MCNP code—enable not only the tracing of particle trajectories through a given detector geometry (and magnetic field) but also allow accounting for the interactions between particles and the detector material. Depending on the mass and energy of the incident particles, such interactions—primarily energy loss, absorption, and scattering—can have a large effect on the size of the geometric factor. Using such software, it is thus possible to determine energy- and particle-dependent geometric factors that enable a precise calculation of particle fluxes from the count rates in the detector.

If we do not apply any reconstructibility conditions, the ADU tracking calorimeter is, to first order, equally sensitive from all directions. For its entrance aperture, we can thus either use the effective surfaces illustrated in Figure 9.3 or simply a sphere with a radius large enough that the full detector is contained in it. Using the latter does not depend on the effective areas being accurately modeled and is therefore the more general approach.

Geometric Factor for the Total Count Rate

The geometric factor for *any* detectable interaction of the space radiation field with the ADU is a crucially important quantity because we can use it to compare the total count rate in the detector to those recorded by other sensors that have a similar range of sensitivity, even if they cannot resolve the nature or energy of particles as well. Being able to do so is a fundamental requirement for assessing the on-orbit performance of the RadMap Telescope. It is also the quantity that we can most easily compare to the analytic results of Equations 9.7 and 9.12.

To first order, we disregarded the instrument's housing and internal systems except for the detector itself, implicitly assuming that they do not appreciably shield the latter. For the simulation of particle trajectories, we used a spherical aperture centered on the ADU stack. The origin of trajectories is distributed randomly on this surface; their angular distribution follows a cosine profile to achieve an isotropic flux inside the sphere. As test particles, we used minimum-ionizing protons with an energy of 3 GeV. We considered every particle that deposited at least 0.4 MeV (corresponding to the energy deposition of a MIP in 2 mm of PS) in a single fiber as registered by the detector.

According to Equation 9.13, the geometric factor can be calculated via

$$G_{\mathrm{F}} = \frac{n_{\mathrm{hit}}}{n_{\mathrm{tot}}} G_{\mathrm{sphere}} \,, \tag{9.14}$$

where n_{hit} is the number of simulated particles creating a measurable signal, n_{tot} the total number of simulated particles, and $G_{\mathrm{sphere}} = 4\pi^2 r^2$ the geometric factor of a sphere with radius r. With this definition and a Geant4 simulation of 100 million minimum-ionizing protons, we obtain a geometric factor for the ADU of [Pös22]:

$$G_{\mathrm{F}}^{\mathrm{MC}} = 1013.16 \pm 0.24\,\mathrm{cm}^2\mathrm{sr} \tag{9.15}$$

This value is consistent wih the analytic approximations of Equations 9.7 and 9.12, showing that our calculation approach works. In contrast to the analytic solutions, however, the simulation method allows us to easily calculate the geometric factors for arbitrary event-selection conditions—for example requiring a particle to traverse a minimum number of fibers or to deposit a minimum total energy in the detector.

Dependence on Number of Fibers Hit

For reasons summarized in Section 9.3 above, a minimum number of fiber hits are needed for track reconstruction, particle identification, and energy reconstruction to work. To gain a general understanding of how a respective detection condition affects the geometric factor, we can perform a simulation study to determine the G_{F} as a function of fiber hits along a trajectory. Though not of interest for the preliminary measurement results presented in this thesis, doing so will be crucial to derive particle-type dependent fluxes from the data gathered by the RadMap Telescope.

Dependence on Particle Type and Energy

One objective of operating the RadMap Telescope in the space radiation field is to gather particle-dependent energy spectra for cosmic-ray ions and determine their individual fluxes, and not just the total flux of particles impinging on the detector. To be able to do so, we need to know the sensitivity of the ADU to a given particle type and energy; for calculating the respective particle flux, we also need to know the energy-dependent geometric factor for each particle type. So again, additional studies are required to understand the geometric factor's dependence on the required event-selection criteria.

Influence of Shielding

So far, we have disregarded the fact that the ADU is located inside the RadMap Telescope instrument—i.e., that it is surrounded by read-out electronics, power converters, the flight computer, the housing, and so on. All of this material is not distributed evenly around the detector but rather concentrated beneath its face pointing in negative y-direction (See. 9.1). The least material is located on top of the detector (in positive y-direction). The lower end of the energy range the detector is sensitive to thus varies with the direction of incidence (see Section 9.3), which also effects the count rate and the geometric factor for low-energy particles. For a precise reconstruction of the total incident particle flux and of its angular distribution, integrating the shielding into the simulation for determining the geometric factor will be necessary.

9.3 Energy Sensitivity

The primary quantity of interest for understanding the sensitivity of the RadMap Telescope's tracking calorimeter to the space radiation environment is the energy range in which particles of a specific type can be detected. Here, we must differentiate between mere detection—i.e., a particle deposits enough energy in a single fiber to cross the noise-suppression threshold of the read-out electronics—and the ability to reconstruct its type and energy. For the latter, a minimum number of ΔE_{vis} measurements are required to record an energy-deposition profile along a clearly identifiable track. The exact number of fiber hits we can only determine once we have gained first experience in operating the detector in a representative radiation field. Simulations (backed by the beam tests we performed) seem to indicate that a minimum of three fiber hits per projection (for a total of six hits) are required for tracking and particle identification to work reliably [Pös22], though this number may change depending on noise, background events, and other aspects that are hard to quantify without on-orbit measurements. For many of our simulations, a total of four fiber hits are required for at the least the energy deposition to be measurable reliably [Los+21].

Figure 9.4 shows the energy sensitivity ranges of the ADU for cosmic-ray nuclei up to iron. The (hatched) blue bars visualize the energies for which each ion type produces a detectable signal in the tracking calorimeter. The ranges are calculated using data from SRIM [ZZB10], assuming that a particle must have a range of at least 2 mm in PS to produce a sufficiently large number

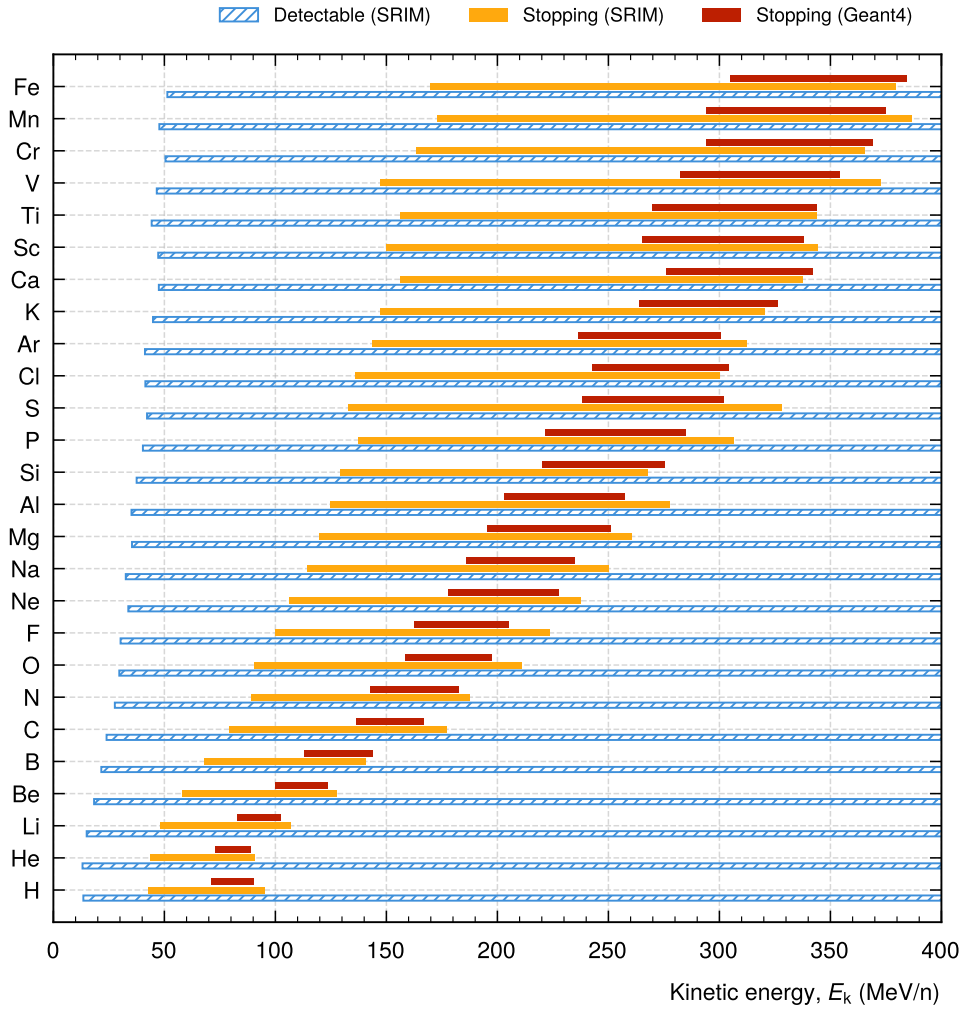

Figure 9.4: Energy sensitivity ranges of the RadMap Telescope's ADU for cosmic-ray nuclei up to iron. The (hatched) blue bars show the energy ranges for which each ion type has a range of at least 2 mm in PS (data from SRIM [ZZB10]). The yellow bars show the range of energies for which the respective nuclei have a range between 16 mm (four fibers per projection) and 64 mm (full detector under perpendicular incidence). The red bars show the same cuts but for a full Geant4 simulation of ADU, including all insensitive materials and the housing surrounding it.

of scintillation photons. Even though particles with shorter range (but higher stopping power) may also be detectable, the left end of the bars nevertheless represent a somewhat ideal lower limit because the calculation does not take into account any material (cladding, coating, structures, and housing) other than the scintillating fibers' cores. The yellow bars show the range of energies for which the respective nuclei have a range between 16 mm and 64 mm in PS, again determined with the help of SRIM. This covers the range between traversing four fibers in each layer orientation and the full detector (32 fibers). Fibers not traveling along the coordinate axes shown in Figure 9.1 obviously can traverse more material. Finally, the red bars show the results of a full Geant4 simulation of the detector, including all insensitive material and the surrounding housing [Los+21]. The condition of stopping particles with at least four fiber hits per projection in this case leads to much narrower sensitivity ranges.

9.4 Event Reconstruction

The ADU is a conceptually simple detector built from functionally simple components. Even though that means it requires, to some degree, less care building it, the unfortunate truth is that the complexity of the data analysis required to achieve high-precision results often scales inversely with the complexity of the instrument. It is certainly true in our case. One of the biggest challenge we had, and still have, to grapple with is the development of data-processing algorithms that can fully reconstruct the characteristics of single particles. Much of this challenge is rooted in the fact that Bragg curve spectroscopy was originally devised for ensembles of particles and suffers largely from range and energy-loss straggling, as well as from nuclear interactions and, in particular, fragmentation. Another important impediment is ionization quenching (see Section 7.1.5).

Since we started working on the tracking-calorimeter concept, we tested multiple approaches for event reconstruction. The initially most promising one was a Bayesian particle filter [Los+17] that calculates a particle's energy loss by inverting its CSDA range, taking into account energy-loss straggling and multiple scattering. It allowed us to tackle the non-Gaussian nature [Aru+02] of the energy loss and straggling via Monte Carlo methods, approaching the optimal Bayesian estimate for a large number of samples. Alternative approaches included simulated annealing [LA87] and a Markov Chain Monte

Carlo [CKK09]. Though some of these methods produced acceptable results in a limited parameter space [Hol19], their biggest drawback was the computing effort required, which resulted in processing times per event upward of 15 minutes [Mil16]. Though some improvement could possibly have been achieved by further parallelizing the Monte-Carlo sampling, we saw little chance of achievable processing rates.

We therefore investigated the use of machine-learning algorithms, in particular different architectures of neural networks. They are trained on data generated by a (somewhat) realistic Geant4 simulation of the ADU. This work has been performed by a number of students under the supervision of my colleague Thomas Pöschl [Kho17; Han18; Aga18; Hol19; Bie19; Hös20]. I therefore do not describe in detail the development that led to the current generation of networks and also do not explain their exact architecture. Instead, I only show the final projected capabilities of the latest networks, which have been developed and are being further refined by my colleague Luise Meyer-Hetling [Mey18; Mey21]. She generated and provided to me all graphs that I show in the remainder of this chapter.

9.4.1 Track Reconstruction

The first step in the analysis of ADU data is the reconstruction of each event's track, that is, the determination of the angles θ and ϕ that describe in what direction the particle traversed the detector. We determine these angles separately from the data of the two projections shown in Figure 9.1, and then combine the information to calculate the track's orientation in three dimensions. We also determine its position in relation to the origin of the coordinate system described in Section 9.1 above. Along the reconstructed track, the direction of motion is encoded in the energy-loss profile, with the particle traveling in the direction of increasing ΔE_{vis} in the fibers. For particles in the minimum-ionizing regime (and beyond) that have a quasi-constant energy-loss density, the direction can therefore not always be identified unambiguously.

Figures 9.5 and 9.6 show the performance of our latest neural network for the reconstruction of the track angles. It was trained with 10 million Geant4-generated events, for the creation of which we exposed the detector to a fully isotropic flux of cosmic-ray nuclei (up to iron) with energies of 70 MeV to 5 TeV. The graphs show the result of a validation with a separately generated set of simulated events with the same flux and energy distributions. We chose a bin width of 1° for the parameter space in θ and ϕ.

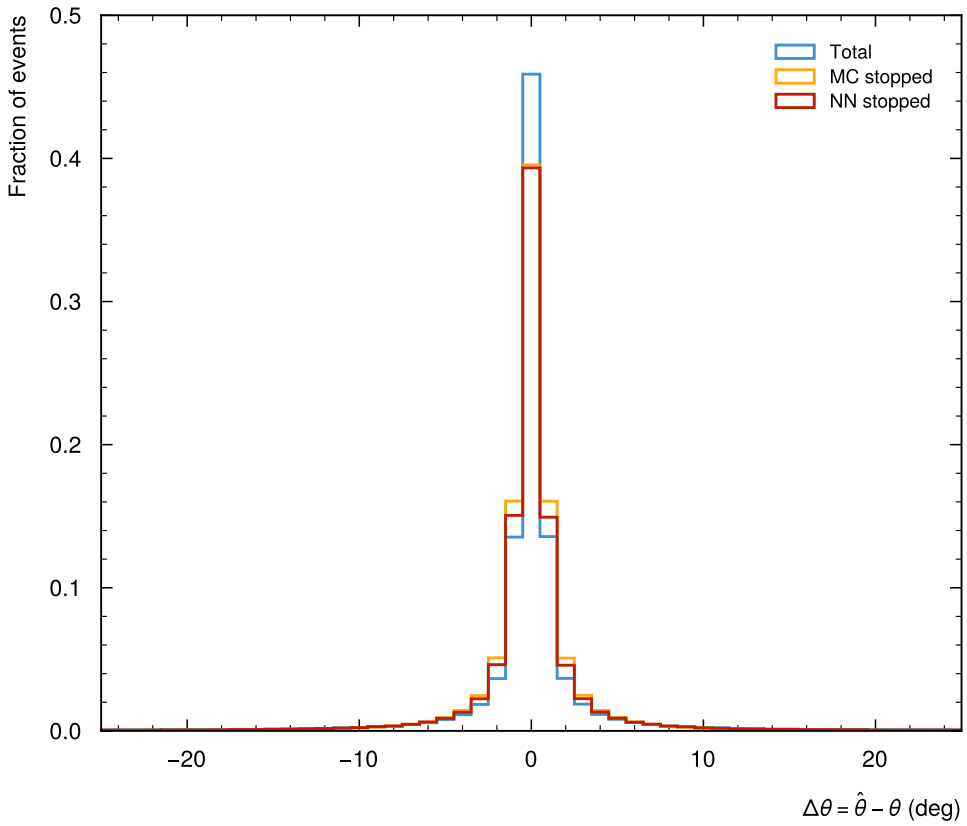

Figure 9.5: Accuracy of the neural network-based reconstruction of the track angle θ, shown as the difference between the reconstructed angle and the true one determined from the Geant4 simulation. See text for an explanation of the three different distributions. Courtesy of Luise Meyer-Hetling.

The histograms show that we can reconstruct the track angles with fairly high precision, considering that the effective pixel size of the two detector projections is approximately 2 mm by 2 mm. They show the distributions for three populations of events: The one for all validation events, including both stopping and through-going particles, is shown in blue. The orange and blue curves show the accuracy of the reconstructed angles for particles that stop in the detector. For the former, we selected events based on our knowledge of the Geant4 track parameters. For the latter, we first used a neural network to determine whether a particle stopped in the ADU, and then fed only those

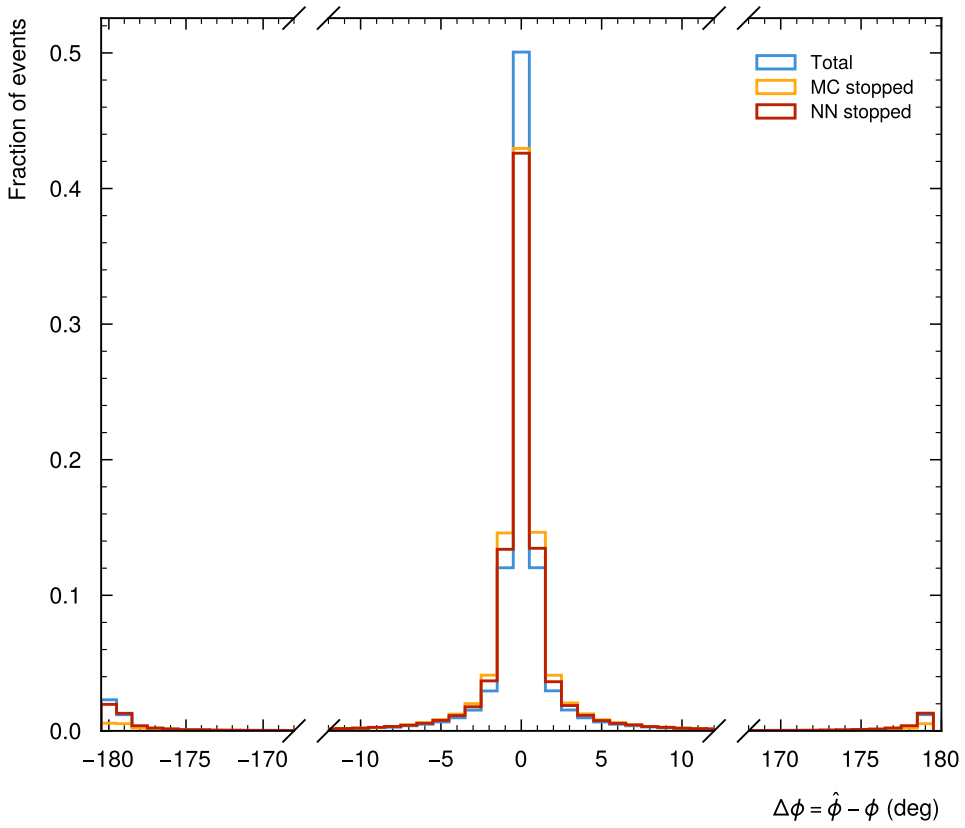

Figure 9.6: Accuracy of the neural network-based reconstruction of the track angle ϕ, shown as the difference between the reconstructed angle and the true one determined from the Geant4 simulation. See text for an explanation of the three different distributions. Courtesy of Luise Meyer-Hetling.

events into the network for the angle reconstruction. The central part of distributions for both angles shows that the reconstruction is apparently a little less accurate for stopping particles.

Figure 9.6 also shows the effect the selection has on the small fraction of events for which the particle's direction is not correctly identified (leading to a 180° shift in ϕ): For the neural-network selected events there is little difference visible; using only Monte Carlo-selected events, on the other hand, leads to a clear decrease in wrongly reconstructed angles. It thus appears that more or less the same fraction of events for which the reconstruction determines

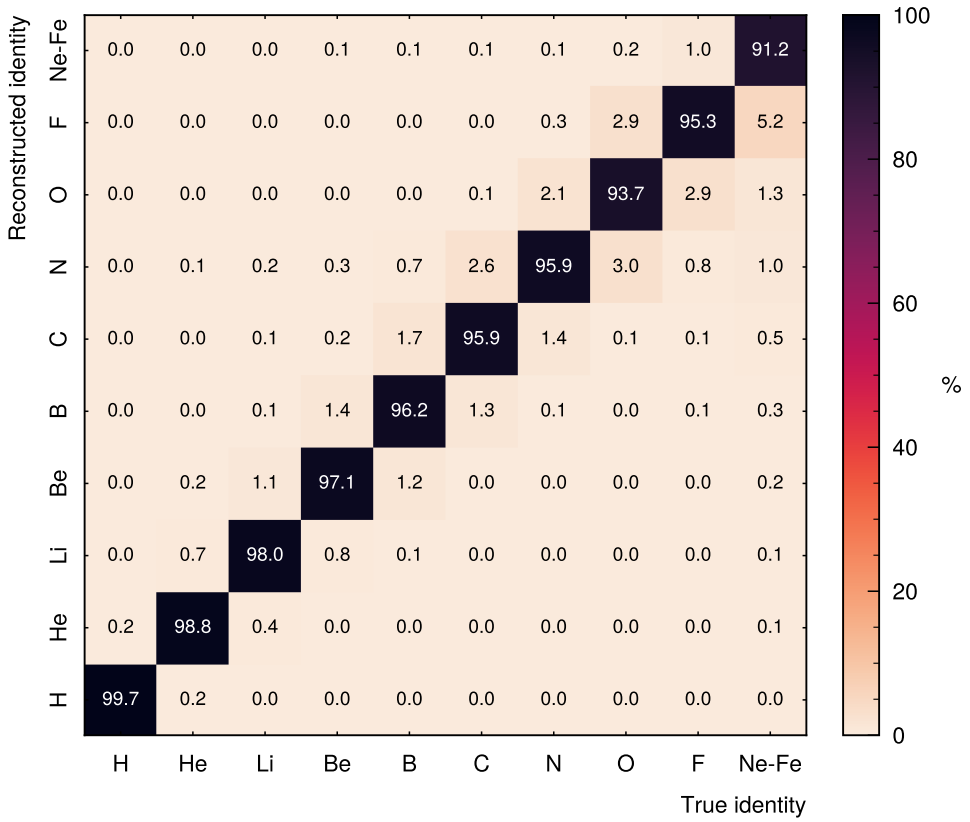

Figure 9.7: Accuracy of the neural network-based identification of cosmic-ray nuclei up to fluorine. The graph compares the reconstructed identity (element) to the true one, revealing how the network misclassifies events.

a wrong direction also confuses the network for detecting stopping particles. Generally, however, the expected overall angular resolutions of $\sigma_\theta = 1.15°$ and $\sigma_\phi = 1.02°$ are excellent for a detector that completely lacks high-resolution tracking elements and more than sufficient for the purposes of operational radiation monitoring.

9.4.2 Particle Identification

One of the core capabilities of the RadMap Telescope is its ability to identify cosmic-ray nuclei on an event-by-event basis. This requires developing an

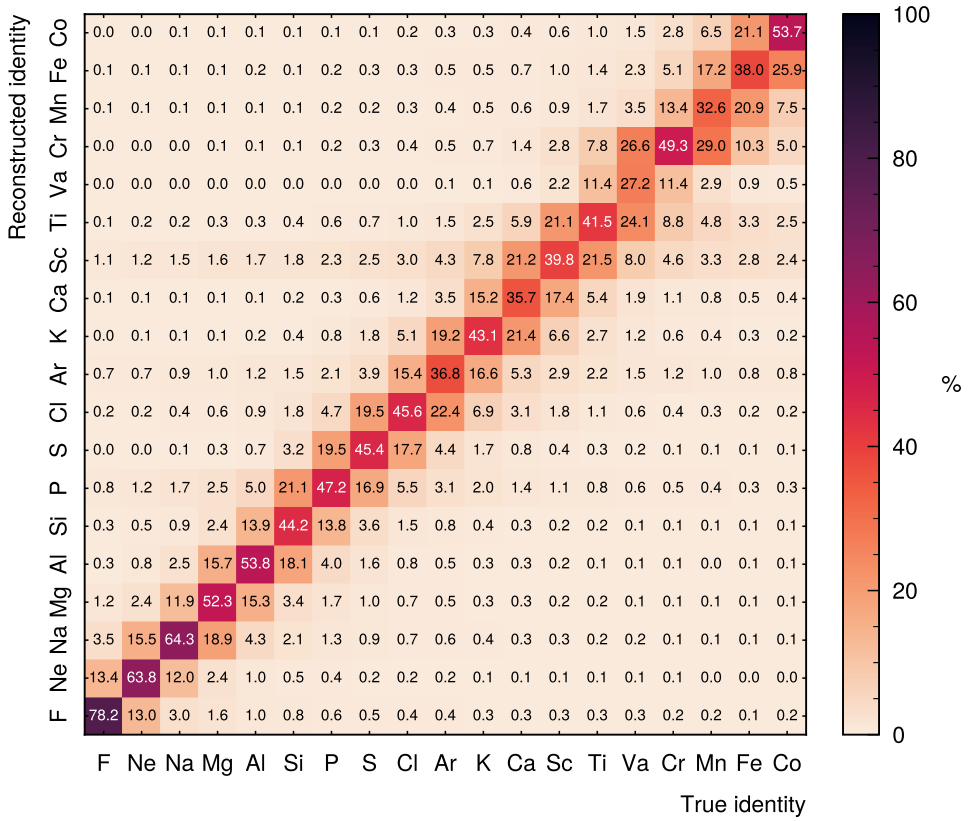

Figure 9.8: Accuracy of the neural network-based identification of cosmic-ray nuclei between fluorine and iron. The graph compares the reconstructed identity (element) to the true one, revealing how the network misclassifies events. Courtesy of Luise Meyer-Hetling.

identification algorithm that can reliably detect a particle's nuclear charge, Z, in the presence of straggling, nuclear reactions, and quenching. The architecture of the neural networks we developed for this task has evolved significantly over the years. For reasons that we have not fully understood yet in physical terms, we achieve better results when we split the identification into two ranges of Z. One network attempts to classify light ions up to fluorine and throws all events that cannot be identified as one of these elements into a 'garbage-collector' bin for heavier elements. A second network attempts to identify elements between fluorine and iron, again moving all unclassifiable events into a bin

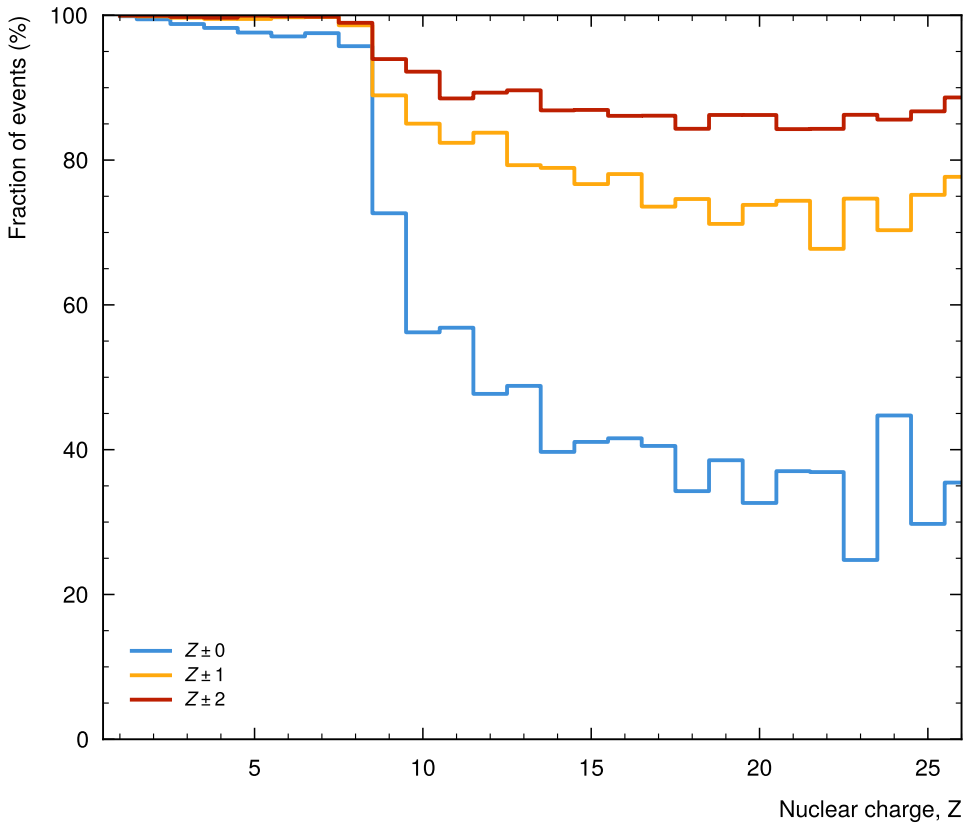

Figure 9.9: Effect of allowing events to be classified with $\Delta Z = 2$ ($Z \pm 1$) or $\Delta Z = 4$ ($Z \pm 2$). Courtesy of Luise Meyer-Hetling.

for even heavier elements. The networks can either run consecutively (as in our case), or potentially be fed by a pre-selection network that classifies events into 'light' and 'heavy' categories, similar to the one separating stopping from through-going particles.

We again trained both networks with Geant4-generated data sets of 10 million events with energies between 70 MeV to 5 TeV, but this time included elements up to cobalt. Figures 9.7 and 9.8 show the results of the validation with independent data sets. The first, immediately obvious observation is that the identification works best for light particles, with an increasing fraction of misclassified events for heavier ones. The accuracy for H (protons) and

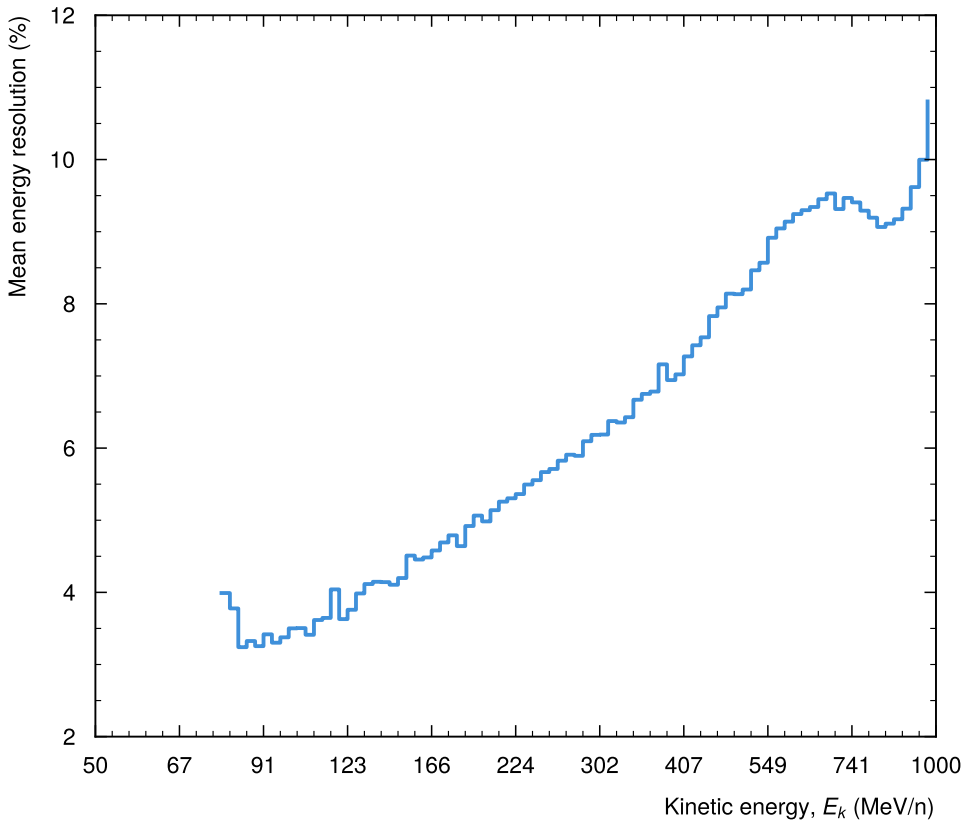

Figure 9.10: Mean energy resolution for protons with energies between 70 MeV and 1 GeV. Courtesy of Luise Meyer-Hetling.

He is at 99.7% and 98.8%, respectively, allowing us to measure the bulk of the cosmic-ray flux with high precision. For the C-N-O group, we still achieve accuracies of about 95%. For heavier elements, the accuracy gets significantly worse and dips well below 50%.

A very precise identification of the nuclear charge of heavy elements is, however, not necessarily required (though it also does not hurt). Figure 9.9 shows what happens if we allow events to be classified with $\Delta Z = 2$ ($Z \pm 1$) or $\Delta Z = 4$ ($Z \pm 2$): The accuracy increases drastically and in the latter case exceeds 85% all the way to iron. For radiation-monitoring purposes, such values are perfectly acceptable. The lower precision can be justified by the

similar biological effectiveness of nuclei with almost the same charge.

9.4.3 Energy Measurement

Lastly, once each event's track and particle type has been identified, we can attempt to reconstruct its energy. Here, we trained separate networks for the individual elements, thus relying on a fully functional particle identification prior to running the energy reconstruction. Figure 9.10 exemplarily shows the mean energy resolution for protons with energies between 70 MeV and 1 GeV (for a network trained with similar data sets as those used for the angle reconstruction). Interestingly, the graph reveals that our initial assumption that we would be able to most accurately determine the energy of particles stopping in the tracking calorimeter (based on the principle of Bragg curve spectroscopy) does not appear to hold true. There at least seems to be a decrease of the resolution at the low-energy end of the graph, though we cannot currently exclude that it is due to edge effects in the network training. Generally, the energy resolution of the detector is surprisingly good, starting at about 3.5% at 100 MeV and decreasing to about 10% at 1 GeV. The transfer of this result to heavier elements is currently ongoing.

Concluding Remarks

The (preliminary) results presented in this chapter demonstrate that the RadMap Telescope's ADU is ideally suited for crew radiation monitoring. Its sensitivity perfectly matches the energy range in which cosmic-ray nuclei are most harmful to the human organism. Its large geometrical acceptance allows gathering statistically significant data sets in short amounts of time. And its ability to accurately determine a particle's identity and energy over a wide range in Z enables the precise determination of the biological effectiveness of incident radiation. The major caveat is, however, that most of these results are based solely on the analysis of simulation data. Though we tried using whatever experimental data we gathered with protons and MIPs for benchmarking our Geant4 framework, we have not yet performed measurements with helium or even heavier ions. Such tests are therefore urgently required to verify the signatures of highly-ionizing nuclei, not least because we need to understand the effects of quenching and nuclear interactions.

Chapter 10

The RadMap Telescope on the International Space Station

The development of what we now call the RadMap Telescope began in 2012. We initially started looking into technologies that would allow us to construct a charged-particle detector for a CubeSat-based astrophysics mission. After investing a few years of effort into the project, we christened the detector the MAPT because we felt the name most accurately reflected its capabilities and working principle. Shortly thereafter, we began pitching the concept to multiple space agencies as a radiation monitor. The proposal that was ultimately accepted, submitted in cooperation with our partners at Airbus U.S. Space & Defense[1], was titled *Multi-Purpose Active-Target Particle Telescope on the International Space Station (MAPT-I)*. Both name and acronym, however, were too cumbersome and unintuitive to be used on a daily basis by a large team of engineers and astronauts not particularly familiar with the device and its function. We thus suggested to NASA to call the instrument the RadMap Telescope—short for *radiation-mapping telescope*—which everyone agreed was a much more descriptive and intuitive name. In light of this re-naming, we decided to also change the name of the detector at the heart of the RadMap Telescope from MAPT to Active Detection Unit (ADU).

In this chapter, I describe the design, development, operational concept, and acceptance testing of the RadMap Telescope, a technology-demonstration experiment whose main objective is the validation of the ADU tracking calorimeter

[1] Formerly called Airbus DS Space Systems, Inc. (ADSH).

as a radiation monitor for applications aboard crewed and uncrewed spacecraft. The primary intention behind the development of the RadMap Telescope (which I often lazily refer to as RadMap) is not necessarily to outperform existing instruments in their respective areas of specialization. Instead, we aim to combine as many measurement capabilities as possible in one compact device to reduce the number of instruments that will be required on future missions. As such, the RadMap Telescope is designed to be a general-purpose instrument for area monitoring. It cannot in any way replace personal dosimeters worn by the crew. We do, however, hope that instruments based on our concept may in the future make the use of simple (active or passive) area-monitoring dosimeters redundant.

The RadMap Telescope comprises multiple radiation sensors, most importantly the tracking calorimeter described at length in the preceding chapters. Additional sensors include the M-42 dosimeter based on a silicon diode and two commercially available transistor-based dosimeters. We had initially foreseen to add a sensor capable of detecting (counting) neutrons as well, but were unable to do so because of time and manpower constraints.

I begin by introducing the scientific, technical, and operational objectives we aimed to achieve by operating the instrument on the ISS. Doing so comes with a range of requirements and constraints specific to human space missions in general and the ISS program in particular, which I also briefly summarize. I then describe one of the most important aspects of the work on RadMap, namely the development of read-out electronics for the ADU that can be reused for future missions. After describing the other radiation sensors, I give an overview of the overall design of the instrument, including its mechanical, electrical, and thermal-control systems. Finally, I discuss the integration into the ISS infrastructure and the tests we were required to perform before deploying the RadMap Telescope to the space station.

10.1 Objectives, Requirements, and Constraints

The RadMap Telescope primarily serves as technology-demonstration experiment for the ADU tracking calorimeter. Most of the objectives therefore relate to this sensor, with additional ones for the two dosimeters. Besides the scientific focus, we also pursued a range of technical and operational objectives concerning the integration of the instrument into the infrastructure of a crewed spacecraft and its operation from the ground.

10.1.1 Scientific Objectives

Based on an analysis of available instruments and the capability gaps identified by NASA and others (summarized in Chapter 5), we formulated a set of core scientific objectives and requirements that, from our perspective, should be at the focus of new sensor and instrument developments for radiation protection of the astronaut crew. These translate into capability objectives for the RadMap Telescope. They are closely related to the general requirements and constraints for the ADU, which I introduced in Chapter 6.

Sensitivity to Cosmic-Ray Protons and Nuclei. The radiation exposure of astronauts and spacecraft is to a large extent caused by cosmic-ray protons and nuclei, with only a small fraction contributed by electrons and other particles (see Section 5.2). It is therefore imperative that an instrument designed to monitor crew radiation exposure is sensitive not only to protons but also to heavier ions. To include all nuclei that significantly contribute to the absorbed dose, the sensitivity range must extend at least up to iron. Electrons and other particles are of minor importance—either because their flux is low or because they can be easily shielded—and need not necessarily be covered, though their detection may help to study secondary radiation created in interactions of cosmic rays with a spacecraft's shielding. Sensitivity to neutrons would likewise be of immense value for investigating secondary radiation, as they can contribute significantly to the total dose astronauts are exposed to. The detection of neutrons is a complicated business, however, and would likely require employing a different measurement principle than is required for charged particles. For RadMap, we therefore concentrated on protons and nuclei and did not investigate in depth how the instrument could be used to detect other (charged and uncharged) particles, though its primary detector material may allow doing so (see Section 12.2.2).

Sensitivity in a Biologically Meaningful Energy Range. Unlike detectors built for astrophysical investigations, the RadMap Telescope is not meant to provide highly accurate data on cosmic rays (i.e., measurements of their kinetic energy) in an unnecessarily broad energy range. Not only would this capability not be particularly useful for radiation-monitoring applications, it would also very likely result in a prohibitively large and power-hungry instrument. Instead, we aim for sensitivity to the part of the cosmic-ray spectrum that is most interesting and important from a medical perspective. The instrument shall, after all, provide biologically meaningful measurements of the radiation dose

and the dose rate astronauts are exposed to. It is therefore designed to be most sensitive to nuclei most harmful to the human organism—i.e., to those with energies of tens to hundreds of MeV per nucleon (see Section 5.2 for details). Faster nuclei must still be detected and their deposited energy recorded; but since their energy loss is near constant along their path through the human body and only depends little on their initial kinetic energy, a precise determination of the latter is not required to accurately determine the delivered dose.

Precise Identification of Protons and Nuclei. A crucial capability of the RadMap Telescope, setting it apart from many existing instruments, is its intended ability to (unambiguously) identify protons and nuclei. Many existing sensors only record the LET and thus cannot do so. While knowledge of the LET allows to determine the biological effectiveness of incident radiation to some degree—and therefore results in a more precise calculation of the effective dose than the measurements of a simple counting dosimeter can provide—it does not allow to unambiguously identify it. The recording of particle-dependent energy spectra, on the other hand, enables the precise determination of the biological effectiveness and of the depth-dose distribution of incident radiation particles. Ideally, the energy range across which particle identification works reliably extends well beyond the core region of interest (see previous paragraph). Though the total energy (dose) deposited by highly energetic nuclei is on average much lower than for stopping ones, the biological effectiveness of the ionization channels created by heavy nuclei is nonetheless much higher than for protons and other light particles.

Omnidirectional Sensitivity and Tracking. A determination of the directionality of incident radiation allows to measure the shielding effectiveness of a spacecraft and identify potential areas of increased production of secondary radiation (e.g., due to inadequate shielding composition). Up to now, gathering such data requires the repeated (manual) turning of, for example, a particle telescope like CPDS [Lee+07] to compensate for its narrow field of view. Doing so leads to significant uncertainties in the gathered data, primarily because measurements usually take place over several days or weeks (mostly owing to low counting statistics and to constraints in the crew schedule). The resulting temporal variations of the radiation environment must be duly corrected before conclusions about the spacecraft shielding can be drawn. The RadMap Telescope is, to our knowledge, the first instrument that can track charged particles with omnidirectional acceptance—i.e., with a field of view covering

the full solid angle. This capability enables the instantaneous measurement of radiation hitting the instrument from random directions and should therefore significantly enhance the resolution of shielding measurements; it also eliminates the need for interventions by the crew.

Real-Time Capability. A sizable contribution to astronaut radiation exposure in missions beyond LEO is expected to come from solar particle events. This is due to the fact that spacecraft and crew are not protected by Earth's (residual) magnetosphere once they leave the planet's vicinity. The nature of these events and our limited understanding of them (see Chapter 2) greatly constrain our ability to predict if and when a burst of high-energy particles emitted by the Sun will hit a spacecraft. However, to minimize their radiation exposure, astronauts must move to areas of a spacecraft or surface habitat that provided better shielding ('shelters') during events with harmfully hard energy spectra. With only limited predictive capabilities, radiation sensors are required that analyze the radiation environment in real time and can alert the crew to shelter. As the onset of powerful solar storms is sudden, and the rise in radiation intensity to dangerous levels can last mere minutes, an analysis on the ground will not be possible for future missions into deep space due to the delay of communications. At least a basic level of real-time analysis on the instrument itself will therefore be required.

To the best of our knowledge, this set of (intended) capabilities is unique to the RadMap Telescope. While there is a number of instruments that meet the first two objectives, few can precisely identify protons and nuclei. Of these, none has omnidirectional sensitivity. Though there are some real-time capable dosimeters (like the M-42 presented in Section 10.3), they at most provide information on the LET of incident radiation. Demonstrating that the ADU tracking calorimeter and its read-out and data-acquisition electronics can meet all of the above objectives is the most important motivation for operating the RadMap Telescope on the ISS.

10.1.2 Technical and Operational Objectives

Besides the scientific objectives aimed at demonstrating the suitability of the ADU as general-purpose radiation monitor, we also formulated a set of technical and operational objectives that aim at demonstrating that RadMap-derived instruments may in the future be used widely aboard crewed spacecraft.

Space-Qualified Read-Out Electronics. The development of a set of space-qualified read-out electronics suitable not only for operations on the ISS but also on future deep-space missions was a central technical objective of the RadMap Telescope project. The electronics we used for our beam tests were not only too large in every respect (volume, mass, and power consumption) but also required a relatively long shaping of the SiPM signals, thus limiting the achievable count rate and risking signal pile up in high-rate environments. Though developed for accelerator-based experiments, they were also not designed with radiation hardness in mind. Besides the requirements and constraints imposed by the space environment, the fact that the detector concept requires electronics that can cope with the large dynamic range of SiPMs presented an additional challenge, as most commercially available ASICs cannot handle the charge released by a fully illuminated sensor.

Real-Time Capable Data Acquisition. With the requirement for the real-time delivery of measurements also comes the requirement for a real-time capable data-acquisition system. In the context of the RadMap Telescope, the term 'real-time' must not be understood as strictly as in some other applications. When we call for a real-time capability, we essentially require three things: (1) the fully parallel digitization of all 1 024 sensor channels of the ADU, (2) a predictable, constant, and short ($< 10\,\mathrm{ms}$) delay between the passage of a particle through the detector and the availability of the digitized SiPM signals, and (3) the ability to cope with the event rate on the ISS. These aspects differentiate the RadMap Telescope from many legacy systems that integrate measurements over a certain time, with data becoming available at fixed intervals.

Real-Time Event Processing and Data Delivery. Alerting the crew in response to the increased radiation intensity of a solar particle events requires not only the sensor data to be acquired in real time but also the real-time processing of it. While a full analysis including particle identification and precise energy determination may not always be required, at least a certain set of parameters—for example the count rate, the approximate energy deposited by each particle, or the rough directionality of tracks—should be determined. The system should also be capable of storing or forwarding its measurements continuously at the maximum event rate achievable by the read-out electronics. This ensures that parameters that are too complicated for real-time analysis can be determined from recorded data at a later point in time.

Integration Into Spacecraft Infrastructure. Operating an instrument on a spacecraft is significantly different in many aspects from operating one in the laboratory or at an accelerator-based experiment. Not only are resources like mass, volume, power, and data bandwidth severely constrained. One of the biggest challenges is that instruments cannot be easily fixed while on orbit, lest they be designed specifically for being maintained by the crew. Since we had never built and operated in instrument in space before, deploying the RadMap Telescope to the ISS gave us the opportunity to gain experience in a lot of the aspects specific to the space environment. At the same time, we also needed to demonstrate that RadMap could seamlessly integrate into the infrastructure of the space station. This included handling of the instrument by the crew.

Semi-Autonomous Operations. Future radiation monitors based on the tracking calorimeter concept shall be able to operate fully autonomously aboard spacecraft that will be travelling as far as Mars. On such missions, the amount of data that can be sent back and forth will be severely limited, and the round-trip communications delay can be as much as 45 minutes. Systems of critical importance to crew health must thus not depend on constant monitoring and control by operators on the ground. An objective of the RadMap Telescope therefore is to demonstrate that it can operate semi-autonomously for extended periods of time.

Data for Fine-Tuning of Simulations. Developing tracking and reconstruction algorithms requires accurate knowledge of the expected signatures that the different cosmic-ray nuclei of interest create in the detector. We generally rely on simulated events generated with the Geant4 framework to develop our algorithms. However, such simulations can approximate the true event signature only as good as we understand aspects like the signal-generation process, crosstalk, background events, and noise. Since the radiation environment inside the ISS can hardly be artificially re-created on Earth, a crucially important objective of RadMap is to collect a large data set that we can use to fine-tune our simulation models.

Benchmarking Against Flight-Proven Instruments. By far one of the most important objectives is the benchmarking of ADU measurements against the data of other, flight-proven sensors. Such comparison allows us to understand to what extent the data we gather delivers an accurate picture of the radiation environment inside the station. In particular, it gives us the possibility to find the detection thresholds we must set to record all particle interactions in the

ADU's active volume, which is a prerequisite for recording accurate dosimetric values. The well-calibrated M-42 dosimeter that is part of the instrument is one source of data for benchmarking; instruments operated by NASA and other agencies can be another, if the RadMap Telescope is operated in close enough proximity that the radiation field the sensors are exposed to can be considered the same.

These major technical and operational objectives are supplemented by a range of minor ones that are of no importance to my thesis and are thus not discussed here.

10.1.3 ISS-Specific Requirements and Constraints

There is a long list of requirements and constraints that must be met before an instrument can be deployed to and operated on the ISS, or any other crewed spacecraft. These range from simple things like material constraints to the rather complicated topic of electromagnetic compatibility. Here, I only give a high-level overview of the most important requirements that the ISS program and NASA's safety engineers placed on the RadMap Telescope.

Material Constraints. The choice of materials that can be used on the space station is generally restricted to those that are neither toxic nor flammable. This, for example, usually limits the use of plastics to expensive high-performance polymers like PTFE, polyetherimide (PEI), and polyether ether ketone (PEEK). Small quantities of flammable plastics may be approved for use if payload developers can credibly show that their instrument does not contain ignition sources and that flames cannot propagate into it from the outside [SSP51721]. Another reason for constraining the use of plastics is outgassing—the release of gas that was trapped, dissolved, or absorbed in the material. The accumulation of such gas must be carefully controlled to prevent the buildup of harmful concentrations of unhealthy chemicals in a spacecraft's atmosphere [SSP50005]. For the ISS, NASA often waives the restriction on outgassing if an instrument contains less than 20 pounds (9 kg) of polymeric material.

Launch Loads. During their ascend into space, payloads must withstand the acceleration, vibration, shock, and acoustic-pressure loads created by the launch vehicle [SSP57000]. The maximum static acceleration loads are specified at 7 g (9.2 g for re-entry upon return to Earth); the design RMS loads due to vibrations follow a frequency-dependent profile with an overall level

of 6.8 g_{rms}. These values also apply if the payload is launched soft-stowed, that is, in a foam-lined transport bag or similar, though reduced limits may be imposed on a case-by-case basis. Shock loads peak at 1 700 g but are generally not relevant for soft-stowed payloads.

Crew-Induced Loads. Depending on where in the ISS the instrument is deployed, it may be subjected to mechanical loads by the crew, especially when it is mounted close to or inside the translation path (i.e., the central corridor in each module through which the astronauts float from one place to another). In this case, the crew may accidentally bump into the payload or use it as a kick-off point, with loads of up to 556.4 N acting on an area of $10 \times 10\,\mathrm{cm}^2$ [SSP50005; SSP57000].

Touch Temperatures. To avoid pain and skin damage, exposed surfaces of a payload that can be touched by the crew must not exceed certain temperature limits. For inadvertent quasi-continuous contact, the maximum allowable temperature is 45 °C [SSP50005]; higher limits apply for incidental contact or for short intentional contact [STD3001]. Exceptions can be made, for example for exhaust vents, if hot surfaces are adequately marked and shielded from accidental contact.

Electromagnetic Compatibility. To ensure that payloads can operate inside the electromagnetic environment aboard the space station and do not disturb others in doing so, the ISS program strictly controls the emissions of every hardware element that draws electrical power to prevent electromagnetic interference (EMI). Tests must be performed to assess whether a payload stays within the limits for conducted (via the power supply) and radiated emissions [SSP30327]. Conversely, payload developers must demonstrate that their hardware is not susceptible to the electromagnetic environment on the ISS, especially if it contains safety-critical circuits that may be adversely affected by external (conducted or radiative) disturbances.

Grounding and Bonding. Proper grounding is crucial for safe crew interactions with the instrument. Electrical systems must be enclosed in a housing that is either non-conductive or whose parts are bonded via low-resistance paths to avoid electrical-shock hazards [SSP57000]. If the payload contains radiofrequency (RF) systems, the bond path must have a resistance of 2.5 mΩ or less. Stricter requirements apply to the housing and electrical connectors if voltages above 32 V are present.

Compliance with these and all other applicable requirements can be established via one of three methods: (1) a certificate of conformity, in which the payload developed certifies that a requirement was adhered to during the design of the payload; (2) an analytical verification that shows through calculations or a review of design documentation that a requirement is met; or (3) a test at a certified facility. As this thesis does not serve as a technical documentation, I only selectively mention when any of the above requirements substantially influenced the design of the RadMap Telescope; I do not discuss in detail how we met all the different requirements placed on the instrument.

10.2 Instrument Overview

Before describing in detail the different subsystems comprising the RadMap Telescope, I first give an overview of the overall instrument and its characteristics. Figure 10.1 shows an annotated computer rendering of RadMap as it was designed for operations on the ISS. Besides the ADU, whose working principle and design is described in detail in Chapters 6 and 8, the instrument contains two additional dosimeter systems (DLR's M-42 and commercially available RADFETs) that are presented in Section 10.3. The three detectors are contained in a light-tight housing that also accommodates read-out and data-acquisition electronics, a flight computer, and a power distribution system. The latter two directly connect to the network and power infrastructure of the space station.

To keep training for astronauts and the crew time required to operate the instrument to a minimum, we designed RadMap to appear as simple as possible on the outside. There are no crew interfaces other than a single LED to indicate that the flight computer is turned on. The system automatically boots up once powered by a 28V supply via its electrical interface; there is no power or reset switch. For the data connection, we use an industry-standard circular Ethernet connector that allows bandwidths of up to 100 Mbit. Data transfer is also possible via a wireless network interface. The only mechanical interface is a stud on bottom of the housing that fits into a seat-track anchor. The fully integrated instrument weighs 3.08 kg and measures $16 \times 14 \times 14\,\mathrm{cm}^3$ (excluding the seat-track stud).

Although the ADU's read-out electronics are already optimized for low power (see Section 10.4), the flight computer is a commercially available Jetson TX2i module from Nvidia, which can consume up to 20 W of power. To

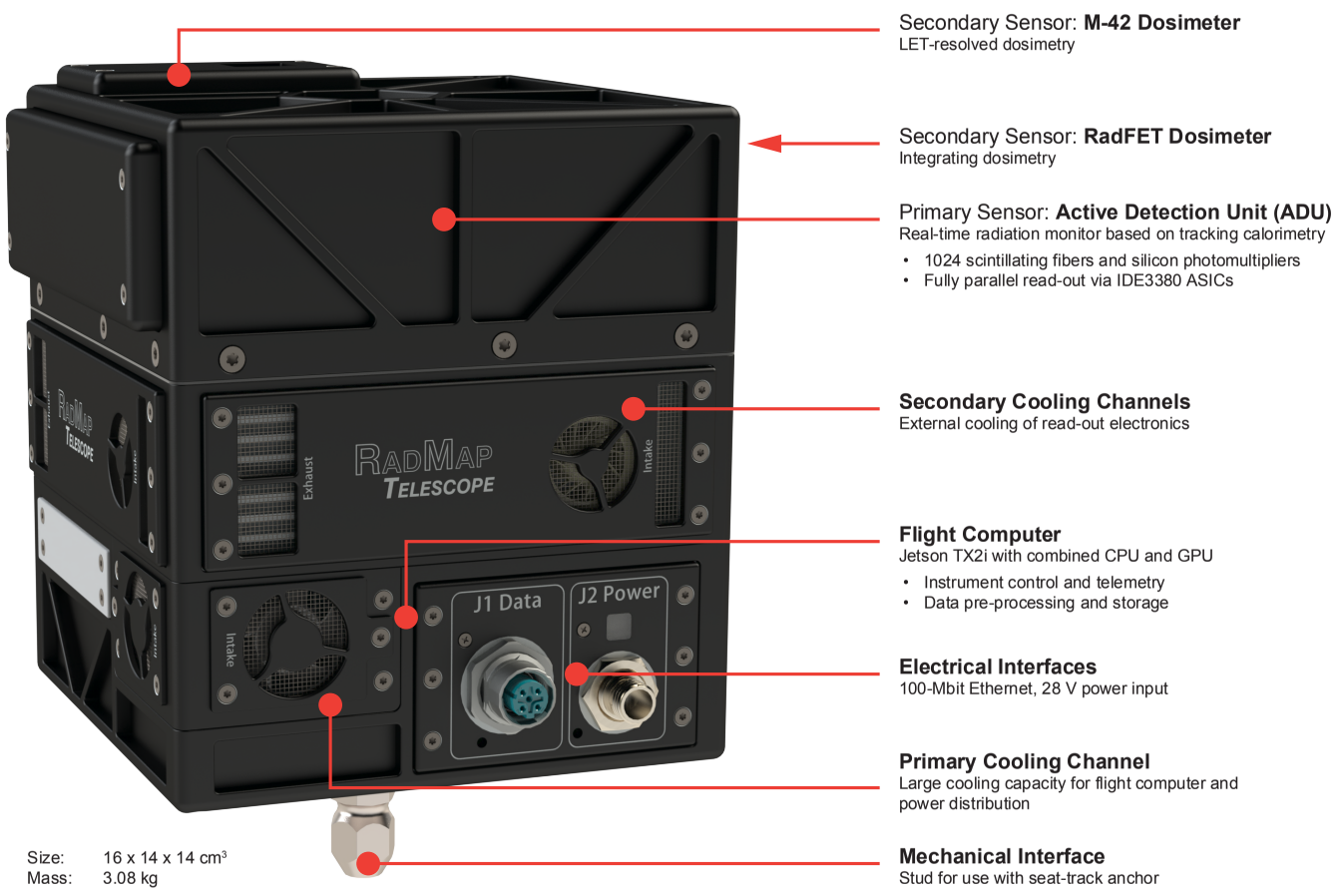

Figure 10.1: Overview of the RadMap Telescope and its subsystems.

prevent the instrument from exceeding the touch-temperature limits (and to keep the dark-count rate of the ADU's SiPMs at an acceptable level), RadMap has five cooling channels. The primary channel has a large cooling capacity and regulates the temperature of the flight computer and the power distribution unit. The four smaller channels have less capacity and keep the temperature of the read-out and data-acquisition electronics stable.

10.3 Primary and Secondary Radiation Sensors

The RadMap Telescope is equipped with three radiation sensors. The primary one is the ADU, which is described at length in earlier chapters of my thesis. It is the most powerful of the three sensors and its on-orbit demonstration is the primary reason for operating RadMap on the ISS. The second sensor is the M-42 dosimeter, which is capable of LET-resolved dosimetric measurements. The least resolved data is gathered by the RADFETs, which can only determine the integrated dose they were exposed to.

10.3.1 Active Detection Unit

The 1024-channel tracking calorimeter comprises four ADU detector modules (see Figure 8.1) that each consist of 256 SCSF-78 scintillating fibers and PM3325-WB-D0 SiPMs. We had initially planned to use the four modules that our calibration measurements had revealed to be the best ones (see Table 8.2) but were not able to do so. Unfortunately, in some modules the material holding the uppermost or lowermost fiber layers slightly deformed while being heated after attaching the SiPM arrays. Excess optical glue formed columns between the fibers and the deformed support structure and cured in place, preventing the latter from reverting into its original shape after cooling down. This prevented us from stacking the modules as intended because we were afraid that pressing down too hard on the deformed structure might break the SiPMs off their PCBs instead of breaking the glue columns. I discuss this issue and our approach to prevent it in the future in detail in Section 12.1.1.

In selecting the ADU modules for the flight detector, we hence needed to settle for a compromise between mechanical fit and module quality. The two best modules, ADU005 and ADU010, were not usable, as was ADU009. The final detector thus consists of (listed in stacking order, from top to bottom): ADU008, ADU003, ADU006, and ADU004. Figure 10.2 shows the fully integrated tracking calorimeter atop the base of the instrument's housing.

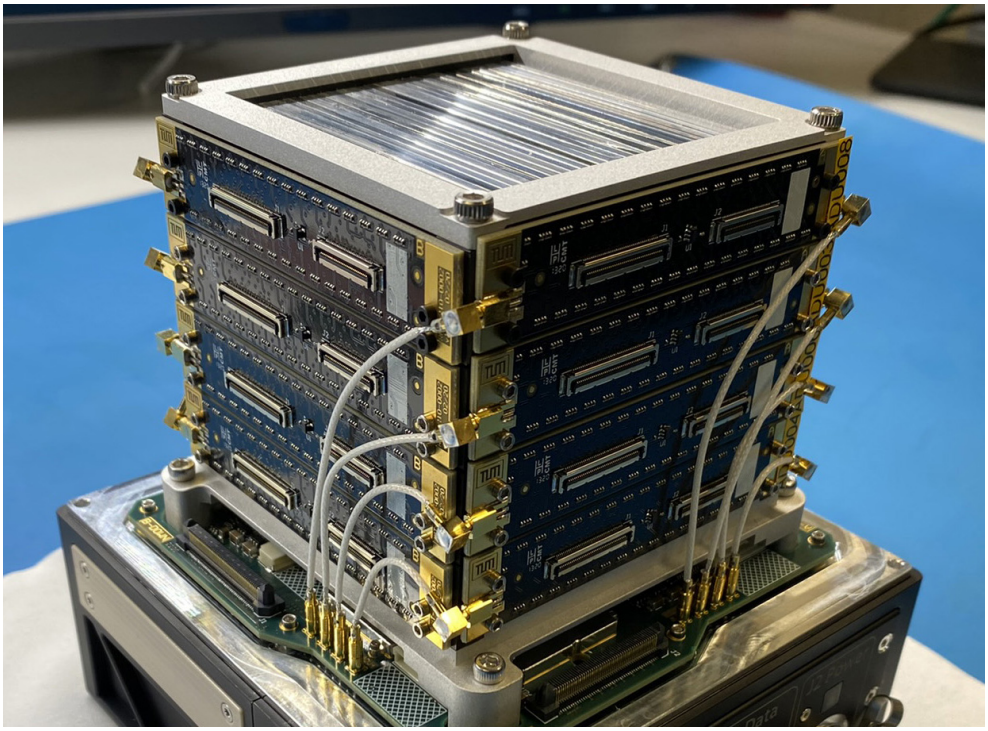

Figure 10.2: Fully integrated flight ADU for the RadMap Telescope. The detector sits atop the base of the instrument's housing, with the coaxial cables for the SiPM bias voltage already attached. From top to bottom, we used the following tracking-calorimeter modules: ADU008, ADU003, ADU006, and ADU004.

10.3.2 M-42 Dosimeter

The M-42 dosimeter integrated into RadMap is a modified version of the M-42 Split (M-42_S) developed by our colleagues at DLR's Institute of Aerospace Medicine [Ber+19]. The sensor measures the energy deposited by charged particles in a Hamamatsu S3590-19 planar silicon PIN photodiode [HAM23b]. The latter has an active area of $11.0 \times 11.2\,\mathrm{mm}^2 = 1.23\,\mathrm{cm}^2$ and a thickness of $300\,\mu\mathrm{m}$. The diode is biased with a reverse voltage of 53 V to ensure full depletion. The charge (electron-hole pairs) created by a particle passing through the silicon [BW69] is amplified before being fed to a shaper and peak-sensing circuit (see Figure 10.3). The peak voltage is then digitized by a 16-bit ADC and stored as a pulse-height spectrum in redundant flash memory that is

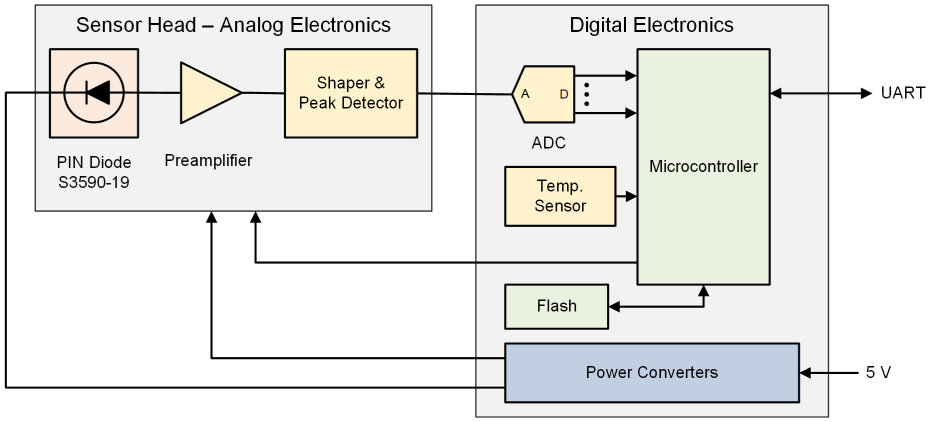

Figure 10.3: Schematic diagram of the M-42 dosimeter in the version modified for the RadMap Telescope. The analog signals are transmitted from the sensor head to the digital electronics via micro-coaxial cables. Adapted from [Ber+19].

attached to a microcontroller. Temperature sensors provide references for correcting temperature effects. The system internally creates and conditions all its required voltage buses, including the PIN diode's bias voltage, from a single 5 V supply. These voltage rails are monitored via the microcontroller's built-in ADC. In the version modified for the RadMap Telescope, the dosimeter's microcontroller communicates with the instrument via a universal asynchronous receiver-transmitter (UART) interface. The firmware allows setting a few selected parameters for controlling the dosimeter operation (e.g., date and time, digitization thresholds, and integration times) via this interface.

The PIN diode and the analog electronics (preamplifier, shaper, and peak detector) are located on a PCB that is optimized for shielding against electromagnetic noise. We refer to this PCB as the sensor head, and it is mounted in a dedicated compartment on the instrument's outer wall to ensure it is well shielded from other systems. The M-42's digital electronics are located on a second PCB that is housed in a separate compartment of RadMap's housing. The analog signals are transmitted from the sensor head to the digital electronics via micro-coaxial cables (see Figure 10.4).

The dosimeter can measure energy depositions between 0.06 MeV and 17.7 MeV. As the amplification and shaping are linear, the 16-bit digitization of the ADC therefore means that the energy deposition of each particle passing the detector can be determined with a resolution of 0.305 keV. To reduce the amount of data produced, the measurements are resampled to 1004 equidis-

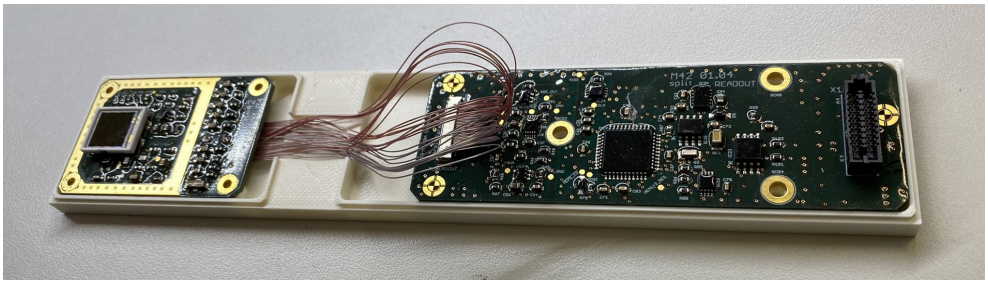

Figure 10.4: M-42 dosimeter before integration into the RadMap Telescope. The sensor head is on the left, the digital electronics on the right. The two PCBs are connected via micro-coaxial cables. The S3590-19 PIN photodiode is the large component in the white ceramic package on the sensor head.

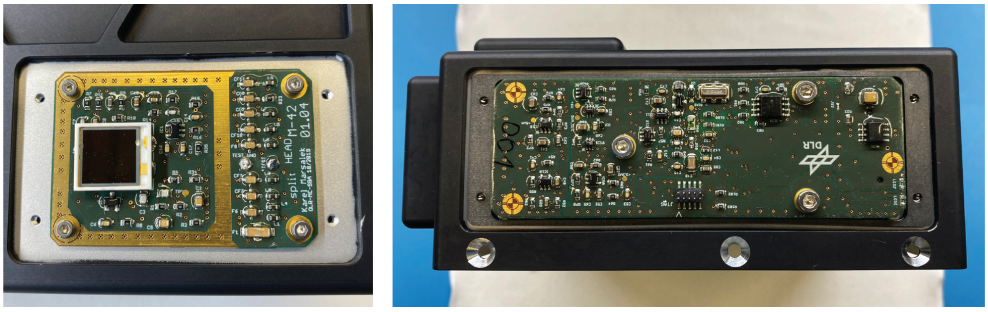

Figure 10.5: The two PCBs (left: sensor head; right: digital electronics) of the M-42 dosimeter integrated into their compartments of the RadMap Telescope housing.

tant bins with a width of 17.6 keV. This width defines the effective resolution of the energy-deposition measurement, which is hence 29.3% at the lower end (0.06 MeV) and 0.1% at the upper end (17.7 MeV) of the energy deposition spectrum. The total absorbed dose is calculated by integrating over the spectrum and dividing by the mass of the detector; a conversion factor of 1.23 is used to convert the result (dose in silicon) to dose in water. Nominally, the LET spectrum is accumulated over an integration time of 300 s before being stored in the flash and cleared; the number of counts, the dose rate, and housekeeping data (temperature and voltages) are stored every 60 s. Both intervals can be adjusted via the UART interface.

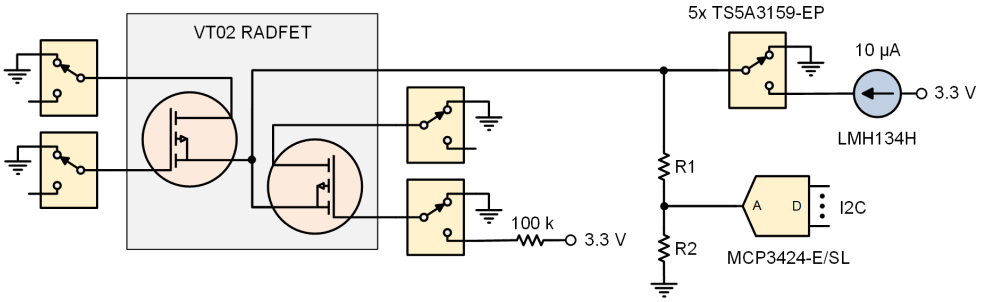

Figure 10.6: Schematic diagram of the read-out circuit for one VT02 RADFET sensor; the circuit for the second one is identical. A 10-µA current forced into the bulk–source terminal generates a voltage that is proportional to the source–drain resistance, which increases through irradiation. During exposure, all terminals of both transistors are grounded, except for the gate of one of them. The latter is biased to 3.3 V to increase its radiation sensitivity. During read-out, one drain terminal is left floating to only measure the voltage across one RADFET. The 18-bit ADC allows the measurement of the absorbed dose with a resolution of 480 mGy or better.

10.3.3 RADFET Dosimeters

For measuring the integrated dose the RadMap Telescope was exposed to during its operational period on the ISS, we use two Varadis VT02 RADFET sensors [Var22]. Each sensor consists of two identical RADFETs with common source and bulk. Their gate has a thickness of 400 nm, a length of 300 µm, and a width of 50 µm, a size which is optimized for the measurement of doses between 1 cGy (1 rad) and 1 kGy (100 krad). Figure 10.6 shows a schematic diagram of the read-out circuit for one VT02 sensor; the circuit for the second one is identical. Via a set of five single-pole double-throw (SPDT) switches, the terminals of the two metal-oxide-semiconductor field-effect transistors (MOSFETs) can either be connected to ground (in the normally closed position), or connected to a potential or additional circuitry (in the normally open position). In exposure mode, all terminals are grounded. In read-out mode, a current of 10 µA is forced into the bulk–source terminal common to both transistors [Tex13], generating a voltage that is proportional to their source–drain resistance, which increases through irradiation [HA86; Pej15]. To only measure the voltage across one RADFET, the drain terminal of the other is left floating during read-out. The gate of one transistor is always grounded, that of the other is biased to 3.3 V to increase its radiation sensitivity [Ris+22].

Figure 10.7: Accommodation of the two RADFETs in the housing of the RadMap Telescope. One VT02 is visible on the left, the other is hidden below a shield made of white POM.

The voltage at the bulk–source terminal is scaled via a voltage divider with $R_1 = R_2 = 100\,\mathrm{k}\Omega$ and then digitized by an 18-bit MCP3424 ADC [Mic09]. RADFETs have a highly non-linear response; the VT02 has a maximum sensitivity of 0.65 mV/cGy, or 325 µV/cGy after the voltage divider. Using its internal reference, the ADC has a maximum resolution of 15.625 µV per least significant bit (LSB), corresponding to a dose of 480 mGy. Its internal programmable gain amplifier (PGA) allows to further improve this resolution by up to a factor of eight. The ADC's measurements are controlled and retrieved via an Inter-Integrated Circuit (I2C) bus. Figure 10.7 shows how the two VT02 sensors are accommodated in the instrument housing, with one being partially shielded by a cover made of POM.

10.4 Read-Out Electronics for the ADU

One particularly important aspect of my work was the development of read-out electronics for the 1 024 SiPMs of the ADU. While of the instrument's other electrical systems were designed only for the technology demonstration on the

space station, our express goal for the read-out system was to find a solution that would also work for future long-term deep-space missions. This did not necessarily mean that each and every component needed to be fully space-qualified but rather that in case non-qualified components were used, they could easily be swapped out in the future. My aim, however, was that at least the actual digitizing circuits should be fully space-qualified.

10.4.1 Requirements

The requirements driving the design of the read-out electronics almost exclusively derive from anticipated future applications. Many of them—especially those relating to size, mass, and radiation hardness—could have been formulated less restrictive if we had designed the system only for an ISS experiment.

1. The most important and at the same time most challenging requirement was that the read-out electronics needed to cope with the large charges released by fully illuminated SiPMs and at the same time be sensitive to the small number of photoelectrons created by MIPs. Such large dynamic range is somewhat unusual in applications of sensors sensitive to single photons. The PM3325-WB-D0 SiPMs we used for the ADU have a terminal capacitance of 1 nF, leading to a charge release of 6 nC for full illumination at the maximum allowable overvoltage of 6 V. At the minimum overvoltage of 2 V, on the other hand, a MIP releases a charge of only 5.6 pC (for 134 photons at a PDE of 29%). Table 10.1 summarizes the charge ranges at different illumination scenarios for a selection of SiPM models, including recent ones that have only become available after the completion of the RadMap Telescope.
2. Achieving a high energy resolution requires that the gain of the SiPMs is as uniform and stable as possible. However, intrinsic differences in the breakdown voltage and its temperature dependence can lead to gain variations of several percent. These can be compensated for by adjusting the bias voltage individually for each photosensor. Since a 1 024-channel bias supply puts a prohibitively large burden on the instrument's mass and power budget, the bias-voltage adjustment must be made by the read-out electronics.
3. The maximum event rate the system can cope with is not a primary driver for its design, as precise knowledge of the so-called 'dead time'—the time a system needs to digitize signals and cannot accept new ones—can be

Table 10.1: Signal properties of a selected range of SiPMs. The PM3325-WB-D0 [KET18] and S13360-3025PE [HAM22] were among the models we considered for RadMap's ADU; we ultimately chose the former. The models marked with an asterisk (*), the AFBR-S4N44P014M [Bro22] and MICROFJ-30020-TSV [ons21], were not yet available at the time we developed the instrument but may be of interest to future versions of the ADU.
The charge released by the SiPMs is calculated by multiplying their terminal capacitance with the respective overvoltage (range). The charge released under full illumination of the complete sensitive area is given as reference. A more realistic upper limit is that of full illumination of the $2 \times 2\,\mathrm{mm}^2$ area covered by a scintillating fiber. However, since the numerical aperture of a fiber end glued to a SiPM is not zero, the real illuminated area, and hence the maximum released charge, may be slightly larger. For the calculation of the charge released by a MIP, I assume that it produces 134 photons that reach the SiPM.

	PM3325-WB-D0	**S13360-3025PE**	**AFBR-S4N44P014M***	**MICROFJ-30020-TSV***
	KETEK	Hamamatsu	Broadcom	onsemi
Active Area	$3 \times 3\,\mathrm{mm}^2$	$3 \times 3\,\mathrm{mm}^2$	$3.72 \times 3.62\,\mathrm{mm}^2$	$3.07 \times 3.07\,\mathrm{mm}^2$
Microcell Pitch	25 µm	25 µm	40 µm	20 µm
# of Microells	13 920	14 400	8334	14 410
Recharge Time, τ	33 ns	-	55 ns	45 ns
Term. Capacitance	1 nF	320 pF	580 pF	1.07 nF
Overvoltage	2.0 to 6.0 V	2.0 to 9.0 V	6.0 to 16.0 V	1.0 to 6.0 V
PDE	29% to 47%	13% to 30%	56% to 65%	37% to 51%
Charge				
Full illumination	2.0 to 6.0 nC	0.64 to 2.88 nC	3.48 to 9.28 nC	1.07 to 6.42 nC
For $2 \times 2\,\mathrm{mm}^2$	0.89 to 2.67 nC	0.28 to 1.28 nC	1.03 to 2.76 nC	0.45 to 2.73 nC
For MIP	5.6 to 27.1 pC	0.8 to 8.0 pC	31.3 to 97.0 pC	3.7 to 30.4 pC

used to calculate the true fluxes from the measured count rate. This only works, though, if the system is not fully saturated, that is, if it is not constantly recording data. In LEO, we expect the highest event rates to occur while a spacecraft passes through the SAA. From simulations, we expect event rates on the other of five to ten kilohertz.

4. Achieving a power consumption that is as low as possible is critical for enabling a wide range of use cases for future radiation monitors based from the RadMap Telescope's design. Radiation measurements are crucially important for ensuring crew health and should therefore be conducted constantly, even when a spacecraft is in a power-saving state. Keeping the power consumption of the read-out electronics well below 5 W is therefore an important objective.
5. During long-term deep-space missions, spacecraft (and crew) may be exposed to radiation doses of tens of krad (hundreds of Gy) or more. All components of the read-out system must therefore survive such exposure. Single event effects (SEU and SEL) are not critical as long as they do not lead to permanent damage.

10.4.2 ASIC Selection

The rising popularity of SiPMs as a compact and easy-to-use alternative to PMTs has led to the development of a broad range of read-out ASICs over the past two decades. Many of them—for example the PACIFIC [Cos+18], KLauS [Yua+19], FastIC [Góm+22], and H2GCROC [Gon23] chips—are designed for accelerator-based high-energy physics experiments. Others are intended for medical (e.g., ANGUS [Tri+18], STiC [She+18], ToT-ASIC2 [Ori+23], and MPPC-CT64 [Ari+23]) applications or for telescopes (e.g., MUSIC [Ber+16b] and SMART [Ara+23]). There are even a few projects that develop ASICs specifically for space applications (e.g., [DiS+23; Ted+23; San+24]). The challenge in using any of the above chips is twofold: (1) Most, if not all, are tailored to the specific use case of the experiment they are intended for and (2) they are developed by small groups at universities and research institutes. This not only means that literally none of them matches the dynamic-range requirements of our application but also that the devices are more often than not poorly documented, with the developers unable to offer the comprehensive support required to use their chips. We therefore decided against considering any of those ASICs for our project.

Table 10.2: Characteristics of selected SiPM read-out ASICs. Data from [Int19; wee19; wee18a].

	IDEAS **IDE3380**	WEEROC **Citiroc 1A**	WEEROC **Petiroc 2A**
Channels	16	32	32
Inputs	negative, $\leq$16 nC positive, $\leq$40 pC	positive, $\leq$400 pC	negative, $\leq$400 pC positive, $\leq$400 pC
Bias correction	1 V / 8 bit	2.5 V / 8 bit	1 V / 8 bit
Modes of Operation	peak-sensing + ADC time-over-threshold analog shaper	peak-sensing photon counting	photon counting analog time / charge digital time / charge
Outputs	serial analog charge (MUX) parallel shaper / ToT trigger OR	low-gain analog MUX high-gain analog MUX parallel discriminator trigger OR	analog charge MUX analog time MUX digital charge / time trigger parallel / OR
Interfaces	serial data out SPI for configuration trigger output clock input (4 MHz)	parallel / MUX out serial for configuration trigger output probe output	serial data out serial for configuration trigger output clock input
Shaper	200 to 1600 ns	15 ns / 12.5 to 87.5 ns	25 to 100 ns
Internal ADC	50 ksps / 12 bit	-	10 bit
Rate Capability	?	?	40 000 events/s
Time Resolution	-	100 ps	18 ps (on trigger out)
Power Consumption For 1024 Channels	30 mW / 15 mW (no CMIS) 1.92 W	225 mW 7.2 W	192 mW 6.2 W
Radiation Hardness	340 krad TID 137 MeV cm^2/mg SEL immunity 18 MeV cm^2/mg SEU threshold	?	?

Table 10.3: Characteristics of selected SiPM read-out ASICs (continued). Data from [wee18b; PET22; Int20].

	WEEROC **Triroc 1A**	PETsys **TOFPET2**	IDEAS **IDE3381**
Channels	64	64	16
Inputs	negative, ≤500 pC positive, ≤500 pC	positive, ≤1.5 nC negative, ≤1.5 nC	negative, ≤800 pC positive, ≤40 pC
Bias correction	2 V / 8 bit	-	1 V / 8 bit
Modes of Operation	peak-sensing + ADC / TDC analog charge	charge integration time-over-threshold	photon counting analog time / charge digital time / charge
Outputs	serial analog charge / time (MUX) trigger OR	digital charge / time	parallel analog shaper parallel analog time digital charge / time trigger OR
Interfaces	serial data out serial for configuration trigger output clock input	serial data out serial for configuration probe output clock input (200 MHz)	serial data out serial for configuration trigger output clock input
Shaper	1.25 to 1280 ns	-	50 to 2000 ns
Internal ADC	10 bit	10 bit	2 Msps / 12 bit
Rate Capability	50 000 events/s	500 000 events/s	1 000 000 events/s
Time Resolution	88 ps	100 ps	-
Power Consumption For 1024 Channels	640 mW 10.3 W	525 mW 8.4 W	360 mW 23 W
Radiation Hardness	?	?	340 krad TID 137 MeV cm^2/mg SEL immunity 18 MeV cm^2/mg SEU threshold

By now, several commercially offered solutions exist, which are (mostly) better documented and come with customer support. Commercial products typically also have a longer life cycle. A broad range of products is offered by WEEROC [Ahm+21], a company working with the OMEGA laboratory at Ecole Polytechnique, with many of them based on the first-generation SPIROC [Aab+21] and EASIROC [Cal+12] chips. PETsys Electronics offers an ASIC originally developed for the read-out for glspetscan scanners that can, however, be used more broadly. And Integrated Detector Electronics AS (IDEAS) has developed multiple ICs that are targeted at space applications. Tables 10.2 and 10.3 list relevant characteristics of the read-out ASICs we considered for our tracking calorimeters. All are essentially based on a signal chain with (charge-integrating) preamplifiers, shapers (with substantially varying shaping times), and peak-sensing circuits, and all except one feature an internal ADC for the digitization of the SiPM charge. The rate capability differs significantly from 10 000 event/s up to 1 000 000 events/s.

All except one option (the IDE3380) would consume more power than the targeted limit of 5 W. More importantly, though: The IDE3380 is the only chip that can cope with the charge range of the PM3325-WB-D0 SiPM, and would also work for all potential replacements listed in Table 10.1. Incidentally, it is to our knowledge also the only IC for which the results of comprehensive radiation tests have been published [Ste+19]. It is therefore the sole product that fulfills all our (most critical) requirements.

The IDE3380 [Int19] has 16 channels and one summing channel (see Figure 10.8 for a schematic diagram), all of which allow measuring charge (pulse height) and trigger time. Each channel has a current-mode input stage (CMIS), to which SiPMs can be direct current (DC)-coupled, that is, without the need for a blocking capacitor. The CMIS has two main purposes: (1) It scales down the charge generated by the SiPM and (2) it provides a stable input voltage offset that allows to individually adjust the effective bias voltage of each photosensor. The stage is designed for large negative charges with a programmable attenuation of 1/10, 1/100, 1/200, and 1/400, corresponding to maximum charges of -0.4 nC, -4 nC, -8 nC, and -16 nC, respectively. It can also cope with large leakage currents of up to -100 μA from dark counts. The input offset is generated via a bias voltage of up to 1 V generated by an 8-bit digital-to-analog converter (DAC). In addition, a configurable bias current of up to 90 μA can be set to compensate for SiPMs with very small dark current.

The voltage generated by the CMIS is fed into a current integrator (CI) stage with programmable gain. This is followed by a shaper that optimizes the

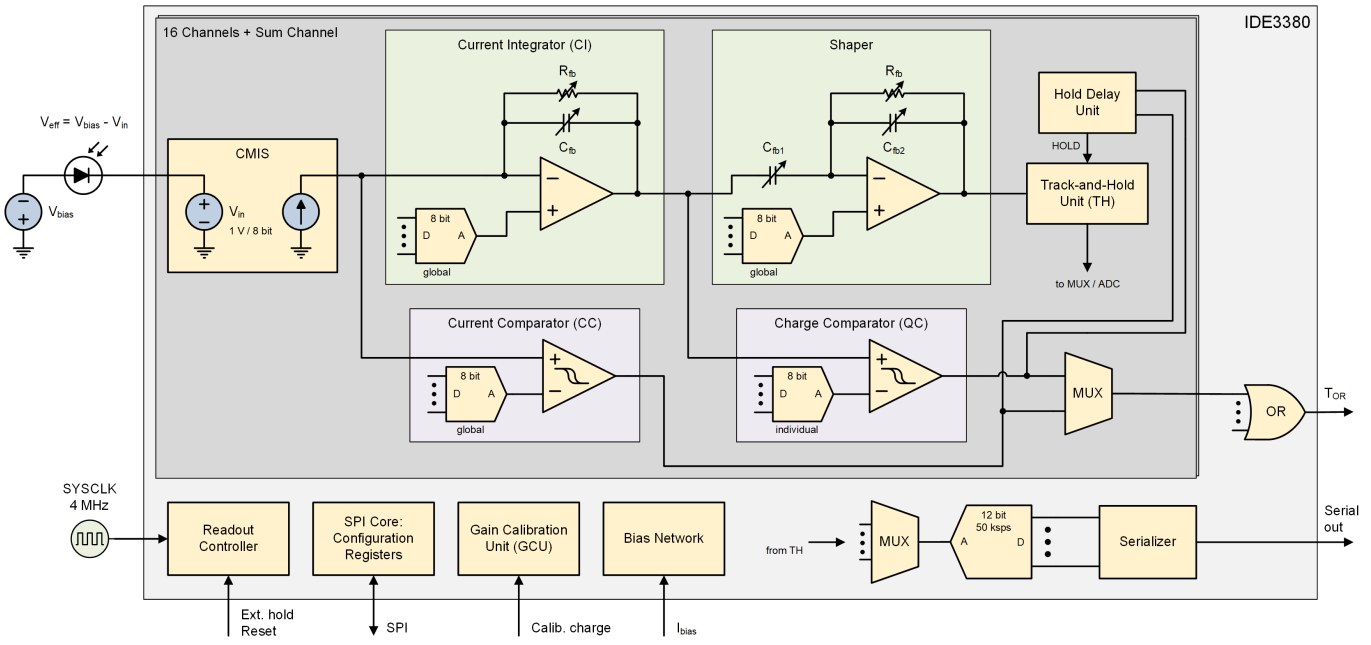

Figure 10.8: Simplified schematic diagram of the IDE3380 ASIC, showing only the elements relevant for understanding its architecture. The parallel-output section and other unused features are omitted. Adapted from [Int19].

signal-to-noise ratio of the integrated pulse. Each shaper has a programmable shaping time, with nominal options of 200 ns, 400 ns, 800 ns, and 1600 ns. The feedback elements (capacitors, resistors, and bias voltage) can, however, be individually adjusted to set (slightly) different values. A track-and-hold (TH) unit tracks the shaper output; its stops tracking and holds the signal upon assertion of a hold signal. The latter is either created from an internal, programmable hold delay (see below) or an external signal. The output of the TH unit can be multiplexed to a 12-bit successive-approximation register (SAR) ADC or accessed via output buffers for digitization by external ADCs.

Every channel (including the summing channel) has two trigger comparators: a charge comparator (QC) for pulse-height discrimination and a current comparator (CC) for fast triggering. Either can be used to (1) trigger the hold delay for the TH unit and to initiate digitization in the ADC, to (2) generate a timing trigger pulse, and to (3) generate a time-over-threshold signal. The QC is a level discriminator (with programmable hysteresis) that compares the output of the CI to a threshold set by an 8-bit voltage DAC individual to each channel. Similarly, the CC compares the current from the CMIS to a threshold set by a global 8-bit current DAC. Setting the reference current right above the noise level allows reducing the time walk inherent to the QC—i.e., the threshold-dependent delay of the QC trigger signal caused by the finite rise time of the CI output. Any combination of the 16 timing trigger pulses can be used to generate a global trigger OR signal.

Because the outputs of the TH units are multiplexed to a single ADC, the channels can only be read out synchronously. The hold delay and the time required to digitize the multiplexed signals thus define the minimum time between consecutive events. The ADC values are sent out via a simple serial interface. The chip requires an external master clock with a nominal frequency of 4 MHz, which can be increased to up to 16 MHz. The configuration registers controlling the chip's operation can be accessed via a standard Serial Peripheral Interface (SPI).

The IDE3380 also contains a gain calibration unit (GCU), which allows identifying and characterizing gain variations and non-linear responses of the signal chain (excluding the CMIS). A calibration charge can either be generated internally or supplied externally, and can likewise be triggered from internal or external sources. Internally, the charge is generated by applying a voltage step to a resistor–capacitor network, producing a current pulse with exponential characteristics and a 100-ns decay constant. The voltage step can be configured with a resolution of 8 bit. The largest charge that can be created is 52.6 pC.

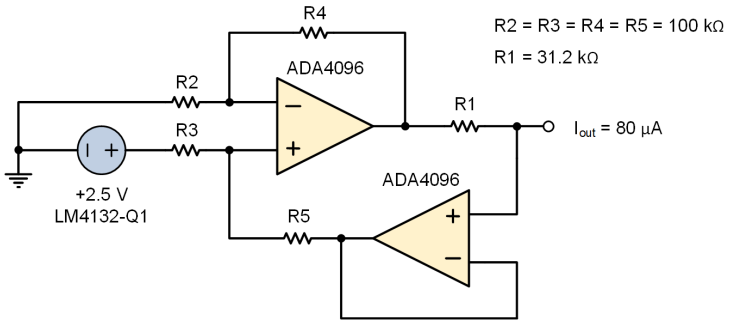

Figure 10.9: Simplified schematic of the precision current pump we use to bias the IDE3380 ASICs. One ADA4096 operational amplifier is used as the current source, the other as a non-inverting voltage follower in the feedback loop to increase the accuracy of I_{out}.

10.4.3 Bias Current Generation

All bias currents and voltages required by the IDE3380 are generated by an internal bias network. This network must be a driven by an external source supplying a nominal current of 80 µA (76 µA to 88 µA). Each ASIC must be supplied by its own current source; the 64 chips for the ADU's 1 024 channels therefore require 64 current sources.

To the best of our knowledge, there is currently no space-qualified source on the market that can be configured for 80-µA current, and we did not want to simply use a resistor to a (potentially unstable) supply voltage. We therefore generate the bias current via a precision current pump based on two operational amplifiers [Ana17]. Figure 10.9 shows the circuit that I adapted from [Won]. The advantage of this design is that the accuracy of the current output is improved by using a non-inverting voltage follower in the feedback loop. The output current of the circuit can be calculated via:

$$I_{\mathrm{out}} = \frac{V_{\mathrm{in}} \cdot A_{\mathrm{V}}}{R_1} \tag{10.1}$$

$$A_{\mathrm{V}} = \frac{R_4}{R_2}, \quad R_2 = R_3, \quad R4 = R_5 \tag{10.2}$$

With $R_2 = R_4 = 100\,\mathrm{k\Omega}$, $R_1 = 31.2\,\mathrm{k\Omega}$, and $V_{\mathrm{in}} = 2.5\,\mathrm{V}$, we get $I_{\mathrm{out}} = 80.13\,\mu\mathrm{A}$. All resistors should have an accuracy of 0.1% or better and a low temperature drift.

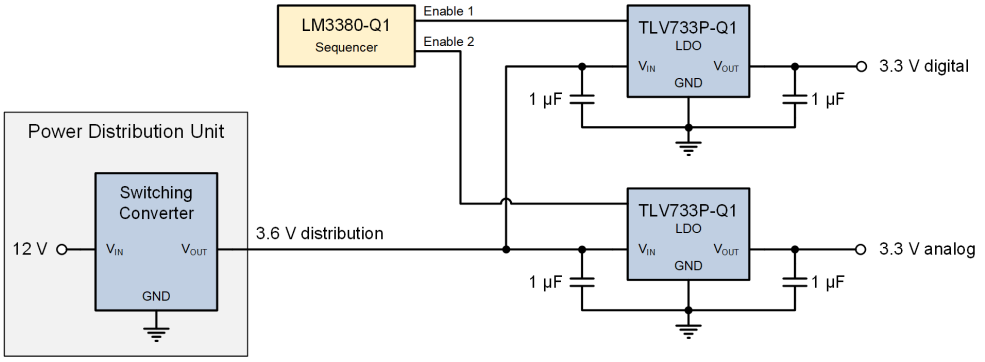

Figure 10.10: Simplified schematic of the power-conditioning circuitry for the read-out electronics. The ASICs and their supporting components are powered by two linear regulators, which are powered by a 3.6 V supply generated by a switching converter in the power distribution unit.

Though neither the operational amplifiers nor the precision voltage source we use (LM4132-Q1 [Tex16b]) are space-qualified, they can easily be replaced by qualified components. For the RadMap Telescope, we chose these particular components because they offer the low drift and noise characteristics we require; the full circuit shown in Figure 10.9 also uses only about 860 µW of power and thus does not add significantly to the overall power consumption of the system.

10.4.4 Power Conditioning

The IDE3380 requires two 3.3 V supplies—one for the analog and one for the digital components. These can in principle be powered from the same supply, at the risk that noise induced by the digital components feeds into the analog part. We thus decided to use separate supplies for the two domains.

In all of the RadMap Telescope, we followed the guiding principle of placing noise-generating components, for example switching converters, as far away as possible from noise-sensitive components, for example the SiPMs and read-out ASICs. The digital and analog supply voltages are therefore generated by two TLV733P-Q1 low-dropout regulators (LDOs) [Tex20], a type of DC linear voltage regulators that can operate when its input voltage is very close to its output voltage. They operate off a 3.6-V supply rail generated

by a switching converter in the power distribution unit (PDU). A LM3380-Q1 sequencer [Tex21] enables the analog LDO 30 ms later than the digital one; this sequence is required to protect the analog circuitry of the IDE3380.

Again, none of the components we used here is radiation-hardened or space-qualified. There exist, however, a sufficiently broad range of products that allow a direct replacement without impacting the design principle.

10.4.5 Clock Distribution

The read-out ASICs require a single-ended clock signal with a nominal frequency of 4 MHz. This clock directly drives the internal timers and ADC, as well as the IC's read-out controller and the serial data output. To improve the conversion speed and rate capability, the clock frequency can in principle be increased to up to 16 MHz, though the manufacturer does not necessarily recommend doing so. We generate the main system clock in the data-acquisition electronics and distribute it to the read-out electronics. There, we use CDCVF2310-EP clock buffers with a 1:10 fan-out [Tex12] to drive the read-out controllers of the IDE3380.

10.4.6 Output Buffers

In the first prototype of the front-end electronics, we added buffers to increase the drive strength of the ASICs serial outputs and other interfaces. Testing did, however, show that the IC's internal buffers are strong enough for the short transmissions paths in the RadMap Telescope. We thus removed them in the design of the flight hardware, though they can easily be added again in future instruments.

10.4.7 Design of the Flight Electronics

Since the SiPM arrays are located on four sides of the ADU, it made sense to split the read-out electronics into four assemblies, each capable of digitizing the signals of 256 photosensors. Each of those assemblies consists of two PCBs (see Figure 10.11): one holding 16 IDE3380 read-out ASICs and one serving primarily as interposer to allow the direct attachment of the micro-coaxial cables of the ADU's SiPM arrays. The addition of the interposer was necessary to comply with the space constraints of the instrument housing, as will become apparent in later sections of this chapter.

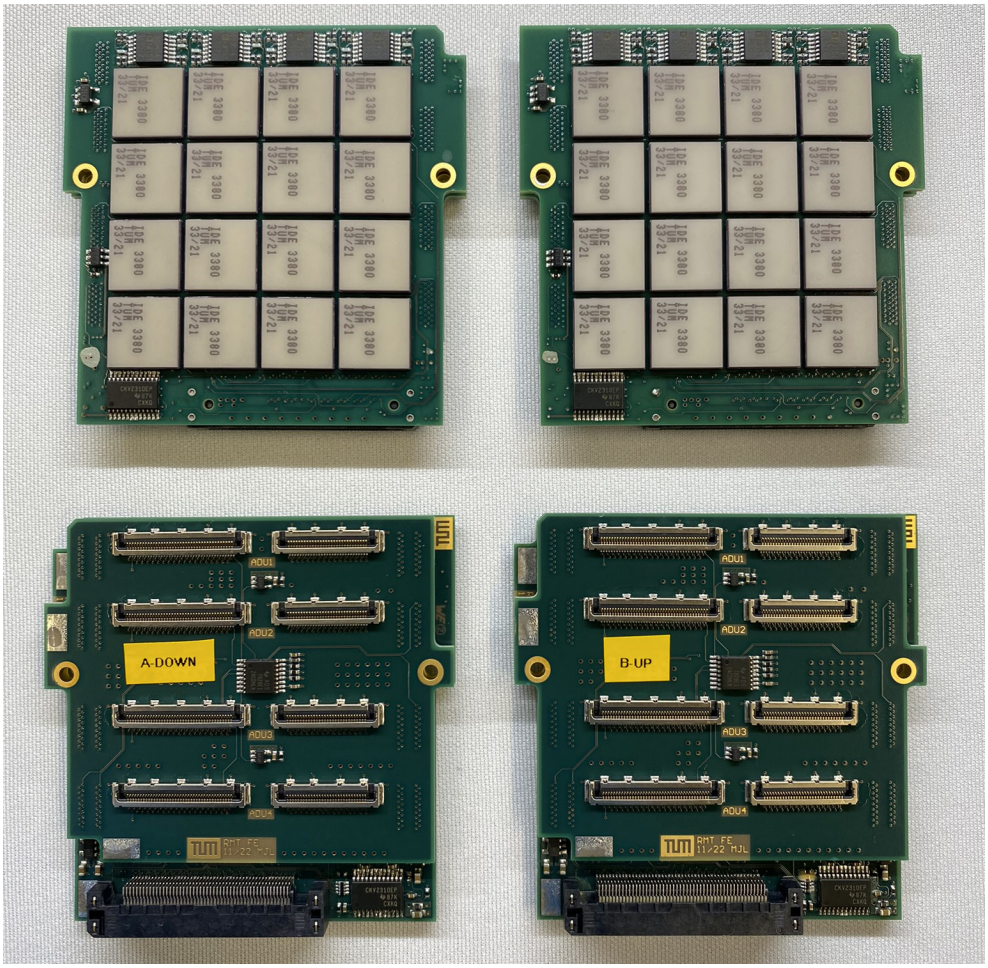

Figure 10.11: The four identical PCB assemblies of the read-out electronics. Each comprises 16 IDE3380 ASICs (recognizable by their white ceramic lids), the bias-current pumps, and clock-distribution circuitry. Due to space limitations, the assemblies consist of two PCBs each; the second one mainly functions as an interposer to allow the direct attachment of the micro-coaxial cables of the ADU's SiPM arrays. The connection to the data-acquisition electronics is made via a board-to-board connector at the bottom of each assembly.

The PCB holding the read-out chips also contains all the circuitry required to operate them, including the bias-current pumps, the clock distribution, and the power conditioning. The electrical connection to the data-acquisition system is made via a 100-pin right-angle board-to-board at the bottom of the PCB. Due to space constraints, the placement of the micro-coaxial receptacles for connecting the SiPM arrays was not possible, which is why we needed to add an interposer that allows routing signal from micro-pitch board-to-board connectors to the receptacles. The only other circuitry on this second PCB is an ADS7828-Q1 8-channel ADC [Tex16a] for reading the temperatures sensors on the SiPM arrays and read-out PCBs. The signals of the latter are transmitted via spare pins on the micro-coaxial cables.

10.5 Electrical Design

Through they are a crucial part of the demonstration of our tracking-calorimeter concept, the read-out electronics are but a small part of the electrical systems of the RadMap Telescope. Figure 10.12 provides a schematic overview of these systems, and of the interconnections between them. Non-essential components—such as temperature sensors, buffers, level translators, etc.—are omitted for clarity. In this section, I briefly describe the systems not already discussed above, focusing on the most important aspects of each of them. In describing the read-out electronics, I have often pointed out in the text which exact components we used. I did so because this system is one which we hope to adapt for future missions. The systems described in the present section are tailored for use on the ISS and thus unlikely to be reused. The exact components we used are therefore of less importance. Nevertheless, for the interested reader, part numbers are given in the figures.

10.5.1 Data-Acquisition Electronics

The data-acquisition electronics record the digitized information generated by the read-out electronics, distribute the system clock for driving the IDE3380 ASICs, generate the bias voltage for operating the SiPMs, and contain a 1:64 SPI demultiplexer through which the flight computer can access the configuration registers of the read-out ICs. Figure 10.13 shows the assembled data-acquisition electronics before integration into the instrument.

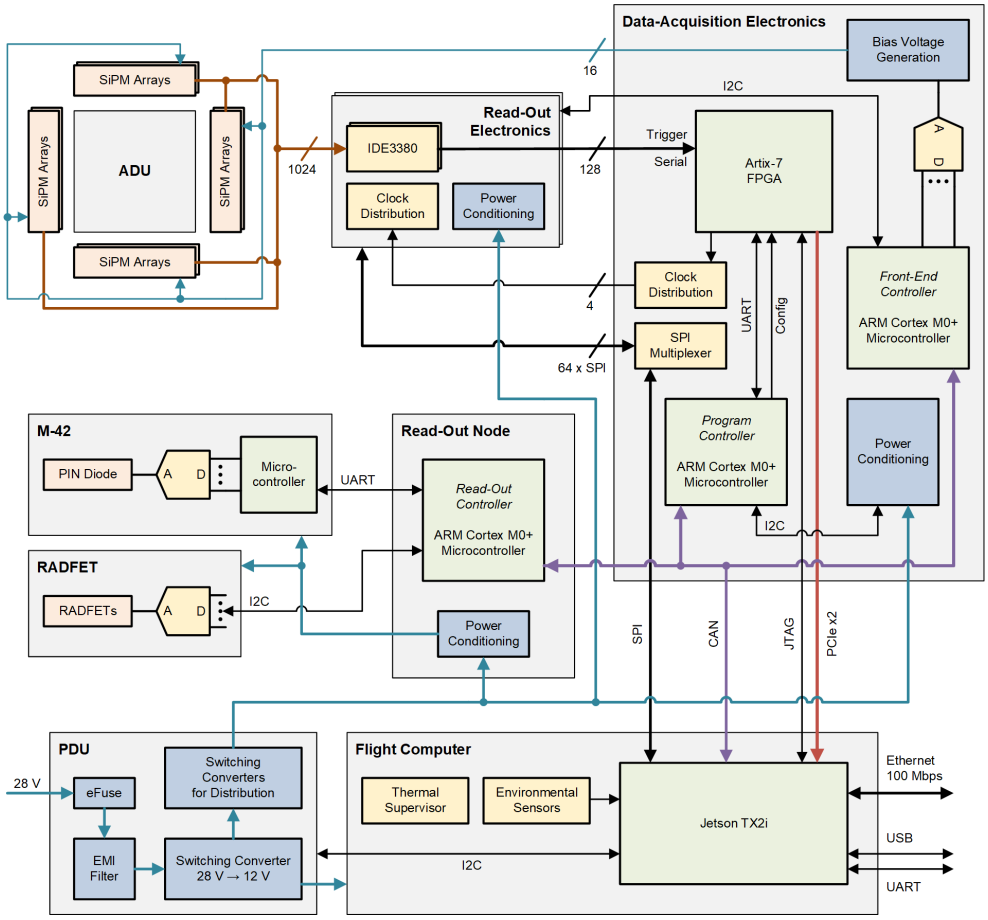

Figure 10.12: High-level schematic overview of the RadMap Telescope's electrical systems. Non-essential components (temperature sensors, buffers, level translators, etc.) are omitted for clarity.

FPGA and Microcontrollers

Despite the comparatively low speed at which the 64 front-end ASICs operate (less than 16 MHz), we chose to use an FPGA for the acquisition of their data for several reasons:

1. Interfacing with the 64 read-out chips requires more than 128 signal pins

Figure 10.13: Data-acquisition electronics of the RadMap Telescope. One the top side of the PCB (left picture), the power condition for the FPGA is visible in the lower left corner, the two bias-voltage converters on the right, and the two microcontrollers near the top. The read-out electronics are plugged into the four long connectors at the edges of the PCB; next to them, the bias voltage is distributed via 16 gold-plated coaxial connectors. The FPGA is located at the center of the bottom side (right picture). The electrical connections to the flight computer are made via the single connector at the left edge of the PCB. The four cutouts are for the feet of the ADU support structure.

(64 serial links, 64 trigger outputs, plus a few additional signal lines). Few, if any, microcontrollers or low-power processors offer that many general-purpose input–output (IO) pins, whereas even the least powerful FPGAs offered by most manufacturers do.

2. The IDE3380 works asynchronously, that is, it starts sending data on its serial output once the trigger hold delay has passed, and it starts multiplexing the TH voltages into its ADC immediately thereafter. That means that the time at which each serial link sends data cannot be controlled, and they can therefore not be multiplexed but must be read fully in parallel. FPGAs are ideally suited for such a task.
3. Even if it were possible, multiplexing the ASICs' serial links would reduce the system's rate capability by at least a factor of 64, or require a high-speed, power-hungry processor (running at about 1 GHz or faster).
4. In high-rate and time-varying environments, real-time capability is crucial. This is especially important for taking trigger decisions, checking for time coincidence, and for being able to with the random nature of the cosmic-ray particle flux. FPGAs are intrinsically real-time capable.

In the selection of a suitable FPGA, we restricted our search to devices manufactured by Xilinx, simply because our group had substantial experience in using them and almost none with chips of other manufacturers. The smallest and least power-hungry device with a large enough number of IO connections offered by Xilinx (now part of Advanced Micro Devices) is the XC7A200T [Xil20]. It belongs to the Artix-7-series of FPGAs and comes in a 676-pin BGA package. Its 215 360 programmable logic cells and up to 16 high-speed transceivers offer sufficient resources not only for implementing the data acquisition but also for first-level event analysis. Being based on static random-access memory (SRAM) technology, which is susceptible to SEUs, Xilinx' devices are not intrinsically radiation tolerant. The Kintex UltraScale XQR (a larger cousin of the Artix-7) and the older Virtex 5QV have been hardened specifically for space applications but have prohibitively large price tags for a technology-demonstration experiment like RadMap. On the space station, however, the Artix-7 will not even remotely approach its TID limit. Since the instrument is not critical to the safety of station and crew, it is acceptable if the occasional SEU is dealt with by reprogramming the device.

Figure 10.14 shows how the FPGA is complemented by two ARM Cortex M0+ microcontrollers [Mic23], which control it, the bias-voltage generation, and parts of the read-out electronics. The *program controller* controls the two

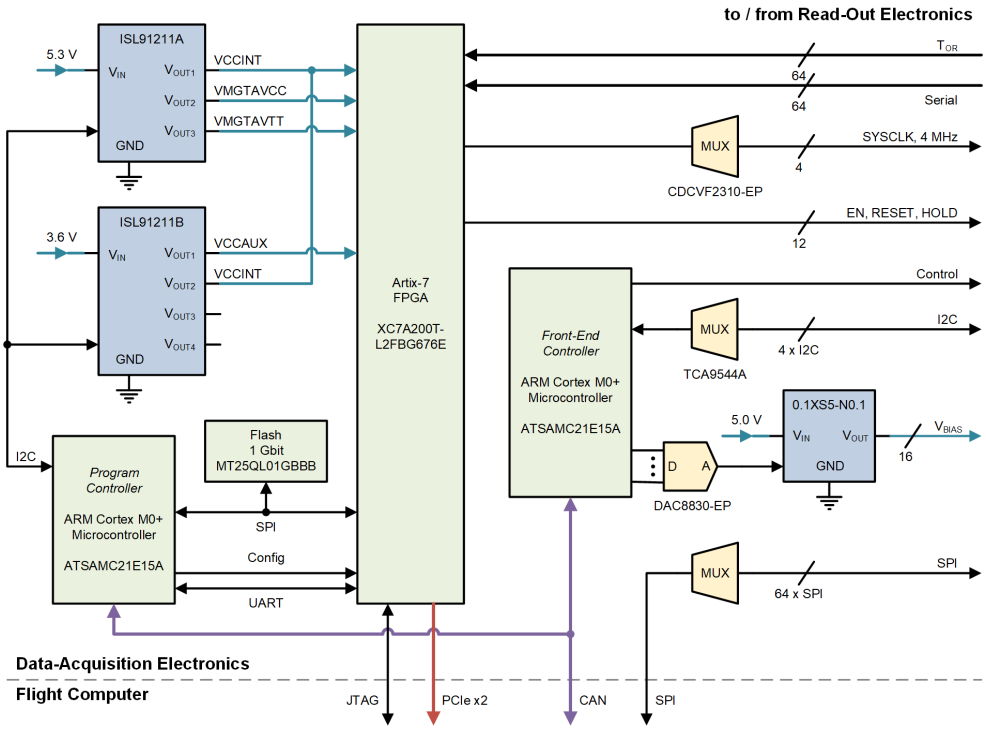

Figure 10.14: High-level schematic overview of the data-acquisition electronics. The system's heart is a Xilinx Artix-7-series FPGA, which is complemented by two ARM Cortex M0+ microcontrollers. Non-essential components (buffers, level-translators, etc.) are omitted for clarity.

power-conditioning ICs (switching converters) for the FPGA; they generate all voltages required by the latter except that for powering the IO banks, which is supplied directly by the PDU. The controller can configure the device for different boot modes and program it from a 1 Gbit flash memory. Through a UART interface, it can also read and write registers in the FPGA. The *front-end controller's* primary task is to provide an interface to the secondary sensors (e.g., temperature) of the read-out electronics and the ADU via a multiplexed I2C bus, as well as to control the fans of the thermal-control system (see Section 10.7 below). Its second task is the control of the bias-voltage generation and read-back (see below). Both microcontrollers are connected to the flight computer via a Controller Area Network (CAN) bus.

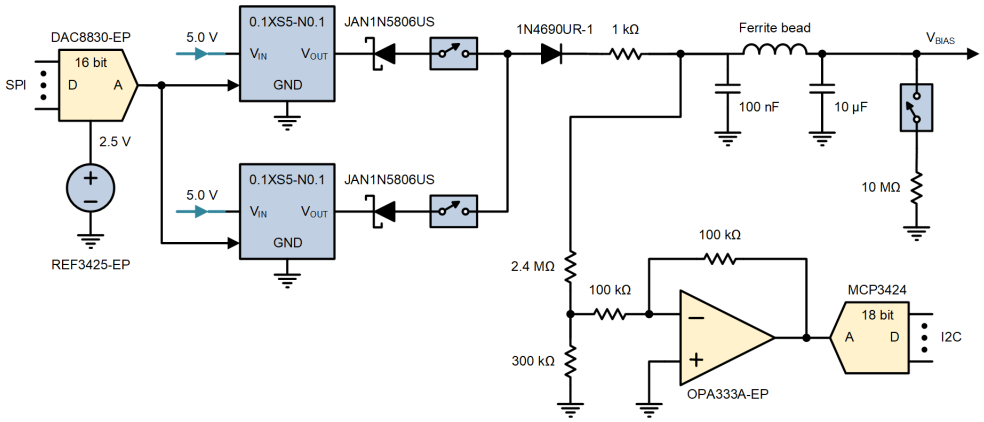

Figure 10.15: The (negative) bias voltage for the ADU's SiPMs is generated by two Advanced Energy 0.1XS5-N0.1 switching converters. Their output voltage is set via a DAC, with closed-loop control provided by an ADC connected to the output via a voltage divider and operational amplifier. The RLC-filter formed by the ferrite bead and capacitors reduces the ripple of the bias voltage.

Clock Distribution

The system clock (SYSCLK) with a nominal frequency of 4 MHz (and a maximum of 16 MHz) for driving the IDE3380 ASICs is created by the FPGA and made available on a standard IO pin. This clock signal is then distributed to the four PCB assemblies of the read-out electronics via a (partially used) clock buffer with a 1:10 fan-out.

Bias Voltage Generation

The stability of the bias voltage supplied to the SiPMs directly impacts their gain stability (see Equation 4.30) and hence the achievable energy resolution. Choosing an adequate supply is therefore of crucial importance to the overall performance of the detector. The number of commercially available converters, especially those capable of supplying negative voltages (the IDE330 ASIC works with negative charges), is limited and the selection of an appropriate one was driven by the volume, mass, and power constraints of RadMap. The only product fulfilling all our requirements is the 0.1XS5-N0.1 switching converter by Advanced Energy [Adv20]. The module's output is proportional to the analog voltage applied to its control input, which we generate using a 2.5-V

precision voltage reference (allowing a maximum voltage of -50 V) and a 16-bit DAC (see Figure 10.15). For closed-loop control, we rely on an 18-bit ADC, driven by a voltage divider and an operational amplifier, to read back the voltage applied to the SiPMs—i.e., after all voltage-altering components. Since one 0.1XS5-N0.1 converter can only provide a maximum of about 3 mA (at 32 V), we use two modules in parallel; blocking diodes at the output of each of them provide reverse-current protection in case of slightly mismatched voltage output. Solid-state relays allow to use the output of one, two, or none of the converters. A third relay allows to connect a 10-MΩ bleed resistor.

The converter has an intrinsic output ripple of $50\,\mathrm{mV_{pk-pk}}$, which would result in a gain instability of 1% at an overvoltage of 5 V. The manufacturer claims that the ripple can be reduced to $10\,\mathrm{mV_{pk-pk}}$, resulting in a 0.2% gain instability, by adding a 100 nF capacitor at the output. The ripple can be even further reduced by adding a ferrite bead in series as shown in Figure 10.15, effectively forming an RLC-filter. The current-limiting resistors and capacitors placed close to each SiPM constitute another layer of low-pass filters that further reduce the remaining noise.

SPI Multiplexing for ASIC Control

The IDE3380 read-out ASICs are not controlled by the data-acquisition electronics but directly by the flight computer. To be able to control 64 ICs from single SPI interface, we use a 1:64 de-multiplexer. This multiplexer only fully switches the chip-select line of the interface; the clock and serial-data lines are switched between the four read-out PCB assemblies, where they are connected to all 16 ASICs in parallel.

10.5.2 Read-Out Node for Secondary Radiation Sensors

The data from both secondary radiation sensors—the M-42 dosimeter and the RADFET sensors—are collected by a read-out node and forwarded to the flight computer without any pre-processing. The node consists of only an ARM Cortex M0+ microcontroller, LDOs for power conditioning, and two temperature sensors. The data from the M-42 and RADFET sensor is gathered via UART and I2C, respectively. Like the other controllers, the read-out node is connected to the flight computer via the instrument's main CAN bus.

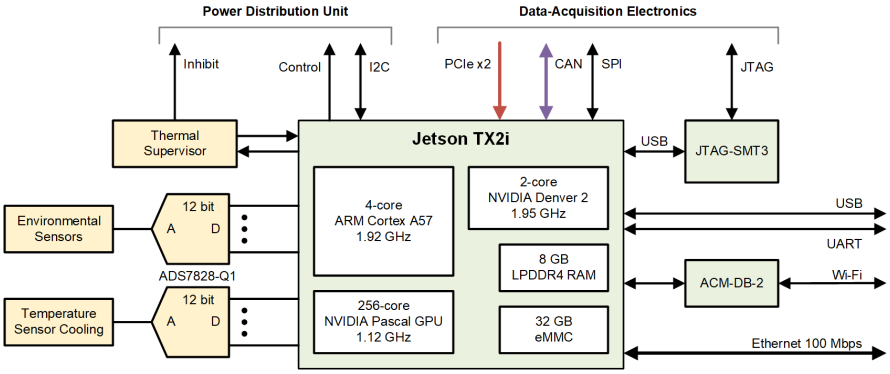

Figure 10.16: Simplified schematic overview of the RadMap Telescope's flight computer. It controls the read-out and data-acquisition electronics, as well as the PDU. Communication with the ISS happens primarily via a 100-Mbit Ethernet interface; a secondary option is the communication via a PCIe-to-wireless module.

10.5.3 Flight Computer

The flight computer consists of an industrial-grade NVIDIA Jetson TX2i computer module [NVI21]. It comes with a quad-core ARM Cortex A57 processor, a dual-core Denver 2 processor, and a 256-core Pascal graphics processing unit (GPU), hence offering more than enough processing power for running the instrument. The processors share 8 GB of low-power DDR4 SDRAM and 32 GB of eMMC flash memory. The module runs a modified version of the Ubuntu 16.04 operating system (OS).

Before settling for the Jetson TX2i module, we tested and benchmarked a variety of compute modules based on different processor architectures, including some of Xilinx' system-on-modules that combine FPGA fabric with ARM microcontrollers [Ang20]. Though the detailed list of requirements was longer, we were essentially looking to fulfill three core ones:

1. The flight computer shall not use more than 15 W of power.
2. The computer module shall have the electrical interfaces and processing power required to simultaneously gather data from all the RadMap Telescope's sensors.
3. The system shall run an operating system and a software stack that allows running algorithms, partially based on neural networks, for processing ADU measurements in real time. Buffering would only be acceptable

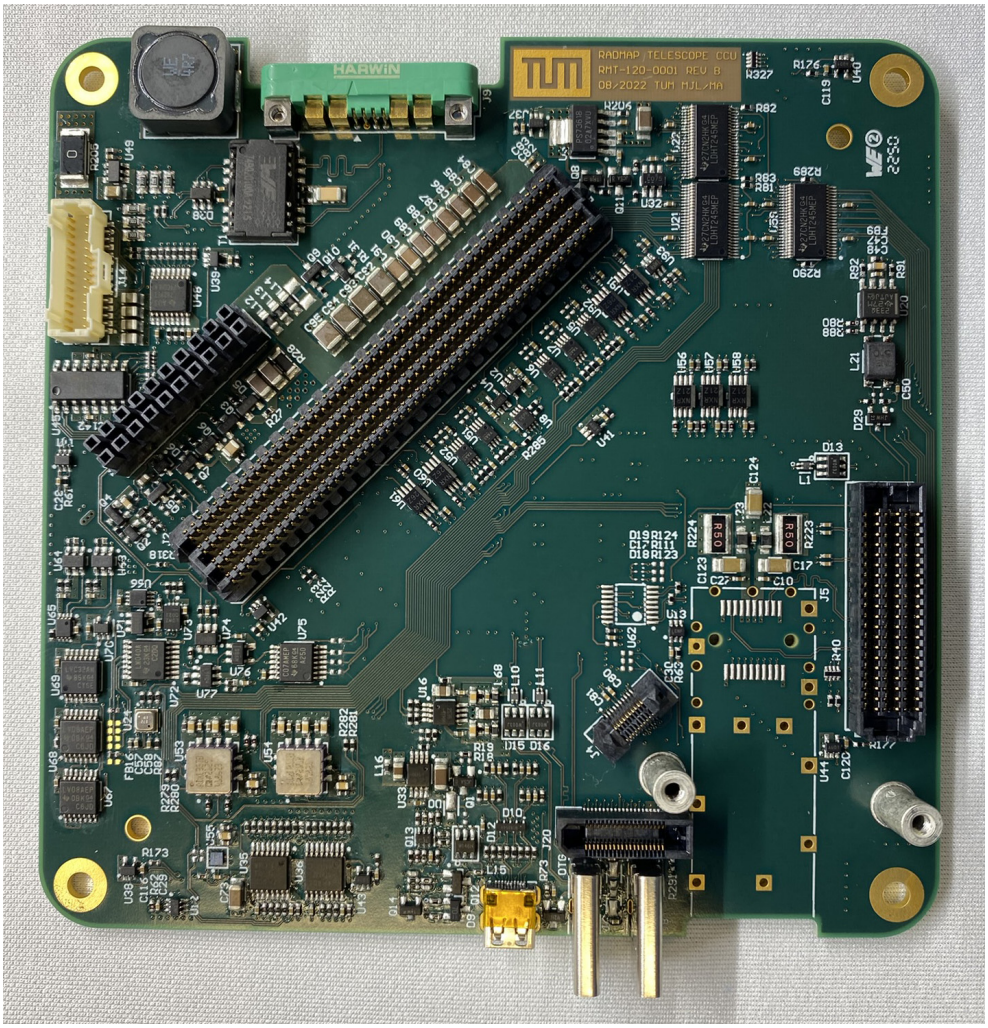

Figure 10.17: Mainboard of the flight computer. The Jetson TX2i modules is plugged into to large, angled connector located roughly at the center of the PCB. The smaller angled connector next to it is for the PDU. The green connector at the top edge is the main power and data interface to the space station infrastructure; an adapter PCB splits it into two circular connectors that are accessible by the crew. The connector on the right interfaces to the rest of the RadMap Telescope's systems, including the read-out and data-acquisition electronics.

during passes of the SAA, where we expected event rates to reach the kilohertz level.

Based on our tests, the only module that fulfilled all these requirements, though the power-consumption requirement can only be fulfilled by setting it to certain power modes, otherwise it uses up to 19 W. At the same time, it was also the only one rated for industrial, vibration-intense applications. As all other candidates, it is neither rated for space applications nor radiation-hardened. Considering the breadth of commercial compute hardware operated on the ISS, we nevertheless concluded that it should survive operations on the station long enough for us to fulfill our technology-demonstration objectives.

The flight computer controls the read-out electronics via a single SPI interface that is de-multiplexed in the data-acquisition electronics (see above). The latter is controlled via a CAN bus (microcontrollers) and a USB-to-JTAG interface (FPGA). The digitized ADU data is sent from the FPGA to the TX2i via a two-lane Peripheral Component Interconnect Express (PCIe) connection. The main connection to the PDU is an I2C interface with some additional lines for control signals. Communication with the ISS happens primarily via a 100-Mbit Ethernet interface; a secondary option is the communication via a PCIe-to-wireless module. USB and UART interfaces provide means for debugging and programming the TX2i module, but are only accessible on the ground.

Figure 10.17 shows the custom mainboard we designed for interfacing with the Jetson TX2i module. Besides the circuitry required to run the computer, it also houses a few environmental sensors (temperature sensors, accelerometers, and a pressure sensor) and the thermal supervisor (see below) that ensures the instrument's outer surfaces stay below the touch-temperature limit imposed by NASA. The PCB also has a connector that provides the main power and data interface to the space station. In flight configuration, an adapter plugged into this connector splits it into two circular ones accessible by the crew.

Thermal Supervisor

The only (somewhat) safety-critical electrical system of the RadMap Telescope is its thermal supervisor, whose task is to monitor the instrument's temperatures and to ensure that the touch temperature is not exceeded anywhere on the outer surface. It is thus implemented in discrete components, i.e., without any software- or firmware-controlled functionality. Figure 10.18 shows a schematic overview of the circuits of the thermal supervisor, omitting non-critical ones.

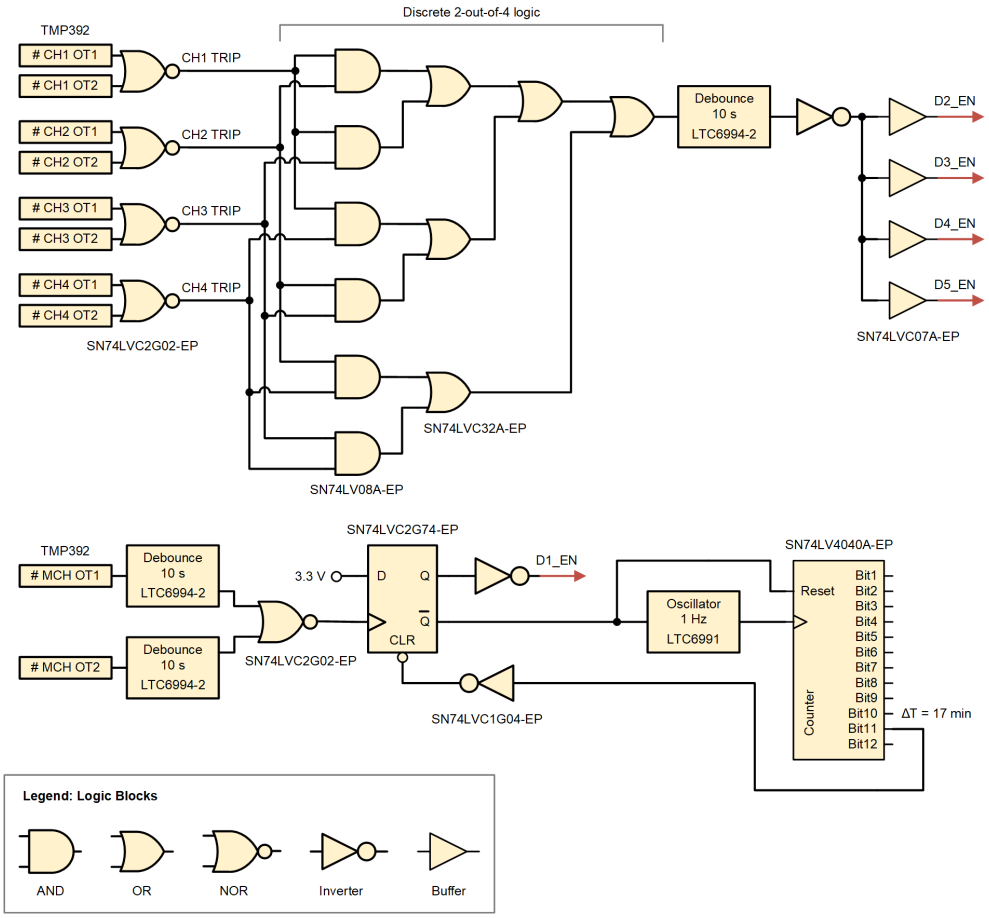

Figure 10.18: Simplified schematic overview of the thermal supervisor, focusing on its functionally important elements. The TMP392 temperature switches monitoring the four cooling channels for the read-out electronics trigger a 'two-out-of-four' circuit, whose output is debounced for ten seconds before turning off all power converters except those powering the flight computer. The sensors monitoring the main cooling channel switch off the instrument's main power converter and trigger a circuit that re-enables power to the flight computer after about 17 minutes.

The system is split into two parts: one part that monitors the temperatures of the four cooling channels of the read-out electronics and one that monitors the main cooling channel. Both rely on TMP392 temperature switches [Tex19] integrated into the housing at the cooling-channel exhausts to monitor whether temperatures exceed the limit of 45 °C, in which case they pull a signal line low. We monitor each location with two sensors and, via a NOR gate, require both of them to indicate a temperature exceedance. This is to prevent the system from triggering due to signal fluctuations in one of the sensors if its temperature is close to the limit.

In the part monitoring the read-out electronics, the trip signals for the four channels are fed into a 'two-out-of-four' logic circuit that only triggers the supervisor in case the temperature is exceeded in at least two channels. The resulting trigger signal is then debounced, i.e., it is only passed on if it is active for at least ten seconds. Any shorter signal will be ignored to ensure the instrument does not switch off as a result of brief spikes in the temperature. If the trigger signal is indeed active for longer than ten seconds, the power supply for the front-end and data-acquisition electronics is switched off.

The part of the supervisor monitoring the main cooling channel has a somewhat different functionality. Here, the debouncing is applied directly to the two TMO392 signals, before they are fed into the NOR gate. If they are active for longer than ten seconds, they trigger a D-type flip-flop, which switches off the instrument's main power supply. The flip-flop's complementary (i.e., inverted) output triggers a 1-Hz oscillator that feeds into a counter. After about 17 minutes, the counter's output resets the flip-flop and re-enables the main power converter. We implemented this circuit for two reasons:

1. The RadMap Telescope's main switching converter is hard-wired to turn on once power is applied from an external source. If the supervisor did not reset itself, a cycling of the external power supply would thus be necessary, which requires intervention by the crew.
2. We wanted to design the instrument to be as maintenance-free as possible. Though disabling the main power obviously switches off all power converters, the automatic reset only enables that required for the flight computer to operate, as those for the read-out and data-acquisition electronics must be enabled manually (see below). The instrument thus boots up in a low-power state, allowing us to investigate the reason for its overheating from the ground, i.e, without crew intervention.

The thermal supervisor thus ensures that the instrument's power consumption is reduced, or the instrument is completely switched off, in case the housing exceeds the touch-temperature limit for longer than ten seconds. The automatic reset after about a quarter of an hour leaves sufficient time for the system to cool down before power to the flight computer is re-enabled. In addition to the thermal switches, temperature sensors are mounted in each location being monitored, and their data is recorded and transmitted to the ground as part of the instrument's telemetry.

10.5.4 Power Distribution Unit

The power distribution unit converts the supply voltage of 28 V to the different voltage rails required to operate the instrument, except for the SiPM bias voltage, which is generated by the data-acquisition electronics. It also ensures compliance with the ISS program's electromagnetic compatibility requirements for conducted and radiated emissions.

Figure 10.19 schematically shows the design of the PDU. The main power converter is a military-grade switching converter of the SynQor MCOTS series [Syn14], which converts an input between 16 V and 40 V to a fixed voltage of 12 V. It can deliver a current of up to 4 A at 84% efficiency, thus drawing a maximum power of 57 W. For EMI suppression, we use a MQPI-18 filter [Vic14] from Vicor rated for the MIL-STD-461F standard[2] that satisfies NASA's requirements. To ensure the instrument can survive spikes in the supply voltage beyond the operational range of the main converter, the input is protected by a transient-voltage suppression (TVS) diode that limits it to voltages below 50 V. The inrush current is limited by a surge stopper that also acts as a resettable fuse: It monitors the current drawn by the instrument via a 0.02 Ω shunt resistor and disconnects the supply if it exceeds 2 [A]. In addition, a slow one-time fuse (not shown in Figure 10.19) sets a hard current limit of 4 A in case the surge stopper malfunctions.

The main converter powers the flight computer and the four switching converters generating the voltages that are distributed throughout the instrument: 5.3 V, 3.6 V, 5.0 V, and 3.3 V. The latter two are used to power components that are not affected by the ripple of the converters or voltage drops caused by resistances of the connectors. The former two are conditioned to 5.0 V and

[2]The standards known as MIL-STD are set forth by the U.S. Department of Defense to establish uniform engineering and technical requirements. Though primarily intended for military applications, they are often used in the civilian aerospace sector, too.

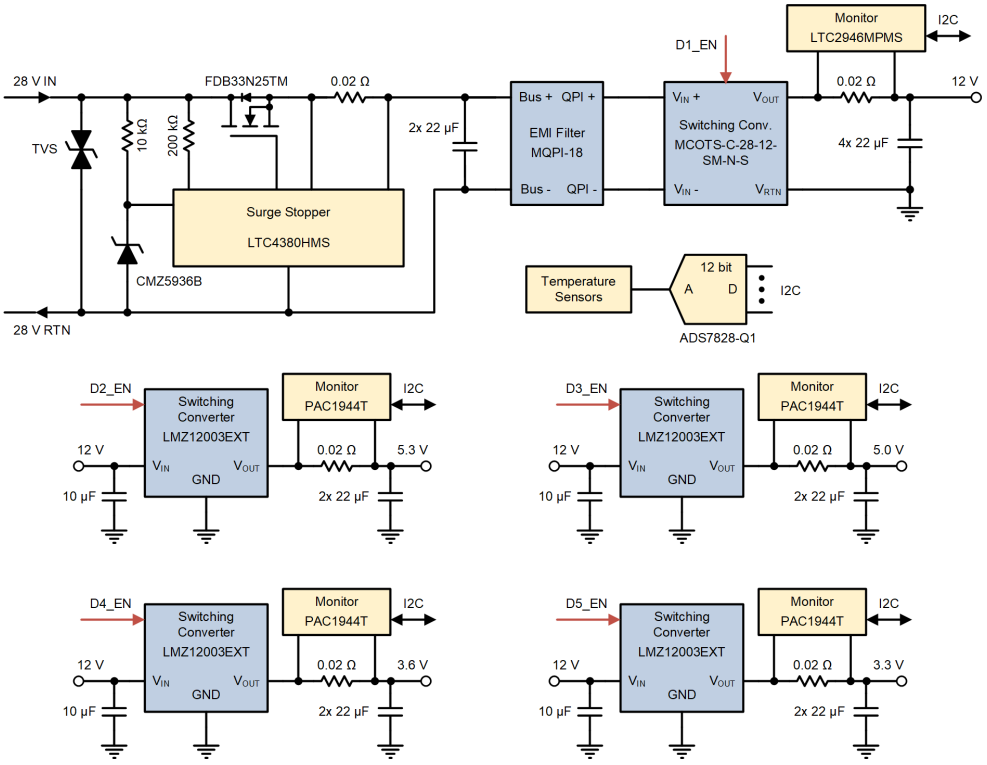

Figure 10.19: Schematic design of the PDU. The main power converter accepts 16 V to 40 V, and generates 12 V at a maximum current of 4 A. This output powers the flight computer and the four switching converters generating the remaining internal supply rails. The PDU is protected against overvoltages by a TVS diode rates at 50 V; the inrush and operational currents are limited by a surge stopper, the latter to 2A. An additional on-time fuse rated at 4 A provides protection in case the surge stopper fails. Electromagnetic compatibility is ensured by a MIL-STD-rated EMI filter.

3.3 V, respectively, by LDOs close to the noise-sensitive components they power, for example in the read-out electronics. The voltages and currents of all supply rails are monitored, as are the temperatures of the converters. Figure 10.20 shows the design of the PDU; all five converters are mounted on the same side of the PCB, allowing a thermal attachment to the main cooling channel.

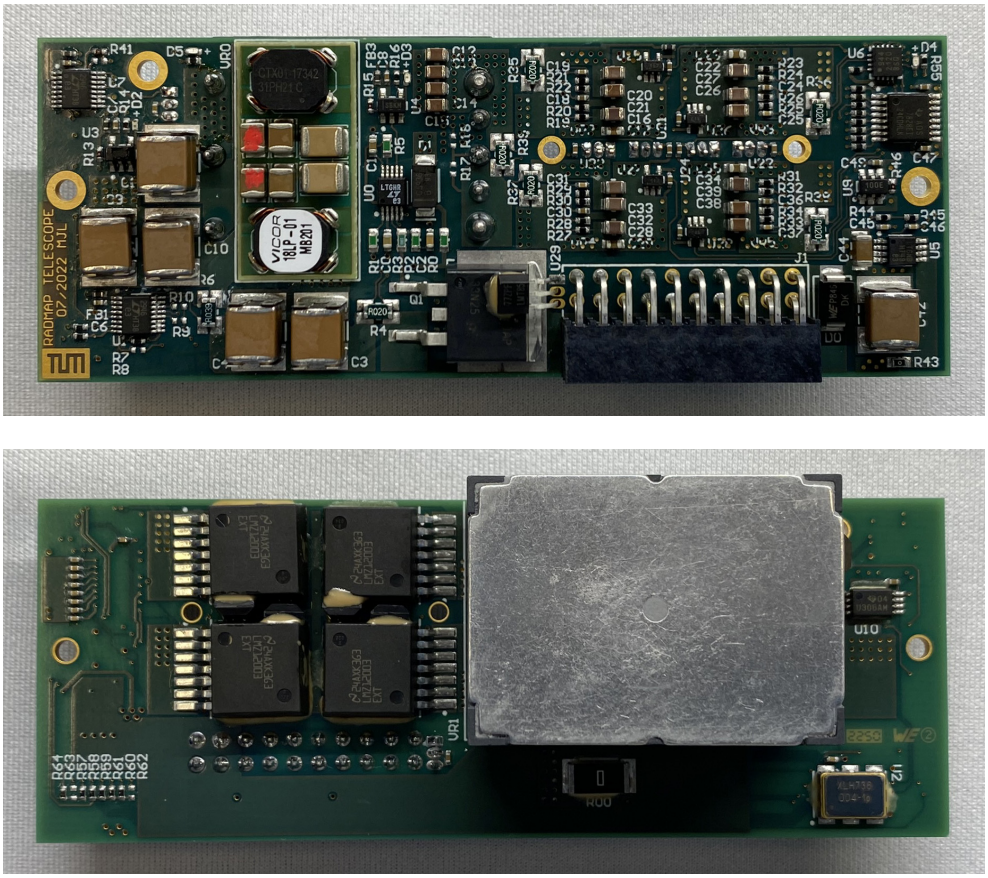

Figure 10.20: Single-PCB design of the PDU. All five switching converters are mounted to the bottom side of the unit (see bottom picture), allowing a thermal attachment to the main cooling channel. The connector that plugs into the flight computer's mainboard is visible at the bottom edge of the PCB's top side (see upper picture).

10.6 Mechanical Design

The RadMap Telescope's structural components are made entirely of aluminum, and specifically of the aerospace-grade Al7075-T651 alloy. The only exposed parts of the instrument not made of aluminum are the covers of the Wi-Fi antennas, which must not be electrically conductive and are made of PEEK. The housing is composed of three primary sections; the top and middle section form

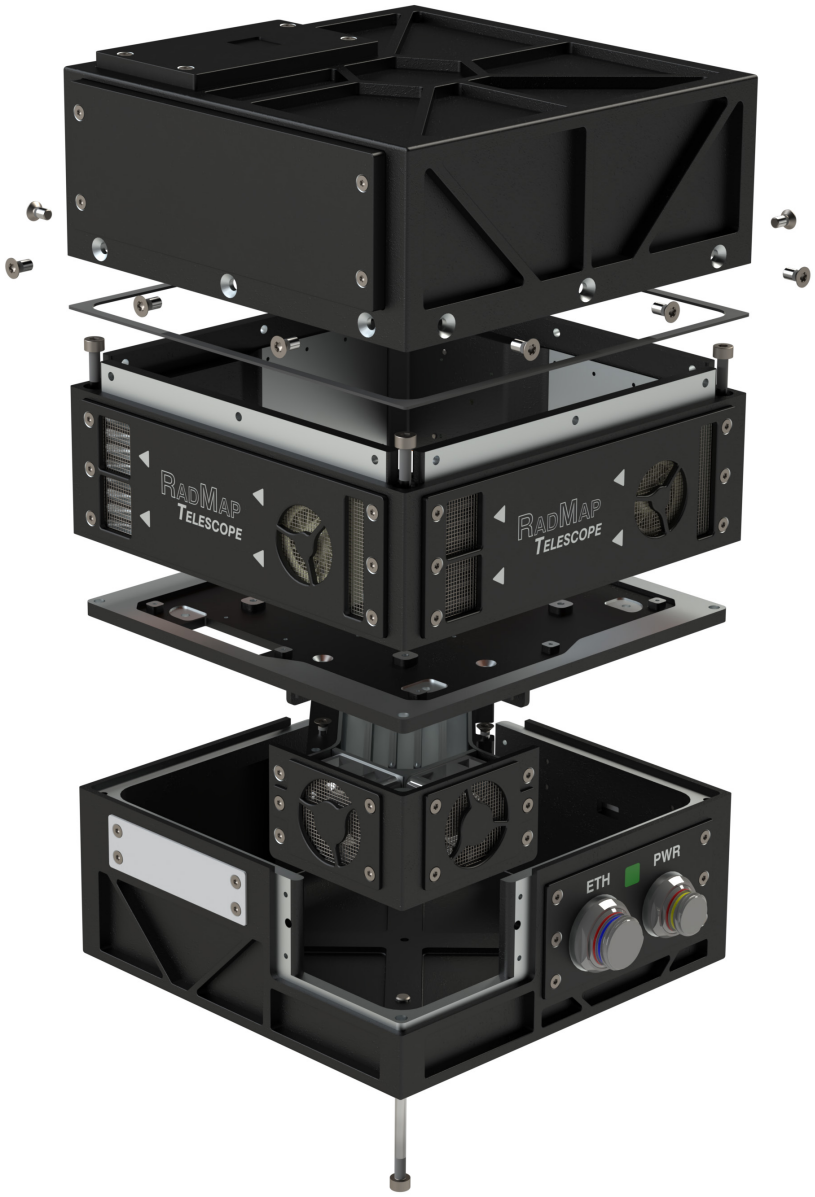

Figure 10.21: Explosion view of the RadMap Telescope's housing components. The top and middle section form the upper, light-tight compartment that house the ADU and the secondary radiation sensors. The bottom section makes up the lower compartment holding the flight computer, PDU, and the main cooling channel.

the upper compartment holding the ADU, and its read-out and data-acquisition electronics; the bottom section makes up the lower compartment holding the flight computer and the PDU. The two compartments are separated by a plate onto which the ADU and the data-acquisition electronics are mounted. The M-42 and RADFET dosimeters are attached to the outside of the top section and protected by individual covers. Since both the ADU and the M-42 are sensitive to light, the upper compartment is fully light-tight. To comply with safety requirements concerning (inadvertent) pressure vessels, a light-tight vent channel enables pressure equalization during launch.

To protect the crew against shock hazards, all exposed parts of the housing are anodized. The contact surfaces between different elements are treated with SurTec 650 [Sur22] to prevent corrosion and ensure good electrical contact for bonding the parts together. An additional electrical path is provided by the stainless-steel screws holding the housing together.

The instrument's only mechanical interface is the stud mounted to the bottom of the housing that fits into one of the standard seat-track anchors available on the space station. It is made from titanium and closely resembles the design of the studs used for the legacy foot restraints.

10.7 Thermal Design

One of the biggest advantages of operating an experiment in the pressurized environment of the ISS is that we do not need to rely on inefficient radiative transfer to get rid of heat but can instead use 'conventional' means of cooling via fans. The thermal design, then, must ensure that the instrument—with all its sensors switched on—can be operated continuously without triggering the thermal supervisor. Ideally, it should also ensure that the SiPMs of the ADU are kept at around 30 °C or less to maintain their dark-count rate, and hence dark current, at an acceptable level. The most challenging constraint is that the upper compartment must be fully light-tight. Other challenges arise from the small size of the RadMap Telescope and from the noise-emission limits of the ISS program. The latter is critical because smaller fans generate higher noise levels for the same air flow, and hence cooling capacity.

To satisfy the light-tightness requirement, the four cooling channels for the read-out electronics are integrated into the outside walls of the housing's middle section. The electronics are thermally attached to the inside walls; exploiting the good thermal conductivity of aluminum, the heat is transferred

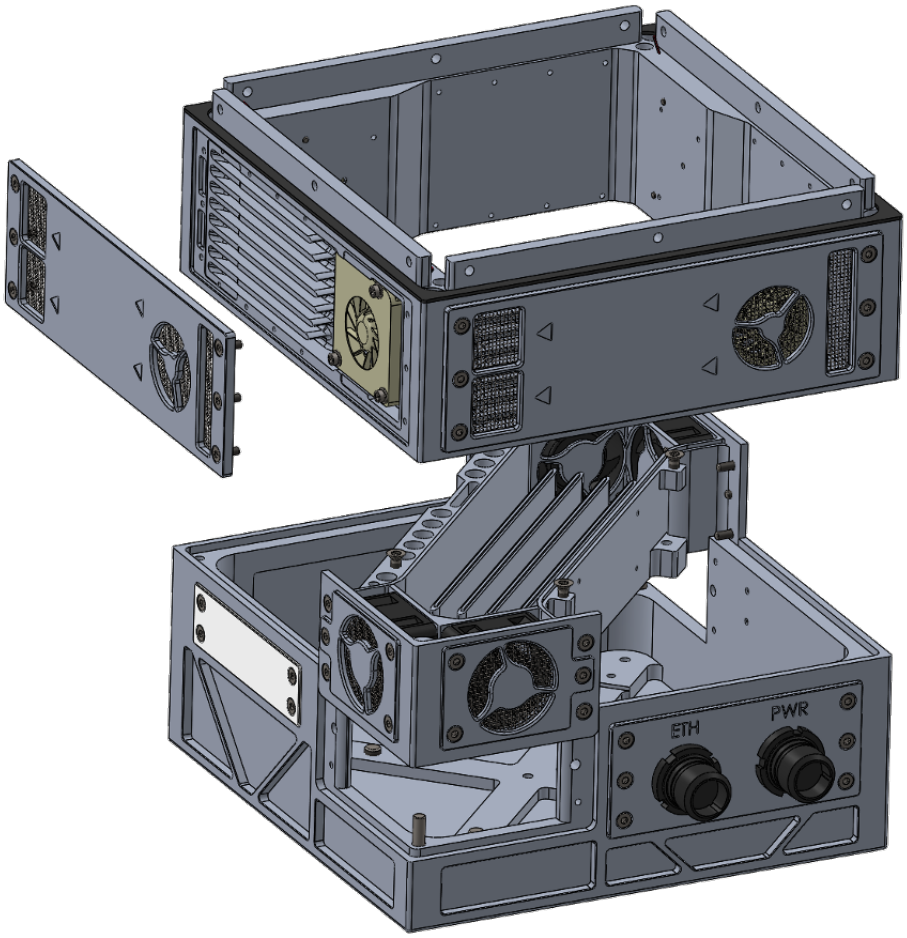

Figure 10.22: Thermal design of the RadMap Telescope. Four cooling channels for the read-out electronics are integrated into the walls of the housing middle section. The main cooling channel for the flight computer runs through the lower compartment.

through the walls to fins in the cooling channels (see Figure 10.22). Two blowers (i.e., radial fans) per channel push air over the fins, thus providing cooling 'through the walls'. Though this approach has the advantage of not requiring openings in the upper compartment's walls for air flow, it has the disadvantage that all heat-producing components must be thermally connected to the housing.

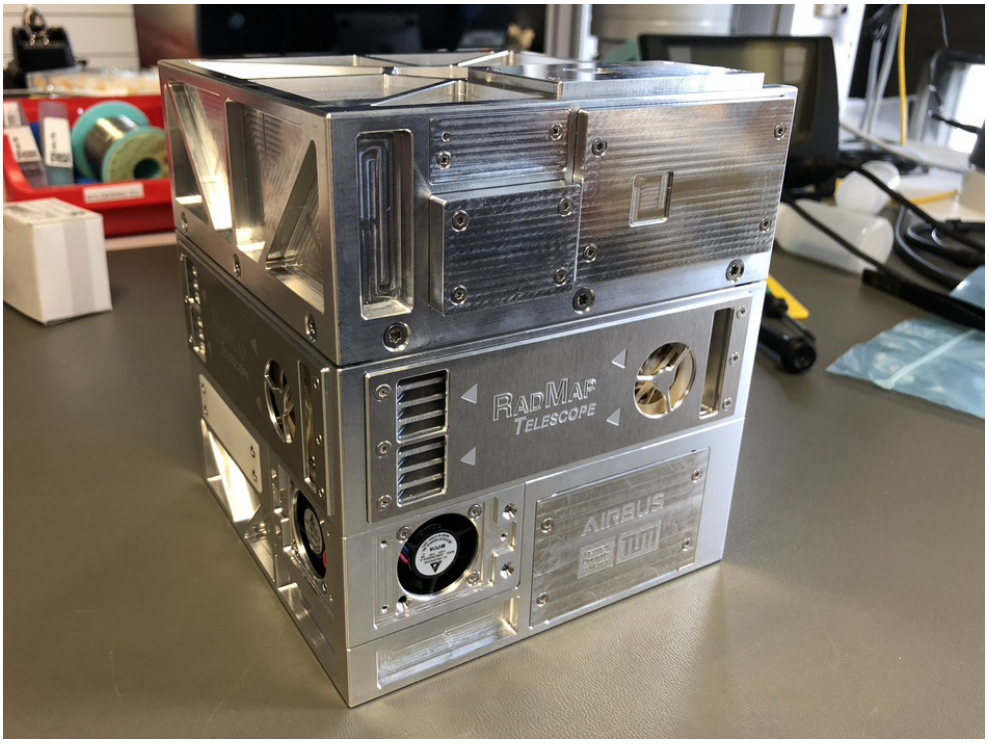

Figure 10.23: Structural engineering model of the RadMap Telescope's housing used for thermal testing. The power dissipation of the major electrical systems was simulated by resistive heaters. The instrument was partially packed in styrofoam to prevent gravitationally induced convective cooling.

The design of the main cooling channel in the lower compartment was less challenging because it did not need to be light-tight. We nonetheless chose to design a central cooling channel instead of just pushing air through the compartment, for two reasons: (1) to better control the air flow and (2) to make it impossible for debris to enter or exit the instrument. The latter made it easier for us to comply with NASA's safety requirements. The cooling channel runs diagonally through the instrument (see Figure 10.22); from the bottom, the Jetson TX2i, the PDU, and the Wi-Fi transceiver are thermally attached to it. The top cover of the channel is the plate separating the two compartments, to which the data-acquisition electronics are thermally attached. Four axial fans push (and suck) air through the heat-exchange fins inside the channel.

To arrive at this final design, we performed extensive finite-element simulations of the system's thermal behavior under different load conditions [ALC20]. Because we initially intended to use a different type of SiPM read-out ASIC, we assumed a total power dissipation of 20 W for the read-out electronics, distributed across the four cooling channels. For the main channel, we assumed a heat load of 17 W. After iteratively optimizing the design of the cooling system, including a change to more powerful fans, simulations of the final design showed that the outer surfaces of the instrument would barely stay below the touch-temperature limit for the full-load case. Within the error margins of the results, slight exceedances were possible in the regions around the exhaust vents. We confirmed the accuracy of our thermal model using a high-fidelity engineering model equipped with heaters, which we partially packed in styrofoam to suppress convective cooling (due to gravity). Figure 10.23 shows the structural engineering model we used.

Despite our analysis showing that the touch temperature may be exceeded in marginal load cases, we stuck to the design. We felt confident doing so because we assumed a power dissipation of the read-out electronics that was a factor of five higher than that of the electronics we actually integrated into the flight instrument. This discrepancy was already apparent when we concluded the thermal simulations, which is why we decided to not unnecessarily invest more effort into the matter. A simulation with reduced thermal load [ALC20], as well as operations on ground and in space confirmed that this decision was a correct one. During nominal operations—i.e., when the instrument is in its average load case, not the maximum one—all fans except for one in the main cooling channel can be switched off.

10.8 Integration into the ISS Infrastructure

We designed the RadMap Telescope for easy integration into the infrastructure of the ISS program and, more importantly, for easy handling by the crew. Mechanically, it can be attached to the seat tracks on the front of any payload rack throughout the U.S. Orbital Segment (USOS) using a standard quick-connect anchor, as shown in Figure 10.24. This has two advantages: (1) Astronauts are intimately familiar with these anchors and as such no crew training is required, and (2) the attachment is rigid, preventing inadvertent changes of the instrument's position and orientation over time (i.e., due to unintended actions by the crew). We use one of NASA's Ku-band Power

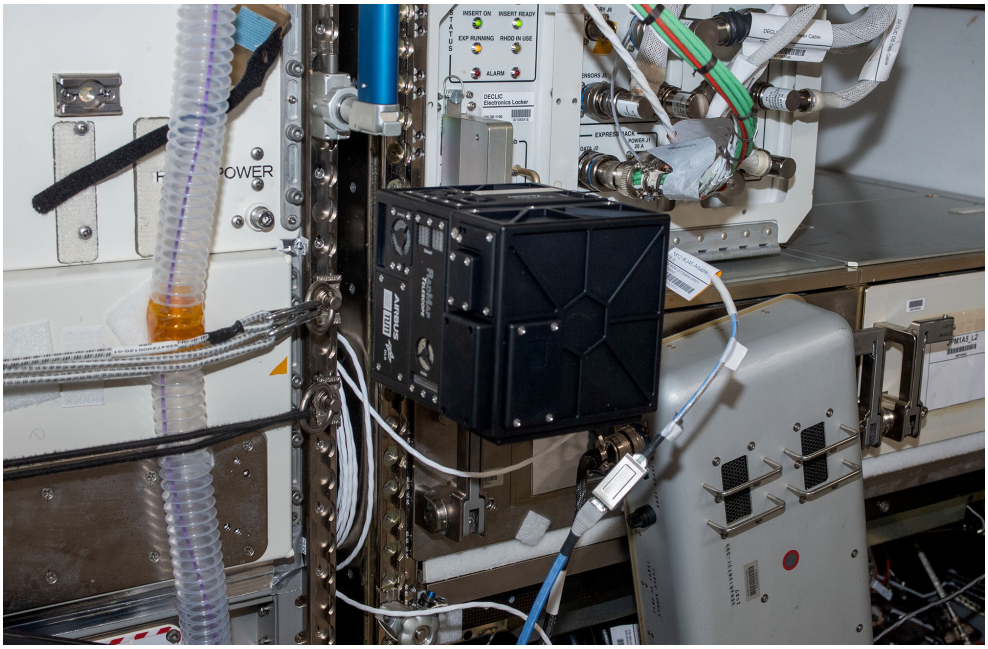

Figure 10.24: The RadMap Telescope mounted to a payload rack on the ISS, showing how it is rigidly attached to a seat track. Such tracks are available on most payload racks throughout the station. Image credit: NASA.

Supplies to convert 120 V into 28 V instead of plugging directly into a 28-V outlet, for two reasons: (1) The external power supply provides additional upstream inhibits, including a manual power switch for the crew, and (2) 120-V outlets are more widely available on the station. One of only two electrical interfaces of the instrument is a miniature four-pin circular connector, to which the crew connects the power supply via a custom cable.

The second electrical interface is an industrial-standard M12 circular connector for the Ethernet connection, which we chose because it is smaller than the widely used RJ-45 standard. Though the flight computer would in principle be able to support bandwidths of up to 1 Gbps, the connector uses a D-coded insert that is limited to 100 Mbps. Using this insert was necessary because all M12 cables and adapters on the ISS use it. When we finalized the choice of electrical interfaces, most Ethernet switches on the station also only had D-coded M12 connectors. While many have since been swapped out for devices

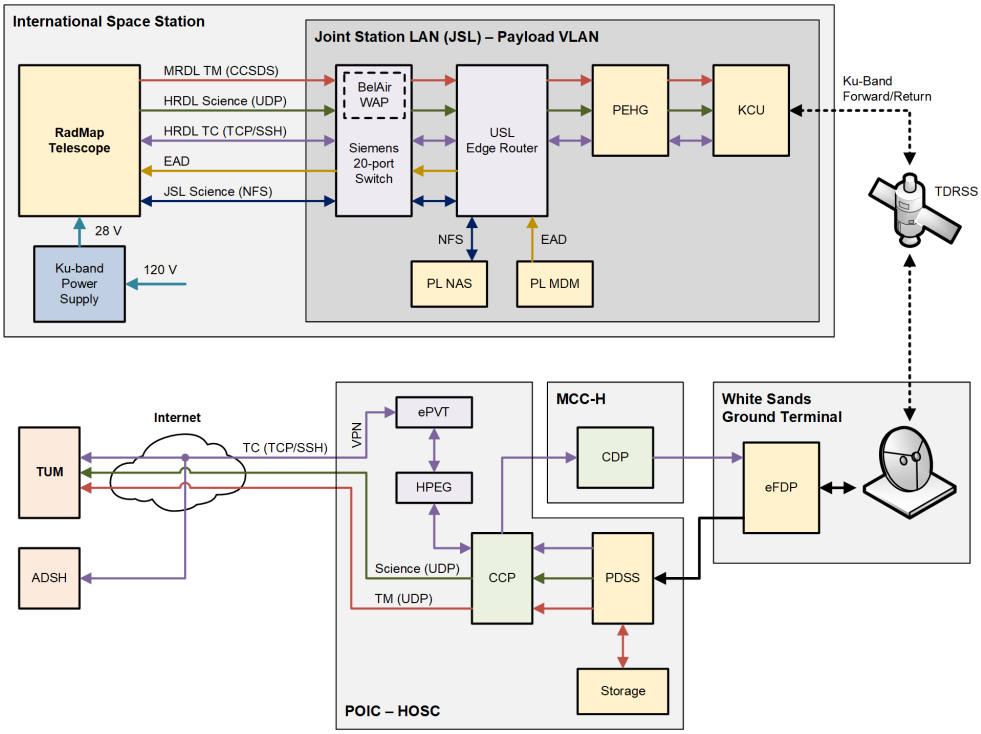

Figure 10.25: Integration of the RadMap Telescope into the communications and data-handling infrastructure of the ISS program.

Acronyms used in this figure: Airbus DS Space Systems, Inc. (ADSH); Central Command Processor (CCP); Consultative Committee for Space Data Systems (CCSDS); Communications Data Processor (CDP); Ethernet Ancillary Data (EAD); enhanced Functionally Distributed Processor (eFDP); external Private (LAN) (ePVT); Huntsville Operations Support Center (HOSC); HOSC Payload Ethernet Gateway (HPEG); High Rate Data Link (HRDL); Joint Station LAN (JSL); Ku-band Communications Unit (KCU); local area network (LAN); Mission Control Center – Houston (MCC-H); Medium Rate Data Link (MRDL); network-attached storage (NAS); Network File System (NFS); Payload Data Services System (PDSS); Payload Ethernet Hub Gateway (PEHG); Payload Multiplexer/Demultiplexer (PL MDM); Payload Network-Attached Storage (PL NAS); Payload Operations and Integration Center (POIC); Secure Shell (SSH); telecommand (TC); Transmission Control Protocol (TCP); Tracking and Data Relay Satellite System (TDRSS); telemetry (TM); Technical University of Munich (TUM); User Datagram Protocol (UDP); U.S. Laboratory (USL); virtual LAN (VLAN); Virtual Private Network (VPN); Wireless Access Point (WAP).

with RJ-45 connectors, the legacy M12 standard remains the smallest one used on the ISS and thus still is the preferred choice. The 100-Mbit bandwidth also is more than sufficient for transmitting all the instrument's raw data, even during passes of the SAA.

Figure 10.25 shows how the RadMap Telescope is integrated into the communications infrastructure of the ISS program. On the station, the instrument's Ethernet cable can be plugged into any of the switches connected to the Joint Station LAN (JSL), the network infrastructure run by NASA for all partners of the ISS program. Via the JSL, we have access to a variety of on-board services: the Payload Network-Attached Storage (PL NAS), which we use to extend the instrument's storage capacity for science data (i.e., measurements recorded with the ADU or the M-42 dosimeter); a Network Time Protocol (NTP) server providing a GPS reference time; and the Payload Multiplexer/Demultiplexer (PL MDM), which sends station telemetry (such as orbital position, attitude, and solar vectors) to the payload in one-second intervals, a service that NASA calls Ethernet Ancillary Data (EAD). All services are also available in case RadMap operates off its Wi-Fi interface (in which case the wired Ethernet must be disabled to avoid network loops).

The RadMap Telescope generates two streams of data: telemetry and science data. Telemetry encompasses information on the current status of the instrument, including: (1) housekeeping data of the flight computer, such as system load and the percentage of storage capacity used, (2) measurements of temperature and other environmental sensors, (3) the status of the PDU, including the power drawn on all supply rails, and (4) station telemetry relevant to the interpretation of our measurements. The values are gathered in a five-second interval, assembled into packets formatted according to the CCSDS Space Packet Protocol [Con22], and sent to one of the station's Payload Ethernet Hub Gateways (PEHGs) as raw Ethernet frames—i.e., on the data link layer of the network connection. The packets are then sent to the ground via the station's Medium Rate Data Link (MRDL). Using the MRDL for telemetry has the advantage that packets are buffered in the Ku-band Communications Unit (KCU) whenever the ISS cannot transmit them to the ground. These packets are downloaded in regular intervals by NASA's flight controllers and can be manually retrieved by payload developers, ensuring gap-less telemetry.

Science data, on the other hand, is sent to one of the PEHGs in the form of User Datagram Protocol (UDP) packets on the network layer, i.e., via the Internet Protocol (IP). These packets are transmitted to the ground via the station's High Rate Data Link (HRDL) and are not buffered. They are thus lost

if sent during times the ISS has no data link to the ground. From the EAD telemetry, the RadMap Telescope can determine whether the link is active or not and store science data on the PL NAS when it is not available.

Both MRDL and HRDL data are transmitted to the ground in the K_u band via the Tracking and Data Relay Satellite System (TDRSS), which has its primary receiving station at White Sands Ground Terminal (WSGT). From there, it is forwarded to the Payload Operations and Integration Center (POIC) at the Huntsville Operations Support Center (HOSC), where both telemetry and science data are encapsulated in an additional layer of UDP packets and sent to the primary RadMap Telescope ground site at TUM. For the telecommand (TC) uplink, the TUM ground site, as well as the secondary site at ADSH, connect to the HOSC Payload Ethernet Gateway (HPEG) via software provided by the Telescience Resource Kit (TReK), and are then able to establish a Secure Shell (SSH) connection to the instrument. This data path can also be used to manually download data from the instrument or from the PL NAS.

10.9 Ground Infrastructure

The ground infrastructure (see Figure 10.26) at TUM consists of the actual ground station, essentially just a collection of servers, and a control room. Telemetry and science data arriving from the POIC is received by redundant gateway servers, which share a common public IP address and hostname. The gateways forward it to a database server, where it is unpacked and stored in a database (telemetry) and files (science data). They can also buffer data packets for several days in case the database server is unavailable. Optionally, science data can be forwarded from the database server to another server for real-time analysis, or to external site like the DLR (e.g., for M-42 measurements). All data (telemetry and science) is regularly backed up to network-attached storage (NAS) servers centrally run by TUM, which are further backed up to tape storage every night.

Telemetry, and a summary of science data, can be accessed from a telemetry (TM) console in the control room using a browser-based interface, which allows displaying live data and browse through past data for troubleshooting purposes. The TM console also connects to the HOSC's Internet Voice Distribution System (IVoDS) for access to the voice loops required for payload operations. The TC console connects via a Virtual Private Network (VPN) and TReK software to the HPEG servers at HOSC for the uplink connection.

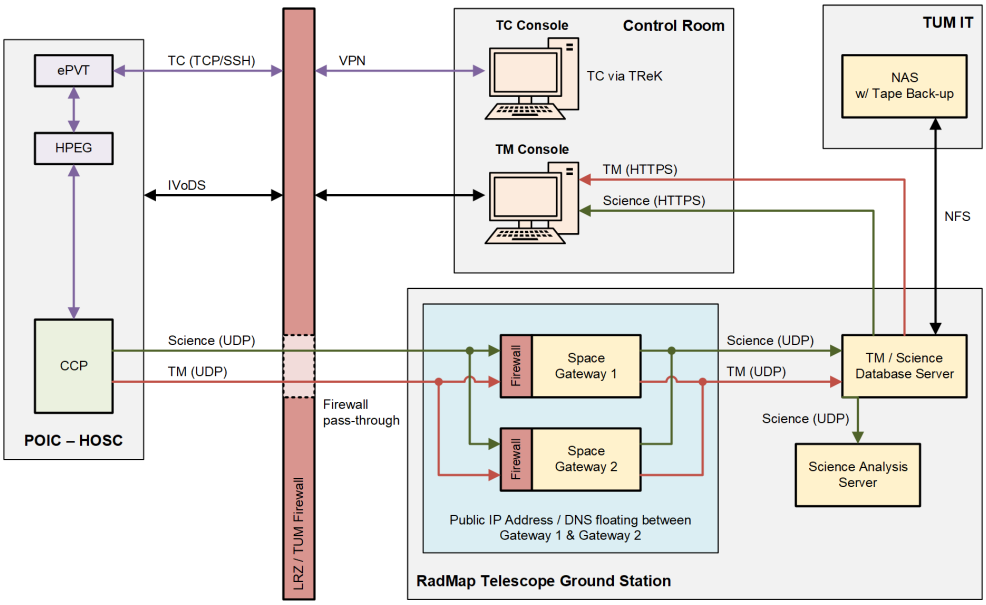

Figure 10.26: Ground station and control room architecture for the RadMap Telescope at TUM.

Acronyms used in this figure: Central Command Processor (CCP); Domain Name System (DNS); external Private (LAN) (ePVT); Huntsville Operations Support Center (HOSC); HOSC Payload Ethernet Gateway (HPEG); Hypertext Transfer Protocol Secure (HTTPS); Internet Protocol (IP); Internet Voice Distribution System (IVoDS); network-attached storage (NAS); Network File System (NFS); Payload Operations and Integration Center (POIC); Secure Shell (SSH); telecommand (TC); Transmission Control Protocol (TCP); telemetry (TM); Telescience Resource Kit (TReK); User Datagram Protocol (UDP); Virtual Private Network (VPN)

10.10 Firmware and Software

In operating the RadMap Telescope, we rely on various firmware and software components.[3] At the heart of the instrument is the FPGA firmware of the data-acquisition electronics, which collects and builds events from the serial-data

[3] I would like to acknowledge the huge support of my colleagues Sebastian Rückerl and Peter Hinderberger, who did most of the software and firmware development. My role has largely been restricted to defining required capabilities and helping to develop architectures. Only in few instances have I needed to write code myself.

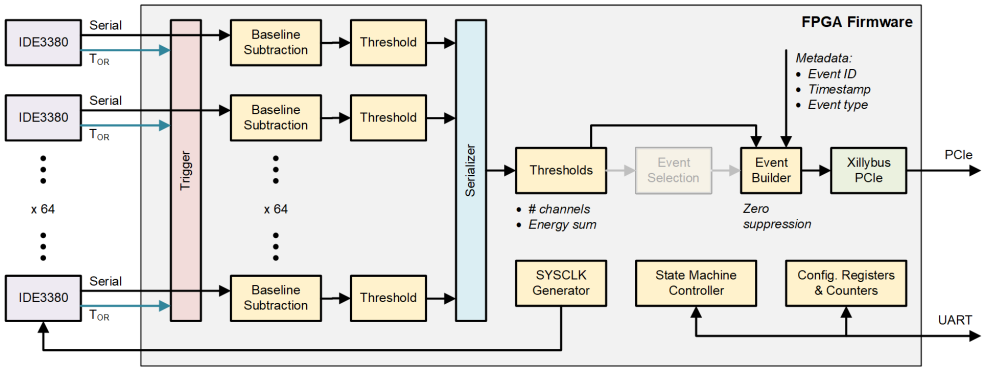

Figure 10.27: Schematic diagram of the FPGA firmware as implemented for the data-acquisition electronics. Event selection on is currently not performed.

streams of the IDE3380 read-out ASICs. Other important components are the remainder of the on-instrument software, as well as the software running on the ground station elements.

10.10.1 FPGA Firmware

The FPGA firmware serves two primary purposes: (1) Using the 64 T_{OR} outputs, it must determine whether serial data sent by the ASICs is relevant or not; and (2) it must record the serial-data streams in parallel, serialize and augment them with metadata, and forward them to the flight computer. Figure 10.27 schematically shows how we implemented this data flow in the firmware. The 64 trigger lines are fed into a trigger module that counts how many ASICs have triggered. Upon receiving an initial trigger signal, a coincidence window of adjustable length is started, which we typically set to one FPGA clock cycle, i.e., 10 ns. While the window is open, the trigger signals arriving from other ASICs are masked (as is the initial one), and only the serial data of those masked chips is recorded. Until the recording is complete, all other serial trigger signals and serial streams are ignored. This approach is required since the IDE3380 operates asynchronously, issuing triggers and starting its internal conversion process whenever a single channel has crossed over the applied threshold. Assuming that all particles traversing the ADU travel at close to light speed, the window length of 10 ns corresponds to a distance of almost three meters, which is an order of magnitude larger than the ADU. At the same time,

the probability for two particles hitting the detector within the 10 ns of each other is very low, even at hit rates in the kilohertz range. Our trigger concept thus ensures that only the data of those fibers that belong to the same particle passing are masked and recorded. Since the conversion process of the ASICs can last up to 100 μs (depending on the SYSCLK frequency and conversion settings), the probability for one or more particles hitting the detector while data from the previous event is still being recorded is not negligible. This is why all triggers must be ignored until the recording is completed.

Once a decision has been taken based on the number of ASICs that triggered, the serial streams of the masked chips are recorded in parallel. Before serializing their data, the firmware allows subtracting the baseline and applying an amplitude threshold for each channel individually. After serialization, an additional layer of thresholds (e.g., a minimum number of detector channels that produced a signal or a minimum total energy deposited in the detector) can be applied before metadata are added to the event. The latter include a continuously incrementing event number, a timestamp, and a string identifying the type of event. During the event-building process, zero suppression can also be applied. Each event is then transmitted individually to the flight computer via the PCIe connection, for the implementation of which we used the Xillybus PCIe core [Xil24].

During nominal operations, the event data is thus sent in its raw form to the flight computer, where it can be stored, forwarded to the ground, or pre-processed. In addition, we have the option of adding a pre-processing step for event selection on the FPGA as well, before the serialized data is built into an event packet. This is what we plan to do in future instruments derived from the RadMap design, which will likely not have flight computer as powerful as the Jetson TX2i, but instead rely on a larger, higher-performance FPGA to perform all data-handling and control tasks.

10.10.2 Microcontroller Firmware

Except for that built into the M-42 dosimeter, none of the microcontrollers in the RadMap Telescope has any control function programmed directly into it. Instead, we use them as extensions of the flight computer by making their hardware interfaces (e.g., SPI, I2C, and UART) controllable via the instrument's CAN bus. This not only reduced the amount of firmware development we needed to perform but also gives us the flexibility to adjust the functionality of the controllers during flight.

10.10.3 Flight Computer Software

The software stack running on the flight computer is to a large extent written in Python, with some supplemental scripts written in Bash. We use the operating system's system scheduler for calling that must be run repeatedly. Another important aspect is the abstraction of the microcontroller interfaces: It separately keeps track of the state an interface should be in and the state it actually is in, allowing us to unwanted configuration changes, for example due to SEUs. Figure 10.28 gives a high-level overview of the most important part of the software, the collection of daemons handling science data from the ADU and the M-42 dosimeter. As they are not fundamental to understanding how we gather scientific data, I do not discuss other parts of the software here.

The ADU events transmitted from the data-acquisition system to the flight computer via PCIe are received by the Xillybus kernel driver, the pendant to the PCIe core we use on the FPGA. Data received by the driver is made available to applications in the form of a pseudo-file, which can be repeatedly read to achieve a stream-like behavior. This is performed by the daqThread inside the DAQ daemon, which parses the PCIe events and re-synchronizes the data in case of missing frames or other errors. The received events are then transmitted to (via process-internal shared memory) and stored in a FIFO buffer, which is primarily required for dealing with the high rates during passes of the SAA. The processorThread retrieves events from the buffer and distributes them sequentially to different data sinks:

1. Storage on the PL NAS in a single, compressed binary file. We use the Python gzip module, which writes files batch-wise to disk.
2. Storage on the PL NAS in hourly rotated, compressed binary files. The files are stored in a folder structure that allows easy retrieval of data for a specific month, day, and time. The same structure is replicated on the database base server on the ground.
3. Event-wise forwarding via UDP to the store-and-forward daemon. Each event is compressed using gzip before being forwarded.
4. Event-wise forwarding to real-time analysis modules. This functionality is currently not implemented on the RadMap Telescope, but may be introduced at a later time.

The UDP-packed events sent to the store-and-forward daemon are once again stored in a FIFO and retrieved by the storeAndForwardThread, which sends them individually to one of the JSL PEHGs via the instrument's Ethernet

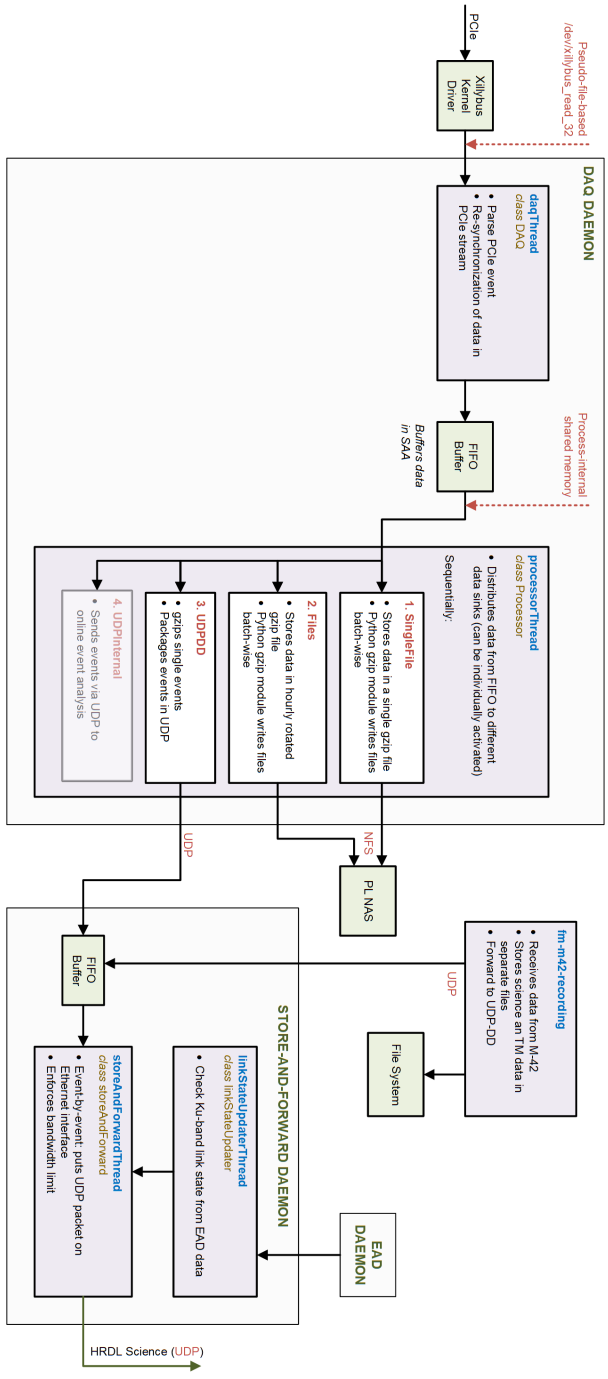

Figure 10.28: Architecture of the data-handling software running on the flight computer. Most of it is written in Python, with only few supplemental scripts written in Bash. See text for detailed explanation.

interface. The thread also enforces the bandwidth limit for the RadMap Telescope. Via the linkStateUpdaterThread, the state of the Ku-band link is retrieved from the EAD telemetry, such that events are only sent when they can be transmitted to ground.

The science and housekeeping data of the M-42 dosimeter is analogously retrieved and encapsulated into UDP packets by the fm-m42-recording service. In the store-and-forward daemon, the M-42 packets are handled exactly as the ADU events.

10.11 Test Campaign at NASA's Johnson Space Center

Before getting approval to be launched to the ISS, the RadMap Telescope was required to complete a set of tests to show that it complied with all functional and safety requirements of the ISS program that needed experimental verification. Though the need for some of the most demanding tests (e.g., vibration) was waived, the program was nevertheless comprehensive, including:

1. Testing the electromagnetic compatibility of the instrument by measuring the conducted and radiated emissions over a wide range of frequencies.
2. Evaluating the power quality by determining the inrush current and the PDU's ability to cope with variations in the power supply.
3. Determining the acoustic noise levels generated by the fans in the different operational modes of the instrument (startup, nominal, and thermal-shutdown).
4. Confirming that the instrument complies with human-factors requirements and is safe to be handled by the crew.
5. Testing all modes of communication with the JSL infrastructure, including sending data via the MRDL and HRDL, access to the PL NAS, and receiving of EAD telemetry from the PL MDM.

We performed all of these at the facilities available at NASA's Johnson Space Center in Houston, Texas. Figure 10.29 shows the RadMap Telescope during some of the tests. Many other requirements were previously closed via analysis, review of design files, and other means of documentation.

We met nearly all test objectives, some much better than anticipated, with two exceptions: (1) The instrument was found to slightly exceed the continuous-noise limits during nominal operations; and (2) the frequency response of the PDU showed a minimally too high capacitive load at some

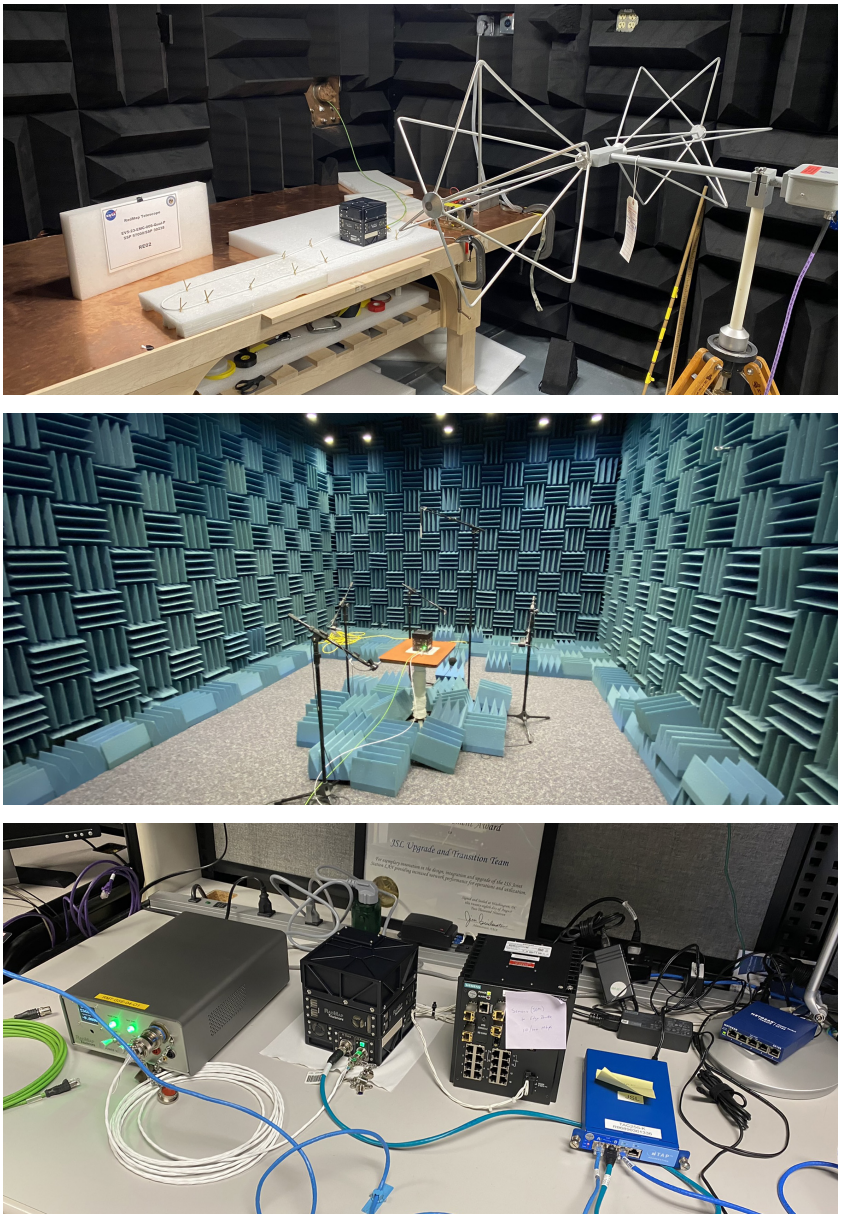

Figure 10.29: The RadMap Telescope during EMI (top), acoustic (center), and JSL (bottom) testing at NASA's Johnson Space Center.

frequencies. We were able to correct the former by adjusting the speed at which the single fan that is active in the main cooling channel during nominal operations turns. A re-test confirmed that this adjustment lead to compliance with requirements. The latter deviation we could not easily mitigate; it was, however, deemed to be minor and the ISS program issued an exemption. We thus received approval to operate the RadMap Telescope on the ISS.

Chapter 11

On-Orbit Operations and A First Look at Data

The RadMap Telescope was launched to space from NASA's Kennedy Space Center aboard the SpaceX CRS-27 mission on 15 March 2023. After the Dragon 2 capsule carrying it docked to the ISS, the instrument was unpacked and installed in the Node 3 module about a month later, on 27 April 2023. In this chapter, I describe our initial concept for operating RadMap aboard the ISS and how we partially deviated from this concept. Though our analysis of the data we recorded is still in its early stages, I also give an initial overview of some early results.

11.1 Concept of Operations

Since the RadMap Telescope was primarily intended to be a technology demonstrator, our initial concept of operations foresaw to operate the instrument for a period of about six months. During this time, it was supposed to rotate through four locations, each in a different module. We requested this rotation schedule to assess the differences in the radiation field in different parts of the station. With RadMap being the first omnidirectionally sensitive radiation monitor with particle-identification capabilities deployed on orbit, we hoped to be able to provide valuable data to the ISS community. The modules and exact locations NASA assigned to us are:

- The Node 3 module, also known as *Tranquility*; location: NOD3D4

- The Japanese Experiment Module (JEM); location: JPM1A5
- The U.S. Laboratory (USL); location: LAB1O6
- The European Columbus module; location: COL1A3

We requested a minimum stay of six weeks for each deployment to gather a large-enough data set for statistical analysis. Since we had no prior experience in operating the ADU and its read-out electronics in space, the instrument was configured to start up with only minimal functionality enabled. Our plan was to incrementally enable autonomous operations as we gained more confidence in the system. We also did not plan on making use of the capability to downlink science data in real time via the HRDL at first, instead relying on the PL NAS for storage.

We anticipated that it would take a few weeks of operating the ADU for us to find the optimal settings for operating the read-out and data-acquisition electronics. Since we did not have the opportunity to perform a beam test with the flight electronics, we did not know how to exactly configure the IDE3380 ASICs. Most importantly, we needed to find optimal settings for the charge attenuation in the CMIS, the shaper, and the various thresholds throughout the system. We therefore planned an initial period of two weeks for determining good settings, followed by another four weeks of data recording without any pre-processing or zero suppression. This would give us a sufficiently large data set for investigating the performance of the system in the space radiation environment.

We also wanted to gather as much data as we could that would allow us to compare our measurements to those of other instruments. We hence requested that RadMap be located close to the ISS-RAD in the USL and next to the DOSimetry TELescope (DOSTEL) in the Columbus module. The former is operated by the Space Radiation Analysis Group (SRAG) of NASA, the latter by DLR's Institute of Aerospace Medicine. We have agreements with both to share and compare measurements.

11.1.1 Crew Activities

Initially deploying RadMap and then rotating it through its various measurement locations requires multiple crew activities. Crew time is the most expensive commodity aboard the ISS, so to minimize it, we designed the instrument's interfaces as simple as possible. Besides the previously described connectors for power and data (Ethernet connection to the JSL)—and the stud for the

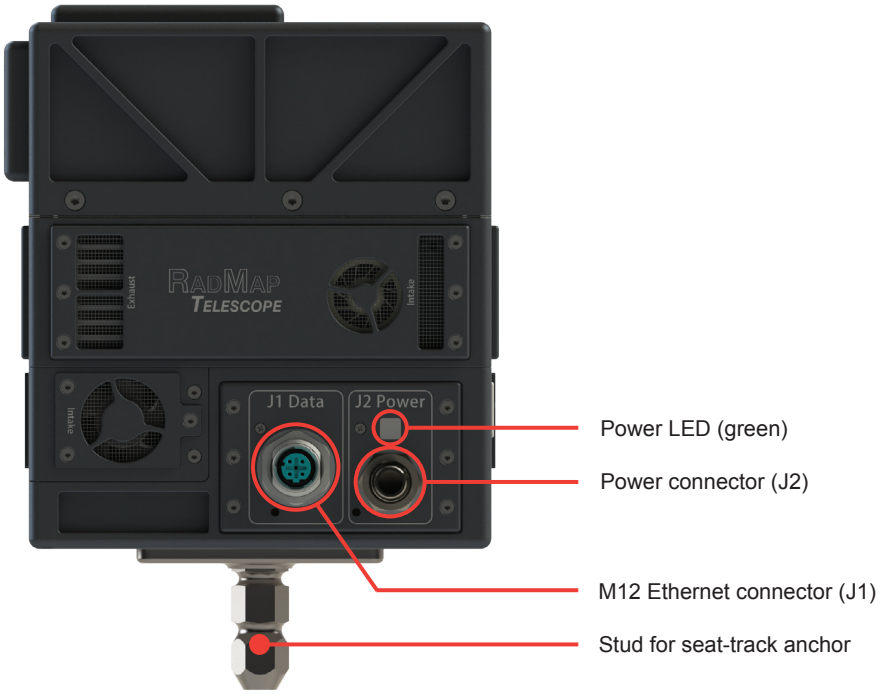

Figure 11.1: Interfaces of the RadMap Telescope that the crew needs to interact with. The power LED lights up as soon as power is supplied to the instrument and the flight computer begins its boot process.

attachment to a seat-track anchor—the only interface for the crew is a single LED that lights up when the instrument is powered and the flight computer starts its boot process. Figure 11.1 shows all four interfaces. Both the seat-track anchor and the Ku-Band Power Supply are widely used items aboard the station, with which most crew members are intimately familiar. We therefore did not need to develop a training program for the crew to go through on Earth before their flight. The set of on-orbit instructions, which we developed in cooperation with our NASA colleagues, consists of simple procedures for deployment, relocation, and packing up the instrument. The time required for each is between ten and twenty minutes.

Upon our request, the crew was instructed to mount the RadMap Telescope such that it would not block items that they need frequent access to. We also wanted to be informed whenever there was a need for temporarily moving the

instrument, in which case we requested that pictures be taken for us to confirm that it was re-mounted in its original orientation.

11.2 Operations Between April 2023 and January 2024

Even though the initial deployment of the instrument went smoothly, and we could promptly connect to it via the HPEG, it took several weeks until all JSL services were working as expected. A configuration error on the part of NASA meant that we could initially not retrieve telemetry sent out by RadMap via the MRDL. Consequently, we did not want to continuously operate the read-out and data-acquisition electronics because we could not monitor their temperatures and other critical parameters. We did, however, switch on the M-42 dosimeter a few hours after installation and thus were able to collect at least some science data from the first day on. Another service that was not immediately available was the retrieval of EAD telemetry, though in this case the reason was us needing to re-test the respective software components at NASA's facilities because we did not have them ready in time for the initial test campaign. Solving these issues took several weeks, during which our ability to work with the payload was limited to the times we could sit on console and establish a SSH connection to it.

Once all problems were solved, we were able to begin our commissioning of the ADU in earnest. Finding a reasonably good configuration for the ASICs was easier than anticipated; only a single chip appeared to have a somewhat noisy channel that we needed to prevent from triggering randomly. We also needed to make minor adjustments to the FPGA firmware to prevent the occasional occurrence of periods of scrambled events caused by problems with one of the buffers. We initially configured the data acquisition to record every event for which at least one chip ASIC issued a trigger; after realizing that we could easily store and download the resulting data, we did not introduce more restrictive event-selection criteria, as originally planned. This allowed us to record essentially every particle hitting the detector.

As of writing this, we successfully operated the RadMap Telescope in three of the four planned locations:

1. Node 3 / NOD3D4; between 27 April 2023 and 23 June 2023;
2. JEM / JMP1A5; between 23 June 2023 and 26 September 2023; and
3. USL / LAB1O6; between 26 September 2023 and 6 January 2024.

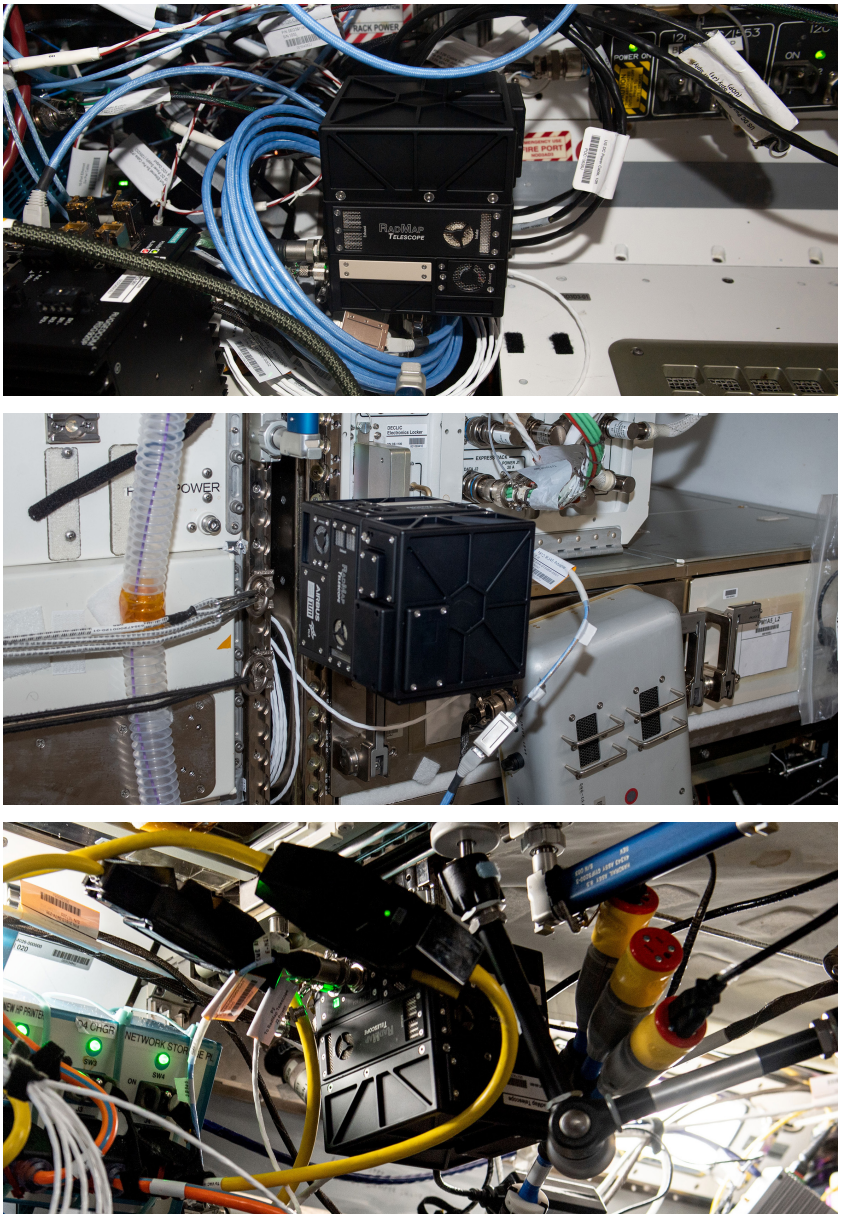

Figure 11.2: The RadMap Telescope deployed in the Node 3 (top), JEM (center), and USL (bottom) modules of the ISS. Image credit: NASA.

Figure 11.2 shows how the instrument was mounted in each module. Though the relocations themselves all went smoothly, wrongly configured network infrastructure at times prevented us from operating immediately. After relocating to the U.S. Laboratory, for example, we could not connect to the payload until October 7 due to a wrongly configured firewall. The connection to the PL MDM was also repeatedly interrupted because switches were rebooted and caused the connection to go stale. In these cases, ground controllers at HOSC need to manually reset the connection, which usually takes a few hours. Fortunately, though, we can retrieve the missing telemetry from NASA servers and match it to our science data via time tags. In November 2023, we transitioned to a fully automatic, real-time downlink of science data via the HRDL. This allowed us to substantially reduce our on-console time.

As is evident from the above list, RadMap operated significantly longer than anticipated in each location. This was in part because additional time was granted to us in light of the network interruptions, and in part because DOSTEL needed be returned to Earth for repair. Since comparing the measurements of RadMap and DOSTEL was an important objective, NASA granted our instrument an extended stay on the station until the latter would be re-installed in Columbus. Unfortunately, we unexpectedly lost the ability to communicate with the instrument on 6 January 2024 for yet unknown reasons. At this point, we had more than met our objective of operating the RadMap Telescope for at least six months on the ISS.

11.3 First Data

Thanks to our ability to store large quantities of data on the PL NAS, we were able to collect hundreds of gigabytes worth of ADU events in the JEM and USL modules, even before we could transition to a real-time downlink. The detailed analysis of this data is still ongoing. Operating an ADU-like detector for the first time in space, we are facing the challenge of interpreting the event signatures we recorded without having performed ground measurements in a representative radiation environment that would have allowed us to perform a detailed calibration. Especially the lack of heavy-ion data means that we need to fully rely on simulations for guiding our particle identification. Another aspect we paid little attention to is the secondary-radiation field (including neutrons, pions, electrons, and gamma rays) created by the interaction of cosmic and solar particles with the station's shielding.

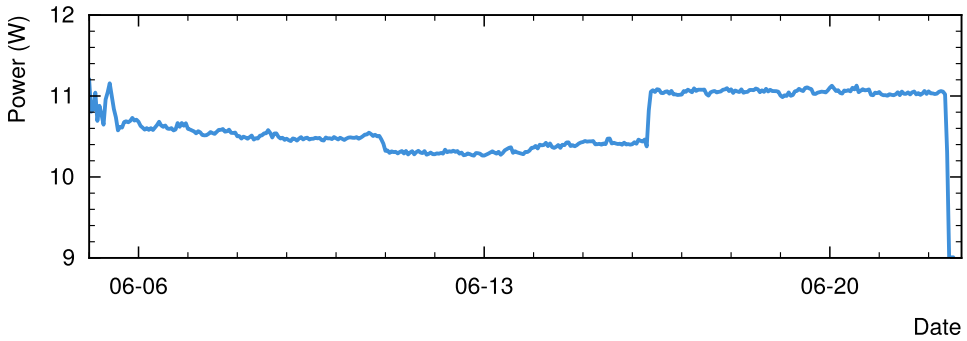

Figure 11.3: The RadMap Telescope's power consumption while deployed in Node 3 during a roughly two-week period in June 2023. During the first two thirds of the period, the read-out and data-acquisition electronics were deactivated. We switched on the latter on June 16, leading to a 600-mW increase of the power draw.

I nonetheless present some of the data we recorded, albeit only as part of a preliminary analysis that does not require tracking and particle identification. Since our tracking algorithms are only partially functional as of writing this, my analysis also relies on uncalibrated data because we cannot correct the position-dependent light yield of the individual fibers yet. In light of the magnitude of these corrections (see Section 7.2), a conversion of the uncorrected signal amplitudes (measured in ADC channels) to units of energy is questionable at best. I therefore do not attempt it here.

11.3.1 General Performance

The instrument in general performed remarkably well. Before building RadMap, we had little experience in the construction of hardware that would operate in space. We were especially anxious about the thermal environment and a potential overheating. Tied to this were concerns about the power consumption and increased temperatures of the PDU, in case we needed to continuously operate fans that were nominally supposed to be off. As it turned out, these concerns were unwarranted. In idle mode—i.e., with the read-out and data-acquisition electronics deactivated—all of RadMap's electrical systems, including the PDU, exhibited temperatures in the range of 30 °C to 35 °C. This translates into a total power consumption of less than 11 W, which is about a fifth of the PDU's maximum power draw. Figure 11.3 shows the power consumption over

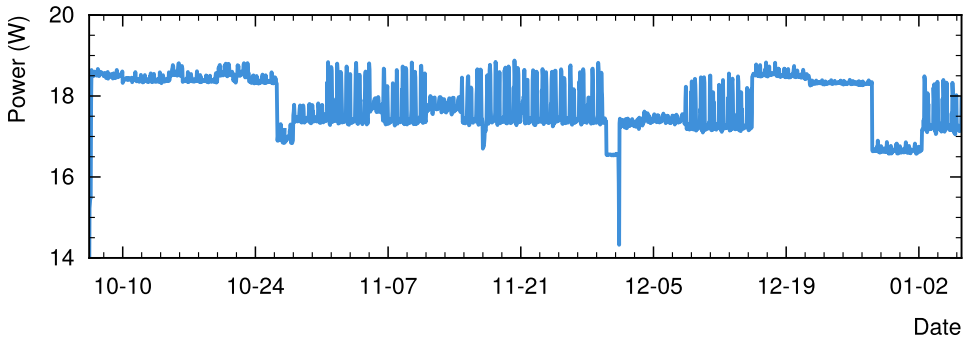

Figure 11.4: Power consumption while the instrument was deployed in the USL. The instrument was fully activate during the whole period. A software update allowed the system to dynamically respond to the processing load, leading to larger variations after October 26. The system was rebooted on December 1.

a roughly two-week period in June 2023 while the RadMap Telescope was deployed in Node 3. During the first two thirds of the period, the instrument was in idle mode, with only the M-42 dosimeter recording data. On June 16, we switched on the data-acquisition electronics, leading to an increase in the power consumption of about 600 mW.

Figure 11.4 shows the instrument's power consumption while it was operational in the USL between early October 2023 and early January 2024. The graph reveals that the steady-state power consumption while all systems are operational is about 18.5 W, as can be seen in the period until October 24. After that date, we updated some elements of the flight computer's software and allowed it to respond dynamically to the processing load. The mean power consumption correspondingly fell by about 1 W, with short periods of increased consumption of about 19 W during passes of the SAA. The figure also shows that we needed to perform a system reboot on December 1, and the dynamic load scaling did not fully function during parts of December.

Temperatures

One of our major concerns relating to temperature were the photosensors of the ADU, for two reasons: (1) In SiPMs, an increased temperature leads to a higher dark-count rate and (2) results in gain variations. In our thermal design, we thus attempted to keep them as cool as possible and to avoid

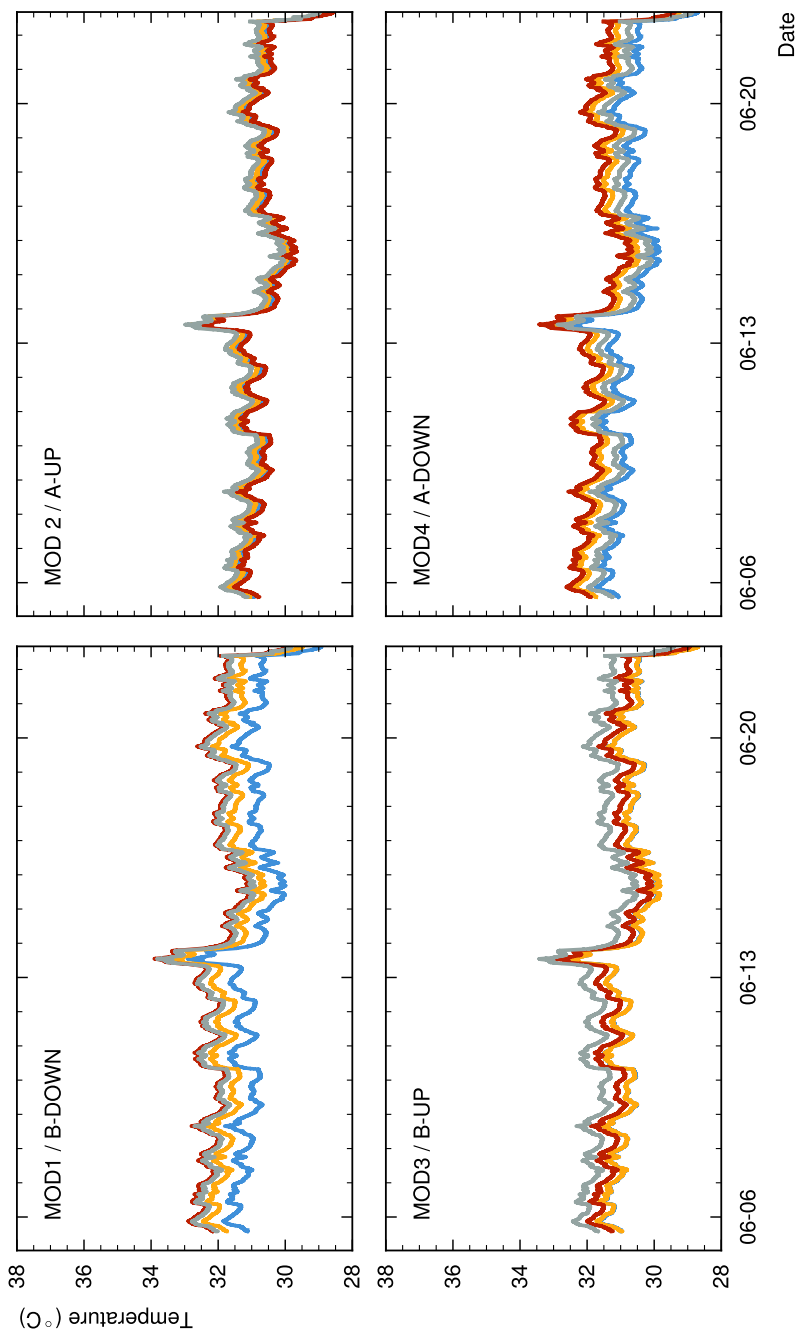

Figure 11.5: Temperatures of the ADU modules while the instrument was deployed in Node 3. The four panels are for the sides of the detector on which SiPM arrays are mounted (see Figure 8.1).

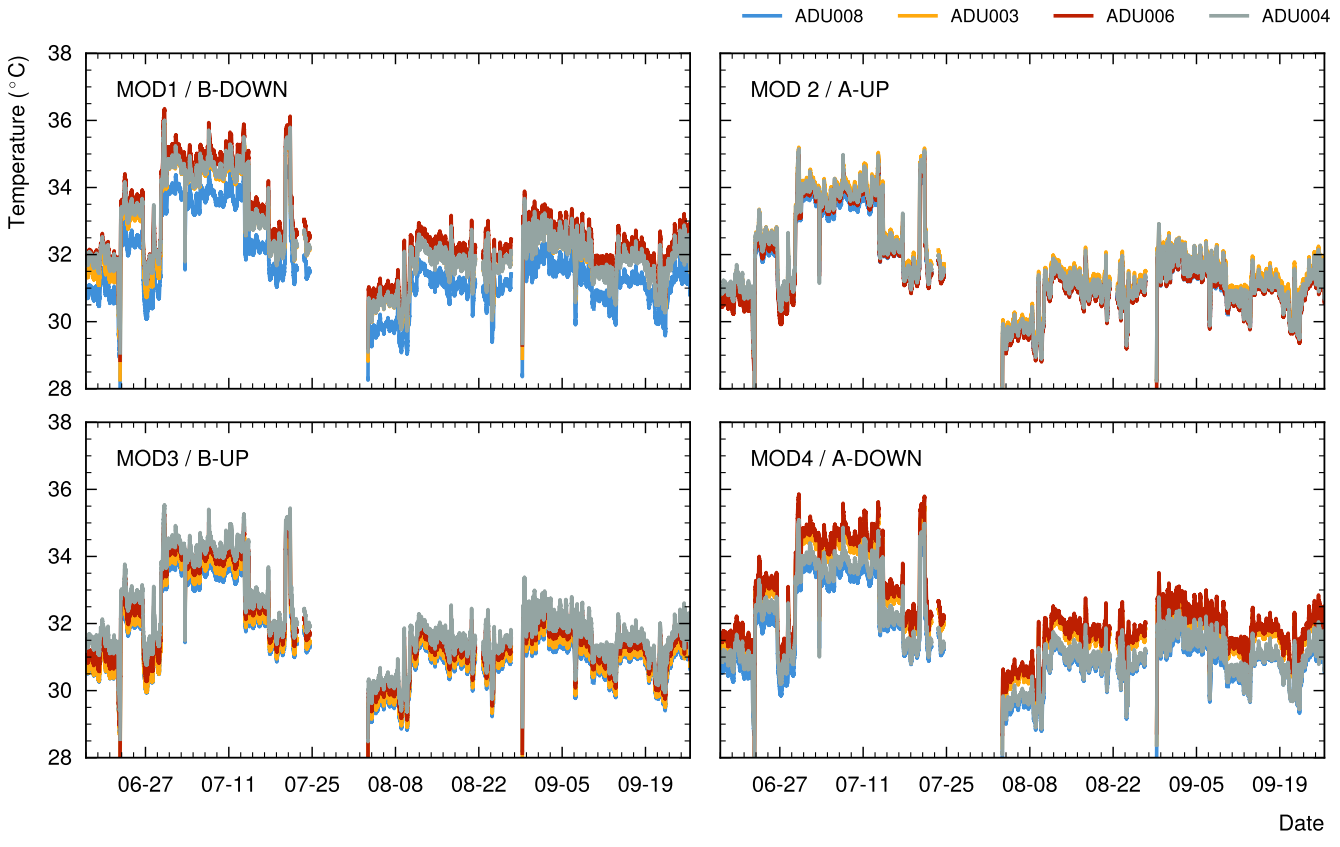

Figure 11.6: Temperatures of the ADU modules while the instrument was deployed in the JEM. The four panels are for the sides of the detector on which SiPM arrays are mounted (see Figure 8.1). Gaps are due to non-functional MRDL.

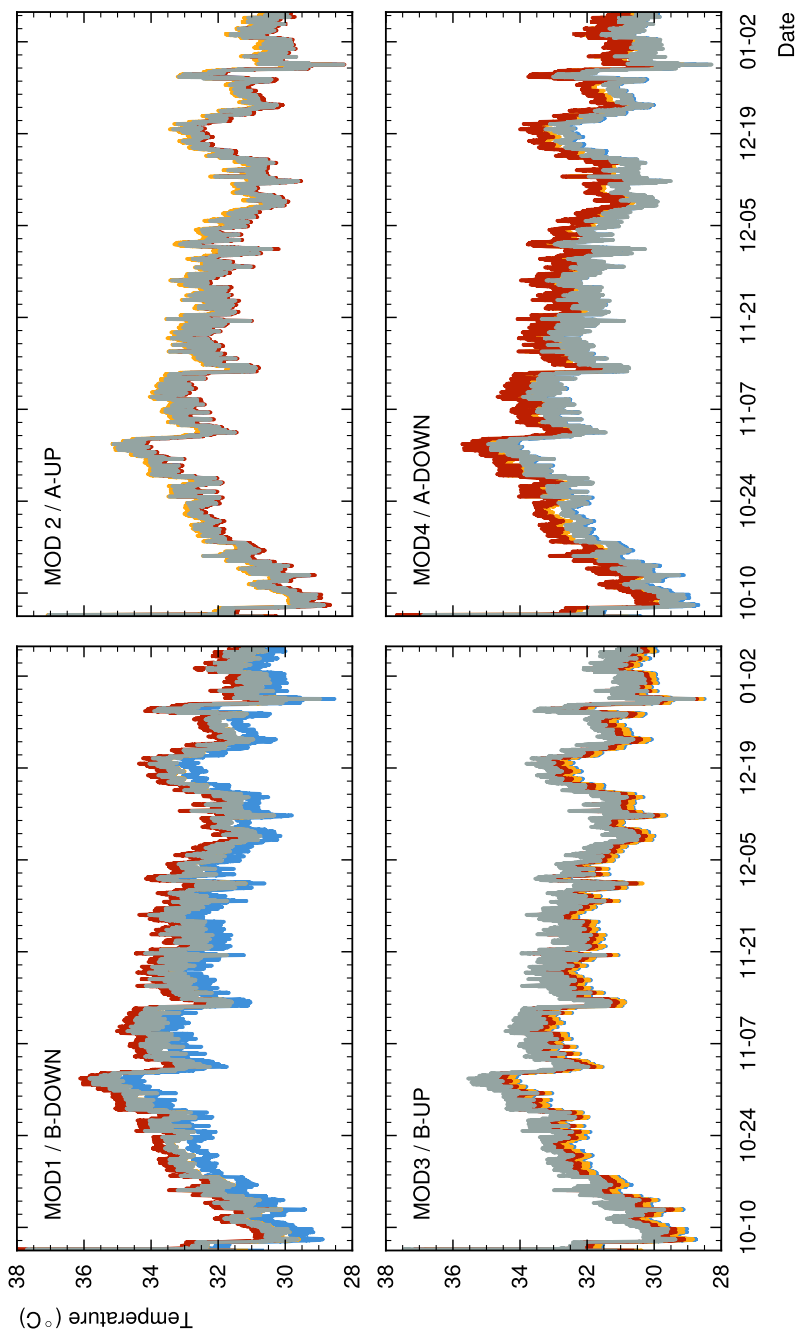

Figure 11.7: Temperatures of the ADU modules while the instrument was deployed in the USL. The four panels are for the sides of the detector on which SiPM arrays are mounted (see Figure 8.1).

large temperature gradients, with the latter being the more important aspect. Figures 11.5, 11.6, and 11.7 show the temperatures recorded by the sensors on each of the ADU's SiPM arrays. They visualize how our initial goal of always keeping the temperature of the SiPM arrays below 30 °C did not work out. After relocating the instrument to the USL, we demonstrated that we could achieve this objective by continuously turning on all fans of the four cooling channels for the read-out electronics (see Figure 11.7). This, however, was not a permanent solution because the instrument would have exceeded NASA's continuous-noise limits had we kept the fans on. We hence were forced to accept the slightly higher temperatures yet could not determine a noticeable degradation in detector performance. Most importantly, we did not notice changes in the overall count rates for different temperatures, indicating that we managed to set the trigger thresholds of the front-end electronics to values well above the dark-count regime.

On the positive side, the three figures show that the temperatures on different arrays and sides of the ADU never drifted apart more than 2 °C. The total range of variation was about 6 °C. For the PM3325's temperature coefficient of $22\,\mathrm{mV\,K^{-1}}$ and our operating overvoltage of 3 V, this range translates into a gain variation of about 4.4%. The continuous recording of all temperature measurements allows us to correct this effect.

Figures 11.7 and 11.4 also show how much the overall temperature of the instrument depends on the ambient temperature. During the deployment in the USL, RadMap's power consumption varied by less than 6%, while the temperature of the ADU varied by roughly 20%. It did so even during times when the power draw, and hence the internal heat dissipation, was nearly constant. Furthermore, the time series of temperature and power consumption show no clear overall correlation, though abrupt changes in the latter appear to induce some change in the former. Without detailed knowledge of the environmental conditions, it is impossible to tell what causes the temperature variations. Possible explanations for higher ambient temperatures include:

1. Though the mean temperature inside the ISS is relatively stable, exhaust vents of power-hungry equipment in the racks can locally create areas of higher temperature. We know that not all equipment is operating continuously, possibly resulting in a time dependence of the ambient-air temperature near the instrument.
2. In microgravity conditions and in the absence of gravitationally driven convection, the main cooling channel's exhaust can create a bubble of

warm air around the instrument. Though the station is equipped with fans creating a constant air flow (mainly to prevent the formation of bubbles of toxic gases like CO_2), local obstructions may at times reduce the rate of air exchange.

Both scenarios would lead to a higher temperature of the cooling channels' air intake, thus reducing their cooling effectiveness. The data we collected shows that the ADU is thermally well-connected to the rest of the instrument, such that temperature changes in the main cooling channel in the lower housing compartment propagate rapidly (in a matter of a few minutes) to it. In future design iterations, a reduced thermal connection between the detector and the electrical systems could be considered. Alternatively, a means of actively controlling the ADU temperature may be an option, if temperature-induced gain variations are to be reduced to the sub-percent level. As long as the increased dark-count rate is not problematic, however, a gain correction during data analysis works just as well.

11.3.2 M-42 Dosimeter

Being a flight-proven system, the M-42 dosimeter provided a good means of collecting scientifically relevant data early during the RadMap Telescope's deployment. It also allowed us to verify the correct operation of the instrument—particularly of the flight computer—and to investigate possible EMI and the measurement noise induced by it. The data we collected was and is being analyzed by our colleagues at the DLR. I therefore discuss here only some early results to highlight the dosimeter's capabilities, as well as the data we used to cross-check the measurements of the ADU. All measurements I show were provided to me in pre-processed form by Thomas Berger and Moritz Kasemann.

Energy-Deposition Spectrum

The M-42 records the energy deposition in a 300-µm thick silicon diode. Since the active material of the diode is not thick enough for absorbing all secondary electrons (δ electrons, see Section 3.2.2), the dosimeter provides a measurement of the LET of each particle passing through it (see Section 3.2.3). With Equation 5.1, the energy deposition can directly be translated into the absorbed dose in silicon.

Figure 11.8 exemplarily shows the energy-deposition spectra for cosmic-ray and radiation-belt particles (measured inside the SAA, see Section 2.5.1)

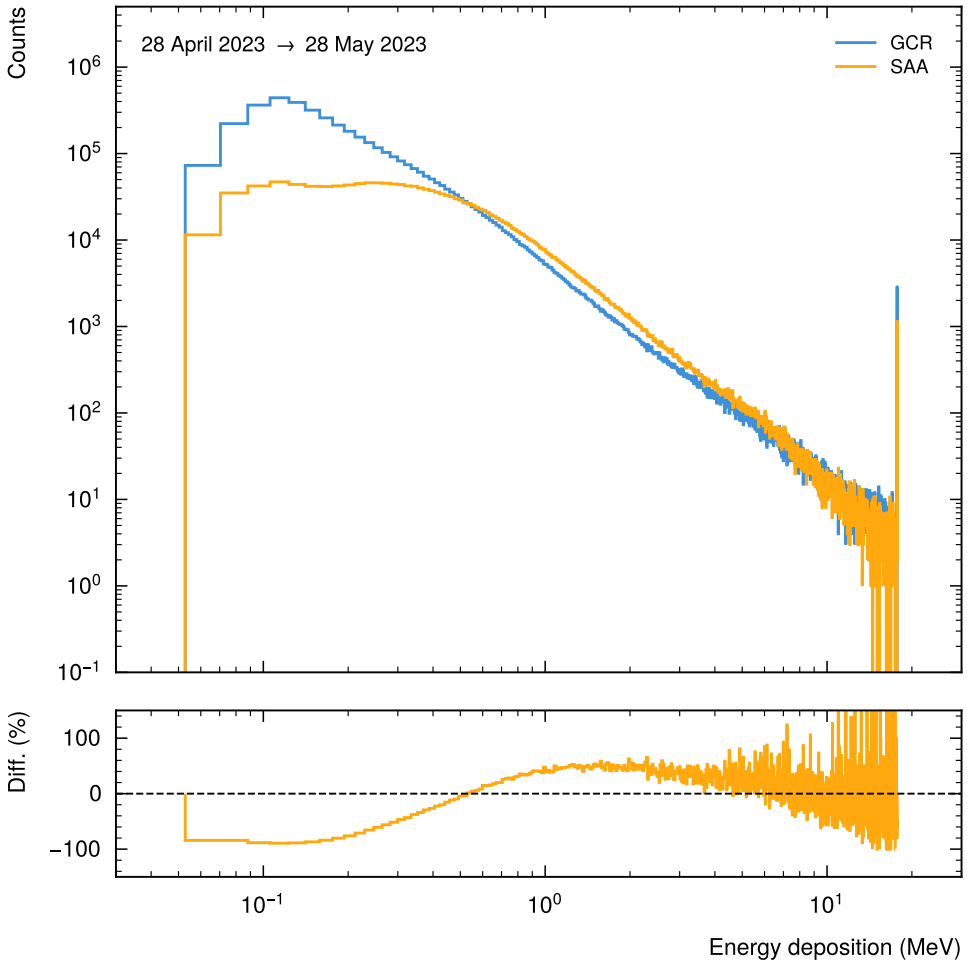

Figure 11.8: Energy-deposition spectra of cosmic-ray (GCR, blue) and radiation-belt (measured inside the SAA, yellow) particles in the M-42 dosimeter, integrated over a one-month period in April and May 2023. The lower panel shows the difference of the two, normalized to the GCR spectrum.

integrated over a one-month period in April and May 2023. The lower panel shows the difference of the two, normalized to the GCR spectrum. The figure illustrates the qualitative difference between the two sources of radiation particles: Though the cosmic-ray spectrum in interplanetary space peaks at a few hundred MeV per nucleon (and at even lower energies outside the

heliosphere), Earth's magnetosphere prevents such low-energy particles from reaching the ISS orbit (see the discussion of the cutoff rigidity in Section 2.5). The cosmic-ray spectrum arriving at the station therefore consists of particles and nuclei with energies of several GeV/n or more. These particles have stopping powers close to the minimum-ionizing regime, thus depositing on average only a small fraction of their kinetic energy in the dosimeter. The energy-deposition spectrum of GCR therefore peaks at small values.

Particles (mostly protons) trapped in the radiation belts, on the other hand, typically have energies of hundreds of MeV (see Section 2.5.1), with their energy further reduced by the station's shielding. A substantial fraction of them consequently has energies that puts them to the left of the minimum-ionization regime (see Figure 3.2), where the stopping power increases drastically. The energy-deposition spectrum of radiation-belt particles measured during passes of the SAA therefore peaks at higher values. In the M-42, there appears to be a second peak-like structure in the first few bins of the spectrum, somewhat obscuring this effect. This structure, however, is not created by the primary radiation field but by secondary particles (mostly electrons and gamma rays) created in interactions of radiation-belt protons with the station's shielding and structures.

Dose Rates in the JEM

Figure 11.9 shows the daily radiation dose absorbed by the M-42's silicon diode while the RadMap Telescope was deployed in the JEM between 23 June 2023 and 25 September 2023. In addition to the daily total dose (drawn in red), the graph also shows the contributions of GCR (blue) and radiation-belt particles (yellow). The relatively higher contribution of the latter is due to their harder energy-deposition spectrum (discussed in the previous section). The dose rate of GCR is fairly constant, only varying on the order of a few percent. The highly variable structure of the total dose is almost exclusively induced by variations of the dose absorbed during passes through the SAA. This is illustrated most graphically by the periods of almost oscillatory behavior in mid-August and mid-September. Here, the daily dose deposited by radiation-belt particles is alternately below and (significantly) above average. This somewhat peculiar behavior is caused by orbital mechanics: Due to the rotation of Earth, the orbit plane of the ISS intersects the SAA only about every twelve hours. Since the time it takes Earth to make a full rotation is not an exact multiple of the ISS' orbital period, the station's daily cycle of ground tracks shifts slightly eastward

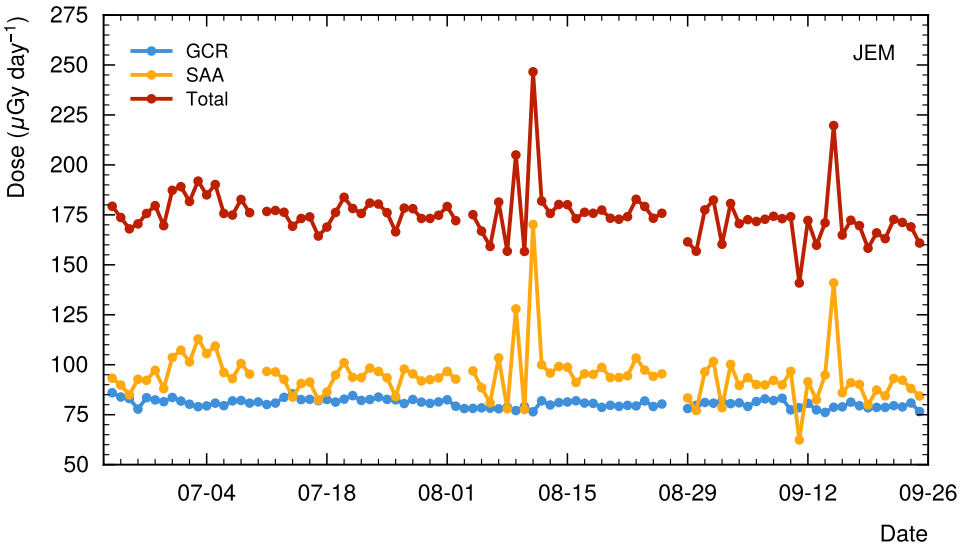

Figure 11.9: Daily radiation dose absorbed by the M-42 dosimeter while the RadMap Telescope was deployed in the JEM between 23 June 2023 and 25 September 2023. The total dose (red) is simply the sum of the doses of GCR (blue) and radiation-belt (yellow) particles. The large variations in mid-August and mid-September are due to orbital mechanics (see text).

each day, approximately but not exactly repeating every few days.[1] Every couple of weeks, this shift leads to a period where every second day the ISS passes through the SAA less often than on average. Every other day, there is an above-average number of long passes through the anomaly. This effect, which is somewhat exacerbated by the SAA's asymmetric shape, leads to the large day-to-day fluctuation of the absorbed dose visible in Figure 11.9.

11.3.3 Active Detection Unit

In contrast to the M-42, the ADU, as well as its read-out and data-acquisition electronics, are new systems that we have never before operated in space (or in any other complex environment, for that matter). My discussion of our initial data analysis is therefore mostly focused on aspects that help us understand

[1]The magnitude of the shift and the time after which the ground-track pattern repeats depend on the orbit altitude of station, which changes over time due to atmospheric drag and occasional re-boosts.

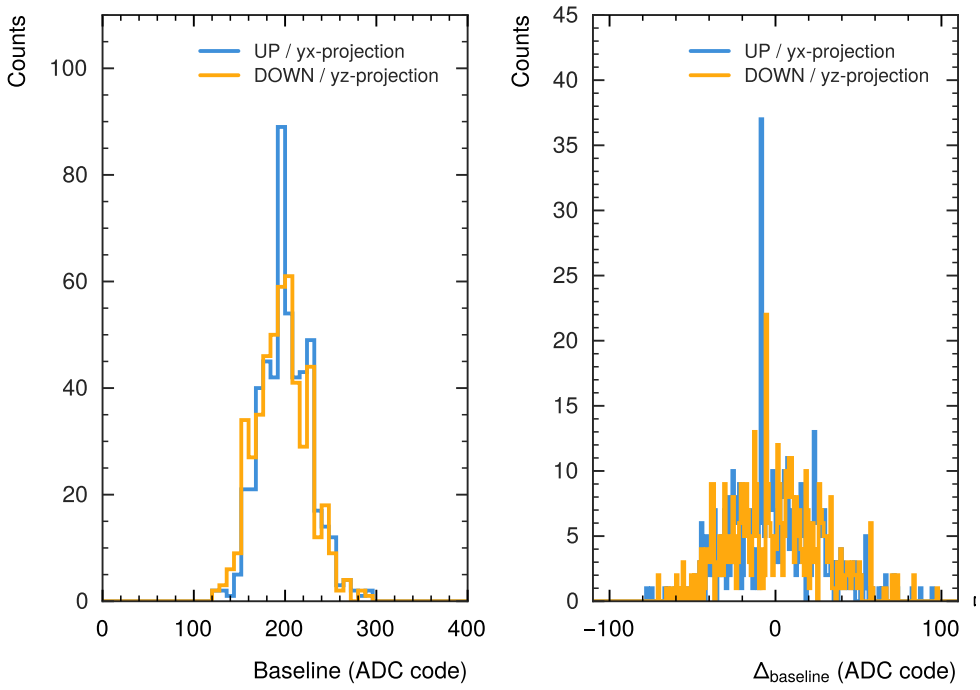

Figure 11.10: Left: Distribution of the baselines of all 1005 read-out channels of the ADU. Two channels have baselines exceeding 1950 and 2750 LSBs, respectively, and are therefore not shown. One ASIC is inoperable, and a single channel on another one is so noisy that we needed to deactivate it. Right: Difference of the baselines from the mean value for all read-out channels.

how the detector performs in the space radiation environment in general, and on the ISS in particular. Where possible, I cross-reference the tracking calorimeter's measurements with those of the M-42 to check for plausibility.

Baselines

One of the primary parameters for characterizing the performance of the read-out ASICs is the height and stability of their baseline, that is, the ADC code[2] returned when a channel is read without a SiPM signal present. The

[2]The ADC code is the number of LSB values corresponding to the applied input signal:

$\frac{\text{signal amplitude}}{\text{LSB value}} = \text{ADC code}$

baseline's height determines the maximum dynamic range of the input signal, and any variation of the baseline translates into an uncertainty of the measured signal amplitudes. To measure the baselines of the ADU's read-out electronics, we switch off the SiPM bias voltage to prevent dark counts from inducing any signals. We force all 64 ASICs into read-out by pulling their external trigger input at a rate of several kilohertz. The baselines can then simply be calculated by taking the mean of the recorded data for each channel. During early operations of the instrument, we performed this procedure manually. Starting in November 2023, we switched from manual baseline measurements to automatic ones (every six hours) to investigate whether the ASICs exhibit a noticeable time dependence but could not observe any.

The left panel of Figure 11.10 shows the distribution of the baseline ADC codes of all 1005 fully functional channels of the read-out electronics for a baseline measurement with 11 000 triggered events. Our investigation revealed that, unfortunately, one ASIC is inoperable; on another one, we needed to deactivate a single channel because it was too noisy. In addition, two channels (on separate ASICs) have baselines exceeding 1950 and 2750 LSBs, respectively, and are therefore practically unusable. The fully functional channels have baselines that are almost symmetrically distributed around a mean value of 200 LSBs. This is also illustrated in the right panel of Figure 11.10, which shows the distribution of $\Delta_{\mathrm{baseline}}$, i.e., the difference of each channel's value from the mean. Hence, the 12-bit dynamic range (corresponding to 4096 LSBs) of the IDE3380's built-in ADC is on average reduced by about 200 LSBs.

The stability of the baseline ADC codes upon repeated read-out determines the uncertainty with which signal amplitudes can be measured. To investigate the baseline stability, we determined the standard deviation, $\sigma_{\mathrm{baseline}}$, of the distribution of the ADC codes for 11 000 baseline measurements for each channel. The left panel of Figure 11.11 shows the distribution of the $\sigma_{\mathrm{baseline}}$ for all functional channels of the ADU. It has a peak at around 1 LSB for both projections (fiber orientations), with nearly all channels having a value smaller than 2 LSBs. Assuming an average dynamic range of 3900 LSBs, this means that the signal-amplitude uncertainty due to baseline fluctuations is less than 0.05% for most channels, and less than about 0.1% for all channels. The right panel of Figure 11.11 shows that there is no apparent correlation between $\Delta_{\mathrm{baseline}}$ and $\sigma_{\mathrm{baseline}}$.

Figures 11.12 and 11.13 show the baselines' difference from the mean and their standard deviation for each individual channel in the two projections defined in Figure 9.1. The graphs reveal that there is neither a particular

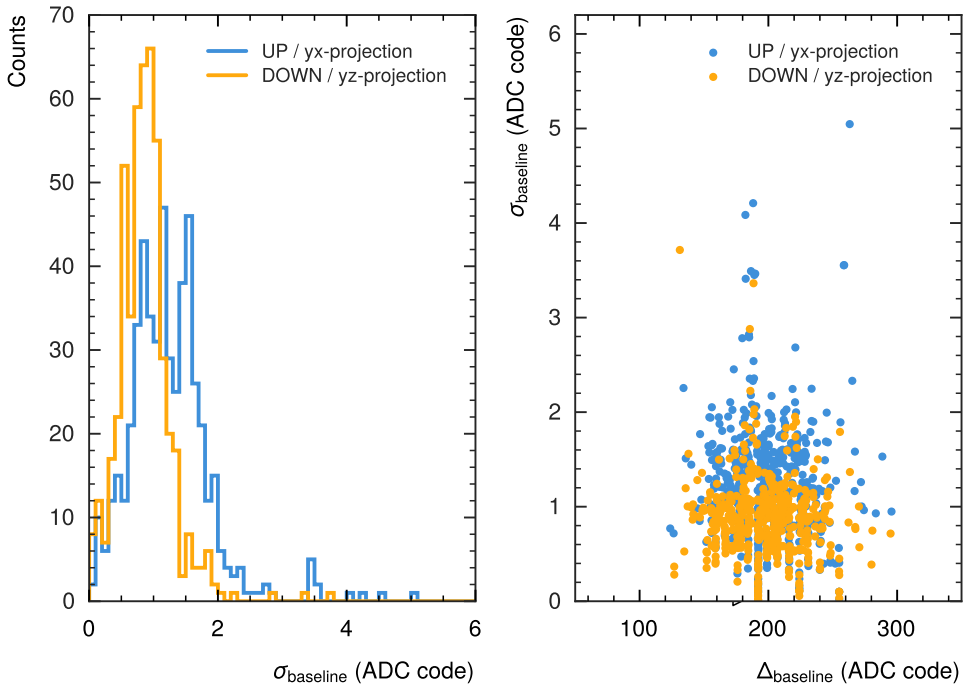

Figure 11.11: Left: Distribution of the standard deviation of 11 000 baseline measurements for each fully functional ADU channel. Right: σ_{baseline} plotted against Δ_{baseline} for each channel.

pattern to larger and smaller Δ_{baseline} values, nor to the magnitude of σ_{baseline}. The only somewhat noticeable trend is that the latter seems to be on average a little higher for the yx-projection, which is visible in Figure 11.11. Overall, the apparent lack of patterns or features in the spatial distribution of Δ_{baseline} and σ_{baseline} indicates that the analog signal paths and read-out ASICs are not systematically affected by internal or external disturbances.

Channel Hit Rates

We also investigated the rate at which each detector channel was hit, that is, traversed by particles. For this analysis, we used data from a period where we could be sure that the ISS was not passing through the SAA, such that the instrument would only be exposed to GCR. This allowed us to assume that a majority of particles had enough energy for traversing at least half the detector,

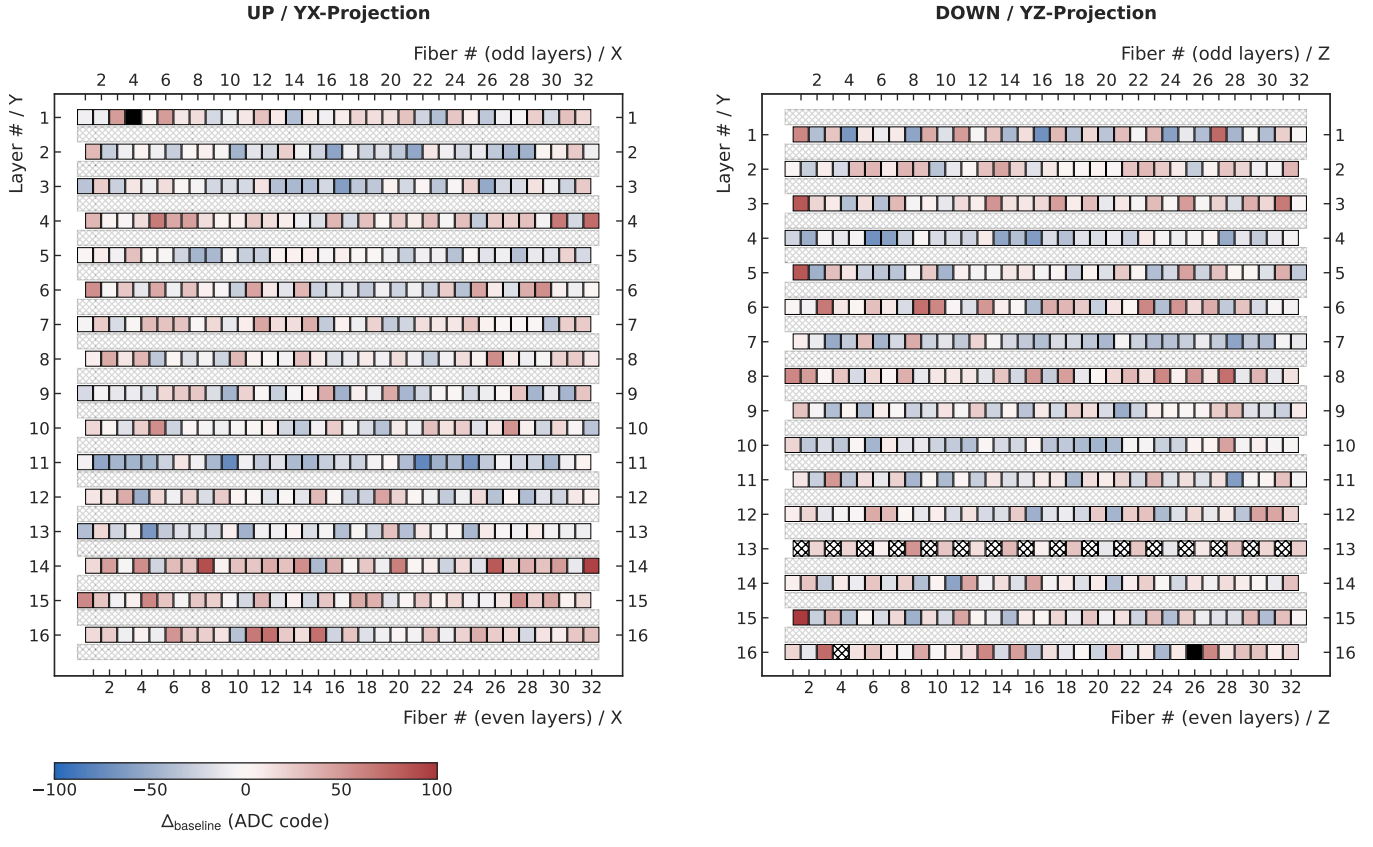

Figure 11.12: Difference of the baseline from the mean value for each ADU channel, shown in the two projections defined in Figure 9.1. The 17 inoperable channels are marked with a cross-hatch pattern; the two channels with abnormally high baselines are marked in black.

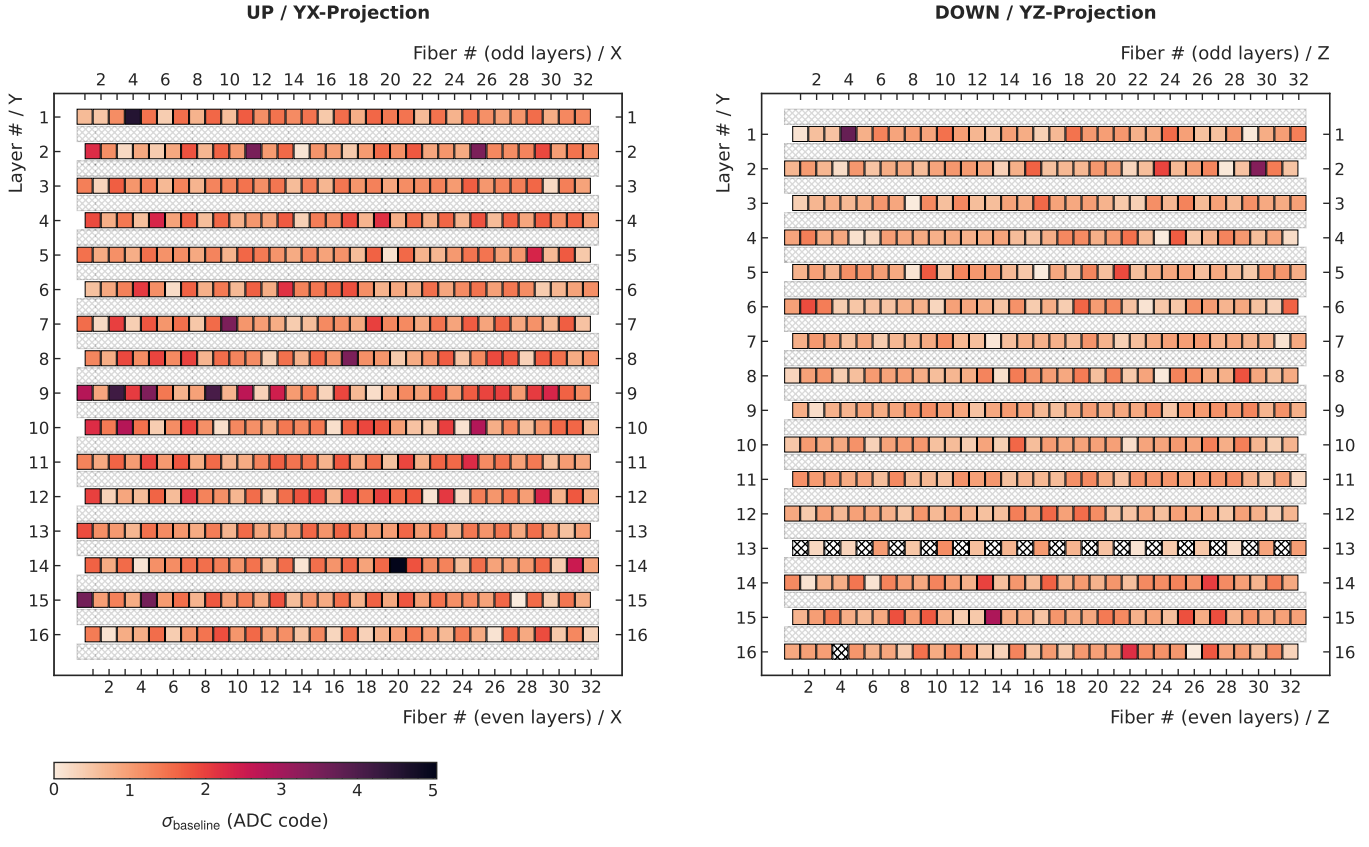

Figure 11.13: Standard deviation of 11 000 baseline measurements for each ADU channel, shown in the two projections defined in Figure 9.1. The 17 inoperable channels are marked with a cross-hatch pattern; the two channels with abnormally high baselines are marked in black.

if not all of it. Further, we assumed that the flux of cosmic rays is to first order isotropic (though that assumption is, strictly speaking, not entirely true because of the shielding of Earth). In this simplified picture, every detector channel should be hit by particles at about the same rate. To verify this, we analyzed the data of one million events, counting the number of times each channel produced a signal that was at least 10 LSBs larger than its baseline ADC code.

Figure 11.14 illustrates the result of this analysis, showing the percentage of events for which each channel produced a signal. In the extremes, values range between 0.1% and 2%, suggesting that there are large differences in either gain or light-collection efficiency (i.e., light yield) in some channels. For one ASIC, all 16 fibers never produced a signal, as did an additional two channels on another chip. Since all these channels produced acceptable baselines when being force-triggered by the data-acquisition electronics, we suspect that there are ASIC-internal problems of yet unknown nature. For the chip in which none of the 16 channels produces a signal, an issue with the internal trigger mechanism seems most likely. As of writing this, we have no credible hypothesis for what is causing the other two channels to working as they should. In either case, a detailed investigation into the root cause of the problem is still pending.

To better visualize the observed variation in the rate at which the individual channels produce signals, Figure 11.15 illustrates the deviation of each channel's signal rate from the mean. The graph shows that in many cases, whole rows of fibers show a consistently lower or higher rate. This suggests that the deviations are unlikely to stem from differences in the actual hit rate but are more likely caused by the channels' lower probability to produce a signal that crosses the 10-LSB threshold. This could, for example, be caused by improper alignment of the scintillating fibers and SiPMs (see detailed discussion in Section 12.1.1), causing an overall lower light yield in some layers. The majority of channels, however, deviates less than 50% from the mean count rate, a fact that is even better highlighted in Figure 11.16.

Crosstalk

Assessing the optical and electrical crosstalk between neighboring channels is difficult without prior knowledge of the channels that were hit by a particle and those that were not. Until our track reconstruction algorithms are fully operational, determining the channel-by-channel crosstalk probability is there-

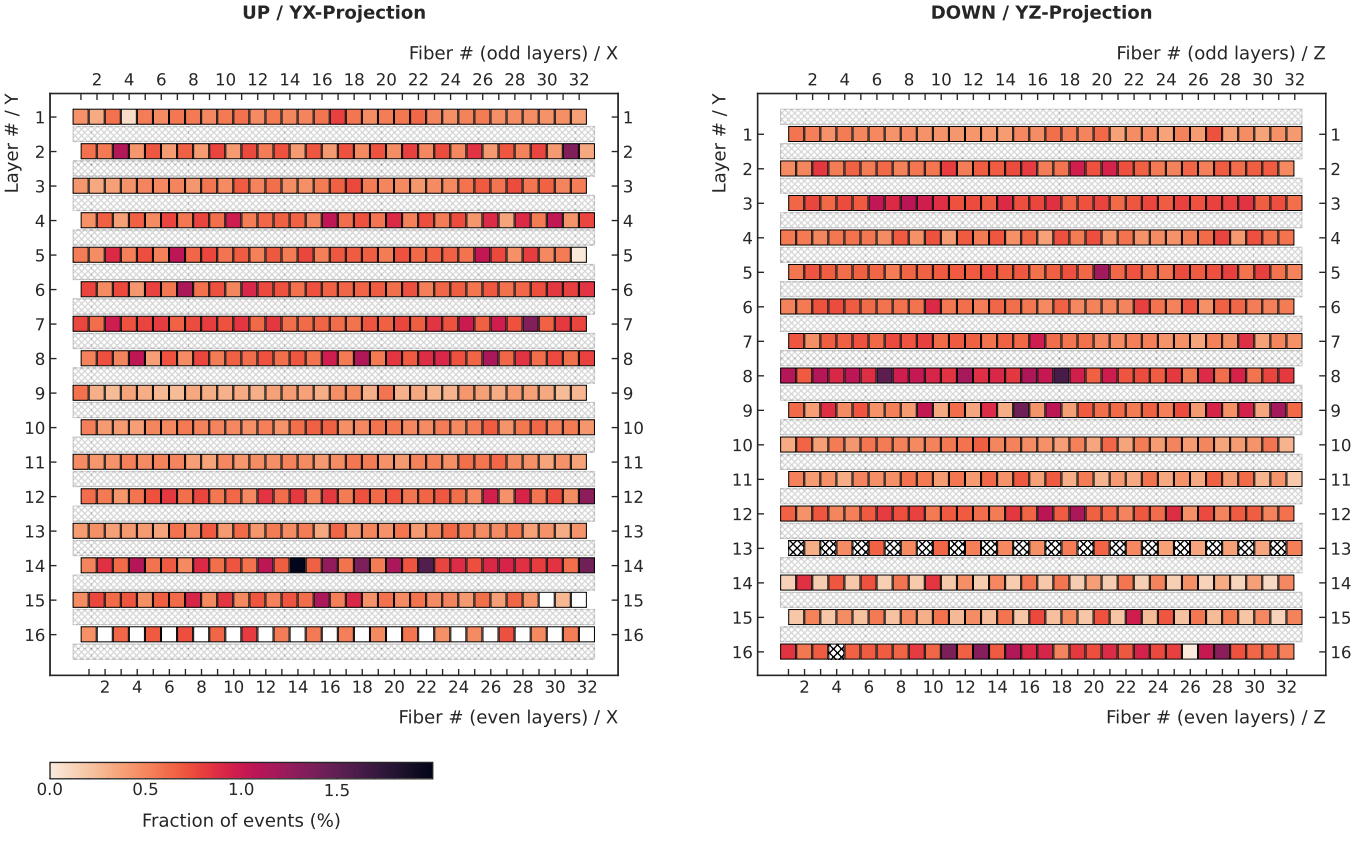

Figure 11.14: Fraction of one million GCR events for which each ADU channel produced a signal that was at least 10 LSBs larger than its baseline ADC code. The 18 channels drawn in white never showed a signal but produce acceptable baselines (see Figure 11.12).

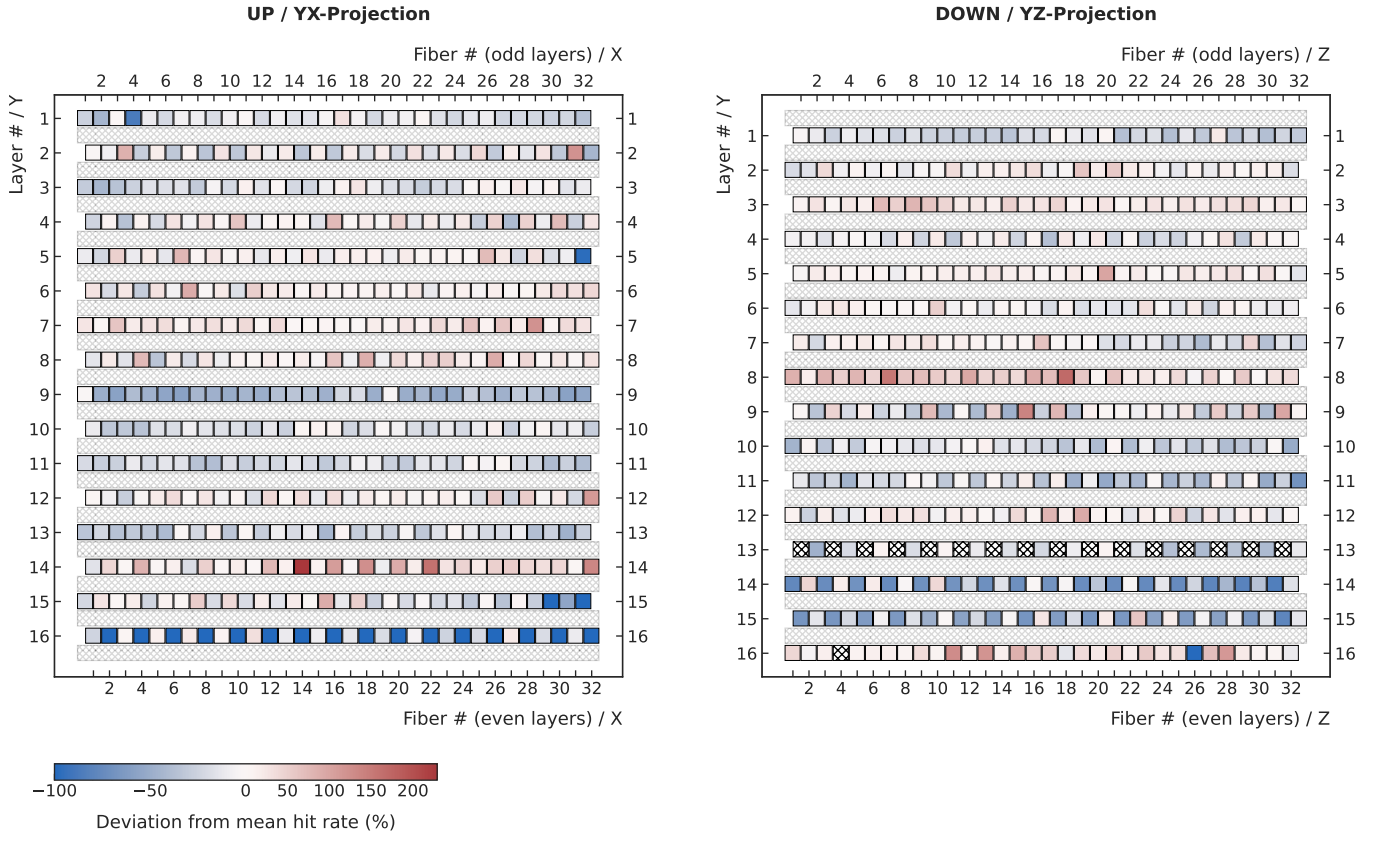

Figure 11.15: Deviation of each channel's hit rate from the mean. The 16 channels not showing signals at all were not masked and thus have a deviation of -100%.

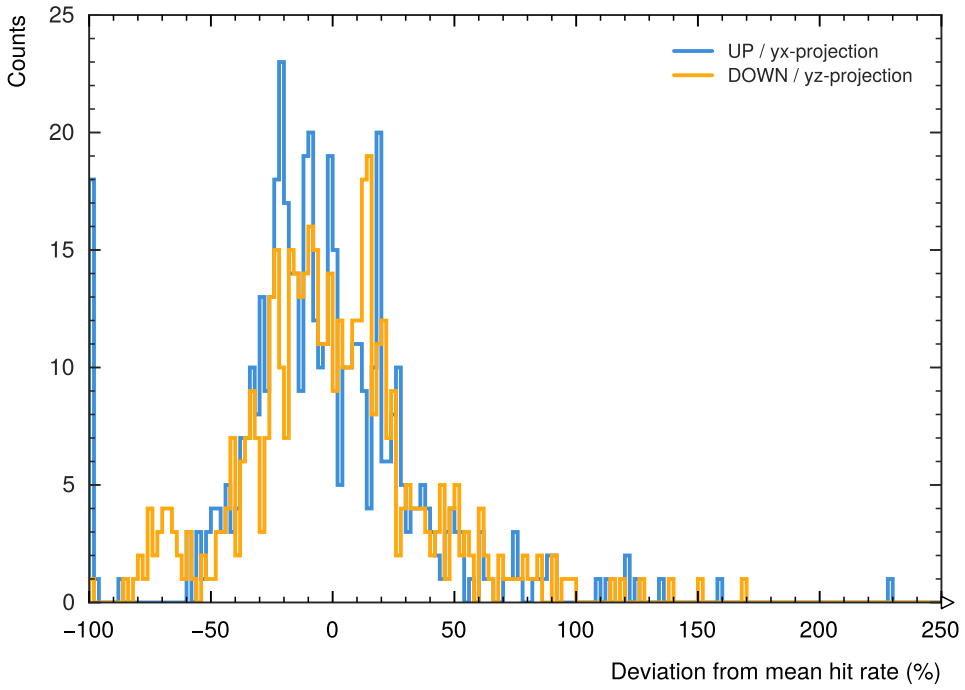

Figure 11.16: Distribution of the deviation of each channel's hit rate from the mean. Same data as shown in Figure 11.15.

fore only possible to a very limited extent. Thus, I here provide only a first and rather simple analysis, which should nonetheless help to at least assess the approximate magnitude of the effects.

For my analysis, I only consider optical crosstalk, mostly because I expect the electrical crosstalk to be smaller than the uncertainties due to the missing track information. There are two scenarios that can lead to photons from one fiber being detected in another fiber's SiPM (see illustration in Figure 11.19). First, damage to the aluminum coating of a fiber's end face (e.g., due to scratches or flaking) can lead to photons leaving the fiber and impinging on the SiPM that is supposed to detect the scintillation light of the neighboring one. This effect can be exacerbated through the creation of light guides by excess optical epoxy (see Section 12.1.1). Second, a fraction of the photons impinging on a SiPM is reflected off its surface [PG19] and may reach a neighboring one. Again, the probability for this to happen may be increased by the presence

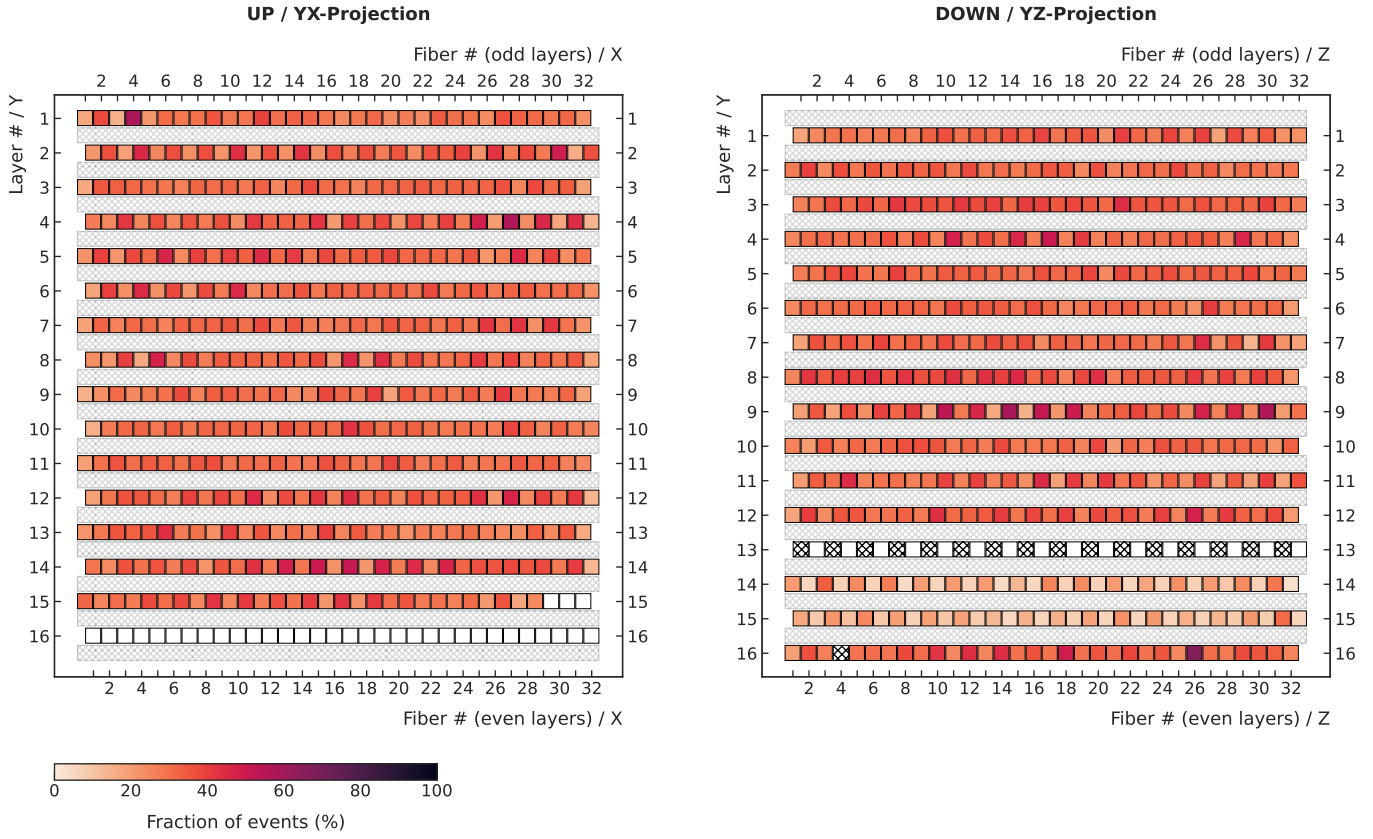

Figure 11.17: Fraction of 100 000 GCR events for which a signal crossing a 10-LSB threshold also crossed a 50-LSB threshold in the neighboring channel either to the left or to the right.

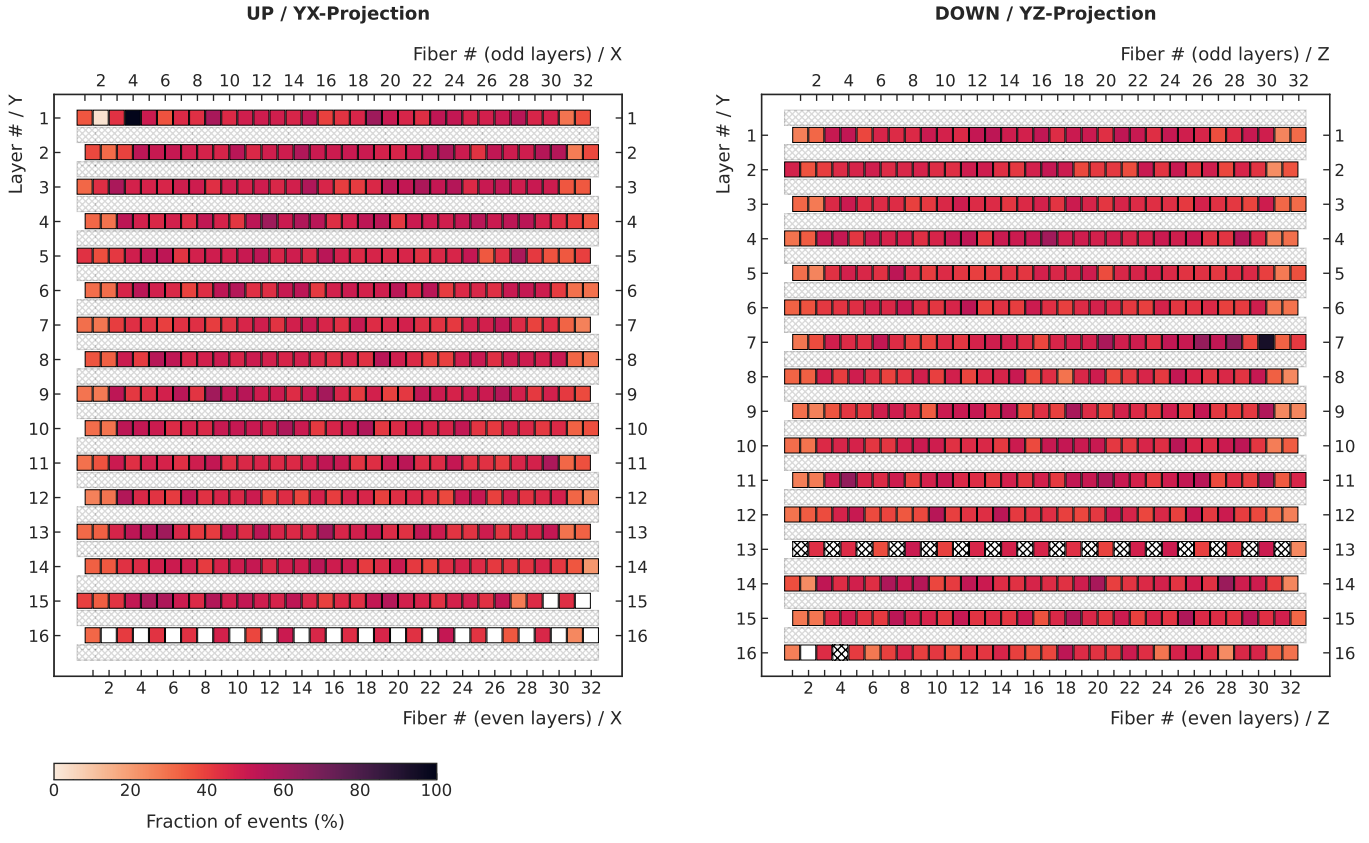

Figure 11.18: Fraction of 100 000 GCR events for which a signal crossing a 10-LSB threshold also crossed a 50-LSB threshold in the second next channel either to the left or to the right.

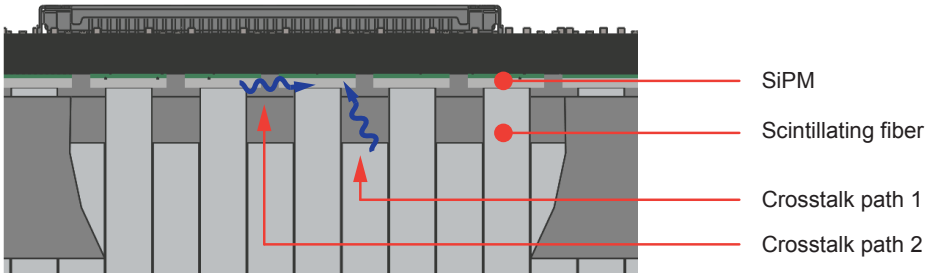

Figure 11.19: The two possible paths for photons of one scintillating fiber to the SiPM of another one. Photons may either exit a fiber end due to damage to the aluminum coating (path 1) or be reflected off a neighboring SiPM (path 2). The presence of excess optical epoxy can improve the photons' optical path towards the photosensor experiencing crosstalk.

of excess glue. Any misalignment of fibers and SiPMs (see Section 12.1.1) is likely to have a much larger effect, though.

I attempted to assess the probability for both crosstalk scenarios separately. For the first path, I analyzed the probability for a signal in one fiber to be caused by a particle hitting its direct neighbor. To do so, I counted the number of times a signal in a given fiber crossed a 10-LSB threshold *and* a signal in the neighboring one, either to left or to right, crossed a 50-LSB threshold at the same time. The larger threshold for the neighbor reflects that a crosstalk signal is likely to be smaller than the original one. I analyzed a data set of 100 000 GCR events; the results of this analysis are shown in Figure 11.17. The graph shows that there is no strong spatial correlation, though some fiber layers appear to have an overall lower probability for coincident signals in neighboring fibers. It is the same layers that also exhibit lower overall hit rates, so it seems likely that this effect is primarily due to a lower acceptance in these channels (caused by a lower gain or light yield). Fibers for which both neighboring channels are non-functional obviously do not exhibit any crosstalk and are thus drawn in white.

Without tracking, we cannot tell whether a signal being present in adjacent fibers is due to crosstalk or because a particle actually traversed both. However, the overall magnitude of the probabilities, which lie in the range of 20% to 40% (see left panel of Figure 11.20), suggests that much of the coincident signals may actually stem from particles and not from crosstalk. This hypothesis is

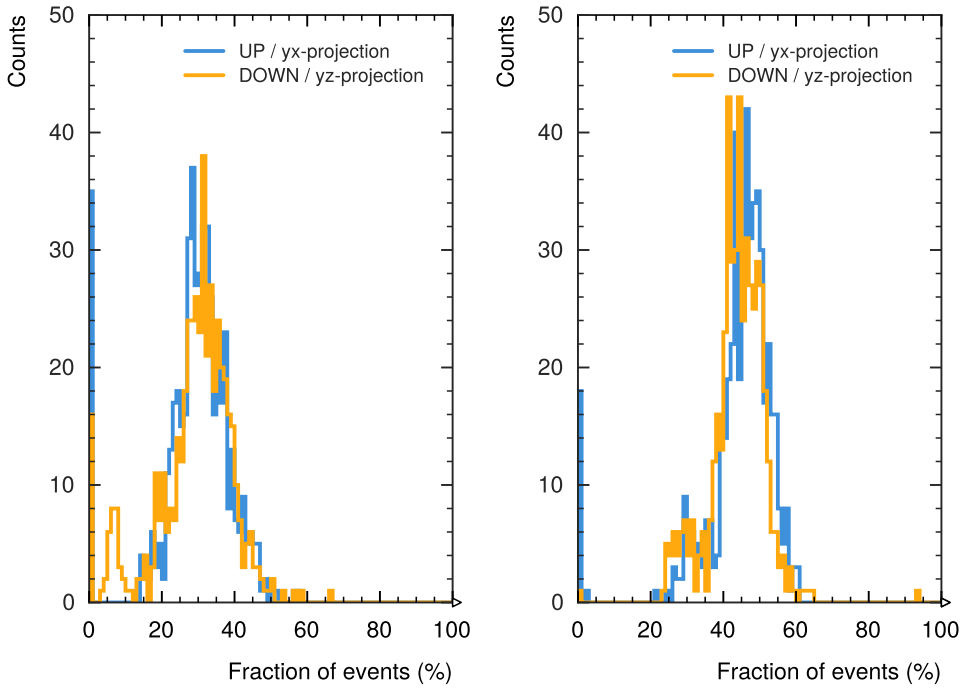

Figure 11.20: Summary of the data shown in Figures 11.17 and 11.18: Distribution of the fraction of events per channel for which the adjacent (left) or second next fibers also produced a signal.

based on simple geometrical considerations: The fraction of the solid angle subtended by adjacent fibers is approximately 25%. Assuming an isotropic particle flux, 25% of particles hitting a fiber should thus also traverse one of its neighbors. The maximum of the distribution shown in the left panel of Figure 11.20 is only slightly higher than that, suggesting that the crosstalk probability, while not zero, is rather small. Any crosstalk in this case must be optical, as adjacent fibers are read out on opposite ends of their fibers (and hence different SiPM arrays), thus eliminating the possibility of electrical crosstalk. A more detailed analysis will only be possible with a fully functional track reconstruction.

For the second crosstalk path, I analogously counted the number of times a signal in a given fiber crossed a 10-LSB threshold *and* a signal two fibers to the left or to the right crossed a 50-LSB at the same time. The results

for this analysis are shown in Figure 11.18. What is immediately obvious is that the overall coincident-signal probability is higher and slightly more uniform than for the first crosstalk path. This is also apparent in the right panel of Figure 11.20. The fibers at the edges of each layer show lower values, which does make sense considering that they only have neighbors to one side. Intriguingly, two channels have values of more than 90%, suggesting that they see a lot of light of the neighboring channels. Overall, the analysis shows that there is a significant probability for optical (or electrical) crosstalk between fibers that are read out on the same side of the detector. Again, a more detailed analysis will only be possible with track reconstruction.

Energy-Deposition Spectra in Individual Channels

Central to understanding whether we operate the ADU with appropriately chosen bias voltage and read-out settings is an assessment of the energy spectra in the individual detector channels. Figure 11.21 shows such spectra for five randomly selected channels with different hit rates (from high to low) for one full day of recorded data (about 20 million events). The events are baseline-corrected, that is, I subtracted each channel's baseline ADC code from the recorded signal height. To account for baseline fluctuations, any resulting values smaller than 5 LSB were set to zero. To avoid large peaks in the first bin, the spectra only show entries for which the signal was greater than zero. I used the SAA detection algorithm presented below to record separate spectra for GCR and radiation-belt particles.

The spectra show that the settings we operated the ADU with are chosen well for a majority of events. The small peaks at the right end are due to energy depositions that exceed the dynamic range of the respective channel. They do, however, make up only a negligible fraction of the recorded events. These signals could likely be resolved by decreasing the charge sensitivity of the CMIS in the IDE3380 ASICs. Doing so would come at the cost of a decreased resolution for the energy deposition and is thus not advisable given that the vast majority of signals are well resolved. It can also be seen that four of the five channels have a very similar response (i.e., spectral shape), though the one drawn in gray shows significantly fewer events at low signal amplitudes. The channel drawn in red has a substantially different response, which is likely due to either a lower gain or a lower light yield.

Comparing the spectra for GCR and radiation-belt particles reveals that they have a somewhat different shape, with the latter having a stronger contribution

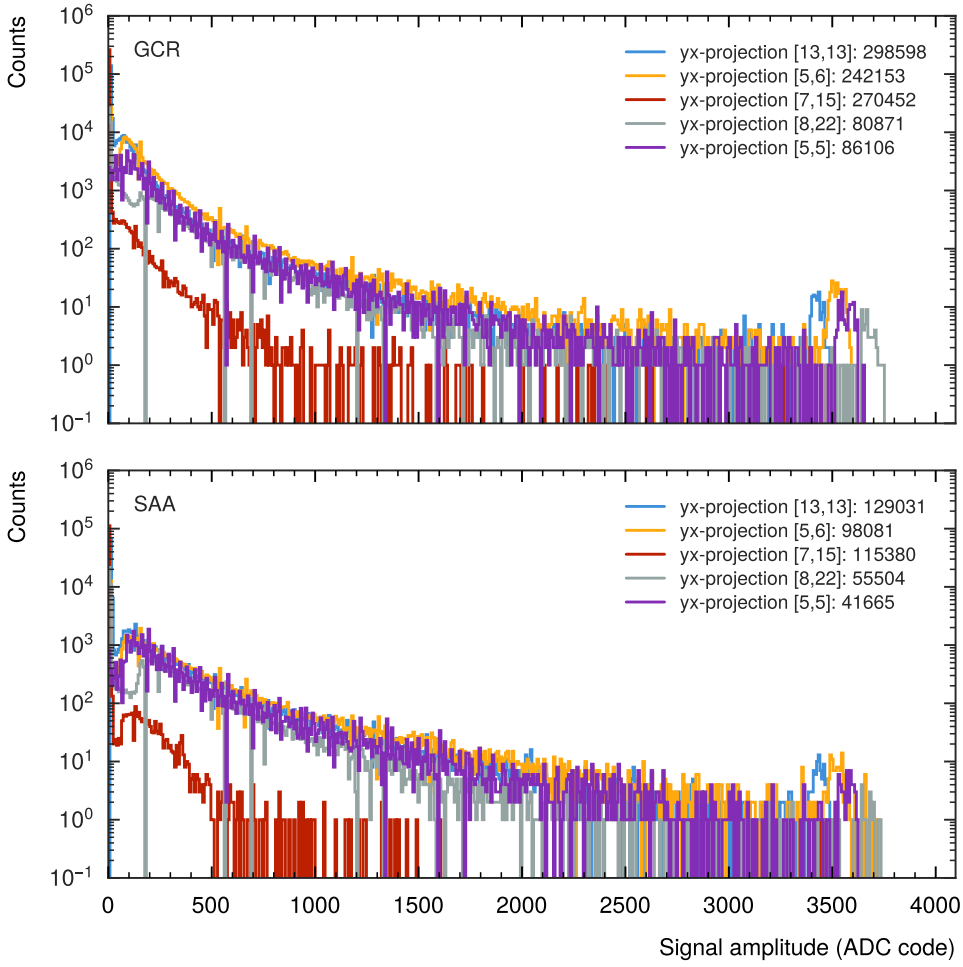

Figure 11.21: Energy-deposition spectra for GCR (top) and radiation-belt particles (bottom) in five randomly selected ADU channels with different hit rates (from high to low) for one full day of recorded data (about 20 million events). The events are baseline-corrected with a threshold of 5 LSB (see text for explanation). Only entries larger than zero are shown to avoid large peaks in the first bin. The numbers in the legend are the total entries in each spectrum.

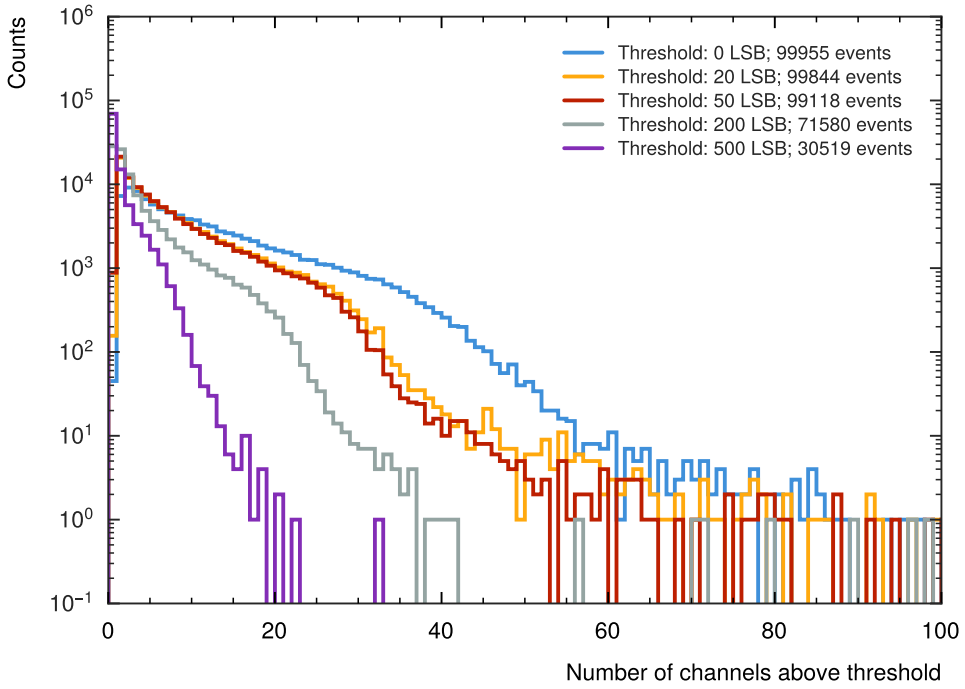

Figure 11.22: Distribution of the number of channels per event (multiplicity) with above-threshold signal amplitudes for increasing threshold values. The data is from 100 000 GCR events; the numbers in the legend give the total entries in each distribution. The events are baseline-corrected with a threshold of 5 LSB.

of large signal amplitudes. The explanation for this effect is the larger stopping power of low-energy protons trapped in the radiation belt, as discussed in the context of the M-42 energy-deposition spectra in Section 11.3.2 above. The differences in the spectral response thus confirm that the individual channels perform roughly as expected, except for the few that show a similar response to the one drawn in red.

Event Signatures

After this first quantitative assessment of the performance of the read-out electronics and the response of individual detector channels, I give a qualitative overview of some of the event signatures we observed. This overview is by no means exhaustive and is only intended to give the reader a feeling for the data

we are working with. A full assessment of event signatures requires comparison with simulated detector responses and is currently ongoing.

Figure 11.22 shows distributions for the number of detector channels per event that have above-threshold signal amplitudes. This quantity is often referred to as the *hit multiplicity*. I chose five different thresholds between 0 and 500 LSB above baseline to illustrate that the majority of events contain mostly signals with small amplitudes. Figures 11.23 through 11.26 show a selection of events for which I required that at least 10 channels pass a 20-LSB threshold cut, corresponding to the tail of the yellow distribution in Figure 11.22. These four events represent only the tiny fraction of signatures that are somewhat interpretable by simply looking at the uncorrected signal amplitudes. A large portion of the data we recorded consists of events with only few fiber hits, many of which do not form recognizable tracks or structures.

Figure 11.23 shows the event signature of a proton or nucleus entering the ADU from below. The particle stops in the active material, producing a clearly recognizable Bragg peak. The energy-deposition profile does not exhibit large fluctuations because the particle traverses the detector almost along the central vertical axis; the position dependence of the light yield is therefore nearly the same for all channels, no matter from which side they are read out. Figure 11.24, on the other hand, shows a much messier event signature, with a broad channel of energy deposition and multiple fiber hits per layer. However, the individual signal amplitudes are not particularly large. The signature is not easily interpretable, though a possible explanation could be the interaction of a high-energy cosmic-ray particle with, for example, the instrument housing, producing a Lorentz-boosted jet of lighter secondary particles that traverse the detector nearly in parallel.

Figure 11.25 shows the signature of what could be the interaction of a (low-energy) particle with the detector material. The particle appears to enter the detector from the right in the yz-projection, supposedly interacting with a target atom after traversing about eight fibers. The interaction produces on short-range particle that deposits a significant fraction of its energy shortly before stopping, as well as another particle exhibits an almost Bragg peak-like energy-loss profile (though it may not completely stop in the detector's active material). Without quantitative analysis, this interpretation is of course speculative. The event nonetheless demonstrates that we can identify particles that interact with the detector.

Lastly, Figure 11.26 shows a clear example of pileup, with two particles entering the ADU from the top at the same time (i.e., within the 10-ns trigger

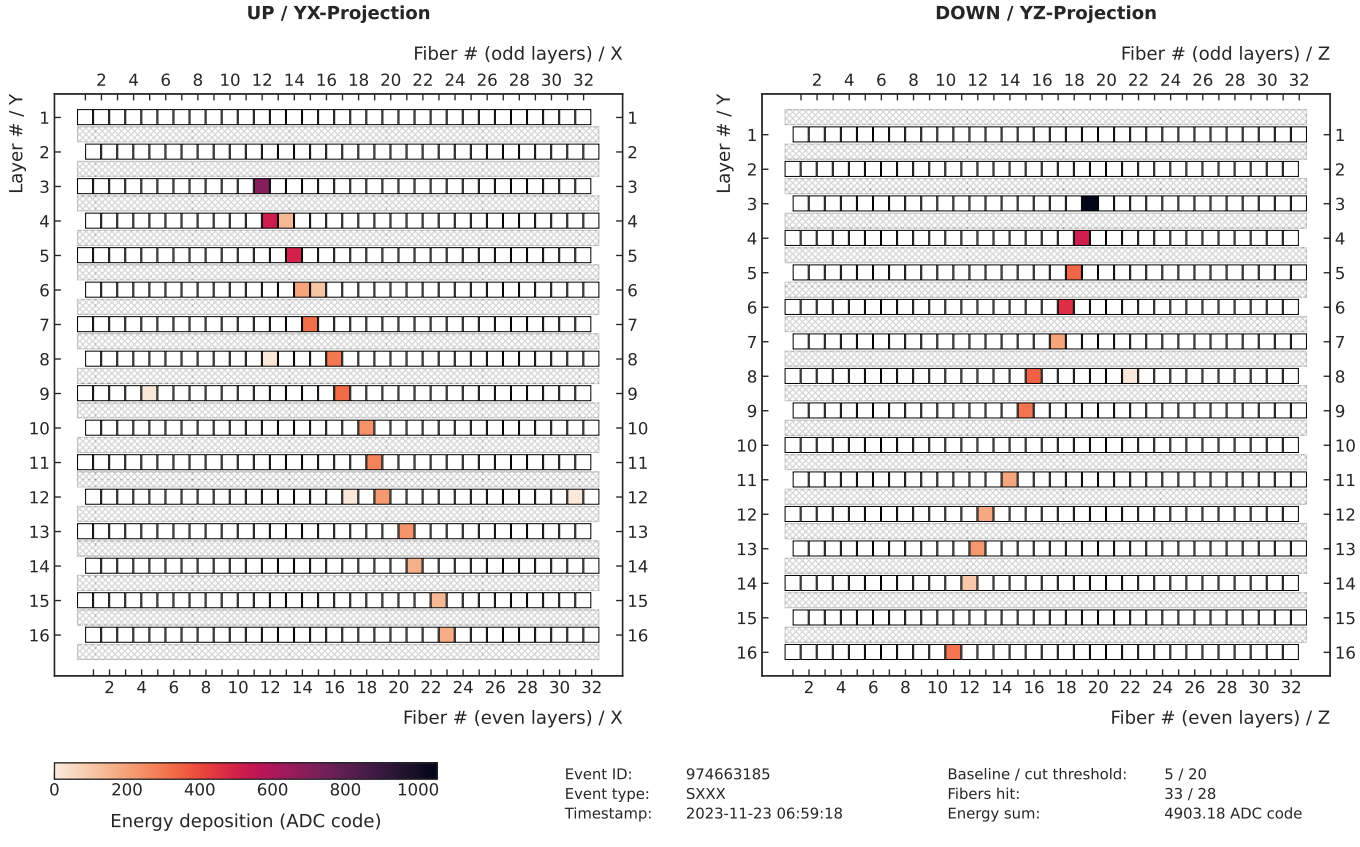

Figure 11.23: Event signature of a low-energy proton or nucleus entering the ADU from below and stopping in its active material. The particle traverse the detector almost along the central vertical axis, leading to a rather clean energy-loss profile because the position-dependent light yield is nearly the same for all fibers.

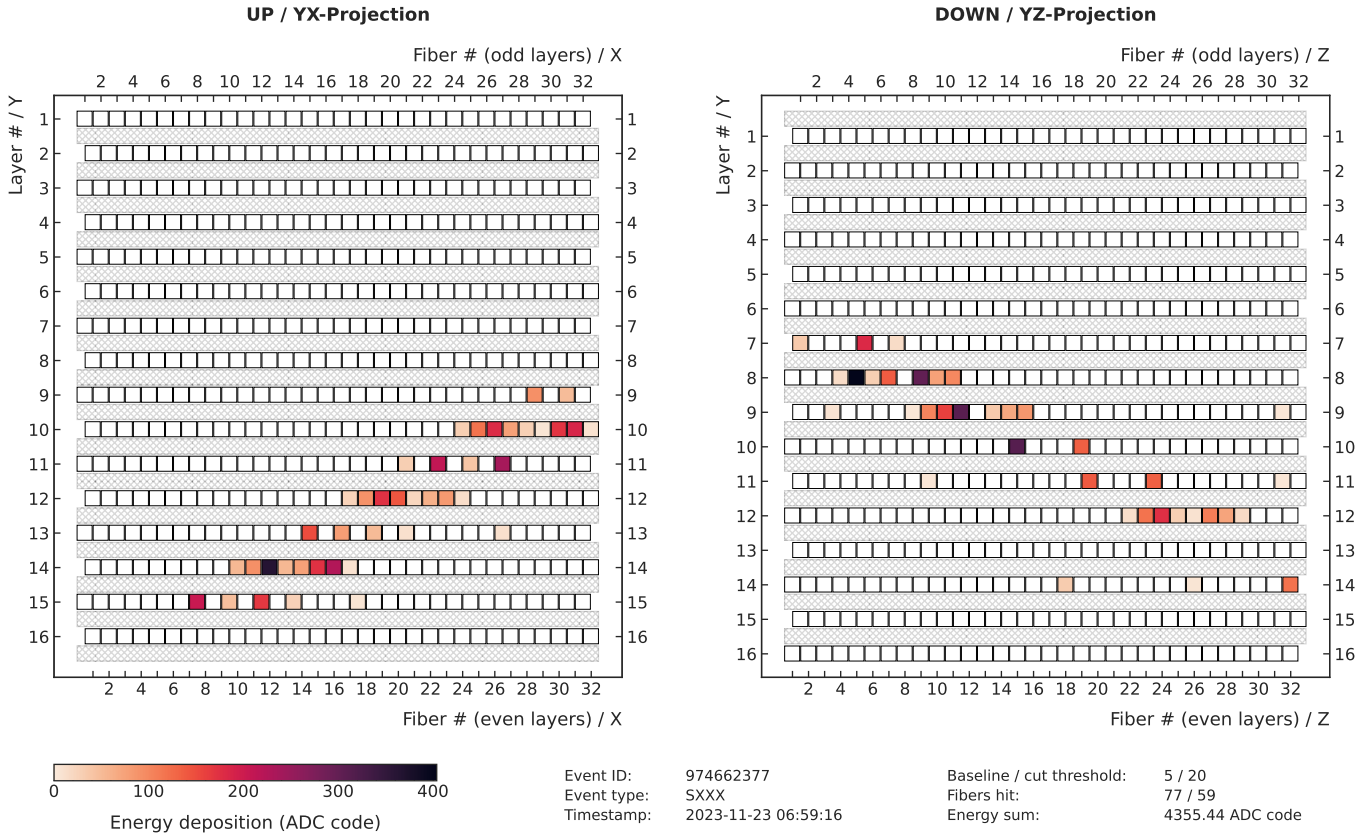

Figure 11.24: Event signature of a broad energy-deposition channel, possibly stemming from a Lorentz-boosted jet of secondary particles created by the interaction of a high-energy cosmic ray with the instrument's shielding.

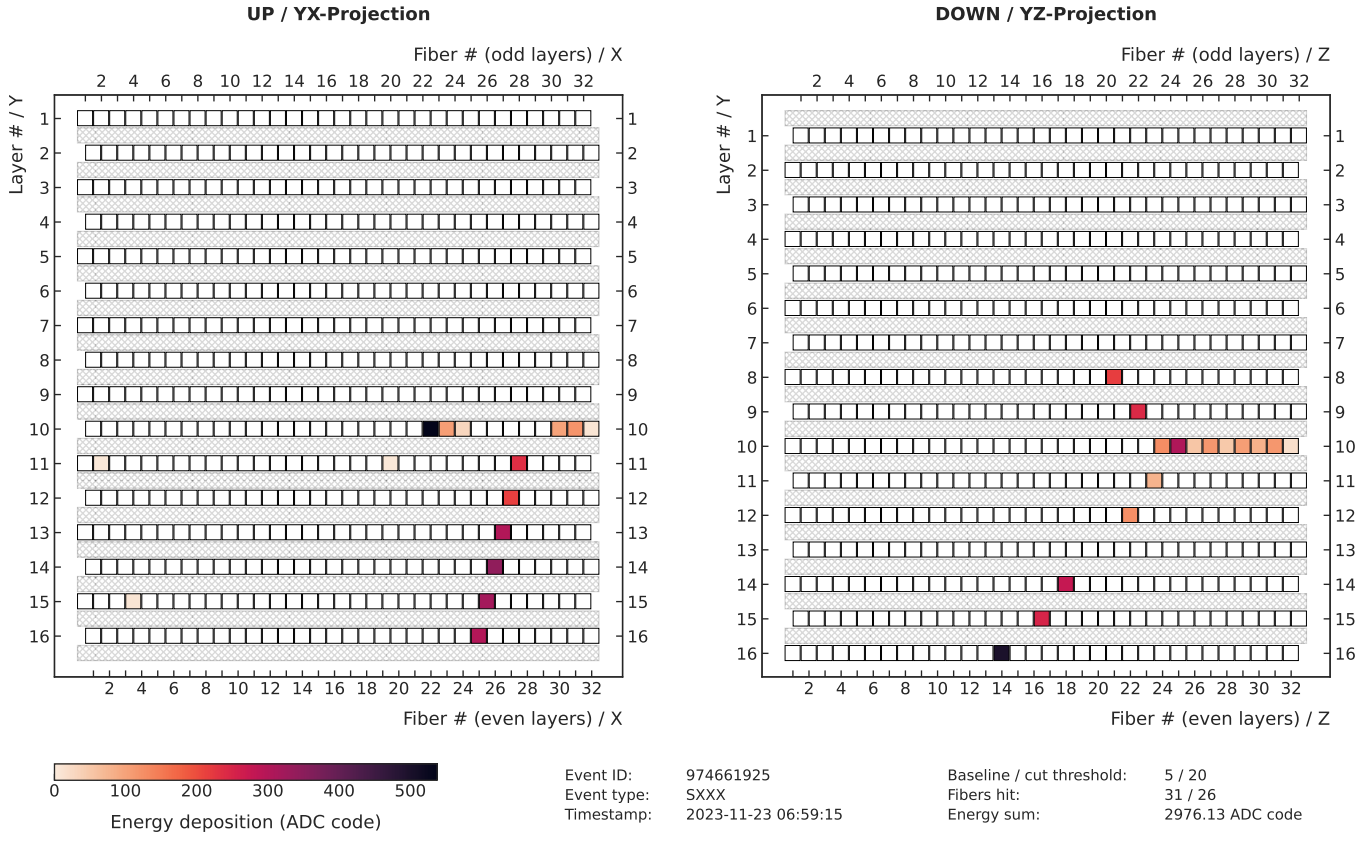

Figure 11.25: Example of a (low-energy) particle that enters the detector (from the right in the yz-projection) and appears to interact with the detector material. A short-ranged secondary particle stops after traversing only a few fibers. Another secondary particle exhibits an energy-loss profile that resembles a Bragg curve, though it is not apparent whether it stops in the detector or not.

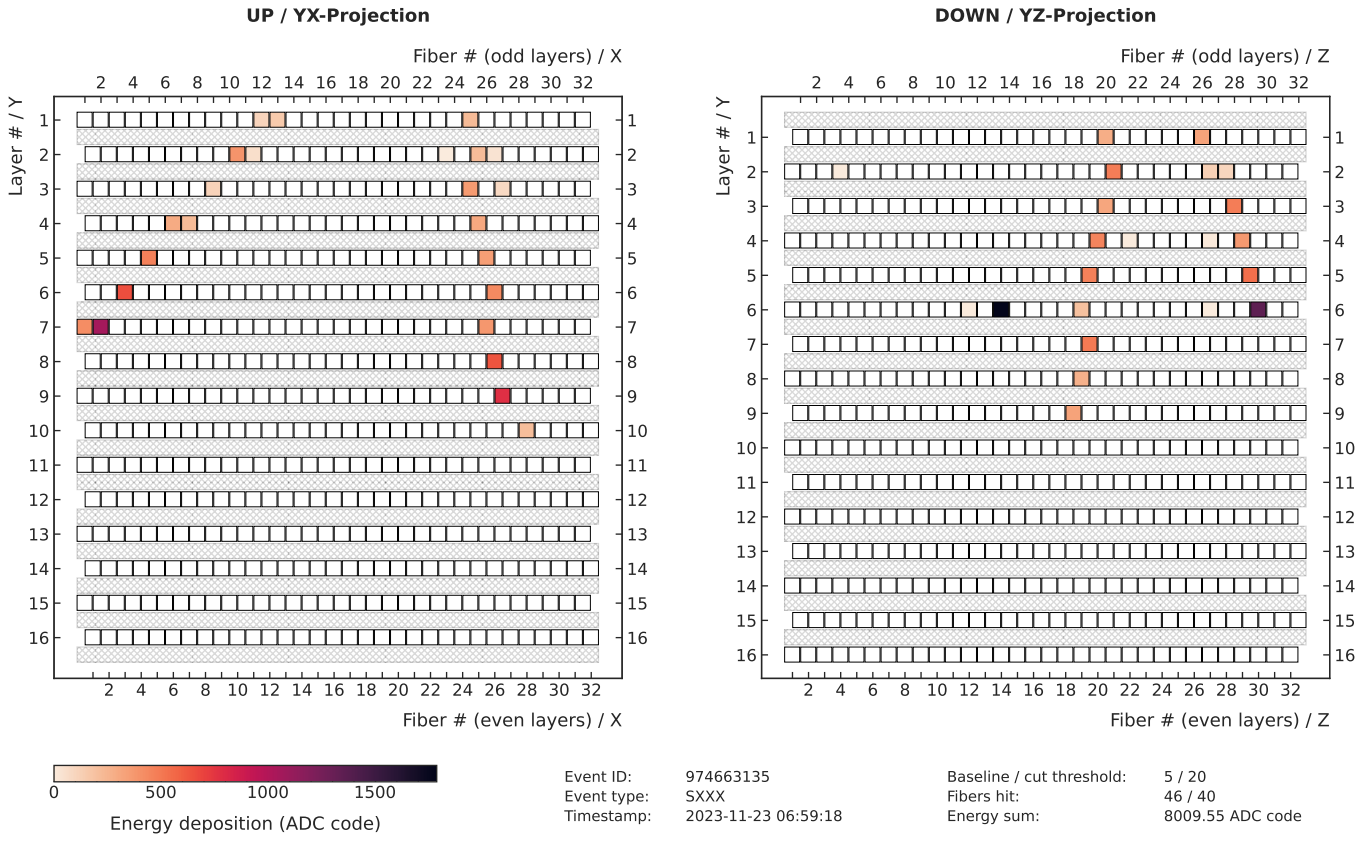

Figure 11.26: Example of an event with two particles entering the detector at the same time (i.e., within the 10-ns trigger window of the data-acquisition electronics). The isolated hit may be from another charged particle traveling along the fiber, or from an uncharged particle (neutron).

window of the data-acquisition electronics). One particle appears to stop in the detector, exhibiting an energy-loss profile resembling a Bragg curve. The yx-projection suggests that the other particle exits the detector. Interestingly, the event also shows an isolated hit with large amplitude in the yz-projection. It is unclear whether this hit is created by a secondary emitted from one of the tracks, or stems from a third particle—either form a charged one traveling along the fiber or possibly from a neutron.

Count Rates

One of the biggest advantages of integrating the M-42 dosimeter into the RadMap Telescope is that we can use its data to gain insights into the performance of the ADU. Especially in light of the fact that many of the events we gathered do not show readily recognizable signatures (track-like or otherwise), determining whether we actually record particles interacting with the detector, or simply trigger into the (electronic) noise of the read-out electronics, is of crucial importance. I therefore present here my initial comparison of data gathered by the two detector systems.

The quantity that can be most straightforwardly compared between detectors based on as different detection principles as the M-42 and the ADU is the count rate—i.e., the number of particles detected per unit of time. Even though it is vastly different for sensors with sensitive volumes of such substantially different size, we can use the geometric factor of each system to calculate the incident flux of particles. Assuming an isotropic flux of incident particles, and integrating over all particle energies, Eq. 4.7 tells us that we can determine the particle flux, I_0, via

$$I_0^{\mathrm{M42}} = \frac{C_{\mathrm{M42}}}{G_{\mathrm{F}}^{\mathrm{M42}}} \tag{11.1}$$

$$I_0^{\mathrm{ADU}} = \frac{C_{\mathrm{ADU}}}{G_{\mathrm{F}}^{\mathrm{ADU}}} \tag{11.2}$$

Here, C_{M42} and C_{ADU} are the measured count rates, and $G_{\mathrm{F}}^{\mathrm{M42}}$ and $G_{\mathrm{F}}^{\mathrm{ADU}}$ the geometric factors of the M-42 dosimeter and the ADU, respectively. Assuming that, to first order, the two detectors have about the same sensitivity, we expect that $I_0^{\mathrm{M42}} \sim I_0^{\mathrm{ADU}}$. Though this assumption is probably somewhat simplistic and thus not entirely accurate, it is certainly good enough for assessing whether we measure particles or noise.

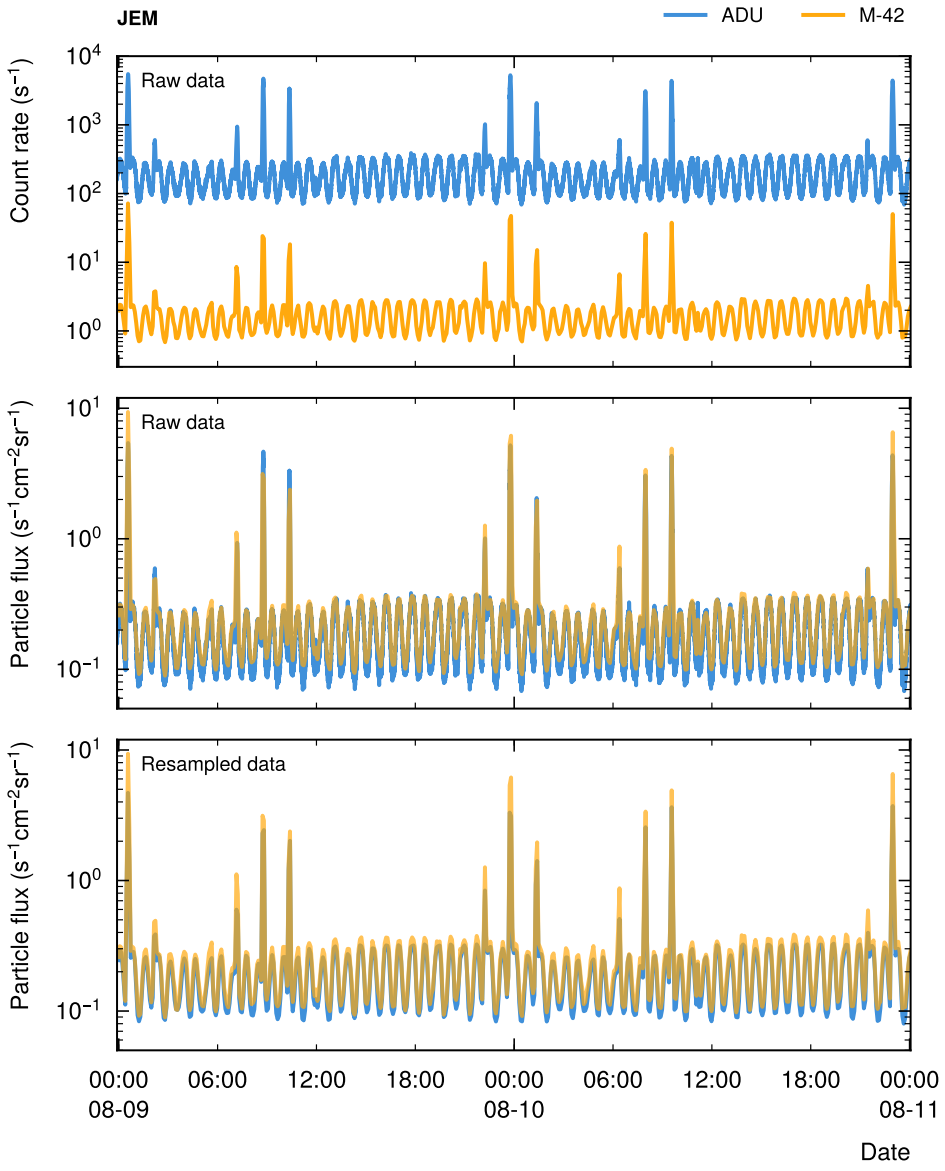

Figure 11.27: Comparison of the count rates and particle fluxes measured by the ADU and M-42 dosimeter in the JEM on 9 August 2023 and 10 August 2013. For the lower panel, the ADU data was resampled to match the five-minute integration windows of the M-42.

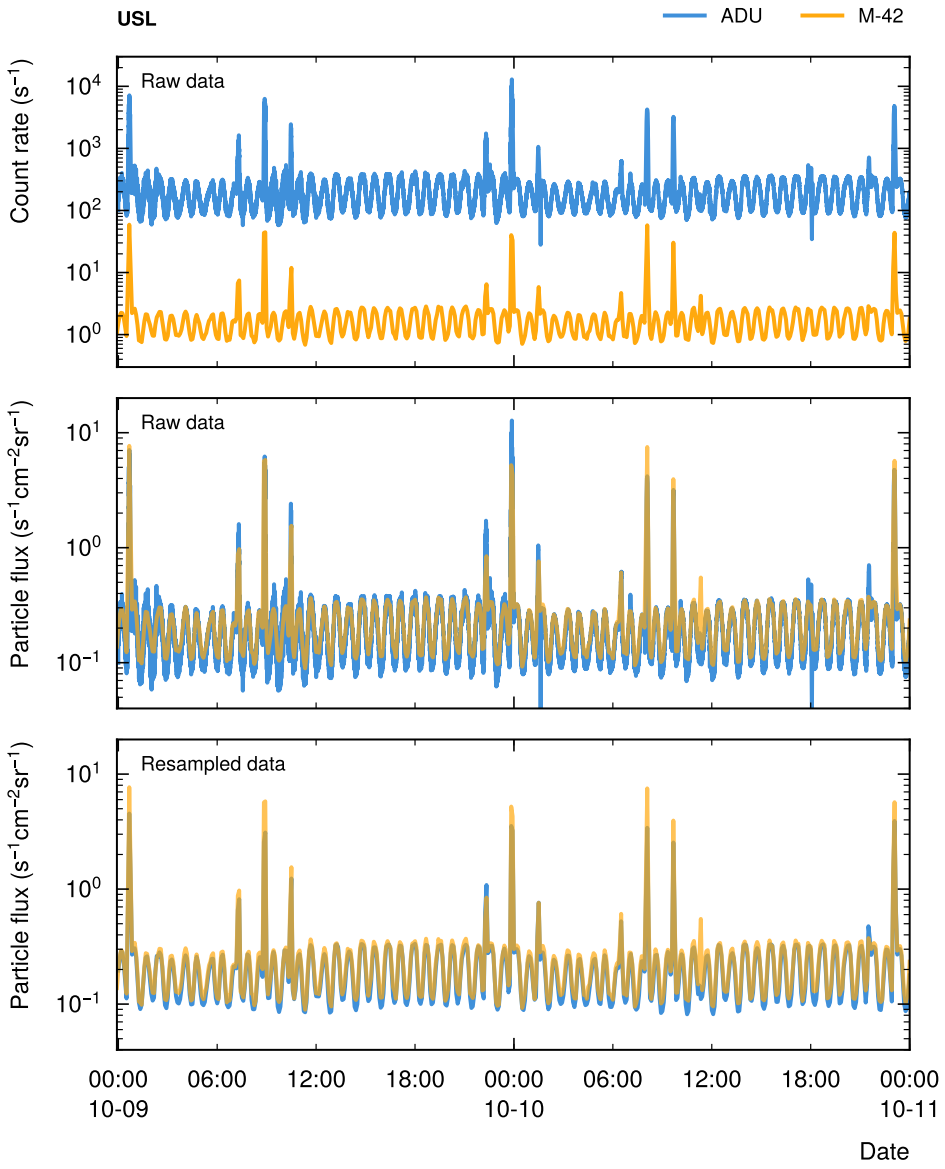

Figure 11.28: Comparison of the count rates and particle fluxes measured by the ADU and M-42 dosimeter in the USL on 9 October 2023 and 10 October 2013. For the lower panel, the ADU data was resampled to match the five-minute integration windows of the M-42.

A minor challenge is the different rate at which the two systems produce measurements of the count rates. The M-42 integrates particle hits over a period of five minutes and calculates the average count rate by simply dividing the cumulative number of events by the elapsed time. Usually, we take the middle of the integration window as absolute reference time for the measurement. The data-acquisition electronics of the ADU, on the other hand, have a much shorter integration window of only five sections, which is why its count rate typically shows much stronger fluctuations. At the same time, the shorter window and the higher count rate allow resolving time- and (orbit) position-dependent features much better. To be able to compare the data from the two detectors, I resampled the ADU's count rate to the integration window of the M-42. To do so, I added up the number of counts over a period of 2.5 minutes before and 2.5 minutes after each M-42 reference time and divided it by the window length, effectively replicating the dosimeter's internal calculation approach.

Figures 11.27 and 11.28 show this methodology applied to compare the count rates of the ADU to those of the M-42 for two two-day periods in the JEM and the USL in August and October 2023, respectively. The upper panels of the figures show the raw count rates of the detectors, presented in a logarithmic scale. Both exhibit the expected dependence on the orbit position: lower rates in the equatorial regions where the magnetospheric shielding is highest, and higher rates closer to the poles, where the shielding is weaker. The M-42's count rate varies between values of roughly $0.07\,\mathrm{s}^{-1}$ and $0.2\,\mathrm{s}^{-1}$, the ADU's between approximately $100\,\mathrm{s}^{-1}$ and $300\,\mathrm{s}^{-1}$. The data of both sensors also exhibits the characteristic increase of the count rates during passes of the SAA, which normally happen in bunches of three or four. During these, the ADU at times detects in excess of 6000 particles per second.

The middle panels of the two figures compare the particle fluxes calculated from the count rates of the two sensors. They are in remarkably good agreement, even without accounting for the much higher sampling rate of the ADU. The latter is apparent in the substantially larger fluctuations in the tracking calorimeter's data during the minima (in the equatorial region) and maxima (towards the poles). Finally, the lower panels show that a resampling of the ADU's count rates significantly improves the agreement between the data of the two sensors, and in particular reduces the discrepancies in the equatorial region and during passes of the SAA.

Figures 11.29 through 11.32 show a more detailed comparison of the measured particle fluxes for the same periods in August and October. In all

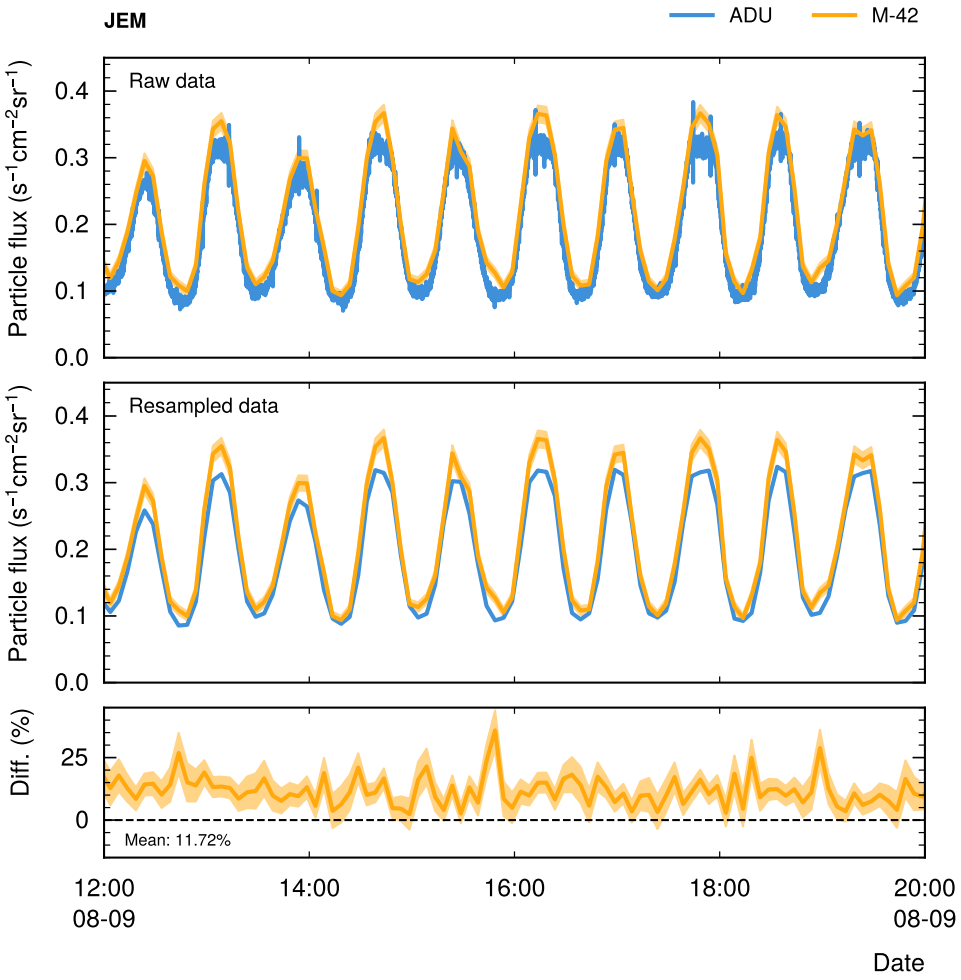

Figure 11.29: Detailed comparison of the GCR particle fluxes measured by the ADU and the M-42 dosimeter in the JEM for an eight-hour period on 9 August 2023. The upper panel shows the raw data, i.e., the fluxes calculated from the unaltered count rates. The middle panel shows the ADU data resampled to the integration windows of the M-42. The lower panel shows the difference between the two, normalized to the ADU data. The uncertainty band on the M-42 data is the square root of the count rate. Analysis of the ADU data is not yet advanced enough to determine errors on the count rate.

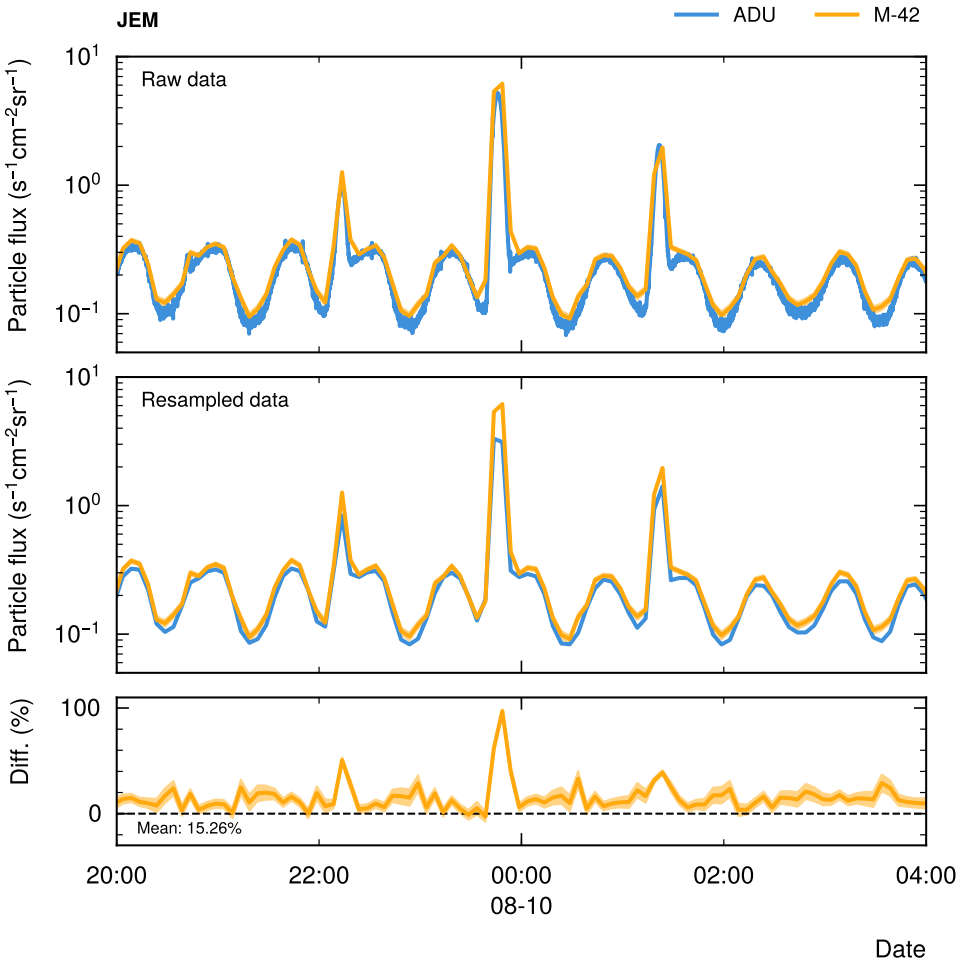

Figure 11.30: Detailed comparison of the GCR and radiation-belt particle fluxes measured by the ADU and the M-42 dosimeter in the JEM for an eight-hour period on 10 August 2023. The upper panel shows the raw data, i.e., the fluxes calculated from the unaltered count rates. The middle panel shows the ADU data resampled to the integration windows of the M-42. The lower panel shows the difference between the two, normalized to the ADU data. The uncertainty band on the M-42 data is the square root of the count rate. Analysis of the ADU data is not yet advanced enough to determine errors on the count rate.

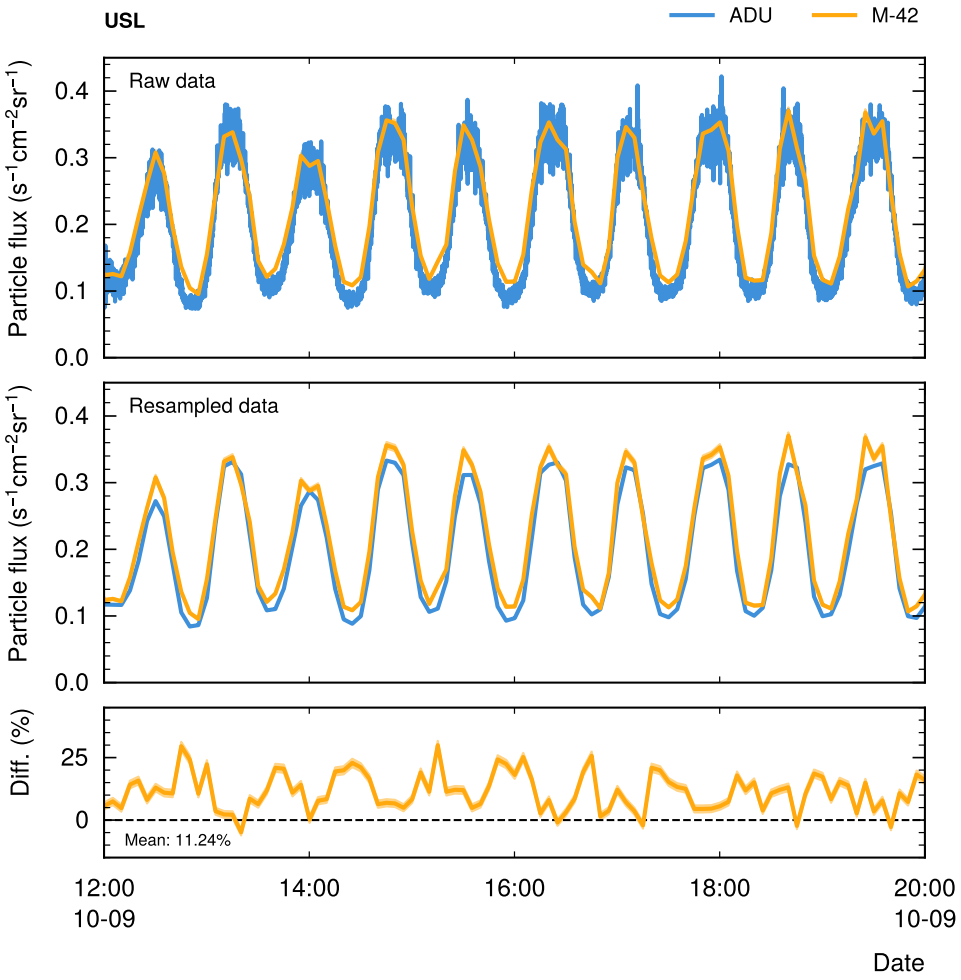

Figure 11.31: Detailed comparison of the GCR particle fluxes measured by the ADU and the M-42 dosimeter in the USL for an eight-hour period on 9 October 2023. The upper panel shows the raw data, i.e., the fluxes calculated from the unaltered count rates. The middle panel shows the ADU data resampled to the integration windows of the M-42. The lower panel shows the difference between the two, normalized to the ADU data. The uncertainty band on the M-42 data is the square root of the count rate. Analysis of the ADU data is not yet advanced enough to determine errors on the count rate.

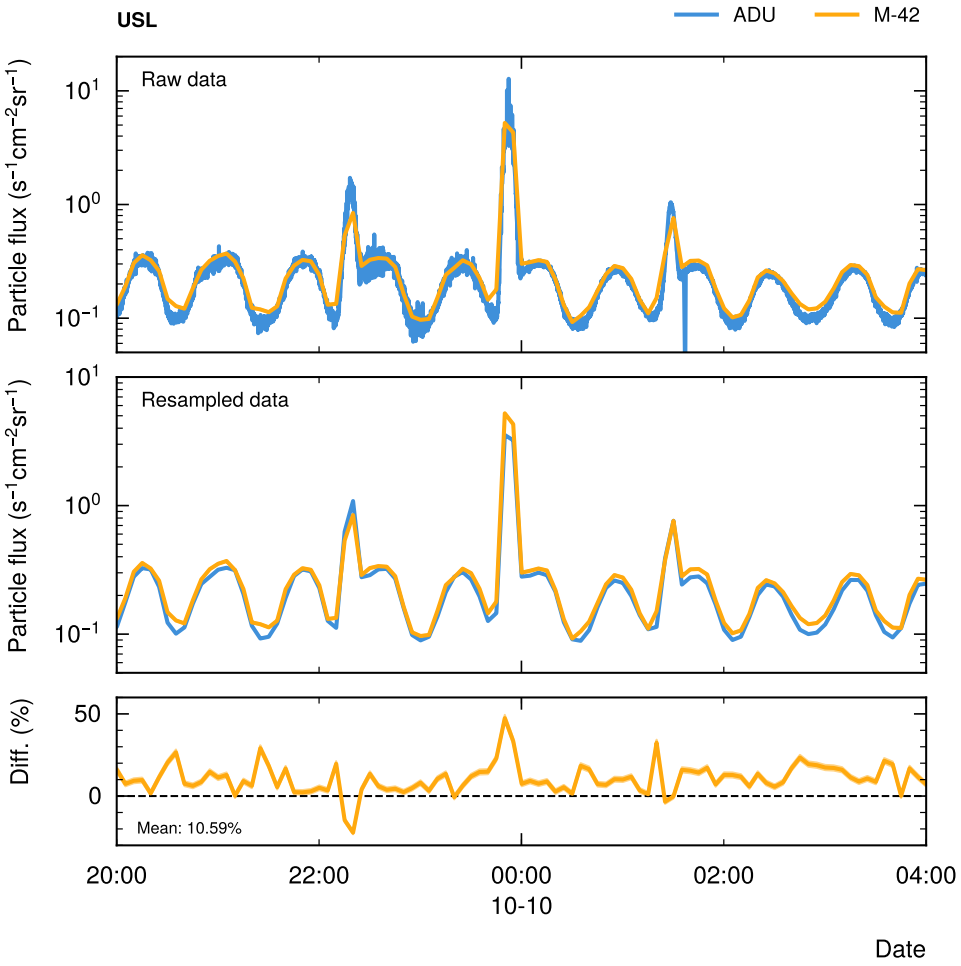

Figure 11.32: Detailed comparison of the GCR and radiation-belt particle fluxes measured by the ADU and the M-42 dosimeter in the USL for an eight-hour period on 10 October 2023. The upper panel shows the raw data, i.e., the fluxes calculated from the unaltered count rates. The middle panel shows the ADU data resampled to the integration windows of the M-42. The lower panel shows the difference between the two, normalized to the ADU data. The uncertainty band on the M-42 data is the square root of the count rate. Analysis of the ADU data is not yet advanced enough to determine errors on the count rate.

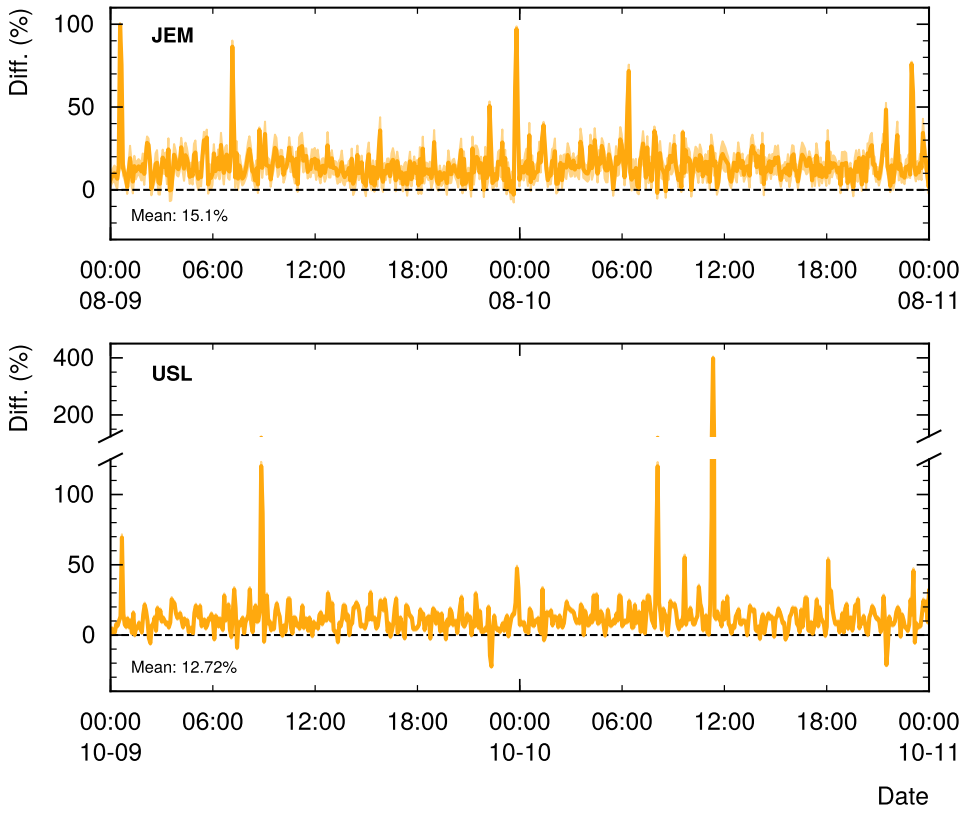

Figure 11.33: Difference between the resampled ADU flux values and the M-42 data for the full two-day periods covered in Figures 11.27 and 11.28.

four figures, the upper panel compares the fluxes as measured, and the middle panel compares the resampled ADU data to the unaltered M-42 measurements. The lower panel shows the difference of the two, normalized to the values of the ADU, as well as the mean difference over the eight-hour period. The uncertainty band on the M-42 data is the square root of the count rate.

The overall agreement between the measurements of the two sensors is remarkable, especially when considering that we chose operating parameters for the ADU's read-out electronics without previously having had the chance to extensively test and calibrate the system on the ground. Across the four periods covered in the figures, the mean difference is in the range of approximately 10% to 15%. The disagreement is strongest in the minima and maxima of the

time series, where the measurements of the M-42 tend to be a little higher. For some periods, however, the agreement is better than for others. To complete the picture, Figure 11.33 shows the overall difference for the full two-day periods covered in Figures 11.27 and 11.28. On average, the M-42 measurements are about 15.1% and 12.7% larger than the ADU's in the JEM and in the USL, respectively. During some, though not all, of the passes of the SAA, the difference approaches or exceeds a factor of two. Further investigation is required to try to understand whether these instances are indeed of a physical nature or an artifact of the resampling of ADU data.

The good agreement between the measurements of the two sensors and the fact that the ADU nearly always produces slightly lower values than the M-42 suggest that we have found good operating parameters for the tracking calorimeter. We can certainly exclude that a significant fraction of the events we record are purely noise—though we can not, conversely, argue that the chances of an event being triggered by noise are zero. Further investigation is required to understand the origin of the residual differences between the measured fluxes. One hypothesis revolves around the fact that the M-42 silicon sensor is much more sensitive to low-energy electrons and gamma rays created in interactions of cosmic and solar radiation with the space station's hull and structures. Since secondary production is higher when the incident primary particle flux is larger, this might explain the increased count rates towards the poles and during passes of the radiation belt. It is, however, unclear so far whether the increased sensitivity to small energy depositions could also cause the differences in the equatorial regions.

One interesting case, for example, is the excessively large discrepancy shortly before noon on October 10. The timing suggests that the increased count rate of the M-42 is likely to be caused by a peripheral passage of the SAA, but the data of the ADU shows that it barely registers any particle flux exceeding the equatorial GCR intensity. The question arises what could cause this vastly different response. Since the ADU is operating in a configuration where it triggers whenever a single channel crosses the noise threshold, it must be caused by particles that it is not (particularly) sensitive to. These could most likely be electrons or gamma rays. So, two possibilities are that there either was a significant flux of electrons trapped in the radiation belt, or that the energy of the typically encountered protons was so low that they were completely absorbed by the shielding of the station (and, possibly, the instrument), thereby producing secondary gamma rays that were registered by the M-42. Either way, a more detailed analysis over a longer period is required

to shed light onto such discrepancies.

Another hypothesis that might explain why the measured fluxes in the SAA sometimes agree better than at other times is connected to the assumption of an isotropic flux. This assumption is generally not true for particles trapped in Earth's magnetosphere, as they gyrate around and move along the field lines, thus creating a directional flux. However, if both detectors had the same omnidirectional sensitivity, the inaccurate assumption of an isotropic flux would not explain the different count rates. The calculated particle fluxes would be (slightly) wrong, but the relative difference between the values of the two detectors would be constant. Yet, even though the M-42 is technically sensitive to particles arriving from any direction, due to its planar geometry its acceptance is smaller for particles incident at small angles to the plane than for those impinging (nearly) perpendicular to it. When it is exposed to a directional particle flux, the count rate of the sensor thus depends on its orientation relative to the direction of the flux. If not properly accounted for, this effect might explain why the data of the M-42 and ADU in the SAA sometimes agrees better and sometimes not as well. A test of this hypothesis will be possible once we can reconstruct the orientation and arrival direction of tracks in our detector.

SAA–GCR Separation

For a detailed analysis of the radiation exposure due to GCR and radiation-belt particles, we need to be able to separate measurements taken inside and outside the SAA based on our own data alone. The method I developed for doing so relies on the count rates of the ADU and exploits two of its most apparent features. First, during passages of the SAA—except when the ISS only traverse its peripheral regions—the count rate rises about an order of magnitude above even the most extreme ones at high latitudes. Second, the change in the count rate is nowhere as strong as when the station enters or exits the anomaly. Exploiting these two facts allows to reliably detect whether recorded events are due to GCR or radiation-belt particles. Any such approach implicitly assumes that *all* events recorded while the ISS passes through the SAA are from geomegnetically trapped particles. This is, of course, not fully accurate, as GCR continue to impinge on the detector. Their flux is, however, so much lower that the (relative) error is insignificant, at least to first order.

Figure 11.34 exemplarily shows my method applied to the count rates recorded on 23 November 2023. The upper panel shows the recorded rate,

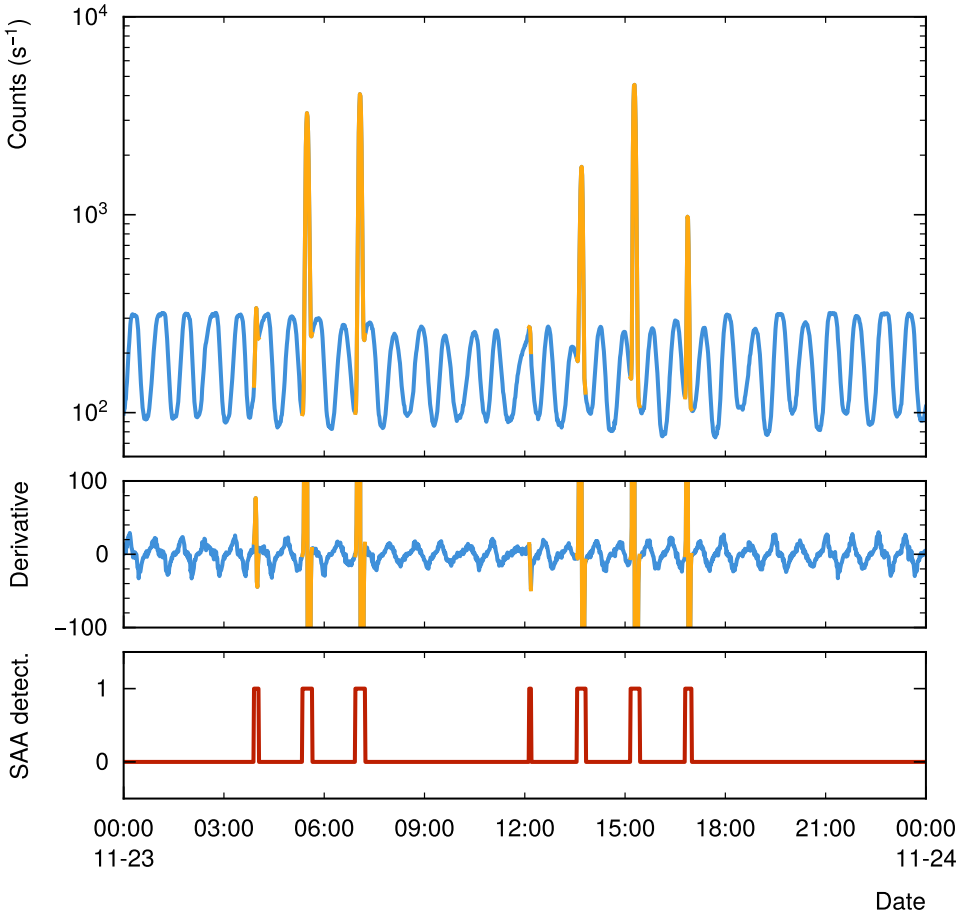

Figure 11.34: Example of the separation of counts induced by GCR and radiation-belt particles based on the count rate (top) and its derivative (middle). The periods the algorithm identifies as passages of the SAA (bottom) are marked in yellow in the upper two panels.

and the middle panel its first derivative. I apply thresholds to both quantities to first detect a potential SAA passage, and then apply a set of conditions and corrections to weed out false positives and to find the exact start and end points of the passage. The lower panel shows the periods my algorithm identifies as passages. The respective portions of the count rate and its derivative are drawn in yellow in the two upper panels. The example shows that my method

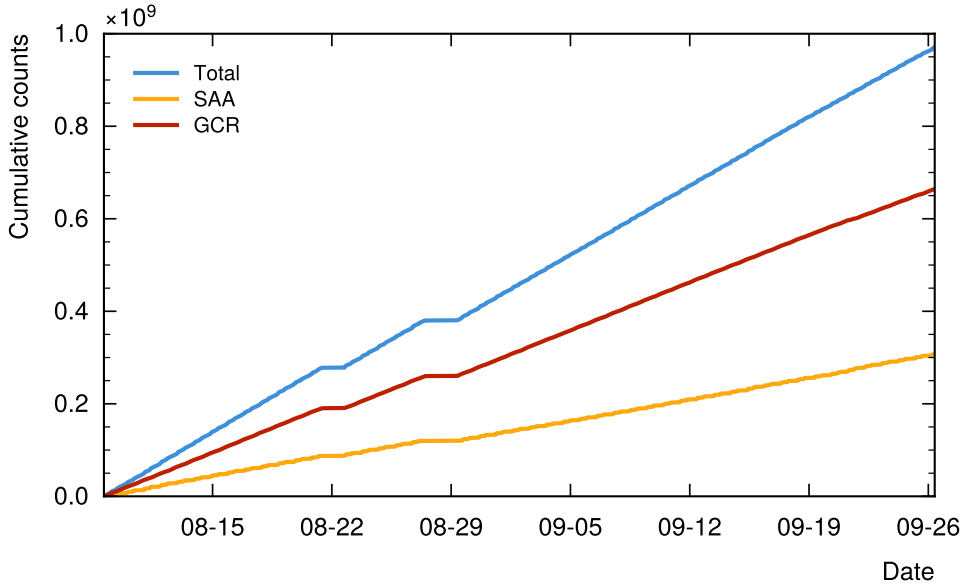

Figure 11.35: Cumulative counts recorded by the RadMap Telescope in the JEM between 8 August 2023 and 26 September 2023. Though data was recorded prior to 8 August 2023, a flaw in the FPGA firmware of the data-acquisition electronics led to scrambled events during passes of the SAA. Earlier data is thus not included.

can accurately detect the start and end times of each SAA passage in the period shown. If applied to all data we collected, it does so with only few exceptions. So, even though some fine-tuning may still be required, we can use the algorithm to separate events recorded inside the radiation belt from those induced by GCR.

Figure 11.35 and 11.36 show the cumulative counts (and hence events) we recorded while the RadMap Telescope was deployed in the JEM and in the USL, respectively. Using my SAA–GCR separation method, I also determined the cumulative counts of SAA and GCR events. In the JEM, we collected a total of about 0.96 billion events, of which 0.66 billion were due to GCR and 0.3 billion due to radiation-belt particles interacting with the detector, respectively. In the USL, we gathered roughly 1.8 billion events, with a little over 1.25 billion and 0.5 billion from GCR and from SAA passages, respectively.

Finally, Figure 11.37 compares the daily total counts of GCR and SAA particles, as well as their sum, recorded by the ADU and the M-42 in the

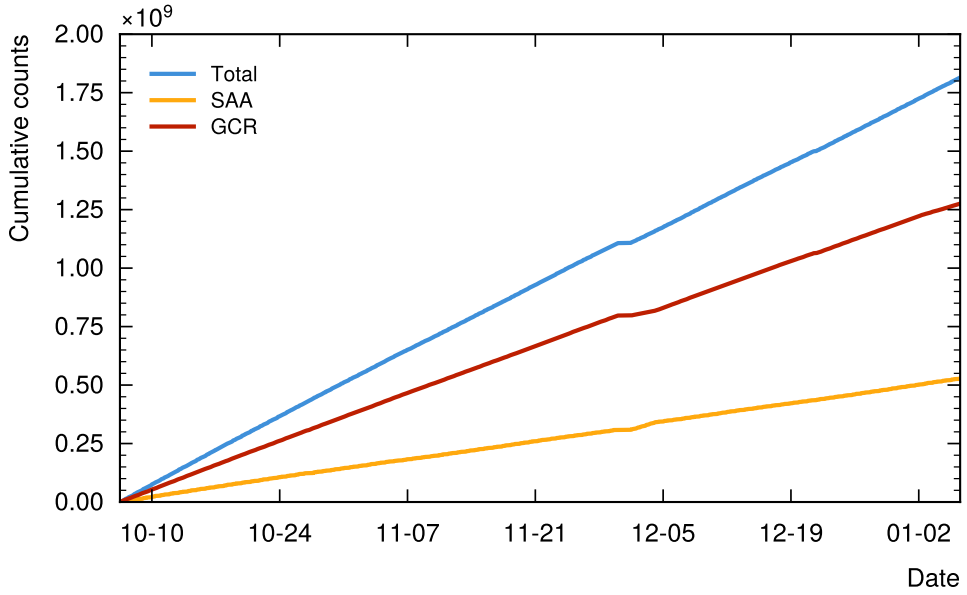

Figure 11.36: Cumulative counts recorded by the RadMap Telescope in the USL between 6 October 2023 and 6 January 2024.

JEM in August and September 2023. The graph shows that the overall count rate for both detectors is quite stable, with only some variance caused by periods of larger fluctuation in the SAA counts. These fluctuations are caused by the orbital-alignment effect explained in Section 11.3.2 above. They are somewhat more pronounced in the M-42 than in the ADU data. The reason for this discrepancy is not yet clear, though it could be connected to the silicon diode's higher sensitivity to secondary radiation (see discussion in the previous section). Overall, however, the comparison again confirms that our tracking calorimeter appears to operate mostly as expected.

Energy-Deposition Spectra

The separation of SAA from GCR events also allows us to assess the difference in the spectra of the total energy deposition of GCR and radiation-belt particles. Since we have not yet completed the calibration of the individual ADU channels—mostly because correcting for the position-dependent light yield requires tracking, which does not work fully automatically yet—I am using the

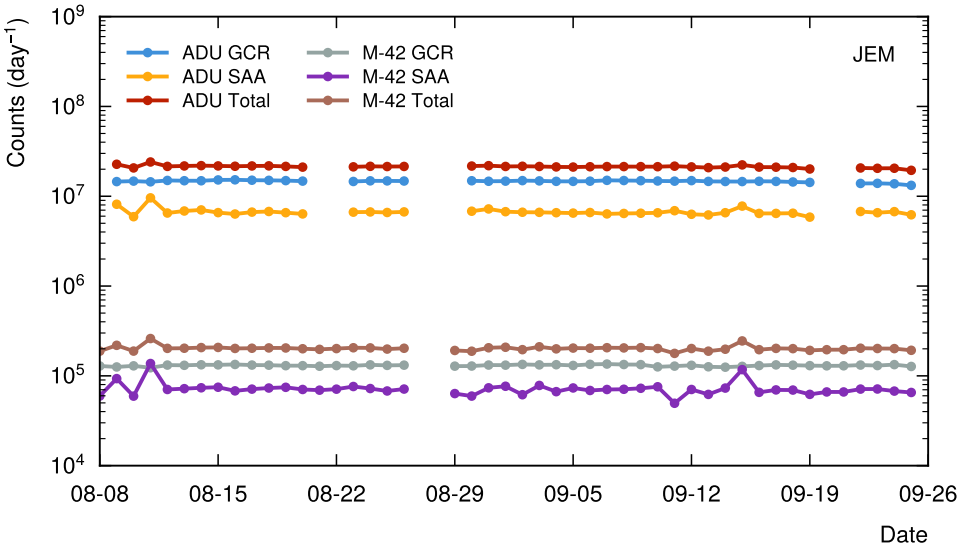

Figure 11.37: Daily GCR, SAA, and total counts of the ADU and the M-42 in the JEM in August and September 2023. The gap in the M-42 data stems from a two-day period during which network connectivity on the ISS was interrupted. The additional gaps in the ADU data are due to unstable operations of the detector that forced us to exclude the recorded events from analysis.

sum of their signal amplitudes (measured in ADC codes) as a measure of the (uncalibrated) total energy deposition. For convenience, I divide the sum by a factor of 1000 to obtain smaller values. Without an event-by-event calibration of the recorded energy depositions, the obtained spectra only approximate the true energy-loss spectrum. However, since the position-dependent hit probability is constant for each fiber because of the (nearly) isotropic incident flux, the uncertainties partially cancel out. Though the spectral shapes will certainly change somewhat once the energy deposition is properly calibrated, my preliminary analysis should nonetheless a first qualitative assessment.

Figure 11.38 shows the spectra of GCR and radiation-belt particles for 200 000 events each, collected in the USL on 23 November 2023. For GCR–SAA separation, I used the method described in the previous section; see Figure 11.34 for the respective count rates. The histograms show a large qualitative difference between the two spectra. The one of the cosmic-ray particles peaks at low energy depositions and falls off exponentially (with

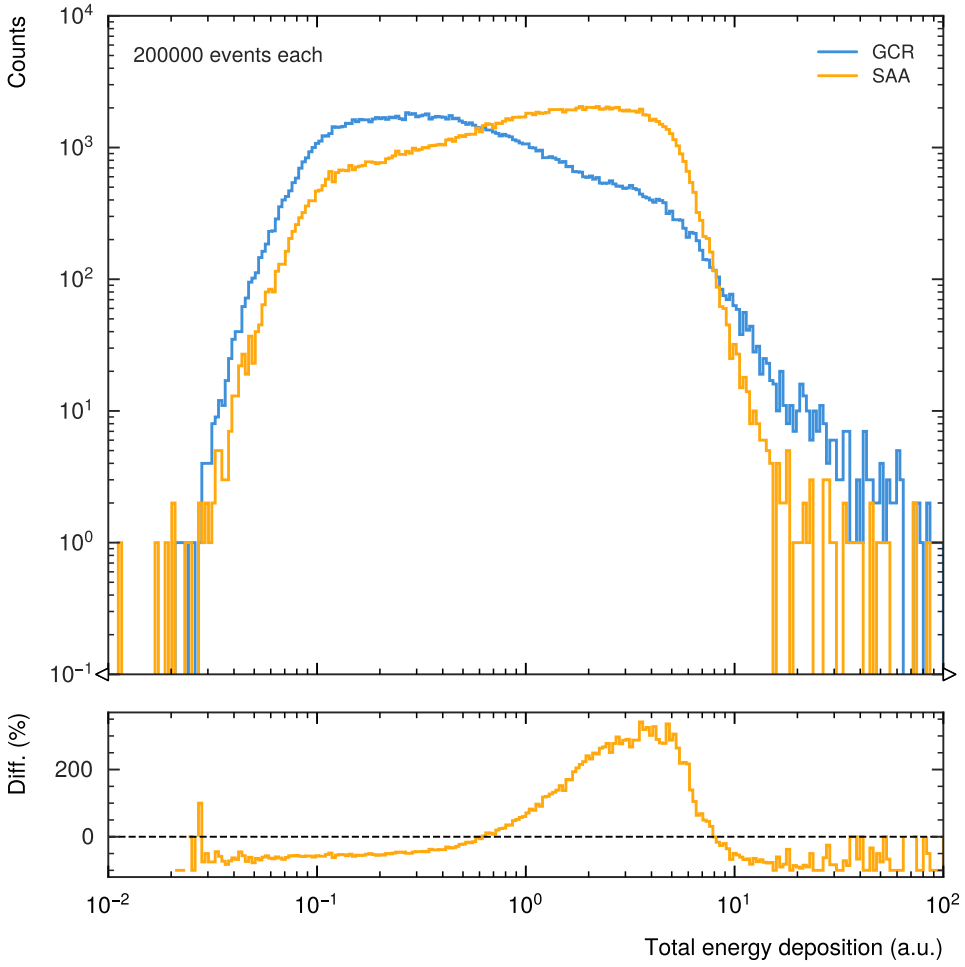

Figure 11.38: Spectra of the total energy deposition per event in the ADU for GCR and radiation-belt particles. In the absence of a full calibration of the detector, the energy deposition is calculated as the sum of the ADC codes of all channels, divided by 1000 to obtain smaller values. Each spectrum represents 200 000 events collected in the USL on 23 November 2023. The lower panel shows the difference of the two.

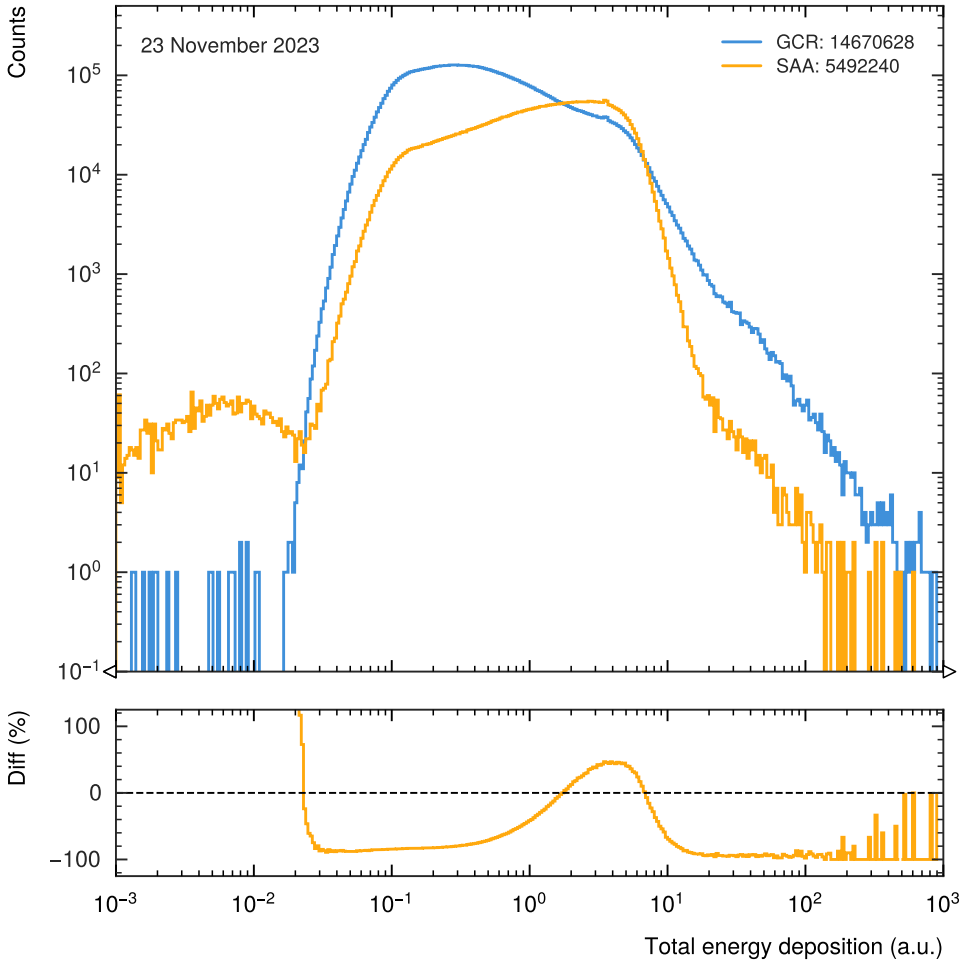

Figure 11.39: Spectra of the total energy deposition per event in the ADU for GCR and radiation-belt particles. In the absence of a full calibration of the detector, the energy deposition is calculated as the sum of the ADC codes of all channels, divided by 1000 to obtain smaller values. Each spectrum represents the total number of respective events collected in the USL on 23 November 2023. The number of entries per histogram is given in the legend. The lower panel shows the difference of the two.

varying slope) toward higher values. The spectrum of radiation-belt particles, on the other hand, peaks at much higher values (note the exponential energy axis) and falls of much sharper. The position of its peak approximately coincides with a noticeable bump in the GCR spectrum, but is about 300% higher (see the lower panel of the figure).

To arrive at a somewhat more conclusive assessment of the total energy deposited in the detector by the two different radiation fields, Figure 11.39 shows the spectra integrated over a full day (23 November 2023). Though their respective shapes are qualitatively similar to those in Figure 11.38, the total number of GCR events (shown in the legend) is more than a factor of 2.5 higher than that collected inside the SAA. This reduces the relative exceedance of radiation-belt particles at higher energy depositions to about 50%. The overall larger number of events also reveals a noticeable bump in the high-energy tail of both spectra, as well as a substantial number of entries in the low-energy tail of the SAA spectrum. Any theory about the origin of either can only be speculative without proper energy calibration (and particle identification). The nature of the latter is particularly intriguing, as they must be caused by particles that deposit less energy than a minimum-ionizing cosmic-ray proton (or any other particle with single charge).

In general, however, the spectral shapes are roughly consistent with those recorded by the M-42 dosimeter shown in Figure 11.8. The peak at lower energy-depositions for GCR is due to the prevalence of high-energy, almost-minimum-ionizing cosmic-ray protons. The relative suppression at higher energy deposition is caused by the suppression of the low-energy part of the GCR spectrum due to magnetospheric shielding. Conversely, the radiation-belt spectrum peaks at higher energy deposition because Earth's magnetic field can only trap particles with lower energies and higher stopping power (and hence larger energy deposition in the detector). The more pronounced structure of both spectra is likely due to the much larger active volume of the ADU, which results in a broader range of possible energy depositions. This is especially true for low-energy particles that can lose a much more significant fraction of their kinetic energy in the ADU's active material. The increased probability for nuclear fragmentation may, for example, cause the bump in the high-energy tail of both spectra. A more detailed interpretation will be possible once we can identify individual particles and perform a particle type-dependent analysis.

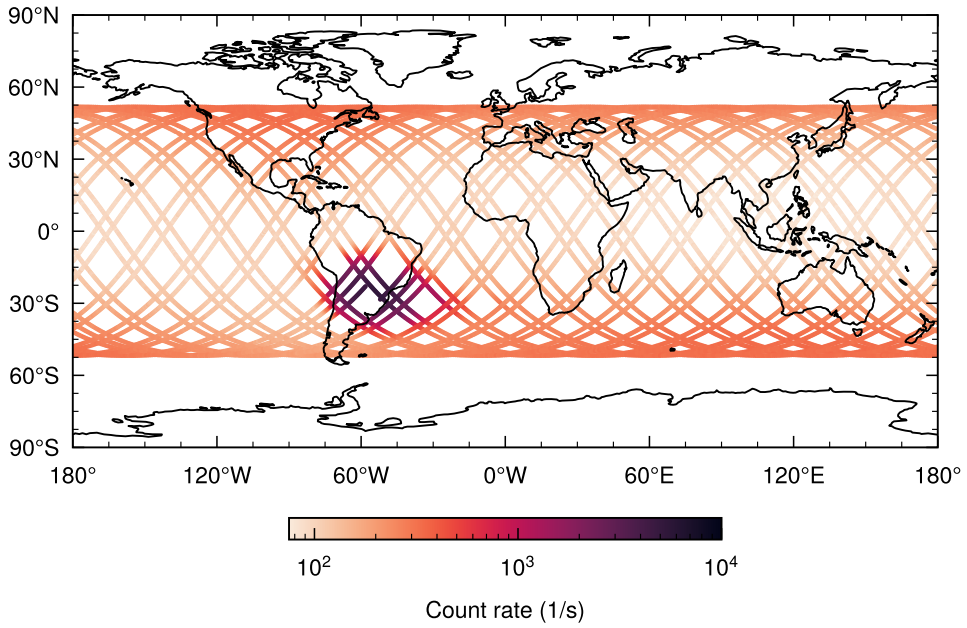

Figure 11.40: ADU count rates in the JEM along the ISS orbit on the first two days of September 2023. The eastward shift of the station's ground track due to the out-of-phase periods of its orbit and Earth's rotation is clearly visible. Note the logarithmic color scale.

Orbit Correlation

Lastly, I assess how the ADU's count rates correlates with the orbit position of the ISS. Such a check is largely qualitative in nature but allows to perform an excellent consistency check. I use the station's orbit parameters provided to the RadMap Telescope by the EAD telemetry to calculate its position every five seconds, that is, at the update frequency of RadMap's MRDL telemetry stream. Every telemetry packet also contains the number of events collected in the past five seconds, which allows me to directly correlate the two. Figure 11.40 shows these data points for the first two days of September 2023. The graph visualizes how the count rate changes along the path of ISS, with higher values at higher latitudes and inside the SAA. The eastward shift of the station's ground track (see discussion in Section 11.3.2) due to the out-of-phase periods of its orbit and Earth's rotation is clearly visible as well. Since the ISS orbits Earth at an inclination of 51.64°, our data does not cover the polar regions.

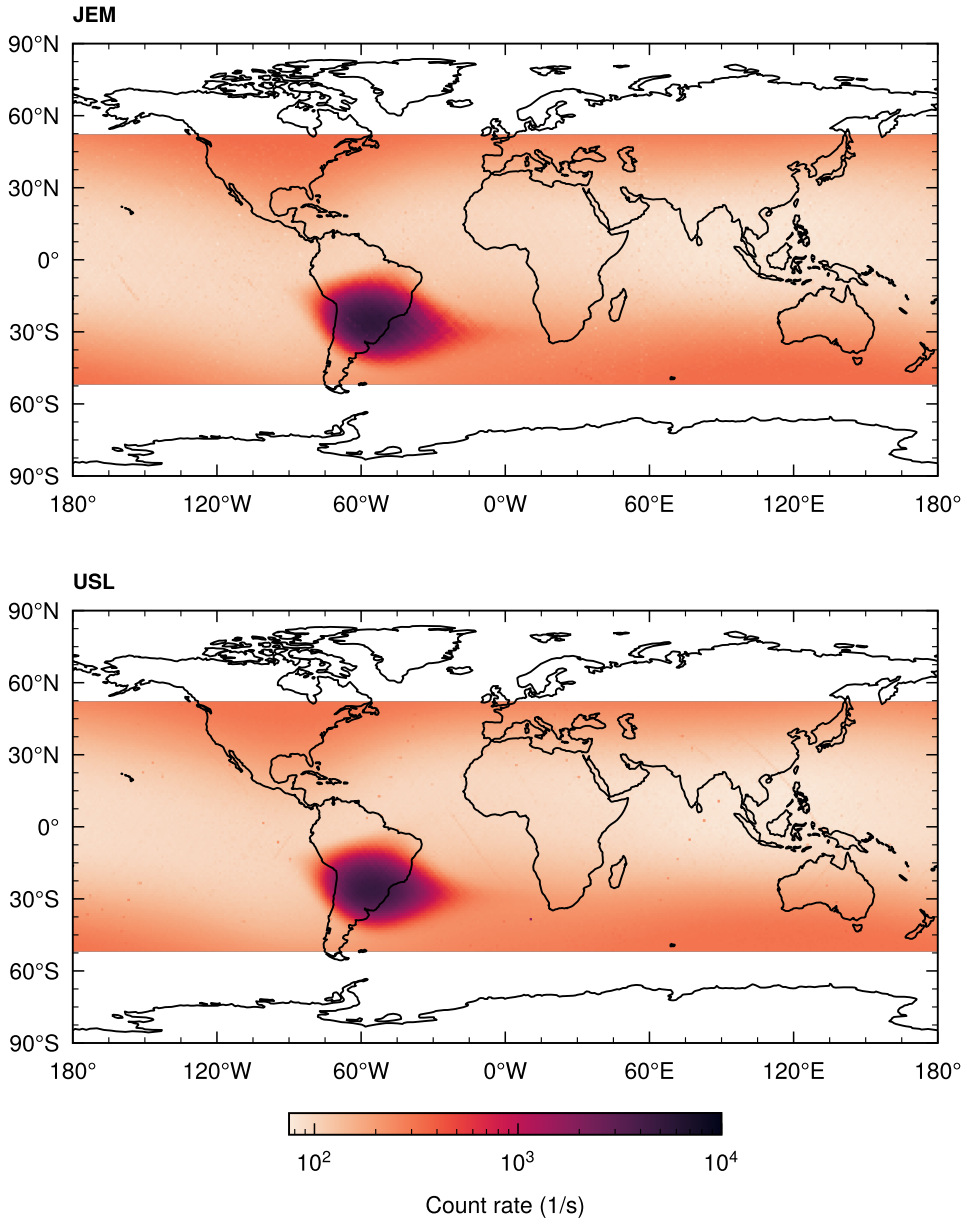

Figure 11.41: Correlation of the ADU's count rates in the JEM (top) and in the USL (bottom) with the orbit position of the ISS. The graphs show the average count rates in bins with a size of 1° in latitude and 1° in longitude.

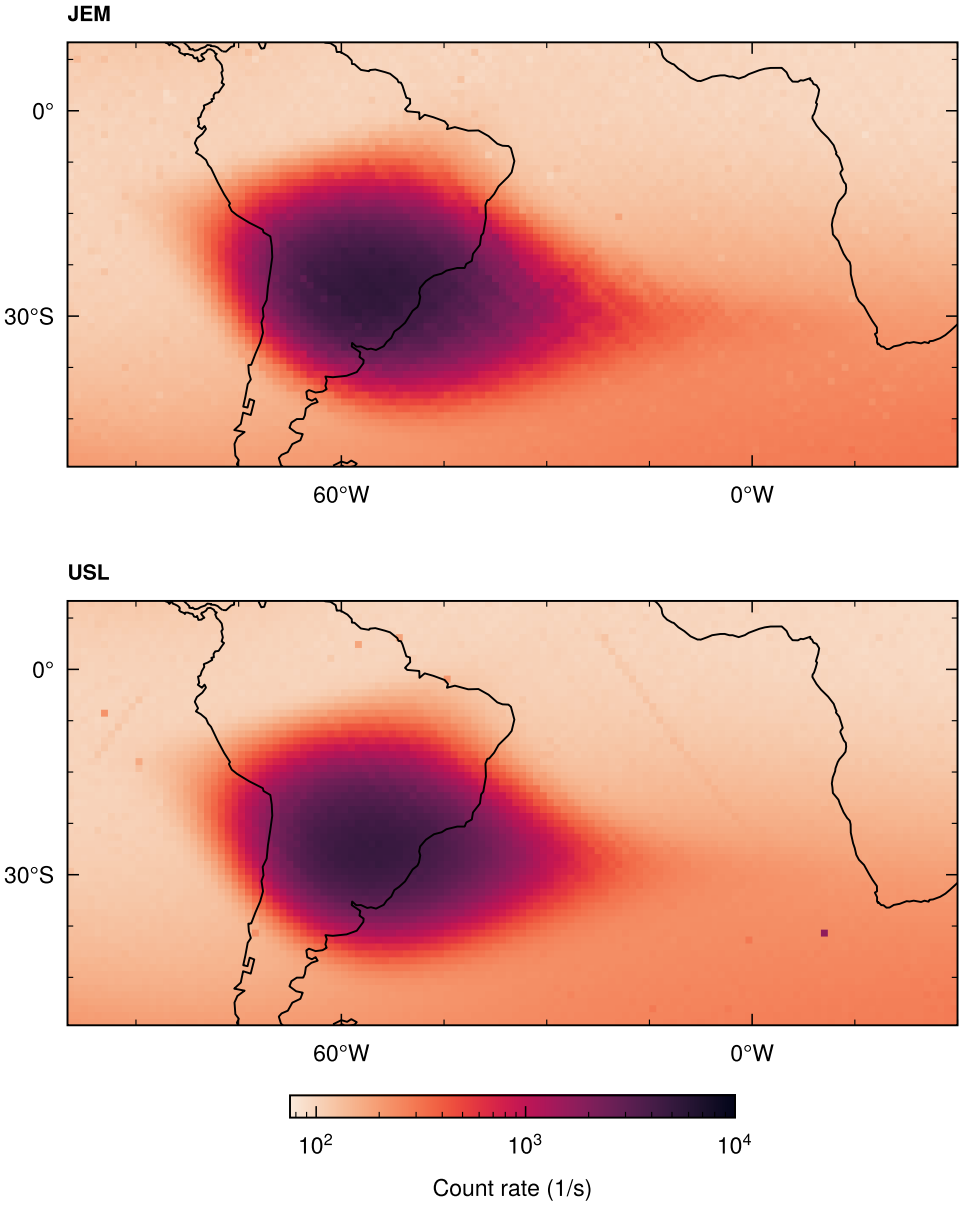

Figure 11.42: Detailed view of the ADU's count rate inside the SAA measured in the JEM (top) and in the USL (bottom). The graphs show the average count rates in bins with a size of 1° in latitude and 1° in longitude.

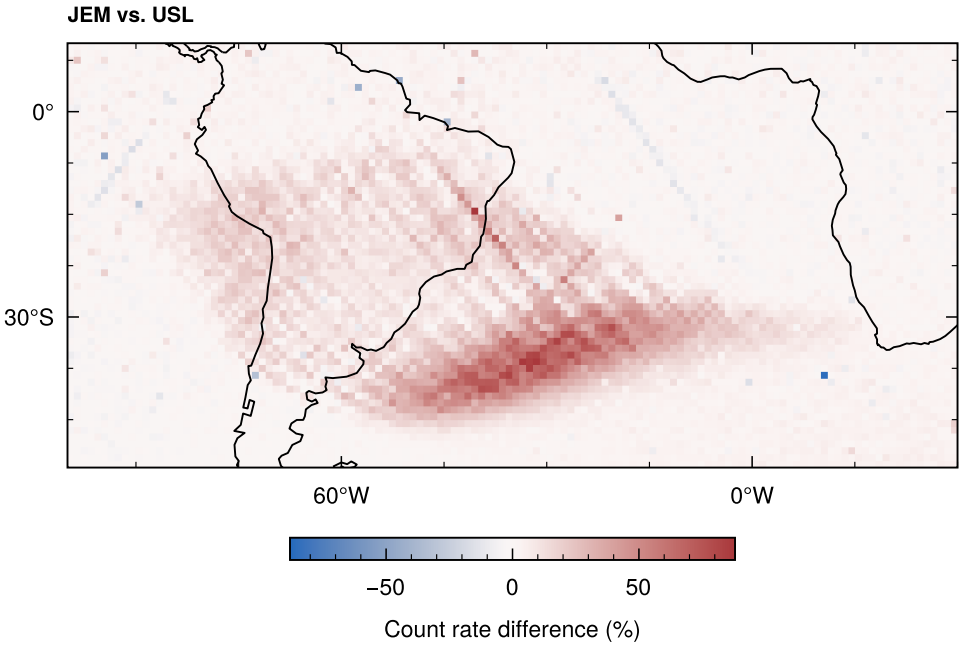

Figure 11.43: Relative difference of the ADU count rate inside the SAA measured in the JEM and in the USL, normalized to the latter.

For a whole-Earth coverage, I accumulated the data in two-dimensional histograms and calculated the average count rates in bins with a size of 1° in latitude and 1° in longitude. Figure 11.41 shows the respective histograms for all data we collected in the JEM and the USL (only some periods are missing because the EAD service did not work). The maps show the expected latitude and longitude dependence (compare, for example, to the data presented in [Ber+20] and [Sem+14]). Figure 11.42 shows detailed views of the count rates inside the SAA recorded in both modules, showing a barely noticeable difference in the anomaly's shape. For better visibility of the latter, Figure 11.43 shows the difference between the two histograms, normalized to the USL data. It reveals that the count rates in a large area of the southeast corner are consistently higher in the JEM, by as much as 70% to 80%. This is likely due to a weaker shielding of the module, strongly affecting radiation-belt particles (protons) that largely have much lower energies than GCR. Why exactly the difference is largest in the southeast region must still be investigated.

Concluding Remarks

Even though the analysis of ADU data I was able to include in my thesis is largely qualitative and only covers first steps, it shows that the tracking calorimeter is performing largely as expected. The consistency of its measurements with those of the M-42 dosimeter is remarkable, as is the fact that I performed no pre-selection of the data I show except for dropping invalid events due to restarts of the detector. For the orbit correlation, I also excluded those without position parameters. In some figures, for example in the detailed views of the count rates inside the SAA, small-scale inconsistencies show that an additional level of filtering can likely further improve the analyses I presented. Overall, however, the ADU's data requires surprisingly few adjustments.

More challenges will likely surface once we attempt particle identification and energy measurement. The significant optical crosstalk and the low light yield of some detector channels foretell as much. And, though not presented here, the track reconstruction has already required a little more effort than we anticipated. Yet, despite these (potential) challenges, the ADU promises to evolve into an excellent tool for the detailed characterization of the radiation environment inside spacecraft like the ISS. If nothing else, the sensor's high count rate and the clean total-energy deposition spectra, though uncalibrated so far, will open new pathways for detailed statistical investigations not possible based on the much sparser data of other instruments.

Chapter 12

Prospects and Outlook

Successfully operating the RadMap Telescope on the ISS has given us confidence that the detector concept of the ADU is worthwhile pursuing further. Though our analysis of on-orbit measurements is still in its early stages, the fact that we could match count rates between the ADU and the M-42 dosimeter without the need for corrections shows that detector can be operated close enough to its noise limit that it records the true intensity of the radiation field inside a spacecraft. The full demonstration of its particle-identification capabilities is still an open task. At the very least, though, we have already demonstrated that it can serve as a tissue-equivalent counter. In this chapter, I describe which lessons we learned that will help us improve future versions of the ADU, and Iriefly highlight a few aspects that we still need to study in more detail. I also compare its capabilities to those of other state-of-the-art instruments to highlight its potential use on future missions.

12.1 Lessons Learned and Future Improvements

Building and operating the RadMap Telescope's ADU has taught us many lessons and has revealed several areas that need improvement. Some are related to the integration of the instrument into the ISS infrastructure but most concern the design of the detector and its electronics. I here focus on those of the latter category which we expect to have a measurable impact on the performance of the detector. I do not discuss issues that only concern aspects very particular to the implementation of the RadMap Telescope and are likely not applicable to future instruments.

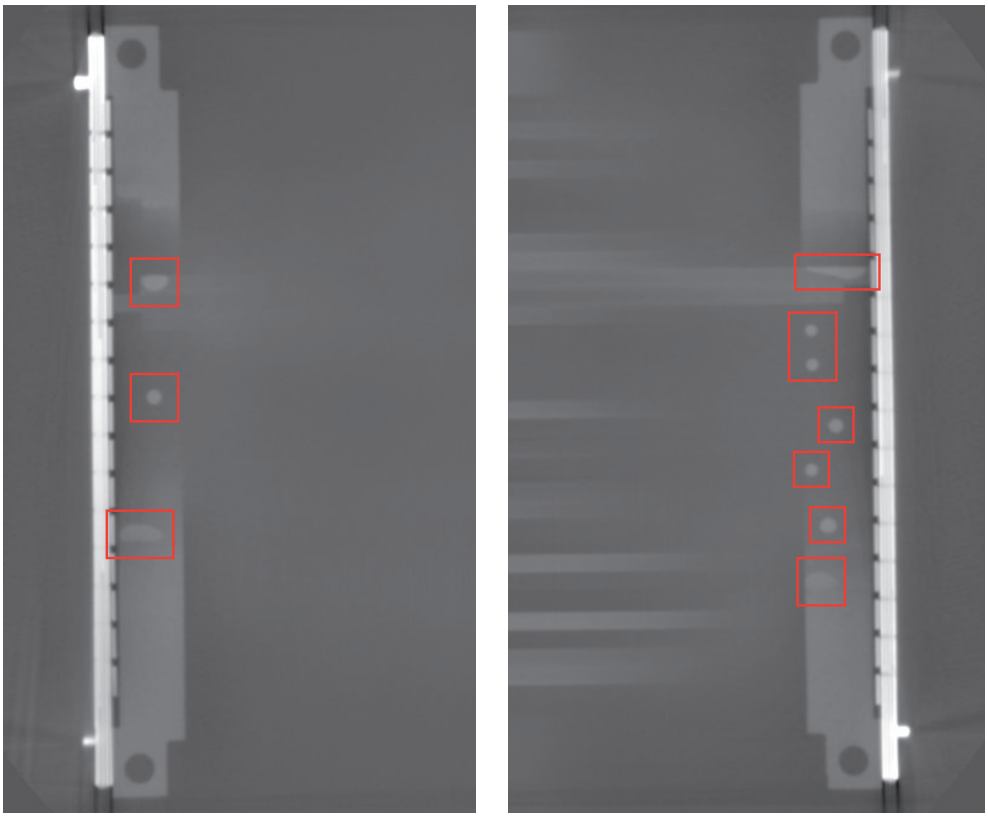

Figure 12.1: Slice of a three-dimensional X-ray image of one of the deformed ADU modules. Columns of optical epoxy formed and hardened in place during assembly, thus preventing the support structure form reverting to its original shape after heating. They are clearly visible (marked in red) below the uppermost layer of the support structure. The bright white structures all the way to the left and right are two of the SiPM arrays.

12.1.1 Mechanical Design

One of the most notable problems in the construction of the ADU was that we could not use some of our best detector modules for the flight instrument because they did not mechanically fit together. As pointed out in Section 10.3.1 above, this was due to the slight deformation of the support structure while the modules were heated to cure the optical epoxy we used for attaching the SiPM arrays. Due to the surface tension of the epoxy, columns of it formed

between the uppermost or lowermost (depending on the orientation of the module during heating) fiber layers and the deformed structure, which then cured in place. The hardened columns prevented the structure from reverting to its original shape. During assembly of the flight detector, we were afraid that pressing down too hard on the modules would likely break the SiPMs off their PCB, and not the columns. The deformed modules were thus practically useless for the RadMap Telescope (though we could use them for other experiments). Figure 12.1 shows a slice of a three-dimensional X-ray image of one of the modules, clearly showing the columns below the (somewhat visible) upper layer of the support structure.

Another issue related to the optical epoxy is that of its previously described tendency to creep into the tight spaces between neighboring fibers, thereby creating light guides that can cause optical crosstalk. With the current design, this could only be avoided if the amount of epoxy used on each SiPM was just enough to attach it to its fiber. At the same time, the glue's tendency to creep would need to be controlled to ensure that it stays where it is supposed to be. This, however, is nearly impossible, resulting in the need to use slightly more than needed. It is thus hardly possible to avoid the creation of such light guides. If you add to this the problems we had with flaking of the fibers' sputter-coated aluminum layer, optical crosstalk is nearly unavoidable.

The third challenge we faced was the residual curvature of the scintillating fibers, which in the future could be avoided by ordering them in straight pieces (an option that is offered by manufacturers). What we cannot avoid, however, is the variation in fiber thickness, which we found in parts to be larger than the 2% stated by Kuraray. Even if we assume that figure is correct, we need to design the slots in the support structure (see Section 8.1.1) assuming that all 32 fibers in a layer are 2% thicker than nominal. This is because the production varies over meters, not centimeters. If, however, the variations in a layer more or less cancel out, the slot is 2% too wide, resulting in quite significant placement uncertainties. Figure 12.2 shows the combined effect of the slot size and the residual curvature, which in some fiber layers led to substantial gaps between individual fibers. Other layers were quite densely packed, highlighting the effect of the thickness variation.

A more severe issue directly follows from the placement uncertainty, and is illustrated in Figure 12.3. Deviations from the nominal placement of the fibers inside their slot can result in non-ideal alignment with respect to their SiPMs. We had purposely chosen photosensors with an active area that is a millimeter larger than the fiber thickness, allowing deviations from the nominal fiber

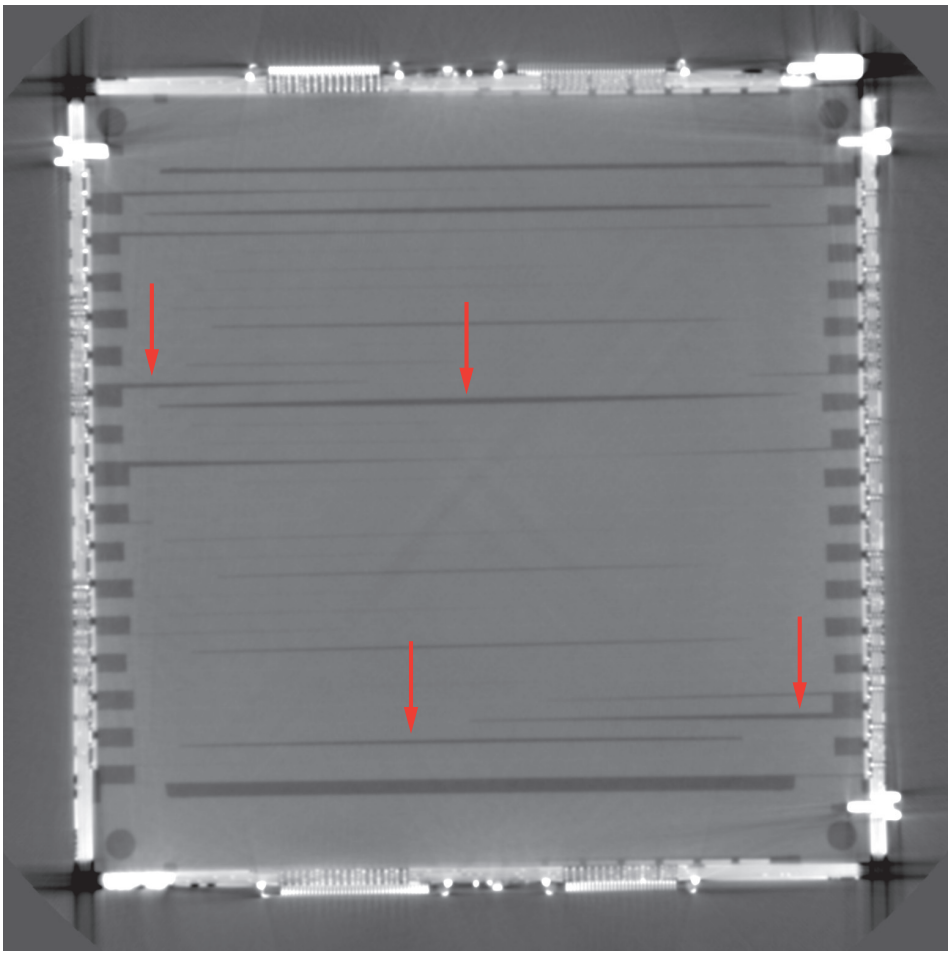

Figure 12.2: Slice of a three-dimensional X-ray image of a non-flight ADU module, showing substantial gaps between individual fibers. They are caused by the combination of thickness variations (necessitating a larger slot size, see text) and residual curvature. This is a particularly bad layer; many others are densely packed, with only small and few gaps. The image also highlights the differences in fiber length resulting from the polishing process.

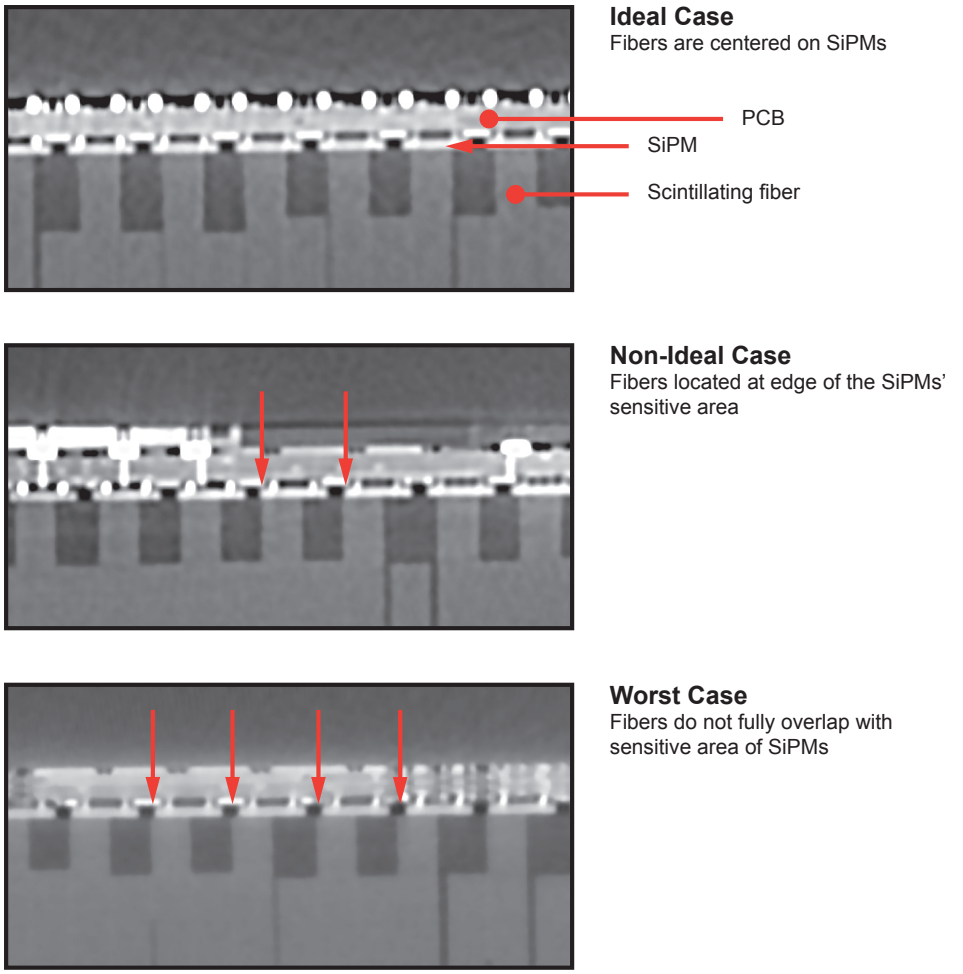

Figure 12.3: Examples of the variation of the fiber–SiPM we observed, caused by off-nominal fiber placement (see Figure 12.2). In the ideal case, the fibers are almost perfectly centered on their SiPMs. In the non-ideal case, the 0.5-mm margin to the left and to the right is completely used up. In the worst-case scenario, fibers do not fully overlap with the sensitive area of their photosensors. The latter we observed only in a few cases of extremely non-uniform fiber layers.

position of up to 0.5 mm to the left and to the right. The upper image of the figure shows the ideal case, in which fibers are almost perfectly centered on their SiPMs. However, in layers with large gaps, we also encountered cases like the one depicted in the center image, where fibers are located right at the edge of the sensors' active area. And in a few extreme cases, we even found that fibers did not fully overlap with their SiPMs, as shown in the bottom image. This is obviously a worst-case scenario, for two reasons: (1) The signal amplitude in these channels is significantly reduced and (2) there is a higher chance for substantial optical crosstalk because the fibers are positioned close to the neighboring photosensors. It is crucial that we avoid such variations in the fiber–SiPM alignment in future detectors.

Updated ADU Design

The combination of these challenges and issues led us to the conclusion that we needed to investigate different approaches of constructing ADU modules. The primary advantage of the design used for the RadMap Telescope is that it results in a densely packed stack of fibers with only little insensitive volume. Whatever of the latter there was would be filled either with air or vacuum. Particles traversing the detector thus deposit almost all of their energy in active scintillator material, allowing us to record their total deposited energy with little uncertainty. We could not, however, identify a clear path to an improved design that would allow us to address all issues we identified. Especially the aspect of coating fibers for crosstalk suppression is a thorny one that we had already invested a lot of time in, without a clear candidate technology that would result in better adhesion of the coating.

Abandoning the objective of maximizing the active volume opens a new design space, for example allowing to cast the fiber stack into opaque epoxy resin. Doing so comes with a drawback: Determining the total energy deposited by a particle in the detector requires correcting for the energy loss in the insensitive material. It does, however, also have several advantages:

1. It results in a mechanically very stable detector.
2. Using opaque (e.g., black) epoxy comes with inherent crosstalk suppression, such that the scintillating fibers do not need to be coated individually prior to assembly.
3. The placement of the fibers, and hence the fiber–SiPM alignment, can be controlled much better.

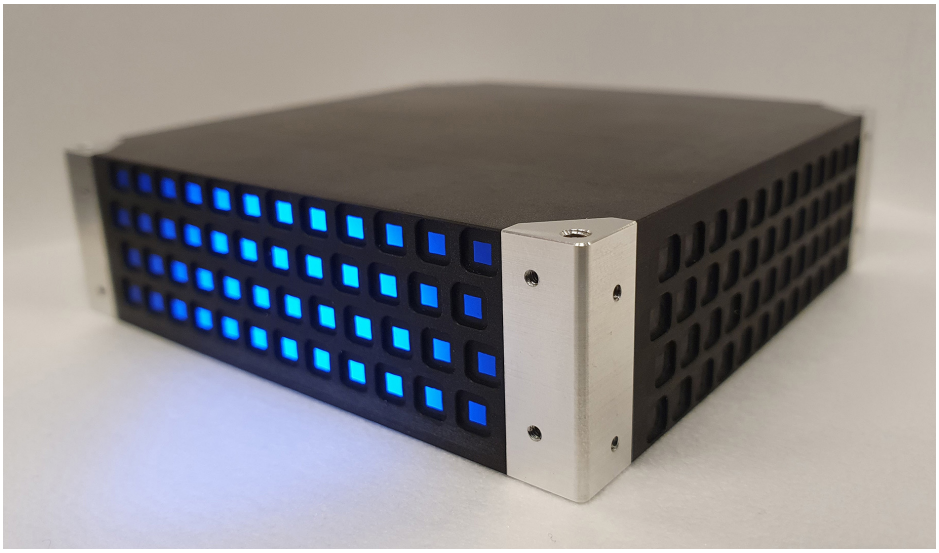

Figure 12.4: First prototype of an ADU module in which the fiber stack is cast into black epoxy resin. The principal design elements of the RadMap modules (SiPMs at alternating ends of neighboring fibers, alternating layer orientation) remain; the intra-layer fiber spacing is, however, larger to allow the resin to fill the voids. For illustration, the left side of the module is illuminated with a UV LED to stimulate the emission of scintillation light.

4. Other elements, for example aluminum pieces for mechanical attachment, can be included in the cast.

We hence attempted the construction of a first prototype module[1] cast into epoxy resin [Eck24]. The highly promising result is shown in Figure 12.4. For its production, we used a mold with cutouts for the individual fibers, which ensures that their ends are placed within less than 100 μm of their nominal position. To deal with the residual curvature of the fibers we still had available, we manufactured distance pieces from the same resin material that we inserted between them. We also incorporated aluminum pieces for mounting the SiPM arrays and for mounting the module. After casting, the mold and was removed with a computer numerical control (CNC) mill and the module machined into its final shape.

[1]This work was largely performed by Liesa Eckert for her Master's thesis, under my supervision.

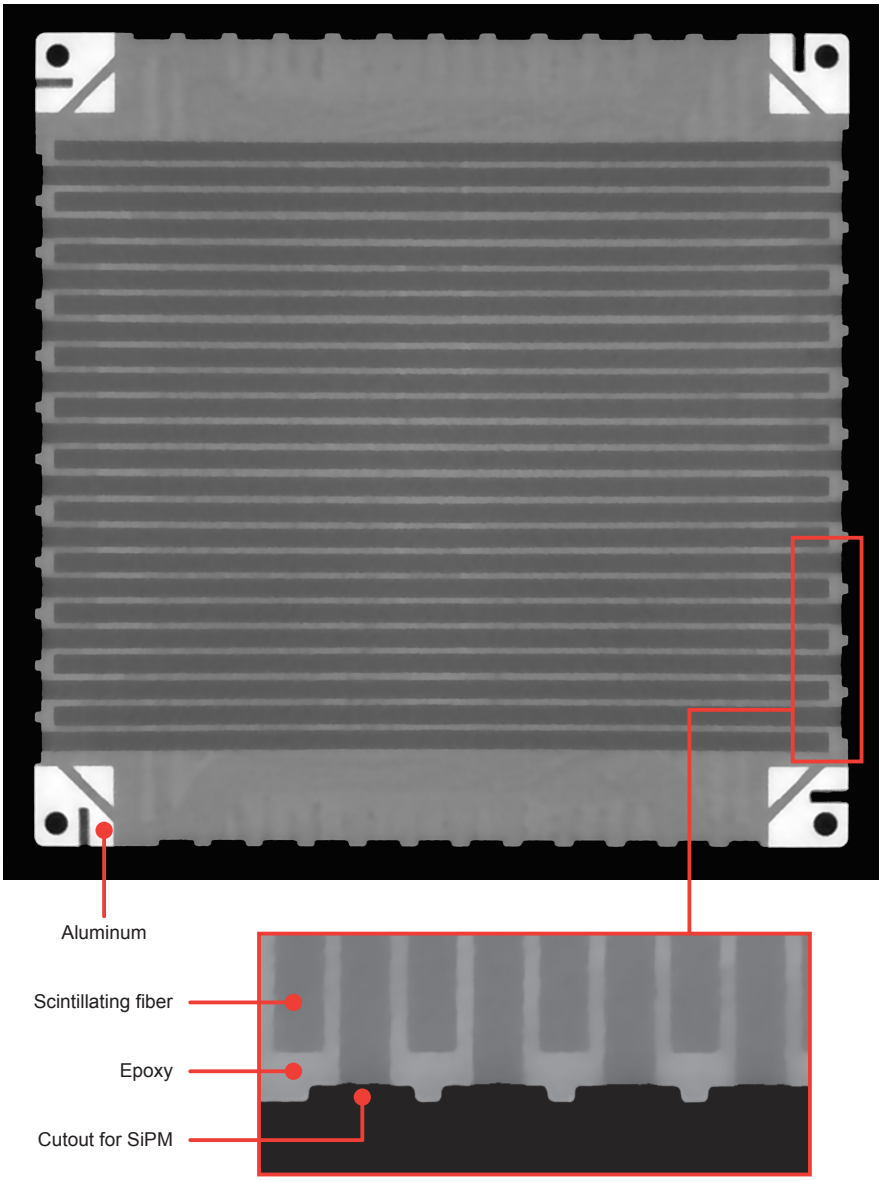

Figure 12.5: Slice of a three-dimensional X-ray of the prototype module shown in Figure 12.4. The image reveals the remarkably uniform distance between fibers. The zoomed-in portion shows how the end of each second fiber is recessed into the epoxy for crosstalk suppression, as well as the individual cutouts for the SiPMs.

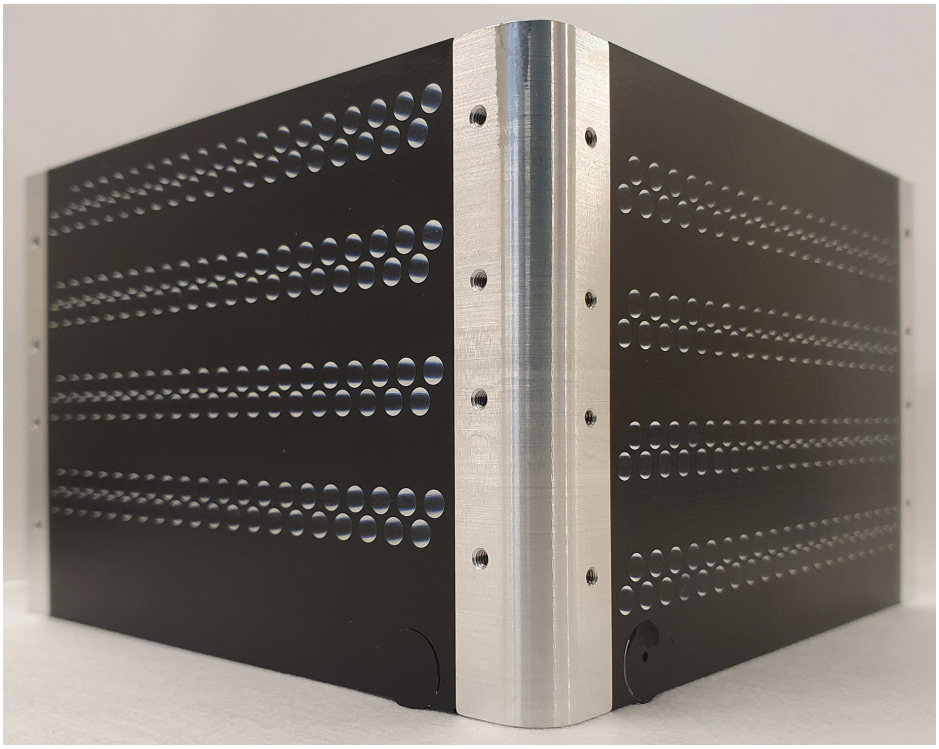

Figure 12.6: First prototype of a module made from round BCF-12 scintillating fibers with a diameter of 2.75 mm. The fiber are arranged in a double-layer design that increase the detection efficiency and resolution for particle traversing the detector at small angles to the vertical axis.

Figure 12.5 shows a slice of a three-dimensional X-ray image of the module. It reveals not only the remarkably uniform distance between adjacent fibers but also how we can achieve perfect crosstalk suppression. After the initial casting, the end of each second fiber is milled away a few millimeters deep into the module; the resulting hole is then filled with epoxy resin before the module is machined into its final shape. To suppress crosstalk between adjacent SiPMs, we also milled cutouts around the end of each fiber that are deep enough for enclosing all of the sensors' sensitive volume. In Figure 12.5, the cutouts are visible as ridges between fibers read out on the same side; the true geometry of the cutouts can be seen better in Figure 12.4. This approach has the added advantage that the fibers do not need to be polished before assembly, and that

their length is uniform to within 100 μm, which is not the case in the RadMap Telescope's modules (see Figure 12.2).

The casting approach also allows us to experiment with different geometries, for example using round fibers. Figure 12.6 exemplarily shows an early prototype of a module made from round BCF-12 fibers with a diameter of 2.75 mm. The need to try working with these was partially driven by the temporary closure of Kuraray's production facilities, which meant we could not get our hands on a new supply of fibers with a square profile. It allowed us, however, to investigate the possibility of using a double-layer design that increases the detection efficiency and resolution for particles traversing the detector at small angles to the vertical axis of Figure 12.6. Such a layout may be beneficial for the study for directional particle fluxes, for example in Earth's radiation belts, while still retaining the ability to track and identify particles impinging from random directions.

Overall, the approach of casting scintillating fibers into epoxy resin seems to be promising. It is, of course, not a completely new one, though we try to take the concept a step further to achieve full crosstalk suppression. We are also restricted to using low-outgassing materials certified by NASA if we want to be able to use our detectors on a broad range of missions. The range of available resins is this limited and not always ideal in their properties (e.g., viscosity). Though our first attempts have produced good prototypes, we still need to verify that they can deliver the performance we require. A first beam test is currently planned for late 2024.

12.1.2 Integration of Read-Out ASICs into SiPM Arrays

For the RadMap Telescope's ADU, we chose to use completely passive SiPM arrays and transmit the photosensors' signals to the read-out electronics via micro-coaxial cables. We did so for two primary reasons:

1. Decoupling the read-out electronics from the SiPM arrays as much as possible simplified the interfaces between the detector and the rest of the instrument. The production and calibration of the modules was time-consuming; the separation of the read-out electronics allowed us to continue their development while the modules were already being assembled and tested.
2. An integration of photosensors and ASICs was not desirable as we wanted to be able to read out the ADU with different systems for calibration.

Figure 12.7: Photo of the RadMap Telescope's ADU after integration, illustrating how we needed to squeeze the cables between the detector and the PCB assemblies of the read-out electronics

However, making 1024 signal connections between the detector and the electronics via cables also has its drawbacks. This is highlighted by Figure 12.7, which shows how we needed to squeeze the cables between the ADU and the PCB assemblies of the read-out electronics.

Now that we have gained some experience in operating a system based on the IDE3380, we can attempt placing the ASICs directly onto the SiPM arrays. This not only results in a much compacter detector, but also minimizes the path length of the analog signals, thus improving the instrument's noise immunity. In the new design presented in the previous section, the arrays will also be slightly larger, rendering the integration of the read-out chips easier.

12.2 Open Studies

In addition to design improvements, there are several studies relating to the ADU's detection principle that we either have not been able to complete yet or

that we have not even begun. Addressing these will be crucial for assessing the performance of our instrument under a wider range of environmental conditions, and to improve our understanding of its measurement accuracy.

12.2.1 Calibration with Heavy Ions

One of the biggest open questions is the accuracy with which we can identify high-Z nuclei and measure their energy. So far, we were only able to test the ADU with pions and protons, so even in the best of all worlds additional measurements would be required to verify its response to heavy ions. The presence of ionization quenching further complicates the matter and causes much of the uncertainty in particle identification (see Section 9.4.2). Calibration with heavy ions is thus urgently required to fully assess the performance of the detector and understand the effect of ionization quenching. It is also needed for a complete analysis of the data we gathered while operating the RadMap Telescope on the ISS. Testing should comprise the widest range of ions and energies possible, but must at least include protons, helium, carbon, oxygen, silicon, and iron. Investigating the detector response to this range of nuclei should give us a relatively good basis for benchmarking our Geant4 simulation framework, with the help of which we can then interpolate to intermediate nuclear charges.

12.2.2 Sensitivity to Neutrons

Though not specifically engineered for the detection of neutrons, plastic scintillators are in principle nonetheless sensitive to them due to their high hydrogen content [Ham+14; Law+14; Bla+14]. They can also be enriched with neutron-absorbing elements [Dum+16; Nem+21]. In spacecraft and on the surface or airless planetary bodies (such as the Moon), the interaction of high-energy cosmic rays and solar particles with material creates a substantial field of neutrons, which in extreme cases can contribute as much as 40% to 50% to the radiation dose astronauts receive [Rei01; AC01; SBC11; Zei+23a; Zei+23b]. Investigating the response of the ADU to neutrons is thus not only of academic interest but can help to make the RadMap Telescope an even more versatile radiation monitor. Again, a complete analysis of the on-orbit data we already gathered will also require at least an initial understanding of the expected event signatures for neutrons.

12.2.3 Radiation Hardness

On long-term deep-space missions to the Moon, Mars, or other destinations, instruments based on the technology demonstrated in the RadMap Telescope will be exposed to large cumulative radiation doses. It is thus imperative that we investigate the response of all the instrument's systems and components to such exposure. Besides the obvious need for testing electrical components, the behavior of the SiPMs and scintillating fibers is of crucial importance for assessing how the detector response will evolve over time. In contrast to PMTs, SiPMs are silicon-based devices whose characteristics can change significantly under exposure (see Section 4.5) [GM19; Mit+22; Ace+23]. Though we made a first attempt at testing the radiation response of the SiPMs used for the RadMap Telescope, our investigation was neither conclusive nor comprehensive. It is also likely that we are going to build future instruments using a different type (and manufacturer) of sensor, for which data may not yet be available. Not less important is the behavior of the scintillating fibers. Studies available in the literature [Klo+98; Bäh+00; Bis+02] typically investigated the residual light yield of fibers after they were exposed to the maximum dose expected in a given application. Dose-resolved measurements in the range of interest to us are, to our knowledge, not available (most studies test much higher doses, as relevant to accelerator-based experiments), though they are urgently required to understand how the response of our detectors evolves over time.

12.2.4 Temperature Sensitivity

For the RadMap Telescope, we did not concern ourselves too much with the sensitivity of the various detector elements to temperature changes, primarily because the instrument is equipped with a fairly extensive thermal control system and only exposed to moderate variations in the ambient environment. The temperature dependence of the SiPM gain is small enough to not play a large role for variations of only a few degrees. In future missions, however, the ADU may be exposed to much larger ranges, especially if it is deployed on robotic spacecraft. In this case, variations can easily reach on the order of 30 K or more, for which the performance of SiPMs can vary drastically [Bon+19b; Anf+21; Sch+22; GNS22]. For such a range, the temperature dependence of the scintillator's light yield starts to become significant, too [WB13; Wan+17; Per18]. Unfortunately, no data is available in the literature for SCSF-78 fibers, requiring us to perform our own investigations.

12.3 Comparison to the State of the Art

To our knowledge, the ADU in the RadMap Telescope is the first operational radiation monitor that has full particle-discrimination capabilities for radiation impinging from random directions. Though progress has been made in interpreting the heavy-ion induced signatures in Timepix-based devices [SP18; PP20], the information contained in the data produced by these detectors is inherently limited by the two-dimensional nature of their measurements and the limited material thickness. Though the introduction of these detectors has certainly significantly advanced the ability with which the different components of the space radiation field can be resolved, it is unlikely that an event-by-event reconstruction of the particle type with a single Timepix detector will ever be possible for nuclei up to iron.

Other omnidirectionally sensitive instruments—such as dosimeters based on planar diodes or passive materials—can only record the energy deposition of particles, not identify them. Especially with planar detectors, measuring particle fluxes requires a correction of the angular dependence of their response function. The segmented nature of the Timepix chips (and other pixelated sensors) allows doing so quite accurately and thus represents a major step forward in terms of radiation dosimetry. The fact the ADU's sensitivity and measurement resolution is nearly constant across the entire solid angle, on the other hand, means that only minimal corrections are needed for our data, if they are required at all.

Many of the more capable detectors currently deployed on the ISS and other spacecraft are variations of the particle-telescope concept that are sensitive only in a restricted field of view. Even if energy-sensitive layers (mostly made from silicon or scintillators) are combined with, for example, TOF systems, like in the case of LIDAL, these instruments cannot unambiguously identify individual particles. Instead, the composition of the measured radiation field is typically reconstructed via template fits to the recorded LET spectra [DiF+23]. More often than not, the data is used as-is, with quality factors assigned based on LET alone [Zei+23a]. If proven to work as well as projected based on our Geant4 simulations (see Chapter 9), the RadMap Telescope would thus be the first compact radiation monitor with particle-identification capabilities in the energy range relevant to radiation protection. The fact that the heaviest nuclei (within the sensitivity range) will probably only be reconstructable with (more than) 90% efficiency when allowing for $\Delta Z = 2$ or $\Delta Z = 4$ would not significantly diminish this accomplishment or the value of the data.

Another advantage of our instrument is the high count rate of the ADU, which averages about 100 Hz to 300 Hz in the equatorial and high-latitude regions, respectively, and reaches approximately 6 kHz in the central part of the SAA. Such high rates allow us to record statistically significant data sets in very short times, enabling us to perform detailed analyses quicker than others. The count-rate differences inside the SAA shown in Figure 11.43 provide only a first (and by themselves not very meaningful) preview of the type of analysis we will be able to perform. If we can make the track reconstruction work with the expected angular resolution, the high count rate will also allow us to perform detailed investigations of the angular dependence of the particle flux in different parts of the ISS' orbit. If both track reconstruction and energy measurement work as expected, three-dimensional analysis of the shielding distribution may be possible. To our knowledge, no other (single) instrument is capable of delivering data that would allow such investigations. Though many of these aspects are in principle understood from a perspective of the fundamental physical principles, their temporal behavior is often not well known—a deficit that the RadMap Telescope and future ADU-like detectors could help to address. Shielding analysis, in particular, often relies on models and simulations, which could to some extent be improved with the large amount of data our tracking calorimeter is capable of gathering.

A third point I want to highlight is the ADU's composition. Though not exactly a tissue-equivalent counter, the tracking calorimeter consists mostly of scintillating-plastic fibers that are much more similar in composition to the human body than silicon-based devices. We would argue that the difference between the PS–PMMA mix and what is usually regarded as tissue-equivalent plastic is virtually negligible for most purposes. The size of the detector is also roughly similar to the average depth of radiation-sensitive organs in the body. It is hence sensitive to more or less exactly the range of particle energies most relevant to radiation biology. Thus, even without full particle identification and energy reconstruction, our instrument is capable of delivering absorbed-dose measurements in a roughly tissue-equivalent volume of relevant size. Except for TEPCs that record data with much lower resolution and without directional information, we are not aware of any other instrument that could deliver comparable data. Ideally, future ADU-like detectors should even be a bit larger [Cha+18], though this would come at the cost of a significantly increased number of channels.

At the upper end of the capability scale, the RadMap Telescope's ADU obviously cannot compete with the accuracy and precision of charged-particle

spectrometers. And it is not meant to. Except for the PAN concept study [Suk+23], we are not aware of a spectrometer-based radiation monitor comparable in size and mass to our instrument. Obviously, large spectrometers like AMS-02 provide much more precise data over a wider range of higher energies, but they are also not sensitive over the full range of lower energies relevant to radiation protection. The RadMap Telescope thus promises to provide data of less precision and accuracy than spectrometers, while being about as large or smaller than many less capable systems.

12.4 Current Status and Outlook

Almost nine months of operating the RadMap Telescope on the ISS allowed us to gather about 2.7 billion ADU events. From the comparison of count rates between the ADU and the M-42, we know that a majority of these events are due to particles interacting with the former, though only a fraction exhibit clearly identifiable tracks. Three months of gathering data alongside the ISS-RAD detector has also allowed us to collect a substantial amount of data that can be compared to that of a flight-proven instrument. The planned co-location with the DOSTEL instrument in the Columbus model was thwarted by the loss of communication with RadMap in early 2024, a problem that we could not resolve despite extensive troubleshooting activities. As of writing this, we are awaiting the return of the instrument to ground in autumn 2024. Since it was working perfectly and showed no anomalies right until the moment we lost contact (shortly after passing through the SAA), we suspect corrupted memory to be the cause of the problem and therefore expect being able to resolve it quickly. Depending on the outcome of our on-ground troubleshooting, the ISS program has tentatively agreed to a re-flight of the RadMap Telescope, which would allow us to record the data we had hoped to gather in Columbus.

In the meantime, we still have a lot of work ahead of us analyzing the data we already collected. Currently, we are benchmarking first tracking algorithms (based on Hough transforms [HDH13]) that will allow us to correct the position-dependent light yield in each fiber on an event-by-event basis. Initial tests of these algorithms with on-orbit data delivered promising results, but a statistically significant characterization still needs to be completed. Another challenge that we must tackle is the energy calibration of the read-out electronics. Due to limited time and access to heavy-ion accelerator facilities, the only particles we could test our detectors with are protons and pions. Completing

our instrument during the Covid-19 pandemic, we were also not able to do so with the final flight electronics, meaning that we need to cross-reference data gathered with different read-out systems for a full calibration. Luckily, our instrument's built-in calibration modules allow doing so, though the process is far from straightforward.

Once we can work with the corrected and calibrated energy-deposition profiles along clearly identifiable tracks, we can start evaluating how well the neural networks we devised and trained on simulation data can cope with real-world data. Effects like cross-talk and correlated noise are not implemented in our Gent4 framework yet because we could not quantify them before completing and operating the instrument. Implementing them will likely require several time-consuming iterations of modifications to the simulation models, re-training of the networks, and assessing their performance on on-orbit data. Extracting track parameters and the event-wise determination of the total deposited energy for all events will likely be possible soon; particle identification and a reconstruction of the kinetic energy for heavy ions will certainly take longer to get right. The latter will also require us to find a workable solution for dealing with the uncertainties introduced by quenching. In the longer term, however, tests with heavy ions are inevitable to get this effect fully under control.

Another aspect is to interpret those events that to not show clearly identifiable tracks. We know that the majority of them contain the signature of some physical interaction in the detector. The challenge is classifying these signatures and matching them to simulation. This will require further improvements to our simulation framework, possibly including the generation of secondary particle in the station's structures and shielding. At the very least, though, we need to find a solution for correcting energy depositions without precise knowledge of where each fiber was hit (due to the absence of tracks).

In parallel, we are preparing to test and calibrate prototypes of the updated ADU designs with a muon beam at CERN in October 2024. These tests are crucial for benchmarking our simulation models and for accurately assessing the difference in performance between the RadMap Telescope's ADU and the updated design. We are also going to use external silicon tracking detectors (with a resolution of about 20 μm) to determine the path of each muon through the ADU modules, allowing us to perform for the first time a high-precision determination of their detection efficiency.

In the medium term, we are hoping to test at least one updated ADU module as part of another experiment on the ISS. This experiment will be deployed

on the Bartolomeo platform attached to the Columbus module, giving us the opportunity to operate a detector outside the station's shielded volume. We will use this test to verify that we can operate ADU-like tracking calorimeters in the free-space environment—i.e., with full exposure to the thermal stress induced by the day–night cycle in vacuum—and to record data of the largely undisturbed radiation environment that can serve as reference for the RadMap Telescope's measurements.

Part II

The Search for Water on the Moon

Introduction to Part II

In recent years, interest in crewed lunar exploration has surged—not just for the Moon to be a stepping stone on the way to Mars, but also because of the many scientific investigations that would be made possible by the return of humans to the lunar surface [Cra+12]. The comprehensive and long-term human-tended activities envisioned by public and private organizations alike will pose severe logistical challenges if all supplies required to sustain these efforts must be brought from Earth. Local resources may therefore prove to be crucial for the establishment of a sustained human presence on the Moon: ISRU, especially the extraction of water and oxygen, could substantially decrease the amount of material that must be re-supplied to a lunar outpost [MC20]. Lunar water ice may very well be the single most important resource in (cis-lunar) space for decades to come—not just for the exploration of the Moon itself, but also for missions to other destinations in our solar system [Cra15]. Accessible deposits of water could, for example, be exploited to produce consumables of critical importance to both crewed and uncrewed missions, such as breathable air, potable water, and rocket propellant [Ana+12]. They may even help to shield habitats and their inhabitants against cosmic and solar radiation [Sin13; Bai+18], another critical aspect of long-term missions beyond Earth orbit [And+19; Cha+18].

Any assessment of the possible uses of lunar water is, however, still severely constrained by the fact that we do not yet fully understand the extent and distribution of volatile deposits expected to exist at the lunar poles [Lan+22; Luc+21]. Even though several credible theories (solar wind, asteroid and meteorite impacts, and outgassing from the lunar interior) exist, we do not even know the exact origin of water (and other volatiles) on the Moon because the currently available data does not particularly favor any of the hypotheses put forward [DHN20]. While it is likely that all three mechanisms contributed, or still contribute, to the delivery of volatile elements to the polar regions,

further detailed and comprehensive (in-situ) measurements will be required to fully understand the lunar water and volatiles cycle [Luc+21; DHN20].

In this second part of my thesis, I present the results of a concept and design study for a mission that is primarily intended to contribute to addressing the shortage of in-situ data on volatiles and, in particular, water in the polar regions of the Moon. The study, called LUVMI-X, was funded by the European Union's Horizon 2020 research and innovation program; its primary objective was to raise the readiness of the technologies required to realize the mission to levels where a selection for full funding to develop a flight mission can be justified. Our contribution to the study was focused on the development of a concept for a cosmic-ray and neutron spectrometer, though my personal involvement also extended to the selection of the overall science objectives and the mission planning.

I begin this part by summarizing the scientific interest in the exploration of the Moon with a focus on volatiles, mineralogy, and radiation, which are the key areas of interest for the mission's three main instruments. I then describe the tool of neutron spectroscopy and its role in the search for lunar water before presenting our design of a compact spectrometer for both neutrons and cosmic rays. Next, I give a brief overview of the mission's central element, a compact yet versatile rover, and the remaining instrumentation it carries, before summarizing the measurements that can be performed. I also discuss our strategy for identifying scientifically relevant candidate landing sites and present an example traverse on the Shackleton-Faustini range at the lunar south pole. To conclude, I discuss how the LUVMI-X mission fits into the diverse landscape of water- and volatile-focused missions currently under development in the U.S., Europe, and elsewhere.

Much of this part of my thesis, including the preceding paragraphs of this introduction, is based on a journal publication in *The Planetary Science Journal* [Los+22]. I was the lead author of this article and hence wrote all of it myself, though I obviously collaborated with other members of the study team who provided guidance and facts on parts of the project I was not responsible for. Some sections are verbatim copies from the journal publication.

Chapter 13

Water on the Moon

By now, the existence of water ice in the Moon's polar regions is widely accepted, even though there is no consensus yet on the origin, extent and nature of these deposits. Improving our knowledge about the size and distribution of the latter is crucial for understanding whether the Moon can act as a source of water for future exploration missions. Besides these mostly practical aspects, lunar volatiles, and water in particular, may also help us understand the history of the inner solar system [Sto+06], the origin of water on Earth and other planets [CV02; SS15b; Bar+16], and possibly even the delivery of pre-biotic organic materials to the terrestrial planets [CS92; Osi+]. In this chapter, I review the evidence for the water's presence that was gathered so far, our current knowledge about the sources, and the expected distribution and accessibility of water deposits. I also discuss the value of neutron spectroscopy as a tool in the search for water and other hydrogen-rich materials.

13.1 (Observational) Evidence

The first indication for the presence of water ice at the lunar south pole was provided by the bistatic radar experiment aboard Clementine [Noz+96] but was called into question by follow-up investigations [Sta97; ST99]. In the years since, more evidence for lunar water has been gathered via neutron spectroscopy [Fel+98; Mit+12] and via optical observations spanning the infrared, visual, and ultraviolet ranges [Cla09; Sun+09; Pie+09; Hay+15]. The strongest evidence so far was provided by LCROSS, which observed the ejecta plume of an impactor hurled into the permanently shadowed Cabeus

crater and detected a water content of $5.6 \pm 2.9\,\%$ by weight [Col+10]. While its origin is still not entirely clear [DHN20; Luc+20], water ice is thought to be trapped in regions of extremely low surface temperatures, primarily in large permanently shadowed regions (PSRs) and micro cold traps in the Moon's polar regions [Hay+15; LM17; HAS20]. Yet, recent results from the SOFIA airborne observatory suggest the presence of molecular water also in sunlit areas near the poles [Hon+21], which may be caused by spillage of volatiles from the floor of PSRs onto the surrounding terrain due to micro-meteoroid impacts and other processes [FHZ15].

The data available today, collected exclusively by remote-sensing instruments aboard probes in lunar orbit, constitutes a relatively strong but nonetheless preliminary evidence for the existence of water ice on the Moon. Aside from these remote-sensing measurements and with the notable exception of the samples recently collected by the Chang'E 5 and Chang'E 6 missions, our knowledge about the concentration and distribution of water and other volatiles in the lunar rocks and regolith is limited to analyses of the few samples collected by the Apollo and Luna missions in the late 60s and early 70s of the last century. In-situ measurements and sample-return missions, complemented by global high-resolution mapping from orbit, are required to resolve the ambiguities in current data and to identify suitable ISRU locations [Cra15; Ana+12].

13.2 Sources, Distribution, and Accessibility

Since the Moon is a very dry body, the question arises where the water we believe to have observed originated. One possibility is that is most if not all of it was picked up when the Moon was created in the collision of a Moon-sized object with a water-bearing Earth [Kra22]. Another possibility is that water and other volatiles were brought to the Moon by asteroids and meteorites [Pre+15] and by the solar wind [FS93]. Or perhaps it was brought up from the lunar interior by volcanic activity [WHL22]. The viability and possible contribution of all these and other proposed processes is not at all clear yet; better modeling, based on urgently required *in-situ* measurements, is required to gain a deeper understanding.

Simulations confirm that surface ice should be stable on macroscopic scales in permanent cold traps inside PSRs, yet some recent calculations seem to suggest otherwise [Far+19]. If buried under an insulating regolith layer of at least a few centimeters thickness, however, ice is almost certainly stable

on geological time scales, perhaps even in areas covering as much as 15% of the lunar south pole [Pai+10]. The impacts of micro-meteorites over millions of years led to a breakup and mixing of surface-ice layers with the regolith beneath in a process called *impact gardening* [CB20]. Over time, this churning and overturning of material resulted in a heterogeneous and stable sub-surface distribution of water ice and other volatiles up to depths of several meters [Cos+20]. Models predict that the amount of water in these sub-surface reservoirs is much larger than in the more easily accessible surface layers [Can+20].

It is not yet clear whether potential reserves are vast and accessible enough to allow economically attractive extraction operations, either for commercial purposes or to ensure that crews of government-led exploration missions can depend on this water for their survival.

13.3 Neutron Spectroscopy: The Search for Hydrogen

On airless bodies, hydrogen-bearing materials—such as water and hydroxyl deposits—can be detected by measuring the (relative) fluxes of thermal, epithermal, and fast neutrons. These are created by highly energetic (hundreds of MeV and above) cosmic-ray and solar particles that penetrate the lunar surface to depths of several meters. While a fraction of the produced neutrons diffuses upwards through the regolith, they scatter with the soil's constituent nuclei and assume an energy spectrum that is characteristic for the composition of the regolith [PBL16].

The presence of hydrogen (and thus water or hydroxyl) elicits a detectable change in this energy spectrum by lowering the relative flux of epithermal neutrons. That is because:

1. During their upward diffusion, neutrons are being moderated more efficiently by hydrogen than by any other material (see Section 3.4). The larger the hydrogen (water) abundance, the higher the fraction of neutrons that lose a substantial fraction of their energy.
2. The moderation cross-section is considerably larger at epithermal energies than at fast energies. For a given diffusion path, epithermal neutrons hence thermalize to a larger degree than fast neutrons, leading to their relative suppression.

The energy spectrum of neutrons detected at the surface (or in orbit) therefore allows to (1) detect the presence of hydrogen and (2) estimate its abundance. A precise determination of the latter requires knowledge of the average composition of the surface material. The major advantage is that no sampling is required; measurements can in principle be taken on the ground and in orbit, though the spatial resolution decreases with increasing altitude.

Neutron spectroscopy is a well-established tool in planetary science. In its passive form described above, it has, for example, been employed on two missions to the Moon—Lunar Prospector and the Lunar Reconnaissance Orbiter (LRO) (see discussion in Chapter 16). The data from these orbital investigations is, however, limited in resolution. The technique is more widely used in combination with active neutron sources, allowing it to be employed on planets with atmospheres and magnetic fields [Has+18; Mit+12; Bar+21b]. Using neutrons created by cosmic rays in Earth's atmosphere, it can likewise be used for the determination of soil moisture levels over large areas without the need for taking samples [Zre+08; DZF10; Fer+20].

Chapter 14

The Lunar Cosmic-Ray and Neutron Spectrometer

To contribute to the search for water ice and other volatiles on the Moon, we started developing the Lunar Cosmic-Ray and Neutron Spectrometer (LCNS) as part of the LUVMI-X (Lunar Volatiles Mobile Instrumentation – Extended) project funded by the European Commission's (EC) Horizon 2020 program. The aim of the project, which I describe in more detail in Chapter 15 below, was to develop a package of complimentary instrumentation that would allow a detailed characterization of the Moon's resource potential and of the environment on the lunar surface in preparation for future crewed and robotic missions. In this chapter, I summarize our work[1] on a conceptual design for a combined cosmic-ray and neutron spectrometer that shall help to find and analyze water-ice deposits and other areas of increased hydrogen abundance. It shall also characterize the radiation environment on the lunar surface to address the shortage of respective in-situ measurements in preparation for the return of humans to the Moon.

[1] This chapter is based on the final report that I wrote for the LUVMI-X project [LPW21], which we submitted to the EC but have not made publicly available. Any parts of the report that I reused were written exclusively by me. We also published aspects of our work in a peer-reviewed proceedings paper that I presented at the IEEE Aerospace conference. I was the main author of that paper [LEP22]. Some paragraphs are verbatim copies from these documents.

14.1 Requirements and Objectives

We derived the objectives and high-level requirements for the instrument from the scientific objectives of the LUVMI-X reference mission described in the next chapter. Based on an analysis of existing measurements and models, as well as the anticipated profile and operational concept of the reference mission, we concluded that an instrument designed to support the latter's two main scientific objectives should have the following capabilities:

1. It should be sensitive to protons and GCR ions with energies larger than 10 MeV and 50 MeV/n, respectively. This energy range covers not only GCR and SEP but also albedo protons generated by high-energy GCR interacting with the lunar surface [Sch+16].
2. It should be sensitive to protons with energies between 100 keV and 1 MeV to measure solar-wind ions and low-energy protons reflected off the lunar surface [Sai+08].
3. It should be sensitive to electrons and positrons with energies between 0.5 MeV and 100 MeV. This energy range covers secondary electrons and positrons that are generated in interactions of GCR with the lunar surface [Spe+13].
4. It should measure the TID of charged and neutral radiation to determine the expected radiation exposure on the lunar surface.
5. It should measure the LET of charged particles. Knowledge of the LET allows a more precise analysis of the biological effectiveness of radiation.
6. It should be capable of identifying charged particles and precisely determining their energy in the range most harmful to humans (between ten and a few hundred MeV for protons, for example). Such information is not only crucial to a better understanding of the lunar radiation environment but also allows an even more precise analysis of its biological effectiveness and thus a more reliable risk prediction for future crewed missions.
7. It should be sensitive to thermal, epithermal, and fast neutrons with energies between 0.1 eV and at least 8 MeV. This energy range covers most of the secondary neutrons produced in reactions of GCR with lunar regolith. It also spans the entire range that is relevant to the detection of hydrogen.
8. It should have at least basic spectroscopic capabilities for neutrons and be able to distinguish between thermal (0.1 eV to 0.4 eV), epithermal

(0.4 eV to ∼1 MeV), and fast (∼1 MeV to ≥8 MeV) neutrons to allow measurements of the hydrogen abundance. Ideally, it should be able to determine neutron energies with much higher precision.

Additional requirements were closely tied to the design of the rover and the expected operational concept. I do not list them here because they are of little relevance to the instrument's design and expected performance.

14.1.1 Compatibility with Different Spacecraft and Probes

The LUVMI-X project was funded by the EC solely as a technology-development project. Its objective was to raise the technology readiness level (TRL) of the rover and its instrumentation to 4 or 5 (see appendix G of [SP6105] or [ESA08] for a definition of the different TRL levels). Follow-on funding by the EC to develop LUVMI-X into a flight mission was unlikely to be approved and ultimately did not materialize, as such projects are the responsibility of ESA. A continuation of the work on LUVMI-X after the completion of the project was therefore not guaranteed.

The instrumentation developed for the LUVMI-X reference mission shall be complementary, with three main instruments providing different measurement capabilities supporting a common objective—the search for and characterization of water-ice deposits at the lunar poles. But the LCNS does not require the other payloads to operate and can provide a plenty of scientifically interesting data on its own, without the need for any additional instrumentation. One of our goals therefore was to design an instrument that can be part of multiple missions, perhaps even at the same time, to help provide a more comprehensive picture of the hydrogen abundance ad the radiation environment on the Moon. Since we were funded by the EC to develop the LUVMI-X concept, any such consideration was, however, not to impact the performance of the reference mission (see Chapter 15) in any way. Additional requirements that go beyond LUVMI-X needed to be optional and design decisions or trade-off studies were not to be driven by them.

Many of the rover-related requirements and constraints are relatively generic and should allow a fairly straightforward adaption to other platforms, either on the surface or in orbit. The instrument's mechanical envelope is loosely based on the CubeSat standard, which is widely used among providers of hosted-payload flight opportunities (for example, in the context of NASA's Commercial Lunar Payload Services (CLPS) program). Electrically, the rover

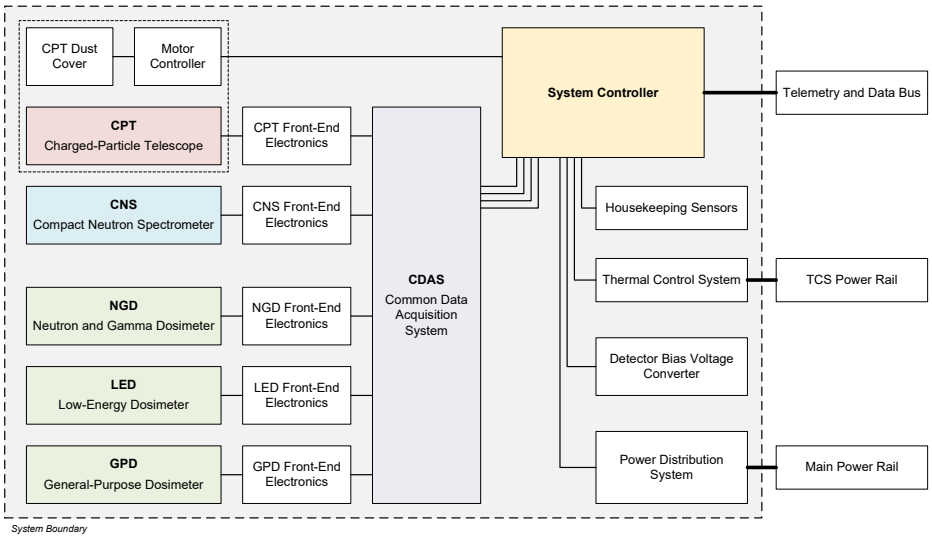

Figure 14.1: The LCNS system architecture.

is equipped with a simple data bus for payloads (RS-485) and provides a single 28 V power bus. Both are widely used standards that are being used or considered for several landers and rovers currently under development. The only major difference between LUVMI-X and some other missions is the mission duration: It is designed for a 14-day operational period and cannot survive a lunar night. At least some other missions are supposed to operate much longer that, requiring payloads to survive extremely low nighttime temperatures and to be less susceptible to (total-dose) radiation damage.

14.2 Overall System Architecture

The operating principle of the LCNS is based on concepts we previously developed for other projects. During the early stages of the LUVMI-X project, we were leaning heavily on this design heritage. But we soon realized that while we would meet the payload's core performance requirements, we would very likely not be able to fulfill many of the optional ones. When the mission's science objectives shifted more and more towards the detection of water ice, we had to abandon the simple architecture we envisioned when we proposed the

project to the EC. Instead, the LCNS now consists of two separate main sensors, a compact neutron spectrometer (CNS) and a charged-particle telescope (CPT), as well as several secondary ones.

The CNS's main task is the identification of water and hydroxyl deposits by measuring the change of the albedo neutron spectrum caused by increased concentrations of hydrogen in the regolith. The detector must have some basic spectroscopy capabilities to perform this task, but it does not need to be a highly precise neutron spectrometer. More importantly, it must consume as little power as possible, so that it can be operated continuously and be used as a scouting instrument to identify locations of interest for follow-up investigations by the more power-intensive instruments that the rover was to be equipped with (see description of the operational concept in Section 15.2). The main task of the CPT is to characterize the lunar surface radiation environment by measuring the energy spectrum of GCR and solar-wind particles. As a secondary objective, the CPT shall also measure charged albedo radiation created in interactions of the solar wind and GCR with the lunar surface.

In addition to these primary sensors, the LCNS is equipped with a set of dosimeters to measure the radiation dose received on the lunar surface: The neutron and gamma dosimeter (NGD) is sensitive to neutrons and gamma rays and provides a reference dose measurement for the CNS; the low-energy dosimeter (LED) measures low-energy charged albedo particles and thus provides a reference for the low-energy section of the CPT (see detailed description of the CPT architecture in Section 14.4); and the general-purpose dosimeter (GPD) measures the TID of all biologically relevant radiation. The design of the dosimeters has, however, not been a central part of our study. We confirmed that state-of-the-art solutions exist that can be adapted for use in the LCNS for all three capability sets we identified to be relevant and that these solutions provide adequate performance.

Figure 14.1 shows the overall system architecture of the LCNS. Both the CNS and CPT, as well as all three dosimeters mostly comprise very similar sensor components and can thus share a common data acquisition system (CDAS). Even though the (analog) front-end electronics are mostly identical as well, they are shown separately as they are integrated directly into the sensors. This common electronics design and the shared data acquisition reduce system complexity and allow us to lower the risk of critical system failures through more comprehensive testing.

At the heart of the system is the system controller (SC), which performs all telemetry and control tasks, processes and stores the sensor data, and interacts

with the rover's command and data handling system via a redundant data interface. The SC is supplemented by a separate controller for the CPT dust cover motor and by a number of housekeeping sensors distributed throughout the instrument. The power distribution system (PDS) converts the rover's main power rail to the voltage busses required to operate the system; a separate bias voltage converter (BVC) generates the highly stable bias voltage required to operate most of the LCNS sensors. To ensure the instrument is kept within its survival temperature range even when the main power rail has been switched off (e.g., to conserve power when the rover is in survival mode during the lunar night), the thermal control system (TCS) is powered by a separate supply rail that must be kept on at all times.

14.2.1 Heritage Considerations

During the development of the LCNS concept, we tried to strike a balance between using state-of-the-art sensor components and materials on the one hand, and relying on our experience and proven designs wherever practical on the other. This allowed us to concentrate on the optimization of the instrument using technologies we understand well. I am convinced this has ultimately led to a more robust design than we would have otherwise been able to achieve.

When we started working on the project, our team already had extensive experience with developing radiation detectors based on scintillators and SiPMs. Chief among our reference projects was the RadMap Telescope, whose flight ADU we were in the process of constructing at the time. We proposed the use of scintillators for the LCNS as well; they are ideally suited for space applications because they are mechanically robust, can be machined into almost any desired geometry, and can be exposed to vacuum. They are also readily available and can be manufactured to the desired specifications in-house, which is not the case for most semiconductor detectors. Our reasoning for using SiPMs analogous to the one we put forward in the context of RadMap. They are a modern replacement for PMTs and offer a number of advantages over them: They are comparatively inexpensive, commercially available, and mechanically robust. Detectors constructed from scintillators and SiPMs require no pressure vessels, gas supplies, or high voltages. They can be exposed to vacuum directly and fare comparatively well in the space radiation environment.

For these technical reasons and because we have most experience with these technologies, we decided to make use of them to the largest extent possible. This approach not only simplified the instrument design by getting

rid of the engineering challenges associated with gas and high-voltage systems but also provided a more robust design based on proven technologies. It is, however, not possible to fulfill all requirements listed in Section 14.1 above with a detector built solely from scintillators. We therefore needed to add other technologies (mostly silicon-based sensors) but tried to use proven components with flight heritage wherever possible. As repeatedly mentioned throughout the following sections, we often excluded other candidate technologies or devices because of these heritage considerations and technological challenges. Though a different approach could have been taken, we believe this has ultimately led to a more reliable design.

14.3 The Compact Neutron Spectrometer

To detect the presence of hydrogen, the CNS must have basic spectroscopy capabilities but does not need to be a highly precise neutron spectrometer. It must be able to determine a neutron's energy with sufficient precision to distinguish between the thermal, epithermal, and fast energy regimes. At the very least, it must be able to count how many neutrons in each of the three energy ranges it detects in a given period of time. Relative changes of these count rates indicate differences in the composition of the regolith below the instrument. The epithermal range in particular is a good indicator for the presence of hydrogen (see Section 13.3). I use the following definition for the energy ranges, which is based on the one used for the analysis of orbital neutron data [Fel+00] but may differ from the that used in other disciplines:

Thermal	0.1 eV to 0.4 eV
Epithermal	0.4 eV to 600 keV
Fast	600 keV to 8 MeV

We thus require at least three detectors that are sensitive to neutrons with energies in the respective ranges. The spectral resolution can be enhanced by increasing the number of detectors and making the sensitivity ranges narrower.

14.3.1 Technology Selection

Measuring neutron energies is a comparatively challenging task: Since they carry no (net) electric charge, neutrons do not interact with matter in a useful (i.e., detectable) manner via ionization over a wide range of energy (in contrast to charged particles, which frequently interact with a material's constituent

atoms, see Chapter 3). In most applications, we therefore make use of the fact that neutrons can most easily be detected when they have thermal energies (about 0.025 eV) and can be captured by a nucleus in the detector material. In a process called thermalization, neutrons are slowed down (moderated) through scattering interactions with a material (the moderator) until they have the same average energy, and thus temperature and velocity, as the surrounding atoms.

This approach is, for example, widely used in neutron spectrometers based on the Bonner sphere principle[2] [AS85; TA02]: Thermal-neutron detectors are embedded in spheres made from a material that effectively moderates higher-energy neutrons to thermal energies. The sensitivity of the detectors is altered by varying the thicknesses of the spheres: The higher the initial energy of a neutron, the more moderator material it must traverse to thermalize and be detected. The relative count rates of detectors with different moderator thicknesses can give an accurate measurement of neutron energies, if a sufficient number of spheres is used. The spheres are typically made from plastics with high concentrations of hydrogen, which thermalize neutrons effectively. Bonner spheres can be produced using simple detectors (mostly gas proportional detectors) and simple electronics, but take up a relatively large volume. They are also omnidirectionally sensitive; this is generally a desirable capability but not required on the lunar surface, where most of the neutrons are traveling upwards from the surface.

Neutrons are often detected with modified gas proportional chambers filled with rare ^{3}He gas (which give only count rates, no energy) [MCM62; Kle21] or with scintillators (crystals, glass, or plastic; often enriched with elements that capture thermal neutrons and subsequently emit charged particles, see Section 4.4) [Car+14; GKT17; Li+24]. Advances have also been made in developing neutron-sensitive semiconductor detectors [Fro+15; Osi+16; Cou+21; Tam+23], but many concepts and devices are neither ready for widespread use nor commercially available.

14.3.2 Detector Concept

We adapted the concept of the Bonner sphere to the requirements of the LUVMI-X reference mission. Instead of an isotropic geometry, we implemented a linear

[2]The same measurement principle is used in many other neutron detectors as well. I reference the Bonner sphere here because the original sphere developed by Bramblett, Ewig, and Bonner [BEB60] was one of the earliest detectors to employ it.

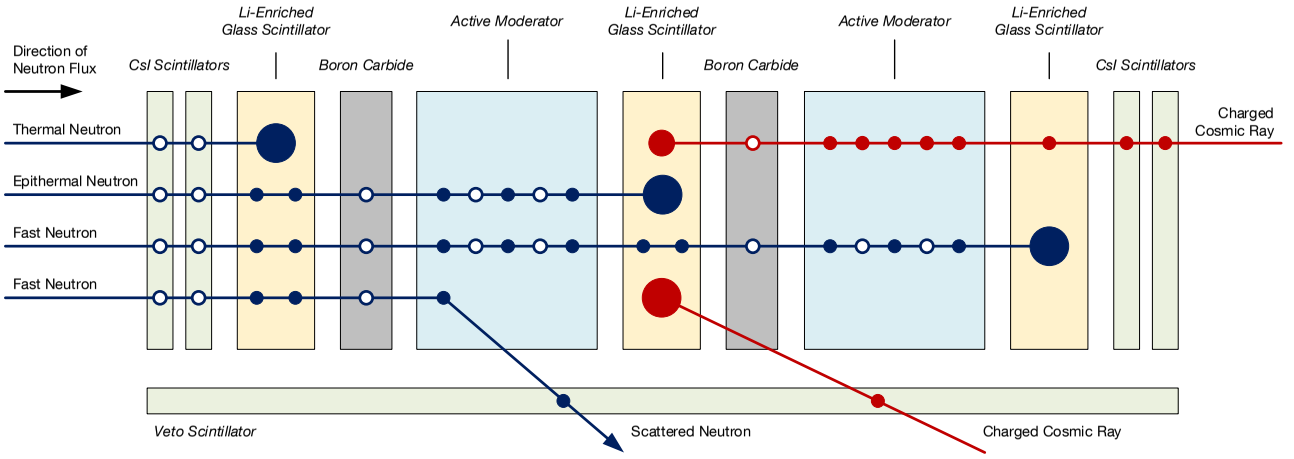

Figure 14.2: Schematic design of the CNS. The detector is shown lying on its side; the left-hand side points to the lunar surface, the right-hand side to free space. Neutrons enter the detector from below with a narrow angular distribution and charged cosmic-ray particles enter from the top and from the sides.

Neutrons (blue tracks) and charged particles (red tracks) traversing the detector lose energy in the detector (glass, CsI, and plastic scintillators) and absorber (boron carbide) materials. The circles along their tracks symbolize this energy loss: the larger the circle, the more energy the particle deposits in a particular layer of the detector. Filled circles denote energy that can be measured in the form of generated photons, open circles denote energy that cannot be measured.

The figure shows the energy-loss signatures of neutrons with different energies. Thermal neutrons are only detected in the lower layer of lithium-glass scintillator. Epithermal neutrons are thermalized in the lower moderator (made from plastic scintillator) and then detected by the middle glass scintillator. Fast neutrons require more material to thermalize and thus only have a significant chance of being detected in the upper glass scintillator. Charged particles generate signals in the tube-like veto scintillator surrounding the detector and in the CsI layers on the top and bottom of the sensor stack. From [LPW21].

one, which allows us to combine the detectors for different neutron energies into one sensor. Figure 14.2 schematically shows the design of the CNS sensor stack, which is based on the assumption that the neutron flux is directional with only a narrow angular distribution. Even though the figure already shows what scintillators we use, the exact choice of materials is not important at this point and will be discussed later.

We use three thermal-neutron detectors (yellow) to count the number of neutrons with thermal, epithermal, and fast energies. The first (left) detector counts thermal neutrons with a very high efficiency. Similar to a Bonner sphere, we then use plastic to moderate epithermal neutrons to thermal energies. But instead of passive material, we use a plastic scintillator (blue) in which the energy the neutron loses during thermalization is converted into detectable light. This allows us to measure the excess energy of the neutron (over the thermal energy). The thermalized neutrons are detected in the second thermal-neutron detector. A layer of highly efficient neutron absorber (grey) between the first neutron detector and the moderator prevents neutrons that were not detected (and thus stopped) from producing a signal in the moderator. Using this simple geometry, we can effectively distinguish between thermal and epithermal neutrons and even measure the total energy of the epithermal neutrons. To detect fast neutrons and measure their energy, we use another set of moderator and thermal-neutron detector of identical dimensions. Fast neutrons therefore pass through double the amount of material and only have a significant chance of being captured in the last detector. Again, we use a layer of absorber to capture epithermal neutrons that were not stopped in the second neutron detector.

High-energy protons and other GCR particles entering one of the scintillators from the side generate signals that can be almost identical to those created by neutrons. The stack is therefore enclosed in a tube made from plastic scintillator (green) to detect charged particles entering from the side, generating veto signals to identify false neutron-like events. On the top and on the bottom of the stack, additional layers of scintillator (green) generate much higher signals for charged particles than for neutrons and thus provide veto signals for charged particles traversing the detector along its vertical axis.

14.3.3 Materials

We decided against using gas proportional chambers or semiconductors as primary neutron detectors early in the project. We found that the latter are

neither mature nor available enough and would therefore add significant risk to the project. Gas proportional chambers have, as mentioned earlier, two major disadvantages: (1) They require a leak-tight pressure vessel to hold the detector gas without introducing impurities and (2) they must be operated at voltages of hundreds of volts. Both aspects necessitate significantly more engineering effort than is required for scintillation detectors. Furthermore, the fact that we use scintillators for other parts of the CNS (and also for the CPT) further reduces risk: The scintillators that we eventually chose have very similar emission spectra, allowing us to use the same type of photodetector and read-out electronics for all of them. This synergy significantly decreases the system's complexity. Furthermore, we excluded liquid scintillators from our considerations, as they would require a pressure vessel as well.

Neutrons only interact weakly with matter and are therefore more difficult to detect with scintillators than gamma rays or charged particles. For our purposes, we mainly looked at detecting neutrons in the fast and thermal energy regimes (see Section 14.3.2 to understand how this is motivated by our detector concept). Fast neutrons can be detected in organic scintillators that have a high concentration of hydrogen atoms: While traversing the material, the neutrons elastically scatter with the hydrogen nuclei (protons) of the material, transferring energy to them that is subsequently converted into scintillation light. Most commonly available plastic scintillators can thus be used to detect fast neutrons with varying but generally low detection efficiencies. Thermal neutrons can most effectively be detected indirectly through absorption reactions. The most widely used absorber material is ^{6}Li (lithium-6): It is readily available and has a relatively large cross-section for the absorption of thermal neutrons through the ^{6}Li(n, α) reaction. In this process, a tritium ion and an alpha particle are created for every absorbed neutron and subsequently interact with the scintillator base material (often a cerium-doped glass matrix) to produce scintillation light.

Table 14.1 lists all neutron-sensitive scintillators we evaluated for this project. We use colors (green, yellow, orange, red) to highlight the suitability of each material's properties. For the evaluation, we fixed the choice of photosensor to SiPMs sensitive in the blue range (with a peak sensitivity of about 430 nm) because most manufacturers offer devices with roughly these characteristics. The emission spectrum of the scintillators should closely match the sensitivity of the SiPMs. Another important property is the decay time of the scintillator (a measure for the time the material produces light after excitation through a neutron). The longer the time, the lower is the rate at

Table 14.1: Evaluated solid organic and inorganic scintillators that are sensitive to neutrons. The characteristics of each material are colored according to their suitability (green – ideal, yellow – acceptable, orange – barely acceptable, red – unacceptable).

Scintillator	Neutron Energy	Light Yield	Peak Emission nm	Decay Time ns	Temp. Range	Comments	Ref.
Ce:$LiCAF_6$	thermal	5000 ph./n	388	40	?	-	[CAC20]
Eu:$LiCAF_6$	thermal	40 000 ph./n	372	1600	?	-	[CAC20]
NaI(Tl+Li)	thermal	35 000 ph./MeV	419	230	?	γ background	[Lux23c]
CLLB	thermal	40 000 ph./MeV	420	180 / 1080	?	γ background, hygroscopic	[Lux18b]
GS20	thermal	6000 ph./n	395	18 / 57 / 98	-200 to 250 °C	-	[Sci20]
BC-702 or EJ-420	thermal	60 000 ph./MeV	450	200	?	No custom sizes	[Lux20a]
BC-720 or EJ-410	fast	?	450	200	90 °C max.	No custom sizes	[Lux20b]
EJ-276	fast	8600 ph./MeV	425	13 / 59 / 460	?	γ background	[Elj20]
BC-400 or EJ-212	fast	13 000 ph./MeV	423	2.4	-20 to 60 °C	-	[Lux23d]
BC-408 or EJ-200	fast	12 800 ph./MeV	425	2.1	-20 to 60 °C	-	[Lux23d]
BC-412 or EJ-208	fast	12 000 ph./MeV	434	3.3	-20 to 60 °C	-	[Lux23d]
BC-416	fast	7600 ph./MeV	434	4.0	-20 to 60 °C	-	[Lux23d]
BC-448 or EJ-248	fast	12 800 ph./MeV	425	2.1	-20 to 90 °C	high-temp. version of BC-408	[Lux18a]
BC-448M	fast	12 800 ph./MeV	425	2.1	-20 to 150 °C	cross-linked version of BC-448	[Lux18a]
BC-440 or EJ-244	fast	12 000 ph./MeV	434	3.3	-20 to 90 °C	high-temp. version of BC-412	[Lux18a]
BC-440M	fast	12 000 ph./MeV	434	3.3	-20 to 150 °C	cross-linked version of BC-440	[Lux18a]

Table 14.2: Evaluated solid organic and inorganic scintillators that are sensitive to charged particles. The characteristics of each material are colored according to their suitability (green – ideal, yellow – acceptable, orange – barely acceptable, red – unacceptable).

Scintillator	**Neutron Energy**	**Light Yield**	**Peak Emission** nm	**Decay Time** ns	**Temp. Range**	**Comments**	**Ref.**
BC-400 or EJ-212	fast	13 000 ph./MeV	423	2.4	-20 to 60 °C	-	[Lux23d]
BC-408 or EJ-200	fast	12 800 ph./MeV	425	2.1	-20 to60 °C	-	[Lux23d]
BC-412 or EJ-208	fast	12 000 ph./MeV	434	3.3	-20 to 60 °C	-	[Lux23d]
BC-416	fast	7600 ph./MeV	434	4.0	-20 to 60 °C	-	[Lux23d]
BC-448 or EJ-248	fast	12 800 ph./MeV	425	2.1	-20 to 90 °C	high-temp. version of BC-408	[Lux18a]
BC-448M	fast	12 800 ph./MeV	425	2.1	-20 to 150 °C	cross-linked version of BC-448	[Lux18a]
BC-440 or EJ-244	fast	12 000 ph./MeV	434	3.3	-20 to 90 °C	high-temp. version of BC-412	[Lux18a]
BC-440M	fast	12 000 ph./MeV	434	3.3	-20 to 150 °C	cross-linked version of BC-440	[Lux18a]
CsI(Tl)	-	54 000 ph./MeV	550	1000	<600 °C	slightly hygroscopic	[Lux18c]
CsI(Na)	-	41 000 ph./MeV	420	630	<600 °C	hygroscopic	[Lux18c]
NaI(Tl)	-	38 000 ph./MeV	415	250	<600 °C	hygroscopic	[Lux23b]
$LaBr_3$(Ce)	-	63 000 [ph./]MeV	380	16	<700 °C	hygroscopic	[Lux23a]

which neutrons can be detected; a decay time of 1 μs, for example, allows detection rates of several kilohertz. A third crucial property is the temperature range in which a scintillator can be used (and is mechanically stable). In principle, the amount of light (i.e, number of photons) generated per captured neutron would also be an important property, but all scintillators we evaluated fulfilled our requirements.

As is evident from Table 14.1, many thermal-neutron sensitive scintillators we evaluated did not fully meet the requirements of the LCNS, mostly because of too long decay times. The material which is best suited is a type of cerium-activated lithium glass scintillator manufactured by Scintacor under the name GS20. In the ^{6}Li(n, α) reaction described above, GS20 produces about 6000 photons per captured thermal neutron, which allows the use of a wide variety of photodetectors, but most definitely allows us to work with SiPMs. Neutrons can be distinguished from background-producing gamma rays via pulse-height discrimination, with several tens to hundreds of gammas required to hit the scintillator simultaneously to produce the same number of photons as one neutron capture. Due to the relatively short decay time, this is unlikely to happen even in environments with a high gamma background.

For the active moderator, the choice was naturally narrowed down to plastic scintillators because they are the only scintillator material with a sufficiently high hydrogen content for effectively moderating neutrons. The choice of plastic scintillator is mostly restricted by the low softening point of about 70 °C of the base material most widely used for commercially available products, PVT. PS-based scintillators have a somewhat higher softening point but are not commercially available in bulk form. Modifications of the PVT base can extend the working range and cross-linking of the polymer chains prevents the plastic from flowing even if the softening point is exceeded for prolonged periods of time. We chose to use BC-448M, a high-temperature and cross-linked version of the BC-408 scintillator manufactured by Luxium Solutions (formerly Saint-Gobain Crystals). Its scintillation properties are identical to those of BC-408, allowing us to use this cheaper material for prototyping and functional tests.

Tab. 14.2 lists the scintillators we evaluated for detecting charged particles. For plastic scintillators, there is a significant overlap with the materials useful for neutron moderation. In addition, we evaluated some commonly used scintillation crystals. For the veto scintillator, materials must be available in large dimensions ($>$10 cm) and must be machinable into the desired shape. This requirement again restricts the choice to plastic scintillators, of which BC-448M is the best choice for detecting charged particles. Choosing BC-448M

has the additional benefit of keeping the number of different materials low. We have not made a final material choice for the top and bottom veto scintillators yet. On the one hand, the material should be an ineffective neutron absorber and ideally detect X-rays and gamma rays with a high efficiency. For these reasons, some inorganic crystal scintillator would be an obvious choice. But such crystals have critical disadvantages: Most candidates have rather long decay times, some are intrinsically radioactive (thus producing background counts), and almost all are brittle and tend to cleave. We therefore still need to perform a trade-off study to select the best-suited material. Since the material thickness required to produce a sufficient signal intensity is about the same for all materials, the final choice of material does not impact the design much. We can thus safely defer the final decision until the detector layout optimization has been finalized (see Section 14.3.5).

The last critical material choice is that of the neutron absorber. Again, we restricted our evaluation to solid materials to reduce the system complexity. The most important material property to evaluate is the absorption cross-section, which is a measure of the probability of neutron capture. The larger the cross-section, the less material is required (on average) to stop and absorb a neutron. The choice was mostly restricted by the limited availability of many candidate materials. We decided to use B_4C (boron carbide), which is frequently used in control rods for fission reactors due to the wide absorption spectrum. B_4C is one of the hardest known materials and its mechanical properties make it an ideal match for our application.

14.3.4 Neutron Signatures

Figure 14.2 shows the signatures created in the CNS by neutrons of different energies and by charged particles entering the detector from the side or from the top. Both neutrons (blue tracks) and charged particles (red tracks) lose energy while traversing the detector and absorber materials. The energy-loss signatures they create in the detector, however, are very different. Neutrons of all energies interact only weakly with most materials and thus part with only little of their energy; this small energy loss is depicted by small circles in the figure. We can measure the energy deposited in active materials (i.e. in the thermal-neutron detectors, the moderators, and the veto scintillators) via the created scintillation light but must rely on modeling to estimate how much energy was deposited in passive materials (i.e., the absorbers and all structures). In the figure, detectable and invisible energy loss are symbolized

as full and open circles, respectively.

Neutrons of different energies create distinct energy-loss signatures in the CNS. Thermal neutrons pass through the lower veto detectors and are then captured by the lithium atoms in the lower GS20 scintillator, creating a scintillation signal equivalent to the excess energy of the ^{6}Li(n, α) reaction of 4.78 MeV (or about 6000 photons). This signal is many times higher than the one created by faster neutrons that are not captured by lithium atoms but instead lose energy through elastic collisions and is symbolized in Figure 14.2 by a large circle. There is a chance that neutrons of higher energies are captured by lithium atoms while they traverse the material as well. The additional energy they bring into the ^{6}Li(n, α) reaction is transferred to the reaction products (a tritium ion and an alpha particle) and converted into scintillation light, creating a signal that is larger than the 4.78 MeV excess energy of the reaction. A 1-MeV neutron, for example, would thus create a signal of 5.78 MeV. Thermal neutrons can therefore be identified by a characteristic energy loss of 4.78 MeV in the lower GS20 layer. Those thermal neutrons that are not captured enter a layer of boron carbide, whose large absorption cross-section ensures that they stop in this layer with almost 100% efficiency.

Epithermal and fast neutrons have a much lower absorption probability and continue to traverse the detector. They lose energy in the lower active moderator before entering the next layer of GS20. The length of the moderator must be chosen such that neutrons with energies in the relevant epithermal range are thermalized and thus have a high probability of being detected as thermal neutrons in the GS20 scintillator. Epithermal neutrons therefore can be identified via two signatures: They either traverse the first GS20 scintillator and moderator and then produce a thermal-neutron signal in the second GS20 layer, or they are captured in the first GS20 scintillator and produce a signal higher than that of a thermal neutron. In the first case, the kinetic energy of the neutron is given by the sum of the energy losses in the layers the neutron traverses before being captured (GS20, absorber, and moderator), with a some modeling required to estimate the invisible energy loss in the absorber. In the latter case, the kinetic energy can be measured directly as the excess over the energy freed up in the ^{6}Li(n, α) reaction.

Epithermal neutrons not captured in the second GS20 layer are absorbed in a second layer of boron carbide. Fast neutrons passing through are then further moderated by a second layer of BC-448M moderator, and before they enter the third layer of GS20. Since the energy range attributed to fast neutrons is rather large, a significant fraction of them will not be captured in the scintillator

but exit the detector through the top veto scintillators. There are hence four types of signatures for fast neutrons: (1) They traverse all previous scintillator and absorber layers and produce a thermal-neutron signature in the third (and last) GS20 layer; (2) they traverse all previous layers and produce a signal exceeding that of thermal neutrons in the third GS20 layer; (3) they are captured in either of the first two GS20 layers and produce a signal exceeding that of an epithermal neutron; or (4) they are not captured in any of the GS20 scintillators and pass through all detector layers. In the first three cases, the kinetic energy of the neutron is given by the sum of the detectable and invisible energy loss and the energy exceeding that of a thermal-neutron capture. In the last case, the kinetic energy of the neutron cannot be determined.

For both epithermal and fast neutrons there is also the possibility of being absorbed in a moderator or absorber layer, where they deposit a part of their energy in non-detectable form. Additionally, while traversing the spectrometer, neutrons with higher energies can be scattered out of the detector stack, generating a very similar signature. The two cases can be told apart by the additional detectable energy loss in the outer veto scintillator, which a neutron scattered out of the stack must traverse.

Charged particles with sufficient energy to enter the CNS (above a few MeV) may generate signals very similar in signature to neutrons, especially when they enter the detector stack from the side (see Figure 14.2). High-energy protons or nuclei can easily generate scintillation signals as large as or exceeding that of a thermal neutron. If a charged particle enters one of the GS20 scintillators from the side, it may be mistaken for a neutron whose energy loss in the moderator layer(s) was below the detection threshold. The main task of the veto scintillator tube is to reliably detect such events. Charged particles entering the detector stack from the top (or bottom) generate signals in the planar veto detectors and can thus be identified as well.

Table 14.3 summarizes the signatures neutrons of different energies generate in the CNS. For a reliable and accurate analysis of CNS data, these signatures must be understood well. To reconstruct the neutron energy spectrum on the lunar surface, it is crucial to know the detection efficiency for neutrons of different energies, what percentage of neutrons in each energy range creates a particular signature, and how many events are (on average) attributed a false signature. It is also crucial to understand the probability of a charged particle creating a neutron-like signature despite the presence of veto scintillators. The next two sections summarize the simulations we performed and data-analysis algorithms we developed to evaluate all these parameters.

Table 14.3: Tabular overview of signatures generated in the CNS by neutrons of different energy. x and y denote the additional energy of a neutron captured in flight that is converted into scintillation light in the ^{6}Li(n, α) reaction.

Neutron Energy	Signature	GS20 #1	Moderator #1	GS20 #2	Moderator #2	GS20 #3	Veto Tube
Thermal	1	4.78 MeV	-	-	-	-	-
	2	$\mathcal{O}(100\,\mathrm{keV})$	-	-	-	-	-
Epithermal	1	$4.78\,\mathrm{MeV} + x$	-	-	-	-	
	2	$\mathcal{O}(100\,\mathrm{keV})$	$\mathcal{O}(100\,\mathrm{keV})$	-	-	-	-
	3	$\mathcal{O}(100\,\mathrm{keV})$	$\mathcal{O}(100\,\mathrm{keV})$	4.78 MeV	-	-	-
	4	$\mathcal{O}(100\,\mathrm{keV})$	$\mathcal{O}(100\,\mathrm{keV})$	$\mathcal{O}(100\,\mathrm{keV})$	-	-	-
	5	$\mathcal{O}(100\,\mathrm{keV})$	-	-	-	-	$\mathcal{O}(100\,\mathrm{keV})$
	6	$\mathcal{O}(100\,\mathrm{keV})$	$\mathcal{O}(100\,\mathrm{keV})$	-	-	-	$\mathcal{O}(100\,\mathrm{keV})$
Fast	1	$4.78\,\mathrm{MeV} + y$	-	-	-	-	-
	2	$\mathcal{O}(100\,\mathrm{keV})$	$\mathcal{O}(100\,\mathrm{keV})$	$4.78\,\mathrm{MeV} + y$	-	-	-
	3	$\mathcal{O}(100\,\mathrm{keV})$	$\mathcal{O}(100\,\mathrm{keV})$	$\mathcal{O}(100\,\mathrm{keV})$	$\mathcal{O}(100\,\mathrm{keV})$	4.78 MeV	-
	4	$\mathcal{O}(100\,\mathrm{keV})$	$\mathcal{O}(100\,\mathrm{keV})$	$\mathcal{O}(100\,\mathrm{keV})$	$\mathcal{O}(100\,\mathrm{keV})$	$4.78\,\mathrm{MeV} + y$	-
	5	$\mathcal{O}(100\,\mathrm{keV})$	$\mathcal{O}(100\,\mathrm{keV})$	$\mathcal{O}(100\,\mathrm{keV})$	$\mathcal{O}(100\,\mathrm{keV})$	$\mathcal{O}(100\,\mathrm{keV})$	-
	6	$\mathcal{O}(100\,\mathrm{keV})$	-	-	-	-	$\mathcal{O}(100\,\mathrm{keV})$
	7	$\mathcal{O}(100\,\mathrm{keV})$	$\mathcal{O}(100\,\mathrm{keV})$	-	-	-	$\mathcal{O}(100\,\mathrm{keV})$
	8	$\mathcal{O}(100\,\mathrm{keV})$	$\mathcal{O}(100\,\mathrm{keV})$	$\mathcal{O}(100\,\mathrm{keV})$	-	-	$\mathcal{O}(100\,\mathrm{keV})$
	9	$\mathcal{O}(100\,\mathrm{keV})$	$\mathcal{O}(100\,\mathrm{keV})$	$\mathcal{O}(100\,\mathrm{keV})$	$\mathcal{O}(100\,\mathrm{keV})$	-	$\mathcal{O}(100\,\mathrm{keV})$
	10	$\mathcal{O}(100\,\mathrm{keV})$	$\mathcal{O}(100\,\mathrm{keV})$	$\mathcal{O}(100\,\mathrm{keV})$	$\mathcal{O}(100\,\mathrm{keV})$	$\mathcal{O}(100\,\mathrm{keV})$	$\mathcal{O}(100\,\mathrm{keV})$

14.3.5 Layout Optimization

We performed extensive Monte Carlo simulations using the Geant4 simulation toolkit to optimize the detector layout.[3] The primary Geant4 physics list we used is QGSP_BERT_HP, which includes a data-driven high-precision neutron package that simulates the transport of neutrons through matter below 20 MeV and down to thermal energies. We used two different particle sources: a neutron source producing a flat energy distribution to simulate the detector response to neutrons and a charged-particle source producing protons and helium ions to simulate the detector response to GCR background radiation. The neutron source created neutrons directly below the CNS with velocity vectors pointing straight upwards; the charged-particle source created ions randomly on a sphere surrounding the detector with velocity vectors following a cosine law to create an isotropic particle flux inside the sphere.

The primary goal of the detector-layout optimization was to understand the effect of changing the height of the detector layers (thermal-neutron sensitive scintillators, active moderators, and absorbers) within the constraints imposed by the LUVMI-X reference mission. Initial simulations showed that thermal neutrons can be detected with 98.8% efficiency by a GS20 scintillator of 7 mm thickness, with little improvement for thicker layers. We therefore fixed the height of all three GS20 layers to 7 mm to lower the complexity of the optimization. Similarly, a 2 mm layer of B_4C is able to absorb close to 100% of thermal neutrons that were not already detected, and therefore absorbed, in the GS20 scintillator. Based on the mechanical constraints for the CNS, the remaining combined thickness for the two moderator layers is 120 mm.

In our simulations, we varied the height of the two moderators between 30 mm and 60 mm and first investigated the classification efficiency for neutrons of epithermal and fast energies. The classification efficiency measures how well the detector can correctly identify a neutron's energy regime (thermal, epithermal, and fast) based on the signatures listed in Table 14.3. We did not include any detector efficiencies or other (noise) effects in the simulation. Figure 14.3 shows the results of the optimization. As expected, the second moderator has very little influence on the system's ability to identify epithermal neutrons, as the majority of them are detected in the second GS20 layer. The first layer marginally increases the efficiency by about 0.2%. For fast neutrons, the increase is more pronounced at roughly 2.5% but only depends on the total

[3] The simulations were performed in large parts by Patrick Wastian for his Master's thesis [Was21] under the supervision of me and my colleague Thomas Pöschl.

moderator height, with little influence of the individual layer heights. The overall classification efficiency for fast neutrons is lower than for epithermal ones (62.8% compared to 97.2%), which is due to the higher probability of fast neutrons being scattered out of the detector stack and therefore being misidentified as epithermal ones.

We also investigated the absolute detection efficiency for epithermal and fast neutrons as a function of moderator height. The results of this analysis are shown in Figure 14.4. Agin, the first moderator primarily influences the efficiency for epithermal energies, and the total moderator height determines the efficiency for fast energies. The increase for epithermal energies is rather low (2.5%); for fast neutrons, we observe a more substantial increase of about 7%. We therefore concluded that total moderator height should be as large as possible given the mechanical constraints of the project, in order to maximize the efficiency for fast neutrons. For simplicity, the two moderators can be chosen to have the same height, as the increase in classification efficiency for epithermal neutrons is only marginal.

Finally, we investigated the required geometries and thicknesses of the veto scintillators that are just to distinguish events caused by neutrons from those caused by charged particles. For the tube-like scintillator surrounding the detector stack, we found that a thickness of 3 mm should be sufficient to reliably detect any charged particle of cosmic or solar origin. The analysis also confirmed that two 'endcap' veto detectors on the top and the bottom of the stack are required to prevent ions from hitting the detector stack without traversing at least one veto scintillator.

14.3.6 Simulated Performance

Based on the simulations described in the previous sections, we analyzed the expected performance of the CNS. The results for the final configuration (GS20 thickness of 7 mm, absorber thickness of 2 mm, and moderator height of 60 mm each) are shown in Figure 14.5 in the form of so-called confusion matrices. In these matrices, the true energy class (thermal, epithermal, and fast) of a neutron event is plotted against the one reconstructed from detector data. Entries on the diagonal therefore correspond to the fraction of events that was analyzed correctly, while off-diagonal entries correspond to incorrectly identified events. For thermal energies, the CNS is able to classify more than 98% of events correctly, yielding an overall identification efficiency of almost 90%. For epithermal energies, the classification is even a bit better at more

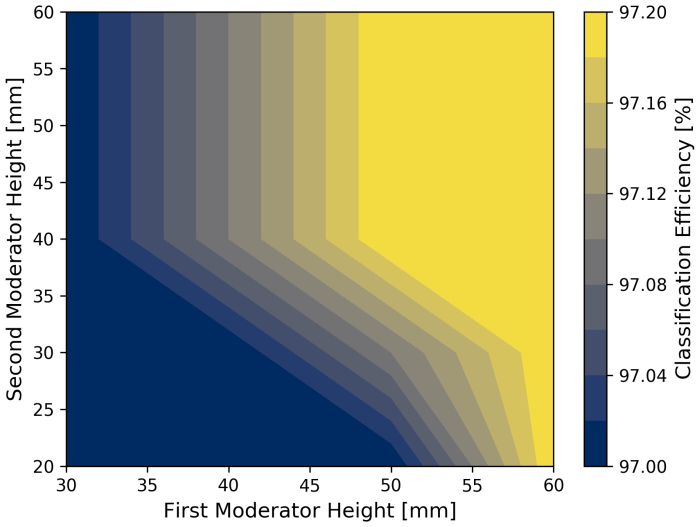

(a) Epithermal

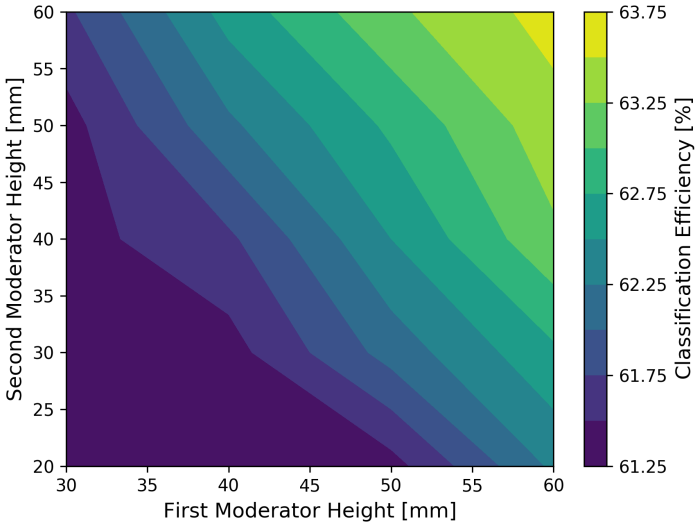

(b) Fast

Figure 14.3: Classification efficiencies for epithermal and fast neutrons as a function of moderator height. From [LPW21].

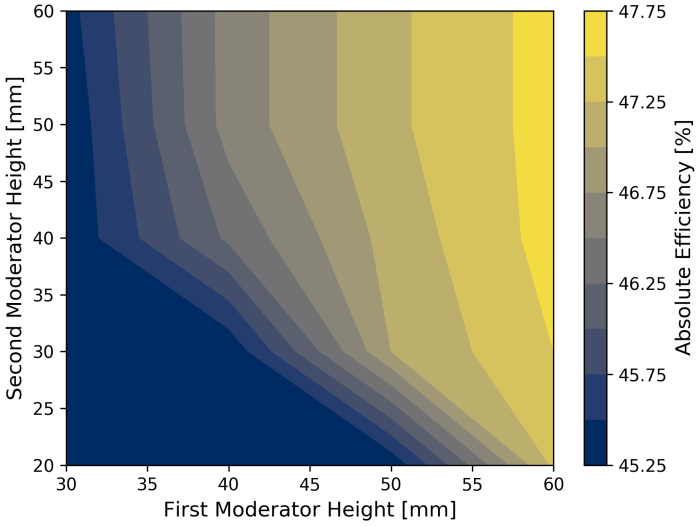

(a) Epithermal

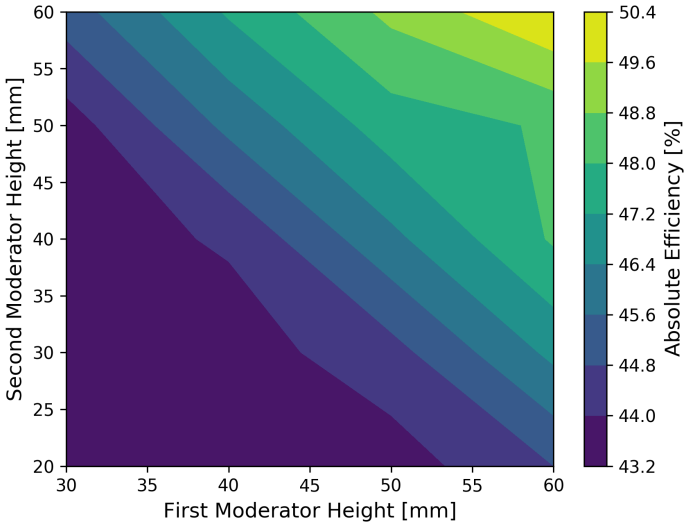

(b) Fast

Figure 14.4: Absolute detection efficiencies for epithermal and fast neutrons as a function of moderator height. From [LPW21].

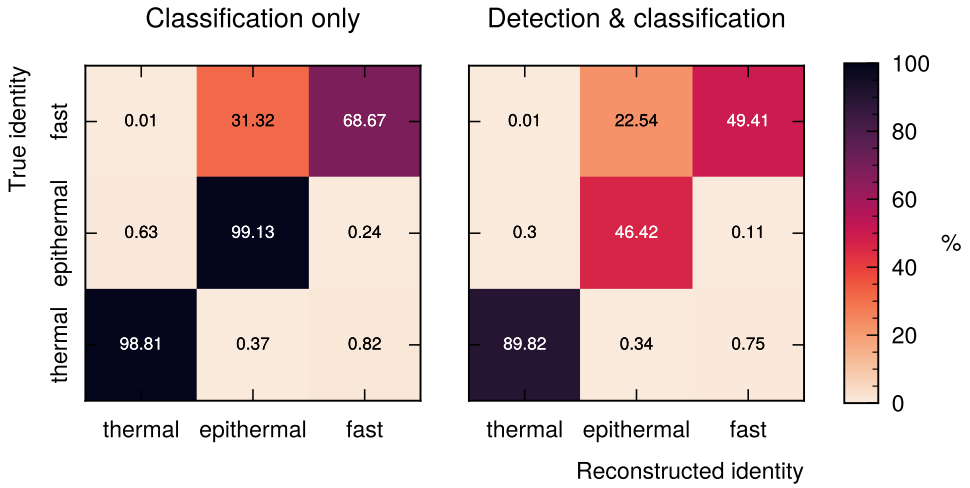

Figure 14.5: Confusion matrices showing the optimized overall performance of the CNS based on simulated events generated with Geant4. The left panel shows only the accuracy of the energy classification. The right panel shows the combined detection and classification efficiencies, thus giving the absolute fraction of incident neutrons that is correctly or incorrectly identified. Adapted from [LPW21].

than 99%, but the detection efficiency drops significantly, giving a combined value of about 46%. This is to be expected, as epithermal neutrons have a much lower interaction cross-section (i.e., interaction probability) than thermal ones. Interestingly, the classification efficiency for fast neutrons drops to about 69% but the combined value is slightly higher (49%) due to a substantially higher detection efficiency. We also observe a larger fraction of fast-neutron events that are being misidentified as epithermal neutrons. This is also to be expected, as fast neutrons have a significant probability of being scattered out of the detector stack, therefore producing signatures resembling those of epithermal energies. With proper calibration of the instrument, this effect can be compensated and thus does not present an issue.

Test and calibration campaigns with neutron sources will obviously be required to verify the simulation results, but the overall performance presented here is surprisingly good for an instrument as simple and compact as the CNS. The absolute detection efficiencies for epithermal and fast neutrons are much higher than we had originally anticipated and should be sufficient for collecting a statistically meaningful data set even on moving surface vehicles.

14.4 The Charged-Particle Telescope

To measure GCR, SEP, and solar-wind particles, the CPT must be sensitive to charged particles over a wide range in mass and energy. The lower sensitivity limits in energy are 10 MeV and 50 MeV/n for protons and heavier nuclei, respectively. The challenge of designing the CPT is making it as small and compact as possible while still achieving an adequate energy range and resolution. For a study of the interaction between GCR and the lunar surface the MeV–to–GeV region is of particular importance.

14.4.1 Detector Concept

For the CPT, we opted for an integrated design: A simple telescope comprised of three silicon pixel detectors encloses a calorimeter stack made from scintillators, the most widely used class of material for such detectors. Figure 14.6 shows a schematic overview of the design, with cosmic-ray and solar particles entering the detector stack from the right.

The three silicon-based tracking detectors are shown in red; two are located at the top of the stack to provide directional information for particles with energies too low to traverse the full calorimeter. The third detector is placed on the bottom, giving a longer lever arm for achieving a better angular resolution. The calorimeter between the tracking detectors consists of multiple layers of plastic scintillators (shown in blue) that measure the energy loss of particles traversing the stack. If a particle deposits its full energy in the calorimeter (i.e. it stops), its total energy can be determined. For particles not stopping in the detector, we extrapolate the characteristic energy-loss curve to be able to determine their total energy, albeit with a larger uncertainty. To maximize the energy range the CPT is sensitive to, we placed layers of passive material between the scintillator layers (shown in gray). Particles lose energy more efficiently in these so-called absorbers, therefore enlarging the maximum energy a particle stopping in the CPT can have. To determine a particle's identity, we just like for the ADU use the method of Bragg curve spectroscopy, exploiting a particle's energy-loss profile to unambiguously identify it. The technique works for a limited energy range and is the primary reason for the segmentation of the calorimeter's detection volume. The energy-loss measurements of the silicon-pixel detectors can be used in addition to those of the scintillators.

Figure 14.6: Signatures of charged particles with different energies in the CPT. The particles (red tracks) traversing the detector lose energy in the detector material. The circles along their tracks symbolize this energy loss: the larger the circle, the more energy the particle deposits in a particular layer of the detector. Filled circles denote energy that can be measured in the form of scintillation photons, open circles denote energy that cannot be measured. The veto scintillator fully encloses the sensor stack but is only shown in parts for clarity. From [LPW21].

Similar to the CNS, the sensor stack of the CPT is enclosed in a tube made from plastic scintillator (shown in green) that allows us to detect particles being scattered out of it or entering from the side. Additional rings of scintillator around the tracking detectors on the top and the bottom of the stack ensure that particles not going through the telescope layers can also be identified.

To be able to measure albedo protons with energies below 1 MeV, we added what we call the low-energy section of the CPT (LE-CPT): a stack of three planar silicon detectors forming a separate telescope for very low-energy particles. The LE-CPT can provide up to three measurements of the LET of particles travelling upwards and also further extends the energy range that the calorimeter can cover. The detection of albedo radiation requires that the LE-CPT can be directly exposed to the lunar surface without any additional material in between.

14.4.2 Materials

To keep the overall design of the LCNS as simple as possible, we opted to use as few detector materials as possible. The CPT calorimeter is therefore made from the same plastic scintillator material we use for the moderator layers of the CNS, as is the veto scintillator. We therefore evaluated the same materials already presented in Table 14.2 and ultimately chose BC-448M. The choice of absorber materials was strongly guided by the simulation-based optimization process. The range of commercially available silicon-pixel detectors suitable for use in space and with approximately the right dimensions is very limited. We chose the TimePix3 (or TimePix4) detectors [Poi+14; BCL20] that have already been used in radiation monitors deployed aboard multiple spacecraft in Earth orbit [Sto+15; Gra+16]. NASA will also rely on TimePix-based detectors for monitoring crew exposure during the upcoming Artemis missions to the Moon, and has already done so during the first in one (Artemis I) in late 2022 [Sto+23].

14.4.3 Event Signatures

Figure 14.6 shows the signatures of events in the CPT. Charged particles (red tracks) traversing the detector lose energy in the detector material. The circles along their tracks symbolize this energy loss: the larger the circle, the more energy the particle deposits in a particular layer of the detector. Filled circles denote energy that can be measured in the form of scintillation photons, open

circles denote energy that cannot be measured. The figure also qualitatively shows how Bragg curves, i.e., the increasing energy loss toward the end of a stopping particle's track, would look like in the detector. As in the RadMap Telescope's ADU, recording these energy-loss profiles allows us to identify particles and measure their energy.

14.4.4 Detector Layout Optimization

As with the CNS, we also performed extensive Monte Carlo simulations using the Geant4 simulation toolkit to optimize the layout of the CPT. Using the same physics lists, we simulated the signatures of different ions in the detector to understand how thick the individual scintillator and absorber layers need to be. We used a particle source covering the full range of cosmic-ray ions and energies; the source created ions randomly on a sphere surrounding the detector with velocity vectors following a cosine law to create an isotropic particle flux inside the sphere.

To understand the performance of the detector, we used reconstruction algorithms that are simple enough to implement on a microcontroller, in order to not come up with a design that requires complicated algorithms that we would later not be able to implement in the CDAS. These algorithms use a combination of the total energy deposited by a particle in the detector and its energy loss in selected detector layers (for details, see [Was21]). We also fixed the number of active scintillator layers in the stack to 12; assuming the use of one 16-channel read-out chip, the remaining four channels are reserved for reading out the veto scintillator. During the optimization process, we concluded that the use of three different kinds of absorber layers would deliver the desired performance: copper layers of two different thicknesses and yet thicker layers of lead.

14.4.5 Simulated Performance

We used the simulations described in the previous section to determine the expected performance of the CPT. Figures 14.7 and 14.8 visualize the identification accuracy for stopping and through-going particles, respectively. We limited to our analysis to elements lighter than neon. The latter we only included so that any edge effects would not occur for fluorine. I again present the data in the form of confusion matrices to show to what element misidentified events were assigned. The accuracy for stopping light ions is close to 100%, only

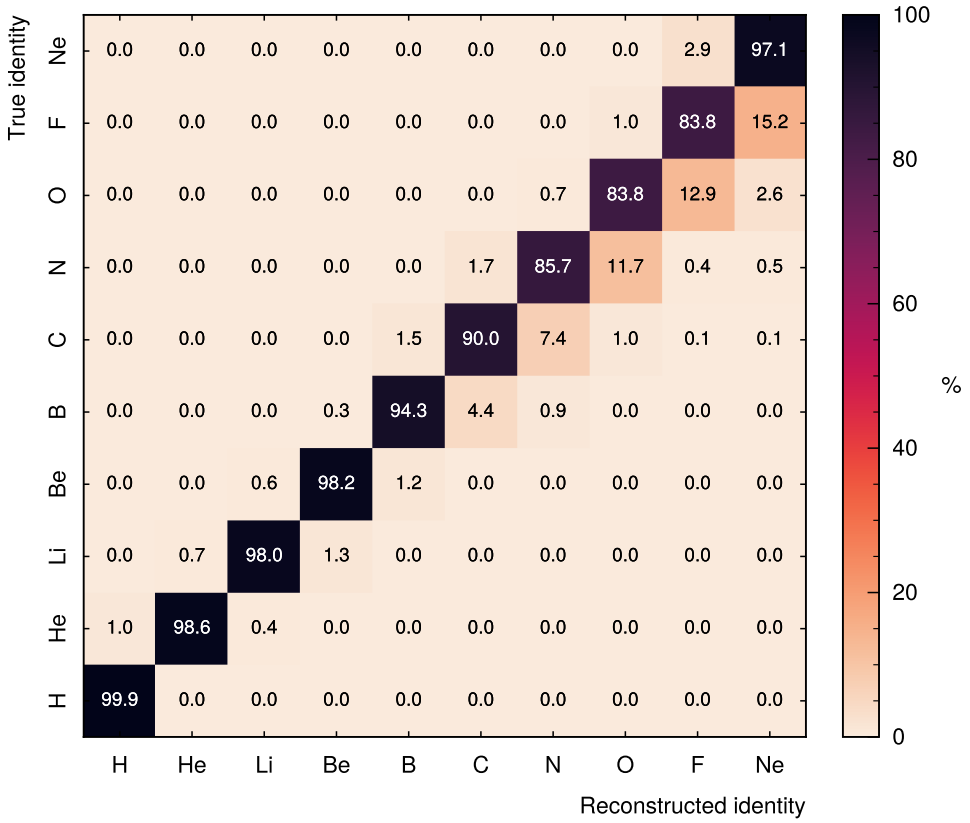

Figure 14.7: Identification accuracy of light GCR nuclei stopping in the sensor stack of the CPT. Adapted from [LPW21].

dropping to below 90% for elements beyond carbon. For higher Z_1, misidentified events are mostly assigned to heavier elements. A classification allowing $\Delta Z = 1$ would yield a nearly 100% accuracy for all elements considered.

Figure 14.8 shows that the situation is qualitatively similar for nuclei that do not fully stop in the detector. The overall accuracy is a little lower, though it is still larger than 99% and 95% for hydrogen and helium, respectively. Interestingly, it jumps from below 80% to almost 95% between oxygen and fluorine. We have not yet fully understood the origin of this effect. Similar to the CNS, the overall performance of the CPT is surprisingly good for a detector of such small size. For through-going heavier elements, a classification with $\Delta Z = 1$ or $\Delta Z = 2$—similar to our particle identification for the RadMap

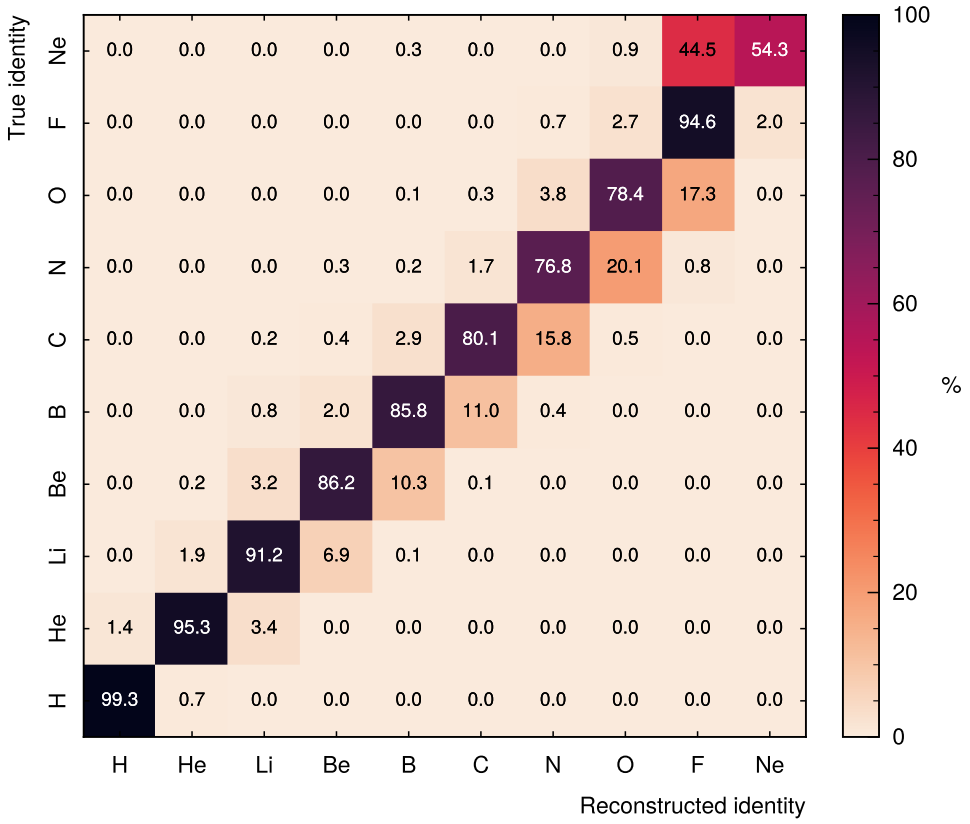

Figure 14.8: Identification accuracy of light GCR nuclei passing through all layers of the CPT's sensor stack. Adapted from [LPW21].

Telescope—will likely be required to keep classification efficiencies in the range of 80% to 90%. For the purposes of characterizing the radiation environment on the lunar surface, this approach is certainly acceptable. And for referencing against the measurements of the CNS, hydrogen and helium are the most important elements due to their abundance that is orders of magnitude higher than those of other nuclei.

14.5 Mechanical and Electrical Design

The main objective of the LUVMI-X project was to raise the TRL of the technologies critical to the rover and to its instrumentation. For the LCNS, we therefore concentrated on developing a robust overall (mechanical) design to show that the capability requirements listed in Section 14.1 above can be fulfilled by an instrument that meets the constraints of the reference mission. We did, however, only develop a detailed design of the critical parts of the LCNS, which are the two main sensors. For all other systems, including most of the electronics, we only performed design studies to identify solutions that either have flight heritage or that we have worked with ourselves before. In this section, I therefore focus on the description of the CNS and CPT designs, and only briefly summarize the architecture of the CDAS and the SC. We have not investigated design options for the NGD, LED, and GPD.

14.5.1 Compact Neutron Spectrometer

As they both have a telescope-like, linear layout, we tried to keep the structural design of the CNS and the CPT as similar as possible. This would in particular allow us to keep the dimensions of the veto scintillator approximately the same, significantly reducing the manufacturing costs.

Figure 14.9 shows a cross-sectional view of the CNS design. The sensor stack—consisting of the three GS20 scintillator blocks, two longer blocks of plastic scintillator (BC-408 or BC-448M) acting as active moderators, and two neutron absorbers made from boron carbide—are enclosed in a lightweight aluminum structure. This structure consists of two half shells that are screwed together after the scintillator and absorbers were inserted. Besides providing structural integrity, the aluminum shells are also light-tight, i.e., they prevent external light from entering the sensor stack. Thin aluminum windows prevent optical crosstalk between the GS20 and plastic scintillators. The scintillators are read out with Hamamatsu S13360-2050VE and S13360-3050VE SiPMs [HAM16] that are optically attached using EPO-TEK 301 epoxy through cutouts in the aluminum shell. They are soldered onto a PCB that is mounted to the back of the sensor stack (and is thus not visible in Figure 14.9).

The veto scintillator is a tube with rounded edges (see Figure 14.17) and a wall thickness pf 5 mm. It completely encloses the sensor stack and is secured in place with end caps that attach to the aluminum shell of the stack. These end caps also hold two layers of CsI scintillator each and provide attachments

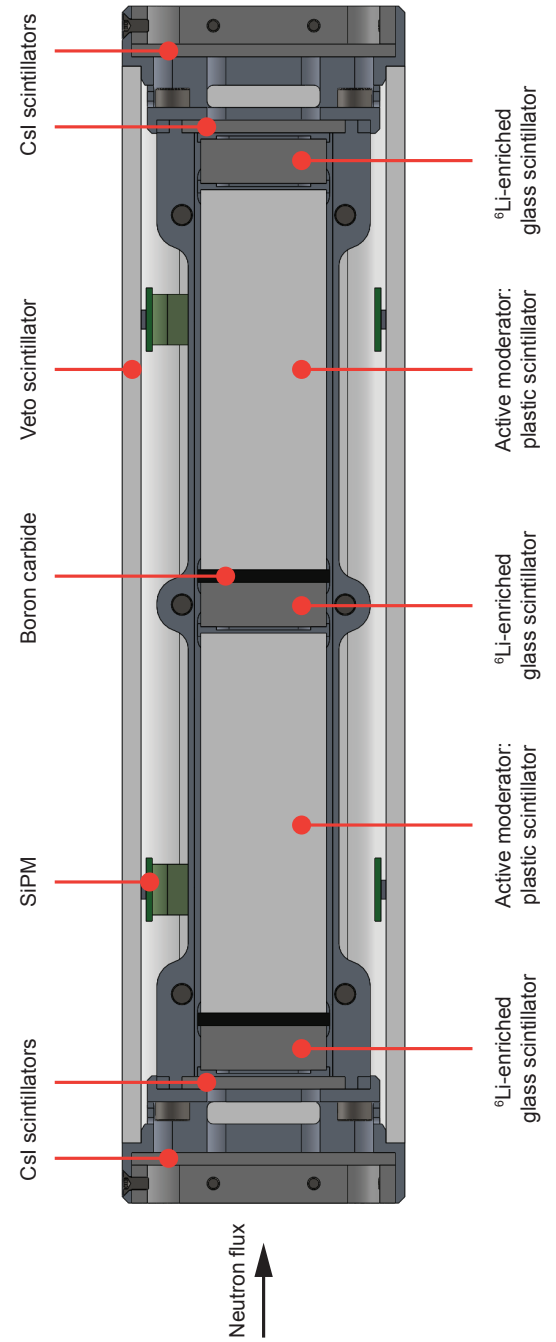

Figure 14.9: Cross-sectional view of the design of the CNS, showing the three blocks of GS20 ^{6}Li-enriched glass scintillator with plastic scintillators acting as active moderators in between. The tube-like veto scintillator is likewise made from plastic scintillator (BC-408 four ground tests and BC-448M for the flight instrument). The SiPMs for the veto tube are mounted on rigid-flex PCBs and glued to it from the inside; the photosensors for reading out the main scintillators are located behind the sensor stack are thus not visible. Neutrons traverse the sensor stack from the left.

points for the whole assembly. The veto is read out by 12 Hamamatsu S13360-6050VE SiPMs [HAM16], which are mounted on rigid-flex PCBs and glued to it from the inside.

14.5.2 Charged-Particle Telescope

The design of the CPT, shown in Figure 14.10, is very similar to that of the CNS. 12 layers of plastic scintillator (BC-408 or BC-448M) are enclosed in an aluminum structure made of two half shells. The first seven absorber layers are made of copper (three with a thickness of 2 mm and four with one of 4 mm), the last three are made of lead. The veto scintillator is nearly identical to that of the CNS, except that it is shorter. The TimePix3 silicon-pixel detectors are embedded into the mechanical end caps attaching the veto scintillator to the main sensor stack. We use the same models of SiPMs of Hamamatsu's S13360 series as for the CNS to read out the various scintillators.

For the LUVMI-X project, we focused on the development of the main part of the CPT because its extension for detecting low-energy albedo particles, the LE-CPT, was deemed optional by the team. We therefore did not integrate it into the main sensor stack shown in Figure 14.10. Instead, we performed a limited design study to identify candidate components for a future detailed design. Figure 14.11 shows the result of this study in the form of an approximate model of a possible detector configuration. We found a number of suitable commercially available silicon sensors that can be used for the direct detection of charged particles, among them the S14536 and S14537-series large-area PIN diodes by Hamamatsu [HAM23a]. In the model, we placed three such planar detectors on top of each other with minimal distance in between.

Since the detector stack must be exposed directly to the lunar surface (i.e., without any material in between) to maximize its acceptance to low-energy particles, it is mounted to a baffle-like entrance window that is 10 mm deep. This protects it against inadvertent impacts or other mechanical influences that could damage the diodes. It does, however, not prevent abrasive lunar dust (regolith) [Col+07; ZDB23] kicked up by a moving rover from reaching the lowermost sensor. As this should be absolutely avoided, the LE-CPT is protected by a rotating lid (see Figure 14.12) whenever the rover moves.

Figure 14.10: Cross-sectional view of the design of the CPT. TimePix3 silicon-pixel detectors are mounted on the left and right ends of the sensor stack. The calorimeter consists of alternating layers of plastic scintillator and passive absorber (copper and lead) with increasing thickness from right to left. The veto scintillator is nearly identical to that of the CNS, except that it is shorter. Again, the SiPMs for reading out the main scintillators are located behind the sensor stack are thus not visible. Cosmic-ray particles traverse the sensor stack from the right with a nearly isotropic angular distribution over the full hemisphere. Albedo particles from the lunar surface arrive from the left.

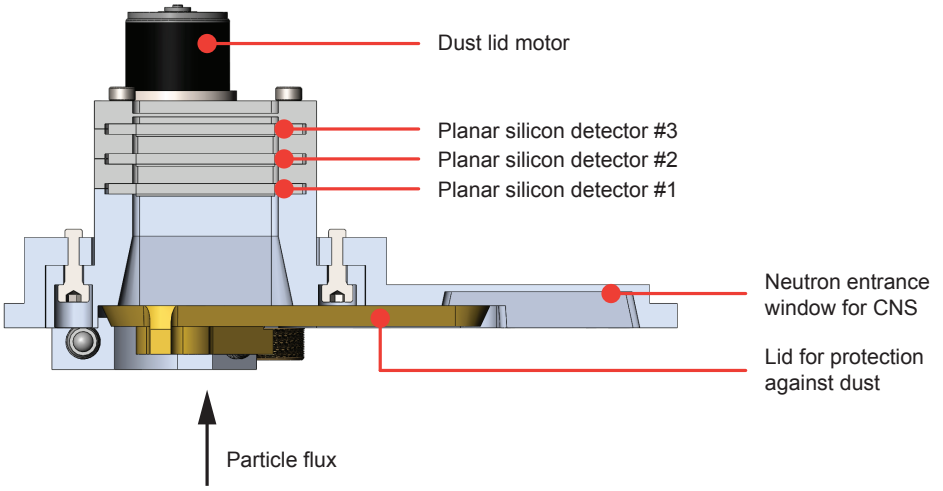

Figure 14.11: Cross-sectional view of the design of the LE-CPT, showing the three planar silicon detectors behind a 10-mm deep entrance window.

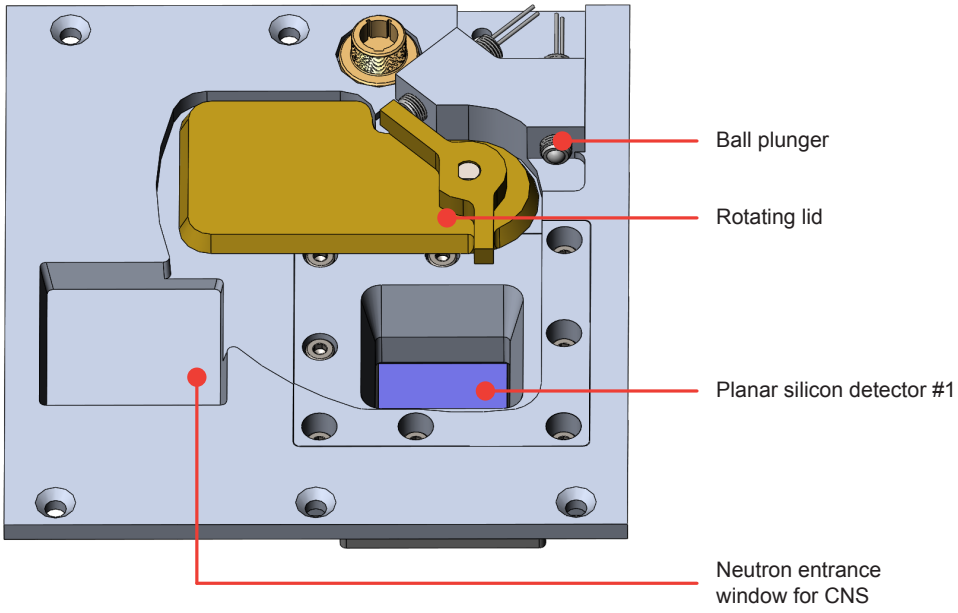

Figure 14.12: Rotating lid to protect the LE-CPT from abrasive lunar dust kicked up by a moving rover. Two ball plungers act as end switches for the rotation.

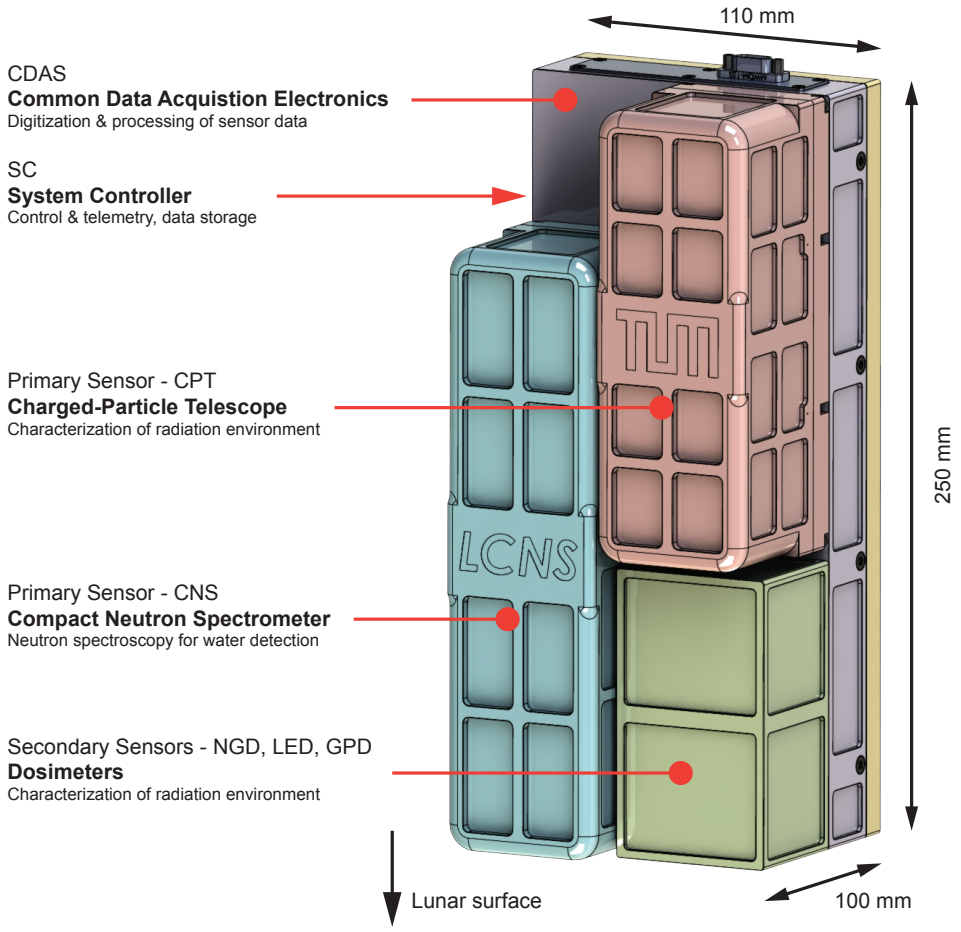

Figure 14.13: Rendering of the LCNS version without LE-CPT in flight configuration. The required external thermal protection is not shown. The color coding is the same as in the schematic system architecture shown in Figure 14.1. Adapted from [LEP22].

14.5.3 Overall (Mechanical) Design

Figure 14.13 shows a rendering of the overall LCNS instrument without LECPT in flight configuration. It does not show the external thermal protection required for surviving the lunar surface environment, especially during the night. During the study, we did not invest much effort into miniaturizing systems beyond the two main detectors, but were able to fit the instrument in an envelope of 250 mm by 110 mm by 100 mm. Its mass should be below 5 kg, including margins of 10% to 40% for most subsystems. Both the volume and the mass of the instrument can likely be further reduced. The backplane of the instrument is formed by the SC and the CDAS, which are housed in a common aluminum structure that also provides the external electrical interfaces and the attachment points for the instrument. The CNS and CPT are both housed in their own aluminum compartments that are attached directly to the main housing. The three dosimeters (NGD, LED, and GPD) share a common compartment. All structural and housing components are made from corrosion-resistant 7075 aluminum alloys and are anodized for increased surface hardness.

14.5.4 Electrical Design

The avionics and data acquisition of the LCNS consist of two primary subsystems: the system controller (SC) and the common data acquisition system (CDAS). Even though the sensors' front-end electronics are mostly embedded directly into them, we logically see them as part of the CDAS, as they are a core part of the data acquisition. The BVC and the motor controller are subsystems with only minimal integration into the SC or CDAS, and they would most rely on design heritage from the RadMap Telescope. I therefore do not describe them here.

System Controller

A schematic overview of the SC is shown in Figure 14.14. Central to the SC is a radiation-hardened (micro)processor. We selected and tested the VA41620 microcontroller manufactured by Vorago Technologies, which is a space-qualified variant of the ARM Cortex-M4. The processor is supplemented by three memory components: a low-capacity MRAM chip for storing the processor's program and operating system, a radiation-hardened SDRAM IC as main working memory, and a radiation-hardened NAND flash for storing data.

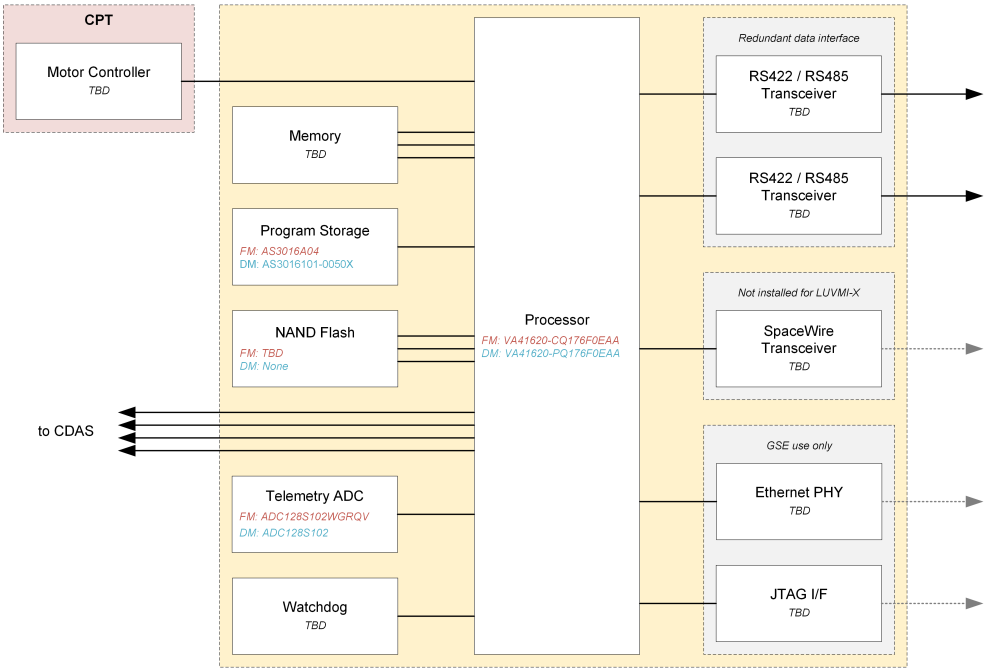

Figure 14.14: Schematic overview of the SC, which is built around a radiation-hardened variant of the ARM Cortex-M4 microcontroller. All critical components are space-qualified to ensure reliable operations in the lunar surface environment.

Choosing MRAM for storing the processor program is motivated by the fact that its underlying technology is intrinsically radiation-hard, i.e., radiation cannot alter the physical state of memory bits at all. This ensures that a so-called 'golden' copy of the program is preserved at all times.

An external watchdog circuits acts as the system's main supervisor and resets the SC in case of execution errors. A low-power ADC with a low sampling rate digitizes the signals of several housekeeping sensors, mostly for temperature monitoring throughout the instrument. The SC communicates with the motor controller of the dust cover via a low-level digital interface and with the CDAS via a yet-to-be-specified parallel interface. The main data interface to the rover's payload data bus is realized via redundant radiation-hardened RS-422/RS-485 transceivers. For potential flight opportunities aboard other landers or rovers, we decided to also include a SpaceWire interface, which would not be installed for the LUVMI-X reference mission. Ethernet and JTAG

interfaces are available for ground use, in particular for programming and monitoring the SC during integration and testing of the instrument.

Common Data Acquisition System and Front-End Electronics

Figure 14.15 shows a schematic overview of the CDAS. I arranged all sensors and their front-end electronics on the left-hand side of the figure and the interface to the SC on the right-hand side. For the CPT and the CNS, we use the same type of ASIC to digitize the signals of the SiPMs that we already used for the RadMap Telescope's read-out electronics. For easier reference, I again provide a brief summary of its characteristics here (see Section 10.4 for details): The IDE3380 (see Figure 10.8) is a 16-channel ASIC with a programmable parallel input stage to shape the SiPM signals to a length suitable for the built-in ADC operating at 50 ksps. Signals are multiplexed internally before being fed to the ADC to achieve a low power consumption of 30 mW per IC; the multiplexed signal is also available on an output pin to be used with an external ADC running at a higher sampling rate, if required. For high data rates, the outputs of the parallel input stage are also available of individual outputs, such that a system with no multiplexing of signals can be constructed. For the LCNS, we plan to use the internal ADC to keep the power consumption as low as possible. The IDE3380 is controlled via an SPI interface and the ADC data is made available via a single-ended serial output. The IC is a space-grade component that was developed under contract for ESA.

The CPT is equipped with two additional front-end ICs for digitizing the signals of the Silicon-Pixel Sensor (SiPX) and the Planar Silicon Sensors (SiPL). A component evaluation to identify suitable candidate ICs was not completed within the project timeframe. Since only a few sensor channels are required, the front-end electronics of the three dosimeters are a lot simpler than those of the CPT and the CNS. We use radiation-hardened ADCs with discrete input and shaper stages to digitize the signals of the SiPMs of the dosimeters. The ADCs are connected via low-level digital interfaces to the CDAS.

Due to the high number of (serial) interface and the fact that pre-processing and analysis of the data must happen in real-time, we decided to use an FPGA as the core processing component of the CDAS. A lot of our prototyping work is performed on SRAM-based devices, mostly those manufactured by AMD (formerly Xilinx), but the code required for our purposes can in principle run on any other technology as well. SRAM-based FPGAs generally are the most powerful and versatile devices on the market, but suffer the disadvantage of a

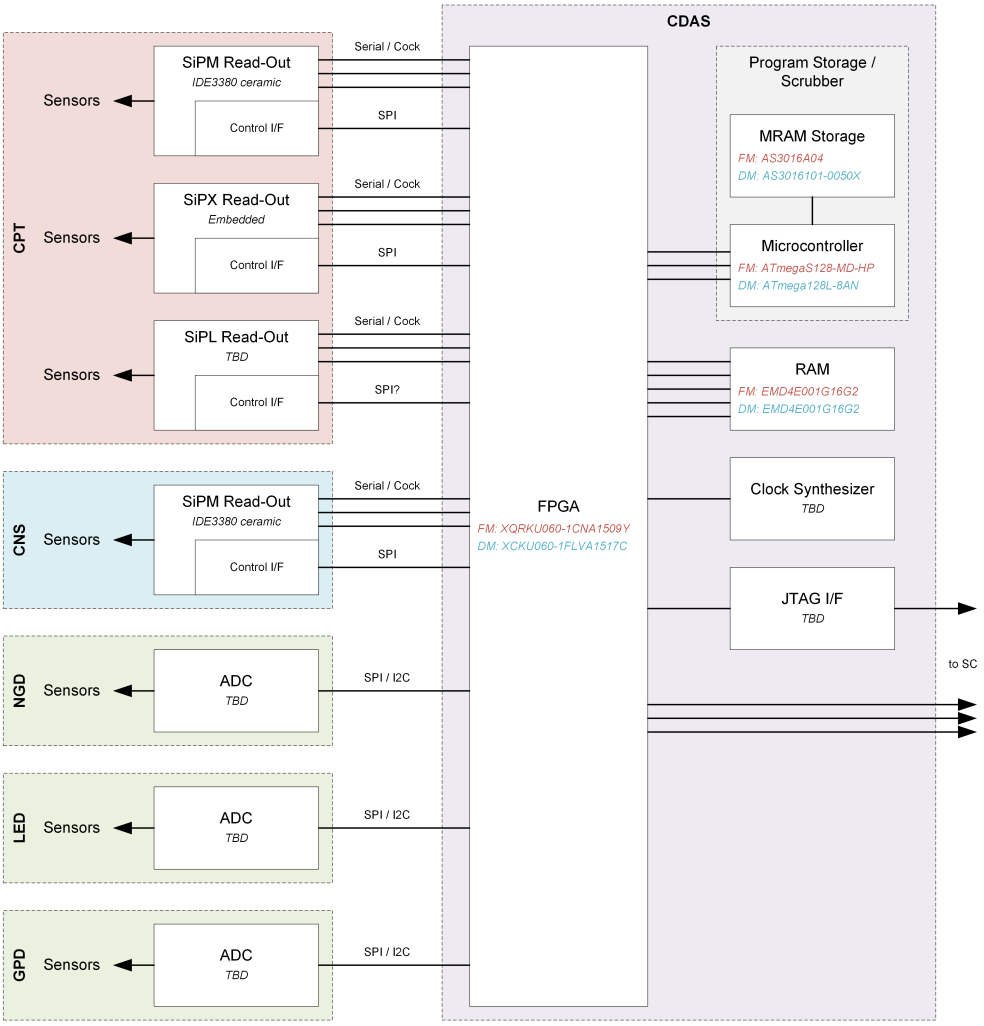

Figure 14.15: Schematic overview of the CDAS. At its heart is a radiation-hardened variant of AMD's Kintex Ultrascale FPGA. For the CNS and the CPT, we rely on the IDE3380 ASIC for the read-out of the SiPMs; we previously used the chip successfully for the RadMap Telescope.

fairly large susceptibility to radiation effects. AMD has released a radiation-hardened version of the Kintex Ultrascale series (the XQRKU060), which should perform adequately in terms of radiation hardness. Alternatively, we could use a flash-based FPGA that is less susceptible to radiation effects.

Similar to the SC, we use MRAM to store the FPGA program to prevent damages to the program from radiation effects. In addition, a small radiation-hardened microcontroller acts as a scrubber and can (partially) reconfigure the FPGA while it is operational. The FPGA may be equipped with additional external memory in the form of an SDRAM IC to improve its data-handling capabilities. The CDAS communicates with the SC via a yet-to-be-specified parallel interface. Direct access to the FPGA during integration and testing is possible via a JTAG interface.

14.6 Test Campaign at Paul Scherrer Institute

Unfortunately, the funding foreseen for test campaigns in the budget of the LUVMI-X project was limited. Much of the project was also performed during the Covid-19 pandemic, which meant that our ability to travel was severely limited. Most impactful, though, was the complete shutdown of the FRM II research reactor at our own university, which completely thwarted our plans for testing the CNS with neutrons. Our ability to investigate the real-world performance of the detector concepts we developed was therefore severely limited. Luckily, though, we were once again granted access to the πM1 beamline of PSI for detector for a variety of detectors and thus were able to at least perform some model verifications.

Figure 14.16 shows the prototype of the CPT that we used for testing at PSI. The upper panel shows that the main structure of the sensor stack was almost identical to the one shown in Figure 14.10, except that we did not use a through-going cutout for the scintillators and absorbers. Instead, we milled an individual compartment for each layer directly into the structure, thus improving the accuracy of the mechanical placement of each of them. The walls between the compartments add about 4 mm of aluminum to the thickness of the lead layers, which for sure does not negatively impact the calorimeter's performance. More important is that they block the path for optical crosstalk. For the absorber layers made of copper, we simply produced a respective insert made from copper. The middle panel shows the scintillators and lead layers integrated into one of the half shells. Due to material shortages, we were

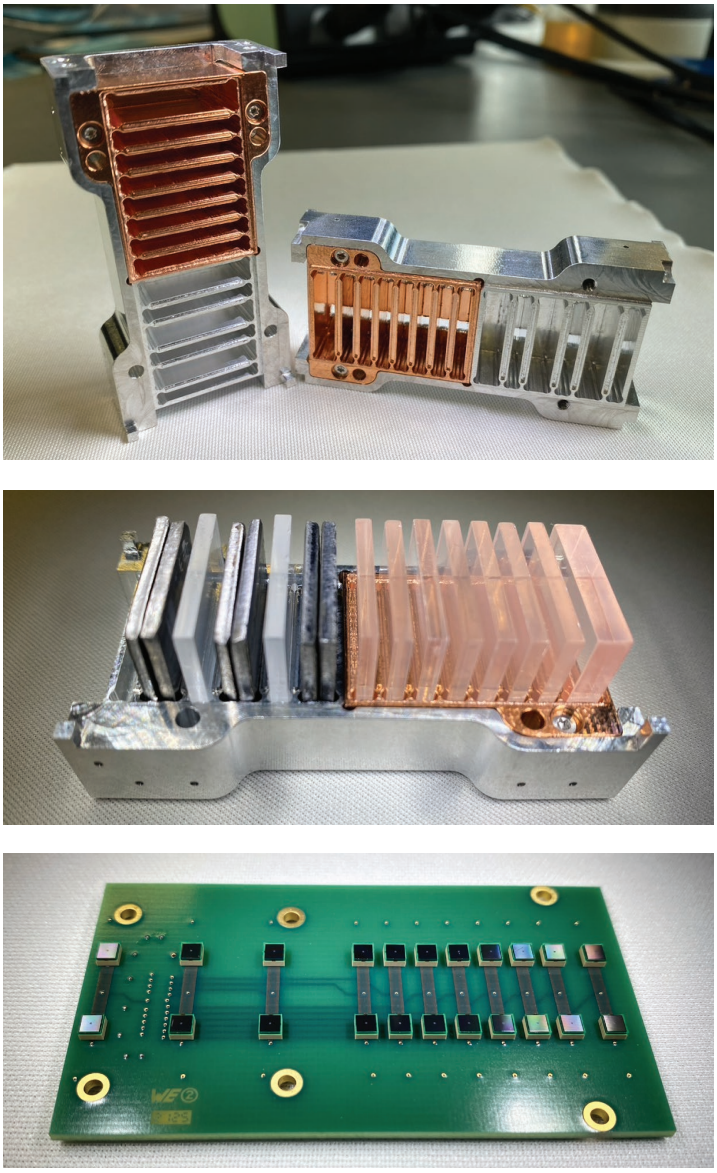

Figure 14.16: Prototype of the CPT calorimeter used for testing at PSI. Top: The two half shells of the aluminum structure, with copper inserts forming absorber layers. Middle: Scintillator and lead layers integrated into one of the half shells. Bottom: The PCB with S13360-2050VE SiPMs used for reading out the sensor's scintillators.

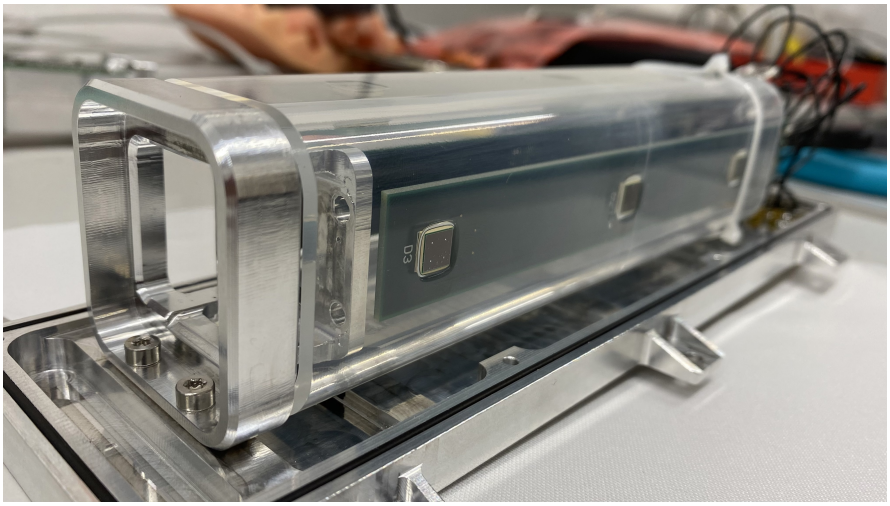

Figure 14.17: Prototype of the CNS veto scintillator that we used for testing at PSI. It is identical to that of the flight instrument, except that the S13360-6050VE SiPMs are mounted on regular PCBs and not rigid-flex ones.

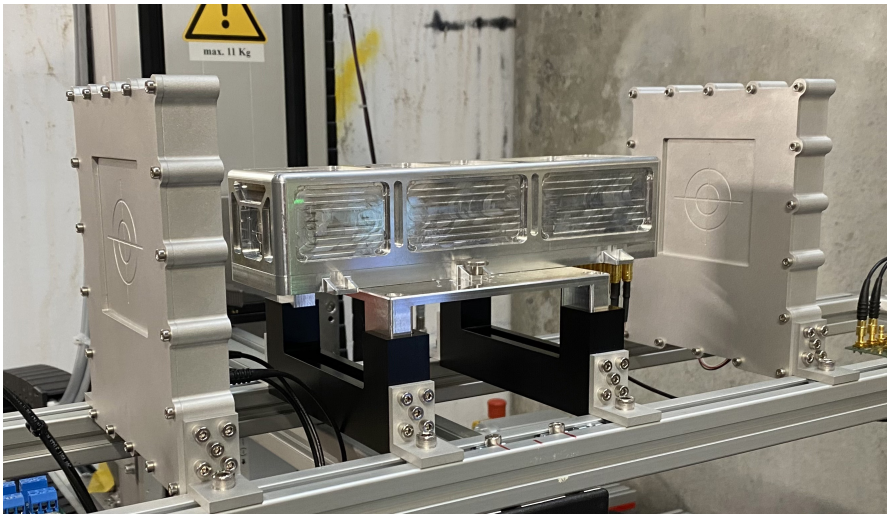

Figure 14.18: The CPT prototype (center) during testing at PSI. The detector sits in top of a table that allows to change its angle to the beam at pre-defined intervals. The devices to the left and to right are trigger detectors.

forced to stack pieces of lead that we had available next to each other. The lower panel shows the PCB with S13360-2050VE SiPMs that we used to read out the scintillators.

Figure 14.17 shows a prototype of the veto scintillator of the CNS that we used for testing its detection efficiency, which is critical to the detector's performance because it helps to identify background events. It is identical to that of the flight instrument, except that the S13360-6050VE SiPMs are mounted on regular PCBs and not rigid-flex ones.

To digitize the SiPM signal of both detectors, we used the sampling-ADC system that we previously used for many of the tests in the context of the RadMap Telescop project (e.g., see Section 7.1.3). We also used the same support equipment (shapers, power and bias-voltage supplies, and trigger detectors). Figure 14.18 shows the test setup, with the CPT prototype placed between an upstream and a downstream trigger detector. It is mounted on a table the allows to change its orientation to the beam at pre-defined intervals. We subjected both detectors to beams of minimum-ionizing pions (at 450 MeV/c) and protons with a momentum of about 400 MeV/c.

Though this did not allow us to perform a comprehensive test campaign to assess the CPT's energy resolution and particle-identification capabilities, we were nonetheless able to gather vital data that allowed to benchmark our Geant4 simulation models. However, our main objective was to confirm that the mechanical design shown in Figure 14.16 produced adequate light yields and uniformity, which could. The test of the CNS veto scintillator was even more crucial: We never before machined such large structures from bulk scintillator material and had little idea about its real-world light-yield. Though we used Geant4 simulations to optimize the scintillator's geometry and the placement of the SiPMs, we were not sure how well the real system would perform. Our skepticism was mainly rooted in the difficulties we initially encountered in producing the tube-shaped structure. Unexpectedly, however, the scintillator performed even better than predicted by our simulations.

Chapter 15

The LUVMI-X Reference Mission

The primary goal of the LUVMI-X project was the maturation of technologies and instrumentation for a future European lunar resource-prospecting mission using a compact rover. The main scientific objective of this endeavor would be to identify regions with abundant water deposits in the Moon's polar regions. To guide the technology development for both the rover and its prospective instruments with a set of realistic capability requirements and constraints, an important cornerstone of the project was to devise a reference mission—including scientific requirements rooted in the current state of the art, an operational concept, and an analysis of potential landing sites given the capabilities of the to-be-developed rover, as well as the current and near-future generation of lunar landers. I present all of these in the following chapter and highlight how they influenced the design of the LCNS.[1]

The reference mission's primary objective is to measure the concentration and distribution of volatiles in fully illuminated, partially illuminated, and permanently shadowed regions at the lunar poles. The principal target is water, both in the form of ice and in chemically bound states, but the abundances of other volatiles identified by LCROSS and found in Apollo samples—such as hydroxyl, hydrogen sulfide, ammonia, ethylene, and carbon dioxide [Col+10]—shall also be determined. Measurements shall be taken through both remote sensing at stand-off distances ($\sim$1 m) and direct sampling; the former having the advantage that it requires less time while the latter can deliver higher levels

[1]This chapter is largely a verbatim copy of a journal article that we published in *The Planetary Science Journal* [Los+22]. Though I obviously needed to rely on technical input from the rest of the team, I was the lead author of that article and wrote all of it myself.

of confidence. The combination of both techniques allows an efficient survey of volatile abundances over a relatively large area. To support the investigation of the solar-wind implanted particle (SWIP) implantation and retention mechanisms, we aim to attempt the technically more challenging measurement of hydrogen and helium abundances with both techniques as well. An important secondary objective is the determination of the regolith's elemental composition in regions for which no reliable in-situ or sample data exists yet, again with a focus on the polar regions. This shall be achieved through means of remote sensing, as an instrument for the in-depth mineralogical analysis of samples is beyond the envisioned scope of the LUVMI-X mission. Another secondary objective is the characterization of the lunar surface radiation environment in preparation for future crewed exploration missions. Here, we do not merely intend to measure the radiation dose astronauts will receive but aim to conduct a full spectral analysis of charged and uncharged radiation from both primary and secondary sources. Figure 15.1 shows an artistic rendering of the LUVMI-X surface elements, i.e., its rover and instrumentation.

15.1 Mission Elements

The scope of the concept and design study I present here was intentionally limited to the development of the surface element of the LUVMI-X mission. We did not devise a broader mission concept encompassing launch, transfer, and landing elements. Instead, we tried to make as few constraining design decisions as possible to be able to take advantage of the growing landscape of commercial and government missions to the lunar surface, assuming that each of them will have identified appropriate means of getting to the Moon. The nature of the investigations we envision does, however, absolutely necessitate mobility and thus the development of a suitable rover. Investigations using only lander-attached instrumentation were therefore excluded from our concept studies. Another constraint of the study was that any form of nuclear power source was prohibited to not constrain the choice of launch provider and due to lack of access to the required materials; the rover must therefore be powered by solar illumination only. This constraint significantly impacts the design of the surface element if it must survive the lunar night, during which temperatures drop well below 100 K in some regions [Wil+17; Wil+19]. To limit the complexity and development time of the mission, we thus assumed a nominal operational period of 14 days during the lunar day, with only brief

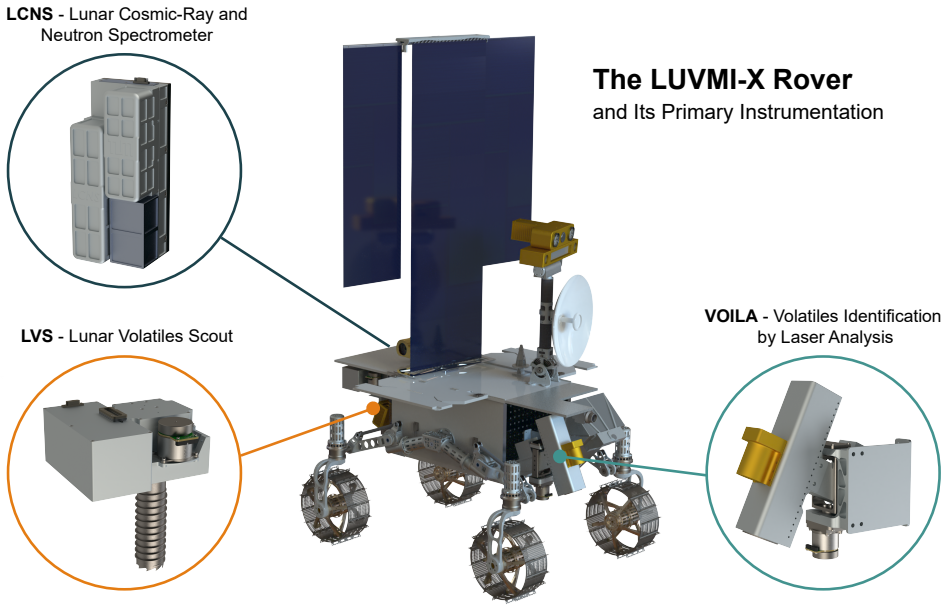

Figure 15.1: The LUVMI-X rover and its instrumentation. The LCNS is one of three primary instruments with both overlapping and complimentary capabilities supporting the characterization of the lunar surface environment. From [Los+22].

incursions into shadowed areas of no more than 8 hours. In principle, the rover and instrument designs presented here may, at specific landing sites and under certain conditions, be able to survive the lunar night—which at the poles can be as short as a few days—and could therefore allow much longer missions. Since we did not have the time to study nighttime survivability in detail and to reliably estimate the maximum time the rover could operate in shadow, we settled on conservative assumptions for these capabilities and leave detailed investigations to future studies.

15.1.1 The Rover

LUVMI-X's surface element is a compact four-wheeled rover capable of traversing a distance of at least 5 km during a 14-day mission. The rover is optimized for operations in the lunar polar regions and is well suited for short-term investigations of PSRs and other cold traps. It is equipped with four independently

steerable wheels in a rocker configuration with an internal differential, has a ground clearance of 30 cm, and drives at a nominal speed of up to 10 cm/s. We chose a four-wheeled design because it allows substantial mass savings over a six-wheeled configuration but has, if combined with a rocker mechanism, only marginally worse stability and traction. Though the design offers less redundancy than one with six wheels, we consider this to be an acceptable drawback given the short mission duration and our goal of designing an affordable platform. The wheels consist of two lightweight aluminum rims connected to a hub via spokes; the running surface is made of wire mesh to prevent the rover from sinking into loose soil and is equipped with grousers for increased traction. To achieve high drive torque, we embedded frame-less and brush-less motors with harmonic gears directly into the wheels' hubs.

One of the distinguishing features of the vehicle is its actuated suspension, which allows bringing chassis-mounted instruments into contact with the lunar surface. It also allows modifying the rover's center of mass, and hence stability, to adapt to different terrain conditions. The vehicle is designed to traverse obstacles up to 40 cm in height and climb slopes composed of loose material with inclinations of up to 25 degrees. Figure 15.2 shows a prototype rover whose drive train and wheel design closely resemble those of the flight version. Using the prototype, we were able to demonstrate most of the rover's mobility capabilities. The surface composition at the test site did not, however, allow us to fully verify the rover's ability to climb slopes of material that is representative of lunar regolith. Power is generated by a vertically mounted, rotatable solar panel conceived to work best at high latitudes; our models indicate that the panel should be capable of delivering up to 150 W. About half of the generated power is available for the scientific instrumentation. The thermal control system is likewise optimized for low illumination angles and hence features upward-facing radiators. Nominally, the rover will communicate via an X-band direct-to-Earth link, though relaying signals through a lander or satellite is possible and preferred, should these options be available.

The mission is nominally teleoperated, mainly relying on a suite of cameras for visual feedback; we do, however, plan to have the option of performing a limited set of supervised, semi-autonomous operations should environmental conditions or operational constraints require it. To aid both operational modes, the rover is equipped with hazard-detection and navigation cameras; the former are mounted on its forward- and backward-facing surfaces while the latter are mounted on a pan-tilt unit on top of the antenna mast. The navigation cameras are based on commercially available, space-grade camera modules.

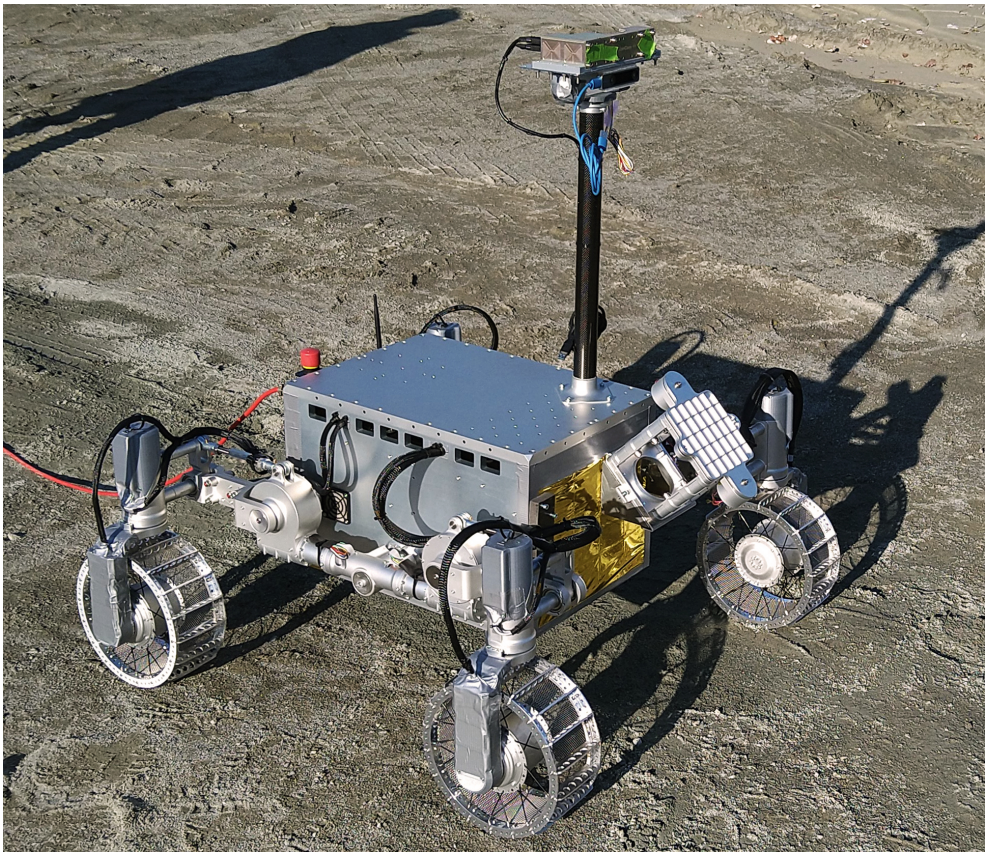

Figure 15.2: Prototype of the LUVMI-X rover, optimized for operations in Earth's gravity, during field-testing in a quarry. A prototype of the spring-loaded mechanism for deploying payloads is mounted on its front face (right). From [Los+22].

They provide three-dimensional images with multi-spectral resolution for short focus distances (0.1 to 1 m) and regular three-dimensional images for medium distances (1 to 10 m). They also include a long-range telescope for traverse planning and for identifying potential sites for investigation with the rover's scientific instruments. The pan-tilt mechanism and the distance information encoded in the three-dimensional images also allow the acquisition of panoramic digital elevation models (DEMs) to support rover navigation.

As an alternative to this relatively traditional setup, we developed a technology demonstrator of a 360° stereo camera. The system is integrated into

the antenna mast—avoiding the need for the mass and complexity of a pan-tilt mechanism—and would allow a more efficient use of mission time as only a single exposure is required to image the surroundings of the rover. The camera's stereo capability also allows for the creation of DEMs of the entire local area visible to the rover and for calibrated distance measurements of specific features. Such a 360° camera system could vastly reduce the number of cameras required on the rover and thereby reduce the mass, required power, and complexity of the mission.

The rover can accommodate instruments (payloads) with a total mass of 25 kg, distributed mainly on the forward- and backward-facing surfaces of its chassis. A limited volume inside the chassis is available for payload systems that need to operate in a more tightly controlled thermal environment than achievable on the outside (within the volumetric, mass, and power constraints). This payload capacity matches the one required for the instruments of the LUVMI-X concept mission described here, but would also allow the rover to carry a wider variety of payloads in future missions due to its modular design. Instruments can either be mounted directly to the rover chassis or can be deployed to the lunar surface using custom release mechanisms (and the rover's actuated suspension). This allows us to place instruments in areas of interest for long-term investigations while the rover continues its journey. The mechanism also allows the retrieval of payloads after they completed their investigation. Such instruments would be self-sufficient, rely on battery or solar power, and use low-power radio links to stay in contact with the rover or to communicate directly with orbital relay satellites. We also devised a spring-loaded mechanism that can deploy instruments with masses up to 1 kg into areas that are inaccessible to the rover, such as deep craters, at distances of up to 50 m (in lunar gravity). This capability allows us to investigate extremely hazardous areas that would otherwise be unreachable but may hold large PSRs or other scientifically interesting features.

15.1.2 Scientific Instruments and Objectives

We selected the rover's scientific instruments such that they provide complementary data on the mission's primary target, water. The focus of our work were three major instruments that can search for water and other volatiles on the surface and at different depths.

The Lunar Volatiles Identification by Laser Analysis (VOILA) Instrument

Starting on the surface, the Volatiles Identification by Laser Analysis (VOILA) instrument will be able to detect the signatures of hydrogen and oxygen in the upper few millimeters of the regolith, allowing us to determine the amount of surface ice present in the areas we investigate. VOILA uses laser-induced breakdown spectroscopy (LIBS) to rapidly analyze the composition of samples along the rover's path. LIBS relies on ablating material from a sample by focusing a pulsed laser onto its surface, producing a micro-plasma of atoms, ions, and electrons [DH17] in a plume several millimeters in size. We developed a compact Yb:YAG laser emitting at a wavelength of 1030 nm that can generate pulses at a rate of 10 Hz, each with a length of 8 ns and an energy of more than 15 mJ. Laboratory measurements have shown that this energy is large enough to produce a sufficiently bright plasma even in loosely grained regolith simulant at near-vacuum pressures [Ric+21]. Figure 15.3 exemplarily shows plasma plumes generated by laser pulses of different energies.

The light emitted by the plasma is collected by the instrument's optical head with an aperture of 50 mm and its spectrum is analyzed to identify and quantify elements based on their characteristic emission lines. We use a crossed Czerny Turner spectrometer that provides spectral coverage from 350 nm to 790 nm at a resolution of better than 0.5 nm and that is optimized for the detection of hydrogen at 656.3 nm and of oxygen at 777.4 nm. To save mass and reduce the complexity of the system, the same confocal optics are used to collect the plasma light and to focus the laser onto its target. The focusing mechanism produces a laser spot size of less than 190 μm and guarantees repeatable measurement conditions on the uneven lunar surface at distances between 0.3 m and 0.5 m; a pointing mechanism allows analyzing targets within a lateral field of view of about 40 degrees in front of the rover. The light of an LED operating in the visible spectrum can be coupled into the receiving path of the optical system and be focused on the target the instrument is observing. The resulting visible spot of light can be detected by the rover's forward-facing hazard-detection cameras and be used to calculate the distance to the target.

A dedicated camera is mounted to the instrument for monitoring the target before and after sampling, providing information on the ablation pattern to aid the analysis of measurements. Our laboratory measurements with prototypes and simulants mixed from basalt and gypsum indicate that water concentrations of at least 1.0% by weight are clearly detectable with the VOILA

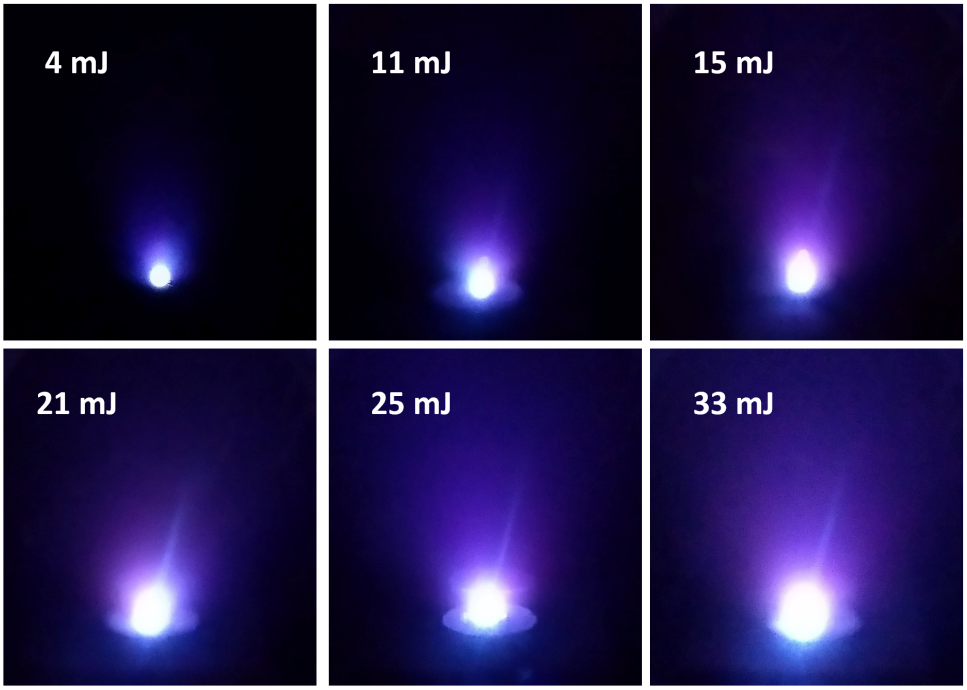

Figure 15.3: Testing of VOILA prototype: plasma plumes generated by laser pulses of different energies on regolith simulant. From [Los+22].

instrument. We are performing further studies to demonstrate even lower detection limits of 0.5% by weight or better. Besides gathering data on surface ice, the instrument will also be able to detect and quantify all major rock-forming elements—i.e., magnesium, titanium, aluminum, silicon, calcium, sodium, and potassium—and can thus determine the composition of regolith and rocks for a more comprehensive geochemical analysis of the mineralogical composition of the lunar surface. Laboratory tests are still ongoing, but early measurements showed that relevant minerals can be clearly distinguished from each other.

The Lunar Volatiles Scout (LVS)

To investigate the shallow sub-surface, the Lunar Volatiles Scout (LVS) will be able to sample the lunar soil to depths of about 15 cm and gather data on

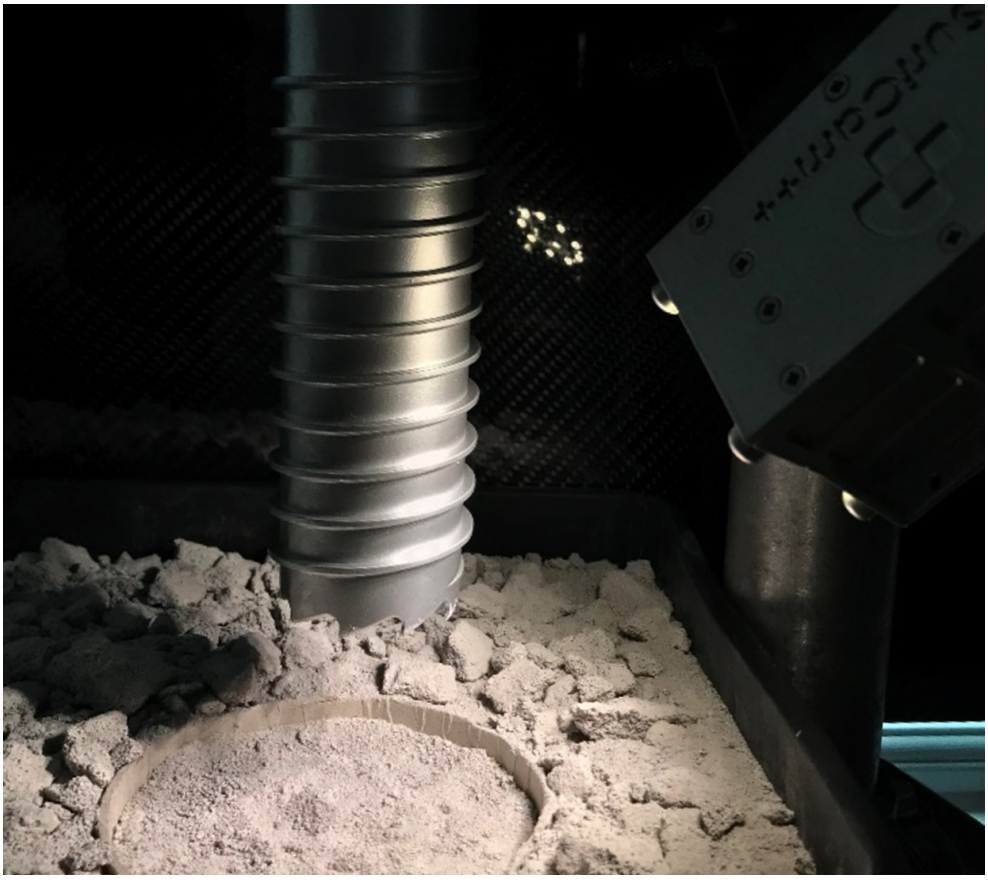

Figure 15.4: Prototype of the LVS drill illuminated by its dedicated multi-spectral camera during testing with regolith simulant. From [Los+22].

the changing volatile content with depth [Bis+20]. It consists of a combined sample drill and volatile-extraction oven that can be inserted into the regolith to release volatiles, and of a miniature ion-trap mass spectrometer (ITMS) for the elemental analysis of the released gases. The sampler consists of a hollow auger drill shell that encloses a sample volume. A resistive heater located at the center of the sample volume can heat the surrounding regolith to a maximum temperature of about 750 °C, depending on the abundance of volatiles in the enclosed sample (a higher abundance leads to a higher thermal conductivity and hence to a lower temperature). Such temperatures allow to

release loosely bound (physisorbed) volatiles like water [Pos+13; Kle+18] and are likely also sufficient for releasing chemically bound ones [Hib+11]. Based on laboratory tests with JSC-1A simulant, we foresee a baseline heating duration of 90 minutes at a constant power of 15 W, which will allow us to reach 750 °C while avoiding sintering at the heating rod. Shorter sampling durations would, for example, be used inside a PSR, where the focus of investigations lies on physisorbed volatiles and lower temperatures are therefore sufficient. Taking the additional time required for drilling, extraction, and imaging of the sample site into account, the nominal duration for a sampling operation is approximately two hours.

Pirani sensors measure the gas pressure inside the sample volume to provide some initial indication of the abundance of volatiles. The released gases are detected and characterized by the miniature ITMS whose design we derived from the Ptolemy instrument that provided the first in-situ measurements of volatiles on the surface of the comet 67P/Churyumov-Gerasimenko during the Rosetta mission [Wri+15; Mor+12]. The ITMS is mounted directly on top of the drill and is connected to the sample volume via a small orifice for pressure control. Even though it is a mechanically simple device, it is capable of detecting a wide range of ion species (with mass-to-charge ratios, m/z, of 10 to 200) with a parts-per-million sensitivity across the detection range. This sensitivity allows the LVS to detect all volatiles species that have previously been detected in the Lunar Crater Observation and Sensing Satellite (LCROSS) ejecta plume, though we were not yet able to determine whether individual compounds could be unambiguously identified if they are all present in the same sample. Due to the inherent sensitivity limitations of an ITMS at low masses, it will however be challenging to determine the relative concentrations of smaller molecules such as water, hydroxyl, and ammonia due to their similar fragmentation patterns [Bis+20]. We are studying the feasibility of using a miniature magnetic-sector mass spectrometer to measure hydrogen and its isotopes and developed a prototype as part of the study presented here.

A dedicated camera provides multi-spectral three-dimensional images and videos of the drilling operations, allowing us to assess the geotechnical properties of the regolith at the sampling site. It can also monitor the tracks left by the rover's wheels to aid operations. Figure 15.4 shows a drill prototype being illuminated by the camera during testing. In its prototype configuration, the system is sensitive to the wavelengths of 450 nm, 540 nm, 600 nm, 660 nm, 725 nm, 840 nm, 940 nm, and 970 nm, which lie in the typical range for lunar-exploration instruments [Rob+10; Gre+11]. With the LVS data, we

will be able to provide new insights into the vertical distribution of water ice and other volatiles in the surface layer and to help improve our understanding of the mixing processes resulting from impact gardening.

The Lunar Cosmic-Ray and Neutron Spectrometer (LCNS)

The third major instrument we conceptualized for the LUVMI-X mission is the LCNS (see Chapter 14), which will measure the abundance of hydrogen in the soil beneath the rover down to depths of about a meter and characterize the radiation environment on the lunar surface. Using the instrument's CNS, we will search for water and hydroxyl deposits by measuring the (relative) fluxes of thermal, epithermal, and fast neutrons. Its performance parameters (presented in the previous chapter) should be sufficient for collecting statistically meaningful data even during rover traverses. If combined with data from the LVS, the measurements of the CNS will allow us to help refine our understanding of the vertical distribution of water in the lunar soil. To measure cosmic and solar radiation, the CPT must be sensitive to radiation particles with a wide range of charge, mass, and energy. It allows us to measure particle-dependent spectra for protons with energies larger than 10 MeV and ions with energies larger than 50 MeV per nucleon. Since the lunar proton albedo may also contain information about the distribution of volatiles in the regolith [Sch+16], we have the option of adding the LE-CPT, which is sensitive to protons and electrons with energies of less than 1 MeV scattering off the lunar surface. The CPT's measurement capabilities, combined with those of the CNS and the additional dosimeters, allow us to fully characterize the radiation environment on the lunar surface—including the dose contributed by neutrons—which is a crucial prerequisite for future crewed exploration missions [RBM12]. Its data is also crucial for the analysis of CNS measurements, which requires knowledge of the intensity of cosmic and solar radiation for normalization.

Secondary Instruments

These three primary instruments are complemented by the Volatiles and Context Analysis Suite (VCAS), a self-sufficient instrument suite that can measure volatiles in locations that are difficult or too hostile for a rover to access, for example on steep slopes or inside deep craters and lava tubes. At the core of the VCAS is a miniaturized magnetic-sector mass spectrometer optimized to fit into a form factor that fits inside the rover's spring-loaded deployment mechanism.

It will allow us to detect molecular water and other volatiles outgassing from the regolith, for example in locations with changing illumination conditions. The instrument will also provide supplementary information about the site it has been deployed to, including images of the local geology, rock formations, and illumination, as well as measurements of the physical, mechanical, and thermal properties of the regolith. Several additional sensors can measure the local temperature and dust distribution to study the near-surface exospheric particulate environment. VCAS units will be released from the rover using the deployment mechanisms described above, depending on the accessibility of the area that shall be investigated.

15.2 Concept of Operations

As the launch, transfer, and landing elements for the LUVMI-X mission were not part of the study presented here, we focus our discussion of the operational concept on the time after landing. Due to the rover's low mass of about 75 kg (including instrumentation) and its compact stowage configuration, we can hitch a ride on many of the lunar landers currently under development—including Astrobotic's Peregrine and Lockheed Martin's McCandless landers, which we used as representative references during the study. Given that these or other (commercial) landers with comparable capabilities will be available very soon, we expect at least one, if not several, missions to target the lunar south pole. Nonetheless, even though our main scientific interest lies in investigating volatiles in the Moon's polar regions, the rover and its instruments are also compatible with non-polar landing sites in case a suitable flight opportunity presents itself before a polar opportunity arises. The scientific return of such a non-polar mission would, however, most likely not be as comprehensive as the scenario we aim for and present here. Since the rover's nighttime survival capabilities are limited, we assume a maximum mission duration of 14 days at latitudes of 75° or higher, during which the mission will need to operate under almost continuous illumination. Excursions into partially illuminated and permanently shadowed regions are, however, possible and can last about six hours at a time, with significantly more time required between consecutive excursions to recharge batteries. We design all systems to survive short lunar nights of up to 24 hours in hibernation mode.

Figure 15.5 provides a visual guide for the discussion of the mission's concept of operations. After a successful deployment to the lunar surface, we

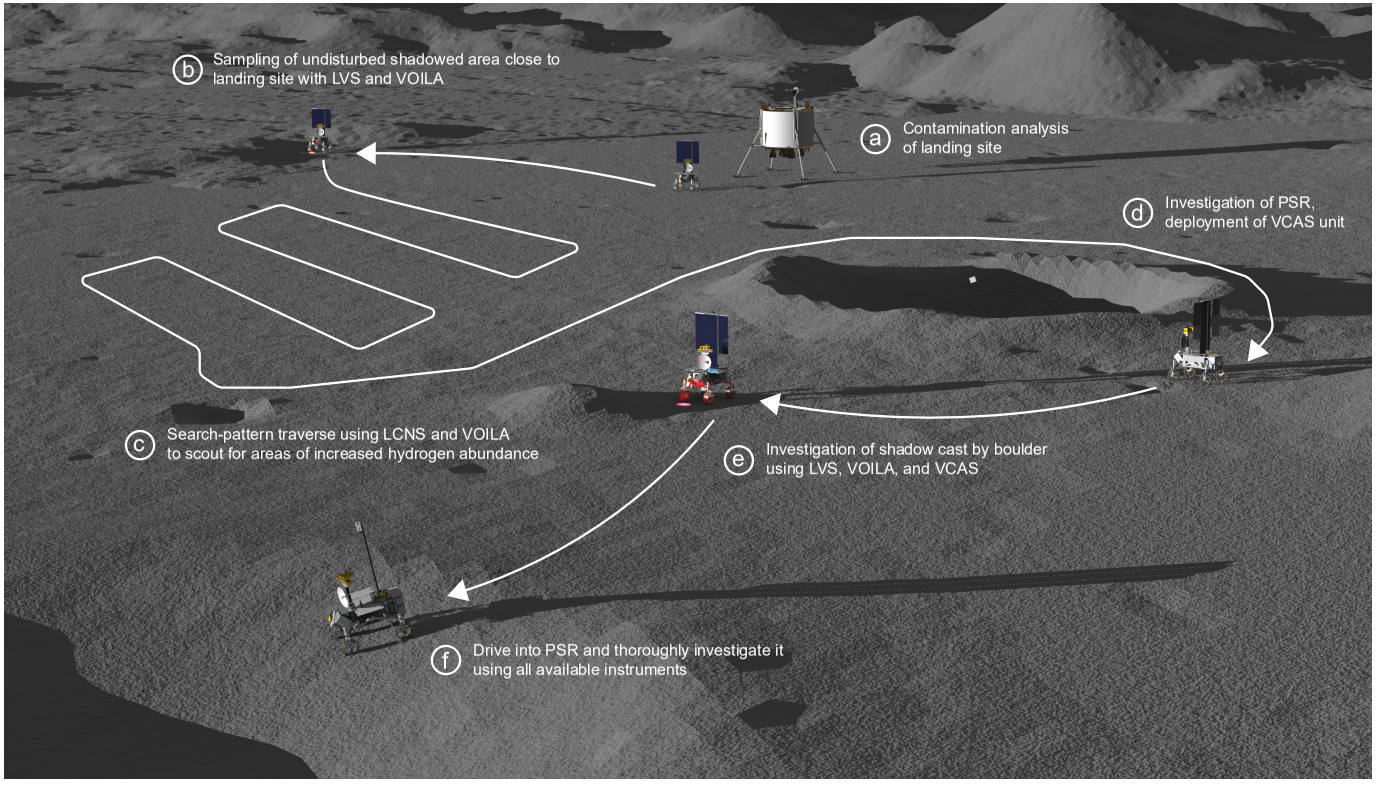

Figure 15.5: Visual guide (not to scale) to the mission's concept of operations: contamination analysis of the landing site (a), sampling with the LVS and VOILA (b), scouting for increased hydrogen abundance during traverse (c), investigation of PSR and deployment of a VCAS unit (d), sampling of an area in temporary shadow with VOILA and LVS (e), and drive into PSR (f). From [Los+22].

will first use the LVS and VOILA instruments to perform a detailed investigation of the landing site. The primary objective of this early phase of the mission is to assess the degree to which the surrounding area was disturbed and altered by the lander. A thorough understanding of the nature and extent of the contamination and alteration of the lunar surface resulting from the action of the lander's engines during descent will be of great importance to follow-on missions, in particular those without a mobile element. In these missions—where it is unlikely that the lander's instruments will be able to access uncontaminated regolith, even if using a robotic arm—knowledge of the distribution of contamination and how it varies with distance from the lander, as well as empirical data on how the exospheric abundance of volatiles freed or generated by the lander's motors evolves with time, is crucial for a correct interpretation of measurements. If a suitable rock or boulder is located close to the lander, we also plan to assess how much shielding from the descent motor's exhaust plume it provides. During this early phase, the LVS will mostly operate in what we call *sniffing mode*, in which the instrument's mass spectrometer measures exospheric volatiles freed from the regolith by mechanical and thermal perturbations caused by the lander and rover. Using VOILA, we will be able to assess the degree to which volatiles of the lander's exhaust were implanted into the top layer of the regolith by performing measurements at increasing distance from the landing site. To determine how deep volatiles were implanted, we will also use the LVS to sample the sub-surface volatile abundance at different depths in select locations.

To further our understanding of the processes leading to the accumulation of surface ice, we will first direct the rover to an undisturbed site at which a boulder or some other rise in the terrain creates an area of temporary shadow. Orbital observations revealed a global cycle of hydration and dehydration due to diurnal illumination (and hence temperature) changes [Cla09], which likely drives the migration of volatiles towards permanent cold traps at the poles [CV02]. In the polar regions, even small boulders can cast large and long-lasting shadows due to the Sun's low elevation and the Moon's long diurnal cycle of 29 days. The regolith in these shadowed areas can cool down significantly enough for volatiles to freeze onto its surface, while the illuminated side of the boulder will become very hot. Sampling the soil on both sides of a suitable boulder with the LVS and VOILA instruments will provide new insights into the diurnal hydration cycle and may help us understand how water ice and other volatiles accumulate in transient cold traps. If the timing is right, further data could be provided by a VCAS unit placed into a

shadowed area shortly before the night-day terminator moves over it. The sudden increase in temperature after sunrise frees volatiles from the regolith, leading to an increased exospheric abundance that can be detected by the mass spectrometer in the unit. A retrieval of the instrument would allow to repeat and compare measurements in locations with different illumination (and hence temperature) conditions.

After these initial investigations that can be performed directly at or close to the landing site, we will instruct the rover to begin its traverse towards nearby volatile-rich locations (e.g., cold traps inside PSRs). The LCNS, which will be switched on upon landing and continuously operate from then on, will allow the identification of areas with increased hydrogen abundance during the traverse. Upon detection of such areas, or at regular intervals otherwise, the VOILA instrument will probe the top layer of the regolith to confirm whether a surface-ice layer or, more generally, an increased hydrogen abundance is present. Depending on the significance of the hydrogen signature found by the LCNS and VOILA instruments, the rover will stop its traverse, perform an extended set of measurements with VOILA, and subsequently sample the regolith at different depths with the LVS. The time required for these operations will also allow the LCNS to gather a statistically more significant dataset on the local hydrogen abundance. During the traverse, we will use the rover's navigation cameras to record DEMs and panoramic images of the lunar surface in order to identify sites of interest for the mineralogical analysis of rocks or regolith with the VOILA instrument. Potential micro cold traps identified in the images will be investigated using the VOILA and LVS instruments. Depending on the topography of the surface along the traverse path, the exospheric abundance of volatiles after terminator passages could be characterized with deployable VCAS units or using the LVS in sniffing mode—with the latter option likely providing a higher measurement resolution—in multiple locations to collect additional data on the migration of volatiles.

Once the rover arrives at a sufficiently large PSR harboring a permanent cold trap, we will use its three main instruments to perform a survey of volatile abundances in the surrounding area as a function of distance from the PSR rim. This not only provides a reference for measurements inside the PSR, but also allows us to investigate the spillage of volatiles from the PSR caused by micro-meteoroid impacts. We will then use the rover's spring-loaded mechanism to propel a VCAS unit into the PSR. Equipped only with a mass spectrometer for the measurement of exospheric volatile abundances, the unit will not be able to actively sample the soil. Instead, we must rely on the instrument's waste

heat and the physical disturbance caused by its tumble into the PSR to free physisorbed volatiles in the uppermost layer of the regolith, which can then be detected by the mass spectrometer. Environmental conditions and operational constraints permitting, the rover shall investigate at least one additional PSR in the same manner. Finally, once we have identified a sufficiently shallow and accessible PSR with a permanent cold trap inside, we will direct the rover to drive into it after the survey of the surroundings is completed. Using all available instruments, we will perform a thorough investigation of the surface and sub-surface volatile abundances. We may even discover a solid layer of water ice on the surface or buried by just a few centimeters of regolith. This final and most risky investigation is the nominal end of the LUVMI-X mission. Should the rover make it out of the PSR, additional investigations may be conducted until the onset of the lunar night.

15.3 Candidate Landing Sites and Traverses

To understand how the rover's capabilities drive, or perhaps constrain, the scientific potential of the mission, we performed an analysis of possible landing sites and rover traverses. For simplicity, we focused on the abundance of water (and other volatiles) as the primary criterion for selecting a target area. Even though there may be great scientific interest in performing geological analyses and radiation measurements virtually anywhere on the Moon, we concluded that for practical purposes there is a high priority for performing them in areas with high potential for water deposits. We limited our work to the lunar south pole, within a latitude range from 75°S to 90°S, because of its larger total PSR surface area compared to the north pole and the corresponding higher probability of finding suitable landing sites with surface-ice deposits. The south pole is also the target of many upcoming missions that may provide ride-share opportunities to LUVMI-X. We first performed a regional analysis using multiple criteria to identify ROIs based on our scientific objectives and on the capabilities and constraints of the rover and potential landers. We then performed a high-resolution local analysis of these ROIs to identify possible landing sites and rover traverses that fulfill the scientific objectives of the LUVMI-X mission and are in line with the concept of operations described above. As launch, transfer, and landing elements were not part of the study presented here, we again used Peregrine and McCandless as representative examples of (commercial) lunar landers currently under development.

15.3.1 Data and Methods

We only used peer-reviewed and publicly released sets of data; most of them are available through NASA's Planetary Data System (PDS). Those that are not can be downloaded from the instruments' websites. For the regional analysis, we used datasets with global coverage and varying resolution:

- the most recent version of the Lunar Reconnaissance Orbiter's (LRO) LROC Wide Angle Camera mosaic at 100 m px^{-1} [Spe+11];
- several digital elevation models based on data from LRO's laser altimeter (LOLA) at resolutions between 10 m px^{-1} and 120 m px^{-1} [Smi+17];
- the hydrogen abundance inferred from Lunar Prospector NS data at 15 km px^{-1} [Elp+07];
- the hydrogen abundance inferred from LRO LEND data at 2 km px^{-1} [Mit+12; Boy09];
- the average visibility of the Sun and Earth, and a map of PSRs at 240 m px^{-1}, derived from LRO LOLA data [Maz+11; Glä+18; Bar+21a];
- and a predictive model of ice stability at depth at 200 m px^{-1} based on LRO Diviner data [Pai+10].

For the local analysis we used:

- the LRO's Narrow Angle Camera mosaic at an average resolution of 1 m px^{-1} [Wag+15];
- the digital elevation model derived from LOLA data, but with a resolution of 5 m px^{-1} for the highest latitudes [Smi+17];
- evidence for surface ice from the Moon Mineralogy Mapper [Li+18];
- illumination maps based on LRO data at 60 m px^{-1} [SR13; Glä+18];
- the average visibility of the Sun and Earth and a map of PSRs from LOLA data, but with a higher resolution of 60 m px^{-1} [Maz+11; Glä+18; Bar+21a];
- and the same model for ice stability at depth we used for the regional analysis [Pai+10].

We processed the data with the ArcGIS software, using a polar stereographic projection with a latitude range from $75°$S to $90°$S centered at the south pole. To define and then select ROIs, we first applied a number of constraints: (1) To ensure a safe landing, slopes in the region must be less than $10°$ in an area large enough to hold the landing ellipses of Peregrine (24 km$\times$6 km) or McCandless

(2 km×2 km); (2) at least one PSR must be in close proximity to the landing site, at a distance of no more than 5 km; and (3) the abundance of hydrogen in the general area must be in excess of 100 ppm. We used these constraints to find areas that would generally be suitable for landing a mission. In parallel, we calculated the scientific potential of sites based on a weighted-sum scoring system using four criteria with different weights: the the visibility of the Sun (higher is better; weight of 0.5), the depth at which water ice is expected to be stable (shallower is better; weight of 0.25), the visibility of Earth (higher is better; weight of 0.15), and the hydrogen abundance in excess of 100 ppm (higher is better; weight of 0.1). We assumed the mission to take place in December and January, during the time of higher illumination at the south pole [Bus+10], to adjust for seasonal variations in solar illumination. To account for the fact that sites with high scores of scientific potential may not necessarily lie in areas that are suitable for landing, we then identified lander-compatible areas within 5 km of top-score sites.

In our local analysis using high-resolution datasets, we placed potential landing ellipses inside the most suitable ROI and ranked them by a weighted sum of Earth and Sun visibilities. For each ellipse and its surrounding 5-km area, we identified candidates for the four major waypoints that must lie along the rover's path: (1) a shadowed boulder to place a VCAS unit at; (2) a subsurface cold trap to investigate with the LVS; (3) a cold trap inside a PSR inaccessible to the rover to deploy a VCAS unit into using the spring-loaded deployer; and (4) a PSR harboring a permanent cold trap that the rover can drive into and investigate. We strongly favored regions in which subsurface ice is stable at less than 20 cm depth to allow sampling with the LVS. To select waypoints and construct a traverse path between them, we also took into account two major constraints imposed by the rover: a maximum slope of 20° and a maximum traverse length of 150 m inside a PSR. The latter constraint is caused by the rover's limited ability to survive without sunlight and assumes that it will move at an average of one meter per minute while in shadow. Extended science operations may further reduce the distance it can drive inside the PSR. As the rover will mostly be teleoperated, we favored waypoints and traverses with high Earth visibility.

15.3.2 Results

Figure 15.6 shows the six ROIs we identified, which mostly lie in the vicinity of the Shackleton, Shoemaker, and Faustini craters. The figure also shows

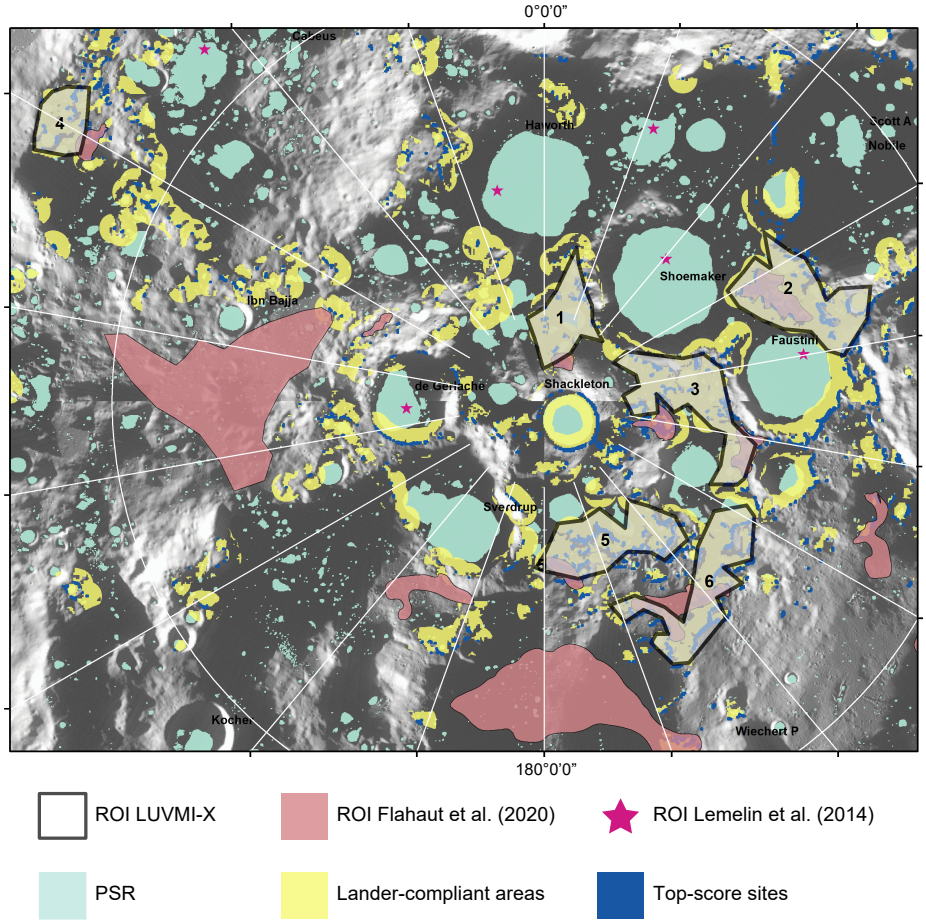

Figure 15.6: Regions of interest for the LUVMI-X mission, compared to those previously identified by [Lem+14] and [Fla+20]. From [Los+22].

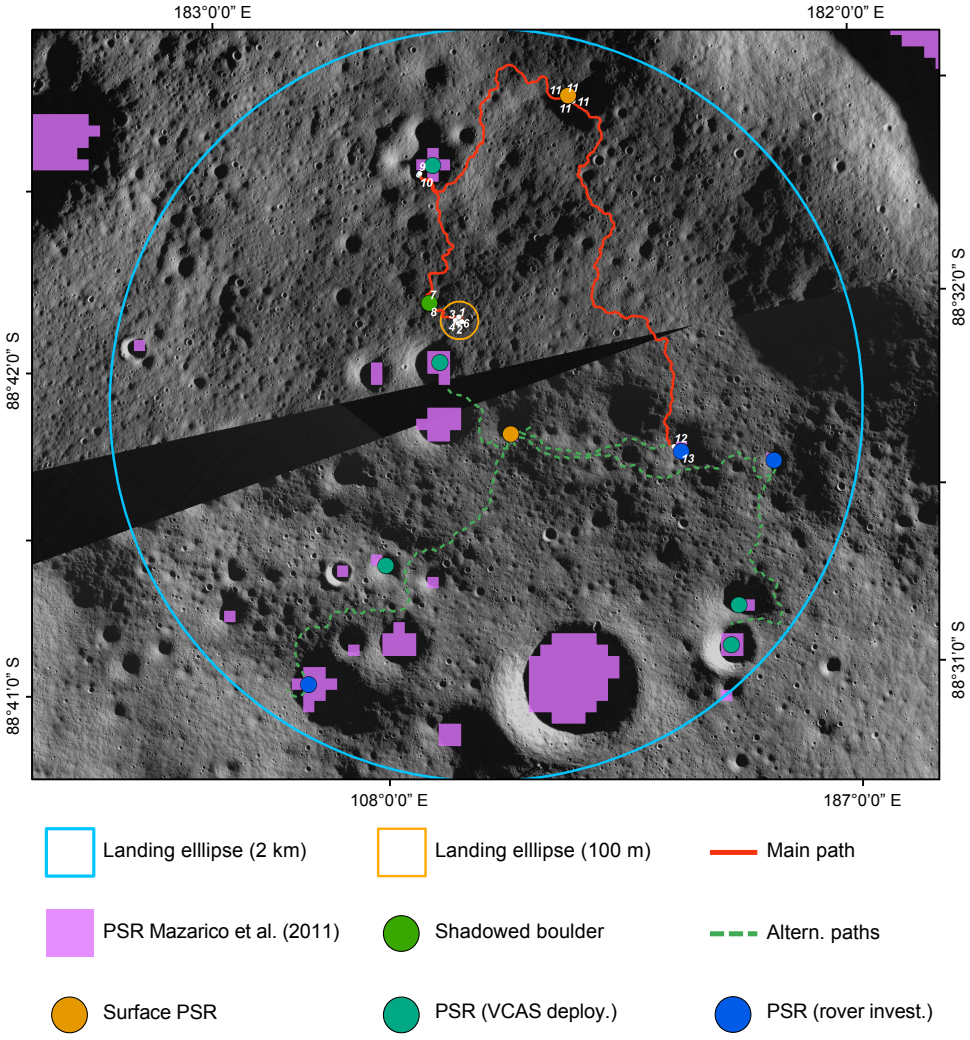

Figure 15.7: A possible traverse path (red line) on the Shoemaker-Faustini ridge fulfilling all requirements for the mission. Alternate paths for landings outside of the 100-m landing ellipse are shown as dashed green lines. From [Los+22].

the ROIs previously identified by [Lem+14] and [Fla+20]. It is evident that our ROIs have little overlap with them, though this can be explained by the different constraints that were applied. Lemelin et al. concentrated on regions inside PSRs [Lem+14], which we excluded because the LUVMI-X rover is solar-powered. Flahaut et al., on the other hand, concentrated on areas with exposed surface ice [Fla+20], so their ROIs only partially intersect with ours. All six ROIs comfortably fit the McCandless landing ellipse of 2 km×2 km, but none of them truly fits the one for the Peregrine lander (24 km×6 km). We therefore limited our subsequent analysis to finding suitable sites for the smaller of the two landing ellipses. We also assumed that the lander is capable of targeting a 100 m×100 m area inside the ellipse once it is close enough to rely on its own optical sensors, based on documentation available from Lockheed Martin [Loc19]. We identified ROIs #2 and #3 as the most promising candidates because of their high abundance of hydrogen and low surface temperatures. Ultimately, we concluded that ROI #3, located on the Shoemaker-Faustini ridge, has the higher potential of capturing and retaining volatiles and should therefore be the primary target of the LUVMI-X mission.

We identified five possible landing ellipses inside ROI #3 and ranked them, again using a weighted sum of Sun visibility, Earth visibility, and topography. Figure 15.7 exemplarily shows a landing ellipse and possible traverse path of 5.6 km length that fulfills all waypoint requirements. It is not, however, optimized for power consumption and also features a relatively large PSR close to the landing site. Besides the primary traverse, the figure also shows optional paths the rover could take depending on the exact landing site and available power. We identified several other possible traverses that fulfill the mission's requirements and constraints to varying degrees.

The analyses we present here have obvious limitations and may only be considered preliminary. The digital elevation model we used does not reflect features under 5 m in size. Even though this can be partially mitigated by relying on the higher-resolution optical images, it still limits our ability to plot a safe traverse for the rover. In addition, some areas in the ROIs we identified were in shadow at the time they were photographed by the LRO cameras, giving us no option to manually identify possible obstacles in these regions either. Earth and Sun visibility were only available at a resolution of 60 m and are averaged over a period of 18.6 years [Maz+11], leading to significant uncertainties in the actual visibility of the Sun and Earth at the time of the mission. The predicted ice-stability and temperature maps have even lower resolutions of 200 m and 240 m, respectively. We also had

to make assumptions about the landers' imaging capabilities and landing accuracy. In our analyses, we did not treat the uncertainties resulting from these limitations and assumptions at all. The results must therefore be understood as a general proof of feasibility of the LUVMI-X mission concept: We were able to demonstrate that—given the constraints imposed by the rover and commercial landers currently under development—the high-level mission requirements derived from our scientific objectives can be met at a number of locations at the lunar south pole.

Chapter 16

Discussion and Outlook

To conclude the second part of my thesis, I discuss how the LUVMI-X mission, and the LCNS in particular, fit into the diverse landscape of planned missions and instruments for lunar exploration. I do so separately[1] because, as previously mentioned, the prospects of the LCNS are not necessarily tied to the fate of LUVMI-X, which is not currently pursued further after the period of funding by the EC came to an end.

16.1 Discussion of the LUVMI-X Mission

For LUVMI-X, our goal was to design a reference mission that is uniquely suited for the detection of water and other volatiles in the Moon's polar regions. Figure 16.1 gives an overview of the instruments we designed to achieve that goal. It also shows the primary areas of scientific interest and how the instruments provide complementary data on common objectives. The main strength of the mission's instrumentation is that every single instrument (the three primary ones plus the deployable units) contributes to the detection of water and hydrogen: The LCNS measures the hydrogen abundance to depths of about a meter or more and can do so (with limited resolution) while the rover is in motion; the VCAS units can detect exospheric hydrogen and water released by thermal or mechanical disturbances of the regolith, either by natural or by artificial means, during the traverse and when they are deployed to locations of interest. While the rover is stationary, the VOILA instrument

[1]The discussion on the reference mission is again largely a verbatim copy of sections of our publication in *The Planetary Science Journal* [Los+22].

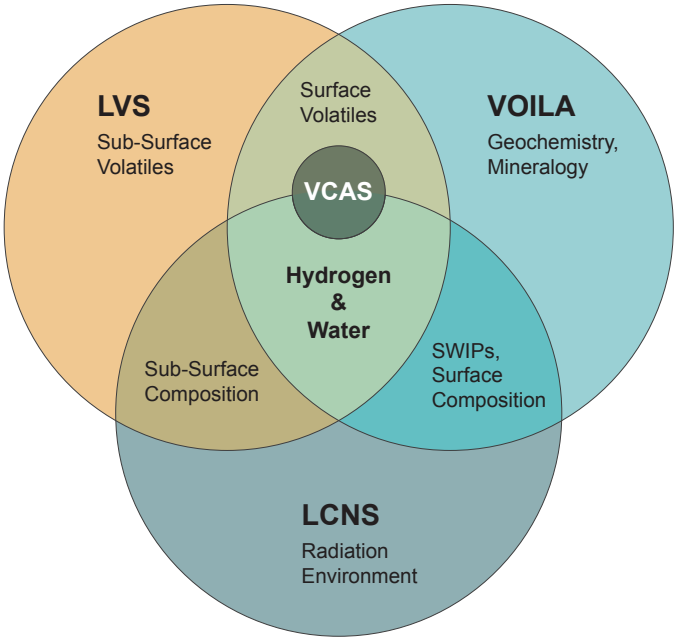

Figure 16.1: The instruments of the LUVMI-X reference mission and the scientific areas investigated by them.

can detect hydrogen and water in the upper few millimeters of the regolith at concentrations of 0.5% by weight or less; and the LVS can sample the shallow sub-surface for water ice with a sensitivity at least an order of magnitude better to depths of about 15 cm and also detect exospheric hydrogen and water.

This not only permits us to formulate an efficient operational concept, with the time-consuming sampling of the LVS mostly conducted at sites where an increased abundance of hydrogen was previously detected by the LCNS and VOILA instruments. It also allows for the combined analysis of instrument data, leading to an increased significance of our findings. This multi-instrument investigation is an important aspect that sets LUVMI-X apart from many other missions currently under development. It allows us to investigate not only the distribution of hydrogen, water, and other volatiles but also their spatial and temporal migration process, which is likely driven by thermal perturbations due to illumination changes [Luc+21]. In addition, there are significant capability overlaps between the instruments in other areas: Both the VOILA and LCNS

instruments will gather data on SWIPs and the composition of surface-layer regolith; the LVS and LCNS will both provide data on the composition of the regolith in the (shallow) sub-surface; and the trio of VOILA, VCAS, and LVS will gather data on physisorbed volatiles in the surface layer. These capabilities are complemented by investigations each instrument can perform on its own: The LVS will gather data on sub-surface, physisorbed volatiles; the VOILA instrument will determine the elemental composition of rocks and regolith along the rover's path; and the LCNS will characterize the radiation environment on the lunar surface. Altogether, these capabilities enable the comprehensive investigation of volatiles and surface chemistry in the polar regions of the Moon. The ability to deploy VCAS units into hard-to-reach places and remotely operate them there adds further versatility and allows us to dynamically respond to the topology of the surveyed area.

Comparable capabilities are currently only foreseen with the Volatiles Investigating Polar Exploration Rover (VIPER), which will use a very similar set of instruments—a drill (TRIDENT), a mass spectrometer (MSolo), and a neutron spectrometer (NSS) [Enn+20]—to search for water at depth and an infrared spectrometer (NRVISS) to passively investigate the surface layer [Rou+21]. Smaller rovers like MoonRanger will only carry a single instrument, in this case a neutron spectrometer, to detect water [Sch+21] and therefore have relatively limited measurement capabilities. Instruments on static landers, such as the Package for Resource Observation and in-Situ Prospecting for Exploration, Commercial exploitation and Transportation (PROSPECT)—formerly part of Luna 27 [Hea+21] and now likely to be launched on a commercial lander—will be able to assess the abundance of water and other volatiles in the immediate vicinity of the lander, but often only at very few locations within the range of a robotic arm. In addition to the obvious spatial limitations of such investigations, the contamination caused by the landers' thrusters [Aro+68; Pre+20] may decisively limit the sensitivity to small abundances of volatiles in the surface layer.

16.1.1 Capabilities of Individual Instruments

On the level of individual instruments, the capabilities of the LVS are inferior to those of the drills of VIPER and PROSPECT, which both can reach depths of about 1 m and have more extensive and precise analysis capabilities. Its low mass, volume, and power consumption, however, make the LVS a good choice for mobile platforms that shall quickly survey large areas and primarily

concentrate on ice in the shallow sub-surface. The in-situ heating capability and the coupling of the mass spectrometer to the sample volume provide operational and sensitivity advantages that facilitate faster and more direct sampling. In PROSPECT, samples must be transferred from the drill to another instrument for analysis [Sef+18]. While this rather complex operation allows the detailed investigation of samples from deep below the surface, it comes at the cost of increased system mass and power consumption and is therefore impractical for a small rover that shall investigate a multitude of sites in as little as 14 days. It also bears a significant risk of loosing or altering volatile content due to thermal disturbances along the sampling chain [Mor+21b]. On VIPER, samples are not analyzed in a closed instrument but instead observed by an infrared spectrometer after being lifted out of the drill hole [Enn+20]. In addition, volatiles sublimating off the samples are detected by a mass spectrometer mounted close to the drill. Investigating samples in open system has the advantage that it is easier to use multiple independent instruments for analysis. The LVS, on the other hand, offers a more controlled environment with less potential for contamination by exospheric volatiles. Even though heating samples in-situ has its own challenges and limitations [Bis+20], overall the LVS design provides a measured balance between sensitivity, instrument size, and complexity for the investigation of volatiles on the surface and in the shallow subsurface.

The LIBS technique has been successfully used on the surface of Mars, most notably in the ChemCam and SuperCam instruments on the Mars Science Laboratory and Mars 2020 rovers, respectively [Mau+16; Mau+21]. The Tianwen-1 rover also carries an instrument that combines the technique with (passive) infrared spectroscopy [Zou+21]. Using LIBS in the quasi-vacuum on the lunar surface presents unique challenges, as the lack of confining atmospheric pressure leads to the plasma dissipating more quickly. So far, the first instrument designed to explore the Moon was supposed to operate on the *Pragyaan* rover on Chandrayaan-2 [Sun18], which unfortunately never made it to the surface intact. A nearly identical copy of the rover (and instrument) landed in August 2023 as part of the Chandrayaan-3 mission and successfully gathered data [Sri+24], thus marking the first time LIBS was employed on the Moon. The VOILA instrument is designed to be more capable than the instrument on Chandrayaan-3; its field of view, working distance, and resolution are, however, inferior to those of the larger and heavier ChemCam and SuperCam instruments operating on Mars. We are not aware of any other LIBS instrument for lunar exploration currently being under development. Because

of its higher complexity, successfully operating VOILA on the Moon would therefore be a technological first. An advantage of the LIBS technique is that it is operationally more versatile and can probe deeper than other techniques that analyze surface composition and volatiles from stand-off distances (e.g., via infrared spectroscopy). This capability allows, for example, to determine the composition of rocks even when they are covered by a (thin) layer of regolith. The instrument is, however, technically and operationally more complicated and requires in-situ calibration [Van+12]. Though VOILA can clearly distinguish between different minerals and rock types, it cannot achieve the sensitivities of a full-scale sample analysis suite.

A discussion of the available data on the lunar-surface radiation environment and a comparison of the LCNS' capabilities to those of other planned instruments are provided in Section 16.2 below.

16.1.2 Existence of Ice Deposits?

Many recent discussions in the lunar-science community revolved around ancient ice reservoirs suspected to exist several meters below the surface [Can+20], created primarily by water delivered through asteroid and comet impacts [Pre+15] or by volcanic outgassing from the lunar interior [WHL22]. The simulations driving these discussions have not yet been verified experimentally, however, and their accuracy and predictive power may, according to their creators, suffer from several free and (partially) unknown parameters [CB20]. The principal challenge is that most reservoirs are predicted to be buried so deep that they can hardly be detected by any of the currently available technologies. The limited depths to which the LVS can sample and to which neutron spectroscopy can provide measurements mean that LUVMI-X will not be able to help shed light on the existence and extent of very deep reservoirs, though ice at depths up to about a meter could be detected by the LCNS. A recent analysis of multiple shadowed and illuminated craters similarly concluded that the smoothing of the surface inside polar craters may not be due to surface ice but rather due to larger deposits at depths that are inaccessible even to neutron spectroscopy and have therefore not been detected yet [Deu+21]. Even though the LUVMI-X instruments cannot prove the existence of deep deposits, they are, at the very least, capable of testing the hypothesized absence of a correlation between surface ruggedness and surface ice.

An updated analysis of LCROSS data, on the other hand, determined that a surface layer of dirty ice—i.e., water ice grains mixed with regolith, and an ice

concentration that increases with depth—can best explain the amount of water (vapor) observed in the ejecta plume [LCS21]. Even though the observations were not sensitive to the first few centimeters of material and therefore cannot be used to determine the stratigraphy in the shallow sub-surface, they seem to be consistent with either a layer of surface frost or older water ice covered with a thin layer of regolith. The LVS could test both hypotheses and therefore contribute to understanding the sources of water ice that accumulated in polar cold traps [DHN20]. Recent analytic models of impact gardening show that even if lunar water has a predominantly primordial origin—e.g., volcanic outgassing from the lunar interior [WHL22]—deposits may be buried by as little as a few centimeters or by as much as several meters of regolith [Cos+20]. The three instruments on LUVMI-X could either help to confirm the presence of shallow deposits down to depths of about a meter or, in case they are absent, provide constraints for future models.

Both the LVS and VOILA are, in general, well suited to search for and quantify young (and possibly transient) surface frost that was detected from orbit in cold traps inside several permanently shadowed craters [Far+19]. They could also investigate the near-surface stratigraphy of such deposits and search for ice at shallow depths. As both instruments are designed for comparatively fast sampling, they allow the time-resolved investigation of transient phenomena; the ability to point VOILA to different targets while the rover is static also reduces operational complexity as the vehicle does not need to move for every measurement. In addition, VCAS units could probe the suspected existence of an exospheric cloud of water molecules and icy grains above the floor of craters containing surface ice [Far+19]. Both VCAS and the LVS can also investigate the thermally driven migration of volatiles, vertically and towards the poles [Rei+21], by analyzing the upper surface layers and the lunar exosphere, particularly in locations with changing illumination conditions [Hen+19]. Exospheric measurements during and after terminator events, e.g. observations of the thermally driven release of water or of its accumulation at dawn [SR22], are key to the validation of simulations models of volatile migration.

Measurements with the SOFIA airborne observatory indicate that the widespread, low-level hydration of the lunar surface at high latitudes observed by infrared spectrometers from orbit [Pie+09; Sun+09; Cla09] may be explained by water that is either confined inside impact glasses or trapped between regolith grains, though they do not allow to distinguish between these two possibilities [Hon+21]. LUVMI-X would be well suited to investigate

which confinement mechanism is the dominant one: If water is trapped in the voids between grains, mechanically disturbing the surface would allow the molecules to be thermally liberated and subsequently be detected with the mass spectrometers in the LVS or in a VCAS unit. If water is predominantly trapped inside glasses, VOILA could reveal its presence there.

16.1.3 Conclusion

We are confident that its primary and secondary instruments and their capabilities render the LUVMI-X rover a unique and powerful tool for studying water and other volatiles on the Moon. Despite the limited depth to which its instruments can actively sample the lunar surface, the mission is nevertheless capable of addressing a wide range of open questions concerning the lunar water cycle—both regarding the origin of volatiles and their migration regionally, as well as globally towards (polar) cold traps. And while it would certainly not be able to conclusively answer many of the questions by itself, it can complement—and in some areas enhance—the capabilities provided by other missions under development. The data gathered by LUVMI-X would also be highly relevant for some of these other investigations. Determining the contamination of the lunar surface in the vicinity of a lander equipped with thrusters, for example, would provide crucial context for the measurements of volatiles by instruments on static platforms like PROSPECT. Another example are maps of the hydrogen abundance in the mission area, which would provide detailed ground truth for past (e.g., Lunar Prospector, LRO) and future orbital measurements, such as those by LunaH-Map [Har+20], Lunar Flashlight [Coh+20], and Lunar Trailblazer [Ehl+21].

To conclude with practical considerations relevant to future exploration efforts, we want to reiterate that ISRU—and especially the extraction of water and oxygen from the lunar regolith—promises to substantially decrease the amount of material that must be supplied to a permanently crewed outpost form Earth. It may also be essential for the development of near-Earth space and form the basis for a cis-lunar economy [Cra15]. Our current knowledge of the Moon's resource potential, however, is too incomplete to accurately assess the technical feasibility and economic viability of ISRU and other resource-extraction efforts. The LUVMI-X mission is well suited to help gather much-needed data about the availability, distribution, and accessibility of water and other volatiles on the Moon. Its unique instrumentation package sets it apart from other missions currently under development because it will be

able to provide complementary measurements by multiple instruments and investigate both the surface layer and the shallow sub-surface. In addition, its ability to provide detailed measurements of both the charged and uncharged components of the lunar radiation environment is highly relevant to future crewed exploration missions. Our intent is to develop an affordable and adaptable system that not only provides scientifically interesting data to help shed light on open questions concerning the Moon's water and volatile cycle but also supports the development of lunar ice as a resource, which more than anything will require comprehensive in-situ measurements by different missions and in multiple locations.

16.2 Discussion and Prospects of the LCNS

During our work on the LUVMI-X project, we devised the design concept for the LCNS, a compact spectrometer capable of measuring both neutrons and charged particles on the lunar surface. As part of the LUVMI-X rover's payload, the LCNS will aid the search for exploitable deposits of water ice in the Moon's polar regions and provide detailed in-situ data on the radiation environment on the lunar surface. The instrument's comparatively compact design and low power consumption also make it an ideal candidate for potential future payload opportunities on other rovers, landers, and orbiters. The preliminary results of our design study are based on extensive simulations of the instrument's two main sensors, the CNS and the CPT, with the Geant4 toolkit. Even though we were unfortunately not able to fully back up our models with real-world data from experimental campaigns, these extensive simulations—paired with our experience of simulating and building similar detectors—give us confidence that we will be able to design the LCNS to meet, and even exceed, all requirements of the LUVMI-X reference mission. We are also confident that the instrument will be able to provide novel data crucial to the understanding of the water cycle on the Moon by itself if it was flown as part of another mission.

Between the Apollo era and the landing of Chang'E 4 in 2019, no radiation measurements had been performed on the lunar surface. Investigations were conducted in lunar orbit, for example by the Cosmic Ray Telescope for the Effects of Radiation (CRaTER) experiment on LRO [Spe+10], but the radiation environment on the lunar surface is believed to differ substantially from the one in orbit [Bha+15]. Any instrument deployed to a location of interest for

future crewed missions will therefore provide immensely valuable data for improving our understanding of the radiation risk to astronauts. The Lunar Lander Neutron and Dosimetry (LND) experiment on Chang'E 4 delivered the first measurement of the radiation field on the Moon, including a contribution of up to $23 \pm 8\%$ by neutrons and gamma rays [Zha+20]. Thanks to the sampling calorimeter at the heart of its telescope, the LCNS can measure charged particles over a much larger range of energy than LND, which essentially is a telescope of planar silicon detectors [Wim+20]. Though it is likely other missions will carry radiation sensors of some form, only limited information about the instrumentation of many upcoming missions is available. Current plans for the Gateway in lunar orbit, for example, seem to focus on dosimetry of biologically relevant radiation, therefore providing less detailed information than LND and the LCNS.

Neutron spectroscopy is by now a standard technique for planetary-science investigations—especially for the detection of water—yet the only measurements for the Moon so far were performed from orbit by the Lunar Prospector and LRO missions. The neutron spectrometer (NS) on Lunar Prospector used two ^{3}He gas proportional counters covered by different neutron-absorbing materials to measure the fluxes of thermal and epithermal neutrons (without energy resolution) [Fel+04]. The Lunar Exploration Neutron Detector (LEND) instrument on LRO similarly uses four gas proportional counters, each equipped with a collimator to increase spatial resolution, but is equipped with a detector for fast neutrons as well [Mit+09]. The LCNS will be able to deliver more accurate data for two primary reasons: Its deployment on the lunar surface significantly increases spatial resolution and its ability to measure neutron energies will result in more accurate and detailed spectra.

Again, LND is the only post-Apollo investigation that measured neutrons on the lunar surface. However, because the instrument was designed to measure the contribution of neutrons to the biologically relevant radiation exposure, it is primarily sensitive to neutrons with energies between 1 MeV and 10 MeV [Wim+20], a range that does not allow the detection of hydrogen or water. Though one of the objectives of LND is to demonstrate that its silicon detectors, paired with a thin foil of gadolinium, can detect small fluxes of thermal neutrons, this capability is experimental and also suffers from relatively large background emitted by the lander's radioisotope generators and heaters. The complete lack of detection capabilities for epithermal neutrons means that LND's ability to detect an increased hydrogen abundance below the Chang'E 4 lander is limited.

Several recent and upcoming missions have carried or will carry neutron detectors, for example the MoonRanger [Sch+21] and VIPER [Enn+20] rovers. Both will be equipped with the Neutron Spectrometer System (NSS), an updated yet functionally equivalent derivative of the Lunar Prospector NS. A version of the instrument was hosted on Astrobotic's Peregrine 1 lander but did not make it to the lunar surface due to a propellant leak that prevented the lander from reaching the Moon. Another noteworthy instrument is Neutron Measurements at the Lunar Surface (NMLS), which was supposed to be hosted on Peregrine 1 as well but has since been deferred to a later mission [Fuq+20]. NMLS is based on the same measurement principle as the NSS (two neutron detectors covered in different neutron-absorbing materials) but uses scintillator detectors instead of the more fragile gas proportional counters. The neutron-spectroscopy capabilities we aim to achieve with the LCNS are superior to those of both the NSS and NMLS instruments. The ability to simultaneously measure the charged-particle radiation environment also provides crucial data for interpreting neutron measurements.

The LCNS is not necessarily limited to deployments on surface assets. Its simple yet effective design allows us to scale it to sizes suitable for orbital measurements, where count rates are intrinsically lower than on the surface. Deploying an array of instruments of the currently envisioned size mounted at different angles on a satellite may also allow to record an angular profile of the neutron flux in orbit. A sensitivity study based on realistic simulations, for example using Geant4, would be required to determine the minimum sensitive area per detector in such an application.

Beyond the Moon, gamma-ray and neutron spectroscopy have become standard techniques for investigating the bulk elemental composition of planetary surfaces, often but not always in combination with active neutron sources [KH12; Has+18; Par20]. Examples are the Dynamic Albedo of Neutrons (DAN) instrument on the Mars Science Laboratory (MSL) *Curiosity* rover [Mit+12], the NS and Gamma-Ray Spectrometer (GRS) aboard MESSENGER [Gol+07; Law+13], the Gamma Ray and Neutron Detector (GRaND) on Dawn [Pre+11], as well as the NS, GRS, and High Energy Neutron Detector (HEND) on Mars Odyssey [Boy+04]. Upcoming instruments include, for example, the Dragonfly Gamma-ray and Neutron Spectrometer (DraGNS) [Bar+21b]. In principle, the LCNS design could easily be adapted to match the sensitivity requirements for such missions, opening an even wider range of possible applications.

Overall Summary and Conclusion

To conclude my thesis, I briefly summarize my work on the RadMap Telescope and the LCNS. Detailed summaries and discussions of the two projects can be found in Chapters 12 and 16, respectively.

With the RadMap Telescope, we developed a new compact yet highly capable radiation monitor for characterizing the radiation environment inside crewed spacecraft. We successfully constructed and calibrated its main sensor, a tracking calorimeter with quasi-omnidirectional acceptance made from scintillating-plastic fibers and SiPMs. We also developed space-qualified read-out electronics suitable for future deep-space missions that, when paired with an upgraded version of RadMap's data-acquisition system, consume less than 5 W of power. The system comes with a flexible Ethernet-based data interface and can easily be adapted to the requirements and constraints of a wide range of mission profiles.

During nine months of operating the RadMap Telescope in multiple modules of the ISS, we gathered about 2.7 billion interactions of cosmic-ray and radiation-belt particles with the tracking calorimeter. I conducted an initial analysis of the collected data and was able to confirm that the instrument performs largely as expected. A comparison of the calorimeter's count rate and its temporal variation to that of the flight-proven M-42 dosimeter (which is integrated into the instrument) confirmed that we operated the read-out electronics at close to optimal settings. It also showed that the recorded events must be almost exclusively due to particle interactions, and the levels of noise and (optical) cross-talk are low. Even though the tracking calorimeter is not fully calibrated yet, its total-energy deposition profile exhibits many commonalities with that of the dosimeter and, overall, appears to be plausible. The

detailed analysis of the recorded data, including particle identification and energy reconstruction, is ongoing. As of writing this, a first version of the track reconstruction is already operational and currently being benchmarked. Once we have further advanced our analysis capabilities, we will compare our data to that gathered by NASA's ISS-RAD detector, close to which RadMap was located while operating in the USL module.

The tracking calorimeter we devised is surely not a one-size-fits-all solution but has several advantages over other state-of-the-art sensors. Most important is its ability to resolve the charge and energy of cosmic-ray nuclei up to iron with omnidirectional acceptance. Its (almost) tissue-equivalent composition results in a sensitivity to exactly those particle energies that are most harmful to the human organism. In contrast to many other instruments that can determine only the LET of incident radiation, our measurements therefore allow a direct and precise calculation of Q_{NASA}, the quality factor NASA uses to describe the biological effectiveness of a radiation field. This allows a more precise determination of the dose equivalent astronauts were exposed to. The large geometric factor, and hence gathering power, and the nearly isotropic acceptance of the tracking calorimeter also enable precise studies of the temporal and spatial variation of the radiation field.

We learned many lessons during the construction and operation of the RadMap Telescope, many of them relating to the placement of scintillating fibers in the detector and to their coating. Most of these lessons were already incorporated into an updated design of the tracking calorimeter, which we plan to comprehensively test for first time later this year and hope to deploy to the ISS for on-orbit verification in the near future. We also identified several aspects that need further study; chief among them is the quenching behavior of the scintillating fibers upon exposure to heavy ions.

The development of the LCNS is not as advanced as that of the RadMap Telescope, mostly because we worked on it as part of a technology-maturation project that did not foresee the construction of a flight instrument, unfortunately, our work was also disrupted by the Covid-19 pandemic. Using simulations, we were, however, able to show that our concept of a scintillator-based neutron spectrometer should perform unexpectedly well. The same appears to be case for the instrument's charged-particle telescope. Comprehensive testing of both detectors is required to confirm these simulation results. The LUVMI-X reference mission we devised in cooperation with our project partners shows that the LCNS can provide valuable data in support of the search for water on the Moon. Its compact size and lower power requirements also allow its use

on many other platforms beyond the rover we chose for the reference mission.

Despite the significant progress on both projects, the work presented in this thesis is but a starting point. The successful operation of the RadMap Telescope on the ISS demonstrated the potential of our detector concept. Tests of the new prototypes, as well as an updated design of the overall instrument are now required to further advance our concept. Continued operations of the current instrument on the space station will allow us to gather more data for verifying our simulations and data-analysis algorithms. The LCNS detector prototypes require testing before the full instrument design can be implemented. With the LUVMI-X project ended, we also need to identify a new flight opportunity.

Appendix A

Some Fundamentals of Particle Physics

The chapter briefly introduces two fundamental concepts of particles: relativistic kinematics and interaction cross-sections.

A.0.1 Relativistic Kinematics

In particle and astrophysics, the motion of particles and nuclei must usually be described in relativistic terms. In the following, we recall some key relativistic kinematic relations that are important for the discussion of the interaction of particles with matter. The information presented here is a selective summary of multiple sources [LR16; And+17; KW20].

The relativistic mass of a particle is

$$m = \frac{m_0}{\sqrt{1 - \left(\frac{v}{c}\right)^2}} = \frac{m_0}{\sqrt{1 - \beta^2}}, \tag{A.1}$$

where $\beta = v/c$, c is the speed of light, and v and m_0 are the particle's velocity and rest mass, respectively. With the definition of the *Lorentz factor*

$$\gamma = \frac{1}{\sqrt{1 - \beta^2}}, \tag{A.2}$$

Eq. A.1 reduces to

$$m = \gamma m_0 \tag{A.3}$$

Using these fundamental relations, we can calculate the kinetic energy of a particle via

$$E_{\mathrm{k}} = \frac{mv^2}{2} = \frac{m_0 c^2 \beta^2}{2\sqrt{1-\beta^2}} = (\gamma - 1) m_0 c^2 \tag{A.4}$$

and, analogously, its momentum via

$$p = mv = \sqrt{2mE} = \frac{m_0 c \beta}{\sqrt{1-\beta^2}} = \beta\gamma m_0 c \tag{A.5}$$

The momentum is commonly expressed in units of pc (see Sec. 3.1), having the dimension of [energy]:

$$pc = \frac{m_0 c^2 \beta}{\sqrt{1-\beta^2}} = \beta\gamma m_0 c^2 \tag{A.6}$$

From Eq. A.5, we can derive another helpful quantity that is often used to compare the energies of particles with substantially different rest masses:

$$\beta\gamma = \frac{p}{m_0 c} \tag{A.7}$$

Finally, the total energy of a particle is given by the sum of its kinetic and rest energies:

$$E = \sqrt{m_0^2 c^4 + p^2 c^2} = mc^2 = \gamma m_0 c^2 \tag{A.8}$$

A.0.2 Interaction Cross-Sections and Mean Free Path

The probability for a particle to interact with matter is usually expressed in terms of characteristic quantities called *cross-sections*. Consider a beam of point-like particles impinging on a target in form of a thin disk of material with area S and thickness l (see Fig. A.1). In this scenario, the probability for a beam particle to interact with a target particle, P_{R}, is given by the ratio of the interaction rate, $\dot{N}_{\mathrm{R}}$—i.e., the total number of particles that interact with the target material per unit time—to the rate of incident particles, $\dot{N}_{\mathrm{in}}$ [KW20]:

$$P_{\mathrm{R}} = \frac{\dot{N}_{\mathrm{R}}}{\dot{N}_{\mathrm{in}}} = \frac{N_{\mathrm{T}}\,\sigma_{\mathrm{tot}}}{S} = n_{\mathrm{T}}\,\sigma_{\mathrm{tot}}\,l \tag{A.9}$$

N_{T} is the number of target particles in the volume $V = S\,l$ and is given by

$$N_{\mathrm{T}} = \frac{\rho V}{A} N_{\mathrm{A}}, \tag{A.10}$$

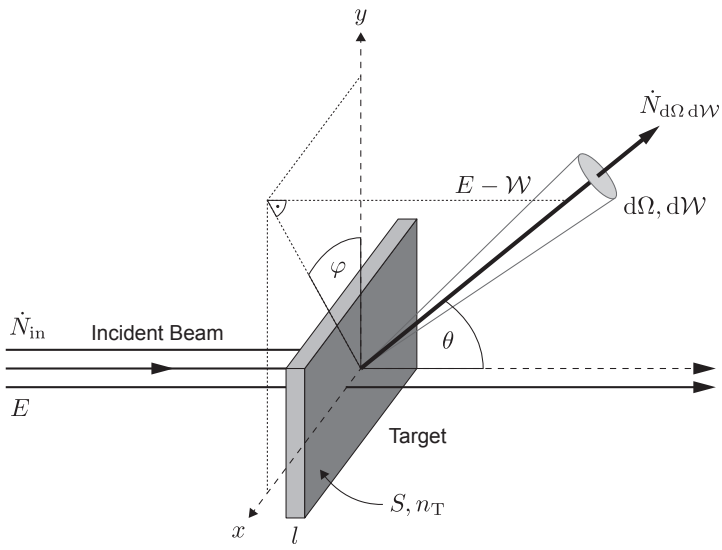

Figure A.1: Illustration of the variables used in the definition of the interaction cross-sections. Adapted from [And+17].

where ρ and A are the target material's mass density and atomic mass number and N_{A} is the Avogadro constant. n_{T} is the corresponding particle number density, $n_{\mathrm{T}} = N_{\mathrm{T}}/V$. The *total* cross-section, σ_{tot}, is hence defined as

$$\sigma_{\mathrm{tot}} = \frac{\dot{N}_{\mathrm{R}}}{\dot{N}_{\mathrm{in}}} \frac{1}{n_{\mathrm{T}}\, l} \tag{A.11}$$

σ_{tot} has the dimension of [area] and can be interpreted as the effective area of a target particle that an incident beam particle 'sees' [KW20]. The total effective area of the target interacting with the beam is thus given by $\sigma_{\mathrm{tot}}\, N_{\mathrm{T}}$.

The *differential* cross-section takes into account that in elastic collisions charged particles of energy E lose a part of their energy, $\mathcal{W}$, and are deflected in a certain direction that depends on $\mathcal{W}$. We now want to know how many particles that lost an energy between $\mathcal{W}$ and $\mathcal{W} + \mathrm{d}\mathcal{W}$ and are deflected within a small solid angle $\mathrm{d}\Omega$ can be detected in a certain direction (θ, φ), where θ and φ are the polar and azimuthal angles (Fig. A.1) [And+17]:

$$\dot{N}_{\mathrm{d}\Omega\,\mathrm{d}\mathcal{W}} \propto \dot{N}_{\mathrm{in}}\, \mathrm{d}\Omega\, \mathrm{d}\mathcal{W} = \frac{\mathrm{d}^2\sigma}{\mathrm{d}\Omega\, \mathrm{d}\mathcal{W}} \dot{N}_{\mathrm{in}}\, \mathrm{d}\Omega\, \mathrm{d}\mathcal{W} \tag{A.12}$$

The *double-differential* cross section per unit solid angle and unit energy loss is hence defined as

$$\frac{\mathrm{d}^2\sigma}{\mathrm{d}\Omega\,\mathrm{d}\mathcal{W}} = \frac{\dot{N}_{\mathrm{d}\Omega\,\mathrm{d}\mathcal{W}}}{\dot{N}_{\mathrm{in}}\,\mathrm{d}\Omega\,\mathrm{d}\mathcal{W}} \tag{A.13}$$

and has dimensions of [area · solid angle^{-1} · energy^{-1}]. Integrating Eq. A.13 over the solid angle yields the differential cross-section in energy loss [And+17]:

$$\frac{\mathrm{d}\sigma}{\mathrm{d}\mathcal{W}} = \int \frac{\mathrm{d}^2\sigma}{\mathrm{d}\Omega\,\mathrm{d}\mathcal{W}}\,\mathrm{d}\Omega = \int_{\varphi=0}^{2\pi}\int_{\theta=0}^{\pi} \frac{\mathrm{d}^2\sigma}{\mathrm{d}\Omega\,\mathrm{d}\mathcal{W}}\sin\theta\,\mathrm{d}\theta\,\mathrm{d}\varphi\,, \tag{A.14}$$

where $\mathrm{d}\Omega = \sin\theta\,\mathrm{d}\theta\,\mathrm{d}\varphi$. Likewise, we obtain the differential cross-section in solid angle by integrating over the energy loss [And+17]:

$$\frac{\mathrm{d}\sigma}{\mathrm{d}\Omega} = \int_0^E \frac{\mathrm{d}^2\sigma}{\mathrm{d}\Omega\,\mathrm{d}\mathcal{W}}\,\mathrm{d}\mathcal{W} \tag{A.15}$$

The total cross-section can be obtained by integrating Eq. A.13 over both the solid angle and the energy loss:

$$\sigma_{\mathrm{tot}} = \int_0^E \left(\int_\Omega \frac{\mathrm{d}^2\sigma}{\mathrm{d}\Omega\,\mathrm{d}\mathcal{W}}\,\mathrm{d}\Omega\right)\mathrm{d}\mathcal{W} = \int_0^E \left(\int_\Omega \frac{\dot{N}_{\mathrm{d}\Omega\,\mathrm{d}\mathcal{W}}}{\dot{N}_{\mathrm{in}}\,\mathrm{d}\Omega\,\mathrm{d}\mathcal{W}}\,\mathrm{d}\Omega\right)\mathrm{d}\mathcal{W} \tag{A.16}$$

Up to now, we did not pay attention to the nature of the interaction between beam and target particles. Both charged and uncharged particles can undergo a number of interactions in matter (many of which I will briefly explain in the following sections of this chapter). To account for this, the *microscopic* total cross-section is defined as the sum of the total cross-sections of the various interactions, $\sigma_i(E)$, at a given energy, E [And+17]:

$$\sigma_{\mathrm{tot}}(E) = \sum_i \sigma_i(E) \tag{A.17}$$

Multiplying Eq. A.17 by the number of atoms per mass of an element, N_{A}/A, yields the *macroscopic* total cross section

$$\Sigma_{\mathrm{tot}}(E) = \sigma_{\mathrm{tot}}(E)\frac{N_{\mathrm{A}}}{A}, \tag{A.18}$$

which has dimension of [area · mass^{-1}] and is typically given in $\mathrm{cm}^2\mathrm{g}^{-1}$.

From Eq. A.18 we can derive the *mass attenuation coefficient*, $\mu(E)/\rho$, which is the macroscopic equivalent of the total cross-section [And+17]:

$$\frac{\mu(E)}{\rho} \equiv \Sigma_{\mathrm{tot}}(E) \tag{A.19}$$

Dividing by ρ yields the *linear attenuation coefficient*, $\mu(E)$, which has the dimension of [length^{-1}] and can be multiplied by a small distance Δs to calculate the probability for an interaction to occur in that distance interval. The *mean free path*, λ, of a particle is defined as [KW20; And+17]

$$\lambda = \frac{1}{\mu(E)} = \frac{A}{\rho N_{\mathrm{A}} \sigma_{\mathrm{tot}}(E)} \tag{A.20}$$

and yields the mean path length between two consecutive interactions. In thick targets, $\mu(E)$ can be used to take into account that the number of beam particles that have not yet interacted with a target particle, $N(x)$, decreases exponentially with the penetration depth x [KW20]:

$$N(x, E) = N_0 \, \mathrm{e}^{-\mu(E)x} \tag{A.21}$$

Here, N_0 is the initial number of beam particles entering the target. Eq. A.21 is known as the Beer-Lambert law and also governs the absorption of photons in matter, in which case $\mu(E)$ is sometimes called the *absorption coefficient*.

Bibliography

Books and Book Chapters

[Aha13] F. A. Aharonian. "Gamma-Ray Emission of Supernova Remnants and the Origin of Galactic Cosmic Rays." In: *Planets, Stars and Stellar Systems*. Ed. by T. D. Oswalt and G. Gilmore. Vol. 5. Dordrecht: Springer, 2013, pp. 789–827. ISBN: 978-94-007-5611-3. DOI: 10.1007/978-94-007-5612-0_15.

[Ald13] B. Aldrin. *Mission to Mars: My Vision for Space Exploration*. Washington, DC: National Geographic Society, 2013. ISBN: 978-1-4262-1468-4.

[Alo+18] R. Aloisio, P. Blasi, I. De Mitri, and S. Petrera. "Selected Topics in Cosmic Ray Physics." In: *Multiple Messengers and Challenges in Astroparticle Physics*. 2018, pp. 1–95. ISBN: 978-3-319-65423-2. DOI: 10.1007/978-3-319-65425-6_1.

[AZ77] H. H. Andersen and J. F. Ziegler. *Hydrogen: Stopping Powers and Ranges in All Elements*. Vol. 3. The Stopping and Ranges of Ions in Matter. Elmsford, NY: Pergamon Press, 1977.

[And+17] P. Andreo, D. T. Burns, A. E. Nahum, et al. *Fundamentals of Ionizing Radiation Dosimetry*. Weinheim: Wiley-VCH, 2017. ISBN: 978-3-527-40921-1.

[Aug+09] N. R. Augustine, M. Austin Wanda, C. Chyba, et al. *Seeking a Human Spaceflight Program Worthy of a Great Nation*. Washington, DC: National Aeronautics and Space Administration, 2009.

[AM15] J.-L. Autran and D. Munteanu. *Soft Errors*. Boca Raton, FL: CRC Press, 2015. ISBN: 978-0-367-65599-0. DOI: 10.1201/b18132.

[Bec21] J. E. Beckman. *Multimessenger Astronomy*. Astronomers' Universe. Cham: Springer, 2021. ISBN: 978-3-030-68371-9. DOI: 10.1007/978-3-030-68372-6.

[Beh+13] O. Behnke, K. Kröninger, G. Schott, and T. Schörner-Sadenius. *Data Analysis in High Energy Physics*. Weinheim: Wiley-VCH, 2013. ISBN: 9783527410583. DOI: 10.1002/9783527653416.

[Bir64] J. B. Birks. *The Theory and Practice of Scintillation Counting*. Oxford, London: Pergamon Press, 1964. ISBN: 978-0-08-010472-0. DOI: 10.1016/c2013-0-01791-4.

[BC21] E. A. Blakely and P. Y. Chang. "Late Effects of Space Radiation: Cataracts." In: *Handbook of Bioastronautics*. Ed. by L. R. Young and J. P. Sutton. Cham: Springer, 2021, pp. 277–286. ISBN: 978-3-319-12190-1. DOI: 10.1007/978-3-319-12191-8_87.

[Bog+22] J. S. Bogard, D. J. Downing, R. L. Coleman, et al. *Atoms, Radiation, and Radiation Protection*. 4th ed. Weinheim: Wiley-VCH, 2022. ISBN: 9783527413522. DOI: 10.1002/9783527805600.

[BW20] M. Born and E. Wolf. *Principles of Optics*. 7th ed. Cambridge: Cambridge University Press, 2020. ISBN: 9781108477437. DOI: 10.1017/9781108769914.

[BG11] H. Budzier and G. Gerlach. *Thermal Infrared Sensors*. Chichester: Wiley, 2011. ISBN: 9780470871928. DOI: 10.1002/9780470976913.

[Bus04] G. W. Bush. *A Renewed Spirit of Discovery: The President's Vision for U.S. Space Exploration*. Washington, DC: White House Executive Office of the President, 2004.

[Büt18] R. Bütikofer. "Cosmic Ray Particle Transport in the Earth's Magnetosphere." In: *Solar Particle Radiation Storms Forecasting and Analysis*. Ed. by O. E. Malandraki and N. B. Crosby. Astrophysics and Space Science Library. Cham: Springer, 2018, pp. 79–94. ISBN: 978-3-319-60050-5. DOI: 10.1007/978-3-319-60051-2_5.

[CD13] A. Castellina and F. Donato. "Astrophysics of Galactic Charged Cosmic Rays." In: *Planets, Stars and Stellar Systems. Volume 5: Galactic Structure and Stellar Populations*. Ed. by T. D. Oswalt and G. Gilmore. 2013, pp. 725–788. DOI: 10.1007/978-94-007-5612-0.

[Cha19] K. H. Chadwick. *Understanding Radiation Biology*. Boca Raton, FL: CRC Press, 2019. ISBN: 9780429288197. DOI: 10.1201/9780429288197.

[CGW12] J. Clayden, N. Greeves, and S. Warren. *Organic Chemistry*. 2nd ed. Oxford, New York: Oxford University Press, 2012. ISBN: 978-0-19-927029-3.

[ES12] S. I. Eidelman and B. A. Shwartz. "Interactions of Particles and Radiation with Matter." In: *Handbook of Particle Detection and Imaging*. Ed. by C. Grupen and I. Buvat. Vol. 1. Berlin, Heidelberg: Springer, 2012, pp. 3–23. ISBN: 978-3-642-13270-4. DOI: 10.1007/978-3-642-13271-1_1.

[EM20] R. W. Erickson and D. Maksimović. *Fundamentals of Power Electronics*. 3rd ed. Cham: Springer, 2020. ISBN: 978-3-030-43879-1. DOI: 10.1007/978-3-030-43881-4.

[FS93] B. Fegley and T. D. Swindle. "Lunar Volatiles: Implications for Lunar Resource Utilization." In: *Resources of Near-Earth Space*. Ed. by J. S. Lewis, M. S. Matthews, and M. L. Guerrieri. Tucson, AZ: University of Arizona Press, 1993.

[GER16] T. K. Gaisser, R. Engel, and E. Resconi. *Cosmic Rays and Particle Physics*. 2nd. Cambridge: Cambridge University Press, 2016. DOI: 10.1017/cbo9781139192194.

[GKT17] N. Z. Galunov, N. L. Karavaeva, and O. A. Tarasenko. "Crystalline and Composite Scintillators for Fast and Thermal Neutron Detection." In: *Engineering of Scintillation Materials and Radiation Technologies*. Ed. by M. Korzhik and A. Gektin. Springer Proceedings in Physics. Cham: Springer, 2017. ISBN: 978-3-319-68464-2. DOI: 10.1007/978-3-319-68465-9_12.

[GL10] C. Gattringer and C. B. Lang. *Quantum Chromodynamics on the Lattice*. Vol. 788. Lecture Notes in Physics. Heidelberg, Berlin: Springer, 2010. ISBN: 978-3-642-01849-7. DOI: 10.1007/978-3-642-01850-3.

[Gom56] P. Gombás. "Statistische Behandlung des Atoms." In: *Atoms II / Atome II*. Ed. by S. Flügge. Encyclopedia of Physics / Handbuch der Physik. Berlin, Heidelberg: Springer, 1956, pp. 109–231. ISBN: 978-3-642-85688-4. DOI: 10.1007/978-3-642-85687-7_2.

[Goo21] D. T. Goodhead. "Particle Track Structure and Biological Implications." In: *Handbook of Bioastronautics*. Ed. by L. R. Young and J. P. Sutton. Cham: Springer, 2021, pp. 287–312. ISBN: 978-3-319-12190-1. DOI: 10.1007/978-3-319-12191-8_29.

[Gri01] P. K. F. Grieder. *Cosmic Rays at Earth: Researcher's Reference Manual and Data Book*. Amsterdam: Elsevier, 2001. ISBN: 9780444507105. DOI: 10.1016/b978-0-444-50710-5.X5000-3.

[Gru20] C. Grupen. *Astroparticle Physics*. 2nd. Cham: Springer, 2020. ISBN: 978-3-030-27341-5.

[Ham21] M. Hamel. *Plastic Scintillators: Chemistry and Applications*. Topics in Applied Physics. Cham: Springer, 2021. ISBN: 978-3-030-73487-9. DOI: 10.1007/978-3-030-73488-6.

[Has+18] N. Hasabe, K. J. Kim, E. Shibamura, and K. Sakurai. *Nuclear Planetary Science: Planetary Science Based on Gamma-Ray, Neutron and X-Ray Spectriscopy*. Advances in Planetary Science. Singapore: World Scientific, 2018.

[Hel+20] C. E. Hellweg, T. Berger, D. Matthiä, and C. Baumstark-Khan. *Radiation in Space: Relevance and Risk for Human Missions*. SpringerBriefs in Space Life Sciences. Cham: Springer, 2020. ISBN: 978-3-030-46743-2. DOI: 10.1007/978-3-030-46744-9.

[Hel+23] C. E. Hellweg, C. Arena, S. Baatout, et al. "Space Radiobiology." In: *Radiobiology Textbook*. Ed. by S. Baatout. Cham: Springer, 2023, pp. 503–569. ISBN: 978-3-031-18809-1. DOI: 10.1007/978-3-031-18810-7_10.

[HDH13] A. Herout, M. Dubská, and J. Havel. "Review of Hough Transform for Line Detection." In: *Real-Time Detection of Lines and Grids*. SpringerBriefs in Computer Science. London: Springer, 2013, pp. 3–16. ISBN: 978-1-4471-4413-7. DOI: 10.1007/978-1-4471-4414-4_2.

[Hey90] K. L. G. Heyde. *The Nuclear Shell Model*. Springer Series in Nuclear and Particle Physics. Berlin, Heidelberg: Springer, 1990. ISBN: 978-3-642-97205-8. DOI: 10.1007/978-3-642-97203-4.

[HR20] H. J. Hilke and W. Riegler. "Gaseous Detectors." In: *Particle Physics Reference Library*. Ed. by C. W. Fabjan and H. Schopper. Cham: Springer, 2020, pp. 91–136. DOI: 10.1007/978-3-030-35318-6_4.

[Hil84b] R. Hillier. *Gamma Ray Astronomy*. Oxford: Clarendon Press, 1984. ISBN: 9780198514510.

[HA02] A. Holmes-Siedle and L. Adams. *Handbook of Radiation Effects*. 2nd ed. Oxford: Oxford University Press, 2002. ISBN: 9780198507338. DOI: 10.1093/oso/9780198507338.001.0001.

[Jac99] J. D. Jackson. *Classical Electrodynamics*. 3rd ed. New York, NY: Wiley, 1999. ISBN: 978-0-471-42764-3.

[Jon15] F. M. Jonas. "Solar Flares." In: *Handbook of Cosmic Hazards and Planetary Defense*. Ed. by J. N. Pelton and F. Allahdadi. Cham: Springer, 2015, pp. 37–46. ISBN: 978-3-319-03951-0. DOI: 10.1007/978-3-319-03952-7_3.

[Joy18] M. Joyce. *Nuclear Engineering*. Oxford: Butterworth-Heinemann, 2018. ISBN: 978-0-08-100962-8. DOI: 10.1016/c2015-0-05557-5.

[KB14] M. G. Kivelson and F. Bagenal. "Planetary Magnetospheres." In: *Encyclopedia of the Solar System*. Ed. by T. Spohn, D. Breuer, and T. V. Johnson. 3rd. Elsevier, 2014, pp. 137–157. ISBN: 9783540463146. DOI: 10.1016/B978-012088589-3/50032-3.

[Kle21] A. Klett. "Neutron Detection." In: *Handbook of Particle Detection and Imaging*. Ed. by I. Fleck, M. Titov, C. Grupen, and I. Buvat. Cham: Springer, 2021, pp. 1041–1073. ISBN: 978-3-319-93784-7. DOI: 10.1007/978-3-319-93785-4_31.

[Kno10] G. F. Knoll. *Radiation Detection and Measurement*. 4th ed. New York: John Wiley & Sons, 2010. ISBN: 978-0-470-13148-0.

[KW20] H. Kolanoski and N. Wermes. *Particle Detectors: Fundamentals and Applications*. Oxford: Oxford University Press, 2020. ISBN: 978-0-19-885836-2. DOI: 10.1093/oso/9780198858362.001.0001.

[KMN17] S. Koltzenburg, M. Maskos, and O. Nuyken. *Polymer Chemistry*. Berlin, Heidelberg: Springer, 2017. ISBN: 978-3-662-49277-2. DOI: 10.1007/978-3-662-49279-6.

[Kra22] G. Kramer. “Origin, Geography, and Geology of the Moon.” In: *Handbook of Lunar Base Design and Development*. Ed. by P. Eckart and A. Aldrin. Cham: Springer, 2022. ISBN: 978-3-030-05323-9. DOI: 10.1007/978-3-030-05323-9_52-1.

[LA87] P. J. M. van Laarhoven and E. H. L. Aarts. *Simulated Annealing: Theory and Applications*. Mathematics and Its Applications. Dordrecht: Springer, 1987. ISBN: 978-90-481-8438-5. DOI: 10.1007/978-94-015-7744-1.

[Leo94] W. R. Leo. *Techniques for Nuclear and Particle Physics Experiments*. 2nd ed. Berlin, Heidelberg: Springer, 1994. ISBN: 978-3-540-57280-0. DOI: 10.1007/978-3-642-57920-2.

[LR16] C. Leroy and P.-G. Rancoita. *Principles of Radiation Interaction in Matter and Detection*. 4th ed. Singapore: World Scientific Publishing Co. Pte. Ltd., 2016. ISBN: 978-981-4603-18-8. DOI: 10.1142/9167.

[Lil82] J. S. Lilley. “Nuclear Reactions Near the Coulomb Barrier.” In: *Contemporary Research Topics in Nuclear Physics*. 1982, pp. 249–273. ISBN: 978-1-4684-1136-2 978-1-4684-1134-8. DOI: 10.1007/978-1-4684-1134-8_13.

[LPG09] K. Lodders, H. Palme, and H. P. Gail. “4.4 Abundances of the elements in the Solar System.” In: *Solar System*. Landolt-Börnstein - Group VI Astronomy and Astrophysics. 2009, pp. 712–770. ISBN: 978-3-540-88055-4. DOI: 10.1007/978-3-540-88055-4_34.

[Lon12] M. S. Longair. *High Energy Astrophysics*. 3rd. Cambridge: Cambridge University Press, 2012. ISBN: 9780521756181. DOI: 10.1017/cbo9780511778346.

[LB23] M. J. Losekamm and S. Burmeister. “Cosmic Rays in the Lunar Environment.” In: *Encyclopedia of Lunar Science*. Ed. by B. Cudnik. Cham: Springer, 2023, pp. 166–176. DOI: 10.1007/978-3-319-14541-9_176.

[MPG21] X. W. Mao, M. J. Pecaut, and D. S. Gridley. “Acute Risks of Space Radiation.” In: *Handbook of Bioastronautics*. Ed. by L. R. Young and J. P. Sutton. Cham: Springer, 2021, pp. 263–276. ISBN: 978-3-319-12190-1. DOI: 10.1007/978-3-319-12191-8_27.

[Mat10] D. M. Mattox. *Handbook of Physical Vapor Deposition (PVD) Processing*. Oxford, UK: Elsevier, 2010. ISBN: 9780815520375. DOI: 10.1016/c2009-0-18800-1.

[Nat12] National Academies of Sciences, Engineering, and Medicine. *Technical Evaluation of the NASA Model for Cancer Risk to Astronauts Due to Space Radiation*. Washington, DC: The National Academies Press, 2012. ISBN: 978-0-309-25305-5. DOI: 10.17226/13343.

[Nat21] National Academies of Sciences, Engineering, and Medicine. *Space Radiation and Astronaut Health: Managing and Communicating Cancer Risks*. Washington, DC: The National Academies Press, 2021. ISBN: 978-0-309-47966-0. DOI: 10.17226/26155.

[Olv+10] F. W. J. Olver, D. W. Lozier, R. F. Boisvert, and C. F. Clark, eds. *NIST Handbook of Mathematical Functions*. New York, NY: Cambridge University Press, 2010. ISBN: 978-0-521-19225-5.

[Pet11] E. Petersen. *Single Event Effects in Aerospace*. New Jersey: Wiley, 2011. ISBN: 978-0-470-76749-8. DOI: 10.1002/9781118084328.

[Pov+15] B. Povh, K. Rith, C. Scholz, et al. *Particles and Nuclei: An Introduction to the Physical Concepts*. 7th ed. Graduate Texts in Physics. Berlin, Heidelberg: Springer, 2015. ISBN: 978-3-662-46320-8. DOI: 10.1007/978-3-662-46321-5.

[Rea21] D. V. Reames. *Solar Energetic Particles*. 2nd. Lecture Notes in Physics. Cham: Springer, 2021. ISBN: 978-3-030-66401-5. DOI: 10.1007/978-3-030-66402-2.

[RZ14] J. G. Roederer and H. Zhang. *Dynamics of Magnetically Trapped Particles: Foundations of the Physics of Radiation Belts and Space Plasmas*. 2nd ed. Astrophysics and Space Science Library. Berlin, Heidelberg: Springer, 2014. ISBN: 978-3-642-41529-6. DOI: 10.1007/978-3-642-41530-2.

[Ros52] B. Rossi. *High-Energy Particles*. New York, NY: Prentice-Hall, 1952.

[RZ96] H. H. Rossi and M. Zaider. *Microdosimetry and Its Applications*. 1996. ISBN: 978-3-642-85186-5 978-3-642-85184-1. DOI: 10.1007/978-3-642-85184-1.

[RCE30] E. Rutherford, J. Chadwick, and C. D. Ellis. *Radiations from Radioactive Substances*. Cambridge: Cambridge University Press, 1930. ISBN: 9781108009010. DOI: 10.1017/cbo9780511707179.

[Shw17] B. A. Shwartz. "Scintillation Detectors in Experiments on High Energy Physics." In: *Engineering of Scintillation Materials and Radiation Technologies*. Springer Proceedings in Physics. 2017, pp. 211–230. ISBN: 978-3-319-68464-2. DOI: 10.1007/978-3-319-68465-9_13.

[Sig14] P. Sigmund. *Particle Penetration and Radiation Effects Volume 2*. Vol. 2. Springer Series in Solid-State Sciences. Cham: Springer, 2014. ISBN: 978-3-319-05563-3. DOI: 10.1007/978-3-319-05564-0.

[Spu18] M. Spurio. *Probes of Multimessenger Astrophysics*. Astronomy and Astrophysics Library. Cham: Springer, 2018. ISBN: 978-3-319-96853-7. DOI: 10.1007/978-3-319-96854-4.

[Sta21] T. Stanev. *High Energy Cosmic Rays*. 3rd. Astrophysics and Space Science Library. Cham: Springer, 2021. ISBN: 978-3-030-71566-3. DOI: 10.1007/978-3-030-71567-0.

[Sve+17] S. Svertilov, V. V. Bogomolov, A. Iyudin, et al. "New Advanced Scintillators for Gamma Ray Spectroscopy and Their Application." In: *Engineering of Scintillation Materials and Radiation Technologies*. Springer Proceedings in Physics. 2017, pp. 281–299. ISBN: 978-3-319-68464-2. DOI: 10.1007/978-3-319-68465-9_17.

[04] *The Vision for Space Exploration*. Vol. NP-2004-01-334-HQ. Washington, DC: National Aeronautics and Space Administration, 2004.

[Wig17] R. Wigmans. "The Physics of Shower Development." In: *Calorimetry: Energy Measurement in Particle Physics*. 2nd ed. Oxford: Oxford University Press, 2017, pp. 30–110. ISBN: 9780198786351. DOI: 10.1093/oso/9780198786351.003.0002.

[Zei21] C. Zeitlin. "Space Radiation Shielding." In: *Handbook of Bioastronautics*. Ed. by L. R. Young and J. P. Sutton. Cham: Springer, 2021, pp. 353–375. ISBN: 978-3-319-12190-1. DOI: 10.1007/978-3-319-12191-8_28.

[Zhm17] P. Zhmurin. "Modification of Plastic Scintillator for Neutron Registration." In: *Engineering of Scintillation Materials and Radiation Technologies*. Springer Proceedings in Physics. 2017, pp. 129–149. ISBN: 978-3-319-68464-2 978-3-319-68465-9. DOI: 10.1007/978-3-319-68465-9_8.

[Zhm+19] P. N. Zhmurin, Y. A. Gurkalenko, V. N. Pereymak, et al. "Plastic Scintillators with the Improved Radiation Hardness Level." In: *Engineering of Scintillation Materials and Radiation Technologies (ISMART 2018)*. Ed. by M. Korzhik and A. Gektin. Springer Proceedings in Physics. Cham: Springer, 2019, pp. 125–145. ISBN: 978-3-030-21969-7. DOI: 10.1007/978-3-030-21970-3_10.

[Zie77] J. F. Ziegler. *Helium: Stopping Power and Ranges in All Elemental Matter*. Vol. 4. The Stopping and Ranges of Ions in Matter. New York: Pergamon Press, 1977.

[ZBL85] J. F. Ziegler, J. P. Biersack, and U. Littmark. *The Stopping and Range of Ions in Solids*. Vol. 1. The Stopping Ranges of Ions in Matter. New York: Pergamon Press, 1985.

[Zor+89] C. Zorn, M. Bowen, S. Majewski, et al. “Development of Improved, Radiation-Resistant Plastic and Liquid Scintillators for the SSC.” In: *Supercollider 1*. Ed. by M. McAshan. Boston, MA: Springer, 1989, pp. 537–550. ISBN: 978-1-4612-8109-2. DOI: 10.1007/978-1-4613-0841-6_50.

Journal Articles

[Aab+20] A. Aab, P. Abreu, M. Aglietta, et al. “Measurement of the cosmic-ray energy spectrum above 2.5×10^{18} eV using the Pierre Auger Observatory.” In: *Physical Review D* 102.6 (2020). DOI: 10.1103/PhysRevD.102.062005.

[Aab+21] A. Aab, P. Abreu, M. Aglietta, et al. “Design, upgrade and characterization of the silicon photomultiplier front-end for the AMIGA detector at the Pierre Auger Observatory.” In: *Journal of Instrumentation* 16.01 (2021), P01026–P01026. DOI: 10.1088/1748-0221/16/01/p01026.

[Aar+19] M. G. Aartsen, M. Ackermann, J. Adams, et al. “Cosmic ray spectrum and composition from PeV to EeV using 3 years of data from IceTop and IceCube.” In: *Physical Review D* 100.8 (2019). DOI: 10.1103/PhysRevD.100.082002.

[Abb+18] R. U. Abbasi, M. Abe, T. Abu-Zayyad, et al. “The Cosmic Ray Energy Spectrum between 2 PeV and 2 EeV Observed with the TALE Detector in Monocular Mode.” In: *The Astrophysical Journal* 865.1 (2018). DOI: 10.3847/1538-4357/aada05.

[Abb+08] R. U. Abbasi, T. Abu-Zayyad, M. Allen, et al. “First observation of the Greisen-Zatsepin-Kuzmin suppression.” In: *Physical Review Letters* 100.10 (2008), p. 101101. DOI: 10.1103/PhysRevLett.100.101101.

[Abb+23] R. U. Abbasi, M. G. Allen, R. Arimura, et al. “An extremely energetic cosmic ray observed by a surface detector array.” In: *Science* 382.6673 (2023), pp. 903–907. DOI: 10.1126/science.abo5095.

[Abe+16] K. Abe, H. Fuke, S. Haino, et al. “Measurements of cosmic-ray proton and helium spectra from the BESS-Polar long-duration balloon flights over Antarctica.” In: *The Astrophysical Journal* 822.2 (2016). DOI: 10.3847/0004-637x/822/2/65.

[Abr+22] S. Abraham, C. Fuentes-Hernandez, S. Mukhopadhyay, et al. “An approach towards plastic scintillators from thermally activated delayed fluorescent dyes and cross-linkable bismuth compounds.” In: *Journal of Materials Chemistry C* 10.46 (2022), pp. 17481–17488. DOI: 10.1039/d2tc04165k.

[Abr+21] P. Abreu, M. Aglietta, J. M. Albury, et al. “The energy spectrum of cosmic rays beyond the turn-down around 10^{17} eV as measured with the surface detector of the Pierre Auger Observatory.” In: *The European Physical Journal C* 81.11 (2021). DOI: 10.1140/epjc/s10052-021-09700-w.

[Acc+22] V. A. Acciari, S. Ansoldi, L. A. Antonelli, et al. “Proton acceleration in thermonuclear nova explosions revealed by gamma rays.” In: *Nature Astronomy* 6.6 (2022), pp. 689–697. DOI: 10.1038/s41550-022-01640-z.

[Ace+23] F. Acerbi, A. R. Altamura, B. Di Ruzza, et al. “Radiation damage effects of protons and X-rays on silicon photomultipliers.” In: *Nuclear Instruments and Methods in Physics Research Section A: Accelerators, Spectrometers, Detectors and Associated Equipment* 1047 (2023). DOI: 10.1016/j.nima.2022.167791.

[Ace+15] F. Acerbi, A. Ferri, G. Zappala, et al. “NUV Silicon Photomultipliers With High Detection Efficiency and Reduced Delayed Correlated-Noise.” In: *IEEE Transactions on Nuclear Science* 62.3 (2015), pp. 1318–1325. DOI: 10.1109/tns.2015.2424676.

[AG19] F. Acerbi and S. Gundacker. “Understanding and simulating SiPMs.” In: *Nuclear Instruments and Methods in Physics Research Section A: Accelerators, Spectrometers, Detectors and Associated Equipment* 926 (2019), pp. 16–35. DOI: 10.1016/j.nima.2018.11.118.

[Ace+19] F. Acerbi, G. Paternoster, M. Capasso, et al. “Silicon Photomultipliers: Technology Optimizations for Ultraviolet, Visible and Near-Infrared Range.” In: *Instruments* 3.1 (2019). DOI: 10.3390/instruments3010015.

[Adr+21a] O. Adriani, A. Agnesi, S. Albergo, et al. “The CaloCube calorimeter for high-energy cosmic-ray measurements in space: performance of a large-scale prototype.” In: *Journal of Instrumentation* 16.10 (2021). DOI: 10.1088/1748-0221/16/10/p10024.

[Adr+20] O. Adriani, Y. Akaike, K. Asano, et al. “Direct Measurement of the Cosmic-Ray Carbon and Oxygen Spectra from 10 GeV/n to 2.2 TeV/n with the Calorimetric Electron Telescope on the International Space Station.” In: *Physical Review Letters* 125.25 (2020), p. 251102. DOI: 10.1103/PhysRevLett.125.251102.

[Adr+21b] O. Adriani, Y. Akaike, K. Asano, et al. “Measurement of the Iron Spectrum in Cosmic Rays from 10 GeV/n to 2.0 TeV/n with the Calorimetric Electron Telescope on the International Space Station.” In: *Physical Review Letters* 126.24 (2021), p. 241101. DOI: 10.1103/PhysRevLett.126.241101.

[Adr+22a] O. Adriani, Y. Akaike, K. Asano, et al. “Cosmic-Ray Boron Flux Measured from 8.4 GeV/n to 3.8 TeV/n with the Calorimetric Electron Telescope on the International Space Station.” In: *Physical Review Letters* 129.25 (2022), p. 251103. DOI: 10.1103/PhysRevLett.129.251103.

[Adr+22b] O. Adriani, Y. Akaike, K. Asano, et al. “Direct Measurement of the Nickel Spectrum in Cosmic Rays in the Energy Range from 8.8 GeV/n to 240 GeV/n with CALET on the International Space Station.” In: *Physical Review Letters* 128.13 (2022), p. 131103. DOI: 10.1103/PhysRevLett.128.131103.

[Adr+22c] O. Adriani, Y. Akaike, K. Asano, et al. “Observation of Spectral Structures in the Flux of Cosmic-Ray Protons from 50 GeV to 60 TeV with the Calorimetric Electron Telescope on the International Space Station.” In: *Physical Review Letters* 129.10 (2022), p. 101102. DOI: 10.1103/PhysRevLett.129.101102.

[Adr+23] O. Adriani, Y. Akaike, K. Asano, et al. “Direct Measurement of the Cosmic-Ray Helium Spectrum from 40 GeV to 250 TeV with the Calorimetric Electron Telescope on the International Space Station.” In: *Physical Review Letters* 130.17 (2023), p. 171002. DOI: 10.1103/PhysRevLett.130.171002.

[Adr+11] O. Adriani, G. C. Barbarino, G. A. Bazilevskaya, et al. “PAMELA Measurements of Cosmic-Ray Proton and Helium Spectra.” In: *Science* 332 (2011), pp. 69–72. DOI: 10.1126/science.1199172.

[Adr+14] O. Adriani, G. C. Barbarino, G. A. Bazilevskaya, et al. “Measurement of Boron and Carbon Fluxes in Cosmic Rays with the Pamela Experiment.” In: *The Astrophysical Journal* 791.2 (2014). DOI: 10.1088/0004-637x/791/2/93.

[Agl23] G. Aglieri Rinella. “Developments of stitched monolithic pixel sensors towards the ALICE ITS3.” In: *Nuclear Instruments and Methods in Physics Research Section A: Accelerators, Spectrometers, Detectors and Associated Equipment* 1049 (2023). DOI: 10.1016/j.nima.2023.168018.

[Ago+03] S. Agostinelli, J. Allison, K. Amako, et al. “Geant4—a simulation toolkit.” In: *Nuclear Instruments and Methods in Physics Research Section A: Accelerators, Spectrometers, Detectors and Associated Equipment* 506.3 (2003), pp. 250–303. DOI: 10.1016/s0168-9002(03)01368-8.

[Agu+15a] M. Aguilar, D. Aisa, B. Alpat, et al. "Precision Measurement of the Helium Flux in Primary Cosmic Rays of Rigidities 1.9 GV to 3 TV with the Alpha Magnetic Spectrometer on the International Space Station." In: *Physical Review Letters* 115.21 (2015), p. 211101. DOI: 10.1103/PhysRevLett.115.211101.

[Agu+15b] M. Aguilar, D. Aisa, B. Alpat, et al. "Precision Measurement of the Proton Flux in Primary Cosmic Rays from Rigidity 1 GV to 1.8 TV with the Alpha Magnetic Spectrometer on the International Space Station." In: *Physical Review Letters* 114.17 (2015), p. 171103. DOI: 10.1103/PhysRevLett.114.171103.

[Agu+17] M. Aguilar, L. Ali Cavasonza, B. Alpat, et al. "Observation of the Identical Rigidity Dependence of He, C, and O Cosmic Rays at High Rigidities by the Alpha Magnetic Spectrometer on the International Space Station." In: *Physical Review Letters* 119.25 (2017), p. 251101. DOI: 10.1103/PhysRevLett.119.251101.

[Agu+23] M. Aguilar, L. Ali Cavasonza, B. Alpat, et al. "Properties of Cosmic-Ray Sulfur and Determination of the Composition of Primary Cosmic-Ray Carbon, Neon, Magnesium, and Sulfur: Ten-Year Results from the Alpha Magnetic Spectrometer." In: *Physical Review Letters* 130.21 (2023), p. 211002. DOI: 10.1103/PhysRevLett.130.211002.

[Agu+19] M. Aguilar, L. Ali Cavasonza, G. Ambrosi, et al. "Properties of Cosmic Helium Isotopes Measured by the Alpha Magnetic Spectrometer." In: *Phys Rev Lett* 123.18 (2019), p. 181102. DOI: 10.1103/PhysRevLett.123.181102.

[Agu+21a] M. Aguilar, L. Ali Cavasonza, G. Ambrosi, et al. "The Alpha Magnetic Spectrometer (AMS) on the international space station: Part II — Results from the first seven years." In: *Physics Reports* 894 (2021), pp. 1–116. DOI: 10.1016/j.physrep.2020.09.003.

[Agu+21b] M. Aguilar, L. A. Cavasonza, M. S. Allen, et al. "Properties of Iron Primary Cosmic Rays: Results from the Alpha Magnetic Spectrometer." In: *Physical Review Letters* 126.4 (2021), p. 041104. DOI: 10.1103/PhysRevLett.126.041104.

[Agu+21c] M. Aguilar, L. A. Cavasonza, B. Alpat, et al. "Properties of a New Group of Cosmic Nuclei: Results from the Alpha Magnetic Spectrometer on Sodium, Aluminum, and Nitrogen." In: *Physical Review Letters* 127.2 (2021), p. 021101. DOI: 10.1103/PhysRevLett.127.021101.

[Agu+21d] M. Aguilar, L. A. Cavasonza, G. Ambrosi, et al. "Periodicities in the Daily Proton Fluxes from 2011 to 2019 Measured by the Alpha Magnetic Spectrometer on the International Space Station from 1 to 100 GV." In: *Physical Review Letters* 127.27 (2021), p. 271102. DOI: 10.1103/PhysRevLett.127.271102.

[AYO19] F. Aharonian, R. Yang, and E. de Oña Wilhelmi. "Massive stars as major factories of Galactic cosmic rays." In: *Nature Astronomy* 3.6 (2019), pp. 561–567. DOI: 10.1038/s41550-019-0724-0.

[Ahl78] S. P. Ahlen. "Z_1^7 stopping-power formula for fast heavy ions." In: *Physical Review A* 17.3 (1978), pp. 1236–1239. DOI: 10.1103/PhysRevA.17.1236.

[Ahl80] S. P. Ahlen. "Theoretical and experimental aspects of the energy loss of relativistic heavily ionizing particles." In: *Reviews of Modern Physics* 52.1 (1980), pp. 121–173. DOI: 10.1103/RevModPhys.52.121.

[Ahm+21] S. Ahmad, S. Blin, S. Callier, et al. "OMEGA SiPM readout ASICs." In: *Nuclear Instruments and Methods in Physics Research Section A: Accelerators, Spectrometers, Detectors and Associated Equipment* 986 (2021). DOI: 10.1016/j.nima.2020.164628.

[Ahn+09] H. S. Ahn, P. Allison, M. G. Bagliesi, et al. "Energy Spectra of Cosmic-Ray Nuclei at High Energies." In: *The Astrophysical Journal* 707.1 (2009), pp. 593–603. DOI: 10.1088/0004-637x/707/1/593.

[Ahn+10] H. S. Ahn, P. Allison, M. G. Bagliesi, et al. “Discrepant Hardening Observed in Cosmic-Ray Elemental Spectra.” In: *The Astrophysical Journal* 714.1 (2010), pp. L89–L93. DOI: 10.1088/2041-8205/714/1/189.

[AMB14] A. Akkerman, M. Murat, and J. Barak. “Delta-electron spectra, inelastic cross sections, and stopping powers of ions in silicon: Comparison between different models.” In: *Nuclear Instruments and Methods in Physics Research Section B: Beam Interactions with Materials and Atoms* 321 (2014), pp. 1–7. DOI: 10.1016/j.nimb.2013.12.002.

[Ako+05] A. B. Akopova, M. M. Manaseryan, A. A. Melkonyan, et al. “Radiation measurement on the International Space Station.” In: *Radiation Measurements* 39.2 (2005), pp. 225–8. DOI: 10.1016/j.radmeas.2004.06.013.

[AlZ+23] M. D. A. Al Zaman, S. Roy, S. Sarker, et al. “Comparative analysis of the effectiveness of natural polymers and conventional space radiation shielding polymers in spacecraft for prolonged space expeditions.” In: *Materials Research Express* 10.11 (2023). DOI: 10.1088/2053-1591/ad05f1.

[Ala+23] Y. Alaghband, P. M. Klein, E. A. Kramar, et al. “Galactic cosmic radiation exposure causes multifaceted neurocognitive impairments.” In: *Cellular and Molecular Life Sciences* 80.1 (2023), p. 29. DOI: 10.1007/s00018-022-04666-8.

[Ale+21] F. Alemanno, Q. An, P. Azzarello, et al. “Measurement of the Cosmic Ray Helium Energy Spectrum from 70 GeV to 80 TeV with the DAMPE Space Mission.” In: *Physical Review Letters* 126.20 (2021), p. 201102. DOI: 10.1103/PhysRevLett.126.201102.

[Ale+78] T. K. Alexander, J. S. Forster, a. C. Ball, et al. “Z1 and Z2 variations in the stopping powers of Z1=10 to 18 ions deduced from Dsam lifetime measurements.” In: *Physics Letters B* 74.3 (1978), pp. 183–186. DOI: 10.1016/0370-2693(78)90548-8.

[Alf+17] R. Alfaro, C. Alvarez, J. D. Álvarez, et al. “All-particle cosmic ray energy spectrum measured by the HAWC experiment from 10 to 500 TeV.” In: *Physical Review D* 96.12 (2017). DOI: 10.1103/PhysRevD.96.122001.

[Ali+88] J. Alitti, A. Baracat, P. Bareyre, et al. “The design and construction of a scintillating fiber tracking detector.” In: *Nuclear Instruments and Methods in Physics Research Section A: Accelerators, Spectrometers, Detectors and Associated Equipment* 273.1 (1988), pp. 135–144. DOI: 10.1016/0168-9002(88)90808-x.

[All+84] L. R. Allemand, J. Calvet, J. C. Cavan, and J. C. Thévenin. “Optical scintillating fibres for particle detectors.” In: *Nuclear Instruments and Methods in Physics Research* 225.3 (1984), pp. 522–524. DOI: 10.1016/0167-5087(84)90098-x.

[All+16] J. Allison, K. Amako, J. Apostolakis, et al. “Recent developments in Geant4.” In: *Nuclear Instruments and Methods in Physics Research Section A: Accelerators, Spectrometers, Detectors and Associated Equipment* 835 (2016), pp. 186–225. DOI: 10.1016/j.nima.2016.06.125.

[AC80] W. W. M. Allison and J. H. Cobb. “Relativistic Charged Particle Identification by Energy Loss.” In: *Annual Review of Nuclear and Particle Science* 30.1 (1980), pp. 253–298. DOI: 10.1146/annurev.ns.30.120180.001345.

[All19] P. Allport. “Applications of silicon strip and pixel-based particle tracking detectors.” In: *Nature Reviews Physics* 1.9 (2019), pp. 567–576. DOI: 10.1038/s42254-019-0081-z.

[Alm+17] M. Almurayshid, Y. Helo, A. Kacperek, et al. “Quality assurance in proton beam therapy using a plastic scintillator and a commercially available digital camera.” In: *Journal of Applied Clinical Medical Physics* 18.5 (2017), pp. 210–219. DOI: 10.1002/acm2.12143.

[Alo+07] R. Aloisio, V. Berezinsky, P. Blasi, et al. “A dip in the UHECR spectrum and the transition from galactic to extragalactic cosmic rays.” In: *Astroparticle Physics* 27.1 (2007), pp. 76–91. DOI: 10.1016/j.astropartphys.2006.09.004.

[ABG12] R. Aloisio, V. Berezinsky, and A. Gazizov. “Transition from galactic to extragalactic cosmic rays.” In: *Astroparticle Physics* 39-40 (2012), pp. 129–143. DOI: 10.1016/j.astropartphys.2012.09.007.

[Alo17] R. Aloisio. “Acceleration and propagation of ultra-high energy cosmic rays.” In: *Progress of Theoretical and Experimental Physics* 2017.12 (2017). DOI: 10.1093/ptep/ptx115.

[Alo23] R. Aloisio. “Ultra High Energy Cosmic Rays an overview.” In: *Journal of Physics: Conference Series* 2429.1 (2023). DOI: 10.1088/1742-6596/2429/1/012008.

[Alt+23] A. R. Altamura, F. Acerbi, B. Di Ruzza, et al. “Radiation damage on SiPMs for space applications.” In: *Nuclear Instruments and Methods in Physics Research Section A: Accelerators, Spectrometers, Detectors and Associated Equipment* 1045 (2023). DOI: 10.1016/j.nima.2022.167488.

[AC33] L. Alvarez and A. H. Compton. “A Positively Charged Component of Cosmic Rays.” In: *Physical Review* 43.10 (1933), pp. 835–836. DOI: 10.1103/PhysRev.43.835.

[Alv+19] R. Alves Batista, J. Biteau, M. Bustamante, et al. “Open Questions in Cosmic-Ray Research at Ultrahigh Energies.” In: *Frontiers in Astronomy and Space Sciences* 6 (2019). DOI: 10.3389/fspas.2019.00023.

[AB18] E. Amato and P. Blasi. “Cosmic ray transport in the Galaxy: A review.” In: *Advances in Space Research* 62.10 (2018), pp. 2731–2749. DOI: 10.1016/j.asr.2017.04.019.

[ABL90] N. A. Amos, A. D. Bross, and M. C. Lundin. “Optical attenuation length measurements of scintillating fibers.” In: *Nuclear Instruments and Methods in Physics Research Section A: Accelerators, Spectrometers, Detectors and Associated Equipment* 297.3 (1990), pp. 396–403. DOI: 10.1016/0168-9002(90)91321-2.

[An+19] Q. An, R. Asfandiyarov, P. Azzarello, et al. “Measurement of the cosmic ray proton spectrum from 40 GeV to 100 TeV with the DAMPE satellite.” In: *Science Advances* 5.9 (2019), eaax3793. DOI: 10.1126/sciadv.aax3793.

[Ana+12] M. Anand, I. A. Crawford, M. Balat-Pichelin, et al. “A brief review of chemical and mineralogical resources on the Moon and likely initial in situ resource utilization (ISRU) applications.” In: *Planetary and Space Science* 74.1 (2012), pp. 42–48. DOI: 10.1016/j.pss.2012.08.012.

[Anc19] L. A. Anchordoqui. “Ultra-high-energy cosmic rays.” In: *Physics Reports* 801 (2019), pp. 1–93. DOI: 10.1016/j.physrep.2019.01.002.

[ASS69] H. H. Andersen, H. Simonsen, and H. Sørensen. “An experimental investigation of charge-dependent deviations from the Bethe stopping power formula.” In: *Nuclear Physics A* 125.1 (1969), pp. 171–175. DOI: 10.1016/0375-9474(69)90836-7.

[And+89] L. H. Andersen, P. Hvelplund, H. Knudsen, et al. “Measurement of the Z13 contribution to the stopping power using MeV protons and antiprotons: The Barkas effect.” In: *Physical Review Letters* 62.15 (1989), pp. 1731–1734. DOI: 10.1103/PhysRevLett.62.1731.

[And33] C. D. Anderson. “The Positive Electron.” In: *Physical Review* 43.6 (1933), pp. 491–494. DOI: 10.1103/PhysRev.43.491.

[AN36] C. D. Anderson and S. H. Neddermeyer. “Cloud Chamber Observations of Cosmic Rays at 4300 Meters Elevation and Near Sea-Level.” In: *Physical Review* 50.4 (1936), pp. 263–271. DOI: 10.1103/PhysRev.50.263.

[And+19] R. Anderton, B. Posselt, M. Komorowski, and P. Hodkinson. “Medical considerations for a return to the Moon.” In: *Occupational Medicine* 69.5 (2019), pp. 311–313. DOI: 10.1093/occmed/kqz099.

[Anf+21] N. Anfimov, D. Fedoseev, A. Rybnikov, et al. “Study of silicon photomultiplier performance at different temperatures.” In: *Nuclear Instruments and Methods in Physics Research Section A: Accelerators, Spectrometers, Detectors and Associated Equipment* 997 (2021). DOI: 10.1016/j.nima.2021.165162.

[Ang+89] C. Angelini, W. Beusch, I. J. Bloodworth, et al. “High-resolution tracking with scintillating fibres.” In: *Nuclear Instruments and Methods in Physics Research Section A: Accelerators, Spectrometers, Detectors and Associated Equipment* 277.1 (1989), pp. 132–137. DOI: 10.1016/0168-9002(89)90544-5.

[Ang+90] C. Angelini, W. Beusch, A. Cardini, et al. “Comparison of glass and plastic scintillating microfibres for high-resolution tracking.” In: *Nuclear Instruments and Methods in Physics Research Section A: Accelerators, Spectrometers, Detectors and Associated Equipment* 295.3 (1990), pp. 299–314. DOI: 10.1016/0168-9002(90)90706-c.

[AT70] R. Anni and L. Taffara. “Heavy-ion elastic scattering and transfer reactions.” In: *La Rivista del Nuovo Cimento* 2.1 (1970), pp. 1–101. DOI: 10.1007/bf02896887.

[Ant+05] T. Antoni, W. D. Apel, A. F. Badea, et al. “KASCADE measurements of energy spectra for elemental groups of cosmic rays: Results and open problems.” In: *Astroparticle Physics* 24.1-2 (2005), pp. 1–25. DOI: 10.1016/j.astropartphys.2005.04.001.

[Ape+09] W. D. Apel, J. C. Arteaga, A. F. Badea, et al. “Energy spectra of elemental groups of cosmic rays: Update on the KASCADE unfolding analysis.” In: *Astroparticle Physics* 31.2 (2009), pp. 86–91. DOI: 10.1016/j.astropartphys.2008.11.008.

[Ape+13] W. D. Apel, J. C. Arteaga-Velàzquez, K. Bekk, et al. “Ankle-like feature in the energy spectrum of light elements of cosmic rays observed with KASCADE-Grande.” In: *Physical Review D* 87.8 (2013). DOI: 10.1103/PhysRevD.87.081101.

[App+97] R. D. Appuhn, C. Arndt, E. Barrelet, et al. “The H1 lead/scintillating-fibre calorimeter.” In: *Nuclear Instruments and Methods in Physics Research Section A: Accelerators, Spectrometers, Detectors and Associated Equipment* 386.2-3 (1997), pp. 397–408. DOI: 10.1016/s0168-9002(96)01171-0.

[Ara+23] C. Aramo, E. Bissaldi, M. Bitossi, et al. “A SiPM multichannel ASIC for high Resolution Cherenkov Telescopes (SMART) developed for the pSCT camera telescope.” In: *Nuclear Instruments and Methods in Physics Research Section A: Accelerators, Spectrometers, Detectors and Associated Equipment* 1047 (2023). DOI: 10.1016/j.nima.2022.167839.

[Arc+05] L. Archambault, J. Arsenault, L. Gingras, et al. “Plastic scintillation dosimetry: Optimal selection of scintillating fibers and scintillators.” In: *Medical Physics* 32.7 (2005), pp. 2271–2278. DOI: 10.1118/1.1943807.

[Ari+23] M. Arimoto, D. Sato, T. Mizuno, et al. “Development of 64-channel LSI with ultrafast analog and digital signal processing dedicated for photon-counting computed tomography with multi-pixel photon counter.” In: *Nuclear Instruments and Methods in Physics Research Section A: Accelerators, Spectrometers, Detectors and Associated Equipment* 1047 (2023). DOI: 10.1016/j.nima.2022.167721.

[AL99] N. R. Arista and A. F. Lifschitz. “Nonlinear calculation of stopping powers for protons and antiprotons in solids: The Barkas effect.” In: *Physical Review A* 59.4 (1999), pp. 2719–2722. DOI: 10.1103/PhysRevA.59.2719.

[AL02] N. R. Arista and A. F. Lifschitz. “Non-linear calculation of antiproton stopping powers at finite velocities using the extended Friedel sum rule.” In: *Nuclear Instruments and Methods in Physics Research Section B: Beam Interactions with Materials and Atoms* 193.1-4 (2002), pp. 8–14. DOI: 10.1016/s0168-583x(02)00719-x.

[Ari02] N. R. Arista. "Energy loss of ions in solids: Non-linear calculations for slow and swift ions." In: *Nuclear Instruments and Methods in Physics Research Section B: Beam Interactions with Materials and Atoms* 195.1-2 (2002), pp. 91–105. DOI: 10.1016/s0168-583x(02)00687-0.

[AC01] T. W. Armstrong and B. L. Colborn. "Predictions of secondary neutrons and their importance to radiation effects inside the international space station." In: *Radiation Measurements* 33.3 (2001), pp. 229–234. DOI: 10.1016/s1350-4487(00)00152-9.

[Aro+68] L. Aronowitz, F. Koch, J. H. Scanlon, and M. Sidran. "Contamination of lunar surface samples by the lunar module exhaust." In: *Journal of Geophysical Research* 73.10 (1968), pp. 3231–3238. DOI: 10.1029/JB073i010p03231.

[Aru+02] M. S. Arulampalam, S. Maskell, N. Gordon, and T. Clapp. "A tutorial on particle filters for online nonlinear/non-Gaussian Bayesian tracking." In: *IEEE Transactions on Signal Processing* 50.2 (2002), pp. 174–188. DOI: 10.1109/78.978374.

[Asa+98] K. Asakimori, T. H. Burnett, M. L. Cherry, et al. "Cosmic-Ray Proton and Helium Spectra: Results from the JACEE Experiment." In: *The Astrophysical Journal* 502.1 (1998), pp. 278–283. DOI: 10.1086/305882.

[ARB72] J. C. Ashley, R. H. Ritchie, and W. Brandt. "Z_1^3 Effect in the Stopping Power of Matter for Charged Particles." In: *Physical Review B* 5.7 (1972), pp. 2393–2397. DOI: 10.1103/PhysRevB.5.2393.

[ARB73] J. C. Ashley, R. H. Ritchie, and W. Brandt. "Z_1^3-Dependent Stopping Power and Range Contributions." In: *Physical Review A* 8.5 (1973), pp. 2402–2408. DOI: 10.1103/PhysRevA.8.2402.

[Ast+22] I. I. Astapov, P. A. Bezyazeekov, M. Blank, et al. "Cosmic-Ray Research at the TAIGA Astrophysical Facility: Results and Plans." In: *Journal of Experimental and Theoretical Physics* 134.4 (2022), pp. 469–478. DOI: 10.1134/s1063776122040136.

[Atk+18] E. Atkin, V. Bulatov, V. Dorokhov, et al. "New Universal Cosmic-Ray Knee near a Magnetic Rigidity of 10 TV with the NUCLEON Space Observatory." In: *JETP Letters* 108.1 (2018), pp. 5–12. DOI: 10.1134/s0021364018130015.

[Atk+19] E. V. Atkin, V. L. Bulatov, O. A. Vasiliev, et al. "Energy Spectra of Cosmic-Ray Protons and Nuclei Measured in the NUCLEON Experiment Using a New Method." In: *Astronomy Reports* 63.1 (2019), pp. 66–78. DOI: 10.1134/s1063772919010013.

[Ave+08] M. Ave, P. J. Boyle, F. Gahbauer, et al. "Composition of Primary Cosmic-Ray Nuclei at High Energies." In: *The Astrophysical Journal* 678.1 (2008), pp. 262–273. DOI: 10.1086/529424.

[Awe+21] C. Awe, P. Barbeau, A. Haghighat, et al. "Measurement of proton quenching in a plastic scintillator detector." In: *Journal of Instrumentation* 16.02 (2021), P02035–P02035. DOI: 10.1088/1748-0221/16/02/p02035.

[AS85] M. Awschalom and R. S. Sanna. "Applications of Bonner Sphere Detectors in Neutron Field Dosimetry." In: *Radiation Protection Dosimetry* 10.1-4 (1985), pp. 89–101. DOI: 10.1093/oxfordjournals.rpd.a079413.

[AGS00] G. d. M. Azevedo, P. L. Grande, and G. Schiwietz. "Impact-parameter dependent energy loss of screened ions." In: *Nuclear Instruments and Methods in Physics Research Section B: Beam Interactions with Materials and Atoms* 164-165 (2000), pp. 203–211. DOI: 10.1016/s0168-583x(99)01074-5.

[Bac+14] B. B. Back, H. Esbensen, C. L. Jiang, and K. E. Rehm. "Recent developments in heavy-ion fusion reactions." In: *Reviews of Modern Physics* 86.1 (2014), pp. 317–360. DOI: 10.1103/RevModPhys.86.317.

[Bag+10] H. Bagan, A. Tarancon, G. Rauret, and J. F. Garcia. "Alpha/beta pulse shape discrimination in plastic scintillation using commercial scintillation detectors." In: *Analytica Chimica Acta* 670.1-2 (2010), pp. 11–7. DOI: 10.1016/j.aca.2010.04.055.

[Bäh+00] J. Bähr, R. Nahnhauer, S. Nerreter, and R. Shanidze. "A fiber detector radiation hardness test." In: *Nuclear Instruments and Methods in Physics Research Section A: Accelerators, Spectrometers, Detectors and Associated Equipment* 449.1-2 (2000), pp. 260–267. DOI: 10.1016/s0168-9002(99)01437-0.

[Bai+18] G. Baiocco, M. Giraudo, L. Bocchini, et al. "A water-filled garment to protect astronauts during interplanetary missions tested on board the ISS." In: *Life Sciences in Space Research* 18 (2018), pp. 1–11. DOI: 10.1016/j.lssr.2018.04.002.

[Bak+17] D. N. Baker, P. J. Erickson, J. F. Fennell, et al. "Space Weather Effects in the Earth's Radiation Belts." In: *Space Science Reviews* 214.1 (2017). DOI: 10.1007/s11214-017-0452-7.

[BCL20] R. Ballabriga, M. Campbell, and X. Llopart. "An introduction to the Medipix family ASICs." In: *Radiation Measurements* 136 (2020). DOI: 10.1016/j.radmeas.2020.106271.

[Bar+20] M. Barella, T. I. Burroni, I. Carsen, et al. "Silicon photomultiplier characterization on board a satellite in Low Earth Orbit." In: *Nuclear Instruments and Methods in Physics Research Section A: Accelerators, Spectrometers, Detectors and Associated Equipment* 979 (2020). DOI: 10.1016/j.nima.2020.164490.

[Bar+21a] M. K. Barker, E. Mazarico, G. A. Neumann, et al. "Improved LOLA elevation maps for south pole landing sites: Error estimates and their impact on illumination conditions." In: *Planetary and Space Science* 203 (2021). DOI: 10.1016/j.pss.2020.105119.

[Bar+16] J. J. Barnes, D. A. Kring, R. Tartese, et al. "An asteroidal origin for water in the Moon." In: *Nature Communications* 7 (2016), p. 11684. DOI: 10.1038/ncomms11684.

[Bar+21b] J. W. Barnes, E. P. Turtle, M. G. Trainer, et al. "Science Goals and Objectives for the Dragonfly Titan Rotorcraft Relocatable Lander." In: *The Planetary Science Journal* 2.4 (2021). DOI: 10.3847/PSJ/abfdcf.

[Bar+15] B. Bartoli, P. Bernardini, X. J. Bi, et al. "Knee of the cosmic hydrogen and helium spectrum below 1 PeV measured by ARGO-YBJ and a Cherenkov telescope of LHAASO." In: *Physical Review D* 92.9 (2015). DOI: 10.1103/PhysRevD.92.092005.

[Bar+23] A. Bartoloni, N. Ding, G. Cavoto, et al. "Astroparticle Experiments to Improve the Biological Risk Assessment of Exposure to Ionizing Radiation in the Exploratory Space Missions: The research topic initiative." In: *Nuclear Instruments and Methods in Physics Research Section A: Accelerators, Spectrometers, Detectors and Associated Equipment* 1047 (2023). DOI: 10.1016/j.nima.2022.167738.

[Bas84] G. Basbas. "Inner-shell ionization and the Z13 and barkas effects in stopping power." In: *Nuclear Instruments and Methods in Physics Research Section B: Beam Interactions with Materials and Atoms* 4.2 (1984), pp. 227–238. DOI: 10.1016/0168-583x(84)90023-5.

[Bat20] R. Battiston. "High precision cosmic ray physics with AMS-02 on the International Space Station." In: *La Rivista del Nuovo Cimento* 43.7 (2020), pp. 319–384. DOI: 10.1007/s40766-020-00007-2.

[Bat08] R. Battiston. "The antimatter spectrometer (AMS-02): A particle physics detector in space." In: *Nuclear Instruments and Methods in Physics Research Section A: Accelerators, Spectrometers, Detectors and Associated Equipment* 588.1-2 (2008), pp. 227–234. DOI: 10.1016/j.nima.2008.01.044.

[Bau+13] A. E. Baulin, Y. Cao, J. Chan, et al. “Attenuation length and spectral response of Kuraray SCSF-78MJ scintillating fibres.” In: *Nuclear Instruments and Methods in Physics Research Section A: Accelerators, Spectrometers, Detectors and Associated Equipment* 715 (2013), pp. 48–55. DOI: 10.1016/j.nima.2013.03.027.

[Bay82] G. Baym. “Confinement and deconfinement of quarks in nuclear matter.” In: *Progress in Particle and Nuclear Physics* 8 (1982), pp. 73–101. DOI: 10.1016/0146-6410(82)90006-0.

[Bea+02] R. Beaujean, J. Kopp, S. Burmeister, et al. “Dosimetry inside MIR station using a silicon detector telescope (DOSTEL).” In: *Radiation Measurements* 35.5 (2002), pp. 433–8. DOI: 10.1016/s1350-4487(02)00074-4.

[Bei+10] B. Beischer, H. Gast, R. Greim, et al. “A high-resolution scintillating fiber tracker with silicon photomultiplier array readout.” In: *Nuclear Instruments and Methods in Physics Research Section A: Accelerators, Spectrometers, Detectors and Associated Equipment* 622.3 (2010), pp. 542–554. DOI: 10.1016/j.nima.2010.07.059.

[Bel50] E. H. Belcher. “Measurement of gamma-ray energies with the scintillation counter.” In: *Nature* 166.4228 (1950), p. 826. DOI: 10.1038/166826a0.

[Ben+22] V. Benghin, V. Shurshakov, V. Osedlo, et al. “Results of long-term radiation environment monitoring by the Russian RMS system on board Zvezda module of the ISS.” In: *Life Sciences in Space Research* (2022). DOI: 10.1016/j.lssr.2022.11.002.

[BHB75] E. V. Benton, R. P. Henke, and J. V. Bailey. “Heavy Cosmic-Ray Exposure of Apollo Astronauts.” In: *Science* 187.4173 (1975), pp. 263–265. DOI: 10.1126/science.187.4173.263.

[Ben+19] E. R. Benton, T. Berger, Y. Uchihori, and H. Kitamura. “5.2.2 Intercomparison of Radiation Detectors and Dosimeters for Use in Manned Space Flight.” In: *Radioisotopes* 68.6 (2019), pp. 411–418. DOI: 10.3769/radioisotopes.68.411.

[Ben+16] D. Benyamin, E. Nakar, T. Piran, and N. J. Shaviv. “The B/C and Sub-Iron/Iron Cosmic Ray Ratios—Further Evidence in Favor of the Spiral-Arm Diffusion Model.” In: *The Astrophysical Journal* 826.1 (2016). DOI: 10.3847/0004-637x/826/1/47.

[BV07] E. G. Berezhko and H. J. Völk. “Spectrum of Cosmic Rays Produced in Supernova Remnants.” In: *The Astrophysical Journal* 661.2 (2007), pp. L175–L178. DOI: 10.1086/518737.

[BGG06] V. Berezinsky, A. Gazizov, and S. Grigorieva. “On astrophysical solution to ultrahigh energy cosmic rays.” In: *Physical Review D* 74.4 (2006). DOI: 10.1103/PhysRevD.74.043005.

[BSE20] J. van den Berg, D. T. Strauss, and F. Effenberger. “A Primer on Focused Solar Energetic Particle Transport.” In: *Space Science Reviews* 216.8 (2020). DOI: 10.1007/s11214-020-00771-x.

[Ber+19] T. Berger, K. Marsalek, J. Aeckerlein, et al. “The German Aerospace Center M-42 radiation detector–A new development for applications in mixed radiation fields.” In: *Review of Scientific Instruments* 90.12 (2019), p. 125115. DOI: 10.1063/1.5122301.

[Ber+20] T. Berger, D. Matthiä, S. Burmeister, et al. “Long term variations of galactic cosmic radiation on board the International Space Station, on the Moon and on the surface of Mars.” In: *Journal of Space Weather and Space Climate* (2020). DOI: 10.1051/swsc/2020028.

[Ber+16a] T. Berger, B. Przybyla, D. Matthiä, et al. “DOSIS & DOSIS 3D: long-term dose monitoring onboard the Columbus Laboratory of the International Space Station (ISS).” In: *Journal of Space Weather and Space Climate* 6 (2016), A39. DOI: 10.1051/swsc/2016034.

[BB07] D. R. Bergman and J. W. Belz. “Cosmic rays: the Second Knee and beyond.” In: *Journal of Physics G: Nuclear and Particle Physics* 34.10 (2007), R359–R400. DOI: 10.1088/0954-3899/34/10/r01.

[Ber+24] B. Bergmann, S. Gohl, D. Garvey, et al. “Results and Perspectives of Timepix Detectors in Space—From Radiation Monitoring in Low Earth Orbit to Astroparticle Physics.” In: *Instruments* 8.1 (2024). DOI: 10.3390/instruments8010017.

[BHS14] G. H. Bertrand, M. Hamel, and F. Sguerra. “Current status on plastic scintillators modifications.” In: *Chemistry* 20.48 (2014), pp. 15660–85. DOI: 10.1002/chem.201404093.

[BAB80] F. Besenbacher, J. U. Andersen, and E. Bonderup. “Straggling in energy loss of energetic hydrogen and helium ions.” In: *Nuclear Instruments and Methods* 168.1-3 (1980), pp. 1–15. DOI: 10.1016/0029-554x(80)91224-0.

[Bet30] H. Bethe. “Zur Theorie des Durchgangs schneller Korpuskularstrahlen durch Materie.” In: *Annalen der Physik* 397.3 (1930), pp. 325–400. DOI: 10.1002/andp.19303970303.

[Bet32] H. Bethe. “Bremsformel für Elektronen relativistischer Geschwindigkeit.” In: *Zeitschrift für Physik* 76.5-6 (1932), pp. 293–299. DOI: 10.1007/bf01342532.

[BH34] H. Bethe and W. Heitler. “On the stopping of fast particles and on the creation of positive electrons.” In: *Proceedings of the Royal Society of London. Series A, Containing Papers of a Mathematical and Physical Character* 146.856 (1934), pp. 83–112. DOI: 10.1098/rspa.1934.0140.

[Bet53] H. A. Bethe. “Molière’s Theory of Multiple Scattering.” In: *Physical Review* 89.6 (1953), pp. 1256–1266. DOI: 10.1103/PhysRev.89.1256.

[Bet68] H. A. Bethe. “Thomas-Fermi Theory of Nuclei.” In: *Physical Review* 167.4 (1968), pp. 879–907. DOI: 10.1103/PhysRev.167.879.

[BL70] H. D. Betz and G. Lee. “Charge States and Excitation of Fast Heavy Ions Passing Through Solids: A New Model for the Density Effect.” In: *Physical Review Letters* 25.4 (1970), pp. 211–214. DOI: 10.1103/PhysRevLett.25.211.

[Bha36] H. J. Bhabha. “The scattering of positrons by electrons with exchange on Dirac’s theory of the positron.” In: *Proceedings of the Royal Society of London. Series A - Mathematical and Physical Sciences* 154.881 (1936), pp. 195–206. DOI: 10.1098/rspa.1936.0046.

[Bha+15] A. Bhardwaj, M. B. Dhanya, A. Alok, et al. “A new view on the solar wind interaction with the Moon.” In: *Geoscience Letters* 2 (2015), p. 10. DOI: 10.1186/s40562-015-0027-y.

[Bic90] H. Bichsel. “Barkas effect and effective charge in the theory of stopping power.” In: *Physical Review A* 41.7 (1990), pp. 3642–3647. DOI: 10.1103/physreva.41.3642.

[Bic02] H. Bichsel. “Shell corrections in stopping powers.” In: *Physical Review A* 65.5 (2002). DOI: 10.1103/PhysRevA.65.052709.

[Bic88] H. Bichsel. “Straggling in thin silicon detectors.” In: *Reviews of Modern Physics* 60.3 (1988), pp. 663–699. DOI: 10.1103/RevModPhys.60.663.

[BP82] H. Bichsel and L. E. Porter. “Stopping Power of protons and alpha particles in H_2, He, N_2, O_2, CH_4, and air.” In: *Physical Review A* 25.5 (1982), pp. 2499–2510. DOI: 10.1103/PhysRevA.25.2499.

[BS75] H. Bichsel and R. P. Saxon. “Comparison of calculational methods for straggling in thin absorbers.” In: *Physical Review A* 11.4 (1975), pp. 1286–1296. DOI: 10.1103/PhysRevA.11.1286.

[Bil+18] B. Bilki, Y. Onel, E. Tiras, et al. “Development of radiation-hard scintillators and wavelength-shifting fibers.” In: *Journal of Instrumentation* 13.02 (2018), pp. C02052–C02052. DOI: 10.1088/1748-0221/13/02/c02052.

[Bim+89a] R. Bimbot, C. Cabot, D. Gardes, et al. “Stopping power of gases for heavy ions: Gas-solid effect.” In: *Nuclear Instruments and Methods in Physics Research Section B: Beam Interactions with Materials and Atoms* 44.1 (1989), pp. 1–18. DOI: 10.1016/0168-583x(89)90683-6.

[Bim+89b] R. Bimbot, C. Cabot, D. Gardes, et al. “Stopping power of gases for heavy ions: Gas-solid effect.” In: *Nuclear Instruments and Methods in Physics Research Section B: Beam Interactions with Materials and Atoms* 44.1 (1989), pp. 19–34. DOI: 10.1016/0168-583x(89)90684-8.

[Bin+89] W. R. Binns, T. L. Garrard, P. S. Gibner, et al. “Abundances of ultraheavy elements in the cosmic radiation - Results from HEAO 3.” In: *The Astrophysical Journal* 346 (1989). DOI: 10.1086/168082.

[Bir51] J. B. Birks. “Scintillations from Organic Crystals: Specific Fluorescence and Relative Response to Different Radiations.” In: *Proceedings of the Physical Society. Section A* 64.10 (1951), pp. 874–877. DOI: 10.1088/0370-1298/64/10/303.

[Bir52] J. B. Birks. “Theory of the Response of Organic Scintillation Crystals to Short-Range Particles.” In: *Physical Review* 86.4 (1952), pp. 569–569. DOI: 10.1103/PhysRev.86.569.

[BB51] J. B. Birks and F. A. Black. “Deterioration of Anthracene under α-Particle Irradiation.” In: *Proceedings of the Physical Society. Section A* 64.5 (1951), pp. 511–512. DOI: 10.1088/0370-1298/64/5/112.

[Bis+02] J. Bisplinghoff, D. Eversheim, W. Eyrich, et al. “A scintillating fibre hodoscope for high rate applications.” In: *Nuclear Instruments and Methods in Physics Research Section A: Accelerators, Spectrometers, Detectors and Associated Equipment* 490.1-2 (2002), pp. 101–111. DOI: 10.1016/s0168-9002(02)01064-1.

[Bis+23] A. Biswas, B. B. Karak, I. Usoskin, and E. Weisshaar. “Long-Term Modulation of Solar Cycles.” In: *Space Science Reviews* 219.3 (2023). DOI: 10.1007/s11214-023-00968-w.

[Bis+20] J. Biswas, S. Sheridan, C. Pitcher, et al. “Searching for potential ice-rich mining sites on the Moon with the Lunar Volatiles Scout.” In: *Planetary and Space Science* 181 (2020), p. 104826. DOI: 10.1016/j.pss.2019.104826.

[Biz+12] P. G. Bizzeti, L. Carraresi, F. A. Danevich, et al. “Response of CdWO4 crystal scintillator for few MeV ions and low energy electrons.” In: *Nuclear Instruments and Methods in Physics Research Section A: Accelerators, Spectrometers, Detectors and Associated Equipment* 696 (2012), pp. 144–150. DOI: 10.1016/j.nima.2012.08.106.

[Bjo+50] R. Bjorklund, W. E. Crandall, B. J. Moyer, and H. F. York. “High Energy Photons from Proton-Nucleon Collisions.” In: *Physical Review* 77.2 (1950), pp. 213–218. DOI: 10.1103/PhysRev.77.213.

[BCL62] D. Blanc, F. Cambou, and Y. G. de Lafond. “Cinétique de la composante rapide de la scintillation dans un milieu organique pur. Application au cas de l’anthracène.” In: *Comptes rendus de l’Académie des Sciences* 254 (1962), p. 3187.

[Bla+14] P. Blanc, M. Hamel, C. Dehé-Pittance, et al. “Neutron/gamma pulse shape discrimination in plastic scintillators: Preparation and characterization of various compositions.” In: *Nuclear Instruments and Methods in Physics Research Section A: Accelerators, Spectrometers, Detectors and Associated Equipment* 750 (2014), pp. 1–11. DOI: 10.1016/j.nima.2014.02.053.

[BBO00] A. Blažević, H. G. Bohlen, and W. von Oertzen. “Charge-state changing processes for Ne ions passing through thin carbon foils.” In: *Physical Review A* 61.3 (2000). DOI: 10.1103/PhysRevA.61.032901.

[Blo33a] F. Bloch. “Bremsvermögen von Atomen mit mehreren Elektronen.” In: *Zeitschrift für Physik* 81.5-6 (1933), pp. 363–376. DOI: 10.1007/bf01344553.

[Blo33b] F. Bloch. “Zur Bremsung rasch bewegter Teilchen beim Durchgang durch Materie.” In: *Annalen der Physik* 408.3 (1933), pp. 285–320. DOI: 10.1002/andp.19334080303.

[BW69] P. Bloch and C. S. Worrilow. “Portable radiation and light detector using a p-i-n silicon diode.” In: *Physics in Medicine & Biology* 14.2 (1969), pp. 277–81. DOI: 10.1088/0031-9155/14/2/006.

[BB92] H. Blumenfeld and M. Bourdinaud. “Aging of plastic scintillating fibers.” In: *Applied Optics* 31.15 (1992), pp. 2791–5. DOI: 10.1364/AO.31.002791.

[Blu+89] H. Blumenfeld, M. Bourdinaud, P. Rebourgeard, and J. C. Thevenin. “Production and test of coherent bundles of plastic scintillating microfibers.” In: *Nuclear Instruments and Methods in Physics Research Section A: Accelerators, Spectrometers, Detectors and Associated Equipment* 278.2 (1989), pp. 619–621. DOI: 10.1016/0168-9002(89)90891-7.

[BL50] O. Blunck and S. Leisegang. “Zum Energieverlust schneller Elektronen in dünnen Schichten.” In: *Zeitschrift für Physik* 128.4 (1950), pp. 500–505. DOI: 10.1007/bf01330032.

[BEH84] R. Bock, H. Emling, and K. D. Hildenbrand. “Nuclear Reactions Induced by Heavy Ions.” In: *Interdisciplinary Science Reviews* 9.4 (1984), pp. 305–312. DOI: 10.1179/isr.1984.9.4.305.

[Boe+03] M. Boezio, V. Bonvicini, P. Schiavon, et al. “The cosmic-ray proton and helium spectra measured with the CAPRICE98 balloon experiment.” In: *Astroparticle Physics* 19.5 (2003), pp. 583–604. DOI: 10.1016/s0927-6505(02)00267-0.

[Boh+09] P. Bohn, A. Clough, E. Hazen, et al. “Radiation damage studies of silicon photomultipliers.” In: *Nuclear Instruments and Methods in Physics Research Section A: Accelerators, Spectrometers, Detectors and Associated Equipment* 598.3 (2009), pp. 722–736. DOI: 10.1016/j.nima.2008.10.027.

[Boh13a] N. Bohr. “On the constitution of atoms and molecules.” In: *The London, Edinburgh, and Dublin Philosophical Magazine and Journal of Science* 26.151 (1913), pp. 1–25. DOI: 10.1080/14786441308634955.

[Boh13b] N. Bohr. “On the theory of the decrease of velocity of moving electrified particles on passing through matter.” In: *The London, Edinburgh, and Dublin Philosophical Magazine and Journal of Science* 25.145 (1913), pp. 10–31. DOI: 10.1080/14786440108634305.

[Boh15] N. Bohr. “On the decrease of velocity of swiftly moving electrified particles in passing through matter.” In: *The London, Edinburgh, and Dublin Philosophical Magazine and Journal of Science* 30.178 (1915), pp. 581–612. DOI: 10.1080/14786441008635432.

[Boh21] N. Bohr. “Atomic Structure.” In: *Nature* 107.2682 (1921), pp. 104–107. DOI: 10.1038/107104a0.

[Boh40] N. Bohr. “Scattering and Stopping of Fission Fragments.” In: *Physical Review* 58.7 (1940), pp. 654–655. DOI: 10.1103/PhysRev.58.654.

[Boh41] N. Bohr. “Velocity-Range Relation for Fission Fragments.” In: *Physical Review* 59.3 (1941), pp. 270–275. DOI: 10.1103/PhysRev.59.270.

[BL54] N. Bohr and J. Lindhard. “Electron Capture and Loss by Heavy Ions Penetrating through Matter.” In: *Mat Fys Medd Dan Vid Selsk* 28.7 (1954).

[Boh48] N. Bohr. “The Penetration of Atomic Particles Through Matter.” In: *Mat Fys Medd Dan Vid Selsk* 18.8 (1948), pp. 1–144.

[BTG62] L. M. Bollinger, G. E. Thomas, and R. J. Ginther. "Neutron detection with glass scintillators." In: *Nuclear Instruments and Methods* 17.1 (1962), pp. 97–116. DOI: 10.1016/0029-554x(62)90178-7.

[Bon+19a] D. K. Bond, B. Goddard, R. C. Singleterry, and S. Bilbao y León. "Comparing the Effectiveness of Polymer and Composite Materials to Aluminum for Extended Deep Space Travel." In: *Nuclear Technology* 206.8 (2019), pp. 1120–1139. DOI: 10.1080/00295450.2019.1681221.

[Bon67] E. Bonderup. "Stopping of Swift Protons Evaluated from Statistical Atomic Model." In: *Mat Fys Medd Dan Vid Selsk* 35.17 (1967).

[Bon+19b] M. Bonesini, T. Cervi, A. Falcone, et al. "Study on SiPM breakdown voltage, dark current and gain from room down to liquid nitrogen temperature." In: *Nuclear Instruments and Methods in Physics Research Section A: Accelerators, Spectrometers, Detectors and Associated Equipment* 936 (2019), pp. 192–194. DOI: 10.1016/j.nima.2018.08.111.

[BPS81] S. R. Borenstein, R. B. Palmer, and R. C. Strand. "Optical Fibers and Avalanche Photodiodes for Scintillator Counters." In: *Physica Scripta* 23.4A (1981), pp. 550–555. DOI: 10.1088/0031-8949/23/4a/030.

[BS82] S. R. Borenstein and R. C. Strand. "Scintillating Optical Fibers for Fine Grained Hodoscopes." In: *IEEE Transactions on Nuclear Science* 29.1 (1982), pp. 402–404. DOI: 10.1109/tns.1982.4335874.

[Bos+20] D. Boscolo, D. Scognamiglio, F. Horst, et al. "Characterization of the Secondary Neutron Field Produced in a Thick Aluminum Shield by 1 GeV/u 56Fe Ions Using TLD-Based Ambient Dosimeters." In: *Frontiers in Physics* 8 (2020). DOI: 10.3389/fphy.2020.00365.

[Bou+15] M. Boudaud, S. Aupetit, S. Caroff, et al. "A new look at the cosmic ray positron fraction." In: *Astronomy & Astrophysics* 575 (2015). DOI: 10.1051/0004-6361/201425197.

[Boy+04] W. V. Boynton, W. C. Feldman, I. G. Mitrofanov, et al. "The Mars Odyssey Gamma-Ray Spectrometer Instrument Suite." In: *Space Science Reviews* 110.1/2 (2004), pp. 37–83. DOI: 10.1023/b:Spac.0000021007.76126.15.

[BK05] W. H. Bragg and R. Kleeman. "On the α particles of radium, and their loss of range in passing through various atoms and molecules." In: *The London, Edinburgh, and Dublin Philosophical Magazine and Journal of Science* 10.57 (1905), pp. 318–340. DOI: 10.1080/14786440509463378.

[BEB60] R. L. Bramblett, R. I. Ewing, and T. W. Bonner. "A new type of neutron spectrometer." In: *Nuclear Instruments and Methods* 9.1 (1960), pp. 1–12. DOI: 10.1016/0029-554x(60)90043-4.

[BK82] W. Brandt and M. Kitagawa. "Effective stopping-power charges of swift ions in condensed matter." In: *Physical Review B* 25.9 (1982), pp. 5631–5637. DOI: 10.1103/PhysRevB.25.5631.

[BS07] P. Braun-Munzinger and J. Stachel. "The quest for the quark-gluon plasma." In: *Nature* 448.7151 (2007), pp. 302–9. DOI: 10.1038/nature06080.

[BD22] A. Bravar and Y. Demets. "Timing properties of blue-emitting scintillating fibers." In: *Journal of Instrumentation* 17.12 (2022). DOI: 10.1088/1748-0221/17/12/p12020.

[Bre+16] T. Bretz, T. Hebbeker, M. Lauscher, et al. "Dynamic range measurement and calibration of SiPMs." In: *Journal of Instrumentation* 11.03 (2016), P03009–P03009. DOI: 10.1088/1748-0221/11/03/p03009.

[BRS18] J. C. Brient, R. Rusack, and F. Sefkow. “Silicon Calorimeters.” In: *Annual Review of Nuclear and Particle Science* 68.1 (2018), pp. 271–290. DOI: 10.1146/annurev-nucl-101917-021053.

[Bri+24] L. Brinkmann, E. Garutti, S. Martens, and J. Schwandt. “Correcting the Non-Linear Response of Silicon Photomultipliers.” In: *Sensors* 24.5 (2024). DOI: 10.3390/s24051671.

[Bri+93] G. I. Britvich, A. I. Peresypkin, V. I. Rykalin, et al. “Radiation damage studies on polystyrene-based scintillators.” In: *Nuclear Instruments and Methods in Physics Research Section A: Accelerators, Spectrometers, Detectors and Associated Equipment* 326.3 (1993), pp. 483–488. DOI: 10.1016/0168-9002(93)90849-d.

[BKT41] J. H. M. Brunings, J. K. Knipp, and E. Teller. “On the Momentum Loss of Heavy Ions.” In: *Physical Review* 60.9 (1941), pp. 657–660. DOI: 10.1103/PhysRev.60.657.

[BV21] A. Burrows and D. Vartanyan. “Core-collapse supernova explosion theory.” In: *Nature* 589.7840 (2021), pp. 29–39. DOI: 10.1038/s41586-020-03059-w.

[Bus+10] D. B. J. Bussey, J. A. McGovern, P. D. Spudis, et al. “Illumination conditions of the south pole of the Moon derived using Kaguya topography.” In: *Icarus* 208.2 (2010), pp. 558–564. DOI: 10.1016/j.icarus.2010.03.028.

[BZB17] C. Bustard, E. G. Zweibel, and E. Brooks. “Cosmic Ray Acceleration by a Versatile Family of Galactic Wind Termination Shocks.” In: *The Astrophysical Journal* 835.1 (2017). DOI: 10.3847/1538-4357/835/1/72.

[But22] N. Butchart. “The stratosphere: a review of the dynamics and variability.” In: *Weather and Climate Dynamics* 3.4 (2022), pp. 1237–1272. DOI: 10.5194/wcd-3-1237-2022.

[CH11] J. A. Caffrey and D. M. Hamby. “A review of instruments and methods for dosimetry in space.” In: *Advances in Space Research* 47.4 (2011), pp. 563–574. DOI: 10.1016/j.asr.2010.10.005.

[CKK09] A. Caldwell, D. Kollár, and K. Kröninger. “BAT – The Bayesian analysis toolkit.” In: *Computer Physics Communications* 180.11 (2009), pp. 2197–2209. DOI: 10.1016/j.cpc.2009.06.026.

[CGA94] J. Calera-Rubio, A. Gras-Martí, and N. R. Arista. “Stopping power of low-velocity ions in solids: inhomogeneous electron gas model.” In: *Nuclear Instruments and Methods in Physics Research Section B: Beam Interactions with Materials and Atoms* 93.2 (1994), pp. 137–141. DOI: 10.1016/0168-583x(94)95678-2.

[Cal+12] S. Callier, C. D. Taille, G. Martin-Chassard, and L. Raux. “EASIROC, an Easy & Versatile ReadOut Device for SiPM.” In: *Physics Procedia* 37 (2012), pp. 1569–1576. DOI: 10.1016/j.phpro.2012.02.486.

[Cal+19] M. Calvi, P. Carniti, C. Gotti, et al. “Single photon detection with SiPMs irradiated up to 10^{14} cm^{-2} 1-MeV-equivalent neutron fluence.” In: *Nuclear Instruments and Methods in Physics Research Section A: Accelerators, Spectrometers, Detectors and Associated Equipment* 922 (2019), pp. 243–249. DOI: 10.1016/j.nima.2019.01.013.

[CB20] K. M. Cannon and D. T. Britt. “A geologic model for lunar ice deposits at mining scales.” In: *Icarus* 347 (2020). DOI: 10.1016/j.icarus.2020.113778.

[Can+20] K. M. Cannon, A. N. Deutsch, J. W. Head, and D. T. Britt. “Stratigraphy of Ice and Ejecta Deposits at the Lunar Poles.” In: *Geophysical Research Letters* 47.21 (2020). DOI: 10.1029/2020gl088920.

[Can+11] E. D. Cantero, C. C. Montanari, M. Behar, et al. “Experimental and theoretical study of the energy loss of C and O in Zn.” In: *Physical Review A* 84.1 (2011). DOI: 10.1103/PhysRevA.84.014902.

[Car18] P. A. Caraveo. “Neutron Stars as Particle Accelerators.” In: *Nuclear and Particle Physics Proceedings* 297-299 (2018), pp. 96–101. DOI: 10.1016/j.nuclphysbps.2018.07.015.

[Car+20] N. Cartiglia, R. Arcidiacono, G. Borghi, et al. “LGAD designs for Future Particle Trackers.” In: *Nuclear Instruments and Methods in Physics Research Section A: Accelerators, Spectrometers, Detectors and Associated Equipment* 979 (2020). DOI: 10.1016/j.nima.2020.164383.

[Car+14] S. M. Carturan, T. Marchi, E. Fanchini, et al. “Scintillator and solid-state neutron detectors and their applications.” In: *The European Physical Journal Plus* 129.10 (2014). DOI: 10.1140/epjp/i2014-14212-2.

[Cha+98] M. Chabot, M. Nectoux, D. Gardès, et al. “Charge state dependence of the stopping power for chlorine ions interacting with a cold gas and a plasma (1.5MeV/u).” In: *Nuclear Instruments and Methods in Physics Research Section A: Accelerators, Spectrometers, Detectors and Associated Equipment* 415.3 (1998), pp. 571–575. DOI: 10.1016/s0168-9002(98)00377-5.

[CF54] K. F. Chackett and J. H. Fremlin. “The forward displacement of the nitrogen isotope of mass 13 produced by bombardment of aluminium with the isotope 14.” In: *The London, Edinburgh, and Dublin Philosophical Magazine and Journal of Science* 45.366 (1954), pp. 735–741. DOI: 10.1080/14786440708520481.

[Cha+55] O. Chamberlain, E. Segrè, C. Wiegand, and T. Ypsilantis. “Observation of Antiprotons.” In: *Physical Review* 100.3 (1955), pp. 947–950. DOI: 10.1103/PhysRev.100.947.

[Cha+18] J. C. Chancellor, R. S. Blue, K. A. Cengel, et al. “Limitations in predicting the space radiation health risk for exploration astronauts.” In: *npj Microgravity* 4 (2018), p. 8. DOI: 10.1038/s41526-018-0043-2.

[Cha+17] J. Chang, G. Ambrosi, Q. An, et al. “The DArk Matter Particle Explorer mission.” In: *Astroparticle Physics* 95 (2017), pp. 6–24. DOI: 10.1016/j.astropartphys.2017.08.005.

[Che+15] B. Chen, T. S. Bastian, C. Shen, et al. “Particle acceleration by a solar flare termination shock.” In: *Science* 350.6265 (2015), pp. 1238–42. DOI: 10.1126/science.aac8467.

[CKR95] J. Chen, A. M. Kellerer, and H. H. Rossi. “On the revised concept of linear energy transfer.” In: *Radiation and Environmental Biophysics* 34.1 (1995), pp. 29–35. DOI: 10.1007/BF01210542.

[Che+23] X. Chen, S. Xu, X. Song, et al. “Astronaut Radiation Dose Calculation With a New Galactic Cosmic Ray Model and the AMS-02 Data.” In: *Space Weather* 21.4 (2023). DOI: 10.1029/2022sw003285.

[Che93] S. Cherny. “Problems in the use of plastic scintillators in intense radiation fields.” In: *Radiation Physics and Chemistry* 41.1-2 (1993), pp. 181–184. DOI: 10.1016/0969-806x(93)90054-x.

[Che+18] D. O. Chernyshov, P. Caselli, K. S. Cheng, et al. “Interaction of cosmic rays with molecular clouds.” In: *Nuclear and Particle Physics Proceedings* 297-299 (2018), pp. 80–84. DOI: 10.1016/j.nuclphysbps.2018.07.012.

[Cho+22] G. H. Choi, E. S. Seo, S. Aggarwal, et al. “Measurement of High-energy Cosmic-Ray Proton Spectrum from the ISS-CREAM Experiment.” In: *The Astrophysical Journal* 940.2 (2022). DOI: 10.3847/1538-4357/ac9d2c.

[Cho+09] I. Cholis, L. Goodenough, D. Hooper, et al. “High energy positrons from annihilating dark matter.” In: *Physical Review D* 80.12 (2009). DOI: 10.1103/PhysRevD.80.123511.

[CK22] I. Cholis and I. Krommydas. “Utilizing cosmic-ray positron and electron observations to probe the averaged properties of Milky Way pulsars.” In: *Physical Review D* 105.2 (2022). DOI: 10.1103/PhysRevD.105.023015.

[Cho52] C. N. Chou. “The Nature of the Saturation Effect of Fluorescent Scintillators.” In: *Physical Review* 87.5 (1952), pp. 904–905. DOI: 10.1103/PhysRev.87.904.

[Chr+19] J. B. Christensen, E. Almhagen, L. Stolarczyk, et al. “Ionization quenching in scintillators used for dosimetry of mixed particle fields.” In: *Physics in Medicine & Biology* 64.9 (2019), p. 095018. DOI: 10.1088/1361-6560/ab12f2.

[CA18] J. B. Christensen and C. E. Andersen. “Relating ionization quenching in organic plastic scintillators to basic material properties by modelling excitation density transport and amorphous track structure during proton irradiation.” In: *Physics in Medicine & Biology* 63.19 (2018), p. 195010. DOI: 10.1088/1361-6560/aadf2d.

[CP72] W. K. Chu and D. Powerd. “Calculation of mean excitation energy for all elements.” In: *Physics Letters A* 40.1 (1972), pp. 23–24. DOI: 10.1016/0375-9601(72)90181-8.

[Chu90] E. L. Chupp. “Transient particle acceleration associated with solar flares.” In: *Science* 250.4978 (1990), pp. 229–36. DOI: 10.1126/science.250.4978.229.

[CS92] C. Chyba and C. Sagan. “Endogenous production, exogenous delivery and impact-shock synthesis of organic molecules: an inventory for the origins of life.” In: *Nature* 355 (1992), pp. 125–32. DOI: 10.1038/355125a0.

[Cla74] D. Clark. “The intrinsic scintillation efficiency of plastic scintillators for 60Co gamma excitation.” In: *Nuclear Instruments and Methods* 117.1 (1974), pp. 295–303. DOI: 10.1016/0029-554x(74)90412-1.

[Cla09] R. N. Clark. “Detection of adsorbed water and hydroxyl on the Moon.” In: *Science* 326.5952 (2009), pp. 562–564. DOI: 10.1126/science.1178105.

[CGW00] E. G. Clayton, T. G. Guzik, and J. P. Wefel. “CRRES Measurements of Energetic Helium During the 1990–1991 Solar Maximum.” In: *Solar Physics* 195.1 (2000), pp. 175–194. DOI: 10.1023/a:1005251630568.

[CH18] E. W. Cliver and K. Herbst. “Evolution of the Sunspot Number and Solar Wind B Time Series.” In: *Space Science Reviews* 214.2 (2018). DOI: 10.1007/s11214-018-0487-4.

[Cli+22] E. W. Cliver, C. J. Schrijver, K. Shibata, and I. G. Usoskin. “Extreme solar events.” In: *Living Reviews in Solar Physics* 19.1 (2022). DOI: 10.1007/s41116-022-00033-8.

[Coh+20] B. A. Cohen, P. O. Hayne, B. Greenhagen, et al. “Lunar Flashlight: Illuminating the Lunar South Pole.” In: *IEEE Aerospace and Electronic Systems Magazine* 35.3 (2020), pp. 46–52. DOI: 10.1109/maes.2019.2950746.

[Coh+16] E. O. Cohen, E. Piasetzky, Y. Shamai, and N. Pilip. “Development of a scintillating-fiber beam detector for the MUSE experiment.” In: *Nuclear Instruments and Methods in Physics Research Section A: Accelerators, Spectrometers, Detectors and Associated Equipment* 815 (2016), pp. 75–82. DOI: 10.1016/j.nima.2016.01.044.

[Col+10] A. Colaprete, P. Schultz, J. Heldmann, et al. “Detection of Water in the LCROSS Ejecta Plume.” In: *Science* 330.6003 (2010), pp. 463–468. DOI: 10.1126/science.1186986.

[Col+07] J. E. Colwell, S. Batiste, M. Horányi, et al. “Lunar surface: Dust dynamics and regolith mechanics.” In: *Reviews of Geophysics* 45.2 (2007). DOI: 10.1029/2005rg000184.

[Com+05] C. Combet, D. Maurin, J. Donnelly, et al. “Spallation-dominated propagation of heavy cosmic rays and the Local Interstellar Medium (LISM).” In: *Astronomy & Astrophysics* 435.1 (2005), pp. 151–160. DOI: 10.1051/0004-6361:20042459.

[Cor+13] L. Corradi, S. Szilner, G. Pollarolo, et al. “Multinucleon transfer reactions: Present status and perspectives.” In: *Nuclear Instruments and Methods in Physics Research Section B: Beam Interactions with Materials and Atoms* 317 (2013), pp. 743–751. DOI: 10.1016/j.nimb.2013.04.093.

[Cos+18] J. M. de Cos, H. Chanal, A. Comerma Montells, et al. “PACIFIC: SiPM readout ASIC for LHCb upgrade.” In: *Nuclear Instruments and Methods in Physics Research Section A: Accelerators, Spectrometers, Detectors and Associated Equipment* 912 (2018), pp. 354–358. DOI: 10.1016/j.nima.2017.12.044.

[Cos+20] E. S. Costello, R. R. Ghent, M. Hirabayashi, and P. G. Lucey. “Impact Gardening as a Constraint on the Age, Source, and Evolution of Ice on Mercury and the Moon.” In: *Journal of Geophysical Research: Planets* 125.3 (2020). DOI: 10.1029/2019je006172.

[Cou+21] J. Coutinho, V. J. B. Torres, I. Capan, et al. “Silicon carbide diodes for neutron detection.” In: *Nuclear Instruments and Methods in Physics Research Section A: Accelerators, Spectrometers, Detectors and Associated Equipment* 986 (2021). DOI: 10.1016/j.nima.2020.164793.

[Cov+96] S. Cova, M. Ghioni, A. Lacaita, et al. “Avalanche photodiodes and quenching circuits for single-photon detection.” In: *Applied Optics* 35.12 (1996), pp. 1956–76. DOI: 10.1364/AO.35.001956.

[Cow16] R. Cowsik. “Positrons and Antiprotons in Galactic Cosmic Rays.” In: *Annual Review of Nuclear and Particle Science* 66.1 (2016), pp. 297–319. DOI: 10.1146/annurev-nucl-102115-044851.

[CO71] C. J. Crannell and J. F. Ormes. “Geometrical - factor determination using a monte carlo approach.” In: *Nuclear Instruments and Methods* 94.1 (1971), pp. 179–183. DOI: 10.1016/0029-554x(71)90357-0.

[CS70] R. L. Craun and D. L. Smith. “Analysis of response data for several organic scintillators.” In: *Nuclear Instruments and Methods* 80.2 (1970), pp. 239–244. DOI: 10.1016/0029-554x(70)90768-8.

[Cra+12] I. A. Crawford, M. Anand, C. S. Cockell, et al. “Back to the Moon: The scientific rationale for resuming lunar surface exploration.” In: *Planetary and Space Science* 74.1 (2012), pp. 3–14. DOI: 10.1016/j.pss.2012.06.002.

[Cra15] I. A. Crawford. “Lunar resources.” In: *Progress in Physical Geography* 39 (2015), pp. 137–167. DOI: 10.1177/0309133314567585.

[CV02] D. H. Crider and R. R. Vondrak. “Hydrogen migration to the lunar poles by solar wind bombardment of the moon.” In: *Advances in Space Research* 30.8 (2002), pp. 1869–1874. DOI: 10.1016/s0273-1177(02)00493-3.

[CF70] A. Crispin and G. N. Fowler. “Density Effect in the Ionization Energy Loss of Fast Charged Particles in Matter.” In: *Reviews of Modern Physics* 42.3 (1970), pp. 290–316. DOI: 10.1103/RevModPhys.42.290.

[Cuc15a] F. A. Cucinotta. “Biophysics of NASA Radiation Quality Factors.” In: *Radiation Protection Dosimetry* 166 (2015), pp. 282–289. DOI: 10.1093/rpd/ncv144.

[Cuc15b] F. A. Cucinotta. “Review of NASA Approach to Space Radiation Risk Assessments for Mars Exploration.” In: *Health Physics* 108 (2015), pp. 131–142. DOI: 10.1097/HP.0000000000000255.

[Cuc15c] F. A. Cucinotta. “A New Approach to Reduce Uncertainties in Space Radiation Cancer Risk Predictions.” In: *PLoS ONE* 10 (2015), e0120717. DOI: 10.1371/journal.pone.0120717.

[Cuc+15] F. A. Cucinotta, M. Alp, B. Rowedder, and M.-H. Y. Kim. “Safe days in space with acceptable uncertainty from space radiation exposure.” In: *Life Sciences in Space Research* 5 (2015), pp. 31–38. DOI: 10.1016/j.lssr.2015.04.002.

[Cuc+06] F. A. Cucinotta, J. W. Wilson, P. Saganti, et al. “Isotopic dependence of GCR fluence behind shielding.” In: *Radiation Measurements* 41.9-10 (2006), pp. 1235–1249. DOI: 10.1016/j.radmeas.2006.03.012.

[Cue+64] J. Cuevas, M. Garcia-Munoz, P. Torres, and S. K. Allison. “Partial Atomic and Ionic Stopping Powers of Gaseous Hydrogen for Helium and Hydrogen Beams.” In: *Physical Review* 135.2A (1964), A335–A345. DOI: 10.1103/PhysRev.135.A335.

[Cum+16] A. C. Cummings, E. C. Stone, B. C. Heikkila, et al. “Galactic Cosmic Rays in the Local Interstellar Medium: Voyager 1 Observations and Model Results.” In: *The Astrophysical Journal* 831.1 (2016). DOI: 10.3847/0004-637x/831/1/18.

[DAm+96] C. D’Ambrosio, T. Gys, H. Leutz, and D. Puertolas. “Particle tracking with scintillating fibers.” In: *IEEE Transactions on Nuclear Science* 43.3 (1996), pp. 2115–2127. DOI: 10.1109/23.502305.

[Dac+15] T. P. Dachev, J. V. Semkova, B. T. Tomov, et al. “Overview of the Liulin type instruments for space radiation measurement and their scientific results.” In: *Life Sciences in Space Research* 4 (2015), pp. 92–114. DOI: 10.1016/j.lssr.2015.01.005.

[DB17] A. Damyanova and A. Bravar. “Scintillating fiber detectors for precise time and position measurements read out with Si-PMs.” In: *Nuclear Instruments and Methods in Physics Research Section A: Accelerators, Spectrometers, Detectors and Associated Equipment* 845 (2017), pp. 475–480. DOI: 10.1016/j.nima.2016.06.088.

[Dar11] L. R. Dartnell. “Ionizing radiation and life.” In: *Astrobiology* 11.6 (2011), pp. 551–82. DOI: 10.1089/ast.2010.0528.

[Dat+96] S. Datz, H. F. Krause, C. R. Vane, et al. “Effect of Nuclear Size on the Stopping Power of Ultrarelativistic Heavy Ions.” In: *Physical Review Letters* 77.14 (1996), pp. 2925–2928. DOI: 10.1103/PhysRevLett.77.2925.

[Dau+93] H. Dautet, P. Deschamps, B. Dion, et al. “Photon counting techniques with silicon avalanche photodiodes.” In: *Appl Opt* 32.21 (1993), pp. 3894–900. DOI: 10.1364/AO.32.003894.

[DB84] M. S. Daw and M. I. Baskes. “Embedded-atom method: Derivation and application to impurities, surfaces, and other defects in metals.” In: *Physical Review B* 29.12 (1984), pp. 6443–6453. DOI: 10.1103/PhysRevB.29.6443.

[DH17] A. De Giacomo and J. Hermann. “Laser-induced plasma emission: from atomic to molecular spectra.” In: *Journal of Physics D: Applied Physics* 50.18 (2017), p. 183002. DOI: 10.1088/1361-6463/aa6585.

[DBG21] A. De Sarkar, S. Biswas, and N. Gupta. “Positron excess from cosmic ray interactions in galactic molecular clouds.” In: *Journal of High Energy Astrophysics* 29 (2021), pp. 1–18. DOI: 10.1016/j.jheap.2020.11.001.

[Del+16] M. D. Delp, J. M. Charvat, C. L. Limoli, et al. “Apollo Lunar Astronauts Show Higher Cardiovascular Disease Mortality: Possible Deep Space Radiation Effects on the Vascular Endothelium.” In: *Scientific Reports* 6 (2016), p. 29901. DOI: 10.1038/srep29901.

[Dem+16] T. M. Demkiv, O. O. Halyatkin, V. V. Vistovskyy, et al. “Luminescent and kinetic properties of the polystyrene composites based on BaF2 nanoparticles.” In: *Nuclear Instruments and Methods in Physics Research Section A: Accelerators, Spectrometers, Detectors and Associated Equipment* 810 (2016), pp. 1–5. DOI: 10.1016/j.nima.2015.11.130.

[Der+05] V. A. Derbina, V. I. Galkin, M. Hareyama, et al. “Cosmic-Ray Spectra and Composition in the Energy Range of 10-1000 TeV per Particle Obtained by the RUNJOB Experiment.” In: *The Astrophysical Journal* 628.1 (2005), pp. L41–L44. DOI: 10.1086/432715.

[DZF10] D. Desilets, M. Zreda, and T. P. A. Ferré. “Nature’s neutron probe: Land surface hydrology at an elusive scale with cosmic rays.” In: *Water Resources Research* 46.11 (2010). DOI: 10.1029/2009wr008726.

[Det+17] M. Dettmann, V. Herrig, J. Maldonis, et al. “Radiation Hard Plastic Scintillators for a New Generation of Particle Detectors.” In: *Journal of Instrumentation* 12.03 (2017), P03017–P03017. DOI: 10.1088/1748-0221/12/03/p03017.

[DHN20] A. N. Deutsch, J. W. Head, and G. A. Neumann. “Analyzing the ages of south polar craters on the Moon: Implications for the sources and evolution of surface water ice.” In: *Icarus* 336 (2020). DOI: 10.1016/j.icarus.2019.113455.

[Deu+21] A. N. Deutsch, J. L. Heldmann, A. Colaprete, et al. “Analyzing Surface Ruggedness Inside and Outside of Ice Stability Zones at the Lunar Poles.” In: *The Planetary Science Journal* 2.5 (2021). DOI: 10.3847/PSJ/ac24ff.

[DB24] J. M. DeWitt and E. R. Benton. “Secondary proton buildup in space radiation shielding.” In: *Life Sciences in Space Research* 41 (2024), pp. 119–126. DOI: 10.1016/j.lssr.2024.02.005.

[DiF+23] L. Di Fino, G. Romoli, G. Santi Amantini, et al. “Radiation measurements in the International Space Station, Columbus module, in 2020-2022 with the LIDAL detector.” In: *Life Sciences in Space Research* 39 (2023), pp. 26–42. DOI: 10.1016/j.lssr.2023.03.007.

[DiS+23] A. Di Salvo, S. Garbolino, M. Mignone, et al. “A Configurable 64-Channel ASIC for Cherenkov Radiation Detection from Space.” In: *Instruments* 7.4 (2023). DOI: 10.3390/instruments7040050.

[Die+14] S. Diehl, R. W. Novotny, N. Aubry, et al. “Development and Characterization of Inorganic Scintillating Fibers Made of LuAG:Ce and LYSO:Ce.” In: *IEEE Transactions on Nuclear Science* 61.1 (2014), pp. 353–361. DOI: 10.1109/tns.2013.2281277.

[Dlo+92] Z. Dlouhý, A. Kugler, L. Nosek, et al. “The response of BGO scintillation detectors to light charged nuclei.” In: *Nuclear Instruments and Methods in Physics Research Section A: Accelerators, Spectrometers, Detectors and Associated Equipment* 317.3 (1992), pp. 604–606. DOI: 10.1016/0168-9002(92)91008-w.

[DS20] M. I. Dobynde and Y. Y. Shprits. “Radiation environment created with GCRs inside a spacecraft.” In: *Life Sci Space Res (Amst)* 24 (2020), pp. 116–121. DOI: 10.1016/j.lssr.2019.09.001.

[Doe+20] P. von Doetinchem, K. Perez, T. Aramaki, et al. “Cosmic-ray antinuclei as messengers of new physics: status and outlook for the new decade.” In: *Journal of Cosmology and Astroparticle Physics* 8 (2020), p. 035. DOI: 10.1088/1475-7516/2020/08/035.

[Dok+01] T. Doke, T. Hayashi, J. Kikuchi, et al. “Measurements of LET-distribution, dose equivalent and quality factor with the RRMD-III on the Space Shuttle Missions STS-84, -89 and -91.” In: *Radiation Measurements* 33.3 (2001), pp. 373–87. DOI: 10.1016/s1350-4487(00)00149-9.

[DD16] D. J. Doran and S. Dalla. “Temporal Evolution of Solar Energetic Particle Spectra.” In: *Solar Physics* 291.7 (2016), pp. 2071–2097. DOI: 10.1007/s11207-016-0956-4.

[Dre+95] G. Drexlin, V. Eberhard, D. Hunkel, and B. Zeitnitz. “Spectral attenuation length of scintillating fibers.” In: *Nuclear Instruments and Methods in Physics Research Section A: Accelerators, Spectrometers, Detectors and Associated Equipment* 360.1-2 (1995), pp. 245–247. DOI: 10.1016/0168-9002(95)00096-8.

[Dro94] W. Droege. “Transport of solar energetic particles.” In: *The Astrophysical Journal Supplement Series* 90 (1994). DOI: 10.1086/191876.

[Duj+18] C. Dujardin, E. Auffray, E. Bourret-Courchesne, et al. “Needs, Trends, and Advances in Inorganic Scintillators.” In: *IEEE Transactions on Nuclear Science* 65.8 (2018), pp. 1977–1997. DOI: 10.1109/tns.2018.2840160.

[Dum+16] J. Dumazert, R. Coulon, G. H. V. Bertrand, et al. “Compensated bismuth-loaded plastic scintillators for neutron detection using low-energy pseudo-spectroscopy.” In: *Nuclear Instruments and Methods in Physics Research Section A: Accelerators, Spectrometers, Detectors and Associated Equipment* 819 (2016), pp. 25–32. DOI: 10.1016/j.nima.2016.02.083.

[DC11] M. Durante and F. A. Cucinotta. “Physical basis of radiation protection in space travel.” In: *Reviews of Modern Physics* 83 (2011), pp. 1245–1281. DOI: 10.1103/RevModPhys.83.1245.

[Ech+86] P. M. Echenique, R. M. Nieminen, J. C. Ashley, and R. H. Ritchie. “Nonlinear stopping power of an electron gas for slow ions.” In: *Phys Rev A Gen Phys* 33.2 (1986), pp. 897–904. DOI: 10.1103/physreva.33.897.

[Eic+16] D. Eichler, N. Globus, R. Kumar, and E. Gavish. “Ultrahigh Energy Cosmic Rays: A Galactic Origin?” In: *The Astrophysical Journal* 821.2 (2016). DOI: 10.3847/2041-8205/821/2/l24.

[Eis68] F. H. Eisen. “Channeling of medium-mass ions through silicon.” In: *Canadian Journal of Physics* 46.6 (1968), pp. 561–572. DOI: 10.1139/p68-070.

[Elp+07] R. C. Elphic, V. R. Eke, L. F. A. Teodoro, et al. “Models of the distribution and abundance of hydrogen at the lunar south pole.” In: *Geophysical Research Letters* 34.13 (2007), n/a–n/a. DOI: 10.1029/2007gl029954.

[Elw39] G. Elwert. “Verschärfte Berechnung von Intensität und Polarisation im kontinuierlichen Röntgenspektrum1.” In: *Annalen der Physik* 426.2 (1939), pp. 178–208. DOI: 10.1002/andp.19394260206.

[EHP11] R. Engel, D. Heck, and T. Pierog. “Extensive Air Showers and Hadronic Interactions at High Energy.” In: *Annual Review of Nuclear and Particle Science* 61.1 (2011), pp. 467–489. DOI: 10.1146/annurev.nucl.012809.104544.

[Eng+90] J. J. Engelmann, P. Ferrando, A. Soutoul, et al. “Charge composition and energy spectra of cosmic-ray nuclei for elements from Be to Ni - Results from HEAO-3-C2.” In: *Astronomy & Astrophysics* 233 (1990), pp. 96–111.

[ES90] H. Esbensen and P. Sigmund. “Barkas effect in a dense medium: Stopping power and wake field.” In: *Annals of Physics* 201.1 (1990), pp. 152–192. DOI: 10.1016/0003-4916(90)90356-s.

[Fal+23] F. Faldi, B. Bertucci, N. Tomassetti, and V. Vagelli. “Real-time monitoring of solar energetic particles outside the ISS with the AMS-02 instrument.” In: *Rendiconti Lincei. Scienze Fisiche e Naturali* (2023). DOI: 10.1007/s12210-023-01156-2.

[FM18] K. Fang and K. Murase. “Linking high-energy cosmic particles by black-hole jets embedded in large-scale structures.” In: *Nature Physics* 14.4 (2018), pp. 396–398. DOI: 10.1038/s41567-017-0025-4.

[Fan63] U. Fano. “Penetration of Protons, Alpha Particles, and Mesons.” In: *Annual Review of Nuclear Science* 13.1 (1963), pp. 1–66. DOI: 10.1146/annurev.ns.13.120163.000245.

[Fan20] A. Fantoni. “Upgrade of the ALICE inner tracking system: Construction and commissioning.” In: *Physica Scripta* 95.8 (2020). DOI: 10.1088/1402-4896/aba0f7.

[Far+19] W. M. Farrell, D. M. Hurley, M. J. Poston, et al. “The Young Age of the LAMP-observed Frost in Lunar Polar Cold Traps.” In: *Geophysical Research Letters* 46.15 (2019), pp. 8680–8688. DOI: 10.1029/2019gl083158.

[FHZ15] W. M. Farrell, D. M. Hurley, and M. I. Zimmerman. “Spillage of lunar polar crater volatiles onto adjacent terrains: The case for dynamic processes.” In: *Geophysical Research Letters* 42.9 (2015), pp. 3160–3165. DOI: 10.1002/2015gl063200.

[Fel+04] W. C. Feldman, K. Ahola, B. L. Barraclough, et al. “Gamma-Ray, Neutron, and Alpha-Particle Spectrometers for the Lunar Prospector mission.” In: *Journal of Geophysical Research* 109 (2004). DOI: ArtnE07s0610.1029/2003je002207.

[Fel+00] W. C. Feldman, D. J. Lawrence, R. C. Elphic, et al. “Chemical information content of lunar thermal and epithermal neutrons.” In: *Journal of Geophysical Research: Planets* 105 (2000), pp. 20347–20363. DOI: 10.1029/1999JE001183.

[Fel+98] W. C. Feldman, S. Maurice, A. B. Binder, et al. “Fluxes of fast and epithermal neutrons from Lunar Prospector: evidence for water ice at the lunar poles.” In: *Science* 281.5382 (1998), pp. 1496–500. DOI: 10.1126/science.281.5382.1496.

[FT47] E. Fermi and E. Teller. “The Capture of Negative Mesotrons in Matter.” In: *Physical Review* 72.5 (1947), pp. 399–408. DOI: 10.1103/PhysRev.72.399.

[Fer+96] A. Ferrari, J. Ranft, S. Roesler, and P. R. Sala. “Cascade particles, nuclear evaporation, and residual nuclei in high energy hadron-nucleus interactions.” In: *Zeitschrift für Physik C* 70.3 (1996), pp. 413–426. DOI: 10.1007/s002880050119.

[FA84] L. de Ferrariis and N. R. Arista. “Classical and quantum-mechanical treatments of the energy loss of charged particles in dilute plasmas.” In: *Physical Review A* 29.4 (1984), pp. 2145–2159. DOI: 10.1103/PhysRevA.29.2145.

[FLS22] F. Ferrulli, M. Labalme, and M. Silari. “Investigation of CLYC-6 for thermal neutron detection and CLYC-7 for fast neutron spectrometry.” In: *Nuclear Instruments and Methods in Physics Research Section A: Accelerators, Spectrometers, Detectors and Associated Equipment* 1029 (2022). DOI: 10.1016/j.nima.2022.166460.

[Fer+20] B. Fersch, T. Francke, M. Heistermann, et al. “A dense network of cosmic-ray neutron sensors for soil moisture observation in a highly instrumented pre-Alpine headwater catchment in Germany.” In: *Earth System Science Data* 12.3 (2020), pp. 2289–2309. DOI: 10.5194/essd-12-2289-2020.

[Fet+06] A. Fettouhi, H. Geissel, A. Schinner, and P. Sigmund. “Stopping of high-Z ions at intermediate velocities.” In: *Nuclear Instruments and Methods in Physics Research Section B: Beam Interactions with Materials and Atoms* 245.1 (2006), pp. 22–27. DOI: 10.1016/j.nimb.2005.11.058.

[Fin+20] C. C. Finlay, C. Kloss, N. Olsen, et al. “The CHAOS-7 geomagnetic field model and observed changes in the South Atlantic Anomaly.” In: *Earth Planets Space* 72.1 (2020), p. 156. DOI: 10.1186/s40623-020-01252-9.

[Fir57] O. B. Firsov. “Interaction Energy of Atoms for Small Nuclear Separations.” In: *Journal of Experimental and Theoretical Physics* 5.6 (1957), p. 1192.

[Fla+20] J. Flahaut, J. Carpenter, J. P. Williams, et al. “Regions of interest (ROI) for future exploration missions to the lunar South Pole.” In: *Planetary and Space Science* 180 (2020). DOI: 10.1016/j.pss.2019.104750.

[FS16] L. Flamm and R. Schumann. “Die Geschwindigkeitsabnahme der α-Strahlen in Materie.” In: *Annalen der Physik* 355.14 (1916), pp. 655–699. DOI: 10.1002/andp.19163551403.

[For+23] M. J. Ford, E. Aigeldinger, F. Sutanto, et al. “Synthesis and processing of lithium-loaded plastic scintillators on the kilogram scale.” In: *Nuclear Instruments and Methods in Physics Research Section A: Accelerators, Spectrometers, Detectors and Associated Equipment* 1050 (2023). DOI: 10.1016/j.nima.2023.168093.

[För06] T. Förster. “Zwischenmolekulare Energiewanderung und Fluoreszenz.” In: *Annalen der Physik* 437.1-2 (2006), pp. 55–75. DOI: 10.1002/andp.19484370105.

[Fow+87] P. H. Fowler, R. N. F. Walker, M. R. W. Masheder, et al. “Ariel 6 measurements of the fluxes of ultraheavy cosmic rays.” In: *The Astrophysical Journal* 314 (1987). DOI: 10.1086/165101.

[Fre+96] C. M. Frey, G. Dollinger, A. Bergmaier, et al. “Charge state dependence of the stopping power of 1 MeV/A 58Ni ions.” In: *Nuclear Instruments and Methods in Physics Research Section B: Beam Interactions with Materials and Atoms* 107.1-4 (1996), pp. 31–35. DOI: 10.1016/0168-583x(95)01008-4.

[Fro+15] R. G. Fronk, S. L. Bellinger, L. C. Henson, et al. “High-efficiency microstructured semiconductor neutron detectors for direct 3He replacement.” In: *Nuclear Instruments and Methods in Physics Research Section A: Accelerators, Spectrometers, Detectors and Associated Equipment* 779 (2015), pp. 25–32. DOI: 10.1016/j.nima.2015.01.041.

[Fur+19] W. Furnell, A. Shenoy, E. Fox, and P. Hatfield. “First results from the LUCID-Timepix spacecraft payload onboard the TechDemoSat-1 satellite in Low Earth Orbit.” In: *Advances in Space Research* 63.5 (2019), pp. 1523–1540. DOI: 10.1016/j.asr.2018.10.045.

[Gal13] N. Z. Galunov. “Determination of the light yield of organic scintillators.” In: *Functional materials* 20.3 (2013), pp. 304–309. DOI: 10.15407/fm20.03.304.

[Gar+98] D. Gardès, M. Chabot, M. Nectoux, et al. “Experimental study of stopping power for high Z ion in hydrogen.” In: *Nuclear Instruments and Methods in Physics Research Section A: Accelerators, Spectrometers, Detectors and Associated Equipment* 415.3 (1998), pp. 698–702. DOI: 10.1016/s0168-9002(98)00451-3.

[Gar+10] G. Garty, R. Schulte, S. Shchemelinin, et al. “A nanodosimetric model of radiation-induced clustered DNA damage yields.” In: *Physics in Medicine & Biology* 55.3 (2010), pp. 761–81. DOI: 10.1088/0031-9155/55/3/015.

[GM19] E. Garutti and Y. Musienko. “Radiation damage of SiPMs.” In: *Nuclear Instruments and Methods in Physics Research Section A: Accelerators, Spectrometers, Detectors and Associated Equipment* 926 (2019), pp. 69–84. DOI: 10.1016/j.nima.2018.10.191.

[Gaz+23] R. Gaza, A. S. Johnson, B. Hayes, et al. “The importance of time-resolved personal Dosimetry in space: The ISS Crew Active Dosimeter.” In: *Life Sciences in Space Research* 39 (2023), pp. 95–105. DOI: 10.1016/j.lssr.2023.08.004.

[Gaz+17] R. Gaza, M. Kroupa, R. Rios, et al. “Comparison of novel active semiconductor pixel detector with passive radiation detectors during the NASA Orion Exploration Flight Test 1 (EFT-1).” In: *Radiation Measurements* 106 (2017), pp. 290–297. DOI: 10.1016/j.radmeas.2017.03.041.

[Gei+02] H. Geissel, H. Weick, C. Scheidenberger, et al. “Experimental studies of heavy-ion slowing down in matter.” In: *Nuclear Instruments and Methods in Physics Research Section B: Beam Interactions with Materials and Atoms* 195.1-2 (2002), pp. 3–54. DOI: 10.1016/s0168-583x(02)01311-3.

[GHY20] C.-Q. Geng, D. Huang, and L. Yin. “Multicomponent dark matter in the light of CALET and DAMPE.” In: *Nuclear Physics B* 959 (2020). DOI: 10.1016/j.nuclphysb.2020.115153.

[Geo+13] K. A. George, M. Hada, L. Chappell, and F. A. Cucinotta. "Biological effectiveness of accelerated particles for the induction of chromosome damage: track structure effects." In: *Radiation Research* 180.1 (2013), pp. 25–33. DOI: 10.1667/RR3291.1.

[Geo+18] S. P. George, M. Kroupa, S. Wheeler, et al. "Very high energy calibration of silicon Timepix detectors." In: *Journal of Instrumentation* 13.11 (2018), P11014–P11014. DOI: 10.1088/1748-0221/13/11/p11014.

[GNZ19] M. K. Georgoulis, A. Nindos, and H. Zhang. "The source and engine of coronal mass ejections." In: *Philosophical Transactions of the Royal Society A Mathematical, Physical and Engineering Sciences* 377.2148 (2019), p. 20180094. DOI: 10.1098/rsta.2018.0094.

[Ger+21] M. Gerontidou, N. Katzourakis, H. Mavromichalaki, et al. "World grid of cosmic ray vertical cut-off rigidity for the last decade." In: *Advances in Space Research* 67.7 (2021), pp. 2231–2240. DOI: 10.1016/j.asr.2021.01.011.

[Get+04] I. Getselev, S. Rumin, N. Sobolevsky, et al. "Absorbed dose of secondary neutrons from galactic cosmic rays inside the international space station." In: *Advances in Space Research* 34 (2004), pp. 1429–1432. DOI: 10.1016/j.asr.2004.04.002.

[Ghe+17] A. Ghelfi, D. Maurin, A. Cheminet, et al. "Neutron monitors and muon detectors for solar modulation studies: 2. Φ time series." In: *Advances in Space Research* 60.4 (2017), pp. 833–847. DOI: 10.1016/j.asr.2016.06.027.

[Gia23] G. Giacomini. "LGAD-Based Silicon Sensors for 4D Detectors." In: *Sensors* 23.4 (2023). DOI: 10.3390/s23042132.

[Gia+16] A. Giaz, N. Blasi, C. Boiano, et al. "Fast neutron measurements with 7Li and 6Li enriched CLYC scintillators." In: *Nuclear Instruments and Methods in Physics Research Section A: Accelerators, Spectrometers, Detectors and Associated Equipment* 825 (2016), pp. 51–61. DOI: 10.1016/j.nima.2016.03.090.

[GM17] A. Gil and K. Mursula. "Hale cycle and long-term trend in variation of galactic cosmic rays related to solar rotation." In: *Astronomy & Astrophysics* 599 (2017). DOI: 10.1051/0004-6361/201629604.

[GWC93] K. T. Gillen, J. S. Wallace, and R. L. Clough. "Dose-rate dependence of the radiation-induced discoloration of polystyrene." In: *Radiation Physics and Chemistry* 41.1-2 (1993), pp. 101–113. DOI: 10.1016/0969-806x(93)90046-w.

[Gil+18] P. Gillet, M. Munier, N. Arbor, et al. "Evaluation of an optical scintillating fiber detector for CT dosimetry." In: *Radiation Measurements* 119 (2018), pp. 125–131. DOI: 10.1016/j.radmeas.2018.09.012.

[Glä+18] P. Gläser, J. Oberst, G. A. Neumann, et al. "Illumination conditions at the lunar poles: Implications for future exploration." In: *Planetary and Space Science* 162 (2018), pp. 170–178. DOI: 10.1016/j.pss.2017.07.006.

[Gla00] L. Glazov. "Energy-loss spectra of swift ions." In: *Nuclear Instruments and Methods in Physics Research Section B: Beam Interactions with Materials and Atoms* 161-163 (2000), pp. 1–8. DOI: 10.1016/s0168-583x(99)00879-4.

[GS97] L. Glazov and P. Sigmund. "Energy-loss spectra of charged particles in the presence of charge exchange." In: *Nuclear Instruments and Methods in Physics Research Section B: Beam Interactions with Materials and Atoms* 125.1-4 (1997), pp. 110–115. DOI: 10.1016/s0168-583x(96)00928-7.

[Gla02] L. G. Glazov. "Multiple-peak structures in energy-loss spectra of swift ions." In: *Nuclear Instruments and Methods in Physics Research Section B: Beam Interactions with Materials and Atoms* 193.1-4 (2002), pp. 56–65. DOI: 10.1016/s0168-583x(02)00727-9.

[GAP07] N. Globus, D. Allard, and E. Parizot. “Propagation of high-energy cosmic rays in extragalactic turbulent magnetic fields: resulting energy spectrum and composition.” In: *Astronomy & Astrophysics* 479.1 (2007), pp. 97–110. DOI: 10.1051/0004-6361:20078653.

[GB20] N. Globus and R. D. Blandford. “The Chiral Puzzle of Life.” In: *The Astrophysical Journal Letters* 895.1 (2020). DOI: 10.3847/2041-8213/ab8dc6.

[GB23] N. Globus and R. Blandford. “Ultra High Energy Cosmic Ray Source Models: Successes, Challenges and General Predictions.” In: *EPJ Web of Conferences* 283 (2023). DOI: 10.1051/epjconf/202328304001.

[Gol74] A. S. Goldhaber. “Statistical models of fragmentation processes.” In: *Physics Letters B* 53.4 (1974), pp. 306–308. DOI: 10.1016/0370-2693(74)90388-8.

[Gol+07] J. O. Goldsten, E. A. Rhodes, W. V. Boynton, et al. “The MESSENGER Gamma-Ray and Neutron Spectrometer.” In: *Space Science Reviews* 131.1-4 (2007), pp. 339–391. DOI: 10.1007/s11214-007-9262-7.

[Góm+22] S. Gómez, J. Alozy, M. Campbell, et al. “FastIC: a fast integrated circuit for the readout of high performance detectors.” In: *Journal of Instrumentation* 17.05 (2022). DOI: 10.1088/1748-0221/17/05/c05027.

[Gon23] J. D. González-Martínez. “H2GCROC: Design and performance of a dedicated very front-end ASIC for SiPM readout of the CMS High Granularity Calorimeter.” In: *Nuclear Instruments and Methods in Physics Research Section A: Accelerators, Spectrometers, Detectors and Associated Equipment* 1047 (2023). DOI: 10.1016/j.nima.2022.167863.

[GL68] L. Goodman and B. J. Laurenzi. “Probability of Singlet-Triplet Transitions.” In: *Advances in Quantum Chemistry* 4 (1968), pp. 153–169. DOI: 10.1016/S0065-3276(08)60393-7.

[GNS22] S. K. Goyal, A. P. Naik, and P. Sharma. “Characterization of Silicon Photomultipliers (SiPMs) for Space Exploration.” In: *Advances in Space Research* 70.11 (2022), pp. 3750–3768. DOI: 10.1016/j.asr.2022.08.047.

[Gra16] P. L. Grande. “Alternative treatment for the energy-transfer and transport cross section in dressed electron-ion binary collisions.” In: *Physical Review A* 94.4 (2016). DOI: 10.1103/PhysRevA.94.042704.

[GS98] P. L. Grande and G. Schiwietz. “Impact-parameter dependence of the electronic energy loss of fast ions.” In: *Physical Review A* 58.5 (1998), pp. 3796–3801. DOI: 10.1103/PhysRevA.58.3796.

[GS02] P. L. Grande and G. Schiwietz. “The unitary convolution approximation for heavy ions.” In: *Nuclear Instruments and Methods in Physics Research Section B: Beam Interactions with Materials and Atoms* 195.1-2 (2002), pp. 55–63. DOI: 10.1016/s0168-583x(01)01164-8.

[Gra+18] C. Granja, K. Kudela, J. Jakubek, et al. “Directional detection of charged particles and cosmic rays with the miniaturized radiation camera MiniPIX Timepix.” In: *Nuclear Instruments and Methods in Physics Research Section A: Accelerators, Spectrometers, Detectors and Associated Equipment* 911 (2018), pp. 142–152. DOI: 10.1016/j.nima.2018.09.140.

[Gra+16] C. Granja, S. Polansky, Z. Vykydal, et al. “The SATRAM Timepix spacecraft payload in open space on board the Proba-V satellite for wide range radiation monitoring in LEO orbit.” In: *Planetary and Space Science* 125 (2016), pp. 114–129. DOI: 10.1016/j.pss.2016.03.009.

[Gre+19] V. Grebenyuk, D. Karmanov, I. Kovalev, et al. “Energy spectra of abundant cosmic-ray nuclei in the NUCLEON experiment.” In: *Advances in Space Research* 64.12 (2019), pp. 2546–2558. DOI: 10.1016/j.asr.2019.10.004.

[Gre+11] R. O. Green, C. Pieters, P. Mouroulis, et al. "The Moon Mineralogy Mapper (M3) imaging spectrometer for lunar science: Instrument description, calibration, on-orbit measurements, science data calibration and on-orbit validation." In: *Journal of Geophysical Research* 116 (2011). DOI: 10.1029/2011je003797.

[Gre66] K. Greisen. "End to the Cosmic-Ray Spectrum?" In: *Physical Review Letters* 16.17 (1966), pp. 748–750. DOI: 10.1103/PhysRevLett.16.748.

[GMS01] D. E. Groom, N. V. Mokhov, and S. I. Striganov. "Muon Stopping Ppwer and Range Tables 10 MeV—100 TeV." In: *Atomic Data and Nuclear Data Tables* 78.2 (2001), pp. 183–356. DOI: 10.1006/adnd.2001.0861.

[Gru+14] L. Gruber, S. E. Brunner, J. Marton, and K. Suzuki. "Over saturation behavior of SiPMs at high photon exposure." In: *Nuclear Instruments and Methods in Physics Research Section A: Accelerators, Spectrometers, Detectors and Associated Equipment* 737 (2014), pp. 11–18. DOI: 10.1016/j.nima.2013.11.013.

[Gru+82] C. Gruhn, M. Binimi, R. Legrain, et al. "Bragg curve spectroscopy." In: *Nuclear Instruments and Methods in Physics Research* 196 (1982), pp. 33–40. DOI: 10.1016/0029-554X(82)90612-7.

[GH20] S. Gundacker and A. Heering. "The silicon photomultiplier: fundamentals and applications of a modern solid-state photon detector." In: *Physics in Medicine & Biology* 65.17 (2020), 17TR01. DOI: 10.1088/1361-6560/ab7b2d.

[GY18] Y.-Q. Guo and Q. Yuan. "On the knee of Galactic cosmic rays in light of sub-TeV spectral hardenings." In: *Chinese Physics C* 42.7 (2018). DOI: 10.1088/1674-1137/42/7/075103.

[GZH22] Z. Guo, G. Zhou, and W. Hu. "Carcinogenesis induced by space radiation: A systematic review." In: *Neoplasia* 32 (2022), p. 100828. DOI: 10.1016/j.neo.2022.100828.

[HG08] M. Hada and A. G. Georgakilas. "Formation of clustered DNA damage after high-LET irradiation: a review." In: *Journal of Radiation Research* 49.3 (2008), pp. 203–10. DOI: 10.1269/jrr.07123.

[Hag+08] M. Hagiwara, T. Sanami, T. Oishi, et al. "Extension of energy acceptance of Bragg curve counter at the high-energy end." In: *Nuclear Instruments and Methods in Physics Research Section A: Accelerators, Spectrometers, Detectors and Associated Equipment* 592.1-2 (2008), pp. 73–79. DOI: 10.1016/j.nima.2008.03.108.

[Hai+63] R. H. Haitz, A. Goetzberger, R. M. Scarlett, and W. Shockley. "Avalanche Effects in Silicon p—n Junctions. I. Localized Photomultiplication Studies on Microplasmas." In: *Journal of Applied Physics* 34.6 (1963), pp. 1581–1590. DOI: 10.1063/1.1702639.

[Haj+18] T. J. Hajagos, C. Liu, N. J. Cherepy, and Q. Pei. "High-Z Sensitized Plastic Scintillators: A Review." In: *Adv Mater* 30.27 (2018), e1706956. DOI: 10.1002/adma.201706956.

[HB78] A. Hallam and J. B. Birks. "Energy transfer in organic systems. XIII. Plastic scintillators." In: *Journal of Physics B: Atomic and Molecular Physics* 11.18 (1978), pp. 3273–3288. DOI: 10.1088/0022-3700/11/18/019.

[Ham+14] M. Hamel, P. Sibczynski, P. Blanc, et al. "A fluorocarbon plastic scintillator for neutron detection: Proof of concept." In: *Nuclear Instruments and Methods in Physics Research Section A: Accelerators, Spectrometers, Detectors and Associated Equipment* 768 (2014), pp. 26–31. DOI: 10.1016/j.nima.2014.09.029.

[HYP22] Z. Han, H. Yu, and Q. Pei. "Fluorene Derivatives for Efficient Prompt Scintillation in Plastic Scintillators." In: *ACS Applied Polymer Materials* 4.6 (2022), pp. 4424–4431. DOI: 10.1021/acsapm.2c00391.

[Har+20] C. Hardgrove, R. Starr, I. Lazbin, et al. “The Lunar Polar Hydrogen Mapper CubeSat Mission.” In: *IEEE Aerospace and Electronic Systems Magazine* 35.3 (2020), pp. 54–69. DOI: 10.1109/maes.2019.2950747.

[Has+12] D. M. Hassler, C. Zeitlin, R. F. Wimmer-Schweingruber, et al. “The Radiation Assessment Detector (RAD) Investigation.” In: *Space Science Reviews* 170 (2012), pp. 503–558. DOI: 10.1007/s11214-012-9913-1.

[Hat+08] R. Hatcher, M. Beck, A. Tackett, and S. T. Pantelides. “Dynamical effects in the interaction of ion beams with solids.” In: *Physical Review Letters* 100.10 (2008), p. 103201. DOI: 10.1103/PhysRevLett.100.103201.

[Hat15] D. H. Hathaway. “The Solar Cycle.” In: *Living Reviews in Solar Physics* 12 (2015), p. 4. DOI: 10.1007/lrsp-2015-4.

[Hay+22] B. M. Hayes, O. I. Causey, B. B. Gersey, and E. R. Benton. “Active Tissue Equivalent Dosimeter: A Tissue Equivalent Proportional Counter flown onboard the International Space Station.” In: *Nuclear Instruments and Methods in Physics Research Section A: Accelerators, Spectrometers, Detectors and Associated Equipment* 1028 (2022). DOI: 10.1016/j.nima.2022.166389.

[HAS20] P. O. Hayne, O. Aharonson, and N. Schörghofer. “Micro cold traps on the Moon.” In: *Nature Astronomy* (2020). DOI: 10.1038/s41550-020-1198-9.

[Hay+15] P. O. Hayne, A. Hendrix, E. Sefton-Nash, et al. “Evidence for exposed water ice in the Moon’s south polar regions from Lunar Reconnaissance Orbiter ultraviolet albedo and temperature measurements.” In: *Icarus* 255 (2015), pp. 58–69. DOI: 10.1016/j.icarus.2015.03.032.

[Hee+16] A. Heering, Y. Musienko, R. Ruchti, et al. “Effects of very high radiation on SiPMs.” In: *Nuclear Instruments and Methods in Physics Research Section A: Accelerators, Spectrometers, Detectors and Associated Equipment* 824 (2016), pp. 111–114. DOI: 10.1016/j.nima.2015.11.037.

[Hei+98] L. Heilbronn, K. Frankel, K. Holabird, et al. “Production of neutrons from interactions of GCR-like particles.” In: *Acta Astronaut* 42.1-8 (1998), pp. 363–73. DOI: 10.1016/s0094-5765(98)00131-3.

[Hei+06] J. H. Heinbockel, J. W. Wilson, S. R. Blattnig, et al. “HZE ion fragmentation cross-section sensitivity and propagated errors in HZE exposure estimates.” In: *Radiation Measurements* 41.9-10 (2006), pp. 1103–1114. DOI: 10.1016/j.radmeas.2006.02.002.

[Hei+10a] S. Heinz, V. Comas, S. Hofmann, et al. “Investigation of di-nuclear systems as entrance channel to fusion.” In: *The European Physical Journal A* 43.2 (2010), pp. 181–184. DOI: 10.1140/epja/i2010-10914-2.

[Hei+10b] S. Heinz, V. Comas, S. Hofmann, et al. “Study of heavy di-nuclear systems.” In: *Nuclear Physics A* 834.1-4 (2010), pp. 362c–365c. DOI: 10.1016/j.nuclphysa.2010.01.040.

[HD22] S. Heinz and H. M. Devaraja. “Nucleosynthesis in multinucleon transfer reactions.” In: *The European Physical Journal A* 58.6 (2022). DOI: 10.1140/epja/s10050-022-00771-1.

[Hen+19] A. R. Hendrix, D. M. Hurley, W. M. Farrell, et al. “Diurnally Migrating Lunar Water: Evidence From Ultraviolet Data.” In: *Geophysical Research Letters* 46.5 (2019), pp. 2417–2424. DOI: 10.1029/2018gl081821.

[HW80] C. Hepburn and A. H. Windle. “Solid state nuclear track detectors.” In: *Journal of Materials Science* 15.2 (1980), pp. 279–301. DOI: 10.1007/pl00020061.

[HKH13] K. Herbst, A. Kopp, and B. Heber. "Influence of the terrestrial magnetic field geometry on the cutoff rigidity of cosmic ray particles." In: *Annales Geophysicae* 31.10 (2013), pp. 1637–1643. DOI: 10.5194/angeo-31-1637-2013.

[Her+07] M. Herman, R. Capote, B. V. Carlson, et al. "EMPIRE: Nuclear Reaction Model Code System for Data Evaluation." In: *Nuclear Data Sheets* 108.12 (2007), pp. 2655–2715. DOI: 10.1016/j.nds.2007.11.003.

[HJS93] T. E. Herod, K. F. Johnson, and J. B. Schlenoff. "Recovery of radiation-induced color centers in poly(vinyltoluene)." In: *Radiation Physics and Chemistry* 41.1-2 (1993), pp. 65–75. DOI: 10.1016/0969-806x(93)90043-t.

[Her+90] D. W. Hertzog, P. T. Debevec, R. A. Eisenstein, et al. "A high-resolution lead /scintillating fiber electromagnetic calorimeter." In: *Nuclear Instruments and Methods in Physics Research Section A: Accelerators, Spectrometers, Detectors and Associated Equipment* 294.3 (1990), pp. 446–458. DOI: 10.1016/0168-9002(90)90285-e.

[Hes12] V. F. Hess. "Über Beobachtungen der durchdringenden Strahlung bei sieben Freiballonfahrten." In: *Physikalische Zeitschrift* 12 (1912), pp. 1084–1091.

[Hib+11] C. A. Hibbitts, G. A. Grieves, M. J. Poston, et al. "Thermal stability of water and hydroxyl on the surface of the Moon from temperature-programmed desorption measurements of lunar analog materials." In: *Icarus* 213.1 (2011), pp. 64–72. DOI: 10.1016/j.icarus.2011.02.015.

[Hig75] V. L. Highland. "Some practical remarks on multiple scattering." In: *Nuclear Instruments and Methods* 129.2 (1975), pp. 497–499. DOI: 10.1016/0029-554x(75)90743-0.

[Hil84a] A. M. Hillas. "The Origin of Ultra-High-Energy Cosmic Rays." In: *Annual Review of Astronomy and Astrophysics* 22.1 (1984), pp. 425–444. DOI: 10.1146/annurev.aa.22.090184.002233.

[Hil05] A. M. Hillas. "Can diffusive shock acceleration in supernova remnants account for high-energy galactic cosmic rays?" In: *Journal of Physics G: Nuclear and Particle Physics* 31.5 (2005), R95–R131. DOI: 10.1088/0954-3899/31/5/r02.

[Hir+21] N. Hirade, H. Takahashi, N. Uchida, et al. "Annealing of proton radiation damages in Si-PM at room temperature." In: *Nuclear Instruments and Methods in Physics Research Section A: Accelerators, Spectrometers, Detectors and Associated Equipment* 986 (2021). DOI: 10.1016/j.nima.2020.164673.

[HBK68] F. Hirayama, L. J. Basile, and C. Klkuchi. "Energy Transfer and Quenching in Plastic Scintillators." In: *Molecular Crystals* 4.1-4 (1968), pp. 83–108. DOI: 10.1080/15421406808082903.

[Hir+92] M. Hirschberg, R. Beckmann, U. Brandenburg, et al. "Precise measurement of Birks kB parameter in plastic scintillators." In: *IEEE Transactions on Nuclear Science* 39.4 (1992), pp. 511–514. DOI: 10.1109/23.159657.

[Hit21] A. Hitachi. "Luminescence Response and Quenching Models for Heavy Ions of 0.5 keV to 1 GeV/n in Liquid Argon and Xenon." In: *Instruments* 5.1 (2021). DOI: 10.3390/instruments5010005.

[HA86] A. Holmes-Siedle and L. Adams. "RADFET: A review of the use of metal-oxide-silicon devices as integrating dosimeters." In: *International Journal of Radiation Applications and Instrumentation. Part C. Radiation Physics and Chemistry* 28.2 (1986), pp. 235–244. DOI: 10.1016/1359-0197(86)90134-7.

[Hon+15] R. Honda, K. Miwa, Y. Matsumoto, et al. “A beam position fiber counter with scintillation fibers and multi-pixel photon counter for high intensity beam operation.” In: *Nuclear Instruments and Methods in Physics Research Section A: Accelerators, Spectrometers, Detectors and Associated Equipment* 787 (2015), pp. 157–160. DOI: 10.1016/j.nima.2014.11.084.

[Hon02] J. Hong. “The scintillation efficiency of carbon and hydrogen recoils in an organic liquid scintillator for dark matter searches.” In: *Astroparticle Physics* 16.3 (2002), pp. 333–338. DOI: 10.1016/S0927-6505(01)00114-1.

[Hon+21] C. I. Honniball, P. G. Lucey, S. Li, et al. “Molecular water detected on the sunlit Moon by SOFIA.” In: *Nature Astronomy* 5.2 (2021). DOI: 10.1038/s41550-020-01222-x.

[Hoo+17] D. Hooper, I. Cholis, T. Linden, and K. Fang. “HAWC observations strongly favor pulsar interpretations of the cosmic-ray positron excess.” In: *Physical Review D* 96.10 (2017). DOI: 10.1103/PhysRevD.96.103013.

[Hör03] J. R. Hörandel. “On the knee in the energy spectrum of cosmic rays.” In: *Astroparticle Physics* 19.2 (2003), pp. 193–220. DOI: 10.1016/s0927-6505(02)00198-6.

[Hör04] J. R. Hörandel. “Models of the knee in the energy spectrum of cosmic rays.” In: *Astroparticle Physics* 21.3 (2004), pp. 241–265. DOI: 10.1016/j.astropartphys.2004.01.004.

[Hor+04] S. Horikawa, I. Daito, A. Gorin, et al. “Development of a scintillating-fibre detector with position-sensitive photomultipliers for high-rate experiments.” In: *Nuclear Instruments and Methods in Physics Research Section A: Accelerators, Spectrometers, Detectors and Associated Equipment* 516.1 (2004), pp. 34–49. DOI: 10.1016/j.nima.2003.07.038.

[Hor+22] F. Horst, D. Boscolo, M. Durante, et al. “Thick shielding against galactic cosmic radiation: A Monte Carlo study with focus on the role of secondary neutrons.” In: *Life Sciences in Space Research* 33 (2022), pp. 58–68. DOI: 10.1016/j.lssr.2022.03.003.

[HBS20] S. Hu, J. E. Barzilla, and E. Semones. “Acute radiation risk assessment and mitigation strategies in near future exploration spaceflights.” In: *Life Sciences in Space Research* 24 (2020), pp. 25–33. DOI: 10.1016/j.lssr.2019.10.006.

[Ing+11] A. Ingargiola, M. Assanelli, I. Rech, et al. “Avalanche Current Measurements in SPADs by Means of Hot-Carrier Luminescence.” In: *IEEE Photonics Technology Letters* 23.18 (2011), pp. 1319–1321. DOI: 10.1109/lpt.2011.2160533.

[Ito12] T. Itoh. “Fluorescence and phosphorescence from higher excited states of organic molecules.” In: *Chemical Reviews* 112.8 (2012), pp. 4541–68. DOI: 10.1021/cr200166m.

[Jab35] A. Jabłoński. “Über den Mechanismus der Photolumineszenz von Farbstoffphosphoren.” In: *Zeitschrift für Physik* 94.1-2 (1935), pp. 38–46. DOI: 10.1007/bf01330795.

[ELT19] S. El-Jaby, B. J. Lewis, and L. Tomi. “On the decision making criteria for cis-lunar reference mission scenarios.” In: *Life Sci Space Res (Amst)* 21 (2019), pp. 25–39. DOI: 10.1016/j.lssr.2019.02.008.

[JM72] J. D. Jackson and R. L. McCarthy. “z^3 Corrections to Energy Loss and Range.” In: *Physical Review B* 6.11 (1972), pp. 4131–4141. DOI: 10.1103/PhysRevB.6.4131.

[JNP87] K. W. Jacobsen, J. K. Norskov, and M. J. Puska. “Interatomic interactions in the effective-medium theory.” In: *Phys Rev B Condens Matter* 35.14 (1987), pp. 7423–7442. DOI: 10.1103/physrevb.35.7423.

[Jam+19] B. James, L. T. Tran, J. Vohradsky, et al. “SOI Thin Microdosimeter Detectors for Low-Energy Ions and Radiation Damage Studies.” In: *IEEE Transactions on Nuclear Science* 66.1 (2019), pp. 320–326. DOI: 10.1109/tns.2018.2885996.

[Jig+18] P. Jiggens, D. Heynderickx, I. Sandberg, et al. “Updated Model of the Solar Energetic Proton Environment in Space.” In: *Journal of Space Weather and Space Climate* 8 (2018). DOI: 10.1051/swsc/2018010.

[Jiv+17] H. Jivan, J. E. Mdhluli, E. Sideras-Haddad, et al. “Radiation damage effects on the optical properties of plastic scintillators.” In: *Nuclear Instruments and Methods in Physics Research Section B: Beam Interactions with Materials and Atoms* 409 (2017), pp. 224–228. DOI: 10.1016/j.nimb.2017.05.061.

[Joh19] J. A. Johnson. “Populating the periodic table: Nucleosynthesis of the elements.” In: *Science* 363.6426 (2019), pp. 474–478. DOI: 10.1126/science.aau9540.

[JFT20] J. A. Johnson, B. D. Fields, and T. A. Thompson. “The origin of the elements: a century of progress.” In: *Philosophical Transactions of the Royal Society A Mathematical, Physical and Engineering Sciences* 378.2180 (2020), p. 20190301. DOI: 10.1098/rsta.2019.0301.

[JHL15] C. Joram, G. Haefeli, and B. Leverington. “Scintillating Fibre Tracking at High Luminosity Colliders.” In: *Journal of Instrumentation* 10.08 (2015), pp. C08005–C08005. DOI: 10.1088/1748-0221/10/08/c08005.

[Kac19] M. Kachelrieß. “Transition from Galactic to Extragalactic Cosmic Rays.” In: *EPJ Web of Conferences* 210 (2019). DOI: 10.1051/epjconf/201921004003.

[KB57] H. Kallmann and G. J. Brucker. “Decay Times of Fluorescent Substances Excited by High-Energy Radiation.” In: *Physical Review* 108.5 (1957), pp. 1122–1130. DOI: 10.1103/PhysRev.108.1122.

[Kam+97] E. Kamioka, M. Hareyama, M. Ichimura, et al. “Azimuthally controlled observation of heavy cosmic-ray primaries by means of the balloon-borne emulsion chamber.” In: *Astroparticle Physics* 6.2 (1997), pp. 155–167. DOI: 10.1016/s0927-6505(96)00051-5.

[KW12] K.-H. Kampert and A. A. Watson. “Extensive air showers and ultra high-energy cosmic rays: a historical review.” In: *The European Physical Journal H* 37.3 (2012), pp. 359–412. DOI: 10.1140/epjh/e2012-30013-x.

[Kan99] T. Kaneko. “Energy-loss of swift boron and carbon clusters in solids.” In: *Nuclear Instruments and Methods in Physics Research Section B: Beam Interactions with Materials and Atoms* 153.1-4 (1999), pp. 15–20. DOI: 10.1016/s0168-583x(99)00032-4.

[Kan18] H. Kang. “Particle Acceleration at Structure Formation Shocks.” In: *Nuclear and Particle Physics Proceedings* 297-299 (2018), pp. 259–266. DOI: 10.1016/j.nuclphysbps.2018.07.036.

[Kan+23] S. Kang, Y. S. Yoon, H. Kim, et al. “The radiation hardness of 6LiI:Ag for lunar surface neutron measurement from the LVRAD experiment.” In: *Journal of the Korean Physical Society* 83.2 (2023), pp. 96–101. DOI: 10.1007/s40042-023-00846-2.

[Kap+85] J. S. Kapustinsky, R. M. DeVries, N. J. DiGiacomo, et al. “A fast timing light pulser for scintillation detectors.” In: *Nuclear Instruments and Methods in Physics Research Section A: Accelerators, Spectrometers, Detectors and Associated Equipment* 241.2-3 (1985), pp. 612–613. DOI: 10.1016/0168-9002(85)90622-9.

[Kas47] M. Kasha. “Phosphorescence and the role of the triplet state in the electronic excitation of complex molecules.” In: *Chemical Reviews* 41.2 (1947), pp. 401–19. DOI: 10.1021/cr60129a015.

[Kas50] M. Kasha. “Characterization of electronic transitions in complex molecules.” In: *Discussions of the Faraday Society* 9 (1950). DOI: 10.1039/df9500900014.

[Kau93] J. M. Kauffman. “Review of progress on scintillation fluors for the detectors of the SSC.” In: *Radiation Physics and Chemistry* 41.1-2 (1993), pp. 365–371. DOI: 10.1016/0969-806x(93)90073-4.

[Kea+97] A. J. Keane, D. O. Sullivan, A. Thompson, et al. “The charge spectrum of ultra heavy nuclei, including actinides, in the cosmic radiation.” In: *Advances in Space Research* 19.5 (1997), pp. 739–742. DOI: 10.1016/s0273-1177(96)00137-8.

[KHR92] A. M. Kellerer, K. Hahn, and H. H. Rossi. “Intermediate Dosimetric Quantities.” In: *Radiation Research* 130.1 (1992). DOI: 10.2307/3578474.

[KR90] A. M. Kellerer and H. H. Rossi. “A generalized definition of dosimetric quantities.” In: *International Journal of Radiation Biology* 57.4 (1990), pp. 859–64. DOI: 10.1080/09553009014550981.

[Ker+22] D. N. Kernagis, E. Balcer-Kubiczek, S. Bazyar, et al. “Medical countermeasures for the hematopoietic-subsyndrome of acute radiation syndrome in space.” In: *Life Sciences in Space Research* (2022). DOI: 10.1016/j.lssr.2022.06.002.

[Kha15] Y. N. Kharzheev. “Scintillation counters in modern high-energy physics experiments (Review).” In: *Physics of Particles and Nuclei* 46.4 (2015), pp. 678–728. DOI: 10.1134/s1063779615040048.

[Kha19] Y. N. Kharzheev. “Radiation Hardness of Scintillation Detectors Based on Organic Plastic Scintillators and Optical Fibers.” In: *Physics of Particles and Nuclei* 50.1 (2019), pp. 42–76. DOI: 10.1134/s1063779619010027.

[KH12] K. J. Kim and N. Hasebe. “Nuclear Planetology: Especially Concerning the Moon and Mars.” In: *Research in Astronomy and Astrophysics* 12.10 (2012), pp. 1313–1380. DOI: 10.1088/1674-4527/12/10/001.

[KC80] Y.-K. Kim and K.-t. Cheng. “Stopping power for partially stripped ions.” In: *Physical Review A* 22.1 (1980), pp. 61–67. DOI: 10.1103/PhysRevA.22.61.

[Kim+23] Y. Kim, N. Zaitseva, M. J. Ford, et al. “3D printable polyvinyltoluene-based plastic scintillators with pulse shape discrimination.” In: *Nuclear Instruments and Methods in Physics Research Section A: Accelerators, Spectrometers, Detectors and Associated Equipment* 1055 (2023). DOI: 10.1016/j.nima.2023.168537.

[KD01] J. G. Kirk and R. O. Dendy. “Shock acceleration of cosmic rays - a critical review.” In: *Journal of Physics G: Nuclear and Particle Physics* 27.7 (2001), pp. 1589–1595. DOI: 10.1088/0954-3899/27/7/316.

[Kir+04] T. Kirn, C. H. Chung, F. Dömmecke, et al. “Status of AMS-TRD-Straw modules.” In: *Nuclear Instruments and Methods in Physics Research Section A: Accelerators, Spectrometers, Detectors and Associated Equipment* 522.1-2 (2004), pp. 69–72. DOI: 10.1016/j.nima.2004.01.020.

[Kir17] T. Kirn. “SciFi – A large scintillating fibre tracker for LHCb.” In: *Nuclear Instruments and Methods in Physics Research Section A: Accelerators, Spectrometers, Detectors and Associated Equipment* 845 (2017), pp. 481–485. DOI: 10.1016/j.nima.2016.06.057.

[KWB95] P. Kliauga, A. J. Waker, and J. Barthe. “Design of Tissue-Equivalent Proportional Counters.” In: *Radiation Protection Dosimetry* 61.4 (1995), pp. 309–322. DOI: 10.1093/oxfordjournals.rpd.a082802.

[Klo+98] H. A. Klose, P. Goppelt-Langer, M. Sprenger, et al. “On the measurement of degradation and recovery of scintillating plastic fibres.” In: *Nuclear Instruments and Methods in Physics Research Section B: Beam Interactions with Materials and Atoms* 135.1-4 (1998), pp. 555–559. DOI: 10.1016/s0168-583x(97)00629-0.

[KT41] J. Knipp and E. Teller. “On the Energy Loss of Heavy Ions.” In: *Physical Review* 59.8 (1941), pp. 659–669. DOI: 10.1103/PhysRev.59.659.

[KQA60] W. J. Knox, A. R. Quinton, and C. E. Anderson. “Evaporation of Charged Particles from Highly Excited Compound Nuclei.” In: *Physical Review* 120.6 (1960), pp. 2120–2128. DOI: 10.1103/PhysRev.120.2120.

[KM59] H. W. Koch and J. W. Motz. “Bremsstrahlung Cross-Section Formulas and Related Data.” In: *Reviews of Modern Physics* 31.4 (1959), pp. 920–955. DOI: 10.1103/RevModPhys.31.920.

[KR64] Y. Koechlin and A. Raviart. “Analyse par echantillonnage sur photons individuels des liquides fluorescents dans le domaine de la sub-nanoseconde.” In: *Nuclear Instruments and Methods* 29.1 (1964), pp. 45–53. DOI: 10.1016/0029-554x(64)90008-4.

[KHG23] A. Koning, S. Hilaire, and S. Goriely. “TALYS: modeling of nuclear reactions.” In: *The European Physical Journal A* 59.6 (2023). DOI: 10.1140/epja/s10050-023-01034-3.

[Kos22] M. Koshimizu. “Recent progress of organic scintillators.” In: *Japanese Journal of Applied Physics* 62 (2022), p. 010503. DOI: 10.35848/1347-4065/ac94fe.

[KKS92] G. Kraft, M. Kramer, and M. Scholz. “LET, track structure and models. A review.” In: *Radiat Environ Biophys* 31.3 (1992), pp. 161–80. DOI: 10.1007/BF01214825.

[Kre+05] M. Kreuz, T. Soldner, S. Baeßler, et al. “A measurement of the antineutrino asymmetry B in free neutron decay.” In: *Physics Letters B* 619.3-4 (2005), pp. 263–270. DOI: 10.1016/j.physletb.2005.05.074.

[KC23] I. Krommydas and I. Cholis. “Revisiting GeV-scale annihilating dark matter with the AMS-02 positron fraction.” In: *Physical Review D* 107.2 (2023). DOI: 10.1103/PhysRevD.107.023003.

[Kro+16] B. von Krosigk, M. Chen, S. Hans, et al. “Measurement of α-particle quenching in LAB based scintillator in independent small-scale experiments.” In: *The European Physical Journal C* 76.3 (2016). DOI: 10.1140/epjc/s10052-016-3959-2.

[Kro+15] M. Kroupa, A. Bahadori, T. Campbell-Ricketts, et al. “A semiconductor radiation imaging pixel detector for space radiation dosimetry.” In: *Life Sciences in Space Research* 6 (2015), pp. 69–78. DOI: 10.1016/j.lssr.2015.06.006.

[Kro+18] M. Kroupa, A. A. Bahadori, T. Campbell-Ricketts, et al. “Kinetic energy reconstruction with a single layer particle telescope.” In: *Applied Physics Letters* 112.13 (2018). DOI: 10.1063/1.5024920.

[KM18] M. Kusakabe and G. J. Mathews. “Cosmic-Ray Nucleosynthesis of p-nuclei: Yields and Routes.” In: *The Astrophysical Journal* 854.2 (2018). DOI: 10.3847/1538-4357/aaa125.

[Kyr22] D. Kyratzis. “Overview of the HERD space mission.” In: *Physica Scripta* 97.5 (2022). DOI: 10.1088/1402-4896/ac63fc.

[LaT+16] C. La Tessa, M. Sivertz, I. H. Chiang, et al. “Overview of the NASA space radiation laboratory.” In: *Life Sciences in Space Research* 11 (2016), pp. 18–23. DOI: 10.1016/j.lssr.2016.10.002.

[Lac+93] A. L. Lacaita, F. Zappa, S. Bigliardi, and M. Manfredi. “On the bremsstrahlung origin of hot-carrier-induced photons in silicon devices.” In: *IEEE Transactions on Electron Devices* 40.3 (1993), pp. 577–582. DOI: 10.1109/16.199363.

[Lam40] W. E. Lamb. “Passage of Uranium Fission Fragments Through Matter.” In: *Physical Review* 58.8 (1940), pp. 696–702. DOI: 10.1103/PhysRev.58.696.

[Lan44] L. D. Landau. “On the Energy Loss of Fast Particles by Ionization.” In: *Journal of Physics (USSR)* 8.4 (1944), p. 201.

[Lan+22] M. E. Landis, P. O. Hayne, J.-P. Williams, et al. “Spatial Distribution and Thermal Diversity of Surface Volatile Cold Traps at the Lunar Poles.” In: *The Planetary Science Journal* 3.2 (2022). DOI: 10.3847/PSJ/ac4585.

[Lap+22] T. A. Laplace, B. L. Goldblum, J. A. Brown, et al. “Modeling ionization quenching in organic scintillators.” In: *Materials Advances* 3.14 (2022), pp. 5871–5881. DOI: 10.1039/d2ma00388k.

[LMU23] N. Larsen, A. Mishev, and I. Usoskin. “A New Open-Source Geomagnetosphere Propagation Tool (OTSO) and Its Applications.” In: *Journal of Geophysical Research: Space Physics* 128.3 (2023). DOI: 10.1029/2022ja031061.

[Las51a] N. O. Lassen. “The Total Charges of Fission Fragments in Gaseous and Solid Stopping Media.” In: *Mat Fys Medd Dan Vid Selsk* 26.5 (1951).

[Las51b] N. O. Lassen. “Total Charges of Fission Fragments as Functions of the Pressure of the Stopping Gas.” In: *Mat Fys Medd Dan Vid Selsk* 26.12 (1951).

[Lat+47] C. M. G. Lattes, H. Muirhead, G. P. S. Occhialini, and C. F. Powell. “Processes Involving Charged Mesons.” In: *Nature* 159.4047 (1947), pp. 694–697. DOI: 10.1038/159694a0.

[Lau+81] R. Laubert, S. Huldt, M. Breinig, et al. “Convoy electrons from solids in coincidence with emergent projectile charge state.” In: *Journal of Physics B: Atomic and Molecular Physics* 14.5 (1981), pp. 859–862. DOI: 10.1088/0022-3700/14/5/019.

[Lav+13] K. A. Lave, M. E. Wiedenbeck, W. R. Binns, et al. “Galactic Cosmic-Ray Energy Spectra and Composition during the 2009-2010 Solar Minimum Period.” In: *The Astrophysical Journal* 770.2 (2013). DOI: 10.1088/0004-637x/770/2/117.

[Law+14] C. C. Lawrence, M. Febbraro, T. N. Massey, et al. “Neutron response characterization for an EJ299-33 plastic scintillation detector.” In: *Nuclear Instruments and Methods in Physics Research Section A: Accelerators, Spectrometers, Detectors and Associated Equipment* 759 (2014), pp. 16–22. DOI: 10.1016/j.nima.2014.04.062.

[Law+13] D. J. Lawrence, W. C. Feldman, J. O. Goldsten, et al. “Evidence for water ice near Mercury’s north pole from MESSENGER Neutron Spectrometer measurements.” In: *Science* 339.6117 (2013), pp. 292–6. DOI: 10.1126/science.1229953.

[Lee+07] K. Lee, J. Flanders, E. Semones, et al. “Simultaneous observation of the radiation environment inside and outside the ISS.” In: *Advances in Space Research* 40.11 (2007), pp. 1558–1561. DOI: 10.1016/j.asr.2007.02.083.

[Lem+14] M. Lemelin, D. M. Blair, C. E. Roberts, et al. “High-priority lunar landing sites for in situ and sample return studies of polar volatiles.” In: *Planetary and Space Science* 101 (2014), pp. 149–161. DOI: 10.1016/j.pss.2014.07.002.

[Leu95] H. Leutz. “Scintillating fibres.” In: *Nuclear Instruments and Methods in Physics Research Section A: Accelerators, Spectrometers, Detectors and Associated Equipment* 364.3 (1995), pp. 422–448. DOI: 10.1016/0168-9002(95)00383-5.

[LK44] G. N. Lewis and M. Kasha. “Phosphorescence and the Triplet State.” In: *Journal of the American Chemical Society* 66.12 (1944), pp. 2100–2116. DOI: 10.1021/ja01240a030.

[Li+24] J. Li, P. Fan, C. Zhu, et al. “Design and performance evaluation of a compact thermal and fast neutron spectrometer.” In: *Nuclear Instruments and Methods in Physics Research Section A: Accelerators, Spectrometers, Detectors and Associated Equipment* 1063 (2024). DOI: 10.1016/j.nima.2024.169247.

[Li+18] S. Li, P. G. Lucey, R. E. Milliken, et al. “Direct evidence of surface exposed water ice in the lunar polar regions.” In: *Proceedings of the National Academy of Sciences* 115.36 (2018), pp. 8907–8912. DOI: 10.1073/pnas.1802345115. URL: https://www.ncbi.nlm.nih.gov/pubmed/30126996.

[LM17] S. Li and R. E. Milliken. "Water on the surface of the Moon as seen by the Moon Mineralogy Mapper: Distribution, abundance, and origins." In: *Science Advances* 3.9 (2017), e1701471. DOI: 10.1126/sciadv.1701471. URL: https://www.ncbi.nlm.nih.gov/pubmed/28924612.

[LH19] W. Li and M. K. Hudson. "Earth's Van Allen Radiation Belts: From Discovery to the Van Allen Probes Era." In: *Journal of Geophysical Research: Space Physics* 124.11 (2019), pp. 8319–8351. DOI: 10.1029/2018ja025940.

[LA98] A. F. Lifschitz and N. R. Arista. "Velocity-dependent screening in metals." In: *Physical Review A* 57.1 (1998), pp. 200–207. DOI: 10.1103/PhysRevA.57.200.

[LNS68] J. Lindhard, V. Nielsen, and M. Scharff. "Approximation Method in Classical Scattering by Screened Coulomb Fields (Notes on Atomic Collisions, I)." In: *Mat Fys Medd Dan Vid Selsk* 36.10 (1968).

[Lin+63] J. Lindhard, V. Nielsen, M. Scharff, and P. V. Thomsen. "Integral Equations Governing Radiation Effects (Notes on Atomic Collisions, III)." In: *Mat Fys Medd Dan Vid Selsk* 33.10 (1963).

[LS53] J. Lindhard and M. Scharff. "Energy Loss in Matter by Fast Particles of Low Charge." In: *Mat Fys Medd Dan Vid Selsk* 27.15 (1953).

[LS61] J. Lindhard and M. Scharff. "Energy Dissipation by Ions in the kev Region." In: *Physical Review* 124.1 (1961), pp. 128–130. DOI: 10.1103/PhysRev.124.128.

[LSS63] J. Lindhard, M. Scharff, and H. E. Schiøtt. "Range Concepts and Heavy Ion Ranges (Notes on Atomic Collisions, II)." In: *Mat Fys Medd Dan Vid Selsk* 33.14 (1963).

[LS96] J. Lindhard and A. H. Sorensen. "Relativistic theory of stopping for heavy ions." In: *Physical Review A* 53.4 (1996), pp. 2443–2456. DOI: 10.1103/physreva.53.2443.

[Lin76] J. Lindhard. "The Barkas effect - or Z_1^3, Z_1^4-corrections to stopping of swift charged particles." In: *Nuclear Instruments and Methods* 132 (1976), pp. 1–5. DOI: 10.1016/0029-554x(76)90702-3.

[Lin85] J. Lindhard. "On the Theory of Energy Loss Distributions for Swift Charged Particles." In: *Physica Scripta* 32.1 (1985), pp. 72–80. DOI: 10.1088/0031-8949/32/1/010.

[Lin03] G. Lindström. "Radiation damage in silicon detectors." In: *Nuclear Instruments and Methods in Physics Research Section A: Accelerators, Spectrometers, Detectors and Associated Equipment* 512.1-2 (2003), pp. 30–43. DOI: 10.1016/s0168-9002(03)01874-6.

[Lip14] P. Lipari. "Cosmic rays and hadronic interactions." In: *Comptes Rendus. Physique* 15.4 (2014), pp. 357–366. DOI: 10.1016/j.crhy.2014.02.012.

[Lip18] P. Lipari. "Spectral features in the cosmic ray fluxes." In: *Astroparticle Physics* 97 (2018), pp. 197–204. DOI: 10.1016/j.astropartphys.2017.11.008.

[LV20] P. Lipari and S. Vernetto. "The shape of the cosmic ray proton spectrum." In: *Astroparticle Physics* 120 (2020). DOI: 10.1016/j.astropartphys.2020.102441.

[Liu+22] S. Liu, H. Zeng, Y. Xin, and Y. Zhang. "The origin of galactic cosmic rays." In: *Reviews of Modern Plasma Physics* 6.1 (2022). DOI: 10.1007/s41614-022-00080-6.

[LB37] M. S. Livingston and H. A. Bethe. "Nuclear Physics C. Nuclear Dynamics, Experimental." In: *Reviews of Modern Physics* 9.3 (1937), pp. 245–390. DOI: 10.1103/RevModPhys.9.245.

[Llo+07] X. Llopart, R. Ballabriga, M. Campbell, et al. "Timepix, a 65k programmable pixel readout chip for arrival time, energy and/or photon counting measurements." In: *Nuclear Instruments and Methods in Physics Research Section A: Accelerators, Spectrometers, Detectors and Associated Equipment* 581.1-2 (2007), pp. 485–494. DOI: 10.1016/j.nima.2007.08.079.

[LoP+14] D. Lo Presti, D. L. Bonanno, F. Longhitano, et al. “Development of a Real-Time, Large Area, High Spatial Resolution Particle Tracker Based on Scintillating Fibers.” In: *Advances in High Energy Physics* 2014 (2014), pp. 1–13. DOI: 10.1155/2014/692908.

[Los+17] M. J. Losekamm, M. Milde, T. Pöschl, et al. “A new analysis method using Bragg curve spectroscopy for a Multi-purpose Active-target Particle Telescope for radiation monitoring.” In: *Nuclear Instruments and Methods in Physics Research Section A: Accelerators, Spectrometers, Detectors and Associated Equipment* 845 (2017), pp. 520–523. DOI: 10.1016/j.nima.2016.05.029.

[Los+22] M. J. Losekamm, J. Biswas, T. Chupin, et al. “Assessing the Distribution of Water Ice and Other Volatiles at the Lunar South Pole with LUVMI-X: A Mission Concept.” In: *The Planetary Science Journal* 3.10 (2022), p. 229. DOI: 10.3847/PSJ/ac8cfd.

[LPP24] M. J. Losekamm, S. Paul, and T. Pöschl. “Position-dependent light yield in short, coated SCSF-78 scintillating fibers.” In: *Radiation Measurements* 174 (2024). DOI: 10.1016/j.radmeas.2024.107116.

[LC23] Q. Luce and t. P. A. Collaboration. “The energy spectrum of cosmic rays above 6 PeV as measured at the Pierre Auger Observatory.” In: *EPJ Web of Conferences* 283 (2023). DOI: 10.1051/epjconf/202328302004.

[Luc+21] P. G. Lucey, N. Petro, D. M. Hurley, et al. “Volatile interactions with the lunar surface.” In: *Geochemistry* in press (2021). DOI: 10.1016/j.chemer.2021.125858.

[LCS21] K. M. Luchsinger, N. J. Chanover, and P. D. Strycker. “Water within a permanently shadowed lunar crater: Further LCROSS modeling and analysis.” In: *Icarus* 354 (2021). DOI: 10.1016/j.icarus.2020.114089.

[Luo+22] F. Luoni, D. Boscolo, G. Fiore, et al. “Dose Attenuation in Innovative Shielding Materials for Radiation Protection in Space: Measurements and Simulations.” In: *Radiat Res* 198.2 (2022), pp. 107–119. DOI: 10.1667/RADE-22-00147.1.

[Luo+21] F. Luoni, F. Horst, C. A. Reidel, et al. “Total nuclear reaction cross-section database for radiation protection in space and heavy-ion therapy applications.” In: *New Journal of Physics* 23.10 (2021). DOI: 10.1088/1367-2630/ac27e1.

[Lus+10] M. Luszik-Bhadra, P. Beck, T. Berger, et al. “Response calculations for silicon-based direct-reading dosimeters for use at the international space station (ISS).” In: *Radiation Measurements* 45.10 (2010), pp. 1548–1552. DOI: 10.1016/j.radmeas.2010.08.026.

[LHO23] M. Luzum, M. Hippert, and J.-Y. Ollitrault. “Methods for systematic study of nuclear structure in high-energy collisions.” In: *The European Physical Journal A* 59.5 (2023). DOI: 10.1140/epja/s10050-023-01021-8.

[Lv+24] S. Lv, F. Zhang, X. Li, et al. “Online Radiation Beam Tracking by Using Full-Inorganic Scintillating Fibers.” In: *Advanced Optical Materials* 12.10 (2024). DOI: 10.1002/adom.202302306.

[LD91] G. R. Lynch and O. I. Dahl. “Approximations to multiple Coulomb scattering.” In: *Nuclear Instruments and Methods in Physics Research Section B: Beam Interactions with Materials and Atoms* 58.1 (1991), pp. 6–10. DOI: 10.1016/0168-583x(91)95671-y.

[Ma+22] W. Ma, Y. Su, Q. Zhang, et al. “Thermally activated delayed fluorescence (TADF) organic molecules for efficient X-ray scintillation and imaging.” In: *Nature Materials* 21.2 (2022), pp. 210–216. DOI: 10.1038/s41563-021-01132-x.

[Mab+16] A. N. Mabe, A. M. Glenn, M. L. Carman, et al. “Transparent plastic scintillators for neutron detection based on lithium salicylate.” In: *Nuclear Instruments and Methods in Physics Research Section A: Accelerators, Spectrometers, Detectors and Associated Equipment* 806 (2016), pp. 80–86. DOI: 10.1016/j.nima.2015.09.111.

[Mal+19] J. Malimban, U. W. Nam, J. Pyo, et al. “Characterization of a new tissue equivalent proportional counter for dosimetry of neutron and photon fields: comparison of measurements and Monte Carlo simulations.” In: *Physics in Medicine & Biology* 64.17 (2019), 17NT02. DOI: 10.1088/1361-6560/ab2f1f.

[MCB20] I. Maliyov, J.-P. Crocombette, and F. Bruneval. “Quantitative electronic stopping power from localized basis set.” In: *Physical Review B* 101.3 (2020). DOI: 10.1103/PhysRevB.101.035136.

[Man+16] P. .-. Mangeard, D. Ruffolo, A. Sáiz, et al. “Dependence of the neutron monitor count rate and time delay distribution on the rigidity spectrum of primary cosmic rays.” In: *Journal of Geophysical Research: Space Physics* 121.12 (2016). DOI: 10.1002/2016ja023515.

[MS20] B. Manning and R. Singleterry. “Radiation engineering analysis of shielding materials to assess their ability to protect astronauts in deep space from energetic particle radiation.” In: *Acta Astronautica* 171 (2020), pp. 23–30. DOI: 10.1016/j.actaastro.2020.02.020.

[Mar+93] F. Markley, D. Woods, A. Pla-Dalmau, et al. “Development of radiation hard scintillators.” In: *Radiation Physics and Chemistry* 41.1-2 (1993), pp. 135–152. DOI: 10.1016/0969-806x(93)90050-5.

[MN62] F. W. Martin and L. C. Northcliffe. “Energy Loss and Effective Charge of He, C, and Ar Ions below 10 MeV/amu in Gases.” In: *Physical Review* 128.3 (1962), pp. 1166–1174. DOI: 10.1103/PhysRev.128.1166.

[Mas+21] T. Masuda, D. G. Ang, N. R. Hutzler, et al. “Suppression of the optical crosstalk in a multi-channel silicon photomultiplier array.” In: *Optics Express* 29.11 (2021), pp. 16914–16926. DOI: 10.1364/OE.424460.

[MP95] R. J. Mathar and M. Posselt. “Effective-charge theory for the electronic stopping of heavy ions in solids: Stripping criteria and target-electron models.” In: *Physical Review B* 51.1 (1995), pp. 107–116. DOI: 10.1103/physrevb.51.107.

[Mau+16] S. Maurice, S. M. Clegg, R. C. Wiens, et al. “ChemCam activities and discoveries during the nominal mission of the Mars Science Laboratory in Gale crater, Mars.” In: *Journal of Analytical Atomic Spectrometry* 31.4 (2016), pp. 863–889. DOI: 10.1039/c5ja00417a.

[Mau+21] S. Maurice, R. C. Wiens, P. Bernardi, et al. “The SuperCam Instrument Suite on the Mars 2020 Rover: Science Objectives and Mast-Unit Description.” In: *Space Science Reviews* 217.3 (2021). DOI: 10.1007/s11214-021-00807-w.

[Mau+15] D. Maurin, A. Cheminet, L. Derome, et al. “Neutron monitors and muon detectors for solar modulation studies: Interstellar flux, yield function, and assessment of critical parameters in count rate calculations.” In: *Advances in Space Research* 55.1 (2015), pp. 363–389. DOI: 10.1016/j.asr.2014.06.021.

[Mau+20] D. Maurin, H. Dembinski, J. Gonzalez, et al. “Cosmic-Ray Database Update: Ultra-High Energy, Ultra-Heavy, and Antinuclei Cosmic-Ray Data (CRDB v4.0).” In: *Universe* 6.8 (2020). DOI: 10.3390/universe6080102.

[MCG00] G. Maynard, M. Chabot, and D. Gardès. “Density effect and charge dependent stopping theories for heavy ions in the intermediate velocity regime.” In: *Nuclear Instruments and Methods in Physics Research Section B: Beam Interactions with Materials and Atoms* 164-165 (2000), pp. 139–146. DOI: 10.1016/s0168-583x(99)01006-x.

[May+02] G. Maynard, C. Deutsch, K. Dimitriou, et al. “Evaluation of the energy deposition profile for swift heavy ions in dense plasmas.” In: *Nuclear Instruments and Methods in Physics Research Section B: Beam Interactions with Materials and Atoms* 195.1-2 (2002), pp. 188–215. DOI: 10.1016/s0168-583x(02)01334-4.

[Maz+11] E. Mazarico, G. A. Neumann, D. E. Smith, et al. “Illumination conditions of the lunar polar regions using LOLA topography.” In: *Icarus* 211.2 (2011), pp. 1066–1081. DOI: 10.1016/j.icarus.2010.10.030.

[McG83] E. J. McGuire. “Extraction of shell corrections from Born-approximation stopping-power calculations in A1.” In: *Physical Review A* 28.1 (1983), pp. 49–52. DOI: 10.1103/PhysRevA.28.49.

[McI61] R. J. McIntyre. “Theory of Microplasma Instability in Silicon.” In: *Journal of Applied Physics* 32.6 (1961), pp. 983–995. DOI: 10.1063/1.1736199.

[McI85] R. J. McIntyre. “Recent developments in silicon avalanche photodiodes.” In: *Measurement* 3.4 (1985), pp. 146–152. DOI: 10.1016/0263-2241(85)90024-7.

[MAR71] M. Meneguzzi, J. Audouze, and H. Reeves. “The Production of Element Li, Be, B by Galactic Cosmic Rays in Space and its Relation with Stellar Observations.” In: *Astronomy & Astrophysics* 151 (1971), pp. 337–359.

[Men+23] G. Meng, H. Dai, Q. Wang, et al. “High-efficiency and stable short-delayed fluorescence emitters with hybrid long- and short-range charge-transfer excitations.” In: *Nature Communications* 14.1 (2023), p. 2394. DOI: 10.1038/s41467-023-38086-4.

[Més+19] P. Mészáros, D. B. Fox, C. Hanna, and K. Murase. “Multi-messenger astrophysics.” In: *Nature Reviews Physics* 1.10 (2019), pp. 585–599. DOI: 10.1038/s42254-019-0101-z.

[MC20] A. Meurisse and J. Carpenter. “Past, present and future rationale for space resource utilisation.” In: *Planetary and Space Science* 182 (2020). DOI: 10.1016/j.pss.2020.104853.

[Mey94] B. S. Meyer. “The r-, s-, and p-Processes in Nucleosynthesis.” In: *Annual Review of Astronomy and Astrophysics* 32.1 (1994), pp. 153–190. DOI: 10.1146/annurev.aa.32.090194.001101.

[MM94] K. Michaelian and A. Menchaca-Rocha. “Model of ion-induced luminescence based on energy deposition by secondary electrons.” In: *Physical Review B* 49.22 (1994), pp. 15550–15562. DOI: 10.1103/physrevb.49.15550.

[MMB95] K. Michaelian, A. Menchaca-Rocha, and E. Belmont-Moreno. “Scintillation response of nuclear particle detectors.” In: *Nuclear Instruments and Methods in Physics Research Section A: Accelerators, Spectrometers, Detectors and Associated Equipment* 356.2-3 (1995), pp. 297–303. DOI: 10.1016/0168-9002(94)01252-0.

[Mij22] T. Mijatović. “Multinucleon transfer reactions: a mini-review of recent advances.” In: *Frontiers in Physics* 10 (2022). DOI: 10.3389/fphy.2022.965198.

[MF92] H. H. Mikkelsen and H. Flyvbjerg. “Exact stopping cross section of the quantum harmonic oscillator for a penetrating point charge of arbitrary strength.” In: *Physical Review A* 45.5 (1992), pp. 3025–3031. DOI: 10.1103/physreva.45.3025.

[MS89] H. H. Mikkelsen and P. Sigmund. “Barkas effect in electronic stopping power: Rigorous evaluation for the harmonic oscillator.” In: *Physical Review A* 40.1 (1989), pp. 101–116. DOI: 10.1103/physreva.40.101.

[MC28] R. A. Millikan and G. H. Cameron. “The Origin of the Cosmic Rays.” In: *Physical Review* 32.4 (1928), pp. 533–557. DOI: 10.1103/PhysRev.32.533.

[MCM62] W. R. Mills, R. L. Caldwell, and I. L. Morgan. “Low Voltage He3-Filled Proportional Counter for Efficient Detection of Thermal and Epithermal Neutrons.” In: *Review of Scientific Instruments* 33.8 (1962), pp. 866–868. DOI: 10.1063/1.1717994.

[Min+21] S. Min, H. Kang, B. Seo, et al. “A Review of Nanomaterial Based Scintillators.” In: *Energies* 14.22 (2021). DOI: 10.3390/en14227701.

[Mir+15] I. A. Mironova, K. L. Aplin, F. Arnold, et al. "Energetic Particle Influence on the Earth's Atmosphere." In: *Space Science Reviews* 194.1-4 (2015), pp. 1–96. DOI: 10.1007/s11214-015-0185-4.

[Mit+22] L. Mitchell, B. Phlips, W. N. Johnson, et al. "Radiation damage assessment of SiPMs for scintillation detectors." In: *Nuclear Instruments and Methods in Physics Research Section A: Accelerators, Spectrometers, Detectors and Associated Equipment* 1040 (2022). DOI: 10.1016/j.nima.2022.167163.

[Mit+12] I. Mitrofanov, M. Litvak, A. Sanin, et al. "Testing polar spots of water-rich permafrost on the Moon: LEND observations onboard LRO." In: *Journal of Geophysical Research: Planets* 117 (2012), E00H27. DOI: 10.1029/2011JE003956.

[Mit+09] I. G. Mitrofanov, A. Bartels, Y. I. Bobrovnitsky, et al. "Lunar Exploration Neutron Detector for the NASA Lunar Reconnaissance Orbiter." In: *Space Science Reviews* 150 (2009), pp. 183–207. DOI: 10.1007/s11214-009-9608-4.

[Mol47] G. Molière. "Theorie der Streuung schneller geladener Teilchen I. Einzelstreuung am abgeschirmten Coulomb-Feld." In: *Zeitschrift für Naturforschung A* 2.3 (1947), pp. 133–145. DOI: 10.1515/zna-1947-0302.

[Mol48] G. Molière. "Theorie der Streuung schneller geladener Teilchen II Mehrfach-und Vielfachstreuung." In: *Zeitschrift für Naturforschung A* 3.2 (1948), pp. 78–97. DOI: 10.1515/zna-1948-0203.

[Møl32] C. Møller. "Zur Theorie des Durchgangs schneller Elektronen durch Materie." In: *Annalen der Physik* 406.5 (1932), pp. 531–585. DOI: 10.1002/andp.19324060506.

[Møl+97] S. P. Møller, E. Uggerhøj, H. Bluhme, et al. "Direct measurements of the stopping power for antiprotons of light and heavy targets." In: *Physical Review A* 56.4 (1997), pp. 2930–2939. DOI: 10.1103/PhysRevA.56.2930.

[MR19] S. Mollerach and E. Roulet. "A scenario for the Galactic cosmic rays between the knee and the second-knee." In: *Journal of Cosmology and Astroparticle Physics* 2019.03 (2019), pp. 017–017. DOI: 10.1088/1475-7516/2019/03/017.

[MM06] C. C. Montanari and J. E. Miraglia. "Stopping power for swift dressed ions." In: *Physical Review A* 73.2 (2006). DOI: 10.1103/PhysRevA.73.024901.

[Mon+08] C. C. Montanari, J. E. Miraglia, M. Behar, et al. "Theoretical and experimental study of energy loss of Li ions in Zn." In: *Physical Review A* 77.4 (2008). DOI: 10.1103/PhysRevA.77.042901.

[Mon+19] E. Montbarbon, Z. Zhang, A. Grabowski, et al. "The role of the secondary fluorophore in ternary plastic scintillators aiming at discriminating fast neutrons from gamma-rays." In: *Journal of Luminescence* 213 (2019), pp. 67–74. DOI: 10.1016/j.jlumin.2019.04.059.

[Mor+12] A. D. Morse, K. Altwegg, D. J. Andrews, et al. "The Rosetta campaign to detect an exosphere at Lutetia." In: *Planetary and Space Science* 66.1 (2012), pp. 165–172. DOI: 10.1016/j.pss.2012.01.003.

[Mos09] H.-G. Moser. "Silicon detector systems in high energy physics." In: *Progress in Particle and Nuclear Physics* 63.1 (2009), pp. 186–237. DOI: 10.1016/j.ppnp.2008.12.002.

[Mos+93] S. W. Moser, W. F. Harder, C. R. Hurlbut, and M. R. Kusner. "Principles and practice of plastic scintillator design." In: *Radiation Physics and Chemistry* 41.1-2 (1993), pp. 31–36. DOI: 10.1016/0969-806x(93)90039-w.

[MB79] M. Moszyński and B. Bengtson. "Status of timing with plastic scintillation detectors." In: *Nuclear Instruments and Methods* 158 (1979), pp. 1–31. DOI: 10.1016/s0029-554x(79)90170-8.

[Mot29] N. F. Mott. “The scattering of fast electrons by atomic nuclei.” In: *Proceedings of the Royal Society of London. Series A, Containing Papers of a Mathematical and Physical Character* 124.794 (1929), pp. 425–442. DOI: 10.1098/rspa.1929.0127.

[Mot30] N. F. Mott. “The collision between two electrons.” In: *Proceedings of the Royal Society of London. Series A, Containing Papers of a Mathematical and Physical Character* 126.801 (1930), pp. 259–267. DOI: 10.1098/rspa.1930.0006.

[Mot31] N. F. Mott. “On the Theory of Excitation by Collision with Heavy Particles.” In: *Mathematical Proceedings of the Cambridge Philosophical Society* 27.4 (1931), pp. 553–560. DOI: 10.1017/s0305004100009816.

[Mot32] N. F. Mott. “The polarisation of electrons by double scattering.” In: *Proceedings of the Royal Society of London. Series A, Containing Papers of a Mathematical and Physical Character* 135.827 (1932), pp. 429–458. DOI: 10.1098/rspa.1932.0044.

[MOK64] J. W. Motz, H. Olsen, and H. W. Koch. “Electron Scattering without Atomic or Nuclear Excitation.” In: *Reviews of Modern Physics* 36.4 (1964), pp. 881–928. DOI: 10.1103/RevModPhys.36.881.

[Moy54] J. E. Moyal. “Theory of ionization fluctuations.” In: *The London, Edinburgh, and Dublin Philosophical Magazine and Journal of Science* 46.374 (1954), pp. 263–280. DOI: 10.1080/14786440308521076.

[Mue+91] D. Mueller, S. P. Swordy, P. Meyer, et al. “Energy spectra and composition of primary cosmic rays.” In: *The Astrophysical Journal* 374 (1991). DOI: 10.1086/170125.

[MYG93] A. Murakami, H. Yoshinaka, and M. Goto. “Radiation hardness of plastic scintillating fiber against fast neutron and gamma -ray irradiation.” In: *IEEE Transactions on Nuclear Science* 40.4 (1993), pp. 495–499. DOI: 10.1109/23.256607.

[Mus+07] Y. Musienko, D. Renker, S. Reucroft, et al. “Radiation damage studies of multipixel Geiger-mode avalanche photodiodes.” In: *Nuclear Instruments and Methods in Physics Research Section A: Accelerators, Spectrometers, Detectors and Associated Equipment* 581.1-2 (2007), pp. 433–437. DOI: 10.1016/j.nima.2007.08.021.

[Mus09] Y. Musienko. “Advances in multipixel Geiger-mode avalanche photodiodes (silicon photomultiplies).” In: *Nuclear Instruments and Methods in Physics Research Section A: Accelerators, Spectrometers, Detectors and Associated Equipment* 598.1 (2009), pp. 213–216. DOI: 10.1016/j.nima.2008.08.031.

[Mus+95] R. Mussa, M. Onorato, N. Pastrone, et al. “Development of a cylindrical scintillating fiber tracker for experiment E835 at FNAL.” In: *Nuclear Instruments and Methods in Physics Research Section A: Accelerators, Spectrometers, Detectors and Associated Equipment* 360.1-2 (1995), pp. 13–16. DOI: 10.1016/0168-9002(94)01215-6.

[Nag+13] A. Nagamatsu, K. Murakami, K. Kitajo, et al. “Area radiation monitoring on ISS Increments 17 to 22 using PADLES in the Japanese Experiment Module Kibo.” In: *Radiation Measurements* 59 (2013), pp. 84–93. DOI: 10.1016/j.radmeas.2013.05.008.

[Nak+11] H. Nakamura, Y. Shirakawa, S. Takahashi, and H. Shimizu. “Evidence of deep-blue photon emission at high efficiency by common plastic.” In: *EPL (Europhysics Letters)* 95.2 (2011). DOI: 10.1209/0295-5075/95/22001.

[Nak+13] H. Nakamura, Y. Shirakawa, H. Kitamura, et al. “Blended polyethylene terephthalate and polyethylene naphthalate polymers for scintillation base substrates.” In: *Radiation Measurements* 59 (2013), pp. 172–175. DOI: 10.1016/j.radmeas.2013.06.006.

[Nak09] I. Nakamura. “Radiation damage of pixelated photon detector by neutron irradiation.” In: *Nuclear Instruments and Methods in Physics Research Section A: Accelerators, Spectrometers, Detectors and Associated Equipment* 610.1 (2009), pp. 110–113. DOI: 10.1016/j.nima.2009.05.086.

[Nar+17] L. Narici, T. Berger, S. Burmeister, et al. "Exploiting different active silicon detectors in the International Space Station: ALTEA and DOSTEL galactic cosmic radiation (GCR) measurements." In: *Journal of Space Weather and Space Climate* 7 (2017), A18. DOI: 10.1051/swsc/2017016.

[Nei+13] A. Neiser, J. Adamczewski-Musch, M. Hoek, et al. "TRB3: a 264 channel high precision TDC platform and its applications." In: *Journal of Instrumentation* 8.12 (2013), pp. C12043–C12043. DOI: 10.1088/1748-0221/8/12/c12043.

[Nem+21] I. B. Nemchenok, I. I. Kamnev, E. A. Shevchik, and I. A. Suslov. "Lithium-Loaded Plastic Scintillators for the Detection of Thermal Neutrons." In: *Bulletin of the Russian Academy of Sciences: Physics* 85.5 (2021), pp. 476–479. DOI: 10.3103/s1062873821050154.

[Ngu+21] L. Q. Nguyen, G. Gabella, B. L. Goldblum, et al. "Boron-loaded organic glass scintillators." In: *Nuclear Instruments and Methods in Physics Research Section A: Accelerators, Spectrometers, Detectors and Associated Equipment* 988 (2021). DOI: 10.1016/j.nima.2020.164898.

[Nik+98] H. Nikjoo, S. Uehara, W. E. Wilson, et al. "Track structure in radiation biology: theory and applications." In: *Int J Radiat Biol* 73.4 (1998), pp. 355–64. DOI: 10.1080/095530098142176.

[Nol+06] G. A. de Nolfo, I. V. Moskalenko, W. R. Binns, et al. "Observations of the Li, Be, and B isotopes and constraints on cosmic-ray propagation." In: *Advances in Space Research* 38.7 (2006), pp. 1558–1564. DOI: 10.1016/j.asr.2006.09.008.

[NKT13] K. Nomoto, C. Kobayashi, and N. Tominaga. "Nucleosynthesis in Stars and the Chemical Enrichment of Galaxies." In: *Annual Review of Astronomy and Astrophysics* 51.1 (2013), pp. 457–509. DOI: 10.1146/annurev-astro-082812-140956.

[Nor+12] J. W. Norbury, J. Miller, A. M. Adamczyk, et al. "Nuclear data for space radiation." In: *Radiation Measurements* 47.5 (2012), pp. 315–363. DOI: 10.1016/j.radmeas.2012.03.004.

[Nor60] L. C. Northcliffe. "Energy Loss and Effective Charge of Heavy Ions in Aluminum." In: *Physical Review* 120.5 (1960), pp. 1744–1757. DOI: 10.1103/PhysRev.120.1744.

[Nor63] L. C. Northcliffe. "Passage of Heavy Ions Through Matter." In: *Annual Review of Nuclear Science* 13.1 (1963), pp. 67–102. DOI: 10.1146/annurev.ns.13.120163.000435.

[Noz+96] S. Nozette, C. L. Lichtenberg, P. Spudis, et al. "The Clementine Bistatic Radar Experiment." In: *Science* 274.5292 (1996), pp. 1495–1498. DOI: 10.1126/science.274.5292.1495.

[Nyi+14] S. Nyibule, J. Tõke, E. Henry, et al. "Birks' scaling of the particle light output functions for the EJ 299-33 plastic scintillator." In: *Nuclear Instruments and Methods in Physics Research Section A: Accelerators, Spectrometers, Detectors and Associated Equipment* 768 (2014), pp. 141–145. DOI: 10.1016/j.nima.2014.09.056.

[Obe+11] A. Obermeier, M. Ave, P. Boyle, et al. "Energy Spectra of Primary and Secondary Cosmic-Ray Nuclei Measured with Tracer." In: *The Astrophysical Journal* 742.1 (2011). DOI: 10.1088/0004-637x/742/1/14.

[Oga+91] H. Ogawa, I. I. Katayama, H. Ikegami, et al. "Direct measurement of fixed-charge stopping power for 32-MeV 3He1+ in a charge-state nonequilibrium region." In: *Phys Rev B Condens Matter* 43.13 (1991), pp. 11370–11373. DOI: 10.1103/physrevb.43.11370.

[Ori+23] T. Orita, M. Uenomachi, K. Shimazoe, and H. Ikeda. "Time and Energy Resolving Time-over-Threshold ASIC for MPPC module in TOF-PET system (ToT-ASIC2)." In: *Journal of Instrumentation* 18.09 (2023). DOI: 10.1088/1748-0221/18/09/p09033.

[OD63] J. H. Ormrod and H. E. Duckworth. “Stopping Cross Sections in Carbon for Low-Energy Atoms With.” In: *Canadian Journal of Physics* 41.9 (1963), pp. 1424–1442. DOI: 10.1139/p63-142.

[Ort+20] I. Ortega Ruiz, L. Fosse, J. Franchi, et al. “The XBPF, a new multipurpose scintillating fibre monitor for the measurement of secondary beams at CERN.” In: *Nuclear Instruments and Methods in Physics Research Section A: Accelerators, Spectrometers, Detectors and Associated Equipment* 951 (2020). DOI: 10.1016/j.nima.2019.162996.

[Osi+] G. R. Osinski, C. S. Cockell, A. Pontefract, and H. M. Sapers. “The Role of Meteorite Impacts in the Origin of Life.” In: *Astrobiology* 20.9 (), pp. 1121–1149. DOI: 10.1089/ast.2019.2203.

[Osi+16] M. Osipenko, M. Ripani, G. Ricco, et al. “Response of a diamond detector sandwich to 14MeV neutrons.” In: *Nuclear Instruments and Methods in Physics Research Section A: Accelerators, Spectrometers, Detectors and Associated Equipment* 817 (2016), pp. 19–25. DOI: 10.1016/j.nima.2016.02.008.

[Owe+15] M. J. Owens, K. G. McCracken, M. Lockwood, and L. Barnard. “The heliospheric Hale cycle over the last 300 years and its implications for a “lost” late 18th century solar cycle.” In: *Journal of Space Weather and Space Climate* 5 (2015). DOI: 10.1051/swsc/2015032.

[Pac+22] L. Pacini, O. Adriani, E. Berti, et al. “The Impact of Crystal Light Yield Non-Proportionality on a Typical Calorimetric Space Experiment: Beam Test Measurements and Monte Carlo Simulations.” In: *Instruments* 6.4 (2022). DOI: 10.3390/instruments6040053.

[Pag+14] R. Pagano, S. Lombardo, F. Palumbo, et al. “Radiation hardness of silicon photomultipliers under 60Co γ-ray irradiation.” In: *Nuclear Instruments and Methods in Physics Research Section A: Accelerators, Spectrometers, Detectors and Associated Equipment* 767 (2014), pp. 347–352. DOI: 10.1016/j.nima.2014.08.028.

[Pai+10] D. A. Paige, M. A. Siegler, J. A. Zhang, et al. “Diviner Lunar Radiometer observations of cold traps in the Moon’s south polar region.” In: *Science* 330.6003 (2010), pp. 479–82. DOI: 10.1126/science.1187726.

[Pak+18] S. Pak, Y. Shin, J. Woo, and J. Seon. “A Numerical Method to Analyze Geometric Factors of a Space Particle Detector Relative to Omnidirectional Proton and Electron Fluxes.” In: *Journal of the Korean Astronomical Society* 51.4 (2018), pp. 111–117. DOI: 10.5303/JKAS.2018.51.4.111.

[Pal+23] R. Pal Chowdhury, L. A. Stegeman, M. L. Lund, et al. “Hybrid methods of radiation shielding against deep-space radiation.” In: *Life Sci Space Res (Amst)* 38 (2023), pp. 67–78. DOI: 10.1016/j.lssr.2023.04.004.

[Pan+09] A. D. Panov, J. H. Adams, H. S. Ahn, et al. “Energy spectra of abundant nuclei of primary cosmic rays from the data of ATIC-2 experiment: Final results.” In: *Bulletin of the Russian Academy of Sciences: Physics* 73.5 (2009), pp. 564–567. DOI: 10.3103/s1062873809050098.

[PLL08] Z. Papandreou, B. D. Leverington, and G. J. Lolos. “Spectral response of scintillating fibers.” In: *Nuclear Instruments and Methods in Physics Research Section A: Accelerators, Spectrometers, Detectors and Associated Equipment* 596.3 (2008), pp. 338–346. DOI: 10.1016/j.nima.2008.08.136.

[Par+18] V. K. Parihar, M. Maroso, A. Syage, et al. “Persistent nature of alterations in cognition and neuronal circuit excitability after exposure to simulated cosmic radiation in mice.” In: *Experimental Neurology* 305 (2018), pp. 44–55. DOI: 10.1016/j.expneurol.2018.03.009.

[Par+15] V. K. Parihar, B. Allen, K. K. Tran, et al. “What happens to your brain on the way to Mars.” In: *Science Advances* 1 (2015), e1400256. DOI: 10.1126/sciadv.1400256.

[PMS11] C. H. Park, J. H. Moon, and B. K. Seo. “Development of a scintillating fiber-optic sensor for the radioactive contamination measurement in a narrow area.” In: *Radiation Measurements* 46.8 (2011), pp. 687–693. DOI: 10.1016/j.radmeas.2011.06.003.

[Par+14] J. M. Park, H. J. Kim, Y. S. Hwang, et al. “Scintillation properties of quantum-dot doped styrene based plastic scintillators.” In: *Journal of Luminescence* 146 (2014), pp. 157–161. DOI: 10.1016/j.jlumin.2013.09.051.

[Par58] E. N. Parker. “Cosmic-Ray Modulation by Solar Wind.” In: *Physical Review* 110.6 (1958), pp. 1445–1449. DOI: 10.1103/PhysRev.110.1445.

[Par20] A. M. Parsons. “Review of nuclear techniques for planetary science.” In: *International Journal of Modern Physics: Conference Series* 50 (2020). DOI: 10.1142/s2010194520600046.

[PŠ17] R. Pasechnik and M. Šumbera. “Phenomenological Review on Quark–Gluon Plasma: Concepts vs. Observations.” In: *Universe* 3.1 (2017). DOI: 10.3390/universe3010007.

[PD16] F. J. Pavón-Carrasco and A. De Santis. “The South Atlantic Anomaly: The Key for a Possible Geomagnetic Reversal.” In: *Frontiers in Earth Science* 4 (2016). DOI: 10.3389/feart.2016.00040.

[Pej15] M. M. Pejovic. “Dose response, radiation sensitivity and signal fading of p-channel MOSFETs (RADFETs) irradiated up to 50 Gy with (6)(0)Co.” In: *Applied Radiation and Isotopes* 104 (2015), pp. 100–5. DOI: 10.1016/j.apradiso.2015.06.024.

[PBL16] P. N. Peplowski, A. W. Beck, and D. J. Lawrence. “Geochemistry of the lunar highlands as revealed by measurements of thermal neutrons.” In: *Journal of Geophysical Research: Planets* 121 (2016), pp. 388–401. DOI: 10.1002/2015JE004950.

[Per18] L. Peralta. “Temperature dependence of plastic scintillators.” In: *Nuclear Instruments and Methods in Physics Research Section A: Accelerators, Spectrometers, Detectors and Associated Equipment* 883 (2018), pp. 20–23. DOI: 10.1016/j.nima.2017.11.041.

[PB10] D. Perez-Nunez and L. A. Braby. “Effect of wall thickness on measurement of dose for high energy neutrons.” In: *Health Physics* 98.1 (2010), pp. 37–41. DOI: 10.1097/HP.0b013e3181b8d032.

[Per+22] S. Perri, A. Bykov, H. Fahr, et al. “Recent Developments in Particle Acceleration at Shocks: Theory and Observations.” In: *Space Science Reviews* 218.4 (2022). DOI: 10.1007/s11214-022-00892-5.

[Pet61] B. Peters. “Primary cosmic radiation and extensive air showers.” In: *Il Nuovo Cimento* 22.4 (1961), pp. 800–819. DOI: 10.1007/bf02783106.

[PG19] C. Piemonte and A. Gola. “Overview on the main parameters and technology of modern Silicon Photomultipliers.” In: *Nuclear Instruments and Methods in Physics Research Section A: Accelerators, Spectrometers, Detectors and Associated Equipment* 926 (2019), pp. 2–15. DOI: 10.1016/j.nima.2018.11.119.

[Pie+96] D. A. Pierce, Y. Shimizu, D. L. Preston, et al. “Studies of the Mortality of Atomic Bomb Survivors. Report 12, Part I. Cancer: 1950-1990.” In: *Radiation Research* 146.1 (1996). DOI: 10.2307/3579391.

[Pie+09] C. M. Pieters, J. N. Goswami, R. N. Clark, et al. “Character and Spatial Distribution of OH/H2O on the Surface of the Moon Seen by M3 on Chandrayaan-1.” In: *Science* 326 (2009), pp. 568–572. DOI: 10.1126/science.1178658.

[Pin+24] P. Pinczés, A. Hirn, I. Apáthy, et al. “Automatic measurements with the Pille-ISS thermoluminescent dosimeter system on board the International Space Station (2003–2021).” In: *Life Sciences in Space Research* 41 (2024), pp. 52–55. DOI: 10.1016/j.lssr.2024.01.007.

[PP20] L. S. Pinsky and S. Pospisil. “Timepix-based detectors in mixed-field charged-particle radiation dosimetry applications.” In: *Radiation Measurements* 138 (2020). DOI: 10.1016/j.radmeas.2019.106229.

[Pla65] D. J. Plazek. “Temperature Dependence of the Viscoelastic Behavior of Polystyrene.” In: *The Journal of Physical Chemistry* 69.10 (1965), pp. 3480–3487. DOI: 10.1021/j100894a039.

[Plo+23] P. Plotko, A. van Vliet, X. Rodrigues, and W. Winter. “Differences between the Pierre Auger Observatory and Telescope Array Spectra: Systematic Effects or Indication of a Local Source of Ultra-high-energy Cosmic Rays?” In: *The Astrophysical Journal* 953.2 (2023). DOI: 10.3847/1538-4357/acdf59.

[Poi+14] T. Poikela, J. Plosila, T. Westerlund, et al. “Timepix3: a 65K channel hybrid pixel readout chip with simultaneous ToA/ToT and sparse readout.” In: *Journal of Instrumentation* 9.05 (2014), pp. C05013–C05013. DOI: 10.1088/1748-0221/9/05/c05013.

[Por87] L. E. Porter. “Variations of Projectile Effective Charge in Analyses of Stopping Powers for Heavy Ions.” In: *Radiation Research* 110.1 (1987). DOI: 10.2307/3576880.

[Pös+21] T. Pöschl, D. Greenwald, M. J. Losekamm, and S. Paul. “Measurement of ionization quenching in plastic scintillators.” In: *Nuclear Instruments and Methods in Physics Research Section A: Accelerators, Spectrometers, Detectors and Associated Equipment* 988 (2021), p. 164865. DOI: 10.1016/j.nima.2020.164865.

[Pos+13] M. J. Poston, G. A. Grieves, A. B. Aleksandrov, et al. “Water interactions with micronized lunar surrogates JSC-1A and albite under ultra-high vacuum with application to lunar observations.” In: *Journal of Geophysical Research: Planets* 118.1 (2013), pp. 105–115. DOI: 10.1029/2012je004283.

[Pot13] M. Potgieter. “Solar Modulation of Cosmic Rays.” In: *Living Reviews in Solar Physics* 10 (2013). DOI: 10.12942/lrsp-2013-3.

[PCL23] S. Pourashraf, J. W. Cates, and C. S. Levin. “A Scalable Dynamic TOT Circuit for a 100 ps TOF-PET Detector Design to Improve Energy Linearity and Dynamic Range.” In: *IEEE Transactions on Radiation and Plasma Medical Sciences* (2023), pp. 1–1. DOI: 10.1109/trpms.2023.3344399.

[Pra+77] R. H. Pratt, H. K. Tseng, C. M. Lee, et al. “Bremsstrahlung energy spectra from electrons of kinetic energy $1\,\mathrm{keV} \leq T_1 \leq 2000\,\mathrm{keV}$ incident on neutral atoms $2 \leq Z \leq 92$.” In: *Atomic Data and Nuclear Data Tables* 20.2 (1977), pp. 175–209. DOI: 10.1016/0092-640x(77)90045-6.

[Pre+15] P. Prem, N. A. Artemieva, D. B. Goldstein, et al. “Transport of water in a transient impact-generated lunar atmosphere.” In: *Icarus* 255 (2015), pp. 148–158. DOI: 10.1016/j.icarus.2014.10.017.

[Pre+20] P. Prem, D. M. Hurley, D. B. Goldstein, and P. L. Varghese. “The Evolution of a Spacecraft-Generated Lunar Exosphere.” In: *Journal of Geophysical Research: Planets* 125.8 (2020). DOI: 10.1029/2020je006464.

[Pre+11] T. H. Prettyman, W. C. Feldman, H. Y. McSween, et al. “Dawn’s Gamma Ray and Neutron Detector.” In: *Space Science Reviews* 163.1-4 (2011), pp. 371–459. DOI: 10.1007/s11214-011-9862-0.

[Pri50] R. W. Pringle. “The scintillation counter.” In: *Nature* 166.4209 (1950), pp. 11–4. DOI: 10.1038/166011a0.

[Pro+14] V. V. Prosin, S. F. Berezhnev, N. M. Budnev, et al. “Tunka-133: Results of 3 year operation.” In: *Nuclear Instruments and Methods in Physics Research Section A: Accelerators, Spectrometers, Detectors and Associated Equipment* 756 (2014), pp. 94–101. DOI: 10.1016/j.nima.2013.09.018.

[Pug+14] M. Pugliese, F. Loffredo, M. Quarto, et al. "Results of nDOSE and HiDOSE Experiments for Dosimetric Evaluation During STS-134 Mission." In: *Microgravity Science and Technology* 25.6 (2014), pp. 353–358. DOI: 10.1007/s12217-014-9363-3.

[Qia+13] Y. Qiang, C. Zorn, F. Barbosa, and E. Smith. "Radiation hardness tests of SiPMs for the JLab Hall D Barrel calorimeter." In: *Nuclear Instruments and Methods in Physics Research Section A: Accelerators, Spectrometers, Detectors and Associated Equipment* 698 (2013), pp. 234–241. DOI: 10.1016/j.nima.2012.10.015.

[Qu+14] W. W. Qu, G. L. Zhang, H. Q. Zhang, and R. Wolski. "Comparative studies of Coulomb barrier heights for nuclear models applied to sub-barrier fusion." In: *Physical Review C* 90.6 (2014). DOI: 10.1103/PhysRevC.90.064603.

[Rea15] D. V. Reames. "What Are the Sources of Solar Energetic Particles? Element Abundances and Source Plasma Temperatures." In: *Space Science Reviews* 194.1-4 (2015), pp. 303–327. DOI: 10.1007/s11214-015-0210-7.

[Rea18] D. V. Reames. "Abundances, Ionization States, Temperatures, and FIP in Solar Energetic Particles." In: *Space Science Reviews* 214.3 (2018). DOI: 10.1007/s11214-018-0495-4.

[Rea19] D. V. Reames. "Hydrogen and the Abundances of Elements in Gradual Solar Energetic-Particle Events." In: *Solar Physics* 294.6 (2019). DOI: 10.1007/s11207-019-1460-4.

[Reb+99] P. Rebourgeard, F. Rondeaux, J. P. Baton, et al. "Fabrication and measurements of plastic scintillating fibers." In: *Nuclear Instruments and Methods in Physics Research Section A: Accelerators, Spectrometers, Detectors and Associated Equipment* 427.3 (1999), pp. 543–567. DOI: 10.1016/s0168-9002(99)00053-4.

[Rei+21] P. Reiss, T. Warren, E. Sefton-Nash, and R. Trautner. "Dynamics of Subsurface Migration of Water on the Moon." In: *Journal of Geophysical Research: Planets* 126.5 (2021). DOI: 10.1029/2020je006742.

[Rei01] G. Reitz. "Neutron dosimetric measurements in shuttle and MIR." In: *Radiation Measurements* 33.3 (2001), pp. 341–6. DOI: 10.1016/s1350-4487(00)00153-0.

[Rei93] G. Reitz. "Radiation Environment in the Stratosphere." In: *Radiation Protection Dosimetry* 48.1 (1993), pp. 5–20. DOI: 10.1093/oxfordjournals.rpd.a081837.

[Rei+09] G. Reitz, T. Berger, P. Bilski, et al. "Astronaut's Organ Doses Inferred from Measurements in a Human Phantom Outside the International Space Station." In: *Radiation Research* 171 (2009), pp. 225–235. DOI: 10.1667/RR1559.1.

[RBM12] G. Reitz, T. Berger, and D. Matthiae. "Radiation exposure in the moon environment." In: *Planetary and Space Science* 74 (2012), pp. 78–83. DOI: 10.1016/j.pss.2012.07.014.

[RL09] D. Renker and E. Lorenz. "Advances in solid state photon detectors." In: *Journal of Instrumentation* 4 (2009), P04004. DOI: 10.1088/1748-0221/4/04/P04004.

[Ren06] D. Renker. "Geiger-mode avalanche photodiodes, history, properties and problems." In: *Nuclear Instruments and Methods in Physics Research Section A: Accelerators, Spectrometers, Detectors and Associated Equipment* 567.1 (2006), pp. 48–56. DOI: 10.1016/j.nima.2006.05.060.

[Res+95] D. Ress, R. A. Lerche, R. J. Ellis, et al. "High-sensitivity scintillating-fiber imaging detector for high-energy neutrons." In: *Review of Scientific Instruments* 66.10 (1995), pp. 4943–4948. DOI: 10.1063/1.1146179.

[Rey60] G. T. Reynolds. "Present Status of Scintillation Chambers." In: *IRE Transactions on Nuclear Science* 7.2/3 (1960), pp. 115–120. DOI: 10.1109/tns2.1960.4315748.

[RC57] G. T. Reynolds and P. E. Condon. "Filament Scintillation Counter." In: *Review of Scientific Instruments* 28.12 (1957), pp. 1098–1099. DOI: 10.1063/1.1715822.

[RSZ53] H. L. Reynolds, D. W. Scott, and A. Zucker. “Nuclear Reactions with Energetic Nitrogen Ions.” In: *Proceedings of the National Academy of Sciences of the United States of America* 39.9 (1953), pp. 975–85. DOI: 10.1073/pnas.39.9.975.

[RB11] J. D. Richardson and L. F. Burlaga. “The Solar Wind in the Outer Heliosphere and Heliosheath.” In: *Space Science Reviews* 176.1-4 (2011), pp. 217–235. DOI: 10.1007/s11214-011-9825-5.

[Ric+22] J. D. Richardson, L. F. Burlaga, H. Elliott, et al. “Observations of the Outer Heliosphere, Heliosheath, and Interstellar Medium.” In: *Space Science Reviews* 218.4 (2022), p. 35. DOI: 10.1007/s11214-022-00899-y.

[Rie96] J. Rieger. “The glass transition temperature of polystyrene.” In: *Journal of Thermal Analysis* 46.3-4 (1996), pp. 965–972. DOI: 10.1007/bf01983614.

[Rik+20] R. Rikhi, G. Samra, M. Arustamyan, et al. “Radiation induced cardiovascular disease: An odyssey of bedside-bench-bedside approach.” In: *Life Sciences in Space Research* 27 (2020), pp. 49–55. DOI: 10.1016/j.lssr.2020.07.005.

[Rip+20] J. .-. Ripoll, S. G. Claudepierre, A. Y. Ukhorskiy, et al. “Particle Dynamics in the Earth’s Radiation Belts: Review of Current Research and Open Questions.” In: *Journal of Geophysical Research: Space Physics* 125.5 (2020). DOI: 10.1029/2019ja026735.

[Ris+22] G. S. Ristic, S. D. Ilic, M. S. Andjelkovic, et al. “Sensitivity and fading of irradiated RADFETs with different gate voltages.” In: *Nuclear Instruments and Methods in Physics Research Section A: Accelerators, Spectrometers, Detectors and Associated Equipment* 1029 (2022). DOI: 10.1016/j.nima.2022.166473.

[Rit+14] B. Ritter, K. Maršálek, T. Berger, et al. “A small active dosimeter for applications in space.” In: *Nuclear Instruments and Methods in Physics Research Section A: Accelerators, Spectrometers, Detectors and Associated Equipment* 748 (2014), pp. 61–69. DOI: 10.1016/j.nima.2014.02.030.

[Rob+10] M. S. Robinson, S. M. Brylow, M. Tschimmel, et al. “Lunar Reconnaissance Orbiter Camera (LROC) Instrument Overview.” In: *Space Science Reviews* 150.1-4 (2010), pp. 81–124. DOI: 10.1007/s11214-010-9634-2.

[RB47] G. D. Rochester and C. C. Butler. “Evidence for the existence of new unstable elementary particles.” In: *Nature* 160.4077 (1947), pp. 855–7. DOI: 10.1038/160855a0.

[Rol07] C. Rolfs. “Nuclear reactions in stars far below the Coulomb barrier.” In: *Progress in Particle and Nuclear Physics* 59.1 (2007), pp. 43–50. DOI: 10.1016/j.ppnp.2006.12.017.

[Rol+08] E. Rollinde, D. Maurin, E. Vangioni, et al. “Cosmic Ray Production of Beryllium and Boron at High Redshift.” In: *The Astrophysical Journal* 673.2 (2008), pp. 676–685. DOI: 10.1086/524931.

[RWH64] M. L. Roush, M. A. Wilson, and W. F. Hornyak. “Pulse shape discrimination.” In: *Nuclear Instruments and Methods* 31.1 (1964), pp. 112–124. DOI: 10.1016/0029-554x(64)90333-7.

[Ruc96] R. C. Ruchti. “The Use of Scintillating Fibers for Charged-Particle Tracking.” In: *Annual Review of Nuclear and Particle Science* 46.1 (1996), pp. 281–319. DOI: 10.1146/annurev.nucl.46.1.281.

[Rut11] E. Rutherford. “The scattering of α and β particles by matter and the structure of the atom.” In: *The London, Edinburgh, and Dublin Philosophical Magazine and Journal of Science* 21.125 (1911), pp. 669–688. DOI: 10.1080/14786440508637080.

[Rut24] E. Rutherford. "The capture and loss of electrons by α particles." In: *The London, Edinburgh, and Dublin Philosophical Magazine and Journal of Science* 47.278 (1924), pp. 277–303. DOI: 10.1080/14786442408634367.

[Sab24] M. S. Sabra. "Validation of nuclear physics models for the fragmentation of 16O + Al at beam energies from 290A to 1000A MeV." In: *Nuclear Instruments and Methods in Physics Research Section A: Accelerators, Spectrometers, Detectors and Associated Equipment* 1058 (2024). DOI: 10.1016/j.nima.2023.168815.

[Sai+22] M. Saifulin, P. Boutachkov, E. Gorokhova, et al. "Ionoluminescence and optical transmission investigation of ZnO(In) fast ceramic scintillator irradiated with swift heavy ions." In: *Journal of Applied Physics* 132.19 (2022). DOI: 10.1063/5.0110205.

[Sai+08] Y. Saito, S. Yokota, T. Tanaka, et al. "Solar wind proton reflection at the lunar surface: Low energy ion measurement by MAP-PACE onboard SELENE (KAGUYA)." In: *Geophysical Research Letters* 35 (2008), p. L24205. DOI: 10.1029/2008GL036077.

[SK05] V. N. Salimgareeva and S. V. Kolesov. "Plastic Scintillators Based on Polymethyl Methacrylate: A Review." In: *Instruments and Experimental Techniques* 48.3 (2005), pp. 273–282. DOI: 10.1007/s10786-005-0052-8.

[Sal+89] M. Salomon, V. Li, G. Smith, and Y. S. Wu. "Fast tracking detector with fiber scintillators and a position sensitive photomultiplier." In: *IEEE Transactions on Nuclear Science* 36.1 (1989), pp. 94–97. DOI: 10.1109/23.34409.

[Sán+09] S. Sánchez Majos, P. Achenbach, C. Ayerbe Gayoso, et al. "Noise and radiation damage in silicon photomultipliers exposed to electromagnetic and hadronic radiation." In: *Nuclear Instruments and Methods in Physics Research Section A: Accelerators, Spectrometers, Detectors and Associated Equipment* 602.2 (2009), pp. 506–510. DOI: 10.1016/j.nima.2009.01.176.

[SUC19] A. E. Sand, R. Ullah, and A. A. Correa. "Heavy ion ranges from first-principles electron dynamics." In: *npj Computational Materials* 5.1 (2019). DOI: 10.1038/s41524-019-0180-5.

[San+24] A. Sanmukh, S. Gómez, A. Comerma, et al. "Low-power SiPM readout BETA ASIC for space applications." In: *Nuclear Science and Techniques* 35.3 (2024). DOI: 10.1007/s41365-024-01419-z.

[Sch21] D. R. Schaart. "Physics and technology of time-of-flight PET detectors." In: *Physics in Medicine & Biology* 66.9 (2021). DOI: 10.1088/1361-6560/abee56.

[Sch+19] S. Schael, A. Atanasyan, J. Berdugo, et al. "AMS-100: The Next Generation Magnetic Spectrometer in Space - An International Science Platform for Physics and Astrophysics at Lagrange Point 2." In: *Nuclear Instruments and Methods in Physics Research A* 944 (2019). DOI: 10.1016/j.nima.2019.162561.

[SG98a] C. Scheidenberger and H. Geissel. "Penetration of relativistic heavy ions through matter." In: *Nuclear Instruments and Methods in Physics Research Section B: Beam Interactions with Materials and Atoms* 135.1-4 (1998), pp. 25–34. DOI: 10.1016/s0168-583x(97)00639-3.

[Sch+94] C. Scheidenberger, H. Geissel, H. H. Mikkelsen, et al. "Direct observation of systematic deviations from the Bethe stopping theory for relativistic heavy ions." In: *Physical Review Letters* 73.1 (1994), pp. 50–53. DOI: 10.1103/PhysRevLett.73.50.

[Sch+96] C. Scheidenberger, H. Geissel, H. H. Mikkelsen, et al. "Energy-Loss-Straggling Experiments with Relativistic Heavy Ions in Solids." In: *Physical Review Letters* 77.19 (1996), pp. 3987–3990. DOI: 10.1103/PhysRevLett.77.3987.

[Sch51] L. I. Schiff. "Energy-Angle Distribution of Thin Target Bremsstrahlung." In: *Physical Review* 83.2 (1951), pp. 252–253. DOI: 10.1103/PhysRev.83.252.

[SS19] A. Schinner and P. Sigmund. “Expanded PASS stopping code.” In: *Nuclear Instruments and Methods in Physics Research Section B: Beam Interactions with Materials and Atoms* 460 (2019), pp. 19–26. DOI: 10.1016/j.nimb.2018.10.047.

[SKC15] A. Schleife, Y. Kanai, and A. A. Correa. “Accurate atomistic first-principles calculations of electronic stopping.” In: *Physical Review B* 91.1 (2015). DOI: 10.1103/PhysRevB.91.014306.

[Sch+22] W. Schmailzl, C. Piemonte, S. Schelhase, and W. Hansch. “Characterization of the photo-detection efficiency temperature dependence of silicon photomultipliers from -30°C to 70°C.” In: *Journal of Instrumentation* 17.12 (2022). DOI: 10.1088/1748-0221/17/12/p12009.

[Sch+14] F. R. Schneider, T. R. Ganka, G. Şeker, et al. “Characterization of blue sensitive $3\times3\mathrm{mm}^2$ SiPMs and their use in PET.” In: *Journal of Instrumentation* 9.07 (2014), P07027–P07027. DOI: 10.1088/1748-0221/9/07/p07027.

[Sch+16] N. Schwadron, J. Wilson, M. Looper, et al. “Signatures of volatiles in the lunar proton albedo.” In: *Icarus* 273 (2016), pp. 25–35. DOI: 10.1016/j.icarus.2015.12.003.

[Sco63] W. T. Scott. “The Theory of Small-Angle Multiple Scattering of Fast Charged Particles.” In: *Reviews of Modern Physics* 35.2 (1963), pp. 231–313. DOI: 10.1103/RevModPhys.35.231.

[SHK13] R. S. Selesnick, M. K. Hudson, and B. T. Kress. “Direct observation of the CRAND proton radiation belt source.” In: *Journal of Geophysical Research: Space Physics* 118.12 (2013), pp. 7532–7537. DOI: 10.1002/2013ja019338.

[Sel85] I. A. Sellin. “Convoy electron production by heavy ions in solids.” In: *Nuclear Instruments and Methods in Physics Research Section B: Beam Interactions with Materials and Atoms* 10-11 (1985), pp. 156–160. DOI: 10.1016/0168-583x(85)90224-1.

[SB84] S. M. Seltzer and M. J. Berger. “Improved procedure for calculating the collision stopping power of elements and compounds for electrons and positrons.” In: *The International Journal of Applied Radiation and Isotopes* 35.7 (1984), pp. 665–676. DOI: 10.1016/0020-708x(84)90113-3.

[SB85] S. M. Seltzer and M. J. Berger. “Bremsstrahlung spectra from electron interactions with screened atomic nuclei and orbital electrons.” In: *Nuclear Instruments and Methods in Physics Research Section B: Beam Interactions with Materials and Atoms* 12.1 (1985), pp. 95–134. DOI: 10.1016/0168-583x(85)90707-4.

[Sem+10] J. Semkova, R. Koleva, S. Maltchev, et al. “Radiation measurements inside a human phantom aboard the International Space Station using Liulin-5 charged particle telescope.” In: *Advances in Space Research* 45 (2010), pp. 858–865. DOI: 10.1016/j.asr.2009.08.027.

[Sem+14] J. Semkova, T. Dachev, R. Koleva, et al. “Observation of radiation environment in the International Space Station in 2012–March 2013 by Liulin-5 particle telescope.” In: *Journal of Space Weather and Space Climate* 4 (2014), A32. DOI: 10.1051/swsc/2014029.

[Seo+94] E. S. Seo, F. B. McDonald, N. Lal, and W. R. Webber. “Study of cosmic-ray H and He isotopes at 23 AU.” In: *The Astrophysical Journal* 432 (1994). DOI: 10.1086/174604.

[Seo+23] W. .-. Seol, C. .-. Lee, J. Seon, et al. “Estimation of Geometric Factors for the Particle Detecting Instruments of the Geostationary Satellite GK2A at 128.2°E Longitude Based on Observations of the Outer Radiation Belt During Geomagnetically Quiet Periods.” In: *Space Weather* 21.1 (2023). DOI: 10.1029/2022sw003265.

[Šer+22] L. Šerkšnytė, S. Königstorfer, P. von Doetinchem, et al. "Reevaluation of the cosmic antideuteron flux from cosmic-ray interactions and from exotic sources." In: *Physical Review D* 105.8 (2022). DOI: 10.1103/PhysRevD.105.083021.

[SSG87] M. A. Shea, D. F. Smart, and L. C. Gentile. "Estimating cosmic ray vertical cutoff rigidities as a function of the McIlwain -parameter for different epochs of the geomagnetic field." In: *Physics of the Earth and Planetary Interiors* 48.3-4 (1987), pp. 200–205. DOI: 10.1016/0031-9201(87)90145-2.

[She+18] W. Shen, T. Harion, H. Chen, et al. "A Silicon Photomultiplier Readout ASIC for Time-of-Flight Applications Using a New Time-of-Recovery Method." In: *IEEE Transactions on Nuclear Science* 65.5 (2018), pp. 1196–1202. DOI: 10.1109/tns.2018.2821769.

[She+89] W.-q. Shen, B. Wang, J. Feng, et al. "Total reaction cross section for heavy-ion collisions and its relation to the neutron excess degree of freedom." In: *Nuclear Physics A* 491.1 (1989), pp. 130–146. DOI: 10.1016/0375-9474(89)90209-1.

[Shi+12] K. Shimazoe, H. Takahashi, S. Boxuan, et al. "Dynamic Time Over Threshold Method." In: *IEEE Transactions on Nuclear Science* 59.6 (2012), pp. 3213–3217. DOI: 10.1109/tns.2012.2215338.

[Shi+14] K. Shimazoe, H. Takahashi, K. Kamada, et al. "Development of a prototype of time-over-threshold based small animal PET scanner." In: *Nuclear Instruments and Methods in Physics Research Section A: Accelerators, Spectrometers, Detectors and Associated Equipment* 753 (2014), pp. 84–90. DOI: 10.1016/j.nima.2014.04.008.

[Shu+67] P. Shulek, B. M. Golovin, L. A. Kulyukina, et al. "Fluctuations of Ionization Losses." In: *Soviet Journal of Nuclear Physics* 4 (1967), p. 400.

[Sig94] P. Sigmund. "Analysis of charge-dependent stopping of swift ions." In: *Phys Rev A* 50.4 (1994), pp. 3197–3201. DOI: 10.1103/physreva.50.3197.

[Sig96] P. Sigmund. "Low-speed limit of Bohr's stopping-power formula." In: *Physical Review A* 54.4 (1996), pp. 3113–3117. DOI: 10.1103/physreva.54.3113.

[SG98b] P. Sigmund and L. Glazov. "Energy loss and charge exchange: Statistics and atomistics." In: *Nuclear Instruments and Methods in Physics Research Section B: Beam Interactions with Materials and Atoms* 136-138 (1998), pp. 47–54. DOI: 10.1016/s0168-583x(97)00858-6.

[SG03] P. Sigmund and L. G. Glazov. "Interplay of charge exchange and projectile excitation in the stopping of swift heavy ions." In: *The European Physical Journal D - Atomic, Molecular and Optical Physics* 23.2 (2003), pp. 211–215. DOI: 10.1140/epjd/e2003-00048-2.

[SOS11] P. Sigmund, O. Osmani, and A. Schinner. "Charge-exchange straggling in equilibrium." In: *Nuclear Instruments and Methods in Physics Research Section B: Beam Interactions with Materials and Atoms* 269.9 (2011), pp. 804–809. DOI: 10.1016/j.nimb.2010.11.094.

[SS00] P. Sigmund and A. Schinner. "Binary stopping theory for swift heavy ions." In: *The European Physical Journal D* 12.3 (2000), pp. 425–434. DOI: 10.1007/s100530070004.

[SS01a] P. Sigmund and A. Schinner. "Binary theory of antiproton stopping." In: *The European Physical Journal D* 15.2 (2001), pp. 165–172. DOI: 10.1007/s100530170162.

[SS03a] P. Sigmund and A. Schinner. "Barkas effect, shell correction, screening and correlation in collisional energy-loss straggling of an ion beam." In: *The European Physical Journal D - Atomic, Molecular and Optical Physics* 23.2 (2003), pp. 201–209. DOI: 10.1140/epjd/e2003-00032-x.

[SS10] P. Sigmund and A. Schinner. "Impact-parameter-dependent stopping of swift ions." In: *The European Physical Journal D* 58.1 (2010), pp. 105–116. DOI: 10.1140/epjd/e2010-00043-6.

[SS15a] P. Sigmund and A. Schinner. “Velocity dependence of heavy-ion stopping below the maximum.” In: *Nuclear Instruments and Methods in Physics Research Section B: Beam Interactions with Materials and Atoms* 342 (2015), pp. 292–299. DOI: 10.1016/j.nimb.2014.10.020.

[SS16] P. Sigmund and A. Schinner. “Progress in understanding heavy-ion stopping.” In: *Nuclear Instruments and Methods in Physics Research Section B: Beam Interactions with Materials and Atoms* 382 (2016), pp. 15–25. DOI: 10.1016/j.nimb.2015.12.041.

[Sig92] P. Sigmund. “Statistical theory of charged-particle stopping and straggling in the presence of charge exchange.” In: *Nuclear Instruments and Methods in Physics Research Section B: Beam Interactions with Materials and Atoms* 69.1 (1992), pp. 113–122. DOI: 10.1016/0168-583x(92)95746-e.

[Sig97] P. Sigmund. “Charge-dependent electronic stopping of swift nonrelativistic heavy ions.” In: *Physical Review A* 56.5 (1997), pp. 3781–3793. DOI: 10.1103/PhysRevA.56.3781.

[Sig17] P. Sigmund. “Six decades of atomic collisions in solids.” In: *Nuclear Instruments and Methods in Physics Research Section B: Beam Interactions with Materials and Atoms* 406 (2017), pp. 391–412. DOI: 10.1016/j.nimb.2016.12.004.

[SS01b] P. Sigmund and A. Schinner. “Effective charge and related/unrelated quantities in heavy-ion stopping.” In: *Nuclear Instruments and Methods in Physics Research Section B: Beam Interactions with Materials and Atoms* 174.4 (2001), pp. 535–540. DOI: 10.1016/s0168-583x(01)00317-2.

[SS02] P. Sigmund and A. Schinner. “Binary theory of electronic stopping.” In: *Nuclear Instruments and Methods in Physics Research Section B: Beam Interactions with Materials and Atoms* 195.1-2 (2002), pp. 64–90. DOI: 10.1016/s0168-583x(01)01162-4.

[SS03b] P. Sigmund and A. Schinner. “Anatomy of the Barkas effect.” In: *Nuclear Instruments and Methods in Physics Research Section B: Beam Interactions with Materials and Atoms* 212 (2003), pp. 110–117. DOI: 10.1016/s0168-583x(03)01485-x.

[SS20a] P. Sigmund and A. Schinner. “The Bloch correction, key to heavy-ion stopping.” In: *Journal of Applied Physics* 128.10 (2020). DOI: 10.1063/5.0015478.

[SS21] L. C. Simonsen and T. C. Slaba. “Improving astronaut cancer risk assessment from space radiation with an ensemble model framework.” In: *Life Sciences in Space Research* 31 (2021), pp. 14–28. DOI: 10.1016/j.lssr.2021.07.002.

[Sim83] J. A. Simpson. “Elemental and Isotopic Composition of the Galactic Cosmic Rays.” In: *Annual Review of Nuclear and Particle Science* 33 (1983), pp. 323–382. DOI: 10.1146/annurev.ns.33.120183.001543.

[Sim+16] R. Simpson, T. E. Cutler, C. R. Danly, et al. “Comparison of polystyrene scintillator fiber array and monolithic polystyrene for neutron imaging and radiography.” In: *Rev Sci Instrum* 87.11 (2016), p. 11D830. DOI: 10.1063/1.4962040.

[ST99] R. A. Simpson and G. L. Tyler. “Reanalysis of Clementine bistatic radar data from the lunar South Pole.” In: *Journal of Geophysical Research: Planets* 104.E2 (1999), pp. 3845–3862. DOI: 10.1029/1998je900038.

[Sin13] R. C. Singleterry. “Radiation engineering analysis of shielding materials to assess their ability to protect astronauts in deep space from energetic particle radiation.” In: *Acta Astronautica* 91 (2013), pp. 49–54. DOI: 10.1016/j.actaastro.2013.04.013.

[Sla+17] T. C. Slaba, A. A. Bahadori, B. D. Reddell, et al. “Optimal shielding thickness for galactic cosmic ray environments.” In: *Life Sci Space Res (Amst)* 12 (2017), pp. 1–15. DOI: 10.1016/j.lssr.2016.12.003.

[SBC11] T. C. Slaba, S. R. Blattnig, and M. S. Clowdsley. “Variation in lunar neutron dose estimates.” In: *Radiation Research* 176.6 (2011), pp. 827–41. DOI: 10.1667/rr2616.1.

[SS20b] T. C. Slaba and R. C. Singleterry. “Correct modeling results are needed to inform mission planning and shield design.” In: *Life Sci Space Res (Amst)* 25 (2020), pp. 143–147. DOI: 10.1016/j.lssr.2019.11.001.

[Smi+17] D. E. Smith, M. T. Zuber, G. A. Neumann, et al. “Summary of the results from the lunar orbiter laser altimeter after seven years in lunar orbit.” In: *Icarus* 283 (2017), pp. 70–91. DOI: 10.1016/j.icarus.2016.06.006.

[SCF81] C. J. Sofield, N. E. B. Cowern, and J. M. Freeman. “The role of charge-exchange in energy-loss straggling.” In: *Nuclear Instruments and Methods in Physics Research* 191.1-3 (1981), pp. 462–468. DOI: 10.1016/0029-554x(81)91046-6.

[Son+24] Z. Song, J. Wang, Y. Tong, et al. “Enhancement of alpha/beta ratio in NaI:Tl,6Li neutron-gamma scintillators by rare earth co-doping.” In: *Nuclear Instruments and Methods in Physics Research Section A: Accelerators, Spectrometers, Detectors and Associated Equipment* 1064 (2024). DOI: 10.1016/j.nima.2024.169451.

[SJE17] M. de Soria-Santacruz Pich, I. Jun, and R. Evans. “Empirical radiation belt models: Comparison with in situ data and implications for environment definition.” In: *Space Weather* 15.9 (2017), pp. 1165–1176. DOI: 10.1002/2017sw001612.

[Spe+10] H. E. Spence, A. W. Case, M. J. Golightly, et al. “CRaTER: The Cosmic Ray Telescope for the Effects of Radiation Experiment on the Lunar Reconnaissance Orbiter Mission.” In: *Space Science Reviews* 150 (2010), pp. 243–284. DOI: 10.1007/s11214-009-9584-8.

[Spe+13] H. E. Spence, M. J. Golightly, C. J. Joyce, et al. “Relative contributions of galactic cosmic rays and lunar proton “albedo” to dose and dose rates near the Moon.” In: *Space Weather* 11 (2013), pp. 643–650. DOI: 10.1002/2013SW000995.

[SR13] E. J. Speyerer and M. S. Robinson. “Persistently illuminated regions at the lunar poles: Ideal sites for future exploration.” In: *Icarus* 222.1 (2013), pp. 122–136. DOI: 10.1016/j.icarus.2012.10.010.

[Spi10] P. Spillantini. “Active shielding for long duration interplanetary manned missions.” In: *Advances in Space Research* 45 (2010), pp. 900–916. DOI: 10.1016/j.asr.2010.01.025.

[Sta97] N. J. S. Stacy. “Arecibo Radar Mapping of the Lunar Poles: A Search for Ice Deposits.” In: *Science* 276.5318 (1997), pp. 1527–1530. DOI: 10.1126/science.276.5318.1527.

[Ste52] R. M. Sternheimer. “The Density Effect for the Ionization Loss in Various Materials.” In: *Physical Review* 88.4 (1952), pp. 851–859. DOI: 10.1103/PhysRev.88.851.

[SBS84] R. M. Sternheimer, M. J. Berger, and S. M. Seltzer. “Density effect for the ionization loss of charged particles in various substances.” In: *Atomic Data and Nuclear Data Tables* 30.2 (1984), pp. 261–271. DOI: 10.1016/0092-640x(84)90002-0.

[SP71] R. M. Sternheimer and R. F. Peierls. “General Expression for the Density Effect for the Ionization Loss of Charged Particles.” In: *Physical Review B* 3.11 (1971), pp. 3681–3692. DOI: 10.1103/PhysRevB.3.3681.

[SSB82] R. M. Sternheimer, S. M. Seltzer, and M. J. Berger. “Density effect for the ionization loss of charged particles in various substances.” In: *Physical Review B* 26.11 (1982), pp. 6067–6076. DOI: 10.1103/PhysRevB.26.6067.

[SW85] F. H. Stillinger and T. A. Weber. “Computer simulation of local order in condensed phases of silicon.” In: *Physical Review B* 31.8 (1985), pp. 5262–5271. DOI: 10.1103/physrevb.31.5262.

[Sti09] M. Stipcevic. “Active quenching circuit for single-photon detection with Geiger mode avalanche photodiodes.” In: *Applied Optics* 48.9 (2009), pp. 1705–14. DOI: 10.1364/ao.48.001705.

[Sto+23] N. N. Stoffle, T. Campbell-Ricketts, A. Castro, et al. “HERA: A Timepix-based radiation detection system for Exploration-class space missions.” In: *Life Sciences in Space Research* 39 (2023), pp. 59–66. DOI: 10.1016/j.lssr.2023.03.004.

[SP18] N. Stoffle and L. Pinsky. “Identification of stopping ions in a silicon Timepix detector.” In: *Nuclear Instruments and Methods in Physics Research Section A: Accelerators, Spectrometers, Detectors and Associated Equipment* 880 (2018), pp. 35–39. DOI: 10.1016/j.nima.2017.10.068.

[Sto+15] N. Stoffle, L. Pinsky, M. Kroupa, et al. “Timepix-based radiation environment monitor measurements aboard the International Space Station.” In: *Nuclear Instruments and Methods in Physics Research Section A: Accelerators, Spectrometers, Detectors and Associated Equipment* 782 (2015), pp. 143–148. DOI: 10.1016/j.nima.2015.02.016.

[Sto+06] D. Stoffler, G. Ryder, B. A. Ivanov, et al. “Cratering history and lunar chronology.” In: *Reviews in Mineralogy and Geochemistry* 60.1 (2006), pp. 519–596. DOI: 10.2138/rmg.2006.60.05.

[Sto+19] E. C. Stone, A. C. Cummings, B. C. Heikkila, and N. Lal. “Cosmic ray measurements from Voyager 2 as it crossed into interstellar space.” In: *Nature Astronomy* 3.11 (2019), pp. 1013–1018. DOI: 10.1038/s41550-019-0928-3.

[SBD24] U. Straube, T. Berger, and M. Dieckmann. “The ESA Active Dosimeter (EAD) system onboard the International Space Station (ISS).” In: *Zeitschrift für Medizinische Physik* 34.1 (2024), pp. 111–139. DOI: 10.1016/j.zemedi.2023.03.001.

[Str+15] T. Straume, L. A. Braby, T. B. Borak, et al. “Compact Tissue-equivalent Proportional Counter for Deep Space Human Missions.” In: *Health Physics* 109.4 (2015), pp. 277–83. DOI: 10.1097/HP.0000000000000334.

[Str05] S. I. Striganov. “On the theory and simulation of multiple Coulomb scattering of heavy-charged particles.” In: *Radiat Prot Dosimetry* 116.1-4 Pt 2 (2005), pp. 293–6. DOI: 10.1093/rpd/nci107.

[SMP07] A. W. Strong, I. V. Moskalenko, and V. S. Ptuskin. “Cosmic-Ray Propagation and Interactions in the Galaxy.” In: *Annual Review of Nuclear and Particle Science* 57.1 (2007), pp. 285–327. DOI: 10.1146/annurev.nucl.57.090506.123011.

[Sul71] J. D. Sullivan. “Geometric factor and directional response of single and multi-element particle telescopes.” In: *Nuclear Instruments and Methods* 95.1 (1971), pp. 5–11. DOI: 10.1016/0029-554x(71)90033-4.

[Sum+20] S. Suman, P. Jaruga, M. Dizdaroglu, et al. “Heavy ion space radiation triggers ongoing DNA base damage by downregulating DNA repair pathways.” In: *Life Sciences in Space Research* 27 (2020), pp. 27–32. DOI: 10.1016/j.lssr.2020.07.001.

[SHG95] J. Sun, Q. Huang, and J. A. Gilbert. “Comparing cross talk in doped scintillating-fiber bundles.” In: *Appl Opt* 34.9 (1995), pp. 1536–9. DOI: 10.1364/AO.34.001536.

[Sun+09] J. M. Sunshine, T. L. Farnham, L. M. Feaga, et al. “Temporal and spatial variability of lunar hydration as observed by the Deep Impact spacecraft.” In: *Science* 326.5952 (2009), pp. 565–8. DOI: 10.1126/science.1179788.

[SM19] A. D. Supanitsky and G. Medina-Tanco. “Ultra high energy cosmic rays from super-heavy dark matter in the context of large exposure observatories.” In: *Journal of Cosmology and Astroparticle Physics* 2019.11 (2019), p. 036. DOI: 10.1088/1475-7516/2019/11/036.

[SS15b] V. V. Svetsov and V. V. Shuvalov. “Water delivery to the Moon by asteroidal and cometary impacts.” In: *Planetary and Space Science* 117 (2015), pp. 444–452. DOI: 10.1016/j.pss.2015.09.011.

[Swo+90] S. P. Swordy, D. Mueller, P. Meyer, et al. “Relative abundances of secondary and primary cosmic rays at high energies.” In: *The Astrophysical Journal* 349 (1990). DOI: 10.1086/168349.

[SSN22] Á. Szabó, J. Szöllósi, and P. Nagy. “Principles of Resonance Energy Transfer.” In: *Current Protocols* 2.12 (2022), e625. DOI: 10.1002/cpz1.625.

[Sza+24] J. R. Szalay, F. Allegrini, R. W. Ebert, et al. “Oxygen production from dissociation of Europa’s water-ice surface.” In: *Nature Astronomy* (2024). DOI: 10.1038/s41550-024-02206-x.

[TOF23] H. Tajima, A. Okumura, and K. Furuta. “Studies of propagation mechanism of optical crosstalk in silicon photomultipliers.” In: *Nuclear Instruments and Methods in Physics Research Section A: Accelerators, Spectrometers, Detectors and Associated Equipment* 1049 (2023). DOI: 10.1016/j.nima.2023.168029.

[TC98] Y. Takahashi and t. J. Collaboration. “Elemental abundance of high energy cosmic rays.” In: *Nuclear Physics B - Proceedings Supplements* 60.3 (1998), pp. 83–92. DOI: 10.1016/s0920-5632(97)00503-3.

[TK15] M. Takamoto and J. G. Kirk. “Rapid Cosmic-Ray Acceleration at Perpendicular Shocks in Supernova Remnants.” In: *The Astrophysical Journal* 809.1 (2015). DOI: 10.1088/0004-637x/809/1/29.

[Tal79] R. Talman. “On the statistics of particle identification using ionization.” In: *Nuclear Instruments and Methods* 159.1 (1979), pp. 189–211. DOI: 10.1016/0029-554x(79)90348-3.

[Tam+23] A. Tamburrino, G. Claps, G. M. Contessa, et al. “Thermal neutron detection by means of Timepix3.” In: *The European Physical Journal Plus* 138.11 (2023). DOI: 10.1140/epjp/s13360-023-04583-0.

[Tam+15] J. Tammen, R. Elftmann, S. R. Kulkarni, et al. “Quenching comparison of BGO and BSO for heavy ions.” In: *Nuclear Instruments and Methods in Physics Research Section B: Beam Interactions with Materials and Atoms* 360 (2015), pp. 129–138. DOI: 10.1016/j.nimb.2015.07.127.

[TRE22] Y. Tao, A. Rajapakse, and A. Erickson. “Advanced antireflection for back-illuminated silicon photomultipliers to detect faint light.” In: *Sci Rep* 12.1 (2022), p. 13906. DOI: 10.1038/s41598-022-18280-y.

[TG18] V. Tatischeff and S. Gabici. “Particle Acceleration by Supernova Shocks and Spallogenic Nucleosynthesis of Light Elements.” In: *Annual Review of Nuclear and Particle Science* 68.1 (2018), pp. 377–404. DOI: 10.1146/annurev-nucl-101917-021151.

[TH93] A. G. Taylor and J. P. Harmon. “Structure and dose rate effects on optical radiation hardness in scintillator polymers.” In: *Radiation Physics and Chemistry* 41.1-2 (1993), pp. 115–119. DOI: 10.1016/0969-806x(93)90047-x.

[Tay+51] C. J. Taylor, W. K. Jentschke, M. E. Remley, et al. “Response of Some Scintillation Crystals to Charged Particles.” In: *Physical Review* 84.5 (1951), pp. 1034–1043. DOI: 10.1103/PhysRev.84.1034.

[Ted+23] S. Tedesco, A. Di Salvo, A. Rivetti, and M. Bertaina. “A 64-channel waveform sampling ASIC for SiPM in space-born applications.” In: *Journal of Instrumentation* 18.02 (2023). DOI: 10.1088/1748-0221/18/02/c02022.

[Ter14] S. Ter-Antonyan. “Sharp knee phenomenon of primary cosmic ray energy spectrum.” In: *Physical Review D* 89.12 (2014). DOI: 10.1103/PhysRevD.89.123003.

[TA02] D. J. Thomas and A. V. Alevra. “Bonner sphere spectrometers—a critical review.” In: *Nuclear Instruments and Methods in Physics Research Section A: Accelerators, Spectrometers, Detectors and Associated Equipment* 476.1-2 (2002), pp. 12–20. DOI: 10.1016/s0168-9002(01)01379-1.

[TW72] G. R. Thomas and D. M. Willis. “Analytical derivation of the geometric factor of a particle detector having circular or rectangular geometry.” In: *Journal of Physics E: Scientific Instruments* 5.3 (1972), pp. 260–263. DOI: 10.1088/0022-3735/5/3/024.

[Tho+16] S. Thoudam, J. P. Rachen, A. van Vliet, et al. “Cosmic-ray energy spectrum and composition up to the ankle: the case for a second Galactic component.” In: *Astronomy & Astrophysics* 595 (2016). DOI: 10.1051/0004-6361/201628894.

[Til95] I. S. Tilinin. “Quasiclassical expression for inelastic energy losses in atomic particle collisions below the Bohr velocity.” In: *Phys Rev A* 51.4 (1995), pp. 3058–3065. DOI: 10.1103/physreva.51.3058.

[Tin13] S. Ting. “The Alpha Magnetic Spectrometer on the International Space Station.” In: *Nuclear Physics B - Proceedings Supplements* 243-244 (2013), pp. 12–24. DOI: 10.1016/j.nuclphysbps.2013.09.028.

[Tom+93] B. Tomé, A. Gomes, A. Henriques, et al. “Fibre irradiation under air, dry air, argon and nitrogen at low dose rates.” In: *Radiation Physics and Chemistry* 41.1-2 (1993), pp. 185–193. DOI: 10.1016/0969-806x(93)90055-y.

[TM19] S. Torii and P. S. Marrocchesi. “The CALorimetric Electron Telescope (CALET) on the International Space Station.” In: *Advances in Space Research* 64.12 (2019), pp. 2531–2537. DOI: 10.1016/j.asr.2019.04.013.

[Tri+18] P. Trigilio, P. Busca, R. Quaglia, et al. “A SiPM-Readout ASIC for SPECT Applications.” In: *IEEE Transactions on Radiation and Plasma Medical Sciences* 2.5 (2018), pp. 404–410. DOI: 10.1109/trpms.2018.2856201.

[TSJ93] P. C. Trimmer, J. B. Schlenoff, and K. F. Johnson. “Spatially resolved UV-VIS characterization of radiation-induced color centers in poly(styrene) and poly(vinyltoluene).” In: *Radiation Physics and Chemistry* 41.1-2 (1993), pp. 57–64. DOI: 10.1016/0969-806x(93)90042-s.

[Tro+06] S. Trovati, F. Ballarini, G. Battistoni, et al. “Human exposure to space radiation: role of primary and secondary particles.” In: *Radiat Prot Dosimetry* 122.1-4 (2006), pp. 362–6. DOI: 10.1093/rpd/ncl438.

[Tsa74] Y.-S. Tsai. “Pair production and bremsstrahlung of charged leptons.” In: *Reviews of Modern Physics* 46.4 (1974), pp. 815–851. DOI: 10.1103/RevModPhys.46.815.

[Tsa77] Y.-S. Tsai. “Erratum: Pair production and bremsstrahlung of charged leptons.” In: *Reviews of Modern Physics* 49.2 (1977), pp. 421–423. DOI: 10.1103/RevModPhys.49.421.

[Tsa+16] T. Tsang, T. Rao, S. Stoll, and C. Woody. “Neutron radiation damage and recovery studies of SiPMs.” In: *Journal of Instrumentation* 11.12 (2016), P12002–P12002. DOI: 10.1088/1748-0221/11/12/p12002.

[Tsa+18] Y. Tsarfati, S. Rosenne, H. Weissman, et al. “Crystallization of Organic Molecules: Nonclassical Mechanism Revealed by Direct Imaging.” In: *ACS Central Science* 4.8 (2018), pp. 1031–1036. DOI: 10.1021/acscentsci.8b00289.

[Tur+19] V. Turgeon, G. Kertzscher, L. Carroll, et al. “Characterization of scintillating fibers for use as positron detector in positron emission tomography.” In: *Physica Medica* 65 (2019), pp. 114–120. DOI: 10.1016/j.ejmp.2019.08.009.

[Tur+21] A. N. Turundaevskiy, O. A. Vasiliev, D. E. Karmanov, et al. “Main Results from the NUCLEON Experiment.” In: *Bulletin of the Russian Academy of Sciences: Physics* 85.4 (2021), pp. 353–356. DOI: 10.3103/s1062873821040377.

[VUM21] P. Väisänen, I. Usoskin, and K. Mursula. “Seven Decades of Neutron Monitors (1951–2019): Overview and Evaluation of Data Sources.” In: *Journal of Geophysical Research: Space Physics* 126.5 (2021). DOI: 10.1029/2020ja028941.

[VPA20] G. Valdes Santurio, M. Pinto, and C. E. Andersen. “Evaluation of the ionization quenching effect in an organic plastic scintillator using kV x-rays and a modified Birks model with explicit account of secondary electrons.” In: *Radiation Measurements* 131 (2020). DOI: 10.1016/j.radmeas.2019.106222.

[VF59] J. A. Van Allen and L. A. Frank. “Radiation Around the Earth to a Radial Distance of 107,400 km.” In: *Nature* 183 (1959), pp. 430–434. DOI: 10.1038/183430a0.

[VV22] F. Vanhavere and O. Van Hoey. “Advances in personal dosimetry towards real-time dosimetry.” In: *Radiation Measurements* 158 (2022). DOI: 10.1016/j.radmeas.2022.106862.

[Van+12] D. Vaniman, M. D. Dyar, R. Wiens, et al. “Ceramic ChemCam Calibration Targets on Mars Science Laboratory.” In: *Space Science Reviews* 170.1-4 (2012), pp. 229–255. DOI: 10.1007/s11214-012-9886-0.

[Vav57] P. V. Vavilov. “Ionization Losses of High-Energy Heavy Particles.” In: *Journal of Experimental and Theoretical Physics* 32.4 (1957), p. 749.

[VAS81] L. C. Vaz, J. M. Alexander, and G. R. Satchler. “Fusion barriers, empirical and theoretical: Evidence for dynamic deformation in subbarrier fusion.” In: *Physics Reports* 69.5 (1981), pp. 373–399. DOI: 10.1016/0370-1573(81)90094-6.

[Ver20] A. M. Veronig. “Can we predict solar flares?” In: *Science* 369.6503 (2020), pp. 504–505. DOI: 10.1126/science.abb6150.

[VIT17] V. Verzi, D. Ivanov, and Y. Tsunesada. “Measurement of energy spectrum of ultra-high energy cosmic rays.” In: *Progress of Theoretical and Experimental Physics* 2017.12 (2017). DOI: 10.1093/ptep/ptx082.

[Vla+19] L. Vlahos, A. Anastasiadis, A. Papaioannou, et al. “Sources of solar energetic particles.” In: *Philosophical Transactions of the Royal Society A Mathematical, Physical and Engineering Sciences* 377.2148 (2019), p. 20180095. DOI: 10.1098/rsta.2018.0095.

[Vol+66] R. Voltz, J. L. da Silva, G. Laustriat, and A. Coche. “Influence of the Nature of Ionizing Particles on the Specific Luminescence of Organic Scintillators.” In: *The Journal of Chemical Physics* 45.9 (1966), pp. 3306–3311. DOI: 10.1063/1.1728106.

[Voz+24] M. C. Vozenin, Y. Alaghband, O. G. G. Drayson, et al. “More May Not be Better: Enhanced Spacecraft Shielding May Exacerbate Cognitive Decrements by Increasing Pion Exposures during Deep Space Exploration.” In: *Radiation Research* 201.2 (2024), pp. 93–103. DOI: 10.1667/RADE-23-00241.1.S1.

[Wak82] N. I. Wakayama. “Fluorescence and phase transition of p-terphenyl crystal.” In: *Journal of Luminescence* 27.3 (1982), pp. 299–306. DOI: 10.1016/0022-2313(82)90008-4.

[Wal+93] J. S. Wallace, M. B. Sinclair, K. T. Gillen, and R. L. Clough. “Color center annealing in γ-irradiated polystyrene, under vacuum and air atmospheres.” In: *Radiation Physics and Chemistry* 41.1-2 (1993), pp. 85–100. DOI: 10.1016/0969-806x(93)90045-v.

[Wan+12] L. L. Wang, L. A. Perles, L. Archambault, et al. “Determination of the quenching correction factors for plastic scintillation detectors in therapeutic high-energy proton beams.” In: *Physics in Medicine & Biology* 57.23 (2012), pp. 7767–81. DOI: 10.1088/0031-9155/57/23/7767.

[Wan+17] Z.-M. Wang, Y.-H. Yu, Z.-Y. Sun, et al. “Temperature dependence of the plastic scintillator detector for DAMPE.” In: *Chinese Physics C* 41.1 (2017). DOI: 10.1088/1674-1137/41/1/016001.

[Was+15] S. A. Washburn, S. R. Blattnig, R. C. Singleterry, and S. C. Westover. “Active magnetic radiation shielding system analysis and key technologies.” In: *Life Sciences in Space Research* 4 (2015), pp. 22–34. DOI: 10.1016/j.lssr.2014.12.004.

[Wei+00] H. Weick, H. Geissel, C. Scheidenberger, et al. “Slowing down of relativistic few-electron heavy ions.” In: *Nuclear Instruments and Methods in Physics Research Section B: Beam Interactions with Materials and Atoms* 164-165 (2000), pp. 168–179. DOI: 10.1016/s0168-583x(99)01025-3.

[Wen+19] P. W. Wen, C. J. Lin, C. Li, et al. “Evaporation and fission of the primary fragments produced by multinucleon transfer reactions.” In: *Physical Review C* 99.3 (2019). DOI: 10.1103/PhysRevC.99.034606.

[Wer+21] C. M. Werneth, W. C. de Wet, L. W. Townsend, et al. “Relativistic Abrasion–Ablation De-excitation Fragmentation (RAADFRG) model.” In: *Nuclear Instruments and Methods in Physics Research Section B: Beam Interactions with Materials and Atoms* 502 (2021), pp. 118–135. DOI: 10.1016/j.nimb.2021.06.016.

[Wes+17] S. Westerdale, J. Xu, E. Shields, et al. “Quenching measurements and modeling of a boron-loaded organic liquid scintillator.” In: *Journal of Instrumentation* 12.08 (2017), P08002–P08002. DOI: 10.1088/1748-0221/12/08/p08002.

[Whi88] T. O. White. “Scintillating fibres.” In: *Nuclear Instruments and Methods in Physics Research Section A: Accelerators, Spectrometers, Detectors and Associated Equipment* 273.2-3 (1988), pp. 820–825. DOI: 10.1016/0168-9002(88)90102-7.

[Whi+17] K. Whitman, V. Bindi, C. Consolandi, et al. “Implications of improved measurements of the highest energy SEPs by AMS and PAMELA.” In: *Advances in Space Research* 60.4 (2017), pp. 768–780. DOI: 10.1016/j.asr.2017.02.042.

[Whi+22] K. Whitman, R. Egeland, I. G. Richardson, et al. “Review of solar energetic particle models.” In: *Advances in Space Research* (2022). DOI: 10.1016/j.asr.2022.08.006.

[Whi+18] C. Whittaker, C. A. G. Kalnins, D. Ottaway, et al. “Transmission loss measurements of plastic scintillating optical fibres.” In: *Optical Materials Express* 9.1 (2018). DOI: 10.1364/ome.9.000001.

[Wic+91] K. Wick, D. Paul, P. Schröder, et al. “Recovery and dose rate dependence of radiation damage in scintillators, wavelength shifters and light guides.” In: *Nuclear Instruments and Methods in Physics Research Section B: Beam Interactions with Materials and Atoms* 61.4 (1991), pp. 472–486. DOI: 10.1016/0168-583x(91)95325-8.

[WHL22] A. X. Wilcoski, P. O. Hayne, and M. E. Landis. “Polar Ice Accumulation from Volcanically Induced Transient Atmospheres on the Moon.” In: *The Planetary Science Journal* 3.5 (2022). DOI: 10.3847/PSJ/ac649c.

[WC09] H. Wilkens and t. A. L. Collaboration. “The ATLAS Liquid Argon calorimeter: An overview.” In: *Journal of Physics: Conference Series* 160 (2009). DOI: 10.1088/1742-6596/160/1/012043.

[Wil29] E. J. Williams. “The straggling of β-particles.” In: *Proceedings of the Royal Society of London. Series A, Containing Papers of a Mathematical and Physical Character* 125.798 (1929), pp. 420–445. DOI: 10.1098/rspa.1929.0177.

[Wil39] E. J. Williams. “Concerning the scattering of fast electrons and of cosmic-ray particles.” In: *Proceedings of the Royal Society of London. Series A. Mathematical and Physical Sciences* 169.939 (1939), pp. 531–572. DOI: 10.1098/rspa.1939.0015.

[Wil+19] J. P. Williams, B. T. Greenhagen, D. A. Paige, et al. “Seasonal Polar Temperatures on the Moon.” In: *Journal of Geophysical Research: Planets* 124.10 (2019), pp. 2505–2521. DOI: 10.1029/2019je006028.

[Wil+17] J. P. Williams, D. A. Paige, B. T. Greenhagen, and E. Sefton-Nash. “The global surface temperatures of the Moon as measured by the Diviner Lunar Radiometer Experiment.” In: *Icarus* 283 (2017), pp. 300–325. DOI: 10.1016/j.icarus.2016.08.012.

[Wil+95] M. Wilpert, B. Gebauer, T. Wilpert, et al. “Cold multinucleon transfer and formation of a dinuclear complex.” In: *Physical Review C* 51.2 (1995), pp. 680–694. DOI: 10.1103/physrevc.51.680.

[Wil+94] J. W. Wilson, J. L. Shinn, L. W. Townsend, et al. “NUCFRG2: a semiempirical nuclear fragmentation model.” In: *Nucl Instrum Methods Phys Res B* 94 (1994), pp. 95–102. DOI: 10.1016/0168-583x(94)95662-6.

[WMP88] W. E. Wilson, N. F. Metting, and H. G. Paretzke. “Microdosimetric Aspects of 0.3- to 20-MeV Proton Tracks: I. Crossers.” In: *Radiation Research* 115.3 (1988). DOI: 10.2307/3577289.

[Wim+20] R. F. Wimmer-Schweingruber, J. Yu, S. I. Böttcher, et al. “The Lunar Lander Neutron and Dosimetry (LND) Experiment on Chang’E 4.” In: *Space Science Reviews* 216.6 (2020). DOI: 10.1007/s11214-020-00725-3.

[Win77] K. B. Winterbon. “Electronic energy loss and charge-state fluctuations of swift ions.” In: *Nuclear Instruments and Methods* 144.2 (1977), pp. 311–315. DOI: 10.1016/0029-554x(77)90122-7.

[Win94] A. Winther. “Grazing reactions in collisions between heavy nuclei.” In: *Nuclear Physics A* 572.1 (1994), pp. 191–235. DOI: 10.1016/0375-9474(94)90430-8.

[WP48] E. E. Witmer and M. A. Pomerantz. “The effective path length through a vertical cosmic-ray telescope.” In: *Journal of the Franklin Institute* 246.4 (1948), pp. 293–309. DOI: 10.1016/0016-0032(48)90867-9.

[Won+20] W. S. Wong, J. Alozy, R. Ballabriga, et al. “Introducing Timepix2, a frame-based pixel detector readout ASIC measuring energy deposition and arrival time.” In: *Radiation Measurements* 131 (2020), p. 106230. DOI: 10.1016/j.radmeas.2019.106230.

[WB13] L. Wootton and S. Beddar. “Temperature dependence of BCF plastic scintillation detectors.” In: *Physics in Medicine & Biology* 58.9 (2013), pp. 2955–67. DOI: 10.1088/0031-9155/58/9/2955.

[Wor+22] R. L. Workman, V. D. Burkert, V. Crede, et al. “Review of Particle Physics.” In: *Progress of Theoretical and Experimental Physics* 2022.8 (2022). DOI: 10.1093/ptep/ptac097.

[Wri53] G. T. Wright. “Scintillation Response of Organic Phosphors.” In: *Physical Review* 91.5 (1953), pp. 1282–1283. DOI: 10.1103/PhysRev.91.1282.2.

[Wri55] G. T. Wright. “Scintillation Response of Anthracene Crystals to Short Range Electrons.” In: *Physical Review* 100.2 (1955), pp. 588–590. DOI: 10.1103/PhysRev.100.588.

[Wri+15] I. P. Wright, S. Sheridan, S. J. Barber, et al. “CHO-bearing organic compounds at the surface of 67P/Churyumov-Gerasimenko revealed by Ptolemy.” In: *Science* 349.6247 (2015), aab0673. DOI: 10.1126/science.aab0673.

[Yan+22] T. Yanagida, T. Kato, D. Nakauchi, and N. Kawaguchi. “Fundamental aspects, recent progress and future prospects of inorganic scintillators.” In: *Japanese Journal of Applied Physics* 62.1 (2022). DOI: 10.35848/1347-4065/ac9026.

[YWF15] T. Yanagida, K. Watanabe, and Y. Fujimoto. “Comparative study of neutron and gamma-ray pulse shape discrimination of anthracene, stilbene, and p-terphenyl.” In: *Nuclear Instruments and Methods in Physics Research Section A: Accelerators, Spectrometers, Detectors and Associated Equipment* 784 (2015), pp. 111–114. DOI: 10.1016/j.nima.2014.12.031.

[Yan+14] S. K. Yang, J. Lee, S. W. Kim, et al. “Precision measurement of the photon detection efficiency of silicon photomultipliers using two integrating spheres.” In: *Optics Express* 22.1 (2014), pp. 716–26. DOI: 10.1364/OE.22.000716.

[Yar22] S. Yardley. “The unknown origins of solar energetic particles.” In: *Astronomy & Geophysics* 63.3 (2022), pp. 3.28–3.31. DOI: 10.1093/astrogeo/atac038.

[YRB78] B. S. Yarlagadda, J. E. Robinson, and W. Brandt. “Effective-charge theory and the electronic stopping power of solids.” In: *Physical Review B* 17.9 (1978), pp. 3473–3483. DOI: 10.1103/PhysRevB.17.3473.

[Yoo+17] Y. S. Yoon, T. Anderson, A. Barrau, et al. “Proton and Helium Spectra from the CREAM-III Flight.” In: *The Astrophysical Journal* 839.1 (2017). DOI: 10.3847/1538-4357/aa68e4.

[Yos+10] S. Yoshida, T. Ebihara, T. Yano, et al. “Light output response of KamLAND liquid scintillator for protons and 12C nuclei.” In: *Nuclear Instruments and Methods in Physics Research Section A: Accelerators, Spectrometers, Detectors and Associated Equipment* 622.3 (2010), pp. 574–582. DOI: 10.1016/j.nima.2010.07.087.

[Yuk+06] E. G. Yukihara, G. O. Sawakuchi, S. Guduru, et al. “Application of the optically stimulated luminescence (OSL) technique in space dosimetry.” In: *Radiation Measurements* 41.9-10 (2006), pp. 1126–1135. DOI: 10.1016/j.radmeas.2006.05.027.

[Yuk+22] E. G. Yukihara, S. W. S. McKeever, C. E. Andersen, et al. “Luminescence dosimetry.” In: *Nature Reviews Methods Primers* 2.1 (2022). DOI: 10.1038/s43586-022-00102-0.

[Zad+18] M. G. Zadneprianetc, A. V. Boreyko, T. S. Bulanova, et al. “The Influence of Physical Characteristics of Accelerated Heavy Ions on the Formation and Repair of DNA Double-Strand Breaks.” In: *Physics of Particles and Nuclei Letters* 15.6 (2018), pp. 693–699. DOI: 10.1134/s1547477118060183.

[ZG08] V. Zagrebaev and W. Greiner. “Production of new heavy isotopes in low-energy multinucleon transfer reactions.” In: *Physical Review Letters* 101.12 (2008), p. 122701. DOI: 10.1103/PhysRevLett.101.122701.

[Zai+20] N. P. Zaitseva, A. N. Mabe, M. L. Carman, et al. “Plastic scintillators stable for operating in wide ranges of humidity and temperature variations.” In: *Nuclear Instruments and Methods in Physics Research Section A: Accelerators, Spectrometers, Detectors and Associated Equipment* 954 (2020). DOI: 10.1016/j.nima.2018.12.024.

[ZDB23] P. Zanon, M. Dunn, and G. Brooks. “Current Lunar dust mitigation techniques and future directions.” In: *Acta Astronautica* 213 (2023), pp. 627–644. DOI: 10.1016/j.actaastro.2023.09.031.

[ZK66] G. T. Zatsepin and V. A. Kuz’min. “Upper Limit of the Spectrum of Cosmic Rays.” In: *Journal of Experimental and Theoretical Physics Letters* 4 (1966), p. 78.

[Zei+23a] C. Zeitlin, A. J. Castro, K. B. Beard, et al. “Results from the Radiation Assessment Detector on the International Space Station: Part 1, the Charged Particle Detector.” In: *Life Sciences in Space Research* 39 (2023), pp. 67–75. DOI: 10.1016/j.lssr.2023.01.003.

[Zei+23b] C. Zeitlin, A. J. Castro, K. B. Beard, et al. “Results from the Radiation Assessment Detector on the International Space Station: Part 3, combined results from the CPD and FND.” In: *Life Sciences in Space Research* 39 (2023), pp. 86–94. DOI: 10.1016/j.lssr.2023.06.002.

[Zei+07] C. Zeitlin, A. Fukumura, S. B. Guetersloh, et al. "Fragmentation cross sections of ^{28}Si at beam energies from 290 A to 1200 A MeV." In: *Nuclear Physics A* 784.1-4 (2007), pp. 341–367. DOI: 10.1016/j.nuclphysa.2006.10.088.

[Zei+01] C. Zeitlin, A. Fukumura, L. Heilbronn, et al. "Fragmentation cross sections of 600 MeV/nucleon ^{20}Ne elemental targets." In: *Physical Review C* 64.2 (2001). DOI: 10.1103/PhysRevC.64.024902.

[Zei+08] C. Zeitlin, S. Guetersloh, L. Heilbronn, et al. "Fragmentation cross sections of medium-energy ^{35}Cl, ^{40}Ar, and ^{48}Ti beams on elemental targets." In: *Physical Review C* 77.3 (2008). DOI: 10.1103/PhysRevC.77.034605.

[ZL16] C. Zeitlin and C. La Tessa. "The Role of Nuclear Fragmentation in Particle Therapy and Space Radiation Protection." In: *Frontiers in Oncology* 6 (2016), pp. 1–13. DOI: 10.3389/fonc.2016.00065.

[Zha+19a] K. Zhang, X. Li, H. Zhao, et al. "Cosmic Ray Albedo Neutron Decay (CRAND) as a Source of Inner Belt Electrons: Energy Spectrum Study." In: *Geophysical Research Letters* 46.2 (2019), pp. 544–552. DOI: 10.1029/2018gl080887.

[Zha+20] S. Zhang, R. F. Wimmer-Schweingruber, J. Yu, et al. "First measurements of the radiation dose on the lunar surface." In: *Science Advances* 6.39 (2020), eaaz1334. DOI: 10.1126/sciadv.aaz1334.

[ZWX11] Y.-L. Zhang, X.-L. Wang, and Z.-Z. Xu. "Evaluation of particle acceptance for space particle telescope." In: *Chinese Physics C* 35.8 (2011), pp. 774–777. DOI: 10.1088/1674-1137/35/8/014.

[Zha+19b] H. Zhao, D. N. Baker, X. Li, et al. "The Effects of Geomagnetic Storms and Solar Wind Conditions on the Ultrarelativistic Electron Flux Enhancements." In: *Journal of Geophysical Research: Space Physics* 124.3 (2019), pp. 1948–1965. DOI: 10.1029/2018ja026257.

[Zie99] J. F. Ziegler. "Stopping of energetic light ions in elemental matter." In: *Journal of Applied Physics* 85.3 (1999), pp. 1249–1272. DOI: 10.1063/1.369844.

[ZZB10] J. F. Ziegler, M. D. Ziegler, and J. P. Biersack. "SRIM – The stopping and range of ions in matter (2010)." In: *Nuclear Instruments and Methods in Physics Research Section B: Beam Interactions with Materials and Atoms* 268.11-12 (2010), pp. 1818–1823. DOI: 10.1016/j.nimb.2010.02.091.

[Zin+20] A. N. Zinoviev, P. Y. Babenko, D. S. Meluzova, and A. P. Shergin. "Contribution of molecular orbital promotion to inelastic energy losses in ion-solid collisions." In: *Nuclear Instruments and Methods in Physics Research Section B: Beam Interactions with Materials and Atoms* 467 (2020), pp. 140–145. DOI: 10.1016/j.nimb.2019.12.002.

[Zor93] C. Zorn. "A pedestrian's guide to radiation damage in plastic scintillators." In: *Radiation Physics and Chemistry* 41.1-2 (1993), pp. 37–43. DOI: 10.1016/0969-806x(93)90040-2.

[Zou+21] Y. Zou, Y. Zhu, Y. Bai, et al. "Scientific objectives and payloads of Tianwen-1, China's first Mars exploration mission." In: *Advances in Space Research* 67.2 (2021), pp. 812–823. DOI: 10.1016/j.asr.2020.11.005.

[Zre+08] M. Zreda, D. Desilets, T. P. A. Ferré, and R. L. Scott. "Measuring soil moisture content non-invasively at intermediate spatial scale using cosmic-ray neutrons." In: *Geophysical Research Letters* 35.21 (2008). DOI: 10.1029/2008gl035655.

[Zuc60] A. Zucker. "Nuclear Interactions of Heavy Ions." In: *Annual Review of Nuclear Science* 10.1 (1960), pp. 27–62. DOI: 10.1146/annurev.ns.10.120160.000331.

Conference Proceedings

[ALC20] M. Adams, M. J. Losekamm, and M. Czupalla. “Development of the Thermal Control System for the RadMap Telescope Experiment on the International Space Station.” In: *50th International Conference on Environmental Systems*. Lisbon, Portugal, 2020.

[Amb+19] G. Ambrosi, P. Azzarello, B. Bergmann, et al. “The Penetrating particle ANalyzer (PAN) instrument for measurements of low energy cosmic rays.” In: *2019 IEEE Nuclear Science Symposium and Medical Imaging Conference (NSS/MIC)*. Manchester, UK, 2019, pp. 1–8. DOI: 10.1109/nss/mic42101.2019.9059946.

[Bar+24] A. Bartoloni, F. Baffioni, F. Bisello, et al. “Bridging the Gap: Exploring AMS , Astroparticle Experiments and Space Radiobiology.” In: *Proceedings of The European Physical Society Conference on High Energy Physics — PoS(EPS-HEP2023)*. Hamburg, Germany, 2024. DOI: 10.22323/1.449.0090.

[Ber+16b] F. Berghmans, A. G. Mignani, S. Gómez, et al. “MUSIC: An 8 channel readout ASIC for SiPM arrays.” In: *Optical Sensing and Detection IV*. 2016. DOI: 10.1117/12.2231095.

[Dec15] M. Deckenhoff. “Scintillating Fibre and Radiation Damage Studies for the LHCb Upgrade.” In: *Proceedings of Technology and Instrumentation in Particle Physics 2014 — PoS(TIPP2014)*. Amsterdam, Netherlands, 2015. DOI: 10.22323/1.213.0091.

[Ehl+21] B. L. Ehlmann, R. L. Klima, C. L. Bennett, et al. “Lunar Trailblazer: A Pioneering SmallSat for Lunar Water and Lunar Geology.” In: *52nd Lunar and Planetary Science Conference*. Lunar and Planetary Institute, 2021.

[Enn+20] K. Ennico-Smith, A. Colaprete, R. Elphic, et al. “The Volatiles Investigating Polar Exploration Rover Payload.” In: *51st Lunar and Planetary Science Conference*. The Woodlands, TX: Lunar and Planetary Institute, 2020.

[Fuq+20] H. Fuqua Haviland, P. Bertone, J. Caffrey, et al. “Neutron Measurements at the Lunar Surface (NMLS), an Eight Day Mission to Lacus Mortis on Astrobotic Mission One.” In: *51st Lunar and Planetary Science Conference*. The Woodlands, Texas: Lunar and Planetary Institute, 2020.

[Hea+21] D. Heather, E. Sefton-Nash, R. Fisackerly, et al. “The ESA PROSPECT Payload for LUNA 27: Development Status and Science Activities.” In: *Europlanet Science Congress 2021*. online, 2021. DOI: 10.5194/epsc2021-291.

[Iva+93] I. P. Ivanenko, V. Y. Shestoperov, L. O. Chikova, et al. “Energy Spectra of Cosmic Rays above 2 TeV as Measured by the ‘SOKOL’ Apparatus.” In: *Proceedings of the 23rd International Cosmic Ray Conference*. Alberta, Canada: World Scientific, 1993, p. 17.

[Iva16] D. Ivanov. “TA Spectrum Summary.” In: *Proceedings of the 34th International Cosmic Ray Conference — PoS(ICRC2015)*. The Hague, Netherlands, 2016. DOI: 10.22323/1.236.0349.

[Kle+18] J. Kleinhenz, J. Smith, T. Roush, et al. “Volatiles Loss from Water Bearing Regolith Simulant at Lunar Environments.” In: *16th Biennial International Conference on Engineering, Science, Construction, and Operations in Challenging Environments*. Cleveland, USA: ASCE, 2018. DOI: 10.1061/9780784481899.044.

[Leh04] J. Lehti. “Defining the Geometrical Factor of a Particle Detector Using Computer Simulation.” In: *55th International Astronautical Congress*. Vancouver, Canada: International Astronautical Federation, 2004.

[LEP22] M. J. Losekamm, L. Eckert, and T. Pöschl. “The Lunar Cosmic-Ray and Neutron Spectrometer: Phase-A Design and Technology Studies.” In: *IEEE Aerospace Conference*. Big Sky, MT: IEEE, 2022.

[Los+21] M. J. Losekamm, S. Paul, T. Pöschl, and H. J. Zachrau. “The RadMap Telescope on the International Space Station.” In: *2021 IEEE Aerospace Conference*. Big Sky, MT: IEEE, 2021. DOI: 10.1109/AERO50100.2021.9438435.

[Luc+20] P. G. Lucey, E. Costello, D. M. Hurley, et al. “Relative Magnitudes of Water Sources to the Lunar Poles.” In: *51st Lunar and Planetary Science Conference*. 2020.

[Man+09] A. B. Mann, I. Konorov, H. Angerer, et al. “The universal sampling ADC readout system of the COMPASS experiment.” In: *2009 IEEE Nuclear Science Symposium Conference Record (NSS/MIC)*. Orlando, FL, 2009, pp. 2225–2228. DOI: 10.1109/nssmic.2009.5402077.

[Mat+08] T. Matsubara, H. Tanaka, K. Nitta, and M. Kuze. “Radiation damage of MPPC by gamma-ray irradiation with Co 60.” In: *Proceedings of International Workshop on new Photon-Detectors*. 2008. DOI: 10.22323/1.051.0032.

[Mor+21a] J. A. Morales-Soto, J. C. Arteaga-Velázquez, A. U. Abeysekara, et al. “The all-particle cosmic ray energy spectrum measured with HAWC.” In: *Proceedings of the 37th International Cosmic Ray Conference — PoS(ICRC2021)*. Berlin, Germany, 2021. DOI: 10.22323/1.395.0330.

[Mor+21b] J. I. Mortimer, F. A. J. Abernethy, S. J. Barber, et al. “Experimentally-Derived Water Ice Sublimation Rates for Icy Regolith Samples in Support of ESA’s PROSPECT Package.” In: *NASA Exploration Science Forum & European Lunar Symposium*. virtual: Solar System Exploration Research Virtual Institute, 2021.

[Reg+17] D. Reggiani, K. Deiters, L. Desorgher, et al. “Characterization of the PiM1 Beam Line at the PSI-HIPA Facility.” In: *5th Beam Telescopes and Test Beams Workshop*. Barcelona, Spain, 2017. URL: https://indico.desy.de/event/16161/contributions/21635/attachments/14334/18215/talk_final.pdf.

[Ric+21] L. Richter, M. Deiml, M. Glier, et al. “Development of the VOILA LIBS instrument for volatiles scouting in polar regions of the Moon.” In: *International Conference on Space Optics–ICSO 2020*. Ed. by B. Cugny, Z. Sodnik, and N. Karafolas. Vol. 11852. SPIE, 2021, pp. 628–645. DOI: 10.1117/12.2599244.

[Rou+21] T. L. Roush, A. Colaprete, A. Cook, et al. “The Volatiles Investigating Polar Exploration Rover (VIPER) Near Infrared Volatile Spectrometer System (NIRVSS).” In: *52nd Lunar and Planetary Science Conference*. virtual: Lunar and Planetary Institute, 2021.

[Ruc93] R. C. Ruchti. “Performance of multiclad scintillating and waveguide optical fibers read out with visible light photon counters.” In: *Scintillating Fiber Technology and Applications*. SPIE, 1993, pp. 78–94. DOI: 10.1117/12.161933.

[Sch+21] L. Schweitzer, H. Jamal, H. Jones, et al. “Micro Rover Mission for Measuring Lunar Polar Ice.” In: *2021 IEEE Aerospace Conference (50100)*. 2021. DOI: 10.1109/aero50100.2021.9438261.

[Sef+18] E. Sefton-Nash, J. D. Carpenter, R. Fisackerly, and R. Trautner. “PROSPECT: ESA’s Package for Resource Observation and In-Situ Prospecting for Exploration, Commercial Exploitation and Transportation.” In: *49th Lunar and Planetary Science Conference 2018*. The Woodlands, TX: Lunar and Planetary Institute, 2018.

[SR22] A. Smolka and P. Reiss. “Multi-Element Lunar Exosphere Simulation to Improve the Prediction of Ballistic Migration of Water.” In: *Lunar Surface Science Workshop: Defining a Coordinated Lunar Resource Evaluation Campaign*. virtual: Lunar and Planetary Institute, 2022.

[Spe+11] E. J. Speyerer, M. S. Robinson, B. W. Denevi, and L. S. Team. “Lunar Reconnaissance Orbiter Camera global morphological map of the Moon.” In: *42nd Lunar and Planetary Science Conference*. Lunar and Planetary Institute, 2011.

[Sri+24] R. V. L. N. Sridhar, A. Goswami, K. A. Lohar, et al. “Close-Range In-Situ LIBS (Laser Induced Breakdown Spectroscope) Experiment Aboard the Chandrayaan-3 Pragyaan Rover: Operations and Initial Results.” In: *55th Lunar and Planetary Science Conference*. The Woodlands, TX: Lunar and Planetary Institute, 2024.

[Ste+19] T. A. Stein, A. Fredriksen, J.-E. Holter, et al. “Radiation Testing of the IDE3380 SiPM Readout ASIC.” In: *2019 19th European Conference on Radiation and Its Effects on Components and Systems (RADECS)*. Montpellier, France, 2019, pp. 1–7. DOI: 10.1109/radecs47380.2019.9745675.

[Suk+23] D. Sukhonos, G. Ambrosi, P. Azzarello, et al. “Penetrating particle ANalyzer (PAN).” In: *Proceedings of 38th International Cosmic Ray Conference — PoS(ICRC2023)*. Nagoya, Japan, 2023. DOI: 10.22323/1.444.0045.

[Sun18] V. Sundararajan. “Overview and Technical Architecture of India’s Chandrayaan-2 Mission to the Moon.” In: *AIAA Aerospace Sciences Meeting*. Kissimmee, FL: American Institute of Aeronautics and Astronautics, 2018. DOI: 10.2514/6.2018-2178.

[Wag+15] R. V. Wagner, E. J. Speyerer, M. S. Robinson, and L. Team. “New Mosaicked Data Products from the LROC Team.” In: *46th Lunar and Planeray Science Conference*. Lunar and Planetary Institute, 2015.

[Yua+19] Z. Yuan, K. Briggl, H. Chen, et al. “KLauS: A Low-power SiPM Readout ASIC for Highly Granular Calorimeters.” In: *2019 IEEE Nuclear Science Symposium and Medical Imaging Conference (NSS/MIC)*. Manchester, UK, 2019, pp. 1–4. DOI: 10.1109/nss/mic42101.2019.9059888.

Theses

[Aga18] M. Agarwal. “Particle Identification with Neural Networks for a Radiation Monitor.” BSc thesis. Technical University of Munich, 2018.

[Ang20] M. Anger. “Development of the Flight Computer for the RadMap Telescope.” MSc thesis. Technical University of Munich, 2020.

[Bec17] A. Becerra Esteban. “Design of the LED Driver for the Precision Optical CAlibration Module.” MSc thesis. Technical University of Munich, 2017.

[Bie19] L. Bierwirth. “Development of a Neural Network for Online Event Reconstruction for a Radiation Monitor.” MSc thesis. Technical University of Munich, 2019.

[Cse02] A. Csete. “Experimental Investigations of the Energy Loss of Slow Protons and Antiprotons in Matter.” MSc thesis. 2002.

[Eck20] L. Eckert. “Integration and Calibration of the RadMap Telescope Detector Modules.” BSc thesis. Technical University of Munich, 2020.

[Eck24] L. Eckert. “Improved Design of a Compact Scintillating-Fiber Detector for the AFIS Mission.” MSc thesis. Technical University of Munich, 2024.

[Eke16] R. J. Ekelhof. “Studies for the LHCb SciFi Tracker - Development of Modules from Scintillating Fibres and Tests of their Radiation Hardness.” CERN-THESIS-2016-098. PhD thesis. Technische Universität Dortmund, 2016.

[Hah14] A. Hahn. “Charakterisierung von Silizium Photomultipliern zur Auslese von szintillierenden Fasern.” BSc thesis. Technical University of Munich, 2014.

[Han18] M. Hanke. “Energy Reconstruction of Low-Energy Protons using Multi-Layer Perceptrons.” BSc thesis. Technical University of Munich, 2018.

[Hol19] L. Hollender. “A Bayesian Particle Filter for Particle Identification.” MSc thesis. Technical University of Munich, 2019.

[Hös20] M. Höschler. “Particle Identification for a Radiation Monitor based on Neural Networks.” MSc thesis. Technical University of Munich, 2020.

[Kho17] J. Kholdkov. “Development of Neural Networks for Online Track Reconstruction.” BSc thesis. Technical University of Munich, 2017.

[Kre20] S. Kressierer. “Construction of a Scintillator Fiber Detector for Space Applications.” BSc thesis. Technical University of Munich, 2020.

[Men14] L. Meng. “Development of a CubeSat Detector for Measuring the Low-Energy Antiproton Flux in Low Earth Orbit.” Diploma thesis. Technical University of Munich, 2014.

[Mey18] L. Meyer-Hetling. “Particle Tracking with Neural Networks.” BSc thesis. Technical University of Munich, 2018.

[Mey21] L. Meyer-Hetling. “A Neural-Network-Based Event Reconstruction for the RadMap Telescope.” MSc thesis. Technical University of Munich, 2021.

[Mil16] M. Milde. “Development of a Data-Analysis Framework for the Multi-purpose Active-target Particle Telescope.” MSc thesis. Technical University of Munich, 2016.

[Pös15] T. Pöschl. “Modeling and Prototyping of a Novel Active-Target Particle Detector for Balloon and Space Applications.” MSc thesis. Technical University of Munich, 2015.

[Pös22] T. Pöschl. “Modeling of the Galactic Cosmic-Ray Antiproton Flux and Development of a Multi-Purpose Active-Target Particle Telescope for Cosmic Rays.” PhD thesis. Technical University of Munich, 2022. URL: http://mediatum.ub.tum.de/node?id=1659625.

[Ulu21] B. Ulukutlu. “A search for new materials and the development of a readout system for particle detector applications.” MSc thesis. Technical University of Munich, 2021.

[Was21] P. Wastian. “Conception and Design of a Radiation Detector for LUVMI-X.” MSc thesis. Technical University of Munich, 2021.

[Yea13] G. R. Yearwood. “The Development of a High-Resolution Scintillating Fiber Tracker with Silicon Photomultiplier Readout.” PhD thesis. RWTH Aachen University, 2013.

Reports

[Bah+15] A. A. Bahadori, E. J. Semones, R. Gaza, et al. *Battery-operated Independent Radiation Detector Data Report from Exploration Flight Test 1*. NASA/TP-2015-218575. National Aeronautics and Space Administration, 2015.

[BK20] R. Baumann and K. Kruckmeyer. *Radiation Handbook for Electronics*. SGZY002A. Texas Instruments, 2020.

[Ber+17] M. J. Berger, J. S. Coursey, M. A. Zucker, and J. Chang. *ESTAR, PSTAR, and ASTAR: Computer Programs for Calculating Stopping-Power and Range Tables for Electrons, Protons, and Helium Ions (version 2.0.1)*. National Institute of Standards and Technology, 2017. DOI: 10.18434/T4NC7P. URL: http://physics.nist.gov/Star.

[BS64] M. J. Berger and S. M. Seltzer. *Tables of Energy Losses and Ranges of Electrons and Positrons*. NASA SP-3012. Washington, DC: National Aeronautics and Space Administration, 1964.

[Con22] Consultative Committee for Space Data Systems. *Space Packet Protocol*. CCSDS 133.0-B-2. 2022. URL: https://public.ccsds.org/Pubs/133x0b2e1.pdf.

[Cuc11] Cucinotta, F. A. and Kim, M. H. Y. and Chappel, L. J. *Space Radiation Cancer Risk Projections and Uncertainties – 2010*. NASA/TP-2011-216155. National Aeronautics and Space Administration, 2011.

[Cuc13] Cucinotta, F. A. and Kim, M. H. Y. and Chappel, L. J. *Space Radiation Cancer Risk Projections and Uncertainties – 2012*. NASA/TP-2013-217375. National Aeronautics and Space Administration, 2013.

[Dai22] W. Dai. *Output Voltage Ripple Measurement and Reduction for DC/DC Voltage Regulators*. #0032 Rev 1.0. Monolithic Power Systems, Inc., 2022.

[EBS00] L. D. Edmonds, C. E. Barnes, and L. Z. Scheick. *An Introduction to Space Radiation Effects on Microelectronics*. JPL Publication 00-06. National Aeronautics and Space Administration, 2000.

[Eng+73] R. A. English, R. E. Benson, J. V. Bailey, and C. M. Barnes. *Apollo Experience Report - Protection Against Radiation*. NASA TN D-7080. National Aeronautics and Space Administration, 1973.

[HS04] J. J. Hubbell and S. M. Seltzer. *Tables of X-Ray Mass Attenuation Coefficients and Mass Energy-Absorption Coefficients*. National Institute of Standards and Technology, 2004. DOI: 10.18434/T4D01F. URL: http://physics.nist.gov/xaamdi.

[ICRU37] International Commission on Radiation Units & Measurements. *Stopping Powers for Electrons and Positrons (ICRU Report 37)*. In: *Journal of the ICRU* os-19.2, 1984. DOI: 10.1093/jicru_os19.2.1.

[ICRU49] International Commission on Radiation Units & Measurements. *Stopping Powers and Ranges for Protons and Alpha Particles (ICRU Report 49)*. In: *Journal of the ICRU* os-25.2, 1993. DOI: 10.1093/jicru_os25.2.1.

[ICRU73] International Commission on Radiation Units & Measurements. *Stopping of Ions Heavier than Helium (ICRU Report 73)*. In: *Journal of the ICRU* 5.1, 2005. DOI: 10.1093/jicru/ndi001.

[ICRU85a] International Commission on Radiation Units & Measurements. *Fundamental Quantities and Units for Ionizing Radiation (ICRU Report 85a)*. In: *Journal of the ICRU* 11.1, 2011. DOI: 10.1093/jicru_ndr007.

[ICRU90] International Commission on Radiation Units & Measurements. *Key Data for Ionizing-Radiation Dosimetry: Measurement Standards and Applications (ICRU Report 90)*. In: *Journal of the ICRU* 14.1, 2016. DOI: 10.1093/jicru_ndw043.

[ICRP110] International Commission on Radiological Protection. *Adult Reference Computational Phantoms (ICRP Publication 110)*. In: *Annals of the ICRP* 39.2, 2009.

[ICRP123] International Commission on Radiological Protection. *Assessment of Radiation Exposure of Astronauts in Space (ICRP Publication 123)*. In: *Annals of the ICRP* 42.4, 2013.

[SSP30327] International Space Station Program. *Space Station Electromagnetic Emission and Susceptibility Requirements*. SSP 30327 Revision T. National Aeronautics and Space Administration, 2010.

[SSP50005] International Space Station Program. *International Space Station Flight Crew Integration Standard*. SSP 50005 Revision H. National Aeronautics and Space Administration, 2019.

[SSP51721] International Space Station Program. *ISS Safety Requirements Document*. SSP 51721. National Aeronautics and Space Administration, 2019.

[SSP57000] International Space Station Program. *ISS Pressurized Payloads Interface Requirements Document*. SSP 57000 Revision U. National Aeronautics and Space Administration, 2022.

[Kir87] J. Kirkby. *Today and tomorrow for scintillating fibre (SCIFI) detectors*. CERN-EP-87-60. European Organization for Nuclear Research, 1987. URL: https://cds.cern.ch/record/176472.

[Loc19] Lockheed Martin Corporation. *McCandless Lunar Lander User's Guide*. 2019. URL: https://www.lockheedmartin.com/en-us/products/mccandless-lunar-lander.html.

[Los+15] M. J. Losekamm, M. Gareis, D. Gaisbauer, et al. *Student Experiment Documentation: Antiproton Flux in Space - Prototype*. BX18_AFIS-P_SED_v5-0_6Feb16. Technical University of Munich, 2015.

[LPW21] M. J. Losekamm, T. Pöschl, and P. Wastian. *LCNS Detailed Design*. LUVMI-X Project Report D5.2. Technical University of Munich, 2021.

[STD3001] *NASA Spaceflight Human-System Standard - Volume 2: Human Factors, Habitability, and Environmental Health*. NASA-STD-3001, Volume 2, Revision D. National Aeronautics and Space Administration, 2023.

[SP6105] *NASA Systems Engineering Handbook*. SP-2016-6105 Rev2. National Aeronautics and Space Administration, 2016.

[Sin+10] R. C. Singleterry, S. R. Blattnig, M. A. Clowdsley, et al. *OLTARIS: On-Line Tool for the Assessment of Radiation in Space*. NASA/TP-2010-216722. National Aeronautics and Space Administration, 2010.

[ESA08] *Technology Readiness Levels Handbook for Space Applications*. TEC-SHS/5551/MG/ap. European Space Agency, 2008.

[CDS14] The CubeSat Program, Cal Poly SLO. *CubeSat Design Specification Rev. 14.1*. CP-CDS-R14.1. California Polytechnic State University, 2022.

[Won] J. Wong. *A Collection of Amp Applications*. Application Note AN-106. Analog Devices, Inc. URL: https://www.analog.com/media/en/technical-documentation/application-notes/28080533AN106.pdf (accessed on 2024-07-06).

Data Sheets and Online Sources

[AAT24] AAT Bioquest Inc. *Fluorescence Spectrum Viewer*. 2024. URL: https://www.aatbio.com/fluorescence-excitation-emission-spectrum-graph-viewer/ (accessed on 2024-05-09).

[Adv20] Advanced Energy Industries, Inc. *UltraVolt XS Series: Extra-Small High Voltage Biasing Supplies*. 2020. URL: https://www.advancedenergy.com/getmedia/90ae9e81-9107-475c-aba8-175282fd5578/en-hv-xs-series-data-sheet.pdf (accessed on 2024-07-13).

[Ana17] Analog Devices, Inc. *ADA4096-2/ADA4096-4: 30 V, Micropower, Overvoltage Protection, Rail-to-Rail Input/Output Amplifiers*. 2017. URL: https://www.analog.com/media/en/technical-documentation/data-sheets/ada4096-2_4096-4.pdf (accessed on 2024-07-07).

[Boy09] W. V. Boynton. *2009 Lunar Reconnaissance Orbiter Lunar Exploration Neutron Detector RDR Data V1.0*. 2009. DOI: 10.17189/1520636.

[Bro22] Broadcom. *AFBR-S4N44P014M NUV-MT Silicon Photomultiplier*. 2022. URL: https://docs.broadcom.com/doc/AFBR-S4N44P014M-NUV-MT-Silicon-Photomultiplier (accessed on 2024-07-06).

[Bro24] Brookhaven National Laboratory. *NSRL User Guide*. 2024. URL: https://www.bnl.gov/nsrl/userguide/ (accessed on 2024-05-26).

[CAC20] C&A Corporation. *LiCAF for Neutron Detection*. 2020. URL: https://www.c-and-a.jp/assets/img/products/401190521%20LiCAF%20Single%20Crystal.pdf (accessed on 2024-08-03).

[Elj20] Eljen Technology. *PSD Plastic Scintillator EJ-276D & EJ-276G*. 2020. URL: https://eljentechnology.com/images/products/data_sheets/EJ-276D.pdf (accessed on 2024-08-03).

[Elj23] Eljen Technology. *High Temperature Plastic Scintillator EJ-244, EJ-248, EJ-244M, EJ-248M*. 2023. URL: https://eljentechnology.com/images/products/data_sheets/EJ-244_EJ-248_EJ-244M_EJ-248M.pdf (accessed on 2024-05-27).

[Epo23] Epoxy Technology, Inc. *EPO-TEK 301 Technical Data Sheet*. 2023. URL: https://www.epotek.com/docs/en/Datasheet/301.pdf (accessed on 2024-05-14).

[FAS15] FAST ComTec GmbH. *MCA4 Series: Four channel Multichannel Analyzer with USB bus, MCS, RTC*. 2015. URL: https://www.fastcomtec.com/fwww/datashee/mcd/mca4.pdf (accessed on 2024-06-21).

[HAM16] HAMAMATSU PHOTONICS K.K. *S13360-2050VE/-3050VE/-6050VE: MPPCs in a chip size package miniaturized through the adoption of TSV structure*. 2016. URL: https://www.hamamatsu.com/content/dam/hamamatsu-photonics/sites/documents/99_SALES_LIBRARY/ssd/s13360-2050ve_etc_kapd1053e.pdf (accessed on 2024-08-04).

[HAM22] HAMAMATSU PHOTONICS K.K. *S13360 series: MPPCs for precision measurement*. 2022. URL: https://www.hamamatsu.com/content/dam/hamamatsu-photonics/sites/documents/99_SALES_LIBRARY/ssd/s13360_series_kapd1052e.pdf (accessed on 2024-07-06).

[HAM23a] HAMAMATSU PHOTONICS K.K. *S14536/S14537 series: Si detectors for high-energy physics*. 2023. URL: https://www.hamamatsu.com/content/dam/hamamatsu-photonics/sites/documents/99_SALES_LIBRARY/ssd/s14536_series_etc_kpin1090e.pdf (accessed on 2024-08-04).

[HAM23b] HAMAMATSU PHOTONICS K.K. *S3590 series: Large area Si PIN photodiodes*. 2023. URL: https://www.hamamatsu.com/content/dam/hamamatsu-photonics/sites/documents/99_SALES_LIBRARY/ssd/s3590-08_etc_kpin1052e.pdf (accessed on 2024-07-04).

[Int19] Integrated Detector Electronics AS. *IDE3380: 16 Channel Readout for SiPM/ MPPC/PMT*. 2019. URL: https://ideas.no/products/ide3380/ (accessed on 2024-07-06).

[Int20] Integrated Detector Electronics AS. *IDE3381: 16-Channel Readout IC for PMT/ SiPM*. 2020. URL: https://ideas.no/products/ide3381/ (accessed on 2024-07-06).

[KET14] KETEK GmbH. *PM3325-EB / PM3350-EB SiPM Product Data Sheet*. 2014. URL: https://www.ketek.net/wp-content/uploads/2017/01/KETEK-PM3325-EB-PM3350-EB-Datasheet.pdf (accessed on 2024-06-08).

[KET17] KETEK GmbH. *PM3325-WB-B0 SiPM Product Data Sheet*. 2017. URL: https://www.ketek.net/wp-content/uploads/2017/09/KETEK-PM3325-WB-B0-Datasheet.pdf (accessed on 2024-05-24).

[KET18] KETEK GmbH. *PM3325-WB-D0 SiPM Product Data Sheet*. 2018. URL: https://www.ketek.net/wp-content/uploads/2018/12/KETEK-PM3325-WB-D0-Datasheet.pdf (accessed on 2024-05-14).

[Key20] Keysight Technologies. *B2980A Series Femto/Picoammeter and Electrometer/High Resistance Meter*. 2020. URL: https://www.keysight.com/de/de/assets/7018-04484/data-sheets-archived/5991-4878.pdf (accessed on 2024-06-21).

[Key23] Keysight Technologies. *33500B and 33600A Series Trueform Waveform Generators (20, 30, 80, 120 MHz)*. 2023. URL: https://www.keysight.com/de/de/assets/7018-05928/data-sheets/5992-2572.pdf (accessed on 2024-06-25).

[Kur14] Kuraray Trading Co., Ltd. *Plastic Scintillating Fibers*. 2014. URL: http://kuraraypsf.jp/pdf/all.pdf (accessed on 2024-05-14).

[Lux18a] Luxium Solutions. *BC-440, BC-440M, BC-448, BC-448M Premium Plastic Scintillators*. 2018. URL: https://www.luxiumsolutions.com/files/1681/download (accessed on 2024-08-03).

[Lux18b] Luxium Solutions. *CLLB: $Cs_2 Li La Br_6$ (Ce) Scintillation Material*. 2018. URL: https://www.luxiumsolutions.com/files/976/download (accessed on 2024-08-03).

[Lux18c] Luxium Solutions. *CsI(Tl), CsI(Na) Cesium Iodide Scintillation Material*. 2018. URL: https://www.luxiumsolutions.com/files/886/download (accessed on 2024-08-03).

[Lux20a] Luxium Solutions. *BC-702 Thermal Neutron Detector*. 2020. URL: https://www.luxiumsolutions.com/files/2021/download (accessed on 2024-08-03).

[Lux20b] Luxium Solutions. *BC-720 Fast Neutron Detector*. 2020. URL: https://www.luxiumsolutions.com/files/2026/download (accessed on 2024-08-03).

[Lux23a] Luxium Solutions. *Lanthanum Bromide and Enhanced Lanthanum Bromide*. 2023. URL: https://www.luxiumsolutions.com/files/1496/download (accessed on 2024-08-03).

[Lux23b] Luxium Solutions. *NaI(Tl) and Polyscin®NaI(Tl) Sodium Iodide Scintillation Material*. 2023. URL: https://www.luxiumsolutions.com/files/481/download (accessed on 2024-08-03).

[Lux23c] Luxium Solutions. *NaI(Tl+Li) Neutron-Gamma Scintillator*. 2023. URL: https://www.luxiumsolutions.com/files/601/download (accessed on 2024-08-03).

[Lux23d] Luxium Solutions. *Organic Scintillation Materials and Assemblies*. 2023. URL: https://www.luxiumsolutions.com/files/3120/download (accessed on 2024-08-03).

[Lux23e] Luxium Solutions. *Plastic Scintillating and Wavelength-Shifting Fibers*. 2023. URL: https://www.luxiumsolutions.com/files/2501/download (accessed on 2024-05-24).

[Mic09] Microchip Technology, Inc. *MCP3422/3/4: 18-Bit, Multi-Channel $\Delta\Sigma$ Analog-to-Digital Converter with I^2C Interface and On-Board Reference*. 2009. URL: https://ww1.microchip.com/downloads/aemDocuments/documents/OTH/ProductDocuments/DataSheets/22088c.pdf (accessed on 2024-07-05).

[Mic21] Microchip Technology, Inc. *MCP970X: Low-Power Linear Active Thermistor ICs*. 2021. URL: https://ww1.microchip.com/downloads/aemDocuments/documents/MSLD/ProductDocuments/DataSheets/MCP970X-Family-Data-Sheet-DS20001942.pdf (accessed on 2024-06-20).

[Mic23] Microchip Technology, Inc. *SAM C20/C21 Family: 32-bit Arm Cortex-M0+ with 5V Support, CAN-FD, PTC, and Advanced Analog*. 2023. URL: https://ww1.microchip.com/downloads/aemDocuments/documents/MCU32/ProductDocuments/DataSheets/SAM-C20-C21-Family-Data-Sheet-DS60001479.pdf (accessed on 2024-07-13).

[New+23] M. Newville, R. Otten, A. Nelson, et al. *lmfit/lmfit-py: 1.2.1*. Version 1.2.1. 2023. DOI: 10.5281/zenodo.7887568.

[NVI21] NVIDIA Corporation. *Jetson TX2 Series Module Data Sheet*. 2021. URL: http://developer.nvidia.com/embedded/dlc/jetson-tx2-series-modules-data-sheet (accessed on 2024-07-13).

[ons21] onsemi. *J-Series SiPM Sensors*. 2021. URL: https://www.onsemi.com/download/data-sheet/pdf/microj-series-d.pdf (accessed on 2024-07-06).

[PET22] PETsys Electronics Medical PET Detectors, S. A. *TOFPET2 ASIC*. 2022. URL: https://www.petsyselectronics.com/web/website/docs/products/product1/Flyer_ASIC2_V19.pdf (accessed on 2024-07-06).

[Sai11] Saint-Gobain Crystals. *Scintillation Products: Scintillating Optical Fibers*. 2011. URL: https://ethz.ch/content/dam/ethz/special-interest/phys/particle-physics/precisionphysicsatlowenergy-dam/TeachingContent/ASL/bicronfiber.pdf (accessed on 2024-05-27).

[Sci20] Scintacor. *Lithium glass scintillators for neutron detection*. 2020. URL: https://scintacor.com/wp-content/uploads/2015/09/GlassScintillators.pdf (accessed on 2024-08-03).

[SIL24] SILSO World Data Center. *The International Sunspot Number*. Royal Observatory of Belgium, avenue Circulaire 3, 1180 Brussels, Belgium, 1950-2024. URL: http://www.sidc.be/silso/.

[Sur22] SurTec International GmbH. *Technical Data Sheet SurTec 650*. 2022. URL: https://www.surtec.com/ecomaXL/files/650E.pdf (accessed on 2024-07-13).

[Syn14] SynQor. *MCOTS-C-28-12-SM: Military COTS DC-DC Converter*. 2014. (Accessed on 2024-07-13).

[Tex12] Texas Instruments. *CDCVF2310-EP: 2.5-V to 3.3-V High-Performance Clock Buffer*. 2012. URL: https://www.ti.com/lit/ds/symlink/cdcvf2310-ep.pdf (accessed on 2024-07-07).

[Tex13] Texas Instruments. *LM134/LM234/LM334 3-Terminal Adjustable Current Sources*. 2013. URL: https://www.ti.com/lit/ds/symlink/lm134.pdf?ts=1720205878919 (accessed on 2024-07-05).

[Tex16a] Texas Instruments. *ADS7828-Q1 12-Bit 8-Channel Sampling Analog-to-Digital Converter With I2C Interface*. 2016. URL: https://www.ti.com/lit/ds/symlink/ads7828-q1.pdf (accessed on 2024-07-07).

[Tex16b] Texas Instruments. *LM4132, LM4132-Q1 SOT-23 Precision Low Dropout Voltage Reference*. 2016. URL: https://www.ti.com/lit/ds/symlink/lm4132-q1.pdf?ts=1720281432611 (accessed on 2024-07-07).

[Tex19] Texas Instruments. *TMP392: TMP392 Ultra-Small, Dual-Channel (Hot and Warm Trip), 0.5-μA, Resistor-Programmable Temperature Switch*. 2019. URL: https://www.ti.com/lit/ds/symlink/tmp392.pdf (accessed on 2024-07-13).

[Tex20] Texas Instruments. *TLV733P-Q1: Capacitor-Free, 300-mA, Low Dropout (LDO) Linear Regulator*. 2020. URL: https://www.ti.com/lit/ds/symlink/tlv733p-q1.pdf (accessed on 2024-07-07).

[Tex21] Texas Instruments. *LM3880-Q1 Three-Rail Simple Power Supply Sequencer*. 2021. URL: https://www.ti.com/lit/ds/symlink/lm3880-q1.pdf (accessed on 2024-07-07).

[Tho20] Thorlabs, Inc. *CS20K2 – UV Curing LED System, 365 nm*. 2020. URL: https://www.thorlabs.de/thorproduct.cfm?partnumber=CS20K2 (accessed on 2024-06-24).

[Var22] Varadis. *VT02 400nm RADFET*. 2022. URL: https://www.varadis.com/wp-content/uploads/2023/09/VT02-400nm-Datasheet-rev2.2-19-April-2022.pdf (accessed on 2024-07-04).

[Vic14] Vicor. *Quiet Power MQPI-18: 28 Volt input, 7 Amp M-Grade EMI Filter Module*. 2014. URL: https://www.vicorpower.com/documents/datasheets/ds_mqpi-18.pdf (accessed on 2024-07-13).

[wee18a] weeroc. *Petiroc 2A: SiPM read-out for time-of-flight PET*. 2018. URL: https://www.weeroc.com/my-weeroc/download-center/petiroc-2a/17-petiroc2a-datasheet-v2-5a/file (accessed on 2024-07-06).

[wee18b] weeroc. *Triroc 1A: All-in-one SiPM read-out for multimodal PET inserts*. 2018. URL: https://www.weeroc.com/my-weeroc/download-center/triroc-1a/11-triroc1a-datasheet-1-2/file (accessed on 2024-07-06).

[wee19] weeroc. *Citirox 1A; Scientific instrumentation SiPM read-out chip*. 2019. URL: https://www.weeroc.com/my-weeroc/download-center/citiroc-1a/89-citiroc1a-datasheet-v2-53/file (accessed on 2024-07-06).

[Xil20] Xilinx, Inc. *7 Series FPGAs Data Sheet: Overview*. 2020. URL: https://docs.amd.com/v/u/en-US/ds180_7Series_Overview (accessed on 2024-07-08).

[Xil24] Xillbus Ltd. *An FPGA IP core for easy DMA over PCIe with Windows and Linux*. 2024. URL: https://xillybus.com (accessed on 2024-07-16).

List of Figures

List of Tables